COMPUMAG 2003

Conference on the Computation of Magnetic Fields

Saratoga Springs, New York
July 13–17, 2003

Volume IV

COMPUMAG

14th Conference on the Computation of Magnetic Fields

July 13-17, 2003
Saratoga Springs, New York USA

Record of the 14th COMPUMAG Conference
on the Computation of Magnetic Fields

Volume IV: Thursday, July 17

COMPUMAG 2003

14th Conference on the Computation of Magnetic Fields
Saratoga Springs, New York, USA
July 13-17, 2003

Compumag 2003 Committee:

Prof. Sheppard J. Salon, Chairman

Rensselaer Polytechnic Institute, Troy, NY USA

Philippe Wendling, Vice Chairman

Magsoft Corporation, Troy, NY USA

David Burow, Secretariat

Genfo, Inc., Troy, NY USA

Local Organizing Committee:

M. DeBortoli   K. Sivasubramaniam

M. Lean   M. Shah

I. Mayergoyz   S. Babic

U. Deshpande

Editorial Board Chairmen:

J. Webb, McGill University, Montreal, Quebec Canada

D. Giannacopoulos, McGill University, Montreal, Quebec Canada

Email: edboard.compumag2003@mcgill.ca

Correspondence:

Compumag 2003

1223 Peoples Ave

Troy, NY 12180 USA

Email : secretariat@compumag2003.com

Lodging Arrangements Made By:

Sherie Klein, Carlson Wagonlit/Albany Travel

30 Corporate Drive, Clifton Park, NY 12065 USA

Phone: +1 (518) 292-9000

Email: corporate@albanytravel.com

COMPUMAG 2003 Chairman's Welcome

Welcome to COMPUMAG 2003, the 14th Conference on the Computation of Electric and Magnetic Fields!

In the 27 years since the first COMPUMAG Conference in 1976 at Oxford, we have seen the society and the conference continue to grow in numbers, in significance and in international renown and respect. We are honored, therefore, to carry on what has become a well-established tradition of presenting the leading research and thought in the area of computational electromagnetics.

Because of its high standards and rigorous review process, the Conference has become the place to present in our field. This year 429 papers were approved for presentation in 8 oral sessions and 32 poster sessions. The contributors represent 30 different countries. Our deep thanks go to the editorial board and to the co-chairs Jon Webb and Dennis Giannacopoulos, who did an outstanding job.

And welcome to Saratoga Springs, New York! Those of us fortunate to live and work in New York's Capital District can take advantage of some of the best opportunities in the United States for research and education; cultural, historical and recreational resources; and small cities and towns where neighbors still don't lock their doors. Nearby research institutions and universities include Rensselaer, GE Global Research Laboratories, Knolls Atomic Power Laboratory, IBM Research Laboratory and others. New York City, Boston, and Montreal, with their rich historical and cultural resources, are all within a few hours' drive. Finally, there is the peace and friendliness of smaller towns and villages, like Saratoga Springs, where you are sure to enjoy the activities we have planned; we hope you will also take time to explore on your own.

COMPUMAG 2003 offers lively scientific exchange to charm the intellect and convivial activities to warm the heart. Welcome!

Prof. Sheppard J. Salon
COMPUMAG 2003 Chairman

City of Saratoga Springs

Kenneth Klotz, Mayor
Hank Kuczynski, Deputy Mayor

July, 2003

Welcome!

On behalf of the entire City of Saratoga Springs, I would like to welcome the *14th Conference on the Computation of Electromagnetic Fields* to Saratoga Springs!

As you know, Saratoga Springs is a world-class resort destination, which offers cosmopolitan amenities without the drawbacks of a typical metropolitan area. Our city takes great pride in its hospitality to visitors. We offer world-class attractions, wonderful restaurants, unique shops and a host of related activities that your attendees are sure to enjoy!

Saratoga Springs looks forward to hosting the *14th Conference on the Computation of Electromagnetic Fields and its attendees.*

Once again, Welcome to our City, where we invite you to......*Experience Saratoga!*

Sincerely,

Kenneth Klotz
Mayor

COMPUMAG 2003 Editorial Board
Chairmen: J. Webb, D. Giannacopoulos

COMPUMAG 2003 Program at a Glance

Time	July 13 Sunday	July 14 Monday	July 15 Tuesday	July 16 Wednesday	July 17 Thursday
7:00		Continental Breakfast Buffet	Continental Breakfast Buffet	Continental Breakfast Buffet	Continental Breakfast Buffet
8:00		Formulations Saratoga Ballroom	Devices Saratoga Ballroom	Quasistatic Saratoga Ballroom	Inverse Problems Saratoga Ballroom
10:15		Coffee Break	Coffee Break	Coffee Break	Coffee Break
10:45		Numerical Techniques I / Coupled Problems I / Devices I / Statics I	Numerical Techniques II / Coupled Problems II / Machines II / Statics II	Numerical Techniques III / Coupled Problems III / Devices III / Software	Numerical Techniques IV / Coupled Problems IV / Machines IV / Devices IV
12:00		Lunch: Grand Ballroom – High Rock	Lunch: Grand Ballroom – High Rock	Lunch: Grand Ballroom – High Rock	Lunch: Grand Ballroom – High Rock
1:30		Optimization I / Waves I / Machines I / Quasistatic I	Optimization II / Waves II / Devices II / Quasistatic II	Optimization III / EMC / Machines IIII / Materials I	Optimization IV / Materials II / Education – TEAM / Quasistatic III
2:45		Afternoon Break	Afternoon Break	Afternoon Break	Afternoon Break
3:15	Registration❋ 2:00 – 6:00 p.m.	Methodologies Saratoga Ballroom	Materials Saratoga Ballroom	Waves Saratoga Ballroom	Optimization Saratoga Ballroom
5:30		Enjoy Saratoga!	5:00 Short Break (no refreshments) — 5:15 Panel Session: Topic To Be Announced Saratoga Ballroom		Have a safe and pleasant journey home!
6:30	Evening Reception Saratoga Ballroom		6:15 Enjoy Saratoga!	Banquet at the Canfield Casino	

❋ Registration will also be available each day from 7:00 AM to 12:00 noon and from 1:30 to 2:45 PM.

COMPUMAG 2003 Technical Program

Thursday, July 17, 2003

	8:00 − 10:15
Oral Session	
	Inverse Problems Saratoga Ballroom
	10:45 − 12:00
Poster Session	
	Numerical Techniques IV: Solution of Matrix Equations and Error Estimation
	Coupled Problems IV: MHD and Flow
	Machines IV: Special Topics
	Devices IV
	1:30 − 2:45
Poster Session	
	Optimization IV
	Materials II
	Education – TEAM
	Quasistatic III: Eddy Currents: Applications
	3:15 − 5:30
Oral Session	
	Optimization Saratoga Ballroom

Inverse Problems	Chairman
Thursday, July 17, 8:00am - 10:15am	Dr. Song-yop Hahn

Inverse Electromagnetic Problems by Field Visualization

IV - 2

Iliana Marinova, Hisashi Endo, Seiji Hayano, Yoshifuru Saito

P76823

Technical University of Sofia
Sofia - Bulgaria

A new method for choosing the regularization parameter in time dependent inverse problems

IV - 4

Jörg Schreiber, Jens Haueisen, Jukka Nenonen

P34018

University Jena - Biomagnetic Center
Jena - Germany

Multiresolutive Reconstruction of Magnetoencephalography Source Distribution

IV - 6

Chang-Hwan Im, Hyun-Kyo Jung, Hyuk-Chan Kwon, Yong-Ho Lee

P13702

Seoul National University - School of Electrical Engineering and Computer Science
Seoul - Korea

Identification of Multiple Cracks from Eddy Current Testing Signal with Noise Source by Image Processing and Inverse Analysis

IV - 8

Yoshiaki Nagaya, Toshiyuki Takagi, Tetsuya Uchimoto, Haoyu Huang

P52282

Tohoku University - Institute of Fluid Science
Sendai - Japan

A Condition-Number Based Regularization Parameter Estimate for Reconstruction Problems

IV - 10

Bernhard Brandstätter, Gert Holler, Daniel Watzenig

P54635

Graz University of Technology - Inst. of Electrical Measurement and Measurement Signal Processing
Graz - Austria

Topology-Based Inequalities and Inverse Problems for Near Force-Free Magnetic Fields

IV - 12

P. Robert Kotiuga

P35546

Boston University - Department of Electrical and Computer Engineering
Boston, MA - USA

Numerical Techniques IV: Solution of matrix equations and error estimation	Chairmen
Thursday, July 17, 10:45am - 12:00pm	Dr. Charles T. Choi Dr. Xavier Marechal

An efficient preconditioner for linear systems issued from the Finite Element Method for scattering problems

IV - 14

Ronan Perrussel, Laurent Nicolas, François Musy

P61962

Ecole Centrale de Lyon - CEGELY
Ecully - France

Investigation of Parallel Multigrid Method Using Java Language **IV - 34**
Kota Watanabe, Hajime Igarashi, Toshihisa Honma P25607
HOKKAIDO University - Graduate School of Engineering
Sapporo - Japan

Solution of a Magnetostatic Problem Using an Inexact Newton Method **IV - 36**
Carlo A. Borghi, Mario R. Carraro, Andrea Cristofolini P55776
University of Bologna - Dipartimento di Ingegneria Elettrica
Bologna - Italy

An Experimental Study of Equivalence Phenomena for Field Discontinuity and Optimal Discretizations in Finite Element Adaption **IV - 38**
Dennis Giannacopoulos P76807
McGill University - Electrical & Computer Engineering Dept.
Montreal - Canada

Coupled Problems IV: MHD and Flow Chairman
Thursday, July 17, 10:45am - 12:00pm Dr. Kent Davey

Multi-Grid Method for Eigenvalue Problem Associated with Newcomb Equation **IV - 40**
Takashi Kanki P21114
Japan Coast Guard Academy
Kure - Japan

Electromagnetic Analysis of the 3D Effects of the Metallic Structures in JET Tokamak **IV - 42**
R. Albanese, Guglielmo Rubinacci, Fabio Villone P31884
Ass. EURATOM/ENEA/CREATE, DAEIMI - Universita' di Cassino
Cassino - Italy

Equilibrium shape of a liquid metal subject to electromagnetic forces **IV - 44**
R. Moretti, S. Dufour, G. Vinsard, B. Laporte P11290
GREEN INPL
Vandoeuvre-les-Nancy - France

Investigation on Couple Electric Field and Flow Field in High Voltage SF6 Circuit Breaker **IV - 46**
Xiaoming Liu, Erzhi Wang, Yundong Cao P62785
Shenyang University of Technology - Department of Electrical Engineering
Shenyang - China

A Finite Element Analysis of Surface Wave Plasmas **IV - 48**
Hajime Igarashi, K. Watanabe, T. Ito, T. Fukuda, Toshihisa Honma P94342
Hokkaido University - Graduate School of Eng., System & Information Eng.
Sapporo - Japan

3-D MHD Calculation that has considered the Alternating electromagnetic force

Shouji Satoh, Keisuke Fujisaki, Tatsuya Furukawa
Ohita Setubi Sekkei Corp.
Ohita - Japan

IV - 50

P35126

Influence of Model Parameters on 3D Turbulent Flow in an Electromagnetic Stirring System for Continuous Billet Casting

J.D. Lavers, G. Tallbäck, A. Erraki, L. Beitelman
University of Toronto - ECE Department
Toronto, ON - CANADA

IV - 52

P45536

Numerical Solution of the Non Linear Electrodynamics in MHD Regimes with Magnetic Reynolds Number near One

Carlo A. Borghi, Mario R. Carraro, Andrea Cristofolini
University of Bologna - Dipartimento di Ingegneria Elettrica
Bologna - Italy

IV - 54

P35377

Machines IV: Special Topics	Chairmen
Thursday, July 17, 10:45am - 12:00pm	Dr. Dave Lowther
	Dr. CC Hwang

Investigation of Benchmark Model for Estimating Iron Loss in Rotating Machine

Hideo Domeki, Yoshiyuki Ishihara, Chikara Kaido, Yoshihiro Kawase, Shingo Kitamura, Tohru Shimomura, Norio Takahashi, Takashi Yamada, Katsumi Yamazaki
Okayama University - Dept. Electrical and Electronic Eng.
Okayama - Japan

IV - 56

P11181

Numerical Analysis of Coupling 2-D EM Field and Circuits for Rectification Synchronous Generator Taking Account Slot-Skewed

Huaishu Li, Langru Li
Huazhong University of Science & Technology(HUST)
Wuhan - China

IV - 58

P43613

Representation of Laminated and Slotted Configurations in the Finite Element Analysis of Electrical Machines and Transformers

Erich Schmidt
Vienna University of Technology - Institute of Electrical Drives and Machines
Vienna - Austria

IV - 60

P83925

Impact of Magnetic Nonlinearities and Cross Coupling Effects on Properties of Radial Active Magnetic Bearings

Boštjan Polajžer, Gorazd Štumberger, Jože Ritonja, Drago Dolinar, Kay Hameyer
Faculty of Electrical Engineering and Computer Science
Maribor - Slovenia

IV - 62

P13047

Characteristic analysis of eddy current coupling by finite element method considering rotor pole shape and copper-faced drum

IV - 80

Seok Myeong Jang, Seong Kook Cho, Sung Ho Lee, Han Wook Cho

P75311

Chungnam National University - Dept. of Electrical Engineering
Daejeon - Korea

Some Tricks for Modelling Rotating Electrical Machines Using Finite Elements

IV - 82

D. Rodger, H.C. Lai, R.J. Hill-Cottingham

P55113

University of Bath - Department of Electronic and Electrical Engineering
Bath - UK

Devices IV
Thursday, July 17, 10:45am - 12:00pm

Chairman
Dr. Jozsef Pavo

Design and Dynamic Analysis of permanent Magnetic Actuator for Vacuum Circuit Breaker

IV - 84

S.L. Ho, Y. Li, X. Lin, J.Y. Xu, W.C. Lo, H.C. Wong

P41346

Hong Kong Polytechnic University - Dept. of Electrical Engineering
Kowloon - Hong Kong

Numerical Analysis of Transient Force and Eddy Current Loss in a 720 MVA Power Transformer

IV - 86

S.L. Ho, Y. Li, H.C. Wong, S.H. Wang, R.Y. Tang

P71147

Hong Kong Polytechnic University - Dept. of Electrical Engineering
Kowloon - Hong Kong

Magnetic Force Computation in Permanent Magnets Using a Local Energy Coordinate Derivative Method

IV - 88

W.N. Fu, P. Zhou, D. Lin, S. Stanton, Zoltan J. Cendes

P52569

Ansoft Corporation
Pittsburgh, PA - USA

FEM Evaluation of Zero-phase sequence Characteristics of 3-ph 3-limb Core-type Transformers

IV - 90

Cesare Mario Arturi, Luca Di Rienzo

P73616

Politecnico di Milano - Dipartimento di Elettrotecnica
Milano - Italy

Design of Optical Pickup Actuator Using Multi-Pole Magnet for High Performance

IV - 92

In-Ho Choi, Sam-Nyol Hong, Gina Kim, Jin-Yong Kim

P53097

DCT Group - Digital Media Research Lab.
Seoul - Korea

Characteristic Analysis and Modification of PM-type Magnetic Circuit Breaker

IV - 94

K.I. Woo, B.I. Kwon, H.D. Jun

P84201

Pukyong National University - Division of Electrical, Control and Instrument Engineering
Busan - Korea

Local Electric Field Analysis for Evaluation of Charge Transfer System Using Sequential Sub-window Technique

IV - 96

Joon-Ho Lee, Young-Ki Chung, Il-Han Park

P44174

Sungkyunkwan University - School of Information and Communication Eng.
Suwon - Korea

Electrostatic Comb Accelerometer - Filed and Equivalent Circuit Modeling

IV - 98

Sławomir Wiak, Krzysztof Smółka

P14784

Technical University of Lodz - Institute of Electrical Machines and Transformers
Lodz - Poland

Optimization IV	Chairman
Thursday, July 17, 1:30pm - 2:45pm	Dr. Nathan Ida

Optimization of Permanent Magnet Shape for Minimum Cogging Torque Using a Genetic Algorithm

IV - 100

M. Łukaniszyn, M. Jagieła, R. Wróbel

P31609

Technical University of Opole - Dept. of Electrical Engineering and Automatic Control
Opole - Poland

A Novel Topology Optimization using Density Method Combined with Modified Evolution Strategy

IV - 102

Yoshifumi Okamoto, Norio Takahashi

P11318

Okayama University - Dept. Electrical and Electronic Eng.
Okayama - Japan

Crossover-Controlled Genetic Algorithm and Its Application to Inverse Problem in SF6 Interrupter

IV - 104

Youhua Wang, Xiaoguang Yang, Weili Yan, Egon Sommer

P11274

Hebei University of Technology - School of Electrical Engineering & Automatization
Tianjin - China

An Emigration Genetic Algorithm and its Application to Multiobjective Optimal Designs of Electromagnetic Devices

IV - 106

Yuhuai Wang, Shiyou Yang, Guangzheng Ni

P72415

Zhejiang University - Electrical Engineering College
Hangzhou - China

Analysis of Cogging Torque Considering Tolerance of Axial Displacement on BLDC Motor by Using a Stochastic Simulation Coupled with 3D-EMCN

IV - 108

Young-Kyoun Kim, Jeong-Jong Lee, Jung-Pyo Hong, Yoon Hur

P72742

Changwon National University - Dept. of Electrical Engineering
Kyungnam - Korea

Robust design of MR head to minimize side-fringing field and its variation using response surface methodology and finite element method

IV - 126

H.T. Wang, Z.J. Liu, Y.H. Wu, D. You

P55844

Data Storage Institute
Singapore

Materials II: General   Chairman
Thursday, July 17, 1:30pm - 2:45pm   Dr. Ed Della Torre

Modeling of Eddy Currents in Magnetic Materials and Laminated Materials

IV - 128

Bernard Bandelier, Françoise Rioux-Damidau

P41716

Université Paris Sud - U2R2M
Orsay - France

A Computational Effective Material Data Representation for Fast Simulation Models of Giant Magnetostrictive Materials

IV - 130

Y. Sato, G. Engdahl

P71061

Kungliga Tekniska Högskolan - Department of Electrical Engineering
Stockholm - Sweden

3-D Finite Element Analysis of Current Distribution in HTS Power Cable Taking Account of E-J Power Low Characteristics

IV - 132

Daisuke Miyagi, Tomohiro Wakatsuki, Norio Takahashi, Shinji Torii, Kiyotaka Ueda

P51368

Okayama Univ. Tsushima - Dept. Electrical and Electronic Eng.
Okayama - Japan

Power-law Characteristic for 3D Macroscopic Modelling of Superconductors via an Integral Formulation

IV - 134

Guglielmo Rubinacci, Fabio Villone, Walter Zamboni

P32287

Universita' degli Studi di Napoli FEDERICO II - Dipartimento di Ingegneria Elettrica (DIEL)
Napoli - Italy

Micromagnetic Simulation of Fine Structures in Asymmetrical Landau-Lifshitz Domain Pattern

IV - 136

Mai Lu, Paul J. Leonard

P92191

University of Bath - Department of Electronic and Electrical Engineering
Bath - United Kingdom

Time Domain Analysis of Shielding Current Density in HTS by Element-Free Galerkin Method

IV - 138

Atsushi Kamitani, Ayumu Saitoh, Soichiro Ikuno

P13635

Yamagata University - Faculty of Engineering
Yamagata - Japan

Education – TEAM	Chairman
Thursday, July 17, 1:30pm - 2:45pm	Dr. Kyung Choi

Engineering-oriented benchmarking of Problem 21 family and experimental verification

IV - 156

Z. Cheng, R. Hao, N. Takahashi, Q. Hu, C. Fan

P91513

Baoding Tianwei Group - R & D Centre
Baoding - China

Working Transient Eddy Current Problems with Velocity using Modified Green's Functions and Impedance Matrices

IV - 158

Kent R. Davey

P71828

New Smyrna Beach, FL - USA

Surface Current Reconstruction Using Magnetic Field Tomography

IV - 160

Hartmut Brauer, Marek Ziolkowski

P44503

Technische Universitaet Ilmenau - Fakultaet Elektrotechnik und Informationstechnik
Ilmenau - Germany

Development of Network-Oriented Education System for Learning Finite Element Method Using JAVA

IV - 162

Masashi Ohchi, Tatsuya Furukawa, Shin-ichiro Tanaka

P34723

Saga University - Faculty of Science and Engineering, Department of Electronics
Saga - Japan

TEAM Workshop Problem 25: a multi-objective analysis

IV - 164

Luiz Lebensztajn, Jean-Louis Coulomb

P14929

Escola Politécnica da Universidade de São Paulo - Departamento de Engenharia de Energia e Automaçao Eletricas
São Paulo - Brazil

Some results on a SMES device optimization problem using stochastic methods

IV - 166

O. Hajji, S. Brisset, P. Brochet

P54692

Ecole Centrale de Lille - Departement Genie Electric
Villeneuve d'Ascq - France

An NDT pulse shape study with TEAM Problem 27

IV - 168

Derek N. Dyck, Geoff Gilbert, Behzad Forghani, J.P. Webb

P95527

Infolytica Corporation
Montreal - Canada

Optimise: A Computational Environment for Teaching Optimization in Electrical Engineering

IV - 170

Jaime A. Ramírez, Frederico G. Guimaraes, Paulo H.L. Barros

P45930

Universidade Federal de Minas Gerais - Escola de Engenharia, Departamento de Engenharia Eletrica
Belo Horizonte - Brazil

An analysis of the performance of a MEMS micro-mirror   **IV - 172**
J. Wen, X. Hoa, A. Kirk, D. Lowther   P76504
McGill University - Department of Electrical and Computer Engineering
Montreal - Canada

Scalar and Vector Potentials in Electromagnetism   **IV - 174**
José A. Camberos   P76512
AMC PO Box 33878
Dayton, OH - USA

Quasistatic III: Eddy Currents: Applications	Chairman
Thursday, July 17, 1:30pm - 2:45pm	Dr. Andrzej Krawczyk

Analysis of the thin plate eddy current problem by Finite Volume Method   **IV - 176**
J. Zou, Y.Q. Xie, J.S. Yuan, X.S. Ma   P91453
Tsinghua University - Department of Electrical Engineering
Beijing - China

Calculation of Eddy Current Energy Losses in Thin Sheets under Saturation   **IV - 178**
G. Szymanski, M. Waszak   P91067
Ponzan University of Technology - Institute of Control and System Engineering
Ponzan - Poland

Transient 3D FEM Computation of Eddy-Current Losses in the Rotor of a Claw-Pole Alternator   **IV - 180**
Christian Kaehler, Gerhard Henneberger   P51469
Aachen University - Departement of Electrical Machines
Aachen - Germany

Crack detection in ferromagnetical materials   **IV - 182**
Abbas Farschtschi, Amor Benmansour   P91285
Technische Universität Chemnitz - Lehrstuhl für Allgemeine und Theoretische Elektrotechnik
Chemnitz - Germany

Eddy Current Analysis of Surface Permanent Magnet Motor Using 3-D Finite Element Method   **IV - 184**
Yoshihiro Kawase, Tadashi Yamaguchi, Tomohiro Ono, Shinya Sano   P81699
Gifu University - Department of Information Science
Gifu - Japan

Crack Shape Reconstruction in Ferromagnetic Materials using a Novel Fast Numerical Simulation Method   **IV - 186**
Haoyu Huang, Toshiyuki Takagi, Tetsuya Uchimoto   P92981
Tohoku University - Institute of Fluid Science
Sendai - Japan

Eddy currents effects in circuit breakers during arc displacement phase   **IV - 188**
O. Chadebec, Gérard Meunier, Vincent Mazauric, Yann Le Floch,   P43310
Patrice Labie
Laboratoire d'Electrotechnique de Grenoble - ENSIEG
Saint-Martin-d'Hères - France

Generalization of the ideal crack model in Eddy-Current Testing   **IV - 190**
Philippe Beltrame, Noël Burais   P54559
Ecole Centrale Lyon - CEGELY
Ecully - France

Three-dimensional FEM analysis of an eddy current braking system   **IV - 192**
F. Rapetti, L. Santandrea, F. Bouillault, A. Razek   P45375
Universite de Nice et Sophia-Antipolis - Laboratoire J.-A. Dieudonne
Nice - France

Study of the Local Eddy Current Loss Density near the Edges in Steel   **IV - 194**
Laminations of Finite Width
P.G. Pereirinha, Johan Gyselinck, Carlos F.R. Lemos Antunes   P16515
ISR - Dep. Engenharia Electrotécnica
Coimbra - Portugal

Optimization   Chairman
Thursday, July 17, 3:15pm - 5:30pm

Managing Uncertainties in Electromagnetic Design Problems with Robust   **IV - 196**
Optimization
Gerald Steiner, Andreas Weber, Christian Magele   P94140
TU Graz - Inst. f. Elektrische Messtechnik und Messsignalverarbeitung
Graz - Austria

Stochastic Handling of Tolerances in Robust Magnets Design   **IV - 198**
M. Cioffi, A. Formisano, R. Martone   P95669
Seconda Università di Napoli - Dip. Ignegneria dell'Informazione
Aversa - Italy

Optimization Design of Electrode Contour of SF6 Circuit Breaker Using   **IV - 200**
Artificial Neural Network
Yundong Cao, Xiaoming Liu, Dong Liu, Erzhi Wang   P62886
Shenyang University of Technology - College of Electrical Engineering
Shenyang - China

Optimization of an Offset Reflector Antenna using Genetic Algorithms   **IV - 202**
S.L. Avila, W.P. Carpes Jr., João A. De Vasconcelos   P32489
GRUCAD / EEL / CTC / UFSC
Florianópolis - Brazil

Inverse Electromagnetic Problems by Field Visualization

[1]Iliana Marinova, [2]Hisashi Endo, [2]Seiji Hayano, and [2]Yoshifuru Saito

[1]Technical University of Sofia, 1756 Sofia, BULGARIA, [2]Graduate School of Engineering, Hosei University,
3-7-2 Kajino, Koganei, Tokyo 184-8584, JAPAN
E-mail: iliana@ea.vmei.acad.bg

Abstract– The current distribution is of main importance for testing and inspecting of many devices as printed circuit boards, motherboards of personal computers etc. The determination of current distribution is a main inverse electromagnetic problem. The visualization technique is applied to determine the current distribution by locally measured magnetic field. The image of the field distribution is processed using field theory. The color source densities have been evaluated from the color distributions of the field data set. It was found that the color source distribution corresponds to the current distribution. Generating new color distribution with obtained color source densities can essentially reduce the noise of the measured field data. With the proposed approach the quality of the images can be essentially improved. The results obtained show that the current distribution can be obtained and analyzed using visualized information of the field distribution.

INTRODUCTION

Magnetic field distribution is very important considering many inverse electromagnetic problems – identification, NDT, ECT etc. Usually magnetic field is measured over the parallel surfaces during the testing and inspection of the devices as a printed current boards (PCBs), motherboards of personal computers etc. The determination of the current distribution is reduced to the main inverse electromagnetic problem of the two dimensional currents searching on a flat surface. Recently, many different techniques are proposed to solve that problem [1-4]. The locally measured magnetic field is used to determine the current distribution. The field visualization facilitates modeling and analysis of the electromagnetic phenomena and processes. In this paper, the field theory is applied over the image, visualizing the field distribution. The color source distribution is obtained using the image color model. The color source distribution corresponds to the current distribution. Thus, visualizing the color source distribution it is possible to visualize the current distribution. The measured field database is usually insufficient or the data are accompanied with noise. Using the image color model and solving the inverse problem over the image it is possible to improve the quality and to change the characteristics of the image [5]. The Generalized Vector Sampled Pattern Matching method is applied to solve an ill posed linear system of equations. The new color distributions are generated using the obtained color source densities.

IMAGE COLOR MODEL OF THE FIELD DISTRIBUTION

The image is considered as 2D-distribution of color components – Red, Green, and Blue (RGB). Each color component A is expressed utilizing the appropriate Green function G

$$A = \frac{1}{4\pi} \int_S \sigma G dS \qquad (1)$$

The measured magnetic field densities B are presented by the x-, y- and z- components. Applying the relation between vector potential **A** and flux density **B**

$$\mathbf{B} = \nabla \times \mathbf{A} \qquad (2)$$

Also, the components of the magnetic flux densities are determined utilizing the color source densities σ

$$\mathbf{B}_x = \mathbf{D}_x \sigma \qquad (3)$$
$$\mathbf{B}_y = \mathbf{D}_y \sigma \qquad (4)$$
$$\mathbf{B}_z = \mathbf{D}_z \sigma \qquad (5)$$

where the $\mathbf{D}_x$, $\mathbf{D}_y$ $\mathbf{D}_z$ represent the geometrical relations between pixels for corresponding components of the flux density.

The color component source densities σ are determined solving the system of equations,

$$\mathbf{CX} = \mathbf{Y} \qquad (6)$$

where $\mathbf{C}$, $\mathbf{Y}$ and $\mathbf{X}$ are the n by m system matrix, n-th order column vector of the color component and m-th order column vector of unknown color source densities, respectively. For image processing the color components as well as color source densities have to be determine in the x-, y-pixels of the image. The RGB color components are separated. The systems of equations (6) are solved by Generalized Vector Sampled Pattern Matching method (GVSPM) [2]. Visualized color source distribution corresponds to the current distribution. Thus, applying the field theory over the image of the field distribution, it is possible to determine the corresponding current distribution by solving inverse electromagnetic problem. In order to improve the image of measured field distribution the inverse problem for color source density distribution at high resolution is formulated and solved. The new visualization of the color distributions is carried out from the evaluated color source densities. Thus, quality of the field distribution can be enhanced and the noise to be essentially reduced.

The magnetic field is measured over the parallel surface of the single circle coil shown in Fig. 1. The inner and outer diameters are $d_1=0.02m$ and $d_2=0.025m$, respectively. The height is h=0.005m. The components of the magnetic field densities B_x and B_y measured on the parallel surface over the coil are visualized and shown in Fig. 2. The Red, Green and Blue components are separated and presented in Fig. 4 and Fig. 5. Solving the system of equations (6) for each color component - RGB, the color source density distributions are obtained. The Generalized Vector Sampled Pattern Matching method is applied to solve an ill posed linear system of equations of the corresponding inverse image problem. The color source distribution is visualized and shown in Fig. 3. It was found that the color source distribution corresponds to the searched current distribution.
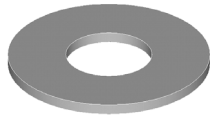
Fig. 1 Single circle coil

| (a) B_x | (b) B_y |
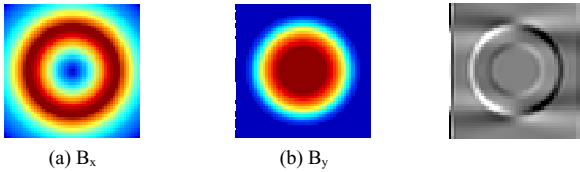
Fig. 2. Magnetic field density distribution (measured data of x- and y-components)

Fig. 3 Current distribution

| Red | Green | Blue |
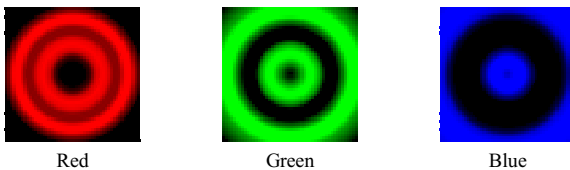
Fig. 4 Color component distribution of B_x

| Red | Green | Blue |
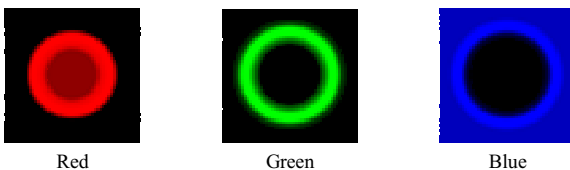
Fig. 5 Color component distribution of B_y

In order to reduce the noise accompanying the measured field data an inverse color problem is formulated and solved over the images of the magnetic field distribution, shown in Fig,

6(a) and Fig. 7(a). The obtained color source densities are used to generate new color distributions shown in Fig. 6(b) and Fig. 7(b). It was found that the quality of the images is essentially enhanced.

| (a) original - B_x | (b) improved - B_x |
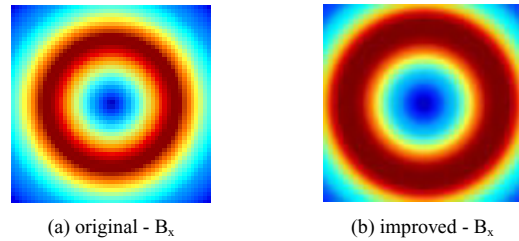
Fig. 6. Original and improved image of magnetic field density distribution (x-components)

| (a) original - B_y | (b) improved - B_y |
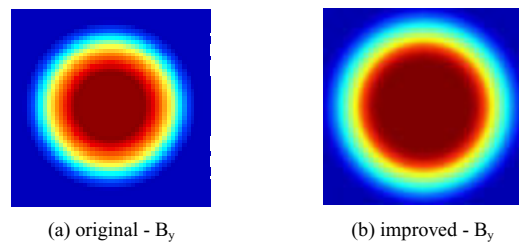
Fig. 7. Original and improved image of magnetic field density distribution (y-components)

CONCLUSION

We have proposed a new inverse approach to determine and visualized the current distribution. The image processing technique using field theory was successfully applied for field visualization of electromagnetic devices. From the locally measured magnetic field distribution it is possible to obtain and visualized the corresponding current distribution. Solving the inverse color problem can essentially reduce the noise of the measured field data.

REFERENCES

[1] T. Doi, S. Hayano, I. Marinova, Y. Saito, "Defect recognition in conductive materials by local magnetic field measurement," Journal of Applied Physics, Vol. 75, No. 10, May, 1994, pp. 5907-5909.
[2] M. Moganti and F. Ercal. Segmentation of Printed Circuit Board Images into Basic Patterns, Computer Vision and Image Understanding, Vol.70, No. 1, pp. 74-86, April 1998.
[3] S. .J. Norton and J. R. Bowler. " Theory of the eddy current inversion," J. Appl. Phys., vol. 73, no. 2, pp. 501-511, 1993.
[4] T. Taniguchi, K. Nakamura, D. Kacprzak, S. Yamada, M. Iwahara, Eddy-current testing image processing for extraction of orientations of defects", In: T. Takagi and M. Uesaka (eds.), *Applied Electromagnetics and Mechanics*, ©2001 JSAEM, pp. 489-490.
[5] I. Marinova, H. Endo, S. Hayano, Y. Saito, "Image reconstruction for electromagnetic field visualization by an inverse problem solution", In: T. Takagi and M. Uesaka (eds.), *Applied Electromagnetics and Mechanics*, ©2001 JSAEM, pp. 699-700.

A new method for choosing the regularization parameter in time dependent inverse problems

Jörg Schreiber[1], Jens Haueisen[1], Jukka Nenonen[2]

[1] Biomagnetic Center, Department of Neurology, Friedrich-Schiller-University, Philosophenweg 3, 07743 Jena, Germany

[2] Laboratory of Biomedical Engineering, Helsinki University of Technology, P.O. Box 2200, 02015 HUT, Espoo, Finland

E-mail: haueisen@biomag.uni-jena.de

Abstract — The current density estimation on the epicardial surface of the heart based on electrocardiographic and magnetocardiographic measurements is one example of an ill-posed inverse problem. Commonly, zero-order Tikhonov regularization is applied to solve such problems. For the determination of the critical regularization parameter a few methods exist. However, none of these methods performed sufficiently in our application. In this paper, we propose a new method for choosing a regularization parameter for a time interval. Our basic assumption for this method is that the optimal solution norm must reflect the temporal properties of the magnetic energy. The performance of our method is tested both on simulated data and patient data.

INTRODUCTION

Magnetocardiography (MCG) provides non-invasively information about the electrical activity of the heart [1]. Estimating and imaging the current density distribution on the epicardial surface of the heart can help diagnosing myocardial infarction and other heart diseases. The determination of this current density distribution requires the solution of an ill-posed inverse problem. Zero-order Thikonov regularization is a commonly applied technique for stabilizing such solutions and leads to the following minimization term

$$\Delta^2 = \left\| \mathbf{B} - L\mathbf{j} \right\|_2^2 + \lambda \left\| R\mathbf{j} \right\|_2^2 \ ,$$

where B is measured magnetic field vector, L the lead-field (kernel) matrix, j the current density vector, R the regularization matrix, and λ the regularization parameter. The equation states that both the residual norm (first term) and the solution norm (second term) should be minimized, whereby the regularization parameter acts as a weight between these terms. Specifying a reasonable value for λ is often very difficult and a few, mainly empirical methods have been proposed [2, 3, 4, 5]. The L-curve [2] and the χ^2 [3] criteria are two most often used methods. However, none of these methods performed well in our application consisting of time interval source reconstructions in patients with myocardial infarction.

Analyzing time intervals is of great importance in MCG (and also in magnetoencephalography, MEG). A possible approach is to determine the regularization parameter for every time point, but in many cases it is convenient to use a mean value for the entire interval. Based on the assumption that the solution should follow the properties of the magnetic energy of the signal, our aim was to develop an algorithm to determine the regularization parameter.

METHODS

The new method The normalized mean global field power (MGFP) integral over a certain time interval in the original signal should be similar to the integral of the current density solution in the same time interval. Moreover, those parts in the MGFP signal containing zero signals should not contribute to the solution. Thus, we normalized both the MGFP and the current density solution, integrated all values above the respective noise levels ($>3\sigma$), and plotted the two integrals for each λ (Fig. 1). The optimal parameter was chosen empirically from the intersection of the tangent in the maximum curve slope and the MGFP integral (dotted line).
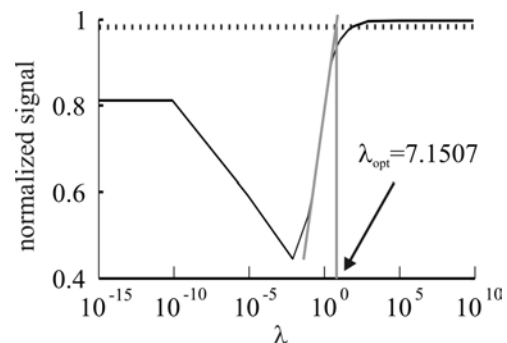
Fig. 1. Normalized MGFP integral (dotted line) and current density solution integral (solid line) over the regularization parameter.

In order to test our method, we performed simulations and analyzed patient data. We compared the results obtained with

our method to the results obtained with often used the L-curve [2] and the χ^2 [3] criteria.

Simulations We modeled the QRS interval of the human heart cycle with the help of 13 dipoles placed around the left ventricle (normal to its surface) representing the basal, medial and apical slice with each containing the four anatomical directions anterior, lateral, inferior and septal. The apex was represented by a separate dipole. Each dipole was fixed in direction and the strength varied over time with a Gaussian shape (maximum of 1 µAm), which was shifted for each dipole according to the measurements in [6]. For the field computation we used a high-resolution boundary element model including the torso (10 mm triangle side length), the lungs (6 mm) and the ventricles (3 mm) [7]. The magnetic field data were calculated in 64 magnetometers arranged in an 8-by-8 array in front of the torso. The forward calculated fields were disturbed with
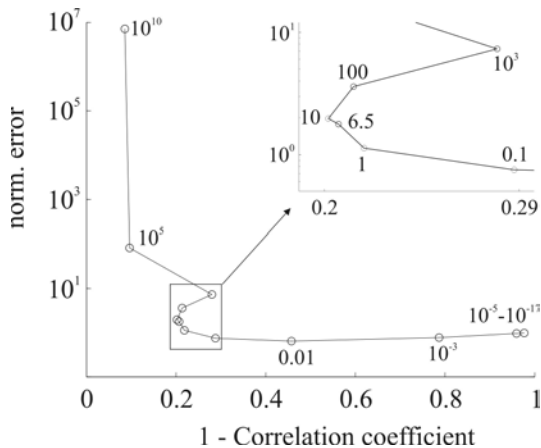
Fig. 2. Normalized squared error over 1- correlation coefficient.

Gaussian noise using 3 different noise levels (0.01, 0.05, and 0.1 pT) and provided the input to our minimum norm current density reconstruction (CDR). The optimal regularization parameter, λ_{opt}, was determined by comparing the strength of the solution from the CDR calculations with the strength of the original dipole distribution. We calculated both the correlation coefficient (CC) and the norm square error (NSE) between the values in each source point and for each time point. The optimal parameter results from the plot NSE versus 1-CC (Fig. 2).

Patient data We tested our new method for determining λ with realistic MCG measurement data. Here, λ_{opt} could be estimated by comparing the CDR with positron emission tomography (PET) data.

RESULTS AND DISCUSSION

Simulations Although our newly proposed method performed better than the other methods, the χ^2 produced similar results (Table I). Since only Gaussian noise was used, a good performance of the χ^2 method was expected.

TABLE I. SIMULATION RESULTS

Noise level	λ_{opt}	λ_{new}	χ^2 [3]	L-curve [2]
0.01 fT	0.1	0.24	0.59	1.1e-16
0.05 fT	0.5	1.83	4.18	2.08e-17
0.1 fT	0.5	7.15	9.14	2.75e-16

Patient data Again our method performed best (Table II), where the L-curve method gave only a one order of magnitude worse regularization parameter for this patient. The χ^2 method failed which is most likely due to the presence of non-Gaussian noise (inherent to real patient data).

TABLE II. PATIENT DATA RESULTS

λ_{opt}	λ_{new}	χ^2 [3]	L-curve [2]
0.5	0.13	6.7e-8	0.015

Further research will focus on the inclusion of a constraint for temporal smoothness of the solution. Moreover, spatial smoothness in the source space might give an additional constraint.

REFERENCES

[1] U. Leder, J. Haueisen, M. Huck, and H. Nowak, "Non-invasive imaging of arrhytmogenic left-ventricular myocardium after infarction," *The Lancet*, vol. 352, p. 1825, 1998.
[2] P. C. Hansen, "Analysis of discrete ill-posed problems by means of the L-curve," *SIAM Review*, *Finite Elements in Electrical and Magnetic Field Problems.* vol. 34, pp. 561 – 580, 1992.
[3] V.A. Morozov, "The error principle in the solution of operator equations," *USSR Comp Math Math Phys,* vol. 28, pp. 69 – 80, 1968.
[4] G.H. Golub, G. Wahba, and M. Heath, "Generalized cross-validation as a method for choosing a good ridge parameter," *Technometrics*, vol. 21, pp. 215-223, 1979.
[5] P.R. Johnston and R.M. Gulrajani, "A new method for regularization parameter determination in the inverse problem of electrocardiography," *IEEE Transactions on Biomedical Engineering*, vol. 44, pp. 19 – 39, 1997.
[6] D. Durrer, R.T. Vandam, G.E. Freud, M.J. Janse, F.L. Meijler, and R.C. Arzbaech, "Total excitation of isolated human heart," *Circulation*, vol. 41, pp. 899, 1970.
[7] J. Haueisen, J. Schreiber, H. Brauer, T.R. Knösche, "The dependence of the inverse solution accuracy in magnetocardiography on the boundary element discretization," *IEEE Transactions on Magnetics*, vol. 38, pp. 1045 – 1048, 2002.

Multiresolutive Reconstruction of Magnetoencephalography Source Distribution

Chang-Hwan Im*, Hyun-Kyo Jung*, Hyuk-Chan Kwon**, and Yong-Ho Lee**

*School of Electrical Engineering, Seoul National University, San 56-1, Shillim-dong, Kwanak-gu, Seoul, 151-742, KOREA
** Korea Research Institute of Standards and Science (KRISS), P.O. Box 102, Yuseong, Daejeon, 305-600, Korea
e-mail : ichich2@snu.ac.kr

Abstract — In this paper, a new technique for multiresolutive reconstruction of magnetoencephalography(MEG) source distribution is proposed. By using the proposed technique, focal solution with higher energy density can be reconstructed and computational cost can be considerably reduced. Moreover, the approach is very easy to implement compared to conventional techniques. The usefulness of the proposed technique is verified by the application to a real head model.

INTRODUCTION

Reconstructing electric activity inside a brain using magnetic measurements outside of the head has attracted a great deal of interest. Usually, such a process is referred to as a magnetoencephalography (MEG) source reconstruction. There have been two source models used to reconstruct brain neural sources from MEG data. Those are usually referred to as a dipolar model and a cortically distributed source model. In the case of the dipolar model, parameters of equivalent current dipoles can be found by using optimization algorithms [1]. Although the method is very simple to apply, it has some critical disadvantages, in that the reconstructed dipoles may not be always located on the real cortical surface and the number of dipoles, i.e., the number of active areas, is not given as *a priori*. Conversely, the cortically distributed source model assumes that the dipoles are located perpendicularly to the cortical surface, and only their magnitudes are reconstructed [2]. Although it can solve the above problems relatively well, it suffers from great computational cost due to highly underdetermined relations between measured data (usually less than 300 sensors) and variables to be reconstructed (usually over 10000 cortical surface meshes). Moreover, conventional minimum norm least square (MNLS) approach provides very smooth-looking intensity patterns but fails to recover focal brain activities.

Recently, multiresolutive reconstruction techniques have been proposed to reduce the search space around emerging active areas [3], [4]. Although they showed improved characteristics in reducing computational cost and finding focal solutions, they still have some problems, especially for their implementation. To implement the conventional methods, multigrid-type surface mesh should be used, which is very hard to generate on highly curved cortical surface. Moreover, ellipsoids used to restrict search spaces are not appropriate to apply to the curved cortical surface.

In this paper, an improved concept for the multiresolutive reconstruction is proposed. The proposed technique is very easy to implement because it is not a node-based but a region-based technique. It uses hexahedra instead of ellipsoids to restrict the search spaces. Interesting regions with higher energy density are split into smaller hexahedra, whereas the others are not considered any more. By applying the process repeatedly, focal brain activations can be found with reduced computational cost. From the simulation for a real head model, the usefulness of the proposed method will be verified.

METHODS

Cortically Distributed Source Reconstruction

Brain neural activity is represented by continuous current flow, which is usually modelled as the distribution of discrete current dipole moments. The aim of the source reconstruction is to estimate the distribution on a brain cortex. The current dipole moments are located perpendicularly to the cortical surface. Because the directions of the dipoles are already determined, their magnitudes at each cortical surface mesh are variables to be reconstructed.

A 122-channel SQUID (Superconducting Quantum Interference Device) magnetometer, capable of measuring normal component of magnetic field at each sensor, was used for simulation. Fig. 1 shows the positions of sensors and the brain cortex, extracted from MRI data. Magnetic flux density at each sensor was calculated using Sarvas's formula, which assumes spherical volume conductor [5].
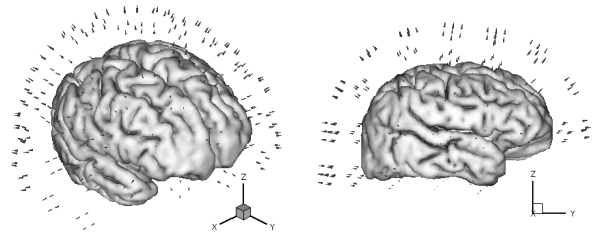
Fig. 1. Positions of SQUID magnetometers (*Neuromag* 122 channel)

Multiresolutive Reconstruction Technique

The unknowns to be reconstructed are the magnitudes of the current dipole moments at the center of each cortical mesh. The basic assumption of the proposed method is that the

meshes within a hexahedron have the same moment value. Fig. 2 shows the 2D schematic illustration to explain the proposed method. Processes for the method are as follows:

Step 1) Generate initial hexahedra. Initial value is zero (0).

Step 2) Calculate sensitivity for each hexahedron. Objective function to be minimized is defined as

$$F = \sum_{j=1}^{N_s} (B_j - B_{ej})^2 \qquad (1)$$

where, N_s is the number of sensors, and B_j and B_{ej} represent the calculated and measured magnetic flux density at a sensor j, respectively. The value of sensitivity, dF/dQ_i, for each hexahedron is calculated analytically, where Q_i is the moment value of i-th hexahedron, $i=1,2,…,N_r$ (number of hexahedra).

Step 3) Variables (moment values of each hexahedron) are updated using steepest decent updating scheme [6].

Step 4) Repeat *Step 2*) – *Step 4*) until a newly calculated objective function decreases below a stopping criterion.

Step 5) If reconstructed moment values of some hexahedra are below a predetermined threshold (0.1×maximum value is used in this paper), remove them from variables. Remained hexahedra are refined and resultant values from previous resolution are used for their initial values. Repeat *Step 2*) – *Step 5*) until satisfactory resolution is obtained.

Fig. 2. 2D Schematic illustration to explain the proposed method

initial domain   initial result   refined domain   high-resolution result
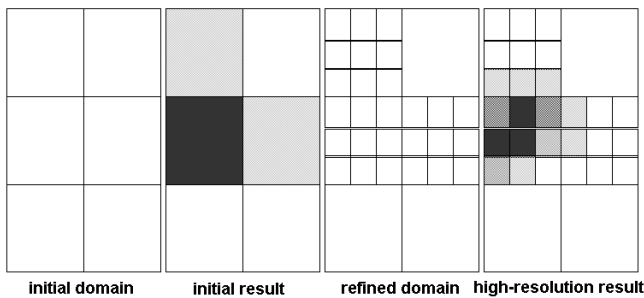
RESULTS

Fig. 3 shows the positions of two original neural activations used for forward calculation. 20-dB Gaussian noise was added to the forward data. Fig. 4 (a), (b) show the reconstructed source distributions for the first and second resolution, respectively. We can see from the figure that focal distribution could be obtained by using higher resolution. To compare the results quantitatively, a measure, named as ε, was proposed to evaluate how well a method can find focal solution. It is defined as the ratio between original and reconstructed energy stored in activation areas. Table I shows the evaluated results. From the table, we can see that the results from the proposed technique yields more focal solution compared to those from conventional MNLS method. More results will be added in the full paper.

CONCLUSION

In this paper, an improved concept for the multiresolutive reconstruction was proposed, which is very easy to implement compared to conventional approaches. From the simulation for a real head model, it was shown that focal brain activations could be found with reduced computational cost.

REFERENCES

[1] C. Wolters, "Comparing regularized and nonregularized nonlinear dipole fit methods : A study in a simulated sulcus structure," *Brain Topography*, vol. 12, no. 1, pp.3-18, 1999.
[2] A. Dale and M. Sereno, "Improved localization of cortical activity by combining EEG and MEG with MRI cortical surface reconstruction : A linear approzch," *J. Cogn. Neurosci., pp. 162-176, 1993.*
[3] R. Srebro, "An iterative approach to the solution of the inverse problem," *Electroencephalogr. Clin. Neurophysiol.*, vol. 98, pp. 349-362, 1996.
[4] L. Gavit, S. Baillet, J.-F. Mangin, J. Pescatore, L. Garnero, "A Multiresolution Framework to MEG/EEG Source Imaging," *IEEE Trans. Biomed. Eng.*, vol. 48, no. 10, pp. 1080-1087, Oct. 2001.
[5] Sarvas, "Basic mathematical and electromagnetic concepts of the biomagnetic inverse problem," *Phys. Med. Biol.*, 32(1), pp. 11-22, 1987.
[6] I. Park, B. Lee, S. Hahn, "Design Sensitivity Analysis for Nonlinear Magnetostatic Problems Using Finite Element Method," *IEEE Trans. Magn.*, vol. 28, no. 2, pp. 1533-1536, March 1992.
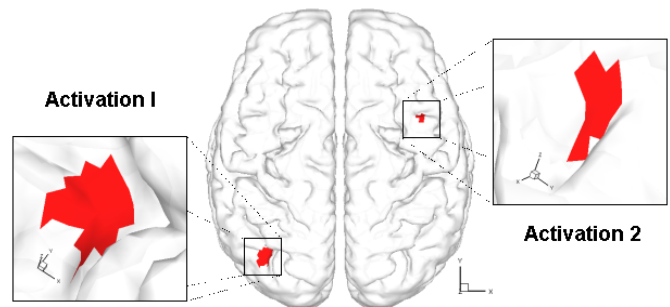
Fig. 3. Positions for two neural activation patches.

(a) First resolution   (b) Second resolution
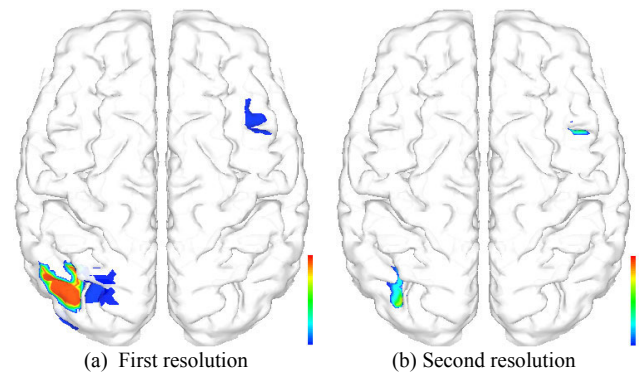
Fig. 4. Reconstruction results for first and second resolution. Normalized values with same cutoff (cutoff = 0.3×maximum value).

TABLE I. COMPARISON OF FOCAL CHARACTERISTICS

Methods	ε (activation region I)	ε (activation region II)
MNLS	0.161	0.090
Resolution I	0.279	0.082
Resolution II	0.389	0.346

Higher ε means the method can find more focal solution.

Identification of Multiple Cracks from Eddy Current Testing Signal with Noise Source by Image Processing and Inverse Analysis

Yoshiaki NAGAYA[*1], Toshiyuki TAKAGI[*2],
Tetsuya UCHIMOTO[*2] and Haoyu HUANG[*2]

[*1]Graduate School of Engineering, Tohoku University, Katahira 2-1-1, Aoba-ku, Sendai, Miyagi, 980-8577, Japan
[*2]Institute of Fluid Science, Tohoku University, Katahira 2-1-1, Aoba-ku, Sendai, Miyagi, 980-8577, Japan
e-mail: takagi@ifs.tohoku.ac.jp

Abstract - **This paper describes a novel method identifying the number and positions of cracks and reconstructing the crack shape. Using the ECT signal obtained by two-dimensional scanning as a picture image, a template matching method with help of genetic algorithms is applied to predict the number and positions of cracks. The present method employs a superposition of crack signals and a nonlinear scaling technique of a signal profile on crack length which are verified by numerical simulation. The number and positions of cracks are predicted sufficiently. Crack shape reconstructions from the predicted positions with help of inverse analysis are achieved with satisfactory accuracy.**

INTRODUCTION

Eddy current testing (ECT) is used for the in-service inspection of tubes in steam generators of pressurized water reactor type nuclear plants. Requirement for testing is not only high sensitivity and detectability but also quantitative evaluation of position and shape of shallow cracks. The steam generator tubes are supported by support structures. The detection of the crack becomes difficult because the noise caused by the support structures is detected as ECT signals.

To predict the number and positions of cracks, this paper proposes a method identifying the number and positions of cracks using the image processing of ECT signals. The method is verified through the application to an experimental ECT signal of multiple cracks. A template matching method, one of image recognition methods, is applied to reconstruction of multiple cracks in this study. The number and positions of cracks are predicted based on the two-dimensional scanning ECT signal as an image picture. The genetic algorithm (GA) is used as a search algorithm so as to improve the search efficiency. Finally crack shapes are reconstructed with help of inverse analysis using predicted positions of cracks by the image processing.

DETAIL OF EXPERIMENT

The testpiece is a tube of INCONEL600 with 300 mm in length, 22.23 mm in the outer diameter, and 19.69 mm in the bore [1]. The support plate is a drilled-hole type of SS400 with 24.1 mm in length, 40 mm in the outer diameter, and 22.7 mm in the bore [2]. This ferromagnetic support plate was installed on the testpiece as shown in Fig. 1.

A differential TR (Transmit-Receive) probe developed by authors was used for this experiment [1]. This probe possesses the feature that the direction of defects can be identified. The parameters of the EC instrument were frequency of 200 kHz and 400 kHz, and gains of 60 dB.

The multiple frequency method [3] is used in an inspection to remove the noise caused by the support structure. This technique is expanding, rotating and subtracting the signals, scanned on the same part with two or more frequencies, on the complex plane.

APPLICATION OF TEMPLATE MATCHING TO ECT SIGNAL

The template matching with help of GA [4] is applied to the reconstruction of multiple cracks. The expansion rate of the crack length and locations of the crack are expressed in the gene. The fitness is calculated by comparing signals of the template after transformation with signals of the input image at the location in the gene using a correlation coefficient. The gene with the highest fitness is supposed to indicate the position of the crack.

In this study, the two assumptions are made on ECT signals. One is that multiple cracks signal can be expressed as a superposition of single crack signals. Another is that signals of cracks of any length can be scaled based on a template. The former assumption enables the searching another crack after one crack is detected. The latter is necessary to search for the various lengths cracks based on one kind of the template. These assumptions are verified through the numerical simulation. The reduced magnetic vector potential method based on edge element is used for forward analysis [5].

The assumption of the crack signals superposition is examined first. Two parallel cracks of OD (Outer Defect) 20% and OD40% were taken here. They have same length of 10 mm and width of 0.2 mm, and three patterns (1 mm, 2 mm and 3 mm intervals) were computed. Scanning line is across the centers of cracks. Examples of numerical results are shown in Fig. 2. The correlation coefficients between the superposition of single crack signals and two cracks signals are shown in Table I. It is possible to reproduce in very high accuracy in every case. Therefore it can be concluded that the assumption of crack signals superposition works out.

Next, asumption of nonlinear scaling of crack length is examined. If the crack is long enough with respect to the probe, the signal of the center of the crack must be equal to the signal of
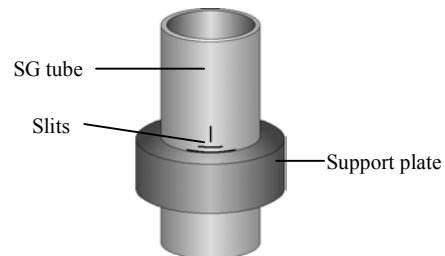
Fig.1 The testpiece and the support plate

(a) 2 mm interval   (b) 3 mm interval
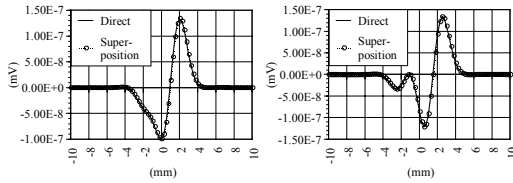
Fig. 2 Signal from cracks 2 mm and 3mm separation

TABLE I. CORRELATION COEFFICIENTS

Crack separation (mm)	Correlation coefficient
1	0.999775441
2	0.999974335
3	0.999994505

TABLE II. CORRELATION COEFFICIENTS

Crack length (mm)	Crack depth (%)	Correlation coefficient
3	20	0.993333741
	40	0.989545998
	60	0.985233249
7	20	0.999426164
	40	0.999014043
	60	0.998457707
10	20	0.998638175
	40	0.997277088
	60	0.995720769

(a) 3 mm length   (b) 7 mm length

Fig. 3 Signal from OD20% crack

Fig.4 ECT signal after signal processing and detected cracks

TABLE III. RECONSTRUCTION OF CRACK SHAPE

Detected No.		R1	R2_3
Depth (%)	Estimated	44.7	29.5
	True	44	21
	Error	+0.7	+8.5
Length (mm)	Estimated	5	11
	True	4.6	10.3
	Error	+0.4	+0.7
Slit No.		#2	#1

the crack having infinite length. If the shape of the edge is the same, the signal of the edge of the crack must always be equal regardless of the crack length. Based on this intuitive consideration, a crack signal is supposed to change depending only on the length of the center part. When the crack increases in length, the signal of the center of the crack is expanded with the value of the center point. When decreasing oppositely, the center of signal is eliminated. Siganls of cracks with 3 mm, 7 mm and 10 mm is transformed based on the signal of the crack of 5 mm in length. Three kinds of depth (OD20%, OD40% and OD60%) are examined. Scanning line is parallel to the crack. Examples of results are shown in Fig. 3. The correlation coefficients between scaled signals and signals computed directly are shown in Table II. It can be concluded that assumption of scaling of length gives good approximation.

RESULTS OF IDENTIFICATION OF THE NUMBER AND POSITIONS OF CRACKS

Using the present method, the number and positions of the cracks are predicted based on ECT signals of multiple cracks sample. Fig. 4 shows results of identification of multiple cracks. The cracks are numbered by the sequence of the detection with the present method. In this search only circumferential cracks can be identified.

As for R2 and R3, it can be judged that they are parts of a single crack and are named R2_3, since the coordinate of the axial direction of the crack is the same. It is found that R1 corresponds to an actual crack #2, R2_3 to #1. The interval between R1 and R2_3 is 1.875 mm, and it agrees with the actual interval 2 mm between #1 and #2 well.

RECONSTRUCTION OF CRACK SHAPES

Crack shapes were reconstructed based on positions of the cracks identified by the present method. Table III shows the shapes of the crack predicted by the inverse analysis [6]. Both
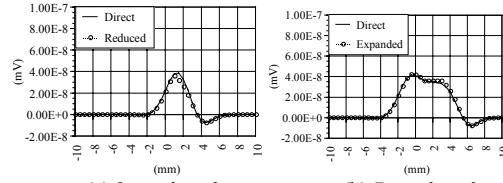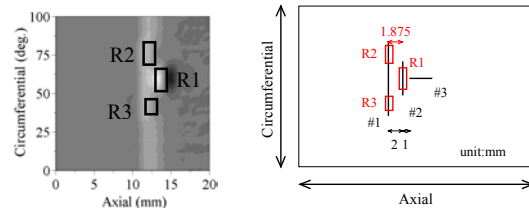
length and depth of the cracks show an excellent agreement. These results imply that even if there are neighboring cracks, the crack shapes can be reconstructed.

SUMMARY

The number and positions of cracks were predicted sufficiently with a template matching method with help of GA. The reconstructions of the crack shape by using positions of detected cracks were confirmed in high accuracy.

ACKNOWLEDGEMENTS

REFERENCES

[1] H. Huang and T. Takagi, "Inverse Analyses for Natural and Multicracks using Signals from a Differential Transmit–Receive ECT Probe", *IEEE Trans. Magnetics*, 38(2), pp. 1009-1012, 2002.

[2] M. Oka and M. Enokizono, "Non-destructive Testing by Using the Rotational Magnetic Flux Type Probe for SG tube", *Electromagnetic Nondestructive Evaluation* (VI), IOS Press, pp. 174-180, 2002.

[3] D. E. Bray, and R. K. Stanley, "Nondestructive Evaluation", *A tool in Design, Manufacturing and Service*, CRC Press, pp. 418-419, 1997.

[4] T. Nagao, T. Agui and H. Nagahashi, "Extraction of Two Dimensional Arbitrary Shapes using a Genetic Algorithm", *SPIE Visual Communications and Image Processing* '93, SPIE 2094, pp. 74-83, 1993.

[5] H. Fukutomi, T. Takagi and M. Hashimoto, "Numerical Evaluation of ECT Impedance Signal due to Minute Cracks", *IEEE Trans. Magnetics*, 33(2), pp. 2123-2126, 1997.

[6] H. Huang and T. Takagi, "ECT Signals for Round-robin Test with Differential TR Probe and their Inverse Analysis", *Electromagnetic Nondestructive Evaluation* (V), IOS Press, pp. 218-225, 2001.

A Condition-Number Based Regularization Parameter Estimate for Reconstruction Problems

Bernhard Brandstätter, Gert Holler and Daniel Watzenig
Institute for Electrical Measurement and Measurement Signal Processing

Abstract— In reconstruction (i. e. determining the model states of a forward problem from measurements of model outputs) one is often forced to search for a regularized solution due to poor sensitivity of model outputs with respect to the model states. The amount of regularization is controlled by the regularization parameter, a scalar value multiplied with the so-called regularization term. The choice of the regularization parameter is crucial for the reconstruction process.

In this paper we propose a new method to estimate the regularization parameter, based on a condition-number estimate of the approximated Hessian matrix, which has to be inverted in the case of sequential quadratic programs (e. g. Newton-like methods). The validity of this method will be demonstrated for a capacitance tomography problem, which is solved applying a Gauss-Newton scheme.

Keywords— Capacitance Tomography, Gauss-Newton, Optimization, Regularization

I. Introduction

For obtaining a reasonable solution for a regularized reconstruction problem, it is necessary to find a good choice for the regularization parameter.

There exist several methods to determine this parameter a priori or a posteriori. The only criterion in the class of a priori estimates is the *discrepancy principle*. The idea behind this criterion is that we cannot expect more accuracy in the approximate solution than the one present in the data. This criterion is attributed to Morozov [1].

Two examples for a posteriori regularization parameter estimates are the *generalized cross validation method* [2], with the disadvantage that some involved operators are difficult (and often with a considerable amount of computation time) to obtain, and the *L-curve criterion* ([3] and [4]), which suffers from high computational cost, as well.

For reconstruction problems where the model states may vary in a wide range, like for Capacitance Tomography, where permittivity values to be reconstructed may be the ones of water (ε_r=80), oil (ε_r=2-3) or air (ε_r=1), the value for the reconstruction parameter is depending on the materials involved (a reconstruction parameter that works for oil and air gives very wrong results for water and oil).

In our investigations we found that the condition number of the approximate Hessian for a Gauss-Newton step, which is a function of the Jacobian matrix and of the regularization parameter multiplied with the regularization term, is less sensitive to the materials involved than the regulariza-

tion parameter itself, and, hence is a suitable criterion with minor additional computational cost to determine a value of the regularization parameter, which leads to a reasonable regularized solution.

II. Description of the Method

For the forward problem solution (determine the potentials at floating electrodes from a given permittivity distribution and a given set of active electrodes (with a prescribed potential)) the governing equations to be solved are Gauss' and Faraday's law for the static case leading to a Poisson equation in the interior of the pipe:

$$\nabla \left(\varepsilon \left(\nabla V \right) \right) = 0, \qquad (1)$$

where ε is the spatial dependent electric permittivity ($\varepsilon = \varepsilon_0 \varepsilon_r$, where ε_0 is the permittivity of air and ε_r is the dimensionless relative permittivity) and V is the electric scalar potential. Dirichlet boundary conditions apply at the position of the electrodes, while homogeneous Neumann boundary conditions apply elsewhere on the boundary. The forward problem is solved by means of a finite element approach with linear triangular finite elements.

The inverse problem can be formulated as follows:

$$\varepsilon_r = \arg \min_{\varepsilon_r} \left\{ \|V_m - V_0\|_2^2 + \alpha \|L\varepsilon_r\|_2^2 \right\}, \qquad (2)$$

where V_0 is a vector of measured potentials and α is a regularization parameter in Volts.

The regularization matrix L is a discrete first order operator (approximated with finite differences), where $L(i, j) = -1$ when finite element j is a neighbor of finite element i and zero otherwise; and $L(i, i) = -\sum_j L(i, j)\ i \neq j$. This choice of the regularization matrix incorporates a smoothness assumption about the interior region into the mathematical model.

A Gauss-Newton update step for ε_r for iteration t is given by

$$\varepsilon_r^t = \varepsilon_r^{t-1} + \gamma \delta \varepsilon_r \qquad (3)$$

with

$$\delta \varepsilon_r = \left(J^T J + \alpha L^T L \right)^{-1} \left(-J^T (V_m(\varepsilon_r) - V_0) - \alpha L^T L \varepsilon_r \right) \qquad (4)$$

and γ being a dimensionless scalar value for adjusting stepsizes.

In (4) J denotes the Jacobian of the transformation between permittivity and potentials. The entry in the ith row and j^{th} column equals

$$J_{i,j} = \frac{\partial V_{m,i}}{\partial \varepsilon_{r,j}} \qquad (5)$$

Prior to the iterative process (3)-(4), the following minimization problem is solved for an optimal value α^* :

$$\alpha^* = \arg\min_{\alpha} \left(\left\| cond\left(J^T J + \alpha L^T L \right) - c \right\|_2^2 \right), \quad (6)$$

where $cond(\cdot)$ is the condition number of $(\cdot)$ (the ratio of the largest singular value of $(\cdot)$ to its smallest) and c is an empirically found condition number, which leads to a good value for α and, hence, to a reasonable reconstruction result.

III. Validation of the Method

For testing the above described method three types of material distributions were chosen:
1. pipe filled with 3/4 oil with ε_r=2 and 1/4 air (ε_r=1) (*distribution 1*)
2. pipe filled with 1/2 oil with ε_r=2 and 1/2 air (ε_r=1) (*distribution 2*)
3. pipe filled with water (ε_r=80) with an oil inclusion of ε_r=2 (*distribution 3*)

In Fig. 1 - Fig. 3 the reconstruction results for *distribution 1* - *distribution 3* are reported. All reconstructions were made with $\gamma = 1$ and $c = 5E - 5$.
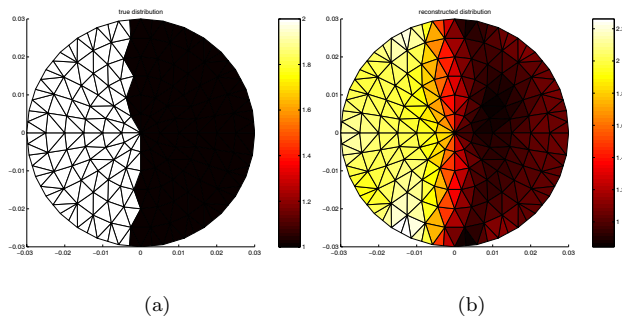
Fig. 1. a) true ε_r distribution (*distribution 1*). b) reconstructed ε_r distribution ($\alpha = 1.2E - 3$)
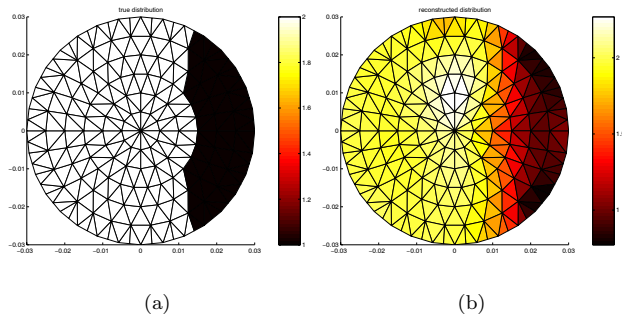
Fig. 2. a) true ε_r distribution (*distribution 1*). b) reconstructed ε_r distribution ($\alpha = 1.2E - 3$)

IV. Conclusions

In this paper a fast and easy to implement method for choosing a good value for the regularization parameter was
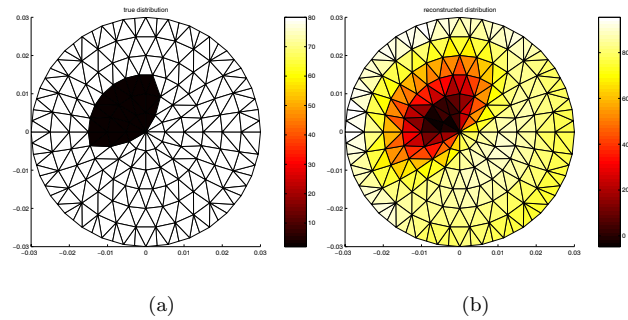
Fig. 3. a) true ε_r distribution (*distribution 1*). b) reconstructed ε_r distribution ($\alpha = 6.7E - 9$)

proposed. The novel method is based on fitting the condition number of the Gauss-Newton system matrix (which is an approximate for the Hessian) to an empirically found value, which is almost insensitive to materials involved (different to the regularization parameter). For the reconstruction of *distribution 1* and of *distribution 2* a value of the regularization parameter of $1.2E - 3$ is suitable, while reconstruction of *distribution 3* with this parameter fails (here $\alpha = 6.7E - 9$ for a good reconstruction). All distributions could be reconstructed with $c = 5E - 5$.

A detailed analysis of the new method will be given in the full paper.

References

[1] V. A. Morozov, *Methods for solving incorrectly posed problems*, Springer, New York, 1984
[2] G. H. Golub, M. T. Heath, and G. Wahba, 'Generalized cross-validation as a method for choosing a good Ridge parameter', *Technometrics*, 21(2), 215-223, 1979
[3] P. C. Hansen, 'Analysis of discrete ill-posed problems by means of the L-curve', *SIAM Review*, 34(4), 561-580, 1992
[4] P. C. Hansen and D. P. O'Leary,'The use of the L-curve in the regularization of discrete ill-posed problems', *SIAM J. Sci. Comput.* , 14(6), 1487-1503, 1993

Topology-Based Inequalities and Inverse Problems for Near Force-Free Magnetic Fields

P. Robert Kotiuga

Department of Electrical and Computer Engineering

Boston University

8 Saint Mary Street, Boston, MA 02215

Email: prk@bu.edu

Abstract— We review a conjecture characterizing the knotting of current paths arising as solutions to an inverse problem involving near force-free magnetic fields. Results about the nonexistence of solutions involving force-free fields supported in a finite domain are then considered, as are explicit constructions of force-free solutions in unbounded domains. This shows why truncating solutions defined on unbounded domains has proven ineffective in the literature, and why the solution to the inverse problem involves a "near force-free magnetic field". Solutions are then characterized by inequalities involving the current distribution's mean asymptotic linking and crossing numbers.

I. INTRODUCTION

Consider the inverse problem of creating an intense magnetic field in a current-free region of space, by currents exterior to the region, with the additional constraint that the Lorentz force in the current carrying region is minimized. If the currents are confined to conductors, the force constraint can be accommodated by twisting conductors in a specific manner [9][10][11]. The resulting knotted conductors resemble nested torus knots. In general, there is a conjecture characterizing the nature of the knotting of the conductors in terms of Thurston and Alexander norms on the cohomology class of the magnetic field intensity vector **H** in the region of space exterior to the conductors [5]. The purpose of this paper is to step back from algebraic characterizations of the knotting of the current paths, and to consider inequalities relating measures of self-force, stored energy, and power dissipation, to topological measures of knotting expressible in terms of the current distribution and the resulting magnetic field. These topological measures amount to the mean asymptotic crossing and linking numbers of the magnetic field [1][2][3][8] [12][13][14].

II. ON THE POSSIBILITY OF FORCE-FREE FIELDS

Theorems asserting the nonexistence of equilibria in electromagnetic systems have a long history. An early well-known result is Earnshaw's theorem which states that that a system of charged conductors, subject only to electrical forces, cannot be in stable equilibrium [15]. Similar results hold for magnetic systems. In astrophysics, the Maxwell stress tensor and the virial theorem are used to show that stars cannot be in a stable equilibrium under magnetic and gravitational forces alone. Hence, it seems unwise to assert that the inverse problem mentioned above has a solution involving a force-free magnetic field.

On the other hand, there is a large literature on force-free magnetic fields. The starting point is an integration by parts formula which reveals that the curl operator is formally self-adjoint. The finite energy eigenfunctions [4] of the curl operator then satisfy:

$$\text{curl}\,\mathbf{H} = \lambda \mathbf{H} \tag{1}$$

In the absence of displacement currents, a force-free magnetic field can then be seen to result from Ampere's law:

$$\mathbf{J} \times \mathbf{B} = (\text{curl}\,\mathbf{H}) \times \mu \mathbf{H} = \lambda\mu(\mathbf{H} \times \mathbf{H}) = 0 \tag{2}$$

Unfortunately, these force-free fields cannot be superimposed since the Lorentz force law is quadratic. Furthermore, since these eigenfunctions are analytic, there is no way to truncate the eigenfunctions to find force-free currents generated by compactly supported currents [16]. Returning to our inverse problem, we make the following definition of a near force-free magnetic field.

> **Definition** Let V be the set theoretic intersection of the supports of the current density **J** and its associated magnetic field **B**. A *near force-free field* is a magnetic field **B** satisfying:
> 1) V is connected.
> 2) $|\mathbf{J}|^2|\mathbf{B}|^2 > |\mathbf{J} \times \mathbf{B}|^2$ throughout V.

The crucial point in the definition is that we have a strict inequality throughout the connected set V.

III. NEAR FORCE-FREE FIELDS

Armed with the above refinement of the notion of a force-free field, and inspired by the trigonometric identity $1 = \sin^2\theta + \cos^2\theta$, we write:

$$|\mathbf{J}|^2|\mathbf{B}|^2 = |\mathbf{J} \times \mathbf{B}|^2 + (\mathbf{J} \cdot \mathbf{B})^2 \tag{3}$$

When the simplest constitutive laws for Ohmic conductors are used, in the absence of displacement current, this becomes:

$$\sigma\mu(\mathbf{J} \cdot \mathbf{E})(\mathbf{B} \cdot \mathbf{H}) = |\mathbf{J} \times \mathbf{B}|^2 + \mu^2(\mathbf{H} \cdot \text{curl}\,\mathbf{H})^2 \tag{4}$$

On the right hand side of this equation, we find the densities of Joule heating and magnetic energy, while the first term on the left is the magnitude of the Lorentz force density squared.

Recognizing that the $\mathbf{H} \cdot \mathrm{curl}\,\mathbf{H}$ term represents a twisting of the magnetic field lines, we see that if $\mathbf{B}$ is a near force-free field, then

1) $\mathbf{H} \cdot \mathrm{curl}\,\mathbf{H}$ is nonzero in V and
2) $\mathbf{H} \cdot \mathrm{curl}\,\mathbf{H}$ cannot change sign in V.

This observation is very useful if we integrate Equation (4) over V, and look at the topological consequences of having a near force-free field.

The first step in relating Equation (4) to global topological results is to integrate the integrand (4) over V and use the identity

$$\int_V (\mathbf{H} \cdot \mathbf{J})^2 = \int_V (\mathbf{H} \cdot \mathbf{J} - \overline{\mathbf{H} \cdot \mathbf{J}})^2 dV + (\overline{\mathbf{H} \cdot \mathbf{J}})^2 \int_V dV \quad (5)$$

where

$$\overline{\mathbf{H} \cdot \mathbf{J}} = \frac{\int_V \mathbf{H} \cdot \mathbf{J}\, dV}{\int_V dV}$$

is the current helicity normalized by the volume of V. Equation (5) relates the integral of the last term in (4) to the current helicity. The next step is to bound the magnitude of the helicity above and below by well understood topological invariants. This exposes the trade-off between power dissipation weighted by energy density, Lorentz force, and topology.

IV. The inequalities

Recall the Biot-Savart Integral

$$\mathbf{H}(\mathbf{r}) = \frac{1}{4\pi} \int_{U'} \frac{(\mathbf{r} - \mathbf{r}') \times \mathbf{J}(\mathbf{r}')}{|\mathbf{r} - \mathbf{r}'|^3} dV' \quad (6)$$

where U' is the support of $\mathbf{J}(\mathbf{r}')$. Two sided bounds on the current helicity are immediate once one considers the three integrals:

$$
\begin{aligned}
I &= \left| \int_U \mathbf{H}(\mathbf{r}) \cdot \mathbf{J}(\mathbf{r}) dV \right| \\
&= \frac{1}{4\pi} \left| \int_U \int_{U'} \frac{\mathbf{J}(\mathbf{r}) \cdot ((\mathbf{r} - \mathbf{r}') \times \mathbf{J}(\mathbf{r}'))}{|\mathbf{r} - \mathbf{r}|^3} dV' dV \right|
\end{aligned}
$$

$$
\begin{aligned}
II &= \int_U |\mathbf{H}(\mathbf{r}) \cdot \mathbf{J}(\mathbf{r})|\, dV \\
&= \frac{1}{4\pi} \int_U \left| \int_{U'} \frac{\mathbf{J}(\mathbf{r}) \cdot ((\mathbf{r} - \mathbf{r}') \times \mathbf{J}(\mathbf{r}'))}{|\mathbf{r} - \mathbf{r}|^3} dV' \right| dV
\end{aligned}
$$

$$
III = \frac{1}{4\pi} \int_U \int_{U'} \left| \frac{\mathbf{J}(\mathbf{r}) \cdot ((\mathbf{r} - \mathbf{r}') \times \mathbf{J}(\mathbf{r}'))}{|\mathbf{r} - \mathbf{r}|^3} \right| dV' dV
$$

where the third integral cannot be expressed in terms of $\mathbf{H}(\mathbf{r})$. Immediately, we have the inequalities:

$$III \geq II \geq I \quad (7)$$

and the following observations:

1) If $\mathbf{H}$ is nearly force-free, then $I = II$.
2) Integral I is the magnitude of the asymptotic linking number of Arnold [1][2][13].
3) Integral III is the mean asymptotic crossing number of Freedman [8][12].

4) The magnitude of the current helicity is bounded below by the magnitude of the mean asymptotic linking number and above by the mean asymptotic crossing number.

The trade-offs coming as a consequence of these observations will be taken up in the extended paper. Surprisingly, they point to the importance of considering Hall voltages and the electric field. This is also important for having a consistent formulation for numerical simulations.

V. Conclusion

Trade-offs between weighted power dissipation, forces on conductors, and topological invariants are articulated by means of inequalities. This exposes the three dimensional nature of high field magnet design when mechanical constraints are incorporated.

References

[1] V.I. Arnold, "The asymptotic Hopf invariant and its applications," *Selecta Mathematica Sovietica*, 5(4), (1986), 327–345.
[2] V.I. Arnold and B.A. Khesin, *Topological Methods in Hydrodynamics*, New York: Springer-Verlag, 1998, Chapter 3.
[3] M.R. Brown, R.C. Canfield, and A.A. Pevtsov editors, *Magnetic Helicity in Space and Laboratory Plasmas*, Washington D.C.: AGU, 1999, pp. 1–9, 17–24, 141–148.
[4] S. Chandrasekhar and P.C. Kendall, "On force-free magnetic fields," *The Astrophysical Journal*, 126, (1957), 457–460.
[5] J.C., Crager and P.R. Kotiuga, "Cuts for the Magnetic Scalar Potential in Knotted Geometries and Force-Free Magnetic Fields," *IEEE Transactions on Magnetics*, MAG-38, (2), March 2002, pp 1309–1312.
[6] Y.M. Eliashberg and W.P. Thurston, *Confoliations*, University Lecture Series, Vol.13, Providence, R.I.: Amer. Math. Soc., 1998.
[7] P.W. Gross and P.R. Kotiuga, *Electromagnetic Theory and Computation: A Topological Approach.* In preparation for the MSRI Monograph series; Cambridge: University Press.
[8] M.H. Freedman and Z.-X. He, "Divergence-Free Fields: Energy and Asymptotic crossing number," *Annals of Math.*, 134(1991), 189–229.
[9] H.P. Furth and R.W. Waniek, "Production and use of high transient magnetic fields I," *The Review of Scientific Instruments,* 27(4), (1956), 195–203.
[10] H.P. Furth and R.W. Waniek, "Production and use of high transient magnetic fields II," *The Review of Scientific Instruments,* 28(11), (1957), 949–958.
[11] H.P. Furth, S.C. Jardin , and D.B. Montgomery, "Force-Free Coil Principles Applied to High-Temperature Superconducting Materials, *IEEE Transactions on Magnetics,* MAG-24,(2), March 1988 1467–1468. *Journal of Applied Physics*," 61(8), April 1987, pp. 3916–3918.
[12] J. Cantarella, R. Kusner, and J.M. Sullivan, "On the Minimum Ropelength of Knots and Links," arXiv:math.GT/0103224 v3 1 Mar 2002 [Online]. Available: http://xxx.lanl.gov/math/archive/
[13] G. E. Marsh, "Topology in Electromagnetics," *Frontiers in Electromagnetics,* New Jersey: IEEE Press, 2000, Chapter 6.
[14] H. K.Moffatt, *Magnetic Field Generation in Electrically Conducting Fluids,*, Cambridge: University Press, 1978.
[15] J. A. Stratton, "*Electromagnetic Theory,* New York: McGraw-Hill, 1941, p.116.
[16] J. Van Bladel, "Some remarks on force-free coils," *Nuclear instruments and Methods,* 16,(1962), 101–112.

An efficient preconditioner for linear systems issued from the Finite Element Method for scattering problems

Ronan Perrussel[(1)], Laurent Nicolas[(2)], François Musy[(1)],

[(1)] MAPLY, UMR CNRS 5585,
Ecole Centrale de Lyon
69134 Ecully Cedex, France
Francois.Musy@ec-lyon.fr

[(2)] CEGELY, UMR CNRS 5005,
Ecole Centrale de Lyon
69134 Ecully Cedex, France
Laurent.Nicolas@eea.ec-lyon.fr

Abstract – **An efficient preconditioner for systems issued from the finite element discretization of time harmonic Maxwell's equations with absorbing boundary conditions is presented. It is based on the Helmholtz decomposition of the electromagnetic field. It is compared to "classical" preconditionners on both simple and realistic problems.**

INTRODUCTION

Electromagnetic scattering problems are classically modeled using time harmonic Maxwell's equations with Silver-Müller conditions. The numerical solution of these equations leads to complex and symmetric matrices [1]. To solve these systems, Krylov subspace methods may be used: BiCGCR [2], symmetric QMR [3] or COCG [4]. Classical preconditioning methods are implemented in order to accelerate the convergence of these iterative algorithms: SSOR, incomplete Cholesky factorization [5], ... An efficient preconditionner based on the Helmholtz decomposition has been previously proposed for simple eddy currents problems [6]. The objective of this paper is to show its efficiency for realistic scattering problems.

PROBLEM FORMULATION

This work deals with time harmonic Maxwell's equations with Silver-Müller conditions. These equations and propagation condition entails the following weak formulation on the domain Ω (in electric field **E** here):
Find **E** in $\mathbf{H}_{\Gamma_d}(\mathrm{curl},\Omega)$ with:

$$\int_\Omega \mathrm{curl}\,\mathbf{E}\cdot\mathrm{curl}\,\mathbf{E}' + i\|\mathbf{k}\|\int_{\Gamma_a}\mathbf{E}\times\mathbf{n}\cdot\mathbf{E}'\times\mathbf{n} - \omega^2\int_\Omega\varepsilon\mu\,\mathbf{E}\cdot\mathbf{E}'$$
$$= -i\omega\int_\Omega\mu\,\mathbf{J}_d\cdot\mathbf{E}', \quad (1)$$

$$\forall\mathbf{E}'\in\mathbf{H}_{\Gamma_d}(\mathrm{curl},\Omega)$$

where ω denotes the wave pulsation, **k** the wave vector, **n** the boundary normal, μ the permeability, ε the permitivity, $\mathbf{J}_d$ the source current density, Γ_a the absorbing boundary, Γ_d the perfect electric conductor boundary (**E**×**n** = 0 on Γ_d). The formulation space of the problem is defined as:
$\mathbf{H}_{\Gamma_d}(\mathrm{curl},\Omega) = \{\zeta\in\mathbf{H}(\mathrm{curl},\Omega),\zeta\times\mathbf{n} = 0\,\mathrm{on}\,\Gamma_d\}$.

Incomplete first order edge elements [7] are used for discretization, leading to the linear system $Ax = b$. A is not hermitian definite positive but is symmetric. These characteristics are essential for the choice of solving methods.

AN EFFICIENT PRECONDITIONER

Following the Helmholtz decomposition, electric field E or magnetic field H can be decomposed into two components [7]:

$$\mathbf{E} = \mathbf{E_s} \oplus \mathrm{grad}\,\phi \quad (2)$$

where:
- grad ϕ is a "static" component with a scalar potential ϕ. It belongs to the kernel of the curl operator.
- $\mathbf{E_s}$ is a "propagation" component called solenoidal component.

In [8], it is underlined that the behaviour of the "curl curl" operator is not the same on these two parts. The existence of the scalar potential ϕ indicates that a secondary problem with "$\Delta\phi$" can be considered. SSOR preconditioner has been shown to be efficient to solve this secondary problem. Moreover, in the discrete setting, the connection between first order nodal elements (space N_h) and first incomplete order edge elements (space $\mathbf{Q_h}$) enables to define a transfer operator $P : N_h \to \mathbf{Q_h}$. The matrix for the scalar potential problem is then assembled by Galerkin product: $A_\phi = P^T A P$ where A is the edge elements matrix.

The algorithm of the preconditioning method is classical for the A matrix and takes into account the second matrix A_ϕ by specifically dealing with the scalar potential component (Fig. 1).

1. $x_n \leftarrow 0, x_\phi \leftarrow 0$
2. k **descents** with Gauss-Seidel algorithm on $A_\phi x_\phi = P^T r_n$
3. $x_n \leftarrow x_n + Px_\phi$
4. 1 **descent and ascent** with Gauss-Seidel algorithm on $Ax_n = r_n$
5. $x_\phi \leftarrow 0$
6. k **ascents** with Gauss-Seidel algorithm on $A_\phi x_\phi = P^T(r_n - Ax_n)$
7. $x_n \leftarrow x_n + Px_\phi$

Fig. 1. One iteration of the preconditioning algorithm using the Helmholtz decomposition. Generally, k=1 or 2.

NUMERICAL RESULTS AND CONCLUSION

To compare this new preconditionner to more "classical" ones, two kinds of problems are considered.

First, a plane wave scattered by a 3D cylinder is studied. From Fig. 2, it is shown that the number of iterations evolves with the number of degrees of freedom (dof.) for the four implemented solving methods: 3 solvers (COCG, BiCGCR, QMR) with SSOR preconditioning, and a COCG solver with the Helmholtz decomposition preconditioner. Table I gives the corresponding CPU times. The new preconditioner needs roughly three time less iterations and twice less CPU time. In addition, COCG is here the fastest solver with SSOR preconditioning. Consequently; in the following, only the results with a COCG solver are given.
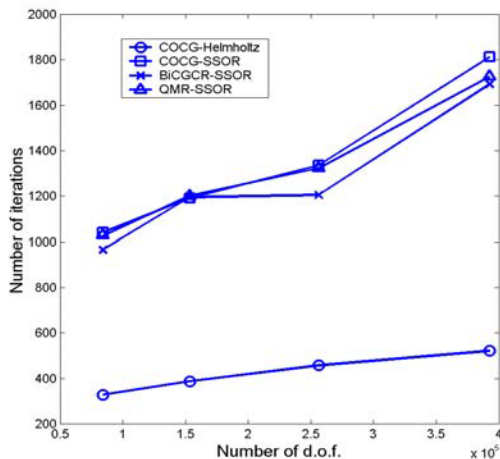
Fig. 2. Increase of the number of iterations with the number of dof.

TABLE I. COMPARISON OF CPU TIME (S) FOR THE 3D CYLINDER.

Number of dof	84 385	153 293	256 121	392 524
QMR – SSOR	2215	5341	9807	19735
COCG – SSOR	1862	4433	8408	17175
BiCGCR – SSOR	2395	5214	10364	22264
COCG – Helmholtz	1111	2317	4455	7992

Different kinds of materials for the cylinder are tested. The difficulty in the indefinite case ($\exists u \neq 0$, $\vec{u}^t A u = 0$) with the lossless cylinder is highlighted (Table II). The efficiency of the new preconditioner is kept in every case.

TABLE II. CPU TIME (S) AND ITERATIONS FOR DIFFERENT CYLINDERS: PERFECT ELECTRIC CONDUCTOR (PEC), LOSSLESS AND LOSSY DIELECTRIC.

Problems	PEC	Lossless diel.	Lossy diel
Number of d.o.f.	34 553	35 713	35 713
COCG – SSOR			
Number of iterations	713	939	790
CPU time (s)	500	731	695
COCG – Helmholtz			
Number of iterations	217	246	216
CPU time (s)	289	364	295

Efficiency of the Helmholtz decomposition preconditioner is observed on two realistic problems: hyperthermia (Fig. 3) and airplane illuminated by a plane wave (Fig. 4). The new preconditioner is interesting in both cases (Table III), and more particularly for the hyperthermia problem.
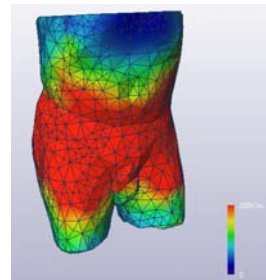
Fig. 3. Hyperthermia RF (27 MHz) for treating deep tumours.
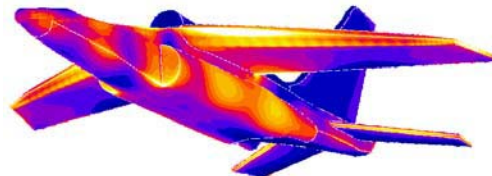
Fig. 4. Illumination of a plane by a 100 MHz plane wave.

TABLE III. CPU TIME (S) AND ITERATIONS FOR TWO REALISTIC PROBLEMS.

Type of problem	Hyperthermia	Plane
Number of dof	202 701	574 151
COCG – SSOR		
Number of iterations	Not convergent after	2890
CPU time (s)	8000 iterations	40096
COCG – Helmholtz		
Number of iterations	474	1210
CPU time (s)	3362	26320

CONCLUSION

A preconditioner based on the Helmholtz decomposition has been developed for scattering problems. This method is efficient because well adapted to the property of the "curl curl" operator. Furthermore it is simple to implement.

REFERENCES

[1] C. Vollaire and L. Nicolas, "Implementation of a finite element and absorbing boundary conditions package on a parallel shared memory computer," *IEEE Trans. On Magn.*, vol. 34, No. 5, pp. 3343-3346, September 1998.
[2] M. Clemens and T. Weiland, "Iterative Methods for the Solution of Very Large Complex Symmetric Linear Systems of Equations in Electrodynamics," *IEEE Trans. On Magn.*, vol. 34, No. 5, pp. 3335-3338, September 1998.
[3] R. W. Freund, G.H. Golub and N. M. Nachtigal, "Iterative solution of linear systems", *Acta Numerica*, vol. 1, pp. 57-100, 1992.
[4] H. A. Van der Vorst and J. B. Melissen, "A Petrov-Galerkin type method for solving $Ax=b$, where A is symmetric complex," *IEEE Trans. On Magn.*, vol. 26, No. 2, pp. 706-708, 1990.
[5] G. Meurant, "Computer Solution of Large Linear Systems", Elsevier Science B.V., Amsterdam, The Netherlands, 1999
[6] R. Beck, "Algebraic Multigrid by Components Splitting for Edge Elements on Simplicial Triangulations", *Technical Report, Konrad-Zuse-Zentrum*, 1999.
[7] J. C. Nédélec, "Mixed finite elements in R^3," *Num. Math.*, vol. 35, No. 3, pp. 315-341, 1980.
[8] R. Hiptmair, "Multigrid method for Maxwell's equations", *SIAM J. Numer. Anal.*, vol. 36, pp. 204-225, 1999.

A Clustering Algorithm for Multi-Level Fast Multipole Methods

K. Barakat and J. P. Webb

Department of Electrical and Computer Engineering
McGill University, 3480 University Street
Montreal, H3A 2A7, Canada
Khalil.Barakat@elf.mcgill.ca

Abstract–The Multi-Level Fast Multipole Method (MLFMM) speeds up the matrix-vector multiply in the iterative solution of the matrix equation arising in the Boundary Element Method. It makes use of a spatial hierarchy of the elements: elements are arranged into groups, and those groups are arranged into higher-level groups, and so on. Ideally, the groups should be widely separated clusters. If the clustering is not adequate, the MLFMM may perform no better than direct matrix-vector multiplication. An efficient clustering algorithm is proposed. It is applied to scattering of electromagnetic waves from buildings at cell-phone frequencies.

Fig. 1. Illustration of FMM grouping, with two of the four groups indicated. Element numbers are in bold.

Fig. 2. Two-level FMM tree

INTRODUCTION

The Multi-Level Fast Multipole Method (MLFMM) is a technique for reducing the time taken to solve field problems by the Boundary Element Method (BEM), and has been widely applied in electromagnetics. The BEM reduces the field problem to:

$$[A]\{x\} = \{b\} \qquad (1)$$

where $\{x\}$ is the unknown vector of size N, $\{b\}$ is a known N-vector, and $[A]$ is a known square matrix [1,2]. Equation (1) may be solved iteratively in $O(N)$ iterations. Normally, the computational cost per iteration is $O(N^2)$. However, The MLFMM makes use of a geometrical hierarchical clustering of the boundary elements to reformulate the $[A]\{x\}$ product such that this cost reduces to $O(N \ln(N))$ instead.

Assume for simplicity that each element gives rise to one unknown in $\{x\}$ (as it commonly does). Then (1) corresponds to N elements. Suppose that these are combined into S groups each containing T_s elements. Let C_s be the center of the sth group, defined, for example, as the center of the smallest rectangular box in which the T_s elements can be inscribed. A group diameter may also be defined, e.g., as the length of a diagonal of this rectangle. Fig. 1. illustrates this grouping scheme for a simple N=8 case in 2D. A multi-level hierarchical tree is obtained by combining groups themselves, shown in Fig. 2. for a two-level structure.

In order for the hierarchical structure to be effective in reducing the computational cost, the groups should be chosen so that any two of them have centers that are sufficiently far apart compared to their diameters, i.e., the groups should, if possible, correspond to well-separated clusters of subgroups or elements. If the clustering is poor, the MLFMM will be only partially effective. Since in general there may be a large number of elements with no particular structure or order, a clustering algorithm (CA) is needed to construct a suitable tree before the MLFMM itself is applied. The algorithm must be carefully designed so that its computational cost is modest in comparison with that of MLFMM. Such an algorithm is the subject of this paper.
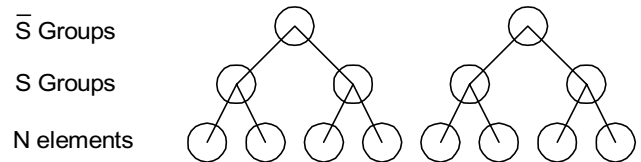
CLUSTERING ALGORITHM

Let the elements be e_i, i=1,...,N. Initially, N groups are defined, each containing one element. The concept is to merge groups that are closest to each other into higher groups in order to maximize the relative distance between the latter. Letting dist(g,h) be a measure of the distance between groups g and h, the algorithm (similar to [3]) is as follows:

0. **Initialize.**
   Set $I = \{1,2,\ldots,N\}$.
   For $i = 1,\ldots,N$:

   Group $g_i = \{e_i\}$.
   $T_{ij} = \text{dist}(g_i, g_j)$, for $j > i$.
   $p_i = \min\limits_{j>i,\ j\in I} T_{ij}$.

   k_i = index j at which minimum occurs.

1. **Merge the two closest groups.**

Find index m such that $p_m \le p_i \ \forall i \in I$.

$g_m = g_m \cup g_{k_m}$ and $g_{k_m} = \varnothing$.

Remove k_m from set I.

2. **Update the distances**.
    For $i \in I$:
        If $i < m$: $T_{im} = \text{dist}(g_i, g_m)$.
        If $i > m$: $T_{mi} = \text{dist}(g_m, g_i)$.
3. **Update the minimum distances**.
    For $i \in I$:
        If $k_i = m$ or $k_i = k_m$ (rare cases):
            $p_i = \min_{j > i, \ j \in I} T_{ij}$.
            k_i = index j at which minimum occurs.
        Otherwise:
            If $i < m$ and $T_{im} < p_i$: $\quad p_i = T_{im}$ and $k_i = m$.
4. **Loop**. If I has only one entry, stop. Otherwise, go to 1.

The initialization is clearly O(N^2). Steps 1 through 4 are performed N-1 times, as the N groups are condensed into one. Step 1-3 are O(N) and step 4 is O(1). Therefore, the overall computational cost is O(N^2), lower than the $O(N^2 \ln(N))$ cost of MLFMM itself.

RESULTS

We have implemented a 2-D MLFMM method in Visual C++ in order to study electromagnetic scattering from perfect conductors at cell-phone frequencies. Fig. 3. shows that its performance is indeed $O(N \ln(N))$ per step. Note that the crossover point at which the MLFMM starts performing better than a direct matrix-vector multiply is for about a thousand elements.
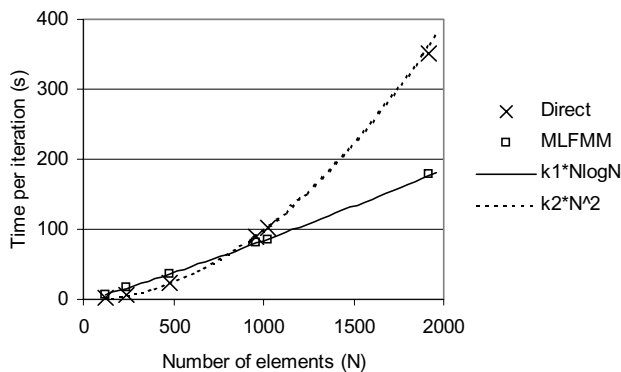
Fig. 3. Simulation times per iteration

To show the importance of an efficient CA, we consider MLFMM implementations with and without the CA using 16384 elements (well above the crossover point). With the total number of elements and the element diameter remaining constant, the first test case has four 40m-side square buildings (16 walls). The elements are input on a wall per wall basis,

but purposefully in such a way that consecutive walls are not geometrical neighbors. In subsequent test cases, the number of buildings (and walls therefore) is multiplied by 4 and the wall size is necessarily divided by 4 as shown in Fig. 4. The last test case has 4096 walls of 4 elements each.
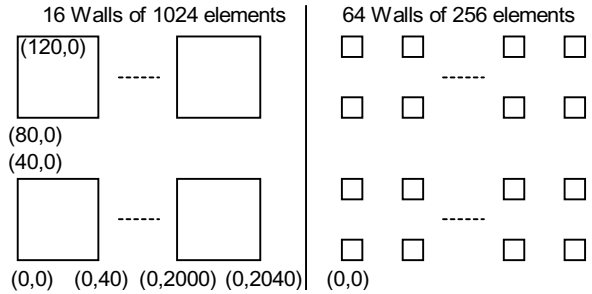
Fig. 4. Test cases with 16 and 64 walls

Since a wall is input as a group, having more walls increases disorder and Fig. 5. shows how the MLFMM implementation without clustering can become very poor and converge towards the direct method.
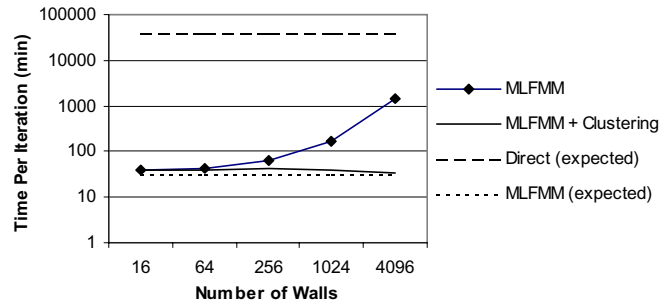
Fig. 5. Importance of Efficient Clustering Algorithm

CONCLUSION

In the absence of a pre-processing stage that constructs a suitable tree structure, the MLFMM may be no more efficient than the direct method. The clustering algorithm presented is an effective yet relatively inexpensive pre-processor.

REFERENCES

[1] Weng Cho Chew, J-M Jin, C-C Lu, E. Michielssen, J M Song, "Fast Solution Methods in Electromagnetics", *IEEE Trans on Antennas and Propagation,* Vol. 45, No 3, pp. 533-543, March 1997.
[2] R. Coifman, V. Rokhlin and S. Wandzura, "The Fast Multipole Method for the Wave Equation: A Pedestrian Prescription", *IEEE Antennas and Propagation Magazine,* Vol. 35, No 3, pp. 7-12, June 1993.
[3] Jung SungYoung, Taek-Soo Kim, "An Agglomerative Hierarchical Clustering using Partial Maximum Array and Incremental Similarity Computation Method", *IEEE International Conference on Data Mining*, November 2001.

Geometric Multigrid Algorithms Using the Conformal Finite Integration Technique

Markus Clemens, Stefan Feigh and Thomas Weiland

Technische Universität Darmstadt, FB 18 Elektrotechnik und Informationstechnik,

Computational Electromagnetics Laboratory (TEMF), Schloßgartenstr. 8, D-64289 Darmstadt, Germany

email: clemens/feigh/weiland@temf.tu-darmstadt.de.

Abstract—**A geometric multigrid algorithm is proposed for the solution of electromagnetic field problem, which uses the mesh independent boundary resolution techniques of the Conformal Finite Integration Technique (CFIT) for the construction of the coarse grid operators. Both an exact and an approximative, merely algebraic construction principle are proposed. A validation of the presented algorithmic approach and first experimental results on the asymptotical complexity of the algorithm are achieved for an electro-static test problem.**

I. INTRODUCTION

The time required for the solution of the algebraic systems of equations arising from the discretization process still dominates the CPU times of most static or low frequency field simulations of computational electromagnetics. For this reason multigrid methods with their superior convergence behavior for very large problems are considered an interesting alternative to preconditioned conjugate gradient such as SSOR-CG or ICCG. The geometric multigrid concept includes the process of smoothing error components, i.e., solving approximately a defect equation using a stationary iterative solution scheme on a sequence of $l + 1$ ever coarser, possibly nested, grid levels L_{h_i} with grid resolutions $h_i, i = 0, \ldots, l$, of the problem [1]. Typically, the number of degrees of freedom on the coarsest grid level L_{h_0} is small enough to use a direct solution method at negligible additional computational costs. In this paper we propose a new combination of a geometric multigrid formulation and the mesh independent discretization scheme for Maxwell's equations, the Conformal Finite Integration Technique (CFIT).

II. CONFORMAL FINITE INTEGRATION TECHNIQUE

The Finite Integration Technique (FIT) transforms the Maxwell equations in their integral form into a set of matrix equations on a dual grid pair $\{G, \widetilde{G}\}$ [2]. In the resulting so-called Maxwell-Grid-Equations (MGE)

$$
\begin{aligned}
\mathbf{C}\widehat{\mathbf{e}} &= -\frac{d}{dt}\widehat{\widehat{\mathbf{b}}} & \widetilde{\mathbf{C}}\widehat{\mathbf{h}} &= \frac{d}{dt}\widehat{\widehat{\mathbf{d}}} + \widehat{\widehat{\mathbf{j}}} \\
\mathbf{S}\widehat{\widehat{\mathbf{b}}} &= \mathbf{0} & \widetilde{\mathbf{S}}\widehat{\widehat{\mathbf{d}}} &= \mathbf{q}
\end{aligned}
, \qquad (1)
$$

the vectors $\widehat{\mathbf{e}}$ and $\widehat{\mathbf{h}}$ contain electric and magnetic grid voltages as components and $\widehat{\widehat{\mathbf{j}}}, \widehat{\widehat{\mathbf{d}}}$ and $\widehat{\widehat{\mathbf{b}}}$ are vectors of electric and magnetic facet fluxes. The discrete rotation matrices $\mathbf{C}, \widetilde{\mathbf{C}}$, the divergence matrices $\mathbf{S}, \widetilde{\mathbf{S}}$ and the gradient matrices $\mathbf{S}^T, \widetilde{\mathbf{S}}^T$ contain information about grid incidence relations of G and $\widetilde{G}$. The approximation of this method is contained in the construction of

the discrete constitutive material equations

$$
\widehat{\widehat{\mathbf{d}}} = \mathbf{M}_\varepsilon \widehat{\mathbf{e}} + \widehat{\mathbf{p}}, \quad \widehat{\widehat{\mathbf{j}}} = \mathbf{M}_\sigma \widehat{\mathbf{e}}, \quad \widehat{\mathbf{h}} = \mathbf{M}_\nu \widehat{\widehat{\mathbf{b}}} + \widehat{\mathbf{m}}, \qquad (2)
$$

featuring the so-called material matrices: $\mathbf{M}_\varepsilon$ for the permittivities, $\mathbf{M}_\sigma$ for the conductivities and $\mathbf{M}_\nu$ for the reluctivities, whereas $\widehat{\mathbf{p}}$ and $\widehat{\mathbf{m}}$ arise from permanent electric and magnetic polarisations. For orthogonal grids, the construction of the equation $\widehat{\widehat{\mathbf{d}}} = \mathbf{M}_\varepsilon \widehat{\mathbf{e}}$ in (2) involves the one-to-one coupling of an electrical grid voltage $\widehat{\mathbf{e}}_i$ along a grid edge $L_i \in G$ with the corresponding flux $\widehat{\widehat{\mathbf{d}}}_i$ through the dual facet $\tilde{A}_i \in \widetilde{G}$, which is intersected perpendicularly by L_i. In the classical FIT this includes an averaging process for the permittivity $\bar{\varepsilon}_i$ over the cell subvolumes of G cut by the dual facet $\tilde{A}_i$, such that

$$
\widehat{\widehat{\mathbf{d}}}_i = \{\mathbf{M}_\varepsilon\}_{i,i}\widehat{\mathbf{e}}_i := \bar{\varepsilon}_i \frac{|\tilde{A}_i|}{|L_i|} \, \widehat{\mathbf{e}}_i \approx \frac{\int_{\tilde{A}_i} \varepsilon(\vec{r}) \, \vec{n} \cdot d\vec{A}}{\int_{L_i} \vec{\tau} \cdot d\vec{s}} \, \widehat{\mathbf{e}}_i \qquad (3)
$$

holds, where $\vec{n}$ and $\vec{\tau}$ denote the unit outer normal vector on $\tilde{A}_i$ and the unit tangent vector along the edge L_i, respectively. The resulting matrix $\mathbf{M}_\varepsilon = \mathbf{D}_{\tilde{A}}\mathbf{D}_{\bar{\varepsilon}}\mathbf{D}_L^{-1}$ of (3) with the matrices of dual facet areas $\mathbf{M}_{\tilde{A}}$, of edge lengths $\mathbf{D}_L$ and of averaged dual facet permittivities $\mathbf{D}_{\bar{\varepsilon}}$ is diagonal.

Recent publications on geometric discretization methods for Maxwell's equations show, that the the lowest order Whitney-Finite Element formulations can be derived in the form of (1), the main difference lying in the construction principle of the material matrices [3]. The introduction of the Conformal Finite Integration Technique (CFIT), first proposed in [4], [5] for high frequency formulations and introduced to quasistatic formulations in [6] is based on the same construction principle (3). The exact evaluation of the integral for the material parameters on the dual grid facets $\tilde{A}_i$ allows to consider curved material interfaces and shape boundaries inside the cells of G during the discretization process while still using an orthogonal grid. With the CFIT method a grid mesh can be set-up independently of the shape contours of the problem, i.e., the mesh only describes the location of the field components, but no longer the material distribution of the problem.

III. GEOMETRIC MULTIGRID METHOD USING CFIT

The construction of a coarser grid level $L_{h_{i+1}}$ involves the restriction of the system matrix $\mathbf{A}_{h_i}$ and the restriction of the L_{h_i} grid level defect vector $\mathbf{r}_{h_i}$. For non-structured, nested grids the system matrix is commonly projected using the restriction and prolongation (interpolation) matrices $\mathbf{R}_{h_i}^{h_{i+1}}$ and $\mathbf{P}_{h_{i+1}}^{h_i}$, respectively [1], with $\mathbf{A}_{h_{i+1}} := \mathbf{R}_{h_i}^{h_{i+1}} \mathbf{A}_h \mathbf{P}_{h_{i+1}}^{h_i}$, which involves

1

sparse matrix-matrix multiplications. Different restriction and interpolation operators have to be devised for the degrees of freedom on the primal and dual nodes $N, \tilde{N}$, edges $L, \tilde{L}$, facets $A, \tilde{A}$ and cell volumes $V, \tilde{V}$ in a straightforward way, resulting in the matrix operators for intergrid restrictions $\mathbf{R}_{h_i,X}^{h_{i+1}}$ and interpolation $\mathbf{P}_{h_{i+1},X}^{h_i}$, respectively. The index X intrinsically denotes the objects on which these operators act. For Cartesian tensor-product grids the coarse grid system matrices $\mathbf{A}_{h_{i+1}}$ can be constructed by newly discretizing the problem for each coarser grid resolution. In standard Finite Difference schemes this approach is typically coupled to a decreasing quality of the mesh representation of the original problem. For this task we propose to use CFIT with its mesh resolution independent discretization capabilities. Here for each grid level L_{h_i} the construction of the system matrix

$$\mathbf{A}_{h_{i+1}} := \mathbf{A}(\mathbf{M}_{h_{i+1}}^{\text{CFIT}}) \tag{4}$$

involves only the corresponding grid incidence matrices and the material matrices $\mathbf{M}_{h_i}^{\text{CFIT}}$, respectively. To attain the CFIT material matrices, the repeated use of a CAD model kernel for the exact evaluation of the averaged material parameters in (3) is required. If this repeated use is too time consuming, we can use this approach just for the fine grid CFIT material matrix $\mathbf{M}_{h_0}^{\text{CFIT}}$. Using this information, a material matrix, e.g. $\mathbf{M}_\varepsilon$, can be constructed algebraically for coarser grid resolutions $h_{i+1}, i \geq 0$, with

$$\mathbf{M}_{\varepsilon\,h_{i+1}}^{\text{CFIT}} =: \Big(\prod_{j=0}^{i} \mathbf{R}_{h_j,\tilde{A}}^{h_{j+1}}\Big) \mathbf{D}_{\tilde{A},h_0} \mathbf{D}_{\bar{\varepsilon},h_0} \Big(\prod_{j=0}^{i} \mathbf{R}_{h_j,L}^{h_{j+1}} \mathbf{D}_{L,h_0}\Big)^{-1}. \tag{5}$$

which yields a new variant of the FIT, the *Algebraic Conformal FIT* (ACFIT), which can be also used starting from fine grid resolutions with the classical FIT.

IV. NUMERICAL RESULTS

First numerical results are presented for a three-dimensional test problem consisting of a dielectric ball in a plate condensator field depicted in Fig. 1. For this problem the linear discrete
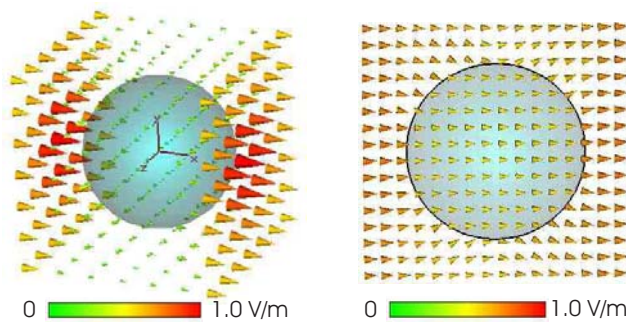

Fig. 1. Dielectric ball ($\varepsilon_r = 4$) in an electrostatic plate condensator field discretized with the Conformal Finite Integration Technique.

Poisson system $\widetilde{\mathbf{S}}\mathbf{M}_\varepsilon^{\text{CFIT}}\widetilde{\mathbf{S}}^T\Phi = 0$ is solved using the proposed algebraic CFIT-MG solution scheme, which requires to apply a stationary iteration method as a smoother to the sequence of defect equations

$$\widetilde{\mathbf{S}}_{h_{i+1}} \mathbf{M}_{\varepsilon,h_{i+1}}^{\text{CFIT}} \widetilde{\mathbf{S}}_{h_{i+1}}^T \phi_{h_{i+1}} = \mathbf{r}_{h_{i+1}} = \mathbf{R}_{h_i,\tilde{V}}^{h_{i+1}} \mathbf{r}_{h_i} \tag{6}$$
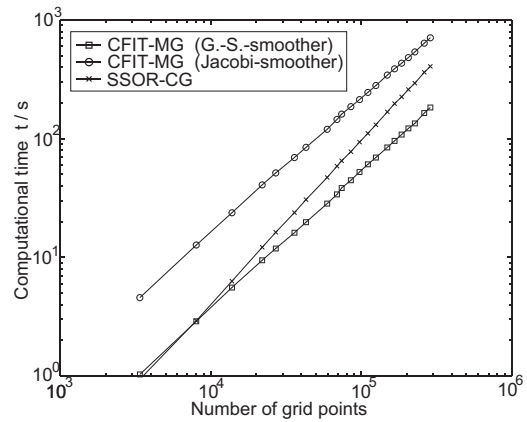
Fig. 2. Asymptotical complexity studies for the algebraic CFIT-MG schemes with Jacobi-/Gauss-Seidel-smoother and an SSOR-preconditioned conjugate gradient scheme (SSOR-CG) for the test problem of Fig. 1

at the each grid level L_{h_i}. In Fig. 2 results of numerical tests performed with a MATLAB implementation are presented. Here, the ACFIT multigrid scheme, using either Jacobi- or Gauss-Seidel-smoothers [1], is compared to a SSOR-preconditioned conjugate gradient method. The iterative processes are terminated if a final relative residual norm accuracy $\epsilon = 10^{-6}$ is reached. The arithmetical work of the SSOR-CG scheme grows approximately similar as $O(N^{1.4})$ for an increasing number of grid points $(N \to \infty)$. Both the CFIT-MG schemes, however, also do not reach the theoretically expected optimal asymptotical complexity $O(N^{1.0})$ in the $\log - \log$-plot in Fig. 2. However, the routine for matrix-vector multiplication in MATLAB features the same slope of 1.1 as the CFIT-MG schemes using it, which explains this non-optimal behavior.

V. CONCLUSION

For the solution of linear systems arising from (quasi-)static electromagnetic field problems a geometric multigrid scheme was proposed, which uses the grid independent modeling capabilities of the Conformal Finite Integration Technique. The new approach maintains the separation of the metric-free grid incidence operators and the material matrices also in the framework of multigrid formulations. Numerical tests of a three dimensional electrostatic test problem illustrate the computational efficiency and improved asymptotical complexity of the new CFIT-MG scheme in comparison to a standard SSOR-CG scheme.

REFERENCES

[1] U. Trottenberg, A. Schuller, and C. Oosterlee, *Multigrid*, Academic Press, London, 2000.
[2] T. Weiland, "A discretization method for the solution of Maxwell's equations for six-component fields," *Electronics and Communications AEÜ*, vol. 31, no. 3, pp. 116–120, 1977.
[3] A. Bossavit and L. Kettunen, "Yee-like schemes on staggered cellular grids: A synthesis between FIT and FEM approaches," *IEEE Trans. Magn.*, vol. 36, no. 4, pp. 861–867, 2000.
[4] B. Krietenstein, P. Thoma, R. Schuhmann, and T. Weiland, "Facing the big challenge of high precision field computation," Proc. 19th LINAC Conf., Chicago, August 1998.
[5] W. Yu and R. Mittra, "A conformal finite difference time domain technique for modeling curved dielectric surfaces," *IEEE Microwave and Wireless Comp. Lett.*, vol. 11, no. 1, pp. 25–27, 2001.
[6] M. Clemens and T. Weiland, "Magnetic field simulation using conformal fit formulations," *IEEE Trans. Magn.*, vol. 38, no. 2, pp. 389–392, 2002.

A New Method for Solving Linear Equations with Large Sparse Symmetric and Non-positively Definite Coefficient Matrix

Wang Jinming, Xie Dexin, Yao Yingying

School of Electrical Engineering, Shenyang University of Technology

Shenyang, Liaoning 110023, P.R.CHINA   E-mail:xiebaiy@mail.sy.ln.cn

Abstract

   A new preconditioned solution with two controlling parameters for linear equations with large sparse symmetric and non-positively definite matrix is presented in this paper. Through theoretical analysis, the proper choice of the controlling parameter can make the preconditioned matrix positively definite and approach the unit matrix, and reduce the number of iteration obviously. Numerical examples show that the method can reduce the computation time over 50% than the conventional ICCG method.

INTRODUCTION

   The coefficient matrix of the linear equations which arise from the finite element analysis of eddy-current field problem of electrical devices is generally symmetric and non-positively definite, and the number of variables of the equations has exceeded 100,000. At the present time, the conventional incomplete Choleski-Conjugate Gradient (ICCG0) method has been widely used for the solution of the equations. The ICCG0 method   is based on the coefficient matrix being positively definite, but in practice it has also been used for the equations with non-positively definite coefficient matrix. Even if for positively definite coefficient matrix, the convergence rate of the ICCG0 method is sometime very slow. For example, for the solution of the TEAM Workshop problem 10, it once appears that the iteration number of the ICCG0 method solving the equations with 4000 or so variables was over 7000. For the equations with symmetric and non-positively definite coefficient matrix, if the preconditioned matrix is just positively definite, the ICCG0 method could converge properly, or else it may not converge. For the equations with positively definite coefficient matrix, M.A.Ajiz and A.Jennings [1] proposed a method that forms preconditioned matrix according to the absolute value of the incomplete decomposition elements, but did not give the mathematical theory inference. The authors' previous paper [2] gave a method with a controlling parameter that can reduce the number of non-zero elements of the incomplete decomposition without increasing the number of the CG iterations, however, the mathematical inference it gave only for the equations with positively definite coefficient matrix.

   This paper presents a new preconditioned solution with two controlling parameters for equations with symmetric and non-positively definite matrix. The parameters ε and δ are used for controlling the elements of the incomplete decomposition in correspondence with non-zero or zero elements of original coefficient matrix to be retained or to be ignored respectively. Through theoretical analysis, the proper choice of the controlling parameter can make the preconditioned matrix positively definite and close to the unit matrix, and reduce the number of iteration obviously.

DESCRIPTION OF THE NEW METHOD

   Consider the system of linear equations

$$\mathbf{Ax = b} \qquad (1)$$

which arises from the finite element analysis of eddy-current field problem of electrical devices, where $\mathbf{A}$ is generally a large sparse real symmetric matrix. The main steps of the method presented here are as follows.

Step1

   Implement the incomplete decomposition of matrix $\mathbf{A}$ with the controlling parameters $\varepsilon, \delta \; (\delta \geq \varepsilon)$, i.e. $\mathbf{A} = \mathbf{LDL}^T + \mathbf{E}$, where $\mathbf{LDL}^T$ are the incomplete decomposed factors, $\mathbf{E}$ is the error matrix. Denote $\mathbf{G} = \mathbf{L} + \mathbf{D} - \mathbf{I}$, where $\mathbf{I}$ is unit matrix. The sparsity pattern of $\mathbf{G}$ is not prescribed beforehand, whereas it is based on a tolerance range. Create $\mathbf{G}$ as follows: Calculate the element of $\mathbf{G}$, g_{ij} , given by

$$g_{ij} = \frac{\left(a_{ij} - \sum_{k=1}^{j-1} g_{ik} \; g_{kk} \; g_{jk} \right)}{g_{jj}} , \left(j = 1, 2, \cdots, i \right) \qquad (2)$$

   1) If the element of $\mathbf{A}, a_{ij}$, is equal to zero and $\left| g_{ij} \right| \geq \delta$, then g_{ij} , the element of $\mathbf{G}$, is filled in, or else ignored.

   2) If $a_{ij} \neq 0$ and $\left| g_{ij} \right| < \varepsilon$, g_{ij} is ignored, or else filled in.

Step2

   Transform (1) into

$$\mathbf{C \, y = d} \qquad (3)$$

where $\mathbf{C} = \left(\mathbf{LD}^{1/2} \right)^{-1} \mathbf{A} \left(\mathbf{LD}^{1/2} \right)^{-T}$ is the preconditioned matrix, the elements of $\mathbf{D}^{1/2}$ are positive real number or pure imaginary [1]. Then solve (3) using CG iteration.

Though the element of $\mathbf{D}^{1/2}$ can be pure imaginary, the CG method for solving (3) [3] only use the elements of $\mathbf{D}$, and the complex operation not occurs.

It is obviously that if δ is very large and $\varepsilon = 0$, the method is equivalent to ICCG0 method, and if $\delta = 0$ and $\varepsilon = 0$, it is the complete Choleski decomposition method.

Reference [1] suggested an idea of using the size of the elements of $\mathbf{A}$ ($\mathbf{A}$ being symmetric positive definite matrix) to create the sparsity pattern of $\mathbf{C}$. We adopt the idea for the symmetric but non-positive definite matrix. With the controlling parameter chosen properly, the method proposed can reduce the total computation time of the incomplete decomposition and the CG iteration considerably. According to the basic theory of numerical algebra, the following theorem is deduced in this paper.

Theorem

Let the matrix $\mathbf{A}$ in (1) is symmetric matrix, and the absolute values of the elements of the error matrix $\mathbf{E}$ are all less than δ. Notate $C = \rho((\mathbf{LD}^{1/2})^{-1}\mathbf{E}(\mathbf{LD}^{1/2})^{-T})$. Then when $\delta < (2 * L_{\max} * \left\|A^{-1}\right\|_2)^{-1}$ ($L_{\max}$ is the biggest value of the sum of the non-zero element number for each row of the matrix $\mathbf{LDL}^T$), $\mathbf{C}$ is positive definite matrix, and the asymptotic rate of convergence for solving (3) with CG method is

$$\frac{(\mathbf{C}(y^{(m)} - y^*), y^{(m)} - y^*)^{1/2}}{(\mathbf{C}(y^{(0)} - y^*), y^{(0)} - y^*)^{1/2}} \le 2(\frac{2M}{\sqrt{1+M}+\sqrt{1-M}})^m$$

where y^* is the exact solution for (3), $y^{(m)}$ is the m-th approximate solution. The deduction for this theorem will be given in the extended paper.

NUMERICAL EXAMPLE

As a numerical model, the 3D eddy-current field analysis of a single-phase transformer of 240MVA/500kV is carried out. The governing equation using $\mathbf{A}, \phi - \mathbf{A}$ method is given by

$$\begin{cases} \nabla \times (\nu\nabla \times \mathbf{A}) - \nabla(\nu\nabla \cdot \mathbf{A}) + \sigma\frac{\partial \mathbf{A}}{\partial t} + \sigma\nabla\phi = J_s \\ \nabla \cdot (-\sigma\frac{\partial \mathbf{A}}{\partial t} - \sigma\nabla\phi) = 0 \end{cases} \quad (4)$$

with proper boundary condition. For analysis of the transient eddy current field of the model at one time-step, the orders of real linear equations are 12458, 43518 and 72555, respectively. Fig.1 shows the magnetic field distribution on the symmetric surfaces of the transformer at the time t = 0.0402s. Table1 shows the comparison of the new method with the ICCG0 method. The CPU times in Table I include the incomplete decomposition time and the CG iteration time. For solving the three sets of equations above, the new method with the optimum values, i.e. $\varepsilon \approx 0.00005$, $\delta \approx 0.005$, can reduce the computation time over 50% than the conventional ICCG0 method. Owing to that the diagonal elements of

coefficient matrix are normalized firstly, the recommended values of the controlling parameters have fairly general meaning for 3D electromagnetic field analysis. The recommended values of ε, δ are $0.00001 \le \varepsilon \le 0.001$, $0.001 \le \delta \le 0.01$ respectively.

CONCLUSIONS

A new method for solving linear equations with large sparse symmetric and non-positive definite coefficient matrix in finite element analysis of electromagnetic field problems is presented in the paper. The proper choice of the controlling parameters can reduce the total computation time of the incomplete decomposition and the iteration. over 50% than the conventional ICCG0 method. The recommended values of the controlling parameters have fairly general meaning for 3D electromagnetic field analysis.

TABLE I. COMPARISON OF THE TWO METHOD
(NUMBER OF EQUATIONS = 43518, $\varepsilon = 0.00005$)

Method	δ	Non-zero element	Number of Iteration	CPU Time (s)
ICCG0		1671517	1834	2139
New	0.05	855346	2212	1638
New	0.01	1012789	822	880
New	0.005	1142325	746	892
New	0.001	1904195	394	909
New	0.0005	2357405	206	903
New	0.00025	3087205	109	1056
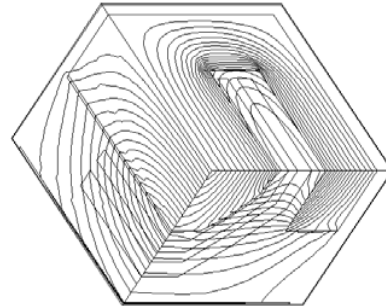
Fig.1 The magnetic field distribution on the symmetric surfaces of a single phase transformer of 240MVA/500kV

REFERENCES

[1] Ajiz M A,Jennings A robust incomplete Cholesky conjugate gradient algorithm.International for numerical methods in engineering, 1984,20:949~9

[2] Wang Jinming,Xie Dexin,Yao Yingying."A Modified solution for large sparse symmetric linear system in electromagnetic field analysis".IEEE Trans.On Mag. Vol.37, No.5, 2001,pp.3494-3497

[3] J. H. Wilkinson. The algebraic eigenvalue problem. Oxford University Press,1965.

Comparison of linear systems solvers on 3-D transient electromagnetic problems

Grégory Vincent[1][2], Marta Costa Bouzo[3], Christophe Guérin[2], Jean-Louis Coulomb[1]

[1]Laboratoire d'Électrotechnique de Grenoble - INPG/UJF-CNRS UMR 5529 ENSIEG,
BP 46, 38402 St Martin d'Hères - France
[2]CEDRAT S.A., 10 Chemin de Pré Carré, 38246 Meylan – France
[3]School of engineering sciences, University of Southampton, S017 1BJ, United Kingdom

Abstract – **The aim of this study is to analyze the effectiveness of linear systems solvers on a well chosen list of 3-D transient electromagnetic problems. This list contains ill-conditioned matrices which are used to compare the solvers robustness. It also contains well-conditioned matrices which are used to compare the time and the memory size taken by each solver.**

The results are disputed and we find that GMRES and Bi-CGStab are more robust than the standard IGBiCG solver. We can also improve computation time by using GMRES or take less memory size by using Bi-CGStab.

INTRODUCTION

The aim of this study is to compare linear systems solvers on different matrices extracted from 3-D transient electromagnetic problems. Those problems are modeled by FLUX3D software which uses the finite element method (FEM). Our criteria to compare the different methods are firstly robustness, and secondly CPU time and memory size taken by the solver.

In the FEM, it is necessary to solve a matrix system. The characteristics of this system depend on material properties which can be linear or non-linear. In the first case, we only solve one linear system, but in the second case, we use an iterative method (for instance the Newton-Raphson method) which solves a linear system at each iteration. The CPU time and the memory size taken by the solving step, which is already important in the first case, become very important in the second case. Also, we must have a solver which is robust, quick and takes small memory size.

First, we will briefly describe the linear systems solvers we used. Second, we will test the robustness of each solver on two electromagnetic problems generating ill-conditioned matrices, that is to say closed to singularity. Finally, we will compare the CPU time and the memory size taken by each solver on various simple problems. Those problems generate well conditioned matrices which enable the solvers to converge.

DESCRIPTION OF THE SOLVERS TESTED

The FEM generates matrices containing a small number of non-zero values, which are called "sparse matrices". In our tests, we use three main iterative methods for this type of matrix.

The first is a coupled solver because it uses "Incomplete Cholesky Conjugate Gradient" (ICCG) [1,2], if the matrix is symmetric and "Incomplete Gauss Bi-Conjugate Gradient" (IGBCG) [3], if the matrix is not symmetric. ICCG is formed by the standard Conjugate Gradient with the LDLT Cholesky preconditioning and IGBiCG is formed by the Bi-Conjugate Gradient with the LDU Gauss preconditioning.

The second solver tested is "Bi-conjugate Gradient Stabilized" (Bi-CGStab), due to Van Der Vorst [4], which uses the ILUT preconditioning.

The last solver is the restarted version of "Generalized Minimum RESidual" (GMRES), due to Y. Saad and M. H. Schultz [5]. It uses the ILUT preconditioning.

OBTAINED RESULTS ON THE ROBUSTNESS TESTS

This part presents two transient electromagnetic problems generating an ill-conditioned matrix. In the first example, the ill-conditioning is caused by the edge element interpolation. In the second example, it is caused by the conductivity properties of the superconductor material. Those two problems are examples where the iterative solvers have difficulties to converge.
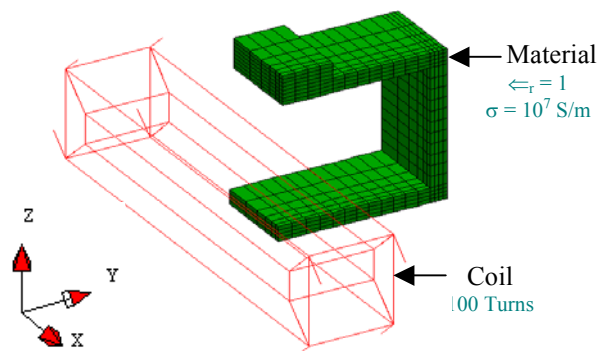

Fig. 1–Description of the first test using the edge elements interpolation

The first problem uses the edge electric vector potential and the tree gauge to assure uniqueness of the solution [6]. The geometry is described on the figure 1. It uses a linear material and a coil supplied with a linear increasing current. There are two symmetry plans : xOz and yOz.

The second problem is showed on the figure 2. It uses the nodal electric vector potential with a superconducting material, which uses the power law :

$$|J| = \frac{|E|}{\dfrac{E_c^{\frac{1}{N}}}{Jc}|E|^{1-\frac{1}{N}} + \dfrac{1}{\sigma_0}}$$

The problem contains also a silver sheet. On each side of this, there are two other superconductor plates. There are three symmetry plans : xOz, yOz and xOy. For those reasons, only one quarter of the geometry is represented.
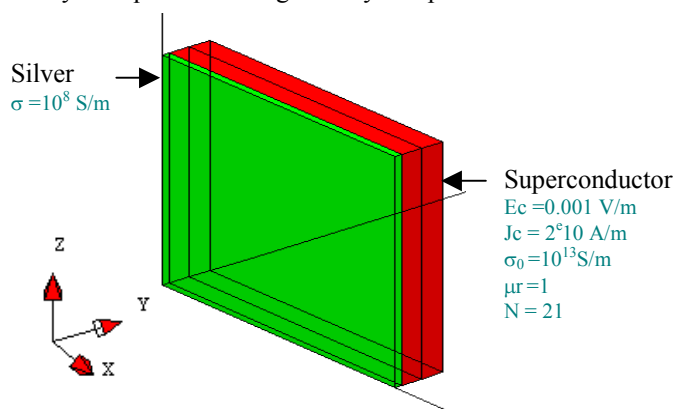

Fig. 2–Description of the second test using superconductor material

For both problems, the coupled solver uses IGBiCG because matrices are not symmetric.

For the case with the edge elements, the matrix of the system to solve has 24 751 lines and 1 036 973 non-zero values. The resolution of the original matrix with IGBiCG does not converge. We need to introduce a rescaling factor, that reduces the differences between the values in the matrix in order for IGBiCG to converge. On the other hand, the Bi-CGStab and GMRES solvers converge without rescaling factor. The obtained results are practically identical to those obtained by using IGBiCG with the rescaling factor.

For the second case, using superconducting material, the matrix to solve has 37 303 lines and 2 579 157 non-zero values. As for the first case, IGBiCG solver does not converge while the two other solvers converge and give the same results.

The results obtained on the two tests show that Bi-CGStab and GMRES solvers seem to be more robust than IGBiCG.

OBTAINED RESULTS ON THE TESTS OF SPEED AND MEMORY SIZE

In this part, we compare the CPU time and the memory size taken by each solver on the first system resolution of the first time step. We use six very simple 3-D transient electromagnetic problems. For example, the first problem represents a cylinder surrounded by a coil supplied with a constant current. The cylinder has linear conductivity and permeability properties.

Those problems generate matrices with a good conditioning and all the solvers converge. The results obtained on the six tests are presented on the table I.

Test	Sym	Time (sec)			Memory place (nb reels/1000)		
		ICCG	GMRES	BCGS	ICCG	GMRES	BCGS
1	N	15	13	19	2 296	3 041	1 633
2	N	6,5	6	7	2 420	3 028	2 275
3	N	7	6	7	1 919	2 403	1 753
4	Y	24	28	26	4 909	9 459	6 515
5	N	52	11	12	2 955	8 042	3 097
6	Y	24	30	36	4 519	9 828	4 379

Table I– Comparative results of ICCG (IGBiCG), GMRES and Bi-CGStab on several electromagnetic problems. The column Sym indicates if the matrix is symmetric or not.

We finally concluded that ICCG takes less time and less memory size for symmetric matrices. For general matrices however, Bi-CGStab uses less memory size whereas GMRES uses less CPU time.

CONCLUSIONS AND PERSPECTIVES

In this paper, we showed results obtained with the solvers ICCG, IGBiCG, GMRES and Bi-CGStab and we compared them. The GMRES and Bi-CGStab solvers are more robust on our 3-D electromagnetic problems and they are also able to improve computation time or to use less memory size on non symmetric matrices.

The two solvers have been tested successfully on transient electromagnetic problems. We can now test them on harmonic problems. It is then necessary to find complex versions of the solvers and to test them on a well-chosen list of harmonic problems.

REFERENCES

[1] Biddlecombe, C., 1980, ICCBCG - A symmetric complex sparse matrix solver. SRC Rutherford Labs. Note CAG/80-14.
[2] D.A.H. Jacobs, Generalisations of the conjugate gradient method for solving non-symmetric and complex systems of algebraic equations, Central Electricity Generating Board, RD/L/N 70/80, August 1980..
[3] K. Fujiwara, T. Nakata and H. Fusayasu " Acceleration of convergence characteristic of ICCG method", IEEE transaction on magnetics, vol 30, no 5, pp. 2877-2880, September 1994.
[4] H.A. Van Der Vorst, Bi-CGSTAB: "A fast and smoothly converging variant of large systems of linear equations", SIAM J. Sci. Statist. Comput., 13 (1992), pp. 631-644.
[5] Y. Saad and M. H. Schultz, GMRES: A generalized minimal residual algorithm for solving nonsymetric linear systems, SIAM J. Sci. Comput. 7 (1986)
[6] N.A. Golias, T.D. Tsiboukis " Magnetostatics with Edge Elements : A Numerical Investigation in the Choice of the Tree", IEEE transaction on magnetics, vol 30, no 5, pp. 2877-2880, September 1994.

Solving Linear FEM Problems Using Hopfield Neural Network

Miklós Kuczmann, Amália Iványi

Abstract-- **The Finite Element Method (FEM) is the most powerful and widely used computational technique to calculate the electromagnetic field quantities in different arrangements. The Hopfield type neural network (HNN) is able to minimize the energy stored in the network; and the system of equations obtained from the weak form of the FEM can be solved by minimizing the energy function of HNN. The HNN can be implemented by hardware as an analogue computational tool. The procedure with some applications and the software simulation of a possible hardware realization are presented in this paper.**

Index Terms-- **Finite Element Method, Hopfield type neural network, electrostatics, magnetostatics.**

I. INTRODUCTION

THE FEM is a widely used technique for the solution of electromagnetic field problems. The inverse of a sparse quadratic matrix must be calculated to obtain the solution, the unknown potential function. The HNN is a recurrent network with feedback from its output to the input of the network. This network can be useful in many ways; they can provide associations or classifications, optimization problem solutions, restoration of patterns and so on. With continuous variables it is useful for the analysis of mathematical programming problems. The structure and main properties of the network, one-, and two-dimensional problems are presented in this paper. Computer simulation of hardware implementation is discussed.

II. THE HOPFIELD TYPE NEURAL NETWORK

The gradient-type HNN is a recurrent, dynamic network, shown in Fig.1 [1-3]. The network consists of N neurons with continuous activation functions $x_i = F_i(v_i)$, where $x_i = x_i(t)$ is the output of the network and

$$v_i = \sum_{j=1}^{N} w_{ij} x_j + b_i \ , \ i = 1,...,N \ . \tag{1}$$

After specifying the weight and bias parameters w_{ij} and b_i (storage phase) the network is ready for operation. The network operates continuously in time during a dynamically stable process (retrieval phase); the output vector of the network is computed recurrently starting from an initial value

$x_i(0), \ i = 1,...,N$. This iteration process continuing until equilibrium stable state is reached. As a dynamical system, the Liapunow's theory can be very useful after defining the energy function of the network as

$$E(\mathbf{x}) = -\frac{1}{2}\sum_{i=1}^{N}\sum_{j=1}^{N} w_{ij} \, x_i \, x_j - \sum_{i=1}^{N} b_i \, x_i + \sum_{i=1}^{N}\int_0^{x_i} F_i^{-1}(x)\,dx \ , \tag{2}$$

which can be described by a set of ordinary equations as

$$\tau_i \frac{dv_i}{dt} = -\left.\frac{\partial E}{\partial x_i}\right|_{x_i(t)} = -v_i + \sum_{j=1}^{N} w_{ij} x_j + b_i$$
$$x_i = F(v_i), \ i = 1,...,N, \tag{3}$$

where τ_i is a time constant. Equations (3) are called HNN evolutionary equations. The stable equilibrium state of the network is defined by the following criteria:

$$\min_{\mathbf{x}} E(\mathbf{x}) = 0 \ \Leftrightarrow \ \frac{d\mathbf{x}}{dt} = 0 \ . \tag{4}$$

The energy function decreases continuously when $w_{ij} = w_{ji}$ and $w_{ii} = 0$. In this case the energy function has to reach its minimum finally under the retrieval phase. These conditions can be fulfilled, when applying the HNN for the solution of linear FEM problems.
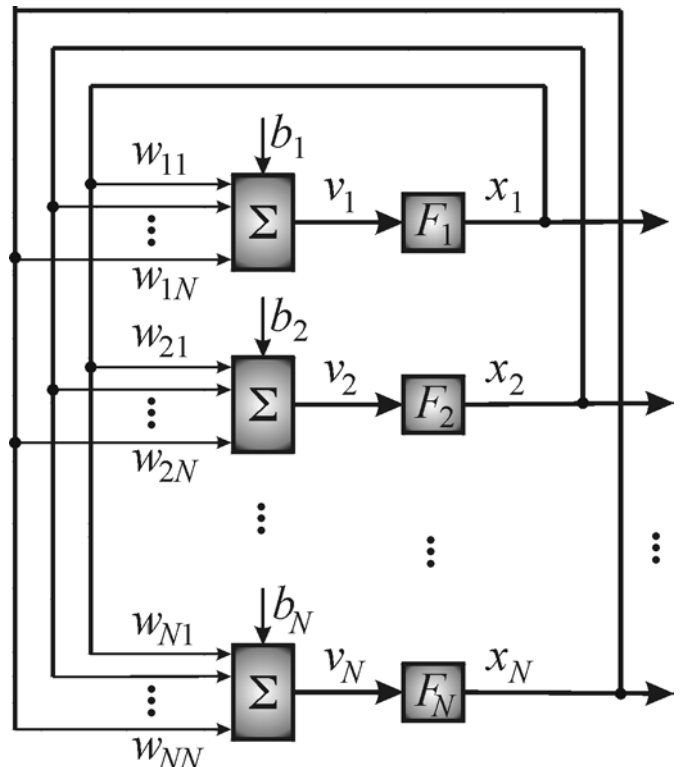

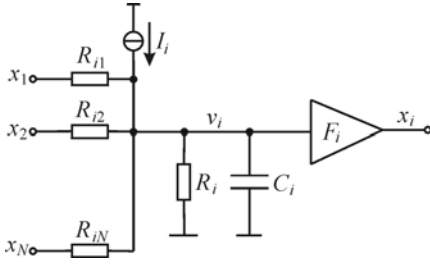Fig.1. Architecture of Hopfield neural network

Fig.2. Electric circuit model of the Hopfield neuron

HNN can be applied to solve Quadratic Programming Problems with bilateral constraints

$$\min_{\mathbf{x}}\left\{\tfrac{1}{2}\mathbf{x}^T\mathbf{Kx}-\mathbf{P}^T\mathbf{x}\right\}, \tag{5}$$

where $\mathbf{Kx}=\mathbf{P}$ is the system of linear equations obtained from FEM, $\mathbf{K}$ is an $N\times N$ quadratic and symmetric matrix, $\mathbf{P}$ and $\mathbf{x}$ are $N\times 1$ vectors. For bilateral constraints the simple identity activation function can be used, $x_i=F_i(v_i)=v_i$, as the values of the unknown potential can be any real number. The system of linear equations $\mathbf{Kx}=\mathbf{P}$ can be rewritten in the form $-\mathbf{Kx}+\mathbf{P}=\mathbf{0}$, and the evolutionary equation (3) can be rewritten in vectorial form as

$$\frac{d\mathbf{v}}{dt}=(\mathbf{W}-\mathbf{E})\mathbf{v}+\mathbf{b}, \tag{6}$$

where $\tau_i=1$, $i=1,...,N$ and $\mathbf{E}$ is the identity matrix. From equation (6) $\mathbf{W}=-\mathbf{K}+\mathbf{E}$ and $\mathbf{b}=\mathbf{P}$. The properties of stable equilibrium are fulfilled.

A neuron of the HNN can be represented by a circuit using electrical components (Fig.2). The neurons mapping its input voltage v_i into the output voltage x_i through the activation function, which is a voltage controlled voltage source, weights and biases can be realized by resistors and current sources. The equation

$$-I_i-\sum_{j=1}^{N}\frac{x_j-v_i}{R_{ij}}+\frac{v_i}{R_i}+C_i\frac{dv_i}{dt}=0 \tag{7}$$

can be obtained for the input node having potential v_i. After substituting $x_i=v_i$ equation (7) leads to the ordinary differential equation

$$C_i\frac{dv_i}{dt}=\sum_{j=1}^{N}\frac{1}{R_{ij}}v_j-\left\{\sum_{j=1}^{N}\frac{1}{R_{ij}}+\frac{1}{R_i}\right\}v_i+I_i. \tag{8}$$

Parameters R_{ij}, R_i and I_i can be expressed by comparing equations (3) and (8),

$$R_{ij}=1/w_{ij},$$
$$\sum_{j=1}^{N}\frac{1}{R_{ij}}+\frac{1}{R_i}=1\Rightarrow R_i=\frac{1}{1-\sum_{j=1}^{N}1/R_{ij}}, \tag{9}$$
$$I_i=b_i.$$

III. Application to Electrostatic Problems

As the simplest illustration, a one-dimensional problem has been investigated for the Laplace-Poisson equation, $\Delta\Phi=-f$, in the region $x\in[0\,\mathrm{mm},10\,\mathrm{mm}]$, and $f=1$. The

prescribed boundary conditions are as follows, $\Phi(0)=0\,\mathrm{V}$, and $\Phi(10)=100\,\mathrm{V}$ are the Dirichlet boundary conditions. The interval has been divided into four elements, and there are three unknown scalar potentials. Applying the weak form for the differential equation, the assembled system of linear equations for three unknown potentials can be obtained as

$$\begin{bmatrix} 2 & -1 & 0 \\ -1 & 2 & -1 \\ 0 & -1 & 2 \end{bmatrix}\begin{bmatrix} \Phi_1 \\ \Phi_2 \\ \Phi_3 \end{bmatrix}=\begin{bmatrix} 6.25 \\ 6.25 \\ 106.25 \end{bmatrix}, \quad \mathbf{Kx}=\mathbf{P}. \tag{10}$$

Using the formulas from section 2, $\mathbf{W}=-\mathbf{K}+\mathbf{E}$ and $\mathbf{b}=\mathbf{P}$,

$$\mathbf{W}=\begin{bmatrix} -1 & 1 & 0 \\ 1 & -1 & 1 \\ 0 & 1 & -1 \end{bmatrix}, \quad \mathbf{b}=\begin{bmatrix} 6.25 \\ 6.25 \\ 106.25 \end{bmatrix} \tag{11}$$

can be got. The diagonal elements of the matrix $\mathbf{W}$ can be neglected, because the resistors R_{ii} are between nodes with the same potential, when using identity activation function. The circuit can be built up according to the equations (9) using network analyzer software, as plotted in Fig.3 (units are in SI system). The processing element (PE) contains a voltage controlled voltage sources and a capacitor, $C_i=1\mu F$.
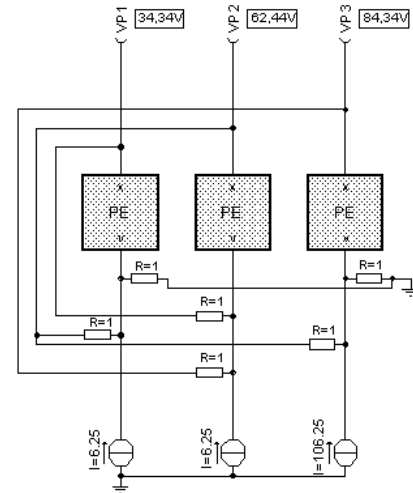
Fig.3. HNN with three neurons

Hopfield type neural networks can be applied as a hardware tool to solve linear FEM problems. Some applications in 2D will be introduced in the full paper.

IV. References

[1] C. Christodoulou, M. Georgiopoulos, *Applications of Neural Networks in Electromagnetics*, Artech House, Boston, 2001.
[2] E. Pabisek, Z. Waszczyszyn, "Neural Networks in the Analysis of Elastoplastic Plane Stress Problem with Unilateral Constraints", *Computational Engineering Using Metaphors from Nature, ed.by B.H.V. Topping,* Civil-Comp Press, Edinburgh, Scotland, 2000, pp. 1-6.
[3] H. Yamashita, V. Cingoski, "On the Application of Hopfield Neural Network in Finite Element Analysis", *Advanced Computational Electromagnetics, ed.by T.Honma,* IOS Press, 1995, pp.37-49.

V. Acknowledgment

Error Estimation in the context of Numerical Optimization of Electromagnetic Systems

S. Vivier, M. Hecquet, P. Brochet

L2EP - Ecole Centrale de Lille
BP 48 - 59651 Villeneuve d'Ascq - France
e-mail: vivier@ec-lille.fr

Abstract – **Different ways to evaluate the modeling error in the context of numerical simulations of electromagnetic devices are proposed. The goal is to validate the use of the Analysis of Variance to discriminate factors acting on responses of an electromechanical system. It allows to reduce the number of factors to be taken into consideration in subsequent optimization processes.**

INTRODUCTION

Numerical models in electromagnetism have reached a so sophisticated level that they now stand as virtual prototypes. Varying the different parameters that control the performances of a given device, provides the designer a powerful tool to explore the design space.

The following step is to use automatic optimization methods. But a question arises: are all the candidate parameters really significant? The answer could be to compare the effect of a factor to the modeling error, assuming that this one exists and can be calculated.

Here, two different approaches are proposed and compared on the 2D finite element model of an eddy current brake used for railway applications.

EXPERIMENTAL DESIGN METHOD

The Experimental Design Method (EDM) gives the ability to pre-determine the experiments (the simulations) to perform, so as to obtain the best modeling of a function, the response, according to input parameters, the factors. EDM is generally split up into two successive stages. The first one is the *Screening analysis* [1]; it is a qualitative study which allows to determine, among a set of factors, the influent ones. The second stage is called *Response Surface Methodology* [2]; its quantitative character gives the possibility to analyze precisely the variations of the response with respect to the influent factors.

Analysis of variance

The Screening analysis is based on 2-level fractional factorial designs that allow to easily compute the aliases, that is the sum of factor and interaction effects. The next step is to perform an Analysis of Variance (ANOVA) to compare the variance of the aliases to the experimental one, calculated as the residual. Under the null hypothesis that aliases have no effect, both variances are the same and their ratio follows the Fisher-Snedecor law.

In the case of experiments, the residual variance can be estimated by repeating the same experiment that give different results. But in the case of numerical simulations, repetitions give always the same result. Does it show that, in the case of numerical modeling, the modeling error does not exist? If two different users simulate the same test case, it is well known that the result will be different, leading to two estimations of the same quantity, and demonstrating the existence of the modeling error.

When using numerical simulations, that is virtual experiments, two approaches can be considered to estimate the modeling error. The first one proposes to build the residual variance from high order interactions between factors. The interaction values can be easily obtained by the calculation of the polynomial model involving the response and the factors; this is achieved by using all the results of an Experimental Design. For the second approach, the experimental errors are estimated, and are used to build the reference variance. The simulations are voluntarily slightly modified in order to create a dispersion of results allowing then to build the experimental variance.

These two construction modes of the experimental variance are presented and compared in two circumstances: a global and a local analysis.

The realization of each design of experiments is made completely automatic thanks to the use of an optimization manager, Sophemis [3].

TEST CASE

To illustrate the evaluation of the experimental error on virtual experiments, a relatively simple example is considered. It is an electromagnetic brake, used for railway applications. This device is fixed under certain bogies, over the rails. It consists of a succession of poles, each of them surrounded by a coil supplied with direct current. The displacement of the brake with respect to the rail, induces eddy currents in the rail, producing then a braking force. In figure 1, a plane view of one pole is presented, with the corresponding geometrical factors. In order to integrate the 3D eddy current trajectory in the rail, the equivalent

conductivity σ of the rail has been considered in the 2D parameterised model [4].
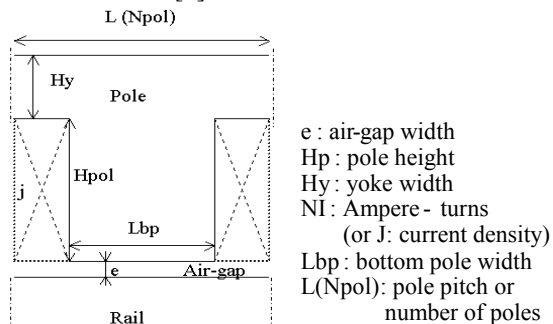

Fig. 1: Plane view of one pole and parameters

e : air-gap width
Hp : pole height
Hy : yoke width
NI : Ampere - turns
    (or J: current density)
Lbp : bottom pole width
L(Npol): pole pitch or
        number of poles

Global analysis over a region

Approach 1 - A Screening Design of Experiments is used, in order to calculate the braking force values for different configurations of the six geometrical factors (Fig. 1).

This analysis allows, in the same time, to determine the significant factors among the six ones. The absolute influence of the different factors and of their interactions on the braking force (brf) variations are obtained thanks to the ANOVA.

By default, the reference residual variance is built from all the interactions terms. Therefore, this variance depends on the model deduced from the design results.

In order to avoid any confusing of effects of the main factors with their interactions, a full factorial design 2^6 (64 simulations) is chosen. The time cost of one simulation is lower than a few minutes.

Tab. 1. Effects of main factors on the braking force (N/mm)
(*v= 200 km/h*) – **Approach 1**

Factors	Effects	Variance	Significant (n %)
Npol	-5.31	1807.4	**Yes** (100)
Hy	1.92	235.65	**Yes** (100)
e	-1.09	76.27	**Yes** (99.9)
NI (j)	0.45	12.96	**Yes** (95.85)
Lbp	-0.264	4.45	No (77.01)
Hp	0.13	1.076	No (43.82)

(NI total constant – the reference residual variance is 3.03)

The ANOVA shows that only 4 parameters are really significant (>95%) with respect to the braking force variations: Npol, Hy, e and NI(j).

Approach 2 - In order to determine the experimental variance, the same design is computed with 4 different models using OPERA-2D [5]:
1. nb of nodes = 1000; up-winding technique not used;
2. nb of nodes = 1500; up-winding technique applied;
3. number of nodes doubled;
4. mesh refinement option selected.

Indeed, for each simulation, different results are obtained, as shown for example in Table 2, for 4 different experiments :

Tab. 2. Effects of different meshes and options on the braking force (N/mm)
(*v= 200 km/h*) – **Approach 2**

Case	Model 1	Model 2	Model 3	Model 4	Variance
1	9.6	9.9	9.95	9.96	0.0255
2	17.8	18.2	18.24	18.248	0.029
3	10.63	10.82	10.86	10.91	0.0157
4	8.5	8.7	8.73	8.8	0.0126

(NI total constant)
Case 1 : Npol = 10, Hy = 30mm, Lbp = -30%, j=6A/mm^2, e=7mm, Hp=101mm; **Case 2** : Npol = 6; **Case 3** : Npol = 10, Hy = 60mm; **Case 4** : e = 9mm.

A global experimental variance can be deduced from the variances calculated for each of the 64 experiments of the design. It equals approximately 0.029.

Tab. 3. Comparison between residual variances

Order of interaction terms	Residual variance (Approach 1)	Experimental variance (Approach 2)
5+6	0.00111524	
4+5+6	0.0234709	0.02907487
3+4+5+6	0.32956587	
2+3+4+5+6	3.03562416	

Table 3 shows how to compare the residual variance built from high order factor interactions and the experimental variance deduced from the repetitions of an experimental design, achieved through different simulation configurations.

Local analysis around a point

The second approach applies well to a single configuration of the factor values. Around this point, the influence of disturbing parameters are tested. In the present case, the precision of the factor values and the mesh construction mode are considered. This approach gives the experimenter an evaluation of the uncertainty relative to the simulation results given by finite element simulations.

This study validates the use of the ANOVA in the particular case of virtual experiments, particularly for screening of significant factors.

In the full paper, more details will be given.

REFERENCES

[1] J.J. Droesbeke, J. Fine, G. Saporta, 'Plans d'Expériences", Editions Technip, Paris, 1997
[2] G.E.P. Box, N.R. Draper, "Empirical Model-Building and Response Sufaces", John Wiley & Sons, New York, 1987
[3] S. Vivier, F. Gillon, M.Hecquet and P.Brochet. 'A design optimisation manager', Compumag 2001, Evian, June 2001, Vol.2, pp.228-229.
[4] S. Vivier, "Stratégies d'optimisation par plans d'expériences et application aux dispositifs électrotechniques modélisés par éléments finis", Thesis, University of Sciences – Techniques, Lille, July 2002.
[5] Vector Fields software: Pc-opera 2D Reference manuals.

GMRES with New Preconditioning for Solving BEM-Type Linear System

Ayumu Saitoh, and Atsushi Kamitani

Faculty of Engineering, Yamagata University

4-3-16, Johnan, Yonezawa

Yamagata 992-8510, JAPAN

saitoh@emperor.yz.yamagata-u.ac.jp

Abstract−A linear-system solver has been developed by using the product-type CG method as a preconditioner and it is applied to the BEM-type linear system. The results of computations show that the CPU time required for the new solver is about half as much as that for the Gaussian elimination. Therefore, the new solver is a powerful tool for solving the BEM-type linear system.

INTRODUCTION

Recently, the boundary element method (BEM) has been applied to the electromagnetic field computations and has yielded excellent results. When discretized by using the BEM, the boundary-value problem of the linear elliptic partial differential equations is transformed to the linear system. Throughout the present paper, the linear system is called the BEM-type linear system. In a large-scale simulation by using the BEM, the linear system solver has become the rate-determining stage. In this sense, the development of the fast solver has been desired.

Since the BEM-type linear system has not a diagonal-dominant coefficient matrix, we can not solve it by using stationary iterative methods such as the RB Gauss-Seidel method and the SOR method. Furthermore, its matrix is dense. For this reason, the Gaussian elimination has been adopted as the solver of the BEM-type linear system. On the other hand, the conjugate gradient (CG) methods have been recently developed to be applied to the nonsymmetric linear system including the BEM-type linear system. In addition, a preconditioning has been investigated to enhance the convergence property of the CG methods.

The purpose of the present study is to develop a new preconditioning for the generalized minimal residual (GMRES) method [1]. In addition, we investigate the applicability of the GMRES with the new preconditioning to the BEM-type linear system.

GMRES WITH VARIABLE PRECONDITIONING

In general, a preconditioning is the technique in which the linear system $A\boldsymbol{x} = \boldsymbol{b}$ is transformed to $A^*\boldsymbol{x}^* = \boldsymbol{b}^*$ by use of the regular matrices, P and Q. Here, A^*, $\boldsymbol{x}^*$ and $\boldsymbol{b}^*$ are given by $A^* = P^{-T}AQ^{-1}$, $\boldsymbol{x}^* = Q\boldsymbol{x}$ and $\boldsymbol{b}^* = P^{-T}\boldsymbol{b}$, respectively. In the following, the residuals $\boldsymbol{r}^*$ and $\boldsymbol{r}$ are defined by $\boldsymbol{r}^* = \boldsymbol{b}^* - A^*\boldsymbol{x}^*$ and $\boldsymbol{r} = \boldsymbol{b} - A\boldsymbol{x}$, respectively. Since the matrix P is chosen such that $P = E$ for the right preconditioning, the residuals satisfy $\boldsymbol{r} = \boldsymbol{r}^*$. Hence, the CG algorithm can be reconstructed easily. For this reason, the right preconditioning is widely used for the CG methods. In using the GMRES with the right preconditioning, we must calculate the product $Q^{-1}\boldsymbol{u}$ at each iteration cycle. The product has been so far evaluated through the backward substitution process after Q was determined by means of the incomplete LU decomposition.

Recently, Abe *et al.* [2] have developed a variable preconditioning in which $Q^{-1}\boldsymbol{u}$ is computed by using the iterative method. Since Q is chosen such that $Q \approx A$ in the preconditioning, $Q^{-1}\boldsymbol{u}$ is nearly equal to $A^{-1}\boldsymbol{u}$. On the other hand, the numerical solution $\boldsymbol{z}$ of the linear system $A\boldsymbol{w} = \boldsymbol{u}$ can be regarded as the approximate value of $A^{-1}\boldsymbol{u}$. For this reason, $Q^{-1}\boldsymbol{u}$ is replaced with $\boldsymbol{z}$ in the variable preconditioned CG method. In order to obtain the approximation solution $\boldsymbol{z}$, we use the iterative method. In the method, both $\|\boldsymbol{u} - A\boldsymbol{z}\| / \|\boldsymbol{u}\| < \delta$ and $n < N_{max}$ are adopted as the termination condition. Here, δ is a constant. In addition, n and N_{max} denote the iteration number and the maximum iteration number, respectively. The above procedure is repeated until the residual norm $\|\boldsymbol{r}\| / \|\boldsymbol{b}\|$ becomes less than 10^{-15}. Throughout this paper, we adopt the product-type CG method [3] as the preconditioner to a variable preconditioned GMRES.

GMRES WITH NEW PRECONDITIONING

As is well known, the residual norm of the GMRES decreases monotonously. After the residual norm falls rapidly in the initial steps, it begins to decrease slowly with an iteration number. In order to improve the reduction rate, we have developed a new preconditioning and have incorporated it to the GMRES. In the resulting solver, the solution of the linear system is iteratively determined by using the following two steps:

Step 1. The product-type method is employed to obtain the solution which satisfies either $\|r\|/\|r_0\| < \varepsilon_p$ or $n < M_{max}$. Here, ε_p is a constant and M_{max} denotes the maximum iteration number.

Step 2. By assuming the above approximate solution as an initial guess, the GMRES is applied to the improvement of the accuracy of the solution.

The above two steps are repeated until the residual norm $\|r\|/\|b\|$ becomes less than 10^{-15}. Throughout the present paper, the above solver is called a restart-preconditioned GMRES.

NUMERICAL RESULTS

As an example, we consider the linear system from the BEM discretization of the 2D Laplace problem over $(0, 2) \times (0, 5)$ with the Dirichlet condition: $u = \cos x \sinh y + \sin x \cosh y$ on the boundary. The resulting linear system has 4000 unknowns and a
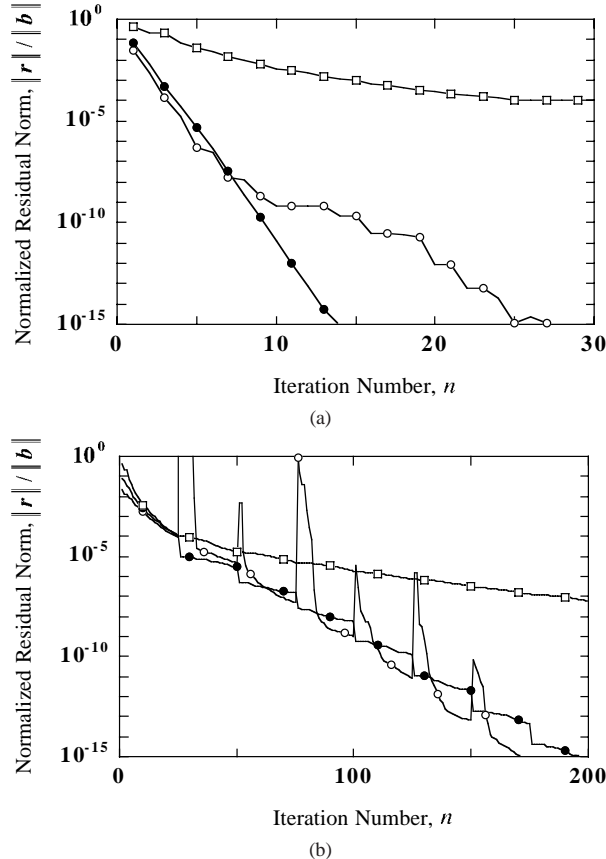

(a)

(b)

Fig. 1. Residual histories of (a) a variable preconditioned and (b) a restart-preconditioned GMRES. Here, the CGS (◯) and the GPBiCG (●) are employed as the preconditioner. In both figures, the residual history of the unpreconditioned GMRES(25) is also indicated by the symbol ☐ .

TABLE I. RATIO τ / τ_G OF CPU TIME.

Preconditioner	Variable Preconditioning	Restart-Preconditioning
CGS	0.63	0.62
GPBiCG	0.41	0.52

nonsymmetric dense matrix. Let us solve the linear system by use of both a variable preconditioned and a restart-preconditioned GMRES. Here, all components of the initial guess vector are assumed to be unity, and the GMRES is restarted in every 25 steps. Moreover, the CGS and the GPBiCG are adopted as the preconditioner to both a variable preconditioned and a restart-preconditioned GMRES. The parameters of the preconditioning are fixed as follows: $\delta = \varepsilon_p = 0.1$ and $N_{max} = M_{max} = 50$.

Figures 1(a) and (b) indicate the residual histories of a variable preconditioned and a restart-preconditioned GMRES, respectively. For the case where the GPBiCG is adopted as a preconditioner, the residual norm of both the preconditioned solvers decreases monotonously with an iteration number. On the other hand, the residual norm shows an irregular behavior when the CGS is adopted as the preconditioner. Furthermore, the iteration number required for the convergence is estimated and is called as a convergent iteration number. The convergent iteration number for the variable preconditioned GMRES is much less than that for the restart-preconditioned GMRES. The CPU time is measured for the Gaussian elimination and the preconditioned GMRESs. The ratio τ / τ_G of the CPU times is tabulated in Table I. Here, τ and τ_G denote the CPU time required for the preconditioned GMRES and that for the Gaussian elimination, respectively. This table indicates that both preconditioned methods give the converged solutions faster than the Gaussian elimination. Moreover, the restart-preconditioned GMRES has almost the same convergence speed as the variable one.

From the above results, we can conclude that the restart-preconditioned GMRES as well as the variable preconditioned one is a powerful tool for solving the BEM-type linear system.

REFERENCES

[1]   Y. Saad and M. H. Schultz, "GMRES: A Generalized Minimal Residual Algorithm for Solving Nonsymmetric Linear Systems," *SIAM. J. Sci. Stat. Comput.*, vol. 7, pp. 856-869, July 1986.

[2]   K. Abe, S. L. Zhang, H. Hasegawa and R. Himeno, "A SOR-base Variable Preconditioned GCR Method," *Trans. JSIAM*, vol. 11, pp. 157-170, December 2001.

[3]   S. L. Zhang, "GPBi-CG: Generalized Product-Type Methods based on Bi-CG for Solving Nonsymmetric Linear Systems," *SIAM J. Sci. Comput.*, vol. 18, pp. 537-551, March 1997.

Iterative Solution for Linear System Obtained by Meshless Approach

[1]Soichiro Ikuno, [2]Ayumu Saitoh and [2]Atsushi Kamitani

[1]Faculty of Engineering, Tokyo University of Technology, 1404-1, Katakura, Hachioji, Tokyo 192-0982, Japan
[2] Faculty of Engineering, Yamagata University, 4-3-16, Johnan, Yonezawa, Yamagata 992-8510, Japan
e-mail: ikuno@cc.teu.ac.jp

Abstract—The iterative solution for the linear system obtained by the meshless approach is investigated. The meshless local Petrov-Galerkin (MLPG) method is based on the local domain weak form, and the trial and the test functions are taken from the different functional spaces. Consequently, the coefficient matrix of the linear system becomes banded and asymmetric. In this study, BiCGSTAB, GPBiCG and GMRES methods are employed for the solution of the linear system obtained by MLPG method. The results of computations show that the BiCGSTAB and the GPBiCG methods do not give a converged solution in finite iterations. On the other hand, the GMRES method converges after 250 iterations in case of the 256×256 linear system.

Introduction

The mesh generation procedure must be needed before using the general finite element method (FEM) for the solution of the partial differential equations. However, it costs a lot of time to divide the region into a set of finite elements. Thus, the time required for discretizing the partial differential equation or solving the resulting linear system is much shorter than that for the element generation. On the other hand, the meshless approach does not require finite elements of a geometrical structure. The necessary information is only locations of nodes which are scattered in the region and on the boundary. For these reasons, various meshless approaches have been developed, such as the diffuse element method [1], the Element-Free Galerkin (EFG) method [2] and the Meshless Local Petrov-Galerkin (MLPG) method [3].

Although the MLPG method is one of the meshless approaches, it is widely different from the diffuse element method and the EFG method. The trial and the test functions are taken from the different functional spaces in the MLPG method, whereas they are taken from the same functional space in other meshless approaches. Furthermore, the weak form is derived on the local domain. Consequently, the coefficient matrix of the linear system becomes banded and asymmetric in the MLPG method.

The purpose of the present paper is to apply the BiCGSTAB [4], the GPBiCG [5] and the GMRES [6] to the solution of the linear system obtained by the MLPG method and to elucidate the numerical character of the linear system obtained by MLPG.

Meshless Approach

In this section, we derive the weak form of the Poisson problem and discretize it by means of the MLPG method. In this study, we use the rectangular two-dimensional region $\Omega \equiv [0, 1] \times [0, 1]$ and its boundary is denoted by Γ. The governing equation is expressed as

$$-\Delta u = f, \tag{1}$$

where $u(x, y)$ and $f(x, y)$ denote the unknown and the given functions, respectively. Furthermore, the boundary condition is assumed as follows:

$$u = \bar{u}. \tag{2}$$

Here, $\bar{u}$ denotes the given function.

To approximate the function $u(x, y)$, let us first scatter M nodes in the domain Ω and on the boundary Γ, and assign the weight functions with compact supports to the nodes. In this study, the weight function is defined as follows:

$$w_i(\boldsymbol{x}) = \begin{cases} \dfrac{e^{(-r_i/c)^2} - e^{-(R/c)^2}}{1 - e^{-(R/c)^2}} & r_i \leq R, \\ 0 & r_i > R. \end{cases} \tag{3}$$

Here, R denotes the size of the support for the weight function $w_i(\boldsymbol{x})$ and r_i is defined as $r_i = |\boldsymbol{x} - \boldsymbol{x}_i|$. Moreover, c is a constant. By using the moving least squares (MLS) approximation, the shape functions are given by

$$\phi_i(\boldsymbol{x}) = \boldsymbol{p}(\boldsymbol{x})^T A(\boldsymbol{x})^{-1} \boldsymbol{b}_i(\boldsymbol{x}), \tag{4}$$

where components of the vector $\boldsymbol{p}(\boldsymbol{x})$ are monomials of the space variables, x and y. In this study, $\boldsymbol{p}(\boldsymbol{x})^T = \begin{bmatrix} 1 & x & y & x^2 & xy & y^2 \end{bmatrix}$ is employed for the quadratic MLS approximation. Furthermore, the matrix $A(\boldsymbol{x})$ and the vector $\boldsymbol{b}_i(\boldsymbol{x})$ are defined by

$$A(\boldsymbol{x}) = \sum_{i=1}^{M} w_i(\boldsymbol{x}) \boldsymbol{p}(\boldsymbol{x}_i) \boldsymbol{p}(\boldsymbol{x}_i)^T, \tag{5}$$

$$\boldsymbol{b}_i(\boldsymbol{x}) = w_i(\boldsymbol{x}) \boldsymbol{p}(\boldsymbol{x}_i). \tag{6}$$

Under the above assumption, the trial function $u(\boldsymbol{x})$ can be expanded in the form,

$$u(\boldsymbol{x}) = \sum_{i=1}^{M} u_i \phi_i(\boldsymbol{x}). \tag{7}$$

In general, the FEM and the EFG are based on the global Galerkin formulation. In this contrast, the MLPG method is essentially based on the weak form over the local sub-domain Ω_i. For the sub-domain Ω_i, we choose a circle of radius R whose center is placed at $\boldsymbol{x}_i$. Thus, the sub-domain Ω_i agrees with the support of the weight function $w_i(\boldsymbol{x})$. Equation (1) and its associate boundary condition on Γ_i are shown to be equivalent to the following local weighted residual expression:

$$\int_{\Omega_i} (\Delta u - f) \, w_i \, d\Omega - \alpha \int_{\Gamma_i} (u - \bar{u}) \, w_i \, d\Gamma = 0, \tag{8}$$

where u is a trial function and α is a penalty parameter. Besides, Γ_i denotes a part of the boundary Γ which is clipped off by the boundary of Ω_i.

Following the standard manners of the MLPG method and the MLS approximation, we can discretize (8) as follows:

$$Bu = f, \tag{9}$$

where the matrix B and vector f are defined by

$$(B)_{ij} = \int_{\Omega_i} \nabla w_i \cdot \nabla \phi_j \, d\Omega + \alpha \int_{\Gamma_i} w_i \, \phi_j \, d\Gamma - \int_{\Gamma_i} w_i \, \frac{\partial \phi_j}{\partial n} \, d\Gamma, \tag{10}$$

$$(f)_i = \alpha \int_{\Gamma_i} u \, w_i \, d\Gamma - \int_{\Gamma_i} f \, w_i \, d\Gamma. \tag{11}$$

Here, $(\ )_{ij}$ and $(\ )_i$ represent the (i, j)-th matrix element and the i-th vector component, respectively. Moreover, n denotes the unit normal vector whose direction is outward to Ω_i. In this way, the solution of the Poisson problem is determined by solving (9) numerically.

NUMERICAL RESULTS

As is apparent from (10), the coefficient matrix of the linear system obtained from the MLPG method becomes asymmetric. In addition, it is not clear whether the matrix becomes diagonal-dominant or not. Therefore, the *LU* decomposition method or the conjugate gradient (CG) method can be employed for the solution. However, as the number of nodes is increased, the coefficient matrix becomes more sparse. For these reasons, the BiCGSTAB, the GPBiCG and the GMRES methods are employed for the solution of the linear system (9).

In Fig.1, we show the residual histories for the BiCGSTAB and the GPBiCG. Here, the residual norm for the approximate solution v is defined by

$$r = \frac{\|f - Bv\|_\infty}{\|f\|_\infty}, \tag{12}$$

where $\|\ \|_\infty$ denotes the infinity norm of the vector. The termination condition for the solver of (9) is $r \leq 10^{-12}$. Through the present paper, the size of the linear system is fixed as 256×256. This figure indicates that both the BiCGSTAB and the GPBiCG method do not give a converged solution even after 300 iterations and that the residual behaves irregularly for both methods. This is mainly because the condition number of the coefficient matrix is large due to the penalty parameter. Besides, the coefficient matrix becomes a nearly singular one.

Next, we show the residual histories for the GMRES method. Figure 2 shows that the residual norm stagnates immediately after the restart. On the other hand, in case of $k = 256$, the residual norm converges after 250 iterations. Here, k denotes the restart parameter. Consequently, this figure suggests that the GMRES method without a restart is more effective for the linear system obtained by the MLPG method than the method with a restart or the BiCGSTAB and the GPBiCG method.
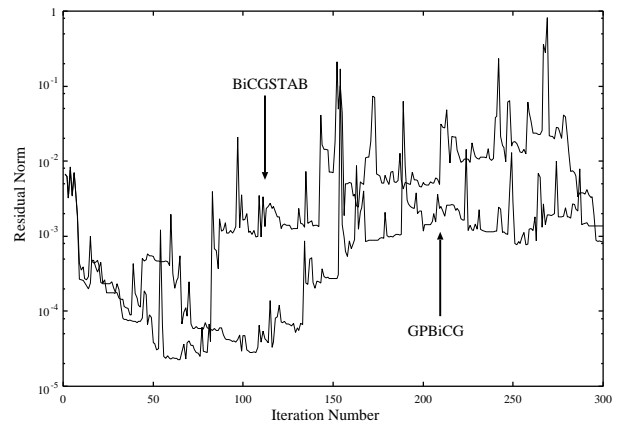

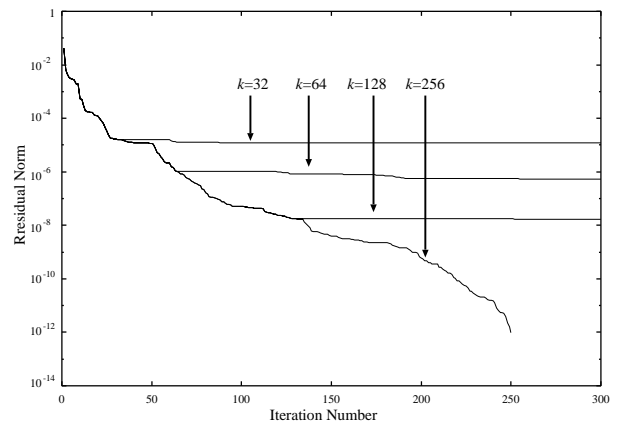Fig. 1. The residual histories for the BiCGSTAB and the GPBiCG.

Fig. 2. The residual histories for the GMRES. Here, k denotes the restart parameter of the GMRES.

From the above results, we can conclude that the BiCGSTAB and the GPBiCG method are unsuitable for the linear system obtained by the MLPG. On the other hand, the GMRES method without a restart is effective for the linear system.

REFERENCES

[1] B. Nayroles, G. Touzot and P. Billon, "Generalizing the finite element method: diffuse approximation and diffuse elements," *Comput. Mech.* vol. 10, pp. 307-318, 1992.

[2] T. Belytschko, Y. Y. Lu and L. Gu, "Element-free Galerkin methods," *Int. J. Numer. Methods Eng.*, vol. 37, pp. 229-256, 1994.

[3] S. N. Atluri and T. Zhu, "A new meshless local Petrov-Galerkin (MLPG) approach in computational mechanics," *Comput. Mech.*, vol. 22, pp. 117-127, 1998.

[4] H. A. Van Der Vorst, "BI-CGSTAB: A Fast and Smoothly Converging Variant of BI-CG for The Solution of Nonsymmetric Linear Systems", *SIAM J. Sci. Stat. Comput.*, vol.13, no.2, pp.631-644, March 1992.

[5] S. L. Zhang "GPBi-CG: Generalized Product-type Methods Based on Bi-CG for Solving Nonsymmetric Linear Systems", *SIAM J. Sci. Stat. Comput.*, vol.18, no.2, pp.537-551, March 1997.

[6] Y. Saad and M. H. Schultz, "GMRES: A Generalized Minimal Residual Algorithm for Solving Nonsymmetric Linear Systems," *SIAM. J. Sci. Stat. Comput.*, vol. 7, pp. 856-869, July 1986.

Estimation of numerical errors due to time and space discretisations

[1]T. Henneron, [2]S. Clénet, [1]F. Piriou

[1]L2EP, USTL
Bat P2
59655 Villeneuve d'Ascq, France
Francis.Piriou@univ-lille1.fr

[2]L2EP, ENSAM CER LILLE
8, Bd Louis XIV
59046 LILLE Cedex, France
Stephane.Clénet@lille.ensam.fr

Abstract – **In this paper, we propose a method to estimate time and space discretisation errors of a 3D FEM model coupled with circuit equations. The estimator is based on the non-verification of the constitutive relationship which requires the calculation of admissible fields. The technique to calculate such fields on the whole time domain is described for the A-formulation. This estimator is tested on a transformer at no load and different methods for time discretisation are studied and compared.**

INTRODUCTION

For a numerical study of magnetostatic problem, FEM is generally employed. The space discretisation using finite element leads to numerical errors. These errors, directly linked with the mesh quality, can be estimated accurately. Among the estimators proposed, those based on the non verification of the constitutive relationship are interesting because they enable to have a direct link with the exact solution [1,2]. To model a magnetostatic system coupled with the external circuit, it is necessary to add to FEM a time differential equation. This one links the time derivative of the flux to the current. Consequently, numerical errors due to the time discretisation appear which add themselves to the numerical error due to space discretisation.

To reduce error due to time discretisation, it is necessary to use a small time step but it also increases the computation time. Moreover, this error becomes negligible versus the error involved by the space discretisation, which is given by the features of the mesh. So, a reduction of the time step doesn't reduce the numerical error significantly. The problem is then the choice of the time step versus the quality of the mesh. To find an issue, a way is to use an estimator, which enables to determine error involved by time and space discretisations.

In this communication, we propose an error estimator in the case of the vector potential formulation coupled with circuit equation. First, we present the error estimator, which requires the calculation of two admissible fields on the time domain from the discrete solutions. This method is developed for the θ-method. As example of application we use this estimator to study a transformer at no-load supplied by a sinusoidal voltage.

ERROR ESTIMATION OF THE SPATIAL DISCRETIZATION

We consider a domain D with a boundary Γ. We assume to have only one inductor flowing by current i. In magnetostatics, the magnetic field **H** and the magnetic flux density **B** verify Maxwell's equations given by:

$$\mathbf{curl}\,\mathbf{H} = \mathbf{N}i \quad \text{with} \quad \mathbf{H} \times \mathbf{n} = \mathbf{0} \text{ on } \Gamma_H \qquad (1)$$

$$\mathrm{div}\,\mathbf{B} = 0 \quad \text{with} \quad \mathbf{B}.\mathbf{n} = 0 \text{ on } \Gamma_B \qquad (2)$$

where **N** is a turn density vector which depends on the inductor shape, Γ_B and Γ_H two complementary parts of Γ and **n** the outward normal of Γ. To take into account the material behavior, the fields **B** and **H** are linked by the constitutive relationship :

$$\mathbf{B} = \mathbf{f}(\mathbf{H}) \qquad (3)$$

This function is supposed to be univoc (hysteresis effect in the ferromagnetic media is neglected) and strictly increasing. To solve these equations, potential formulations are generally used such as, for example, the vector potential formulation (**A**-formulation). The discretisation of such formulations is carried out using functional spaces (Whitney's element spaces for instance) with finite dimensions. The discrete solution is then different from the exact one which satisfies (1),(2) and (3) simultaneously. To estimate the discretisation error, the function Λ_D is introduced such that [1]:

$$\Lambda_D(\hat{\mathbf{H}}, \hat{\mathbf{B}}) = \int_D \left[\int_0^{\hat{\mathbf{B}}} \mathbf{f}^{-1}(\mathbf{b}) \cdot d\mathbf{b} + \int_0^{\hat{\mathbf{H}}} \mathbf{f}(\mathbf{h}) \cdot d\mathbf{h} - \hat{\mathbf{H}} \cdot \hat{\mathbf{B}} \right] dD \qquad (4)$$

with $(\hat{\mathbf{H}}, \hat{\mathbf{B}})$ a couple of admissible fields (i.e. which verifies (1) and (2)). We can note that the function Λ_D is always positive. If it is equal to zero, the couple $(\hat{\mathbf{H}}, \hat{\mathbf{B}})$ is the exact solution because it satisfies (1), (2) and the constitutive relationship (3). In the case of the **A**-formulation, the magnetic flux density denoted $\mathbf{B_A}$ ($\mathbf{B_A}$=**curl A**) is admissible but not $\mathbf{H_A}$ ($\mathbf{H_A}$=**f**($\mathbf{B_A}$)) [3]. Different methods have already been proposed to calculate an admissible $\hat{\mathbf{H}}_\mathbf{A}$ from $\mathbf{H_A}$ to carry out an efficient error estimation using Λ_D [2].

ERROR ESTIMATION WITH THE COUPLING OF THE EXTERNAL CIRCUIT

To couple magnetostatics equations with an external circuit, we use the time differential equation linking the voltage v(t), the current i(t) and the linkage flux flowing the inductor. In the case of **A**-formulation, the equation can be written:

$$\frac{d}{dt} \int_D \mathbf{A} \cdot \mathbf{N}\,dD + r\,i(t) = v(t) \qquad (5)$$

with r the inductor resistance. Then, we have to solve an system of 4 equations (1),(2),(3) and (5) on the domain D and on the time interval [0,T]. More than a space discretisation, we have to carry out a time discretisation of (5). To estimate simultaneously the space and time discretisation error, we introduce a function $\Lambda_{Dx[0,T]}$ such that :

$$\boldsymbol{\Lambda}_{\mathrm{Dx}[0,\mathrm{T}]}(\hat{\mathbf{B}}(t),\hat{\mathbf{H}}(t)) = \int_0^T \boldsymbol{\Lambda}_D(\hat{\mathbf{B}}(t),\hat{\mathbf{H}}(t))\,dt \qquad (6)$$

with $(\hat{\mathbf{B}}(t),\hat{\mathbf{H}}(t))$ a couple of admissible fields which verify (1), (2) and (5) on the time and space domain D x [0,T]. The function $\boldsymbol{\Lambda}_{\mathrm{Dx}[0,\mathrm{T}]}$ is always positive since $\boldsymbol{\Lambda}_D$ is positive as well. The function $\boldsymbol{\Lambda}_{\mathrm{Dx}[0,\mathrm{T}]}$ is equal to zero if the couple $(\hat{\mathbf{B}}(t),\hat{\mathbf{H}}(t))$ is the exact solution since it verifies the constitutive law (3) on D x [0,T]. The problem is then to construct the field $(\hat{\mathbf{B}}(t),\hat{\mathbf{H}}(t))$ from the solution using FEM. A method has been already proposed to calculate such field [5]. However this method can only be used with the Euler implicit scheme for time discretisation and is not very efficient when the resistance value r is weak. In the following, we present a method, which can be applied with the θ-method in the case of the **A**-formulation.

CALCULATION OF ADMISSIBLE FIELDS

The discretisation of equation (5) with the θ-method gives in the case of the **A**-formulation:

$$\int_D \frac{\mathbf{A_n} - \mathbf{A_{n-1}}}{\Delta t}\cdot\mathbf{N}\,dD + (1-\theta)r\,i_n + \theta r\,i_{n-1} = (1-\theta)v_n + \theta v_{n-1} \qquad (7)$$

with Δt the time step, $\mathbf{A_n}$, i_n and v_n are the values of vector potential, current and voltage at $t_n = n\,\Delta t$. The solution using FEM leads a set of value $(\mathbf{A_n},i_n)$ at each time step t_n. Using the construction already developed in magnetostatics (see previous section), we can easily calculate at each time step t_n a magnetic flux density $\hat{\mathbf{B}}_{\mathbf{A},n}$ ($\hat{\mathbf{B}}_{\mathbf{A},n} = \mathbf{curl}\,\mathbf{A_n}$) and a magnetic field $\hat{\mathbf{H}}_{\mathbf{A},n}$ which satisfies (1) with $i=i_n$ [2]. From this set of couples $(\hat{\mathbf{B}}_{\mathbf{A},n},\hat{\mathbf{H}}_{\mathbf{A},n})$, admissible fields $(\hat{\mathbf{B}}(t),\hat{\mathbf{H}}(t))$ on D x [0,T] can be deduced. On each interval $[t_{n-1},t_n]$, The current i(t) is assumed to be constant and equal to $(1-\theta)\,i_n + \theta\,i_{n-1}$. Then, we have on each interval :

$$\hat{\mathbf{H}}(t) = \hat{\mathbf{H}}_{\mathbf{A},n}(1-\theta) + \hat{\mathbf{H}}_{\mathbf{A},n-1}\theta \qquad (8)$$

$$\hat{\mathbf{B}}(t) = \frac{\hat{\mathbf{B}}_{\mathbf{A},n} - \hat{\mathbf{B}}_{\mathbf{A},n-1}}{\Delta t}(t - t_n) + \hat{\mathbf{B}}_{\mathbf{A},n}\left[\frac{\Phi_n + g_n(t)}{\Phi_n}\right] \qquad (9)$$

with $g_n(t) = \int(v(t) - (1-\theta)v_n - \theta v_{n-1})dt$ and $\Phi_n = \int_D \mathbf{A_n}\cdot\mathbf{N}\,dD$

We can note that $\hat{\mathbf{B}}(t)$ verifies (2) and (5) ($\hat{\mathbf{B}}(t) = \mathbf{curl}\,\mathbf{A}(t)$). and $\hat{\mathbf{H}}(t)$ verifies also equation (1) on the whole domain Dx[0,T]. From this couple $(\hat{\mathbf{B}}(t),\hat{\mathbf{H}}(t))$, we can estimate the numerical error by calculating the function $\boldsymbol{\Lambda}_{\mathrm{Dx}[0,\mathrm{T}]}$.

APPLICATION

To test the proposed method of error estimation, we consider a transformer at no load supplied by a sinusoidal voltage. The magnitude is equal to 28 V and the frequency equal to 25KHz. The primary winding resistance is 40mΩ. Two meshes have been considered (fig. 1). The first one, denoted M1 has 2560 elements and 545 nodes. The second one, denoted M2, has 6627 elements and 1281 nodes. The time interval corresponds to the first period of the voltage (T=40 μs). On figure 2, we compare the error $\boldsymbol{\Lambda}_{\mathrm{Dx}[0,\mathrm{T}]}$ of M1 and M2 for different number of time step on T and two values of θ. We can see that the method gives expected results. First, the error decreases with the time step. Best results are obtained with θ=0.5 with large time step but the gap between results with θ=1 decrease with Δt. Finally, the error is weaker with the finest mesh M2. However we can see also that the using of weaker time step doesn't improve the results (from 20 time steps per period to 40).
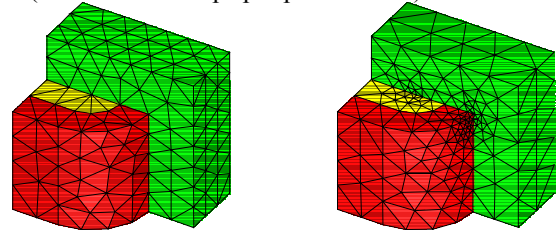

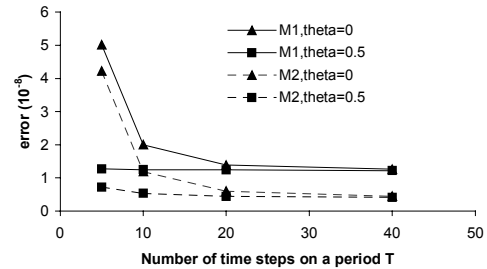Fig. 1. Meshes M1 (left) and M2 (right)

Fig. 2. Evolution of the error

CONCLUSION

A method to estimate the global error due to space and time discretisation has been developed and discussed. Numerical results on a simple example have shown that this one can be used in order to obtain a compromise between computation time and accuracy. In fact, it enables to adapt the time step versus the quality of the mesh.

REFERENCES

[1] J. Rikabi, C.F. Bryant, and E.m. Freeman, "An error based approach to complementary formulation of static field solutions ", Int. Jour. Num. Met. In Eng., vol. 26, pp. 1963-1987, 1988.

[2] G. Marques, S. Clénet, F. Piriou, "Error Estimators in 3D Linear Magnetostatics", *IEEE Trans. Mag*. vol. 36, No. 4, pp 1588-1591, July 2000.

[3] C. Li, Z. Ren and A. Razek, "Application of complementary formulations and adaptive mesh refinement to non-linear magnetostic problems", *IEEE Trans. Mag*, vol. 31, pp. 1376-1379, 1995.

[4] Y. Le Menach, S. Clénet and F. Piriou, "Numerical Model to Discretize Source Fields in the 3D finite element Method ", *IEEE Trans. Mag*, vol. 36, No. 4, July 2000.

[5] G. Marques, Y. Le Menach, S. Clénet and F. Piriou, "Error estimation for 3D magnetostatic problems coupled with electrical circuits", Proc. EPNC'2000, pp. 23-26, Poznan, Sept. 2000.

Investigation of Parallel Multigrid Method Using Java Language

Kota Watanabe, Hajime Igarashi and Toshihisa Honma

Graduate School of Engineering

Hokkaido University

KITA 13, NISHI 8, KITA-KU SAPPORO 060-8628 JAPAN

E-mail: wata@em-si.eng.hokudai.ac.jp

Abstract - **This paper discusses development of the parallel multigrid method for finite element analysis using Java. The multigrid method can significantly reduce computational time in comparison with conventional linear solvers such as ICCG. However, the multigrid method requires a large quantity of memory in large-scale finite element analysis. For this reason, we develop the parallel multigrid method using several computers. This method enables to reduce the required memory of each computer. We adopt Java language that is superior to other languages in developing large-scale programs and programs using network.**

INTRODUCTION

The multigrid method has been applied to electromagnetic field problems so far [1], to show that it can significantly reduce computational time in comparison with conventional linear solvers such as ICCG. However, multigrid method requires a large quantity of memory in large-scale finite element analysis. For this reason, we develop the parallel multigrid method using several computers. This enables to reduce the required memory of each computer.

Java [2] is the computer language which was developed by Sun Microsystems in 1995. Because the syntax of Java is quite similar to C and C++, it is easy to convert from existing source codes to Java source code. Adapting object-oriented style, Java is superior to other old languages such as Fortran in developing large-scale programs and maintenance. Multi-platform is one of the features of Java, whose compiler converts from source code to object code called byte code. The byte code runs on JVM (Java Virtual Machine) which is a kind of program on OS. JVM absorbs the difference of architecture of computer systems. Without recompile, Java program runs on various computer systems where JVM can run. It is another feature of Java that it makes possible to develop network applications with ease.

MULTIGRID METHOD

It is known that the linear solvers such as Gauss-Seidel and CG methods tend to eliminate the high-frequency components of the residue in the system equation more rapidly than the low-frequency components. The multigrid method is based on this property, that is, the high-frequency residual components are eliminated on a fine mesh by small numbers of iterations of the linear solver (smoother). The remained residual components are then projected onto a more coarse mesh, in which they now have high frequency that can again be eliminated by small numbers of the iterations. The multigrid method solves successively performing these processes. This procedure is usually called the coarse grid correction. Although there are many variations in multigrid method, all these variations are based on the coarse grid correction. The procedure of the two-grid V-cycle method that is the simplest multigrid method is described below.

Step1 (Smoothing)

The smoothing operation is applied to the system equation

$$[A_f]\{x\}= \{b\}, \tag{1}$$

for the fine mesh to obtain approximate solution $\{\widetilde{x}\}$, where $[A_f]$ denotes the system matrix defined on the fine mesh. In this step, the high-frequency components in the solution error are eliminated.

Step2

The residual vector $\{r_f\}$ corresponding to the approximate solution $\{\widetilde{x}\}$, is calculated,

$$\{r_f\}=\{b\} - [A_f]\{\widetilde{x}\}. \tag{2}$$

Step3 (Restriction)

The residual vector is projected onto a coarser mesh using the restriction matrix [R],

$$\{r_c\} = [R]\{r_f\}, \tag{3}$$

Step4

The residual equation in coarse mesh is solved to obtain the error vector $\{e_c\}$ corresponding to the residual vector $\{r_c\}$,

$$[A_c]\{e_c\}= \{r_c\}, \tag{4}$$

where $[A_c]$ is the system matrix defined in the coarse mesh. It takes short time to solve (4) because there are small number of unknowns in (4).

Step5 (Prolongation)

The error vector is projected onto the fine mesh using the prolongation matrix [P],

$$\{e_f\}=[P]\{e_c\}, \tag{5}$$

where [P] is usually chosen as the transpose of [R].

Step6

The solution $\{\tilde{x}\}$ obtained in Step1 is corrected using error vector $\{e_f\}$,

$$\{x^{\text{new}}\} = \{\tilde{x}\} + \{e_f\}. \tag{6}$$

Step7 (Post-Smoothing)

The smoothing operation is applied to the system equation again. This procedure is called post-smoothing. After post-smoothing, the convergence of the solution is tested. If convergence condition is not satisfied, we go back to Step-2.

PARALLEL MULTIGRID

In this paper, we pay attention to the Gauss-Seidel smoother that plays a crucial role in multigrid method. The standard Gauss-Seidel algorithm is

$$x_i^{k+1} = \left(b_i - \sum_{j=1}^{i-1} a_{ij} x_j^{k+1} - \sum_{j=i+1}^{n} a_{ij} x_j^{k} \right) / a_{ii}, \tag{7}$$

where

x_i^k　i-th component of the solution vector in k-th iteration step

a_{ij}　i-th row j-th column component of the system matrix

b_i　i-th component of the right hand side vector.

In practical program coding, the diagonal and the upper triangle of the matrix [A] are stored because of symmetry matrix. The proposed algorithm for parallel computing is

```
for (k=1,2, ....) {
    ax[1,2, ... n] = 0 ;
    for (i = 1,2,..., n){
```

$$x_i^{k+1} = \left(b_i - ax[i] - \sum_{j=i+1}^{n} a_{ij} x_j^{k} \right) / a_{ii} \tag{8-1}$$

```
        for (j = i+1, i+2, ... , n){
```

$$ax[j] = ax[j] + a_{ij} x_i^{k+1} ; \tag{8-2}$$

```
        end for(j)
    end for(i)
end for(k)
```

Fig.1 shows an example of parallel calculation using three PC. The suffix f and b in Fig. 1 denote the calculation (8-1) and (8-2) respectively.

NUMERICAL RESULTS

We analyze a simple magnetostatic problem using finite element method. Three personal computers with Pentium3 933MHz~1.26GHz are used. These PC connect the network (100BASE-TX). The data of array $x[]$ and $ax[]$ in (8) are communicated with each PC using TCP/IP Sockets that is one of the standard Java API(Application Program Interface) .

Fig. 2 shows the CPU time of Gauss-Seidel smoothing (10 times iterations). In the small number of unknowns, the proposed method has worse performance than the conventional method due to the time of preparation for TCP/IP Socket. However, we can see that the difference of time between these methods decreases with the number of unknowns. Moreover, the required memory of each PC in proposed method is 1/3 of that in conventional method.
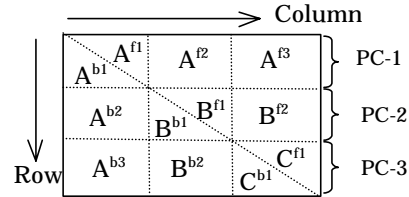
(a) Division of matrix
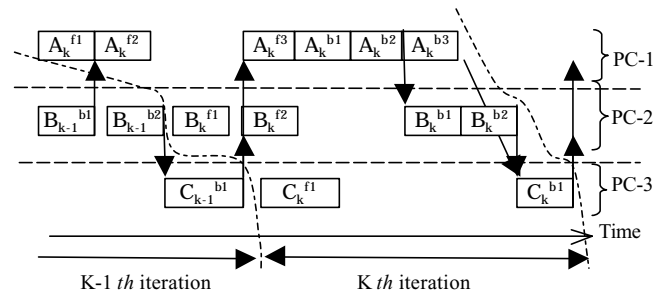
(b) Flow of calculation
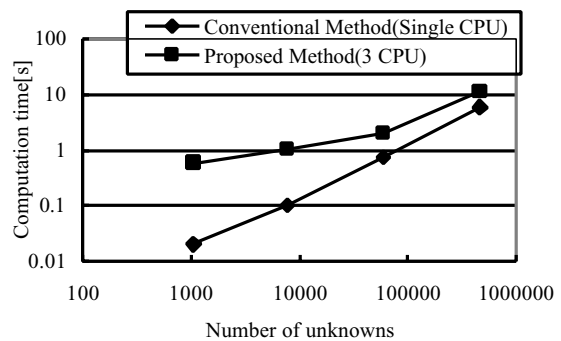
Fig. 1 Example of parallel calculation

Fig. 2 Computation Time

RERERENCES

[1] R. Hiptmair, Multigrid Method for Maxwell's Equations, SIAM J. Numerical Analysis, Vol.36, pp204-225, 1998.

[2] http://wwws.sun.com/software/java/

Solution of a Magnetostatic Problem Using an Inexact Newton Method

Carlo A. Borghi, *Member IEEE,* Mario R. Carraro and Andrea Cristofolini

Department of Electrical Engineering of the University of Bologna,

Viale Risorgimento, 2, I 40135, Bologna, Italy

ca.borghi@mail.ing.unibo.it; mario.carraro@mail.ing.unibo.it; andrea.cristofolini@mail.ing.unibo.it

Abstract — **Inexact Newton solvers can offer many attractive features for the solution of non linear problem in the field of electromagnetics. A critical point for the optimal set up of the solver is the choice of the best algorithm for the evaluation of the approximate solutions of the linear systems at each Newton step, and the most effective preconditioning strategy. In this paper, the NITSOL method is proposed for the solution of a non linear linear magnetostatic problem. The problem has been discretized by means of a finite element approach. The GMRES method has been adopted as linear solver, and four preconditioners have been tested. The performance of the procedure are evaluated for different meshes with increasing number of discretization points.**

INTRODUCTION

Newton solvers are well established methods for the calculation of a zero of a non linear function $\mathbf{F}$, and have successfully applied to large scale problems in various scientific fields. An inexact solvers can improve the performance of the Newton method, utilising the inexact Newton condition [1]:

$$\left\| \mathbf{F}(\mathbf{f}_k) + \mathbf{F}'(\mathbf{f}_k)\mathbf{s}_k \right\| \le \eta_k \left\| \mathbf{F}(\mathbf{f}_k) \right\|, \qquad (1)$$

where $\mathbf{F}'$ is the Jacobian of the function $\mathbf{F}$, $\mathbf{s}_k$ is the solution increment at the k step and $\eta_k \in [0.1)$ is a forcing term enhancing the efficiency of the convergence. Condition (1) yields a linear system at each non linear iteration, which is solved by means of a GMRES algorithm [2]. In the initial non linear iterations, a large forcing term avoids the risk of imposing an accuracy on the solution leading to substantial disagreement between $\mathbf{F}(\mathbf{f}_k + \mathbf{s}_k)$ and its linear approximation $\mathbf{F}(\mathbf{f}_k) + \mathbf{F}'(\mathbf{f}_k)\mathbf{s}_k$. When the solution is getting close to convergence, η_k should tend to zero, and (1) gives the exact Newton condition:

$$\mathbf{F}(\mathbf{f}_k) = -\mathbf{F}'(\mathbf{f}_k)\mathbf{s}_k \qquad (2)$$

As a general rule, the robustness and the convergence rate of GMRES are strictly dependent on the preconditioner quality rather than on the other factors. One of the reasons is that the preconditioner can be changed at each step, to fit the problem in the best possible way. This capability can be really useful for some applications.

MAGNETOSTATIC PROBLEM

A magnetostatic problem with a ferro-magnetic material has been considered. The physical formulation, constituted by the Maxwell equations and the material laws, yields the following equation:

$$\mathbf{B} = \nabla \times \mathbf{A} \, , \ \nabla \times \left(\frac{1}{\mu} \nabla \times \mathbf{A} \right) = \mathbf{J} \, . \qquad (3)$$

The non linear function $\mathbf{F}$ is found discretizing (3) in a two-dimensional symmetry frame by means of a weighted residual FEM approach:

$$\mathbf{K(a)a} - \mathbf{j} \, , \qquad (4)$$

where $\mathbf{a}$ is the vector constituted by the nodal values of the unknown vector potential.

PRECONDITIONING TECHNIQUES

A preconditioner may be defined by performing an incomplete factorization of the original matrix $\mathbf{K}$: such a matrix can be decomposed on the form $\mathbf{K} = \mathbf{LU} - \mathbf{R}$, where $\mathbf{L}$ and $\mathbf{U}$ are respectively the lower an the upper part of $\mathbf{A}$, and $\mathbf{R}$ is the residual error of the factorization.

This technique is rather easy to be implemented, but the residual error $\mathbf{R}$ could detain the convergence of an iterative system, due to the fact that the original matrix $\mathbf{K}$ is replaced by an approximate factorization. To solve this problem, it is necessary to allow more fill-In of L and U over the original terms of lower and upper part of $\mathbf{K}$.

A general algorithm for building an incomplete LU factorisation is to perform a Gaussian elimination, even with the possibility to drop some elements in some predetermined non-diagonal position.

ILUK: As mentioned previously, an incomplete LU factorization may be too rough for bringing to convergence the solver. Thus a certain degree of fill-in is needed in order to supply a more accurate factorisation method. A level of fill-in is given to each element processed with the Gaussian elimination. At the first iteration of the Gaussian elimination, the first value of fill-in of the $k_{i,j}$ element of the sparse matrix $\mathbf{K}$ is:

$$lev_{i,j} = \begin{cases} 0 & k_{i,j} \neq 0; i = j \\ \infty & otherwise \end{cases} . \qquad (5)$$

At every iteration, the level of fill-in of each element is updated by:

$$lev_{i,j} = \min\{lev_{i,j}, lev_{i,k} + lev_{k,j} + 1\} \qquad (6)$$

In ILUK, all elements that have a fill-in value that not exceed the decided fill-in degree are kept, while the others are discarded.

ILUD: In ILUK approach, the elements dropped during the incomplete factorization are simply discarded. ILUD approach make the attempt to compensate this elimination by means of a certain variation to the left elements. The diagonal compensation technique provides to subtract the sum of all dropped elements into the main diagonal of the **U** matrix. At the end of the Gaussian elimination process, the raw i of **U** is:

$$u_{i*} = u_{i*} - (r_{i*}e)e_i^T \cdot \alpha, \qquad (7)$$

were α is a parameter that can change between 0 and 1 for weighting the compensation, and e=$(1,1,\ldots,1)^T$.

ILUT: An ILU algorithm with threshold substitute with zero some matrix elements according to their magnitude. Such a method, allows to determine dynamically the zero-pattern of the approximate matrix. In ILUT (p,τ) technique, two different criteria are adopted. First, elements in upper and lower factorization are dropped when less than the relative tolerance τ_i obtained multiplying τ by the original norm of the i-th row. Second, in each rows is kept a number of elements not exceeding a user specified fill-in value. This in order to control the number of non-zero elements for row.

ILUTP: As a matter of fact, the ILUT algorithm can fail if it encounter a zero pivoting, an over or underflow condition, or it can simply terminate with an incomplete factorization that does not lead to a stable computing of the linear system. To solve these problems, a column pivoting could be implemented quite easily in ILUT algorithm by means of a permutation array. However, pivoting should be advantageous only in diagonal block of a certain size.

APPLICATIONS

In order to gain information on which preconditioner is best suited to the problem requirement, the four preconditioning strategies has been applied to the linear problem. The problem has been discretized with four meshes with increasing number of mesh points: 1621 points (shown in Fig. 1), 6747 points,12150 points and 18830 points.
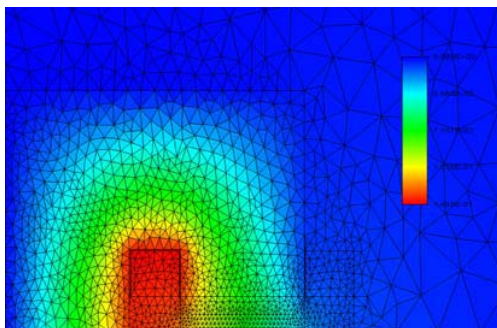

Fig. 1 Computational domain and A potential distribution

In our tests, the best preconditioners seem to be ILUT and ILUTP, with a slight preference for the second, due to the more robust behaviour. In Fig. 2 are reported the best convergence rate of the GMRES algorithm coupled with the ILUT, ILUTP ILUk preconditioners. The convergence rate CR is defined as follow:

$$CR = \log_{10}(IRN/FRN)/(NVMM - NI), \qquad (8)$$

where *IRN* is the initial residual norm, *FRN* the final residual norm, *NVMM* the number of vector-matrix multiply and *NI* the number of initializations of the GMRES solver. Actually, the higher convergence time is not related directly to the higher convergence rate: this is because with a high degree of fill-in increase the computational time requested for preconditioning. In Fig. 3 the best convergence time obtained by the preconditioned solver. The ILUK preconditioner has the best convergence rates slower than ILUT or ILUTP. The fourth preconditioner, the diagonal compensating ILUD, has not shown to be a valid strategy for the considered problem.

When solving the non-linear problem, the NITSOL methods coupled with GMRES has been applied. The Jacobian matrix has been analytically evaluated, to increase the robustness of the procedure. The GMRES solver shows a dependence on the preconditioning strategy similar to the one found in the linear case.
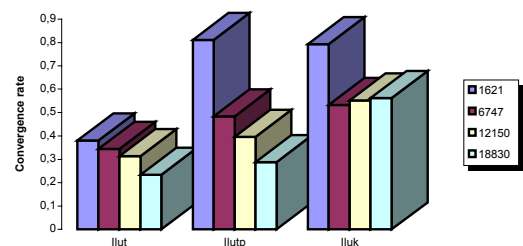

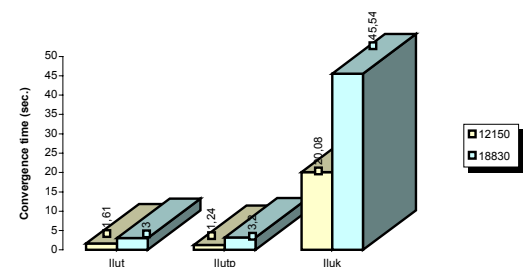Fig. 2 Preconditioned GMRES convergence rate

Fig. 3 Preconditioned GMRES convergence time

REFERENCES

[1] M. Pernice, H. F. Walker, NITSOL: A Newton Iterative Solver for Nonlinear System, *SIAM Journal on Scientific Computing,* Vol. 19, N° 1, pp. 302-318, 1998

[2] J. Saad, " Iterative methods for sparse linear systems", PWS Publishing Co., Boston, 1996

An Experimental Study of Equivalence Phenomena for Field Discontinuity and Optimal Discretizations in Finite Element Adaption

D. D. Giannacopoulos

Department of Electrical & Computer Engineering, McGill University
3480 University Street, Montreal, H3A 2A7, Canada
email: dennis.giannacopoulos@mcgill.ca

Abstract—Equivalence phenomena for field discontinuity and optimal finite element discretizations are reported. The effectiveness of field-discontinuity refinement criteria for achieving optimal finite element discretizations is investigated experimentally. The criteria are examined directly with finite element solutions computed from optimally discretized systems, and for practical adaptive finite element electromagnetic analysis of modern complex systems.

Introduction

In recent years, significant progress has been made on the electromagnetic modeling, simulation and computer-aided design of very complex systems, such as microelectronic system interconnection (MSI) structures [1]. The main difficulty with MSI analysis, for example, is that a very large number of free modeling parameters are needed to compute accurate and reliable simulations for realistic systems. The computational effort required for the electromagnetic analysis of the complex, dense, and irregularly routed arrays of high-speed interconnections that comprise modern MSI structures is often be prohibitive [1]. Yet such analyses are critical if MSI system performance is to be simulated with confidence.

Currently, one promising way to overcome this computational barrier is by using adaptive solver technologies that are capable of intelligently evolving and improving an efficient distribution of DOF over the problem domain [2]. Moreover, the study of error distributions corresponding to optimal finite element discretizations has recently attracted appreciable interest [2], [4], [3], [5]. An incentive for this research focus stems from the potential benefits of identifying effective and reliable refinement criteria, for adaptive finite element analysis (AFEA), based on *a priori* characterizations of optimal discretization solution properties. Such refinement criteria can be used in practice for efficiently guiding adaptive finite element electromagnetic solvers towards optimal accuracy solutions, without incurring the prohibitive computational costs associated with solving the optimal discretization problem directly [2]. This may be useful for overcoming the current computational bottleneck in obtaining accurate electromagnetic simulation results for complex modern systems.

Field Discontinuity in Optimal Discretizations

The primary purpose of the present contribution is to investigate the ability of practical field-discontinuity refinement criteria to effectively reproduce the main modeling characteristics of optimal finite element discretizations. While field-discontinuity refinement criteria are widely used and have been shown to be amongst the most effective for AFEA in electromagnetics, their exact connection to *optimal* finite element discretizations has yet to be reported in the mainstream literature.

In this work it is shown directly, for the first time, that the field-discontinuity criteria considered can correctly identify optimal error distributions, without the expense of actually solving the optimal discretization problem. Specifically, the equivalence phenomenon is demonstrated that field-discontinuity is satisfied precisely for optimally discretized problem domains, whereas it is not for non-optimal meshes. It should be noted that the experimental data supporting this conclusion are based on field solutions obtained using an explicit formulation for computing optimal discretizations directly; thus, the results computed under these conditions cannot be refuted. Namely, the formulation derived for general Helmholtz systems in [3] was employed, which is based on simultaneously satisfying sets of optimization equations defined for both the geometric discretization parameters (i.e., element vertex positions) and the field solution unknowns. In contrast, previous adaption studies reported with practical, but non optimal discretizations, have not been able to provide the sufficiently rigorous conditions required for examining the relationship between field discontinuity refinement criteria and optimal finite element discretizations. Therefore, the novelty of this work is, in part, the use of optimally discretized benchmark systems for evaluating this relationship.

In addition, the operational value of field-discontinuity refinement criteria is evaluated for practical electromagnetic AFEA of principal device features present in modern MSI structures, which are known to pose challenging problems in numerical modeling. Although these types of refinement criteria are well established, the study of their optimal discretization properties in AFEA for electromagnetic simulation is new.

Two simple 1-D free-space examples are presented first, in order to illustrate the equivalence phenomena of field-discontinuity and optimal finite element discretizations. The equivalence phenomena for field-discontinuity and optimal discretizations for practical electromagnetic AFEA are evaluated with a 2-D Laplace test system and a 3-D high-frequency structure in the long version paper.

The 1-D benchmark systems were first studied in [6], and are based on the classical point and line singularity models in free-space. The objective for each benchmark system is to compute the functional value based on the resolution of a radial neighborhood close to the singularity and spanning a 100-fold decay in potential: the point charge and line current, of magnitudes $10^{-9}/9$ C and 5×10^6 A, respectively, are located at the origin, and the two boundaries of both problem domains are set at radial distances of 0.1 m and 10 m away from the singular source distributions. It may be noted, that the field solutions associated with the free-space point charge and line current models contain the types of singularities associated with the sharp material corners and edges that are present in many practical MSI structures [2]. Thus, the primary feature of these test systems is the rapid field solution variation close to the singularity, which has been shown to drastically reduce the finite element convergence rate.

The results for the point and line singularity models are given in Table I and Table II, respectively. To focus ideas, a field discontinuity error measure [7] was evaluated for both uniform and globally optimal second-order meshes. All results were computed using standard second-order Lagrangian elements for the analysis of these 1-D examples. Furthermore, the results corresponding to the optimal meshes, are based on solving the optimization equations for the geometric discretization parameters [3], as previously explained. Hence, each of the optimal discretization results computed for these two benchmark systems represents the ideal mesh for a given number of DOF, i.e., the mesh that produces the most accurate solution possible for the variational finite element formulation used [3]. In each case F Error indicates the error in the global functional value. For the results reported in Table I, E Error indicates the average error in the electric field continuity at the element interfaces. Similarly, in Table II, H Error indicates the average error in the magnetic field continuity at the element interfaces. It should be noted that, for the uniform discretizations, the non-zero field-discontinuity quantities correctly indicate a large error for the functional value. However, for the optimal discretizations, the field-discontinuity errors are identically zero. Hence, field discontinuity is satisfied exactly with respect to these optimal finite element solu-

TABLE I
Numerical Results for Point Singularity Benchmark

No. Elements	Uniform Meshes		Optimal Meshes	
	F Error	E Error	F Error	E Error
2	540.6%	0.6470	35.87%	0.0000
4	242.5%	0.4160	3.756%	0.0000
6	147.9%	0.3605	0.8521%	0.0000
8	102.1%	0.3313	0.2840%	0.0000
10	75.34%	0.3108	0.1192%	0.0000
12	58.01%	0.2994	0.0583%	0.0000
14	46.01%	0.2801	0.0317%	0.0000
16	37.29%	0.2673	0.0187%	0.0000

TABLE II
Numerical Results for Line Singularity Benchmark

No. Elements	Uniform Meshes		Optimal Meshes	
	F Error	H Error	F Error	H Error
2	33.09%	0.2148	9.315%	0.0000
4	16.73%	0.1139	0.8409%	0.0000
6	10.44%	0.0859	0.1801%	0.0000
8	7.155%	0.0706	0.0587%	0.0000
10	5.175%	0.0602	0.0244%	0.0000
12	3.883%	0.0525	0.0118%	0.0000
14	2.994%	0.0463	0.0064%	0.0000
16	2.357%	0.0413	0.0038%	0.0000

tions. For each of the uniform and optimal second-order solutions considered, the average error in field discontinuity was calculated as the mean of the difference in field values over each individual element interface. Thus, these results demonstrate the equivalence phenomena for field discontinuity and optimal discretizations for electrostatic and magnetostatic finite element solutions. The equivalence phenomena will be further invested for a wider range of practical problems in the long version paper.

References

[1] A. Polycarpou, P. Tirkas and C. Balanis, *IEEE Trans. MTT*, vol. 45(10), pp. 1868–1874, 1997.
[2] D. Giannacopoulos, *IEEE Trans. Magn.*, vol. 38(2), pp. 401–404, 2002.
[3] D. Giannacopoulos, *Optimal Discretization-based Adaptive Finite Element Analysis for Electromagnetics*, Ph.D. Thesis, McGill University, 1998.
[4] L. Janicke, A. Kost and P. A. Bastos, *IEEE Trans. Magn.*, vol. 36(4), pp. 1627–1630, 2000.
[5] L. Y. Li and P. Bettess, *Com. Num. Meth. Eng.*, vol. 11, pp. 911–915, 1995.
[6] D. Giannacopoulos and S. McFee, *IEEE Trans. Magn.*, vol. 30(5), pp. 3523–3526, 1994.
[7] J. P. Webb and B. Forghani, *IEEE Trans. Magn.*, vol. 30(5), pp. 3511–3514, 1994.

Multi-Grid Method for Eigenvalue Problem Associated with Newcomb Equation

Takashi Kanki

Japan Coast Guard Academy

5-1 Wakaba, Kure, Hiroshima 737-8512, Japan

e-mail: kanki@jcga.ac.jp

Abstract—In a numerical method to compute the outer region matching data including a plasma close to the marginal ideal MHD stability, it is required to solve an eigenvalue problem and the associated singular equation for the Newcomb equation. An iterative method is developed to solve the eigenvalue problem and the singular equation. In this method, the eigenvalue problem is replaced with an equivalent nonlinear equation and a singular equation is derived from this nonlinear equation by using Newton's method. The multi-grid method can be applied to this method. It is confirmed from the numerical results that this method is powerful for solving the eigenvalue problem and the singular equation with numerical stability and high accuracy.

INTRODUCTION

In the asymptotic matching method to analyze the resistive MHD stability in tokamaks, the plasma is divided into two regions: the outer region far from rational surfaces and the thin inner layer around the rational surfaces [1]. In the outer region, the motion of the plasma can be described by ideal MHD equation without the nonideal MHD effects such as inertia, electrical resistivity and viscosity. The equation in this region is called the Newcomb equation [2] which is a second order ordinary differential equation with regular singular points at the rational surfaces. In the thin inner layer, the nonideal MHD effects must be taken into consideration. However, the equations of the motion in the inner layer can be sufficiently reduced. The solutions in both regions must be asymptotically matched so that the nonideal MHD motion of the plasma is determined. The quantities to be matched are called matching data. The Newcomb equation is homogeneous and the solution is expressed as a linear combination of the square integrable solution (small solution) and the non-square integrable solution (big solution). The ratio of these solutions is called outer region matching data [3]. It is required to compute this matching data with high accuracy.

We developed a numerical method to compute the outer region matching data for the plasma close to the marginal MHD stability by solving the eigenvalue problem and the associated singular equation[4]. This important example of the plasma close to the marginal stability is the $m=1$ instabilities, where m represents poloidal mode number [5]. The multi-grid method [6] is applicable to this method because the multi-grid method is effective not only for the linear equations but also for the singular equation and the eigenvalue problem [7]. The purpose of this study is to solve the singular equation and the eigenvalue problem with regular singular points and to investigate the properties of the numerical convergence. For this purpose, we perform detailed numerical experiment for the Newcomb equation in the $m=1$ theory.

NUMERICAL METHOD

The finite element method based on the variational principle can be applied for the eigenvalue problem and the singular equation associated with the one-dimensional Newcomb equation. As the results, the eigenvalue problem is expressed as

$$A\vec{\xi} = \lambda B\vec{\xi},\qquad(1)$$

where A is a symmrtric matrix, B a symmetric positive definite matrix, $\vec{\xi}$ an eigenvector and λ an eigenvalue. Then the singular equation for $\vec{\xi}$ and v

$$\begin{cases}(A - \lambda B)\vec{\xi} + v\vec{\xi}_0 = \vec{b}, \\ (\vec{\xi},\vec{\xi}_0) = 0\end{cases},\qquad(2)$$

is derived from the variational principle. Here the scalar v is Lagrangian multiplier, $\vec{b}$ a given vector and $\vec{\xi}_0$ the eigenvector corresponding to the eigenvalue in (1).

The eigenvalue problem (1) can be replaced with an equivalent nonlinear equation, and we obtain a linear equation for $\vec{\xi}^{(n+1)}$ and $\delta\lambda$

$$\begin{cases}(A - \lambda^{(n)}B)\vec{\xi}^{(n+1)} - \vec{\xi}^{(n)}\delta\lambda = 0, \\ (\vec{w},\vec{\xi}^{(n+1)}) = 1\end{cases},\qquad(3)$$

derived from Newton's method for the nonlinear equation [6]. Here $\vec{w}$ is a given vector non-orthogonal to the null space N of $A - \lambda B$ and $\|\vec{w}\|^2 = 1$. The algorism of this iterative method can be also applied to solving (2) because (2) is the same form as (3). Consequently, both eigenvalue problem and singular equation can be stably solved by means of this algorism because the global matrix in (3) is always regular.

Next, in order to solve (3) by using the multi-grid method, we consider the following equation

$$L_l\vec{u}_l = \vec{f}_l,\ \ L_l = \begin{bmatrix}\overline{L}_l & \vec{b}_l \\ \vec{\varphi}_l^T & \beta_l\end{bmatrix},\ \vec{u}_l = \begin{bmatrix}\vec{y}_l \\ \rho_l\end{bmatrix},\ \vec{f}_l = \begin{bmatrix}\vec{g}_l \\ \tau_l\end{bmatrix},\qquad(4)$$

where $\overline{L}_l$, β_l, $\vec{\varphi}_l^T$, $\vec{g}_l$ and τ_l are given quantities. The vector $\vec{y}_l$ and the scalar ρ_l are unknown quantities. The scalar ρ_l for all level l requires no prolongation, no restriction,

and in particular, no smoothing process since this component is not defined on a grid. By recognizing this point, the multi-grid method can be applied to solving (4). However, the restriction and the prolongation for the finite element method are required for this application because (1) and (2) are formulated by the finite element method. In order to determine the restriction $\bar{r}$ and the prolongation $\bar{p}$ for $\overline{L}_l \vec{y}_l = \vec{g}_l$, we approximate the basis function at level l-1, $e_j^{(l-1)}(x)$ by the basis function at level l, $e_j^{(l)}(x)$ such that

$$e_j^{(l-1)}(x) = \frac{x_{2j-1}^{(l)} - x_{2j-2}^{(l)}}{x_{2j}^{(l)} - x_{2j-2}^{(l)}} e_{2j-1}^{(l)}(x) + e_{2j}^{(l)}(x) \\ + \frac{x_{2j+2}^{(l)} - x_{2j+1}^{(l)}}{x_{2j+2}^{(l)} - x_{2j}^{(l)}} e_{2j+1}^{(l)}(x), \tag{5}$$

where $x_j^{(l)}$ is grid point at level l. The restriction $\bar{r}$ and the prolongation $\bar{p}$ can be defined by using (5), and we also obtain the characteristic relation $\bar{r} = \bar{p}^T$. Finally, if the matrix $\overline{L}_l$ at level l is symmetric, the symmetry of the matrix $\overline{L}_{l-1}(= \bar{r}\overline{L}_l\bar{p})$ at level l-1 is conserved by the relation $\bar{r} = \bar{p}^T$.

NUMERICAL RESULTS

We apply the numerical method to an ideal $m=1$ internal kink mode for a cylindrical plasma column. Let us use a cylindrical coordinate (r, θ, z). The system is assumed to be periodic in z direction, with length $2\pi R_0$, where R_0 is the major radius. The Newcomb equation for $m=1$ mode is described by

$$\frac{d}{dx}\left(f(x)\frac{d\xi}{dx}\right) - \varepsilon^2 g(x)\xi = 0, \quad x \in [0,a], \\ \xi(x=0) = \xi(x=a) = 0, \tag{6}$$

where $f(x)$ and $g(x)$ are given by

$$f(x) = \frac{x^3}{1+\varepsilon^2 x^2}\left(\frac{1}{q}-1\right)^2, \tag{7}$$

$$g(x) = \frac{2x^2}{1+\varepsilon^2 x^2}\left(\frac{1}{\varepsilon^2}\frac{dp}{dx}\right) \\ + F^2 \frac{x^3}{1+\varepsilon^2 x^2}\left(\frac{1}{q}-1\right)\left[\left(\frac{1}{q}-1\right)-\frac{2}{1+\varepsilon^2 x^2}\left(\frac{1}{q}+1\right)\right]. \tag{8}$$

Here, $\varepsilon=a/R_0$ is the inverse aspect ratio, $x=r/a$, the normalized plasma radius, and $q(x_0)=1$, where a is the plasma radius, q the safety factor, x_0 the position of the rational surface. Also, the toroidal magnetic field F is estimated by the pressure profile p and the safety factor q. For formulating (6) as (1), we employ the finite regular element method with mesh accumulation around the rational surface x_0 and impose the natural boundary condition at the rational surface x_0. We consider set $\vec{w}$, the initial eigenvalue $\lambda^{(0)}$ and eigenvector

$\vec{\xi}^{(0)}$ for Newton's method. The eigenvalue and the eigenvector in the appropriate coarse grid can be determined by the inverse iteration, and thereafter we linear-interpolate the eigenvector from the coarse grid to fine one. The linear-interpolated eigenvector is adopted as $\vec{w}$ and the initial eigenvector $\vec{\xi}^{(0)}$, and the eigenvalue computed by the inverse iteration is chosen as the initial eigenvalue $\lambda^{(0)}$. Fig. 1 shows the convergence of the eigenvalue with respect to the mesh number. It is indicated that the eigenvalue converges inversely with the square of the mesh number.
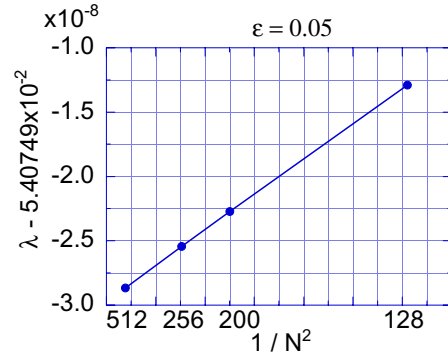
Fig. 1. Convergence of the eigenvalue with respect to the mesh number. This eigenvalue corresponds to the eigenvector left side the rational surface.

CONCLUSIONS

We have developed the iterative method to compute the eigenvalue problem and the associated singular equation for the Newcomb equation. The multi-grid method can be applied to this method. Application to the ideal $m=1$ mode have verified that this method is effective for solving the eigenvalue problem and the singular equation with numerical stability and high accuracy.

REFERENCES

[1] H. P. Furth, J. Killeen and M. N. Rosenbluth, "Finite resistivity instability of a sheet pinch," *Physics of Fluids,* vol. 6, pp. 459-484, April 1963.
[2] W. A. Newcomb, "Hydromagnetic stability of a diffuse linear pinch," *Annals of Physics,* vol. 10, pp. 232-267, June 1960.
[3] B. Coppi, J. M. Greene and J. L. Johnson, "Resistive instabilities in a diffuse linear pinch," *Nuclear Fusion,* vol. 6, pp. 101-117, January 1966.
[4] S. Tokuda and T. Watanabe, "Eigenvalue method for the outer-region matching data in resistive MHD stability analysis," *Journal of Plasma and Fusion Research,* vol. 73, pp. 1141-1154, October 1997.
[5] R. D. Hazeltine and J. D. Meiss, *Plasma Confinement,* Addison-Wesley, New York, 1992.
[6] W. Hackbush, *Multi-Grid Methods and Applications,* Springer-Verlag, Berlin, 1985.
[7] T. Kanki, S. Tokuda, T. Watanabe and T. Uyama, "The multi-grid method for computation of the outer-region matching data in resistive MHD stability analyses," *Nonlinear Electromagnetic Systems*, A. J. Moses and A. Basak (Eds.), pp. 600-603, IOS Press, 1996.

Electromagnetic Analysis of the 3D Effects of the Metallic Structures in JET Tokamak

R. Albanese

Ass. EURATOM/ENEA/CREATE , DIMET, Univ. Mediterranea di Reggio Calabria, Via Cuzzocrea, I-89100, Reggio Calabria, Italy

G. Rubinacci, F. Villone

Ass. EURATOM/ENEA/CREATE, DAEIMI, Università di Cassino, Via Di Biasio 43, I-03043, Cassino (FR), Italy

Abstract — In this paper we analyse the electromagnetic fields in the JET tokamak taking into account the 3D effects of its 3D metallic structures. The systems considered here that interact with the plasma are basically the vacuum vessel, the magnetic circuit, the active poloidal field (PF) coils. Especially the first two have important 3D effects that may cause significant deviations from purely axisymmetric estimates. The numerical results will be compared to the experimental data and utilized to tune approximate equivalent axisymmetric models.

INTRODUCTION

Tokamaks are fusion machines that are conceptually ideally axisymmetric, i.e. symmetric in the toroidal direction. Practical issues of accessibility to the interior of the machine do not allow a perfectly axisymmetric structure. This deviation from the ideal case complicates the interpretation of plasma behaviour.

Aim of this paper is to study such issues with reference to the Joint European Torus, JET, the largest presently operating tokamak [1]. The experience gained in this particular case can be of great importance also in other situations, especially in view of the next-generation tokamaks like ITER.

The first structure that electromagnetically interacts with the plasma is the vacuum vessel, a conducting shell which is supposed to counteract (via the induced currents) unwanted plasma movements. In JET the shell is highly non-axisymmetrical, not only due to the presence of ports and holes as in other tokamaks. We claim that the main deviation from axisymmetry of the vessel that must be taken into account is the presence of bellows, depicted in fig. 1. In this paper we study the effects of such deviations from

Fig.1. Bellows and rigid sectors.

axisymmetry on the eddy currents patterns.

The electrical continuity of the conducting structures ("rigid sectors") is guaranteed by the presence of corrugated conductors ("bellows"), that offer a relatively high resistance. In a purely axisymmetric model, the presence of bellows is usually accounted for by simply enhancing the equivalent toroidal vessel resistivity. Hence, a sudden displacement of the plasma causes the growth of purely axisymmetric currents whose time constants are rather fast due to the relatively high toroidal axisymmetric resistivity. In fact, we can expect that currents on a slower time scale arise only in rigid sectors due to their relatively low resistivity. These saddle currents may have a stabilizing effect on the plasma that is completely neglected in purely axisymmetric model.

A simplified model that is able to take this effect into account has been proposed in [2]. The vacuum vessel is discretized in a number of axisymmetric conductors, through which, in addition to the usual axysimmetric currents, some saddle currents flow. Obviously, these saddle currents have also a poloidal path. In [2] the contributions to the total resistances and inductances of such poloidal paths was roughly estimated on the basis of strongly simplifying assumptions, leaving some calibration coefficients for possible fitting against experiments.

Coupling this simplified equivalent model of the vessel with the linearized CREATE_L plasma response model [3], such non-axisymmetric effects were shown to be responsible for a reduction by a factor of almost 2 in the growth rate of the vertical instability. Surprisingly, this estimate was in rather good agreement (around 5% in standard cases) with experimental results, without any fitting of the above mentioned calibration coefficient, showing that the simplified assumptions were fairly reasonable.

Aim of this paper is to justify this simplified electromagnetic equivalent model. We must also consider that one of the peculiarities of JET, contrary to most present-day and future tokamaks including ITER, is the presence of a ferromagnetic core. This magnetic circuit is fully 3D, although usual models use crude 2D schematisations [4]. Consequently, its effect must be properly taken into account.
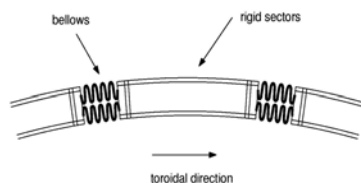
In order to pursue the goals mentioned above, we use the formulation described in [5] and here briefly recalled. The mathematical model consists of the standard eddy currents equations in the time domain. We suppose that the materials have a linear electric resistivity tensor $\underline{\underline{\eta}}$, taking into account possible anisotropies, and that the magnetic characteristic can be represented as:

$$\mathbf{B} = \mu_0(\mathbf{H} + \mathbf{M}), \quad \mathbf{M} = G(\mathbf{B}) \tag{1}$$

where $\mathbf{H}$ is the magnetic field, $\mathbf{B}$ is the magnetic flux density and the magnetization $\mathbf{M}$ is nonlinearly related to $\mathbf{B}$.

We solve the above stated problem using an integral formulation, which is well suited for the analysis of the complex 3D structures under exam, because the regularity conditions at infinity are automatically taken into account, and only the conducting domain V_c and the magnetic region V_f (i.e., neither the air nor the external coils) must be meshed.

Expressing the electric field $\mathbf{E}$ as:

$$\mathbf{E} = -\partial\mathbf{A}/\partial t - \nabla\varphi \tag{2}$$

and using the Biot-Savart law to calculate the magnetic vector potential $\mathbf{A}$ (such that $\mathbf{B} = \nabla\times\mathbf{A}$) we automatically solve (1). We then give a weak form of Ohm's law ($\mathbf{J}$ is the current density):

$$\int_{V_c}\underline{\underline{\eta}}\cdot\mathbf{J}\cdot\mathbf{w}dV + \frac{\partial}{\partial t}\int_{V_c}\mathbf{A}\cdot\mathbf{w}\,dV + \int_{V_c}\nabla\varphi\cdot\mathbf{w}\,dV = 0 \;\forall\mathbf{w} \tag{3}$$

and of the magnetic characteristics:

$$\int_{V_f}\mathbf{P}\cdot[\mathbf{M} - G(\mathbf{B})]dV = 0 \;\;\forall\mathbf{P} \tag{4}$$

In order to guarantee the solenoidality of the current density we introduce the electric vector potential $\mathbf{T}$ (such that $\mathbf{J} = \nabla\times\mathbf{T}$) with a two-component gauge condition [5] to guarantee its uniqueness. We give a finite element discretization of V_c and V_f, using edge elements $\mathbf{N}_k$ to approximate $\mathbf{T}$, so that:

$$\mathbf{T} = \sum_k I_k\mathbf{N}_k \Rightarrow \mathbf{J} = \sum_k I_k\nabla\times\mathbf{N}_k \tag{5}$$

while the magnetization vector is supposed to be piecewise constant ($\mathbf{P}_k$'s are unit vector pulse functions):

$$\mathbf{M} = \sum_k M_k\mathbf{P}_k \tag{6}$$

The gauge condition can be imposed giving a tree-cotree decomposition of the mesh [5], and retaining only the degrees of freedom associated with the edges of the cotree. In order to force $\mathbf{J}\cdot\mathbf{n} = 0$ over ∂V_c, while correctly dealing with multiply connected domains, one could resort to the procedure reported in [6].

Solving (3)-(4) with the Galerkin method, we obtain:

$$\underline{\underline{R}}\,\underline{I} + \underline{\underline{L}}\frac{d\underline{I}}{dt} + \underline{\underline{F}}\frac{d\underline{M}}{dt} = -\frac{d\underline{U}}{dt}$$
$$\underline{\underline{D}}\,\underline{M} = \underline{G}(\underline{B}) \tag{7}$$
$$\underline{\underline{D}}\,\underline{B} = \underline{\underline{E}}\,\underline{M} + \underline{\underline{F}}^{T}\underline{I} + \underline{W}$$

where $\underline{I} = \{I_k\}$, $\underline{M} = \{M_k\}$, $\underline{B} = \{B_k\}$ is the mean value of the components of the magnetic flux density in the elements, and:

$$L(i,j) = \frac{\mu_0}{4\pi}\int_{V_c}\int_{V_c}\frac{\nabla\times\mathbf{N}_i(\mathbf{r})\cdot\nabla\times\mathbf{N}_j(\mathbf{r}')}{|\mathbf{r}-\mathbf{r}'|}dV\,dV'$$

$$R(i,j) = \int_{V_c}\nabla\times\mathbf{N}_i\cdot\underline{\underline{\eta}}\cdot\nabla\times\mathbf{N}_j dV$$

$$U_i = \frac{\mu_0}{4\pi}\int_{V_c}\nabla\times\mathbf{N}_i\cdot\mathbf{A}_0 dV'$$

$$F_{ij} = \frac{\mu_0}{4\pi}\int_{V_c}\int_{V_f}\frac{\nabla\times\mathbf{N}_i(\mathbf{x})\cdot\mathbf{P}_j(\mathbf{x}')\times(\mathbf{x}-\mathbf{x}')}{|\mathbf{x}-\mathbf{x}'|^3}dVdV' \tag{8}$$

$$D_{ij} = \int_{V_f}\mathbf{P}_i\cdot\mathbf{P}_j dV$$

$$G_i(\underline{B}) = \int_{V_f}\mathbf{P}_i\cdot G\left(\sum_k B_k\mathbf{P}_k\right)dV$$

$$E_{ij} = \mu_0\int_{V_f}\mathbf{P}_i\cdot\mathbf{P}_j dV - \frac{\mu_0}{4\pi}\int_{\partial V_f}\int_{\partial V_f}\frac{\hat{\mathbf{n}}\cdot\mathbf{P}_i(\mathbf{x})\hat{\mathbf{n}}'\cdot\mathbf{P}_j(\mathbf{x}')}{|\mathbf{x}-\mathbf{x}'|}dSdS'$$

$$W_i = \frac{\mu_0}{4\pi}\int_{V_f}\int_{V_s}\frac{\mathbf{P}_i(\mathbf{x})\cdot\mathbf{J}_0(\mathbf{x}')\times(\mathbf{x}-\mathbf{x}')}{|\mathbf{x}-\mathbf{x}'|^3}dVdV'$$

The non-linear system of equations (7) can be solved using Picard iterations [5,7] or other suitable methods.

This procedure was already successfully applied to the calculation of the magnetostatic field around the plasma due to some PF coils, evaluated at the positions where some magnetic field sensors are located. In Fig. 2 the discretization of the magnetic circuit is reported. Preliminary results show a good agreement with both the experimental values, and with the predictions of purely 2D iron models.
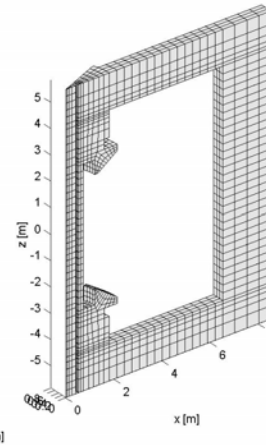
Fig.2. Mesh (2436 elements) of one leg of the JET 3D magnetic circuit.

[1] M. Keilhacker et al., *Nucl. Fusion* **41** 1925 (2001)
[2] R. Albanese, M. Mattei, F. Villone, submitted to *Nuclear Fusion*
[3] R. Albanese, F. Villone, *Nucl. Fusion*, **38** (1998) 723.
[4] E. Solano, G.H. Neilson, L.L. Lao, *Nucl. Fusion* **30** (1990) 1107.
[5] R. Albanese, G. Rubinacci, *Adv. Imag. El. Phys*, **102**, pp. 1-86 (1998)
[6] G. Rubinacci, A. Tamburrino, F. Villone, *IEEE Trans Mag*. Vol. 38, no. 2, pp.581-584
[7] F. I. Hantila, *Rev. Roum. Sci. Tech. El. En.*, **20**, p. 397-407 (1975)

Equilibrium shape of a liquid metal subject to electromagnetic forces

R. Moretti, S. Dufour, G. Vinsard, and B. Laporte

GREEN INPL

2 avenue de la Forêt de Haye

54516 Vandœuvre-lès-Nancy cedex - France

e-mail : Stephane.Dufour@ensem.inpl-nancy.fr

Abstract– **The equilibrium shape of a conductive liquid metal submitted to electromagnetic forces is computed and a comparison with experiments is performed. Meshing techniques are used to spare computation time.**

Introduction

A particular problem of the magnetohydrodynamics is to find the shape of the free boundary of a liquid metal submitted to electromagnetic forces.

Such a problem was studied [1] under the assumption that the depth of penetration is very small behind the dimension of the liquid metal, which allows to use the jump of the magnetic pressure that is introduced in an equation of equilibrium of the free boundary.

The proposed method does not use this assumption, but rather the Helmholtz decomposition of the Laplace forces [2] which allows to use a generic computational software (if it includes local remeshing) to treat such a problem.
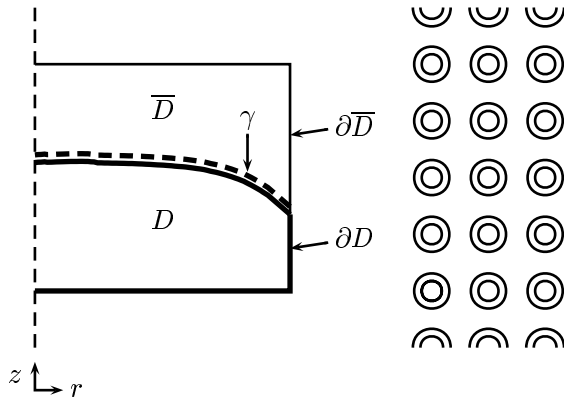
Fig. 1: Geometry of the device : the liquid load (left) and the inductor (right)

The Equilibrium Condition

The inductor made of tubular conductors, as well as the load (liquid tin in a cylindric container) have an axisymmetric geometry (Fig. 1).

In a first time, the axisymmetric time harmonic (of pulsation ω) eddy current problem consists in finding the complex magnetic vector potential (MVP) $\overline{A}$ such as :

$$\nabla \cdot \left(\frac{\nu}{r} \nabla (r\overline{A}) \right) - j\sigma\omega\overline{A} + \overline{J}_s = 0 \tag{1}$$

where $\nu(r,z)$, $\sigma(r,z)$ and $J_s(r,z)$ are respectively the reluctivity, conductivity (which vanishes everywhere except in the load region D where the eddy currents are induced) and the source current density.

In a second time, the mean value of the density of the electromagnetic forces is given by the Laplace law. When the gravity effect is included, the total force density $\vec{f}$ in the load D is :

$$\vec{f} = \sigma\omega \, \Im m \left(\frac{\overline{A}}{r} \vec{\nabla}(r\overline{A}^*) \right) + \rho\vec{g} \tag{2}$$

where $\overline{A}^*$ is the conjugate of $\overline{A}$, $\Im m$ means the imaginary part of. Since the load domain D is simply connected, the force can be split into two components [3] :

$$\vec{f} = \vec{\nabla}\phi + \vec{\nabla} \times \vec{\psi} \tag{3}$$

The rotational part $\vec{\psi}$ of the force density generates inner motions in the fluid. The gradient part ϕ makes the boundary move. If the inner movement of the fluid is not considered (it is assumed not to influence the shape of the liquid), then the equilibrium can be searched with only the gradient component. The field ϕ is solution of the problem :

$$\begin{cases} \Delta\phi = \vec{\nabla} \cdot \vec{f} & \text{in } D \\ \partial\phi/\partial n = \vec{f} \cdot \vec{n} & \text{on } \partial D \end{cases} \tag{4}$$

In this case (similar to the hydrostatic case), if the surface tension on γ is neglected, the Navier-Stokes equation reduces to :

$$\begin{cases} \vec{\nabla}P = \vec{\nabla}\phi & \text{in } D \\ P = P_{\text{atm}} & \text{on } \gamma \end{cases} \tag{5}$$

where P is the pressure field. Full details of this derivation will be given in the final paper.

The field ϕ is equal to the pressure (plus a constant) in D. Then, to satisfy the equilibrium condition, the boundary γ has to be such that the field ϕ, solution of (4), is constant on γ.

Without electromagnetic forces, the domain D is cylindric. Since it extends, under electromagnetic forces, to a part previously occupied by the air (Fig. 1), the domain of computation of ϕ is extended to $D \cup \overline{D}$ (where the air above D is labelled $\overline{D}$).

For a given boundary γ between D and $\overline{D}$, the field ϕ is computed as :

$$\begin{cases} \Delta\phi = \vec{\nabla} \cdot \vec{f_g} & \text{in } D \cup \overline{D} \\ \partial\phi/\partial n = \vec{f_g} \cdot \vec{n} & \text{on } \partial(D \cup \overline{D}) \end{cases} \quad (6)$$

where the generalized force $\vec{f_g}$ is equal to $\vec{f}$ in D, $\vec{0}$ in $\overline{D}$. A new boundary γ is obtained : it is chosen as an equipotential of ϕ under the constraint that the volume of D is constant. When the computation of ϕ is repeated, if the position of the new boundary γ becomes stationary, then ϕ verifies (4) in D, (7) in $\overline{D}$,

$$\begin{cases} \Delta\phi = 0 & \text{in } \overline{D} \\ \partial\phi/\partial n = 0 & \text{on } \partial\overline{D} \end{cases} \quad (7)$$

and is constant on γ : this boundary satisfies the equilibrium condition previously stated.

The practical computation is carried out iteratively. The starting shape is the one without electromagnetic forces. Each iteration of the equilibrium search algorithm is divided into four parts :

1. finite element (FE) computation of the MVP $\overline{A}$ with the help of (1).

2. FE computation of ϕ in the extended domain $D \cup \overline{D}$ with the help of (6).

3. search of the equipotential $\phi(\vec{x}) = k$ which keeps the volume of the liquid metal D constant.

4. modification of the location of the boundary γ corresponding to the equipotential $\phi(\vec{x}) = k$, and definition of the new domains D and $\overline{D}$.

The iterations are repeated until the mean distance between the old and the new boundary is low enough.

The major problem is the modification of the mesh of the domains D and $\overline{D}$ at each iteration. Instead of building the whole mesh at each iteration, the choice was made to use local remeshing techniques (an adaptive scheme is also introduced) : it allows to spare computation time while the quality of the mesh is kept constant.

The fourth step of each iteration is carried out by removing the nodes of the old boundary locally, and adding the nodes of the new boundary locally. Node displacement, edge fusion and edge re-connection around the boundary are made if necessary.

The inductor is made of 30 turns in series. The load which is used is solder tin (tin 63% and lead 37%). Its conductivity at 400^oC is $5.7\ 10^6 (\Omega.m)^{-1}$. The current is $110\,A$ and its frequency is $3800\,Hz$. The load radius is $4.5\,cm$, its height $2\,cm$ and its weight $1\,kg$.

The computed shape of the load has been compared with an experimental shape (Fig. 2). This one is obtained by putting in the load a thin copper sheet (with resin on both sides). Neither the electric behavior (the copper is conductive), nor the magnetic behavior (the dimension of the sheet is too low to take the depth penetration into account) of the load are disturbed by the measurement.
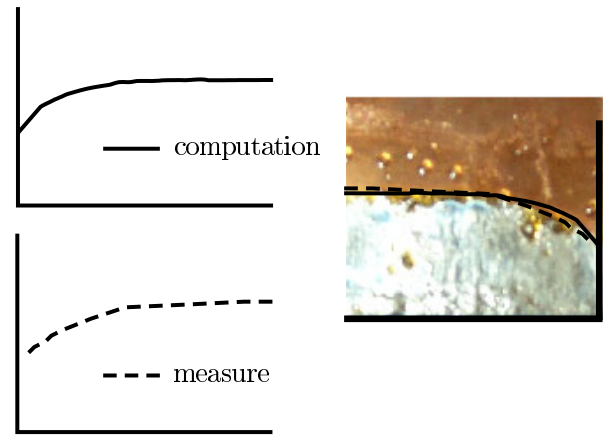
Fig. 2. Shape of the liquid tin

The maximum difference between the computed height shape and the experimental one is lower than $1\,mm$ (which is about 5% of accuracy).

Conclusion

The deformation of the shape of a liquid conductive domain under electromagnetic forces has been computed. Experimental measurements of the shape have been carried out. Results show a good agreement between both.

References

[1] R. Moreau, *Magnetohydrodynamics*, Kluwer Academic Publishers, Dordrecht Boston London, 1990.

[2] G. Vinsard, B. Laporte, N. Takorabet and J.P. Brancher, "An analysis of the rotational forces in the secondary of an electromagnetic pump", *IEEE Transactions on Magnetics*, vol. 34, pp. 3552-3556, September 1998.

[3] R. Dautray and J.L. Lions, *Mathematical Analysis and Numerical Methods for Science and Technology: Spectral Theory and Applications*, Springer Verlag, New-York, 2000.

Investigation on Couple Electric Field and Flow Field in High Voltage SF₆ Circuit Breaker

Liu Xiaoming, Wang Erzhi, Cao Yundong

Shenyang University of Technology

58# , Xinghua South Street, Tiexi District

Shenyang 110023, China

liuxiaoming527@hotmail.com

Abstract- **In this paper, couple electric field and gas flow field for interrupting high current in high voltage (HV) SF6 circuit breaker (CB) has been investigated and analyzed. Moreover, for simulating the insulating performance and interrupting characteristics of SF6 CB, arc model in different interrupting cases have been established. Interrupting performance and dielectric recovery characteristic of HV SF6 CB have been obtained and discussed.**

INTRODUCTION

SF6 is widely used as insulation and arc-quenching medium in electric apparatus because of its excellent insulating performance in uniform electric field. And extended in HV, extra HV and ultra HV CBs. The kernel problem to be investigated is dielectric recovery characteristic and interrupting performance, which mainly depend on the combined effects of electric field and gas flow state in arc quenching chamber during opening process and the arc energy dynamic simulation. Because the breaking process in a CB involves different phases, and considerable knowledge has been covered in understanding of the physical processes, which bring great difficulties for investigating the opening property. However, flow field computation within SF6 CB is extremely difficult due to the complex flow path with supersonic flow, active, viscous, compressible, variable boundary, and some intricate physical phenomena, such as shock wave and vortices during interrupting. Recently, inherent weakness has been reported lies in the simplifications of computing structure and arc modeling. The aim of this paper is to present a novel approach for analyzing the couple electric field and flow field of SF6 CB. Moreover, to solve the numerical problem with complex flow path and space-time processing synchronously, couple field mathematical model of electric field and flow field has been established in this paper. Fairly good representations of interrupting evolutionary processes within the arc-quenching chamber and arc dynamic characteristics have been achieved using the proposed model. And interrupting performance with higher precision has been obtained.

MATHEMATICAL MODELING OF COUPLE FIELD

According to the gas discharge theory, breakdown voltage or dielectric recovery characteristic of CB is determined by

$$U_b = (E/N)^* (U/E) P N_0 (T_0/T) = f(t) \tag{1}$$

where E, U, T, P represents electric field intensity, recovery voltage, gas temperature, gas pressure, respectively. And critical value $(E/N)^*$ is $3.56 \times 10^{-15} V.cm^2$. It can be seen from (1) that the dielectric recovery characteristic is depended on combination of electric field and flow field, and varied with time during interrupting.

The Governing Equation

The following set of governing equations for an couple of electric field and flow field computation can be derived:

Conservation equation of mass：

$$\frac{\partial \rho}{\partial t} + \frac{\partial \rho u}{\partial x} + \frac{\partial \rho v}{\partial y} + \frac{\rho v}{y} = 0 \tag{2}$$

Conservation equation of axial momentum：

$$\frac{\partial \rho u}{\partial t} + \frac{\partial (\rho u^2 + p)}{\partial x} + \frac{\partial \rho u v}{\partial y} + \frac{\rho u v}{y} = \frac{\partial \tau_{xx}}{\partial x} + \frac{\partial \tau_{xy}}{\partial y} + \frac{\tau_{xy}}{y} \tag{3}$$

Conservation equation of redial momentum：

$$\frac{\partial \rho v}{\partial t} + \frac{\partial \rho u v}{\partial x} + \frac{\partial (\rho v^2 + p)}{\partial y} + \frac{\rho v^2}{y} = \frac{\partial \tau_{yx}}{\partial x} + \frac{\partial \tau_{yxy}}{\partial y} + \frac{\tau_{yy} - \tau_{\theta\theta}}{y} \tag{4}$$

Conservation equation of energy：

$$\frac{\partial \rho e}{\partial t} + \frac{\partial \rho u (e + p/\rho)}{\partial x} + \frac{\partial \rho v (e + p/\rho)}{\partial y} + \frac{\rho v (e + p/\rho)}{y} =$$

$$\frac{\partial (u\tau_{xx} + v\tau_{xy} + k\partial T/\partial x)}{\partial x} + \frac{\partial (u\tau_{xy} + v\tau_{yy} + k\partial T/\partial y)}{\partial y} + \frac{u\tau_{xy} + v\tau_{yy} + k\partial T/\partial y}{y} + W \tag{5}$$

$$e = \frac{p}{(\gamma - 1)\rho} + \frac{u^2 + v^2}{2} \tag{6}$$

Equation of gas state：

$$p = \rho R T \tag{7}$$

where $R = \beta R_{SF6}$. β is the correcting parameter, R_{SF6} is gas constant of SF6.

2-D $k - \varepsilon$ Turbulent Flow Equation

To reflect the influence of turbulence in the gas flow process, 2-D $k - \varepsilon$ turbulent equation is introduced in this paper as a part of mathematical model, that is

$$\frac{\partial \mathbf{U}}{\partial t} + \frac{\partial \mathbf{F}_I}{\partial x} + \frac{\partial \mathbf{G}_I}{\partial y} + \mathbf{S}_I = \frac{\partial \mathbf{F}_V}{\partial x} + \frac{\partial \mathbf{G}_V}{\partial y} + \mathbf{S}_V + \mathbf{S} \tag{8}$$

in which, the above mentioned quantities have their traditional meanings, have been given in the full paper.

Electric Field Calculation Equation

Electric field computation satisfies Laplace's equation：

$$\nabla^2 \varphi = 0$$
$$\varphi\big|_{\Gamma_1} = f_1(p) \tag{9}$$
$$\frac{\partial \varphi}{\partial n}\big|_{\Gamma_2} = f_2(p)$$

Arc energy simulation before current zero：

$$W_{i,j} = \frac{G_{i,j}}{(\sum_{k=1}^{n} G_{i,k})^2} I^2 - W_{rad} \tag{10}$$

. Arc energy simulation after current zero：

$$W_{i,j} = \frac{(\sum_{k=1}^{n} G_{i,k})^2}{G_{i,j}} U^2 - W_{rad} \tag{11}$$

Arc energy simulation during current zero：

$$W_{i,j} = \sigma_{i,j}(T,P) S_{i,j} L_{i,j} E_{i,j}^2 - W_{rad} \tag{12}$$

where $G_{i,j}$ is the conductivity value of the element, $\sum_{k=1}^{n} G_{i,k}$ is the total conductivity value of the j th column, I is the interrupting current, and $G_{i,j} = \frac{\sigma_{i,j}(T,P) S_{i,j}}{L_{i,j}}$. And $\sigma_{i,j}(T,P)$ represents the gas conductivity, which is the function of T and P , the distribution of $\sigma_{i,j}(T,P)$ based on Frost's contributions [1], has been given in the full paper. U is the source voltage after current zero. $S_{i,j}$, $L_{i,j}$, $E_{i,j}$ and W_{rad} is the area of the element, arc length, corresponding electric field and the net radiation loss, respectively.

For truly reflecting the state and variation of couple of fields, the TVD Scheme is improved in this paper and combined with the Finite Volume Method to construct a new method for calculating the flow field [2], electric fields with different interrupting stoke have been computed using self-adaptive meshing Finite Element Method. Calculation conditions are as follows: Operating pressure of mechanical actuator $Pa = 32MPa$, gas pressure in arc quenching chamber $p_0 = 0.6MPa$, static state temperature $T = 293K$, gas constant $R = 56.9J/(kg \cdot k)$, and thermal insulation coefficient $k = 1.09$, opening stroke for calculated model is 260mm. As the couple of fields vary continuously during the opening process, the dielectric recovery characteristic is depended on dynamic distribution of couple of fields according to the convergence and stability requirement.

NUMERICAL RESULTS

The calculation model is given in Fig.1. And an arc burning model is illustrated in Fig.2. After solving couple of fields, insulating performance and dielectric recovery characteristic are obtained, as shown in Fig.3 and Fig.4.
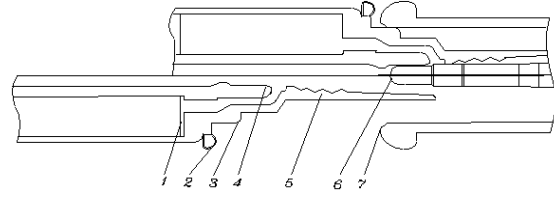
1- plenum chamber；2-shielding；3-movable main contact；
4-movable arc contact；5-nozzle；6-stationary arc contact；
7- stationary main contact

Fig.1. Calculation model of CB
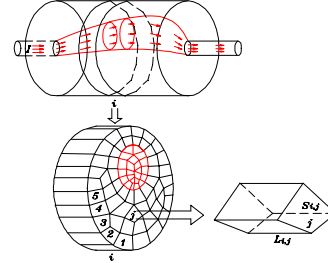
Fig.2. The sketch of equivalent arc model
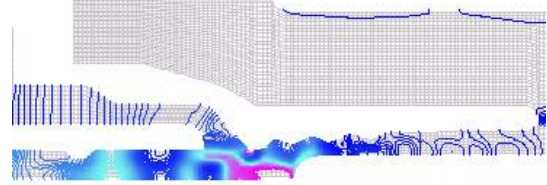
Fig.3. The temperature distribution with 136mm opening stroke
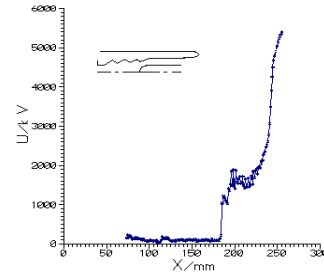
Fig.4. The dielectric recovery characteristics with 13.5ms arcing time

CONCLUSIONS

For investigating the dielectric recovery characteristic, a combined mathematical model, which compactly reflects the regularity of electric field, flow field and dynamic variation of arc burning, has been established. A new method and software with higher precision and resolving power for calculating the couple of fields in SF6 CB has been developed.

REFERENCES

[1] Frost L S, Liebermann R W, "Composition and transport properties of SF6 and their use in simplified enthalpy flow model," Proc. IEEE 59, pp.474-85, 1971.
[2] Cao Yundong, "Computation and analysis on dielectric field characteristic in high voltage SF6 circuit breaker," Shenyang University of Technology Doctor Thesis, 2001.

A Finite Element Analysis of Surface Wave Plasmas

H. Igarashi, K. Watanabe, T. Ito, T. Fukuda and T. Honma

Graduate School of Engineering, Hokkaido University

Kita 13, Nishi 8, Kita-ku, Sapporo, 060-8628, Japan, iga@em-si.eng.hokudai.ac.jp

Abstract— This paper describes a finite element analysis of surface microwaves coupled to a cold non-magnetized plasma for chemical vapor deposition (CVD). The microwave-plasma coupling is taken into account by introducing the frequency-dependent complex permittivity. The electromagnetic mode patters on the plasma-dielectric interface are analyzed using a simple cylindrical model. The present method is further applied to analysis of more realistic models of the CVD device.

I. Introduction

The surface wave plasma, maintained by the standing microwaves on the boundary surface between dielectric and plasma, has advantageous features such as low pressure, high density and large processing area for the chemical plasma deposition (CVD). For this reason, the surface plasma have recently been attracted considerable attention.

It is difficult to optimize the structure of such CVD devices as well as plasma parameters through only the experimental studies, and thus numerical analysis of the surface wave plasma would play a crucial role for those purposes. The microwaves coupled to the surface wave plasma have been analyzed with FDTD [1], and many useful characteristics have been clarified. FDTD, however, requires a lot of time steps to reach steady states which are what we want to know, and are also necessary for the design and parameter optimization. Moreover FDTD has problems in expression of curved shapes.

In this paper, we present a finite element analysis of the surface wave plasma under the time-harmonic condition, which is free from the above drawbacks. The finite element solution will be compared with the analytical results using a simple cylindrical model. Moreover the present method will be applied to more realistic model which has a waveguide, apertures and metallic rings.

II. Formulation

Let us consider the cylinder Ω, shown in Fig.1, consisting of the dielectric and plasma regions. The cylinder surface is assumed to be the electric wall. In the real CVD devices, microwaves propagate along a waveguide mounted on the top surface of the plasma vessel and go through apertures to the dielectric region. In our simple model, a driving line source of microwaves is located near the top surface, which would play the similar role of the aperture.
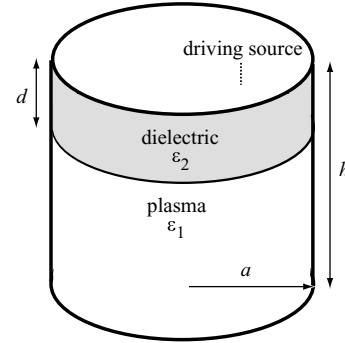
Fig.1 Cylindrical dielectric and plasma

A. Modeling of plasma

The plasma, assumed to be cold and non-magnetized, is governed by the equation of motion

$$m\frac{\partial \boldsymbol{v}}{\partial t} + m\nu\boldsymbol{v} = -e\boldsymbol{E}, \tag{1}$$

where m denotes the electron mass, $\boldsymbol{v}$ the velocity, ν collision frequency, e the elementary charge. The plasma current is given by

$$\boldsymbol{J} = -en\boldsymbol{v} = \sigma\boldsymbol{E}, \tag{2}$$

where n is the electron density and σ the conductivity. Insertion of the Fourier transform of (1) into (2) yields the complex permittivity of the plasma

$$\epsilon_1 \equiv \epsilon_0 + \frac{\sigma}{\mathrm{j}\omega}$$
$$= \epsilon_0 + \frac{\omega_p^2 \epsilon_0}{\omega(\mathrm{j}\nu - \omega)}, \tag{3}$$

where ω_p denotes the plasma frequency defined by $\omega_p = \sqrt{ne^2/m\epsilon_0}$. Consequently the plasma can be modeled by considering the complex permittivity (3) in the analysis of the electromagnetic field.

When $n < n_c$, where n_c is the cut-off density defined by $n_c = m\epsilon_0\omega_p/e^2$, the electrons' motion is slower than the microwaves, which can penetrate deeply into the plasma region. On the other hand, when $n > n_c$, the microwave is confined in the plasma-dielectric interface, and forms the surface wave.

B. Modeling of microwave

The microwaves are governed by

$$\nabla \times (\nabla \times \boldsymbol{A}) - \mu_0\omega^2\epsilon(\boldsymbol{A} + \nabla V) = 0, \tag{4}$$

$$-\mu_0\omega^2\nabla\cdot[\epsilon(\boldsymbol{A}+\nabla V)]=0, \qquad (5)$$

where $\boldsymbol{A}$ and V are the vector and scalar potentials. Note that (5) is valid in both dielectric and plasma which is assumed to be neutral. The weak form of (4) and (5) can be written as

$$\int_\Omega \nabla\times\boldsymbol{w}\cdot\nabla\times\boldsymbol{A}\,dv - \mu_0\omega^2\int_\Omega \epsilon\boldsymbol{w}\cdot(\boldsymbol{A}+\nabla V)\,dv = 0, \quad (6)$$

$$-\mu_0\omega^2\int_\Omega \epsilon\nabla w\cdot(\boldsymbol{A}+\nabla V)\,dv = 0, \qquad (7)$$

where $\boldsymbol{w}$ and w represent the vector and scalar weighting functions.

The region Ω is divided into finite elements with n nodes, e edges and f faces. The finite element discretization of (6) and (7), where the Whitney 1st and 0th forms work as the weighting functions [2], yields a system of equations with the symmetric matrix, that is

$$\begin{bmatrix} [C]^t[f][C]-\mu_0\omega^2[e] & -\mu_0\omega^2[e][G] \\ -\mu_0\omega^2[G]^t[e] & -\mu_0\omega^2[G]^t[e][G] \end{bmatrix}\begin{Bmatrix} A \\ V \end{Bmatrix}=\begin{Bmatrix} 0 \\ 0 \end{Bmatrix}, \tag{8}$$

where $[C]$ and $[G]$ denote the f × e and e × n matrices which are the discrete counterparts of curl and grad with entities ±1 and 0, and satisfy the relation $[C][G]=0$. The matrices $[f]$ and $[e]$ are f × f and e × e positive definite matrices, respectively.

Because of the inclusion grad $W_0\subset W_1$, where W_0 and W_1 represent the spaces spanned by the Whitney 1st and 0th forms, V can be eliminated from (8). This simplification leads to

$$\left[[C]^t[f][C]-\mu_0\omega^2[e]\right]\{A\}=\{0\}. \qquad (9)$$

The method in which (8) or (9) is solved is called A-V method or A method. The convergence of the ICCG method applied to the A-V method is proved to be better than that applied to the A method [3], [4] although the latter is easier for computer implementation.

III. Numerical Results

We set $a=110, h=68, d=17$ [mm], $f=2.45$ [GHz], $\epsilon_2=4\epsilon_0$ and $\nu=0$. The region is divided into $252{,}648$ tetrahedral elements with $314{,}864$ edges. In the solution processes of the finite element equations derived above with the ICCG method, sudden increases in the residue are observed. This is resulted from the fact that the finite element matrix is indefinite. Figure 1 shows $|\boldsymbol{E}|$ just above the plasma-dielectric interface. When $n > n_c$, we can clearly see the standing wave pattern as expected, whereas it becomes unclear when $n < n_c$.

In the long version, the computational times for A and A-V methods are reported. Moreover, the eigenmodes for the former cases will be compared with the theoretical results [5]. More realistic CVD models will also be discussed.
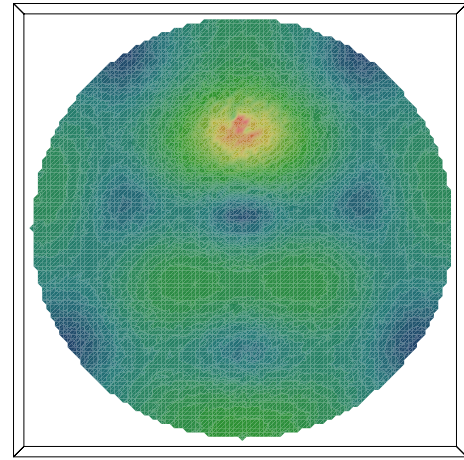
(a) $n < n_c$
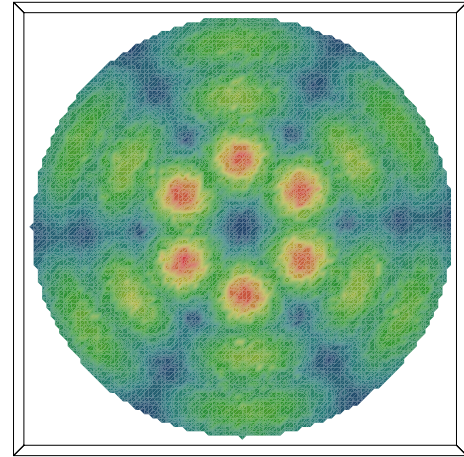
(b) $n > n_c$

Fig.1 $|\boldsymbol{E}|$ distribution near plasma-dielectric interface

IV. Conclusions

In this paper, a finite element analysis of surface microwaves coupled to a cold non-magnetized plasma for CVD has been described. The cold, non-magnetized plasma is modeled with the frequency-dependent complex permittivity. The surface wave is numerically observed when the plasma density is greater then the cut-off density.

References

[1] J. Kim, T. Takagi, M. Katsurai, "Numerical analysis and experimental investigation of discharge characteristics of ring dielectric line surface wave processing plasma apparatus", *Transaction of IEE Japan*, **122-A**, (2002), 639-649 (in Japanese).
[2] A.Bossavit, *Computational electromagnetism*, (1998), Academic Press.
[3] H.Igarashi and T.Honma, "On the convergence of ICCG applied to finite element equation for quasi-static fields", *IEEE Trans. Magn.* **38**, (2002), 565-568.
[4] H.Igarashi and T.Honma, "Convergence of conjugate gradient method applied to driven microwave problems", Proc. CEFC-2002, submitted to *IEEE Trans. Magn.*
[5] I. Ghanashev, M. Nagatsu and H. Sugai, "Surface wave eigenmodes in a finite-area plane microwave plasma", *Jpn. J. Appl. Phys.* **36**, (1997), 337-344.

3-D MHD Calculation that has considered the Alternating electromagnetic force

Shouji Satoh

Ohita Setubi Sekkei Corp., Nisinosu-1, Ohita, 870-0902 Japan.
Sho-sato@daisetsu.co.jp

Keisuke Fujisaki

Environment & Process Technology Center, Nippon Steel Corp., 20-1 Shintomi, Futtsu, 293-8511 Japan.
fujisaki@re.nsc.co.jp

Tatsuya Furukawa

ACE Lab., Saga University, 1 Honjo-machi,Saga-city, Saga 840-8502, Japan.
tach@ace.ec.saga-u.ac.jp

Abstract—In the continuous casting process, as for the movement of free surface at slab-mold, we know that it has an influence on the quality of slab. Then, the free surface at the slab-mold using electromagnetic stirring usually vibrates, and it is making the slab's quality degrade. The conventional magneto hydrodynamic calculation couldn't express the vibration of free surface. In this paper, we researched the new magneto hydrodynamic calculation that has considered the full electromagnetic force including the alternating part, and confirmed that it expresses the vibration of free surface.

INTRODUCTION

The slab-mold in continuous casting process produces "slab" that becomes an origin of the steel sheet by doing cooling molten steel and solidifying. The quality of slab is almost decided in the flow and solidification process in the slab-mold. Therefore, the flow at free surface and the movement of free surface are very important. In recent years, the electromagnetic stirring (EMS) by which the flow of molten steel and solidification process can be controlled was widely introduced because of the slab's quality improvement [1,2]. However, when doing the wrong EMS operation, it causes the degradation of slab's quality, because the free surface that is very sensitive to the quality vibrates.

On the other hand, the 3-D magneto hydrodynamic (MHD) calculation was generally used to evaluate the EMS operation [3,4,5]. The electromagnetic force that was gotten by EMS is combination of constant direct force and cyclic alternating force. Then, the variation of the alternating electromagnetic force would be considered as the disturbance of free surface vibration. However, the conventional MHD calculation uses an only direct part of electromagnetic force, because the mass inertia is enough larger than alternating force variation. Therefore, the conventional MHD calculation couldn't express the vibration of free surface.

ELECTROMAGNETIC FORCE

The electromagnetic field is derived from the Maxwell equations by the A-ϕ method as follows [6].

$$\nabla \times \left(\left[\frac{1}{\mu} \right] \cdot \nabla \times \vec{A} \right) + \sigma \left(\frac{\partial \vec{A}}{\partial t} + \nabla \varphi \right) = \vec{J}_0 \qquad (1)$$

By using the jω method and finite element method in the discrete three-dimensional field, magnetic flux density $\vec{B}$, eddy current density $\vec{J}_e$ and electromagnetic force $\vec{F}$ is defined as follows.

$$\vec{B} = \vec{B}_r + j\vec{B}_i$$
$$\vec{J}_e = \vec{J}_r + j\vec{J}_i \qquad (2)$$
$$\vec{F} = \vec{J}_e \times \vec{B} = \sigma \left(\frac{\partial \vec{A}}{\partial t} + \nabla \varphi \right) \times \left(\nabla \times \vec{A} \right)$$

Here, $\omega = 2\pi f$,(f is Frequency [Hz], $\vec{A}$ is vector potential [Wb/m], φ is scalar potential [V/m], $\vec{J}_0$ is current density [A/m^2], σ is electromagnetic conductivity [S/m], μ is permeability [H/m].

Magnetic flux density and eddy current density in Equation (2) are shown in the jω field. They are derived in the real field as follows.

$$\vec{J}_e = \vec{J}_r \cos \omega t + \vec{J}_i \sin \omega t$$
$$\vec{B} = \vec{B}_r \cos \omega t + \vec{B}_i \sin \omega t \qquad (3)$$

Electromagnetic force is derived in the real field as shown in Equation (4), too. The electromagnetic force is composed of constant direct force $\vec{F}_{DC}$ and cyclic alternating force $\vec{F}_{AC}$. The alternating force $\vec{F}_{AC}$ has cycle of the twice frequency.

However, the coalesced problem in electromagnetic field and fluid dynamic field generally ignores the alternating electromagnetic force, because the mass inertia of fluid dynamic field is enough larger than variation of the alternating electromagnetic force.

$$\vec{F} = \vec{J}_e \times \vec{B} = \begin{Bmatrix} J_y B_z - J_z B_y \\ J_z B_x - J_x B_z \\ J_x B_y - J_y B_x \end{Bmatrix}$$

$$= \begin{Bmatrix} \left\{ \begin{array}{l} \left(J_{ry}B_{rz} - J_{rz}B_{ry}\right)\cos^2 \omega t + \left(J_{iy}B_{iz} - J_{iz}B_{iy}\right)\sin^2 \omega t \\ + \left(J_{rz}B_{iy} + J_{iz}B_{ry} - J_{ry}B_{iz} - J_{iy}B_{rz}\right)\cos \omega t \sin \omega t \end{array} \right\} \\ \left\{ \begin{array}{l} \left(J_{rz}B_{rx} - J_{rx}B_{rz}\right)\cos^2 \omega t + \left(J_{iz}B_{ix} - J_{ix}B_{iz}\right)\sin^2 \omega t \\ + \left(J_{rx}B_{iz} + J_{ix}B_{rz} - J_{rz}B_{ix} - J_{iz}B_{rx}\right)\cos \omega t \sin \omega t \end{array} \right\} \\ \left\{ \begin{array}{l} \left(J_{rx}B_{ry} - J_{ry}B_{rx}\right)\cos^2 \omega t + \left(J_{ix}B_{iy} - J_{iy}B_{ix}\right)\sin^2 \omega t \\ + \left(J_{ry}B_{ix} + J_{iy}B_{rx} - J_{rx}B_{iy} - J_{ix}B_{ry}\right)\cos \omega t \sin \omega t \end{array} \right\} \end{Bmatrix}$$

$$= \begin{Bmatrix} \dfrac{1}{2}\left\{ \begin{array}{l} \left(J_{iy}B_{iz} + J_{rz}B_{ry} - J_{ry}B_{rz} - J_{iz}B_{iy}\right) \\ + \left(J_{ry}B_{rz} + J_{iz}B_{iy} - J_{iy}B_{iz} - J_{rz}B_{ry}\right)\cos 2\omega t \\ + \left(J_{rz}B_{iy} + J_{iz}B_{ry} - J_{ry}B_{iz} - J_{iy}B_{rz}\right)\sin 2\omega t \end{array} \right\} \\ \dfrac{1}{2}\left\{ \begin{array}{l} \left(J_{iz}B_{ix} + J_{rx}B_{rz} - J_{rz}B_{rx} - J_{ix}B_{iz}\right) \\ + \left(J_{rz}B_{rx} + J_{ix}B_{iz} - J_{iz}B_{ix} - J_{rx}B_{rz}\right)\cos 2\omega t \\ + \left(J_{rx}B_{iz} + J_{ix}B_{rz} - J_{rz}B_{ix} - J_{iz}B_{rx}\right)\sin 2\omega t \end{array} \right\} \\ \dfrac{1}{2}\left\{ \begin{array}{l} \left(J_{ix}B_{iy} + J_{ry}B_{rx} - J_{rx}B_{ry} - J_{iy}B_{ix}\right) \\ + \left(J_{rx}B_{ry} + J_{iy}B_{ix} - J_{ix}B_{iy} - J_{ry}B_{rx}\right)\cos 2\omega t \\ + \left(J_{ry}B_{ix} + J_{iy}B_{rx} - J_{rx}B_{iy} - J_{ix}B_{ry}\right)\sin 2\omega t \end{array} \right\} \end{Bmatrix} \quad (4)$$

$$= \vec{F}_{DC} + \vec{F}_{AC}\cos\left(2\omega t + \varphi\right)$$

MHD CALCULATION RESULT

Casting directional electromagnetic force that was gotten by EMS at the slab-mold is shown in Fig. 1. The "DC-part Only" line is direct electromagnetic force only, "DC-part + AC part" line is the full electromagnetic force which is combination of the direct part and the alternating part.
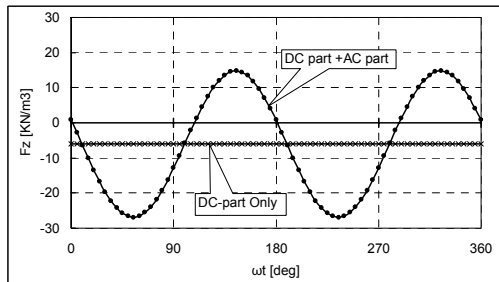
Fig. 1. Electromagnetic force

The result of conventional MHD calculation and new MHD calculation that has considered the full electromagnetic force are shown in Fig. 2. The result of new MHD calculation has vibration of free surface that couldn't express by conventional calculation. The slightly moving of free surface by conventional calculation is because of ripple. The vibration frequency of free surface by new calculation is just twice as large as supplied frequency, as indicated in Equation (4). This vibration of free surface agrees with the knowledge that we have, in case of the producing operation at the slab-mold using EMS.
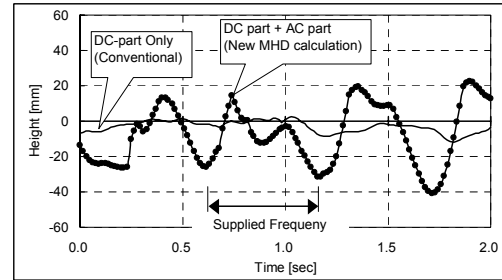
Fig. 2. Movement of free surface

CONCLUSION

With this new MHD calculation, we could express the vibration of free surface, which couldn't be produced in the conventional calculation. Then, we confirmed that the alternating part of electromagnetic force makes serious influence on the vibration of the free surface. Therefore, the consideration of the full electromagnetic force inclusive of the alternating part is very important, in MHD calculation to evaluate the movement of free surface which has a serious influence on the steel quality.

REFERENCES

[1] K.Fujisaki, K.Wajima, K.Sawada, and T.Ueyama, "Application of electromagnetic technology to steel making plant," *Nippon Steel Technical Report*, no.74, 1997.
[2] K.Fujisaki, J.Nakagawa, and H.Misumi, "Fundamental characteristics of molten metal flow control by linear induction motor," *IEEE Transaction on Magnetics*, vol.30, no.6, pp.4764-4766, November 1994.
[3] C.W.Hirt, and B.D.Nichols, "Volume of fluid (VOF) method for the dynamics of free boundaries," *Journal of Computational Physics*, vol.39, pp.201, 1981.
[4] K.Fujisaki, T.Ueyama, and K.Okazawa, "Magnetohydrodynamic calculation of in-mold electromagnetic stirring," *IEEE Transaction on Magnetics*, vol.33, no.2, pp.1642-1645, 1996.
[5] K.Fujisaki, and T.Ueyama, "Magnetohydrodynamic calculation in free surface," *Journal of Applied Physics*, pt.2, vol.83, no.11, pp.6356-6358, June 1997.
[6] T.Ueyama, K.Shinkura, and R.Ueda, "Fundamental equation for analysis by using the A-ϕ method and 3-D analysis of a conducting liquid," *IEEE Transaction on Magnetics*, vol.25, no.5, pp.4153-4155, 1989.

Influence of Model Parameters on 3D Turbulent Flow in an Electromagnetic Stirring System for Continuous Billet Casting

J.D. Lavers[1], G. Tallbäck[2], A. Erraki[1], and L. Beitelman[3]

[1]Dept. of Electrical & Computer Engineering, University of Toronto,
10 King's College Rd., Toronto M5S 3G4, Canada
[2]ABB Automation Systems, SE-721 67, Dept. FJT, Västerås, Sweden
[3]ABB Inc., JME Division, 1450 Hopkins St., Whitby, Ontario L1N 2C3, Canada

Abstract – **Unlike the case with electromagnetic fields, the development of a model for a turbulent flow system has considerable flexibility in terms of choosing model parameters and system equations. This paper examines that effect of several model choices on the turbulent flow that is predicted for an industrial scale electromagnetic stirring system. It is shown that the choice of model parameters can have a profound influence on the predicted flow.**

ELECTROMAGNETIC STIRRING SYSTEMS

Rotary in-mold electromagnetic stirring systems (EMS) are widely used when continuously casting high quality steel. These systems are essentially very crude induction motors where the rotating field in produced by quite simple 2-phase or 3-phase coil arrangements. The rotor, consisting of the casting mold together with the liquid steel, may be either square or rectangular in shape. In order for the electromagnetic fields to penetrate the copper mold, EMS systems typically operate at frequencies in the 1 to 6 Hz range. Typical 2-phase and 3-phase M-EMS systems are shown in Fig. 1.

Fig.1. Typical 2-phase (left) and 3-phase (right) EMS systems with rectangular molds.

The electromagnetic forces that act on the molten steel produce complex 3D turbulent flow. Although the flow has a predominant azimuthal component, there is also significant flow in the axial direction. When designing EMS systems, it is important that the specification on minimum angular velocity be met while maintaining a quiescent free surface (i.e. meniscus). The prediction of flow in systems such as this presents two challenges: (1) There is a strong coupling between the electromagnetic and the flow systems through

the **v x B** field, and (2) Turbulent flow is not characterized by a fully deterministic set of PDEs. This paper addresses several issues related to the selection of an appropriate turbulent flow model for an EMS system. It is shown that the choice of model has a profound effect on the magnitude and distribution of the predicted flow.

TURBULENT FLOW MODEL

Conventional laminar flow is described by the well-known physically derived Navier-Stokes equations (conservation of momentum and mass). When the flow is turbulent, however, the flow model becomes somewhat more empirical. In the simplest approach to turbulence modeling, an effective (turbulent) viscosity can be defined. At a more sophisticated level, diffusion transport equations can be defined to represent the kinetic energy k and the dissipation rate ε of the turbulence (i.e. the k-ε model). More recently, the Reynolds stress terms in the flow equations have been represented in terms of k, ε and a transport equation (i.e. the Reynolds Stress Transport or RST model).

In addition to the choice of model to represent turbulence and its impact on momentum transfer within the flow system, a second issue is numerical in origin. A flow system is governed by both diffusion and convection. As with systems involving velocity dependent convection terms, instabilities can arise which have to be treated through the introduction of an up-winding scheme. The predicted turbulent flow for an EMS system will be strongly dependent on the choice of up-winding. Finally, the predicted flow, particularly in the important meniscus region (which is far from the stirred zone) will depend on all of these factors and on the density of grid that is used.

The impact of each of these factors (choice of model for turbulence; up-winding; grid density) will be examined in this paper. When each is treated properly, and **v x B** effects are accounted for, it is possible to obtain excellent estimates of the velocity distribution. This is illustrated in Fig. 2, which shows the predicted axial distribution of angular velocity compared to data measured using an industrial EMS system acting on a mercury column of 110 x 110 mm square cross-section. The supply frequency was 5.25 Hz and a **v x B** correction was applied to the electromagnetic forces that were predicted by 3D FE software, assuming that the mercury region was stationary. Fig. 2 shows the quality of the results

that a carefully developed model can yield. The final model used approximately 50,000 cells, a RST model of turbulence and higher order up-winding.

Fig. 2. Comparison of measured flow data and values predicted by a fully converged and corrected turbulent model.

INFLUENCE OF TURBULECE MODEL PARAMETERS

The impact of the turbulence model (k-ε or RST) and the up-winding scheme is examined in this section. In all cases, the full **v x B** correction was applied.
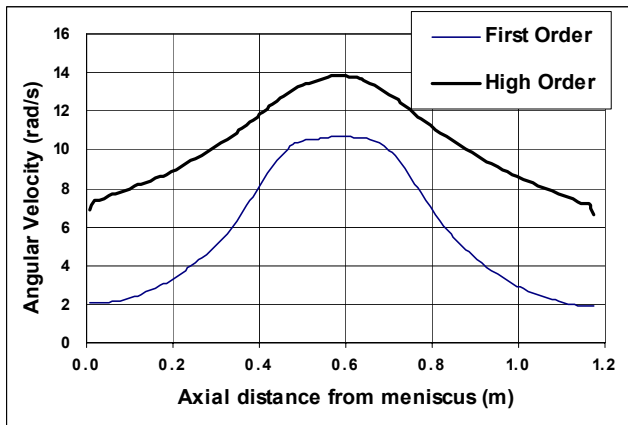
Fig. 3. Axial distribution of angular velocity as a function of the up-winding scheme.

Fig. 3 compares the axial distribution of angular velocity when first order and higher order up-winding schemes are used with a RST model of turbulence. The model in this case used a RST treatment of turbulence. The distribution using the higher order scheme is similar to the one shown in Fig. 2, other than small differences that are due to the use of a slightly different grid. Unless the higher order scheme is used, the predicted angular velocity is under-estimated by 40% at the system mid-plane, and by a factor of more than 3

at the meniscus. The problems at the meniscus are further illustrated in Fig. 4 where the radial distributions are compared. These results, together with Fig. 2, clearly show that predicted flow can be substantially in error at the meniscus unless a higher order up-winding is employed.
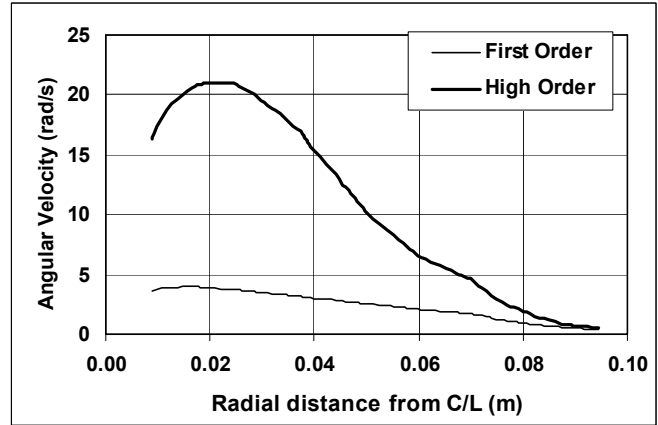
Fig. 4. Radial distribution of angular velocity at the meniscus as function of up-winding.

The impact of the turbulence model itself (k-ε vs. RST) is illustrated in Fig. 5. In this instance, both simulations used higher order up-winding. Clearly, when a k-ε model of turbulence is used with all other parameters being equal, the maximum angular velocity predicted at the meniscus is under-estimated by a factor of 2.
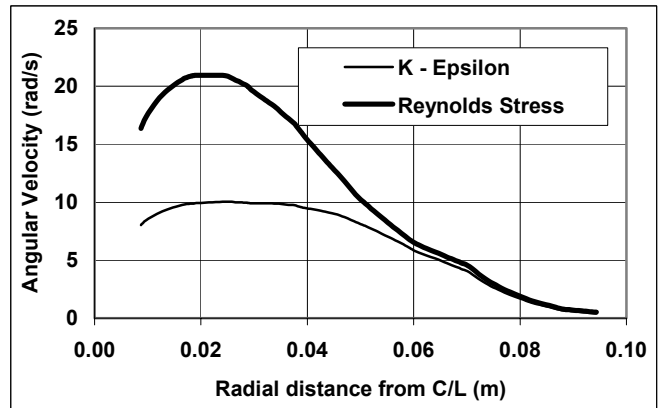
Fig. 5. Radial distribution of angular velocity at the meniscus as function of turbulence model.

CONCLUSIONS

It has been shown that in order to accurately predict the turbulent flow in a continuous casting EMS system, it is necessary to use a Reynolds Stress Transport model of turbulence, higher order up-winding, adequate grid density near the meniscus, and a **v x B** correction.

Numerical Solution of the Non Linear Electrodynamics in MHD Regimes with Magnetic Reynolds Number near One

Carlo A. Borghi, *Member IEEE,* Mario Carraro and Andrea Cristofolini

Department of Electrical Engineering of the University of Bologna,

Viale Risorgimento, 2, I 40135, Bologna, Italy

ca.borghi@mail.ing.unibo.it, mario.carraro@mail.ing.unibo.it, andrea.cristofolini@mail.ing.unibo.it

Abstract — In MHD regimes of plasmas with magnetic Reynolds number comparable to one, electrodynamics exhibits a non linear characteristic. In the present paper, the electrodynamics has been discretzed utilizing a finite element method. The problem unknown is the electric scalar potential. Non linearity are caused by the dependance of the electric transport parameters and of the source terms on the magnetic flux density. Different approach are evaluated to deal with the non linearity. The model has been coupled with a solver of the Navier-Stokes equations The MHD interaction in the boundary layer of an hypersonic flight has been analyzed

INTRODUCTION

In a wide range of MHD applications of technological interest, the magnetic Reynolds number Re_m can be assumed to be much lower than one. Under this circumstance, due to a low fluid conductivity or a low flow velocity, the MHD interaction does not produce sufficient electric current density to generate a significant magnetic flux density. As an example, when modeling the electrodynamics in an MHD power generator, the assumption $Re_m << 1$ allows to neglect the induced by the plasma current density when compared to the externally imposed magnetic flux density. This leads to a significant simplification of the electrodynamics.

However, instances exist where the assumption of a magnetic Reynolds number much lower than one does not hold. In this case, the current density in the fluid depends, on some extent, on the magnetic flux generated by the current density itself. An additional complication arises when dealing with plasmas, where the Hall component of the current density is often not negligible. The Hall current represents the effect of the electrons and ions drift, and depends on the magnetic flux density.

In this paper, a two dimensional model for the analysis of the non linear electrodynamics of the MHD interaction in a plasma with magnetic Reynolds number comparable to one.

PHYSICAL MODEL

The governing equations for the electrodynamics can be obtained from the Maxwell equations and the generalized Ohm's law. The total magnetic flux density $\mathbf{B_T}$ can be decomposed into the flux density $\mathbf{B_p}$ induced by the plasma current and the externally imposed flux density $\mathbf{B_e}$. Given the linearity of the relation linking the magnetic field to its sources, it follows:

$$\frac{1}{\mu_0}\nabla \times \mathbf{B_p} = \mathbf{J_p} \text{ ,} \tag{1.a}$$

$$\frac{1}{\mu_0}\nabla \times \mathbf{B_e} = \mathbf{J_e} \text{ ,} \tag{1.b}$$

where $\mathbf{J_p}$ and $\mathbf{J_e}$ are the current density in the plasma and in the conductors generating the imposed magnetic flux density.

Neglecting the ion slip phenomenon, the generalized Ohm's law can be written as:

$$\mathbf{J_p} = \sigma\left(\mathbf{E} + \mathbf{u} \times \mathbf{B_T}\right) - \beta_e \frac{\mathbf{J_p} \times \mathbf{B_T}}{B_T} \text{ ,} \tag{2}$$

where, naming μ_e the electronic mobility, the electrons Hall parameter β_e is:

$$\beta_e = \mu_e B_T \text{ ,} \tag{3}$$

Equation (3) can be rewritten in a more convenient way as:

$$\mathbf{J_p} = \boldsymbol{\sigma}(\mathbf{B_T})\left(\mathbf{E} + \mathbf{u} \times \mathbf{B_T}\right), \tag{4}$$

where the conductivity tensor $\boldsymbol{\sigma}(\mathbf{B_T})$ is:

$$\boldsymbol{\sigma}(\mathbf{B_T}) = \frac{\sigma}{1+\beta_e^2}\begin{vmatrix} 1+\beta_{e,x}^2 & \beta_{e,x}\beta_{e,y}-\beta_{e,z} & \beta_{e,x}\beta_{e,z}+\beta_{e,y} \\ \beta_{e,x}\beta_{e,y}+\beta_{e,z} & 1+\beta_{e,y}^2 & \beta_{e,y}\beta_{e,z}-\beta_{e,x} \\ \beta_{e,x}\beta_{e,z}-\beta_{e,y} & \beta_{e,y}\beta_{e,z}+\beta_{e,x} & 1+\beta_{e,z}^2 \end{vmatrix},$$

with:

$$\beta_{e,i} = \frac{B_i}{B_T}\beta_e = B_i\mu_e \text{ , } i = x, y, z$$

Neglecting the time derivatives of the magnetic flux density and of the electric charge density, the physical model is completed, by the following equations:

$$\nabla \times \mathbf{E} = 0 \Rightarrow \mathbf{E} = -\nabla\varphi \text{ ,} \tag{5}$$

$$\nabla \cdot \mathbf{J_p} = 0 \text{ ,} \tag{6}$$

NUMERICAL MODEL

Following a finite element approach, and assuming the x-y plane as the plane of symmetry, (4), (5) and (6) yield the

following matrix:

$$\mathbf{K}\,\boldsymbol{\varphi} + \mathbf{p_z} - \mathbf{p_F} + \mathbf{p_J} = 0 \tag{7}$$

where $\boldsymbol{\varphi}$ is the nodal potential vector and the matrix $\mathbf{K}$ is the conductivity matrix, defined as follows:

$$\mathbf{K} = \int_{\Omega} \nabla \mathbf{N^T} \boldsymbol{\sigma}_{xy} \nabla \mathbf{N} dS \;, \tag{8}$$

with $\boldsymbol{\sigma}_{xy}$ obtained by deleting the z row and the z column in the matrix representing the conductivity tensor. It should be noted that, due to the presence of the Hall parameter, the conductivity matrix depends on the magnetic flux density and, as a consequence, on the electric scalar potential, which is the problem unknown. This feature yields a non linear characteristic of the problem. The vector $\mathbf{p_z}$ is the contribution of the current on the x-y plane caused by the E_z component of the electric field, which is supposed to be known; $\mathbf{p_J}$ is the contribution of the current densities on the calculation domain boundary and the vector $\mathbf{p_F}$ represents the effect of the $\mathbf{u} \times \mathbf{B_T}$ term. This term, as the conductivity matrix $\mathbf{K}$, depends on the magnetic flux density $\mathbf{B_p}$.

In order to find out the magnetic flux density $\mathbf{B_p}$, the magnetostatic problem defined by (1.a) and:

$$\nabla \cdot \mathbf{B_p} = 0 \;, \tag{9}$$

has to be solved. This can be done analytically, by means of the Biot-Savart law, or numerically solving the vector potential equation:

$$\mathbf{B_p} = \nabla \times \mathbf{A_p} \;, \quad \nabla \times \left(\frac{1}{\mu} \nabla \times \mathbf{A_p} \right) = \mathbf{J_p} \;, \tag{10}$$

by means of a finite element technique. The former approach is especially attractive because of the possibility to store the matrix representing the linear relationship between the nodal value of current density and magnetic flux density. However, the numerical solution of (10) is often much faster. Moreover, the storing and the operation management of a full matrix is not a viable option for meshes containing more than some thousands of nodes.

Two approach has been implemented for the solution of the non linear problem shown in (7). The first proposed methodology is basically a straight iterative scheme: at each iterative step, the solution of (7) allows to evaluate the current densities in the calculation domain. The values of the magnetic flux density calculated from (10), are then utilized for solving (7) at the next iterative step.

The second approach utilize an inexact Newton method [1] to solve (7). The method utilizes the inexact Newton condition:

$$\left\| \mathbf{F}(\boldsymbol{\varphi}_k) + \mathbf{F'}(\boldsymbol{\varphi}_k) d\boldsymbol{\varphi}_k \right\| \leq \eta_k \left\| \mathbf{F}(\boldsymbol{\varphi}_k) \right\| , \tag{11}$$

where $\mathbf{F'}$ is the Jacobian of the function $\mathbf{F}$, constituted by the left hand terms of (7), $d\boldsymbol{\varphi}_k$ is the solution increment at the k step and $\eta_k \in [0.1)$ is a forcing term enhancing the efficiency of the convergence. The linear system at each iteration is solved by means of a GMRES algorithm.

The proposed electrodynamic model has been coupled with a fluid-dynamic code [2]. The fluid-dynamic equation are given by the continuity equation for mass, momentum and energy, and by the state equations of plasma.

APPLICATIONS AND CONCLUSION

The proposed methodology has been applied for the analysis of the magneto-fluid dynamics in the boundary layer of an hypersonic vehicle. In Fig. 1, a portion of the calculation domain is shown, as well as the position of the conductors generating the externally imposed magnetic flux density. The calculation domain lays on the x-y plane, and the z component of flow velocities is neglected.

The convergence of the direct iterative scheme proved to be robust enough for magnetic Reynolds numbers not exceeding 0.5. The application of the inexact Newton solver presents some critical points, namely the evaluation of the Jacobian matrix and the setting up of an efficient preconditioning technique in order to optimize the convergence of each GMRES run.
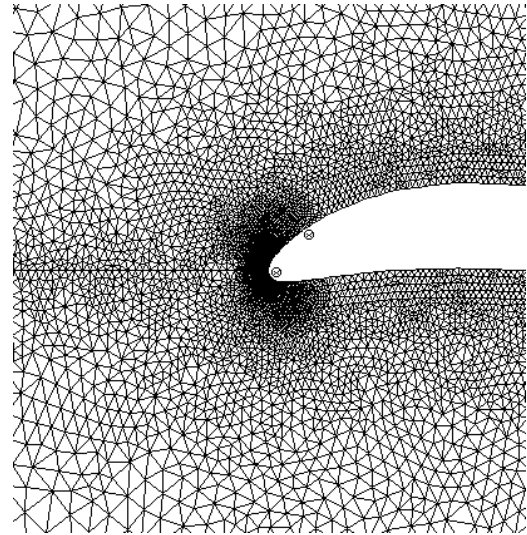
Fig. 1. Calculation mesh and conductors position.

REFERENCES

[1] M. Pernice, H. F. Walker, "NITSOL: A Newton Iterative Solver for Nonlinear System", *SIAM Journal on Scientific Computing,* Vol. 19, N° 1, pp. 302-318, 1998
[2] L. Fezoui, B. Stoufflet, "A Class of Implicit schemes for Euler Simulations on Unstructured Meshes", *Journ. of Comp. Phys.,* 84, pp. 174-206, 1989.

Investigation of Benchmark Model

for Estimating Iron Loss in Rotating Machine

Hideo Domeki[*1], Yoshiyuki Ishihara[*2] , Chikara Kaido[*3], Yoshihiro Kawase[*4], Shingo Kitamura[*5],
Tohru Shimomura[*5],　Norio Takahashi[*6], Takashi Yamada[*7] and Katsumi Yamazaki[*8]

*1:Research & Development Center, Oriental Motor Co., Ltd., Kashiwa 277-0882, Japan (domeki@mb.infoweb.ne.jp)
*2:Dept. Electrical Eng. Doshisha Univ., Kyotanabe 610-0394, Japan (yishihar@mail.doshisha.ac.jp)
*3:Steel Research Labs., Nippon Steel Corp., Futtsu 293-8511, Japan (kaido@re.nsc.co.jp)
*4:Dept. Information Science, Gifu Univ., Gifu 501-1193, Japan (kawase@info.gifu-u.ac.jp)
*5:Development Dep., Kusatsu Electric Co., Ltd., Kusatsu 525-8501, Japan (s-kitamura@kusatsu.co.jp)
*6:Dept. Electrical and Electronic Eng., Okayama Univ., Okayama 700-8530, Japan (norio@elec.okayama-u.ac.jp)
*7:The Japan Research Institute, Ltd., Kudanminami 1-5-3, Tokyo 102-0074, Japan (yamada@sci.jri.co.jp)
*8: Dept. Electrical Eng., Chiba Institute of Tech., Narashino 275-0016, Japan (yamazaki@pf.it-chiba.ac.jp)

Abstract ― **In order to examine estimation methods of iron losses of rotating machines, a verification model of surface permanent magnet (SPM) motor is manufactured and measured by the investigation committee of IEE of Japan. The effect of stress due to the insertion to aluminum case on magnetic characteristics can also be investigated by using the model. In this paper, features of the benchmark model is discussed, and some results of calculation and measurement are shown.**

Ⅰ. INTRODUCTION

It has become more important for design of motors to estimate precisely iron losses under rotating flux. But, the accuracy of the conventional estimation methods have not been sufficient for the practical design of motors. In order to investigate the accuracy of various estimation methods of iron losses, a benchmark model of SPM motor is proposed by the "Investigation Committee on High-ly Advanced Method for Analyzing 3-D Electromagnetic Fields in Rotating Machines" of IEE of Japan.

In this paper, features of the benchmark model is shown, and some problems, such as to examine the effect of stress due to casing the motor core are discussed. Various estimation methods, such as calculating the iron loss as a summation of iron losses under alternating fluxes in x-and y-direction[1], interpolating the measured iron losses under rotating flux, are examined using the model.

Ⅱ. EXAMINATION OF BENCHMARK MODEL

Fig.1 shows a 4-pole SPM motor model. This motor consists of rotor core, permanent magnet, stator core and aluminum case. The stator and rotor cores are made of non-oriented silicon steel (grade: 50A1300). The core length is 40 mm. The permanent magnet is Nd-Fe-B magnet, and the magnetization is 1.26 T (parallel orientation). The motor is rotated without excitation to investigate the iron loss of stator core due to the flux produced by the permanent magnet of rotor. The rotating speed is 1500rpm.

The iron loss of stator core is examined by the following process:

(a) The *B-H* curve and iron loss of a stacked stator core and glued stator core are measured, and those are compared with the result measured by the SST (single sheet tester).

(b) The torque of the motor having glued stator core is measured by a torque meter when the permanent magnet rotor is driven by another motor as shown in Fig.2.

(c) The iron loss of the stator is obtained by subtracting the torque (corresponding to the mechanical loss) measured by driving the rotor having non-magnetized permanent magnet from the torque measured in (b).

(d) The same measurement is also carried out for the stator core with aluminum case having some stress due to casing.

Ⅲ. RESULTS AND DISCUSSION

A. Iron Loss by Sinusoidal Alternating Excitation of Stator Core

First, the stator core is exited by sinusoidal alternating voltage with the toroidal winding as shown in Fig.3(a). The flux flows in the circumferential direction in the stator core. The purpose of this preliminary study is to clarify the increase of the iron loss after manufacturing the stator core from the silicon steel.

In this case, the iron loss wi per weight can be expressed approximately as follows:
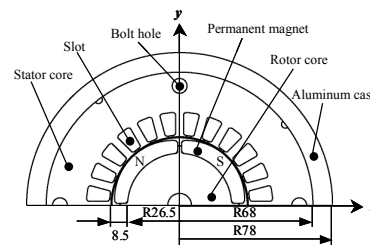
Fig. 1. SPM motor model.
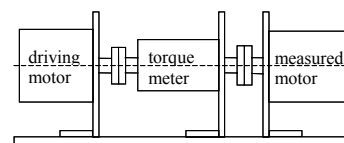
Fig. 2. Measuring equipment of torque.

$$w_i = K_e f^2 B_{max}^2 + K_h f B_{max}^2 \qquad (1)$$

where the K_e, K_h are the eddy current and hysteresis loss coefficients obtained from the iron loss measurement of the silicon steel, f is the frequency, B_{max} is the maximum flux density during the period of AC excitation.

Fig.3(b) shows the experimental and the calculated results, which agree well. One reason of the slight underestimation of the calculated results can be considered as the effect of the strain caused by the manufacturing of the stator.

B. Iron Loss at No Load Condition of Motor

Next, the iron loss at no load condition of the motor is measured and calculated. In this case, the effects of the harmonics and the iron loss due to rotating magnetic field caused by the rotation of the rotor are not negligible. Thus, the following four methods are applied:

(a) Harmonic iron loss calculation using (1) by the Fourier transformation of the waveform of flux density at each finite element. The total iron loss is calculated by the sum of the harmonic losses as follows:

$$W_i = \int_{ron} \sum_{n=1}^{M} D\left\{ (K_e f_n^2 B_{rn}^2 + K_h f_n B_{rn}) + (K_e f_n^2 B_{\theta n}^2 + K_h f_n B_{\theta n}) \right\} dv \qquad (2)$$

where D is the density of the core, M is the number of the harmonics, B_{rn} and $B_{\theta n}$ are the n-th harmonics of the radial and peripheral components of the flux density.

(b) Total iron loss calculation using the waveform of the flux density directly [2]. The eddy current loss W_{ie} and the hysteresis loss W_{ih} are calculated by

$$W_{ie} = \frac{K_e D}{2\pi^2} \int_{ron} \frac{1}{N} \sum_{k=1}^{N} \left\{ \left(\frac{B_r^{k+1} - B_r^k}{\Delta t} \right)^2 + \left(\frac{B_\theta^{k+1} - B_\theta^k}{\Delta t} \right)^2 \right\} dv \qquad (3)$$

$$W_{ih} = \frac{K_h D}{T} \sum_{i=1}^{NE} \frac{\Delta V_i}{2} \left(\sum_{j=1}^{Npr^i} \left(B_{mr}^{ij} \right)^2 + \sum_{j=1}^{Np\theta^i} \left(B_{m\theta}^{ij} \right)^2 \right) \qquad (4)$$

where N is the number of time step per one time period, Δt is the time interval, ΔV_i is the volume of the i-th finite element, B_{mr}^{ij} and $B_{m\theta}^{ij}$ are the amplitudes of each hysteresis loop.

(c) Total iron loss calculation considering the effect of the rotating magnetic field as follows:

$$W_i = W_1(\alpha, B_{max}) + \sum_{n=2}^{M} \left\{ W_n(B_{rn}) + W_n(B_{\theta n}) \right\} \qquad (5)$$

where W_1, W_n are the fundamental and the harmonic iron losses, α is the axis ratio of the rotating magnetic field. In this case, the fundamental iron loss is expressed as the function of both B_{max} and α.

(d) Direct eddy current loss calculation considering skin effect of the laminated silicon steel using the 3-D finite element method.

Fig.4(a) shows the iron loss distribution obtained by the

method (b). The iron loss concentrates at the stator teeth, where the time variation of the flux density includes low order time harmonics caused by the magnetic saturation of the core as shown in Fig.4(b).

Fig.5 shows the calculated iron losses of SPM motor model shown in Fig.1. The accuracy of the iron loss estimation methods can be examined by comparing with measurement. The detailed results of measured and calculated iron losses will be shown and discussed in the extended paper.

(a) Flux distribution (b) Iron loss

Fig. 3. Iron loss by sinusoidal alternating excitation of stator core.

(a) Iron loss distribution (b) Flux density waveform at teeth
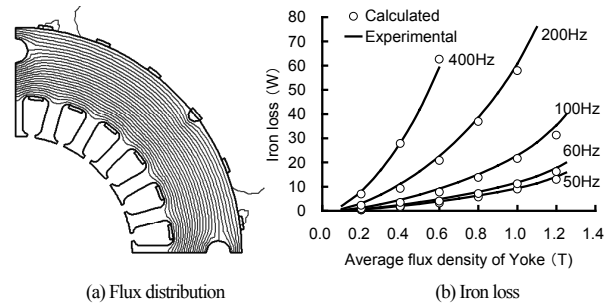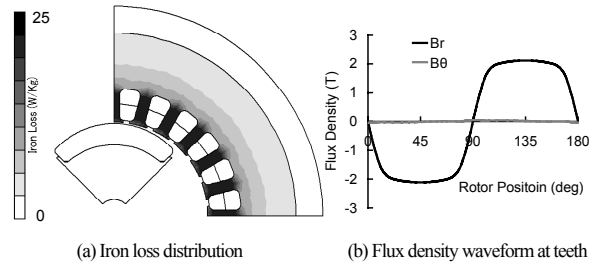
Fig. 4. Iron loss and flux waveform.

(1) eddy current loss (3) Iron loss due to harmonic component
(2) hysteresis loss (4) Iron loss due to alternating flux ($\alpha < 0.1$)
(5) Iron loss due to rotating flux
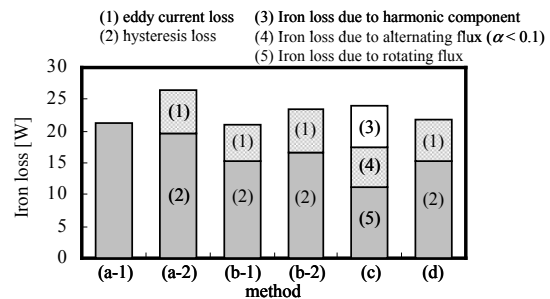
Fig. 5. Comparison of iron loss.

REFERENCES

[1] J.G.Zhu and V.S.Ramsden,"Improved formulations for rotational core losses in rotating electrical machines," *IEEE Trans. Magn.,* vol. 34, no.4, pp.2234-2242, 1998.

[2] K. Yamazaki, "A study on method of loss calculation for rotating machines considering effects of slot harmonics and rotating magnetic field", *Papers of Joint Technical Meeting on Static Apparatus and Rotating Machinery IEE of Japan,* SA-01-32, RM-01-100, 2001.

Numerical Analysis of Coupling 2-D-EM Field and Circuits for Rectification Synchronous Generator Taking Account Slot-Skewed

Huaishu Li   Langru Li

Huazhong University of Science & Technology

#1037 Luoyu Rd., Wuhan, 430074, P.R.China

E-mail: lrli@mail.hust.edu.cn

Abstract—A new approximate method, which uses 2-D finite element technique to calculate 3-D electromagnetic field of electrical machine with slot-skewed, is proposed. Based on this method, the numerical technique of directly coupling the equations of transient eddy-current field and circuits is studied, and the example equations of application to the 12-phase rectification synchronous generator with skewed slots are established. Then, the dynamic voltage of a salient synchronous generator at no-load is calculated, and the regular pattern in which the damper windings affect the voltage waveform is analyzed. The results show that the damper windings can reduce the stator tooth harmonic components of voltage at no-load, and can strengthen the rotor tooth harmonic voltage components which related to the damper winding pitch. These practical calculations demonstrate that this method is effective.

Index Terms—**Electromagnetic field, Slots-skewed, Synchronous generator, Finite element method,**

INTRODUCTION.

It is known that 3-D FEM can achieve very close result in calculating the electromagnetic field in electrical machine. But it is complicated and time consuming. Particularly, it is not suitable to use directly coupling equations of transient eddy-current field and circuits to get the dynamic characters of an electrical machine. The 2-D finite element method, on the other hand, cannot consider the skewed slots or oblique pole effect of electrical machine, and we usually deal with it by multiplying with skewed coefficient, therefore the result is not exact. In this paper, a new approximate method which uses 2-D FEM to calculate 3-D electromagnetic field of electrical machine with slots-skewed is proposed. An example of a 12-phase synchronous generator-rectification system is given to show how to build and solve the direct coupling the equations of transient eddy-current field and circuits. The example demonstrates the feasibility and the effectiveness of this method.

THE PRINCIPLE FOR USING 2-D FEM TO CALCULATE 3-D EM FIELD OF ELECTRICAL MACHINE WITH SLOTS-SKEWED

Because the slot is skewed in electrical machine, the same stator slot has different mechanical angles along the axis direction of stator, as shown in Fig.1a. The idea behind is to get certain number of sections at different axis position of electrical machine, then calculate each magnetic vector potential, and finally average the data got from each areas. The more areas you choose, the more closer the result will be.

If we choose the first section at the one end of the stator iron core and the last section at the other end, the middle of the iron core can be sampled with certain number of identical-distance areas (as shown in Fig.1b). The magnetic vector potential on each section are different as the relative positions between stator and the rotor change. On each section, the numbers of node are same, the distributions of current source are also same.
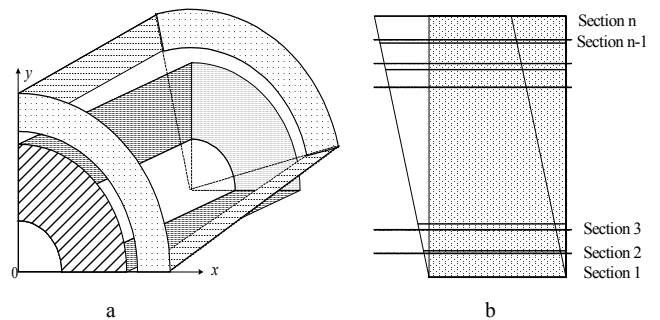
Fig.1 Schematic Diagram of slot-skewed stator

Suppose the number of sections got along the axis is l, and their magnetic vector potential are $\mathbf{A}_1$, $\mathbf{A}_2$,…,$\mathbf{A}_l$. Then the governing equation of magnetic vector potential and the boundary value problem are as follows:

$$
\begin{cases}
\nabla \times \dfrac{1}{\mu} \nabla \times A_i = J - \sigma \dfrac{dA}{dt} \\
A|_{S1}=0 \qquad A|_{R1}=0 \qquad (i=1,\ 2,\ \cdots;\ l) \\
A|_{R2}=-A|_{R3} \qquad A|_{S2}=-A|_{S3} \\
A|_{S4}=-A|_{R4} \qquad A|_{S5}=A|_{R5}
\end{cases} \qquad 1
$$

The boundary conditions are given as fig.2

After the magnetic vector potential on each section is obtained, we can calculate relevant parameters by subsection method. The equation for phase voltage of electrical machine with slots-skewed is as follows:

$$
[e] = -2PL_{eff}[B]\frac{d}{l \cdot dt}\big([A]_1 + [A]_2 + \cdots + [A]_l\big) \qquad 2
$$
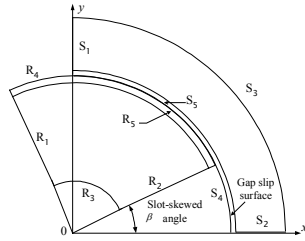
Fig.2 Schematic diagram of the solved region

COUPLING EQUATION OF 2-D NON-LINEAR TRANSIENT EDDY-CURRENT FIELD AND CIRCUITS

For the magnetic field in the skewed generator with the known current source, we can calculate the magnetic vector potential on different sections. But for some systems, the winding current is unknown, and it depends on the magnetic field distribution in the electrical machine and the parameters in outer circuit. Therefore, it is necessary to establish the coupling equation for 2-D transient eddy-current field and outer circuit for all computing sections. The combinative discretization equation is as follows

$$\begin{bmatrix} \{K\}+\dfrac{\{H\}}{\Delta t} & \{B\}^T\{M\}^T \\ \{M\}\{B\} & -\dfrac{[R]\Delta t+[L]}{2PL_{eff}}\cdot l \end{bmatrix}\begin{bmatrix} \{A\} \\ -[I] \end{bmatrix}_t =$$
$$\begin{bmatrix} \dfrac{\{H\}}{\Delta t} & 0 \\ \{M\}\{B\} & -\dfrac{[L]}{2PL_{eff}}\cdot l \end{bmatrix}\begin{bmatrix} \{A\} \\ -[I] \end{bmatrix}_{t-\Delta t}+\begin{bmatrix} 0 \\ -\dfrac{[E_c]\Delta t}{2PL_{eff}}\cdot l \end{bmatrix}$$

3

NUMERICAL ANALYSIS ON ELECTRIOMAGNETIC FIELD OF THE ELECTRICAL MACHINE WITH SLOTS-SKEWED.

It is well known that the classic harmonic permeance can analyze why skewed slot or skewed polar can reduce the stator tooth harmonic voltage. But this method did not consider the effect of damper winding, and therefore cannot quantitatively calculate the stator tooth harmonic voltage. In this paper, we calculate and analyze voltage waveform of a skewed stator 12-phase synchronous rectification generator at no-load situation, and analyze the effects of different pitch slots-skewed on reducing the stator tooth harmonic voltage.

Table shows the basic data of the electrical machine. Fig. 3~4 are the calculation result. Ks is the coefficient of the

Table . Basic data of generator

Basic data	Damper data	Mesh data
P_N=18kW, P=2, Z=48	n_c=7	elements 8780
=196.35mm ,m=12	t_2/t_1=1.187	codes 4700
$_p$=0.74　　g_{min}=		

g_{max}=1mm

skewed slot, which is defined as the ratio between the pitch of slots-skewed and the stator slot pitch; kv(%) is defined as the ratio between the amplitude of v harmonic waves and the base amplitude.

The result shows that the skewed stator can effectively reduces the stator tooth harmonic voltage, especially when the slot-skewed pitch is equal to the stator slot pitch
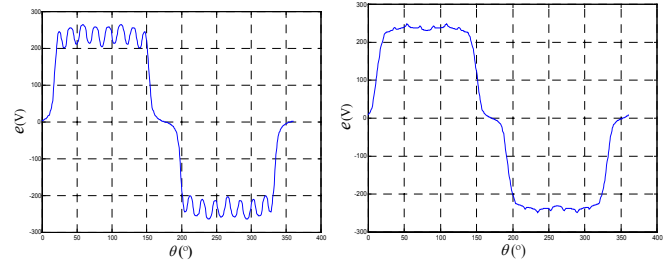
Fig.3 Phase voltage waveform (k_s=0.5) Fig.4 Phase voltage waveform (k_s=1)

Fig. 5 indicates that there is no apparent effect on phase harmonic component after introducing skewed slot. The curve in Fig. 6 shows that the main teeth harmonic voltage changes as the pitch of slots-skewed changes. From the curve, we can see that when ks=0.5, 2-order (47th, 49th) tooth harmonic component can be reduced greatly, while the effect on 1-order (23rd, 25th) is limited. But when ks=1, both 1-order and 2-order tooth harmonic component can be reduced greatly.
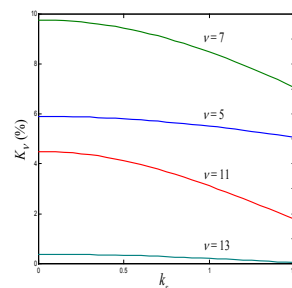
Fig.5 The phase voltage harmonic　　Fig.6 The teeth harmonic
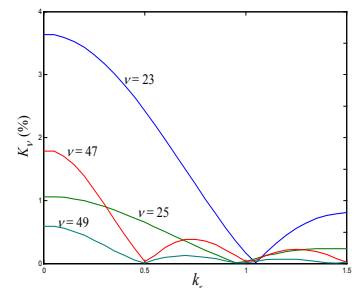
CONCLUSION

This paper introduces the principle to use 2-D finite element to approximately calculate the 3-D electromagnetic field in the skewed electrical machine with an example of a 12-phase (4Y with displace 15° angles) rectification synchronous generator with slots-skewed. A non-linear direct coupling equation of the 2-D transient eddy-current field and circuits is established. We simulate and calculate the electromagnetic field and voltage waveform with no-load. The

Representation of Laminated and Slotted Configurations in the Finite Element Analysis of Electrical Machines and Transformers

Erich Schmidt

Vienna University of Technology, Institute of Electrical Drives and Machines
Gusshausstrasse 25–29, A–1040 Vienna, Austria
Email: erich.schmidt@tuwien.ac.at

Abstract – In the design of electrical machines and transformers, the modelling of the laminated core material is of great importance. Moreover especially in the conceptual phase, a finite element analysis with all details of the slotted geometries might be onerous. Both scopes of duties can be treated by an anisotropic modelling with regard to permeability and conductivity of the used materials. The application of this anisotropic material modelling is shown with some characteristic examples in the field of electrical machines and transformers.

Index Terms – Electrical machine design, Material modelling, Finite element analysis

I. ANISOTROPIC CORE MODEL

The material properties of the laminated iron core are built with anisotropic permeabilities and conductivities related to a cartesian coordinate system as shown Fig. 1.

The laminated iron core can be represented by an effective permeability obtained from the ratio of airgap thickness to lamination thickness as expressed by the well known space factor k_F [1]. Based upon the shown cartesian coordinate system, the anisotropic permeability is given as

$$[\,\mu\,] = \begin{bmatrix} \mu_{xx} & 0 & 0 \\ 0 & \mu_{yy} & 0 \\ 0 & 0 & \mu_{zz} \end{bmatrix} . \qquad (1)$$

The different magnetization directions of legs and yokes are considered with appropriate functions μ_{xx} and μ_{zz}. In dependence of the local saturation, the function

$$\mu_{yy} = \mu_0 \, \frac{\mu}{\mu(1 - k_F) + \mu_0 k_F} \qquad (2)$$

take into account the lamination.

With this anisotropic modelling, modified magnetization characteristics as proposed in [2] can be applied additionally.
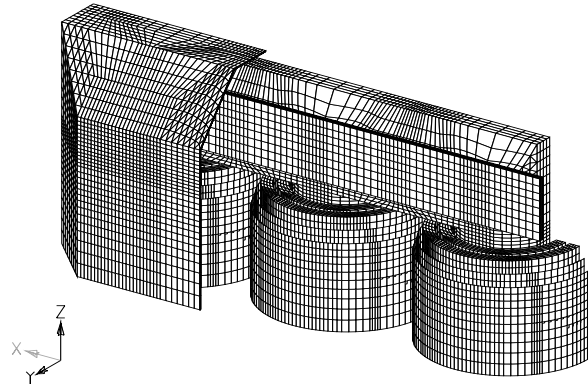
Fig. 1: Active parts of the finite element model of a three-leg power transformer containing core, low and high voltage windings, core clamping plate and steel tank wall (partly shown) [3]

In case of an unsaturated iron core, the eddy currents in the lamination sheets can be modelled with an equivalent conductivity as

$$[\,\sigma\,] = \begin{bmatrix} \sigma_{xx} & 0 & 0 \\ 0 & 0 & 0 \\ 0 & 0 & \sigma_{zz} \end{bmatrix} , \qquad (3)$$

where σ_{xx} ans σ_{zz} denote the iron conductivity with respect to magnetization direction.

The representation of the laminated iron core when considering the eddy currents in the xz-plane of the saturated lamination sheets is more complex. This modelling is based on [4]–[6] and will be shown in the full paper.

II. ANISOTROPIC WINDING MODEL

In frequent cases, both the high voltage and the low voltage windings of power transformers consist of many single turns. Therefore, a replacement method of spreading the multiturn windings with a minimum of changes within the field and energy distribution is necessary.

As shown in [7], [8], this can be done using attached 0D circuit elements and 1D line elements. However, there are noticeable differences in the field and energy distribution in the regions of the windings due to the reduced number of turns of each winding with these proposed modelling methods. Due to this reason, another modelling method will be used when the fields of interest are the multiturn windings themselves.

With regard to Fig. 1, the conductivity of the coil windings is related to three local cylindrical coordinate systems as

$$[\sigma] = \begin{bmatrix} \sigma_{rr} & 0 & 0 \\ 0 & \sigma_{\varphi\varphi} & 0 \\ 0 & 0 & \sigma_{zz} \end{bmatrix} . \qquad (4)$$

In the case of impressed current densities without noticeable eddy currents inside the coil windings, the anisotropic conductivity (4) can be written as

$$[\sigma] = \begin{bmatrix} 0 & 0 & 0 \\ 0 & \sigma & 0 \\ 0 & 0 & 0 \end{bmatrix} . \qquad (5)$$

The anisotropic conductivity (4) can be used with applied voltages, too. Thereby, an assumption of the current density as a screw line with a constant ratio $c = J_z/J_\varphi$ is valid. This yields to an anisotropic conductivity of the coil winding as

$$[\sigma] = \begin{bmatrix} 0 & 0 & 0 \\ 0 & \sigma & c\sigma \\ 0 & c\sigma & c^2\sigma \end{bmatrix} , \qquad (6)$$

where the slope coefficient c can be derived directly from the geometry of the coil winding.

III. ANISOTROPIC SLOT MODEL

As usual, the slotted geometry of an rotating electrical machine is described in the $r\varphi$-plane. Therefore, the anisotropic behaviour can be represented with the permeability as

$$[\mu] = \begin{bmatrix} \mu_{rr} & 0 & 0 \\ 0 & \mu_{\varphi\varphi} & 0 \\ 0 & 0 & \mu_{zz} \end{bmatrix} . \qquad (7)$$

The replacement method as shown here eliminates the circumferential distribution of the magnetic anisotropy. Thus, the slotted geometry will be represented by permeabilities in dependence of the radius only.

Introducing the slot width function $s(r)$ and the slot pitch function $\tau(r)$, the components are given as

$$\mu_{rr}(r) = \mu \frac{\tau(r) - s(r)}{\tau(r)} + \mu_0 \frac{s(r)}{\tau(r)} , \qquad (8)$$

$$\mu_{\varphi\varphi}(r) = \mu_0 \frac{\mu \tau(r)}{\mu_0 \left(\tau(r) - s(r)\right) + \mu s(r)} . \qquad (9)$$

Additionally, the lamination in the axial direction is represented with an analogous form of (2) by

$$\mu_{zz} = \mu_0 \frac{\mu}{\mu(1 - k_F) + \mu_0 k_F} . \qquad (10)$$

As it will be shown in the full paper, the above equations can be used for linear electrical machines with slightly modifications.

IV. CONCLUDING REMARKS

The full paper includes applications of the above material modelling with high-speed induction machines, transverse flux machines and power transformers.

REFERENCES

[1] Hameyer K., Belmans R.: *Numerical Modelling and Design of Electrical Machines and Devices*. WIT Press, Southampton, 1999.

[2] Biro O., Paoli G., Buchgraber G.: "Complex Representation in Nonlinear Time Harmonic Eddy Current Problems". *IEEE Transactions on Magnetics*, Vol. 34, No. 5, March 1998.

[3] Schmidt E., Hamberger P., Seitlinger W.: "Calculation of Eddy Current Losses in Metal Parts of Power Transformers". Submitted for publication in *Proceedings of the 15th International Conference on Electrical Machines, ICEM*, Brugge (Belgium), 2002.

[4] Biro O., Bardi I., Preis K., Renhart W., Richter K.R.: "A Finite Element Formulation for Eddy Current Carrying Ferromagnetic Thin Sheets". *IEEE Transactions on Magnetics*, Vol. 33, No. 2, March 1997.

[5] Hollaus K., Biro O.: "A FEM Formulation to Treat 3D Eddy Currents in Laminations". *IEEE Transactions on Magnetics*, Vol. 36, No. 4, July 2000.

[6] Brauer J.R., Cendes Z.J., Beihoff B.C., Phillips K.P.: "Laminated Steel Eddy-Current Loss versus Frequency Computed Using Finite Elements". *IEEE Transactions on Industry Applications*, Vol. 36, No. 4, July 2000.

[7] Brauer J.R., MacNeal B.E.: "Finite Element Modeling of Multiturn Windings with Attached Electric Circuits". *IEEE Transactions on Magnetics*, Vol. 29, No. 2, March 1993.

[8] Brauer J.R., MacNeal B.E., Hirtenfelder F.: "New Constraint Technique for 3D Finite Element Analysis of Multiturn Windings with Attached Electric Circuits". *IEEE Transactions on Magnetics*, Vol. 29, No. 6, November 1993.

Impact of Magnetic Nonlinearities and Cross Coupling Effects on Properties of Radial Active Magnetic Bearings

Boštjan Polajžer, Gorazd Štumberger,
Jože Ritonja, Drago Dolinar
Faculty of Electrical Engineering and Computer Science
Smetanova 17, 2000 Maribor, Slovenia
E-mail: bostjan.polajzer@uni-mb.si

Kay Hameyer
Katholieke Universiteit Leuven, Dept. E.E.(ESAT)
Kasteelpark Arenberg 10, B-3001 Leuven-Heverlee, Belgium

Abstract— **The current and position dependent flux linkages and forces of radial active magnetic bearings are determined by the finite element method. The results obtained are incorporated into the dynamic model of active magnetic bearings in order to evaluate the influence of magnetic nonlinearities and cross coupling effects on their dynamic and static properties. The presented results show that the magnetic nonlinearities and cross coupling effects can change the electro motive forces considerably. These cross coupling effects are calculated and can be implemented in the control design as additional compensations.**

INTRODUCTION

Active Magnetic Bearings (AMB's) are a system of controlled electromagnets which enable contact-less suspension of a rotor [1]. The electromagnets of the discussed AMB's [2] are placed on the common iron core, which means that their behavior is magnetically nonlinear. Moreover, the individual electromagnets are magnetically coupled.

For the control design of the AMB's the linearized dynamic models are commonly used, where magnetic nonlinearities and cross coupling effects are not considered [1]. The nonlinearities can be taken into account, for example by the nonlinear force characteristics and dynamic inductances [3]. The influence of the disturbing cross coupling effects is neglected in the majority of the dynamic AMB models, which are available in the literature, although the efficient cross coupling compensation is important to get better closed-loop dynamic behavior of the device.

In this paper, the impact of the magnetic nonlinearities as well as cross coupling effects on the properties of AMB's is evaluated. The characteristics of flux linkages and radial forces are determined by using the Finite Element (FE) method and verified by measurements in the entire operating range of the bearing. The determined characteristics are incorporated in the dynamic AMB model. The obtained dynamic model is used to evaluate the impact of magnetic nonlinearities and cross coupling effects on the properties of AMB's. The proposed dynamic model is appropriate for the nonlinear control design.

FINITE ELEMENT COMPUTATION

The geometry and the magnetic field distribution of the studied AMB's is shown in Fig. 1, while the AMB circuit model is shown in Fig. 3.

The magneto-static computation was performed by 2D FE method using (1), where **A** denotes the magnetic vector potential, ν is the magnetic reluctivity, and **J** is the current density.
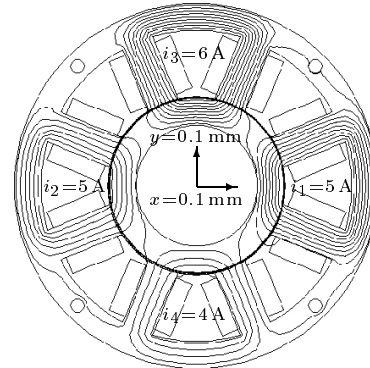
Fig. 1. The AMB geometry and magnetic field distribution.

$$\nabla \cdot (\nu \nabla \mathbf{A}) = -\mathbf{J} \qquad (1)$$

The flux linkages ψ_1, ψ_2, ψ_3 and ψ_4 were calculated in the entire operating range from average values of the magnetic vector potential in the stator coils for different control currents $i_{x\Delta}$ and $i_{y\Delta}$, and for different rotor displacements in the x- and in y-axis. The radial forces F_x and F_y were calculated by Maxwell's stress tensor method.

DYNAMIC AMB MODEL

The dynamic AMB model is according to the circuit model presented in Fig. 3 given by (2) and (3):

$$\begin{bmatrix} u_1 \\ u_2 \\ u_3 \\ u_4 \end{bmatrix} = R \begin{bmatrix} I_0 + i_{x\Delta} \\ I_0 - i_{x\Delta} \\ I_0 + i_{y\Delta} \\ I_0 - i_{y\Delta} \end{bmatrix} + 2 \begin{bmatrix} \frac{\partial \psi_1}{\partial i_{x\Delta}} & \frac{\partial \psi_1}{\partial i_{y\Delta}} \\ \frac{\partial \psi_2}{\partial i_{x\Delta}} & \frac{\partial \psi_2}{\partial i_{y\Delta}} \\ \frac{\partial \psi_3}{\partial i_{x\Delta}} & \frac{\partial \psi_3}{\partial i_{y\Delta}} \\ \frac{\partial \psi_4}{\partial i_{x\Delta}} & \frac{\partial \psi_4}{\partial i_{y\Delta}} \end{bmatrix} \begin{bmatrix} \frac{di_{x\Delta}}{dt} \\ \frac{di_{y\Delta}}{dt} \end{bmatrix} +$$

$$+ \begin{bmatrix} \frac{\partial \psi_1}{\partial x} & \frac{\partial \psi_1}{\partial y} \\ \frac{\partial \psi_2}{\partial x} & \frac{\partial \psi_2}{\partial y} \\ \frac{\partial \psi_3}{\partial x} & \frac{\partial \psi_3}{\partial y} \\ \frac{\partial \psi_4}{\partial x} & \frac{\partial \psi_4}{\partial y} \end{bmatrix} \begin{bmatrix} \frac{dx}{dt} \\ \frac{dy}{dt} \end{bmatrix}$$

$$(2)$$

$$\begin{bmatrix} F_x \\ F_y \end{bmatrix} = m \begin{bmatrix} \frac{d^2 x}{dt^2} \\ \frac{d^2 y}{dt^2} \end{bmatrix} \qquad (3)$$

where u_1, u_2, u_3 and u_4 are the supply voltages, I_0 is the bias current, $i_{x\Delta}$ and $i_{y\Delta}$ are the control currents in the x- and in y-axis. R stands for the coil resistances. F_x and F_y are the radial forces in the x- and in y-axis, respectively. The characteristics $\psi_1(i_{x\Delta}, i_{y\Delta}, x, y)$, $\psi_2(i_{x\Delta}, i_{y\Delta}, x, y)$, $\psi_3(i_{x\Delta}, i_{y\Delta}, x, y)$
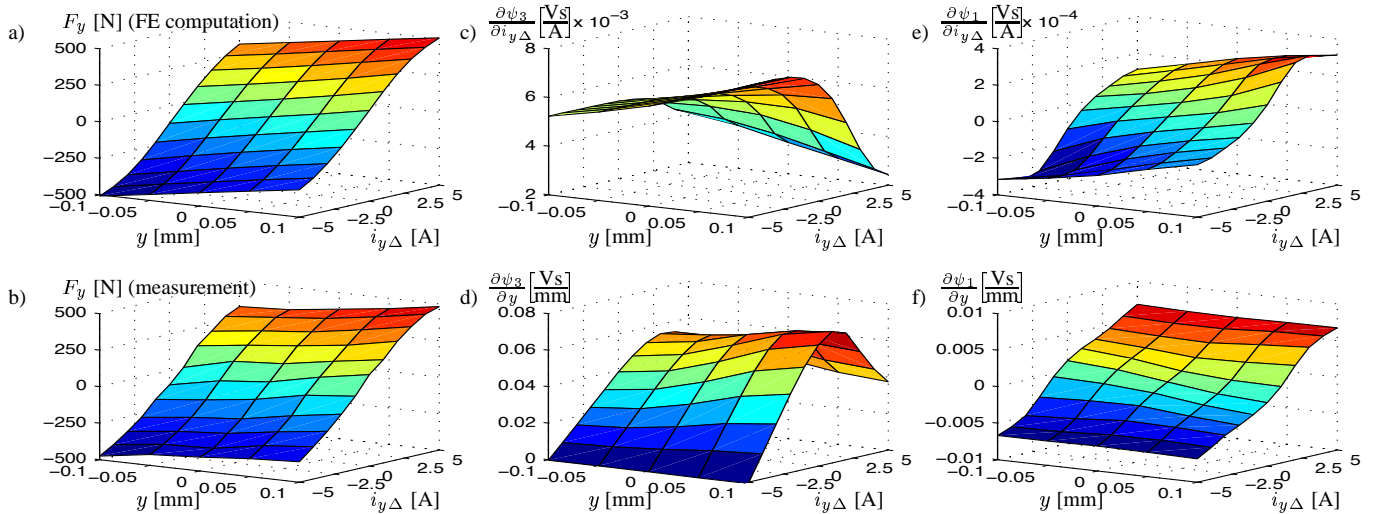
Fig. 2. Results ($x = 0$ mm, $i_{x\Delta} = 0$ A and $I_0 = 5$ A): a) computed force $F_y(i_{y\Delta}, y)$, b) measured force $F_y(i_{y\Delta}, y)$, c) partial derivative $\frac{\partial \psi_3}{\partial i_{y\Delta}}(i_{y\Delta}, y)$, d) partial derivative $\frac{\partial \psi_3}{\partial y}(i_{y\Delta}, y)$, e) partial derivative $\frac{\partial \psi_1}{\partial i_{y\Delta}}(i_{y\Delta}, y)$, f) partial derivative $\frac{\partial \psi_1}{\partial y}(i_{y\Delta}, y)$
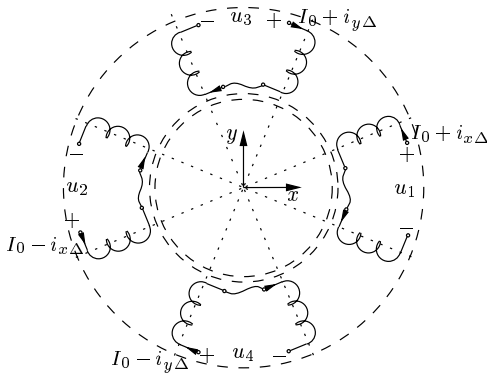
Fig. 3. The circuit AMB model.

and $\psi_4(i_{x\Delta}, i_{y\Delta}, x, y)$, as well as $F_x(i_{x\Delta}, i_{y\Delta}, x, y)$ and $F_y(i_{x\Delta}, i_{y\Delta}, x, y)$ were determined by FE computations. The current and position dependent partial derivatives of flux linkages required in (2) have been determined numerically. Therefore, the magnetic nonlinearities and cross coupling effects are incorporated into the dynamic AMB model (2), (3) by the current and position dependent flux linkages and forces.

In standard AMB models the terms like $\frac{\partial \psi_3}{\partial i_{y\Delta}}$ and $\frac{\partial \psi_3}{\partial y}$ are constant, the terms like $\frac{\partial \psi_1}{\partial i_{y\Delta}}$ and $\frac{\partial \psi_1}{\partial y}$ are neglected, while the forces are given by the linearized functions. Therefore, the dynamic model proposed in this paper is much more consistent in comparison with the standard AMB models.

RESULTS

A good agreement between the computed and measured forces can be seen in Fig. 2a) and Fig. 2b). The partial derivatives $\frac{\partial \psi_3}{\partial i_{y\Delta}}$, $\frac{\partial \psi_3}{\partial y}$, $\frac{\partial \psi_1}{\partial i_{y\Delta}}$ and $\frac{\partial \psi_1}{\partial y}$ are shown in Fig. 2c) – Fig. 2f). The flux linkages were determined by the FE method, while the partial derivatives were calculated numerically. The presented results are given for the case when the control current $i_{x\Delta}$ and the rotor position in the x-axis are equal to zero.

From the computed results shown in Fig. 2c) – Fig. 2f) can be seen that the current and position dependent partial derivatives of flux linkages are different from zero. As a consequence, the electro motive forces (emf's) can vary in a range up to 16 % when compared to those, obtained by the standard AMB models.

CONCLUSION

The impact of magnetic nonlinearities and cross coupling effects on the properties of radial AMB's is studied in the paper. It has been shown that the results of the FE computations can be used to improve the standard AMB models. In this way, the magnetic nonlinearities and cross coupling effects are considered in the proposed dynamic model, which is appropriate for the evaluation of static and dynamic behavior of the AMB's. The presented results show that the influence of magnetic nonlinearities and cross coupling effects is not negligible. In the case of the discussed AMB's, the emf's can vary due to the magnetic nonlinearities and cross coupling effects in the range up to 16 % in comparison with those data obtained by the standard models. These effects have to be considered in the nonlinear control design as cross coupling compensations. Therefore, the closed-loop dynamics can be improved in the best possible way.

REFERENCES

[1] G. Schweitzer, H. Bleuler and A. Traxler, *Active magnetic bearings*. ETH Zürich: Vdf Hochschulverlag AG an der ETH Zürich, 1994.
[2] G. Štumberger, D. Dolinar, U. Pahner and K. Hameyer, "Optimization of radial active magnetic bearings using the finite element technique and the differential evolution algorithm," *IEEE Transaction on Magnetics*, vol. 36, no. 4, pp. 1009–1013, 2000.
[3] M. Antila, E. Lantto and A. Arkkio, "Determination of forces and linearized parameters of radial active magnetic bearings by finite element technique," *IEEE Transaction on Magnetics*, vol. 34, no. 3, pp. 684–694, 1998.

Analysis of Far Field of Permanent Magnet Synchronous Machines

O-Mun Kwon, M.V.K. Chari , S. J. Salon & Kiruba Sivasubramaniam*,

Rensselaer Polytechnic Institute, Troy, New York, 12180, USA

The Electronic Systems Laboratory, GE-CRD, Niskayuna, NY USA

E-Mail: kwono@rpi.edu, charim@rpi.edu, salons@rpi.edu, sivasubr@crd.ge.com

ABSTRACT : Exterior magnetic fields compuation of permanent magnet synchronous motors are of importance in naval applications with respect to electromagnetic interference and detection. For shipboard applications far field effects due to currents in the stator windings, induced magnetic field in the iron parts and permanent magnets in the rotating members of motors are of significance and their accurate evaluation is vital to providing remedial measures. In this paper, the effects due to all the above are analyzed using a scalar potential method.

INTRODUCTION:

Brushless DC (BLDC) motors are presently being considered for naval applications ranging from pumps to propulsion. In some instances these would replace induction motors and in some cases mechanical drives. Of vital importance for naval applications is the electromagnetic signature of these motors. Propulsion motors under consideration are quite large both in rating and physical size. Electromagnetic fields near the motor must not interfere with on-board systems. The far field of these motors must be below specific thresholds to avoid detection. The balanced case for the far field has been presented in [1]. For characterization of motors particularly with regard to their far field performance and to effect design changes to compensate for asymmetries during the manufacturing process, multi-pole decomposition is necessary. Numerical methods, such as finite element analysis, do not give sufficient resolution to accurately compute the small net fields produced by the cancellation of larger components from different poles of the machine, currents in the stator and induced magnetization in the iron parts, far from the source. An integral formulation [1,2] is used in conjunction with finite element analysis to obtain the potentials. These potentials are then used to compute magnetic charges from which the multi-pole decomposition of the magnetic field is obtained. The results for both balanced and unbalanced cases for different number of poles are presented. Several applications are illustrated.

DETERMINATION OF THE FIELD AND ITS MULTI-POLE EXPANSION DUE TO SPHERICAL HARMONICS:

Scalar potentials on a sphere surrounding the permanent magnet machine can be obtained by a combination of finite elements (to determine saturation in iron parts) and integral equations to determine the potentials using numerical integration [4] due to permanent magnets, current sources and induced magnetization in the iron members. From these potentials, a charge simulation method yields magnetic charges on a concentric sphere in close proximity but interior to the first sphere. These charges are then used to find the multi-pole components of the far field at any desired point exterior to the outer sphere.

Magnetic scalar Potential from magnetization

$$\psi = \frac{1}{4\pi} \int \vec{M} \bullet \nabla(\frac{1}{|r'-r|}) dv \tag{1}$$

$\vec{M}$: is magnetization ; $\vec{B} = \mu_0(\vec{H}+\vec{M})$

Magnetic scalar Potential from current source[3]

$$\psi = -\frac{1}{4\pi} \iint_{vol} \int_{\infty}^{\xi} \frac{\vec{J}(x,y,z) \bullet (\vec{l} \times \vec{x})}{|\xi \vec{l} - \vec{x}|^3} d\xi\, dv \tag{2}$$

ξ : the observation point, $\vec{l}$: unit vector, $\vec{x}$: the source point.

Magnetic charge q_i and multi-pole expansion

$$\psi = \sum_{i=1}^{n} \frac{q_i}{4\pi\varepsilon_o |r'-r_i|} = \frac{1}{4\pi\varepsilon_o} \sum_{i=1}^{n} q_i \sum_{l=1}^{\infty} \frac{r_i^l}{r'^{l+1}} P_l(\cos\theta_i) \tag{3}$$

r',r: observation and source points; P: Legendre Polynomial of degree l

Alternate multi-pole decomposition using spherical harmonics [5]

$$\psi = \sum_{i=1}^{n} \frac{q_i}{4\pi\varepsilon_o} \sum_{l=0}^{\infty} \sum_{m=-l}^{l} \frac{4\pi}{2l+1} \frac{r^l}{r'^{l+1}} Y_l^m *(\theta,\phi) Y_l^m(\theta',\phi') \tag{4}$$

Y_l^m : Associated Legendre Polynomial of degree l, order m

APPLICATION:

Model of a Brushless DC Motor (BLDC)

A full model of the motor including magnets, stator iron, winding currents, and endcaps is described. Two such examples of this model are illustrated. One is totally for a balanced case, the other is with the residual flux density of magnet 1 about 5% demagnetization (1.1T→1.05T).
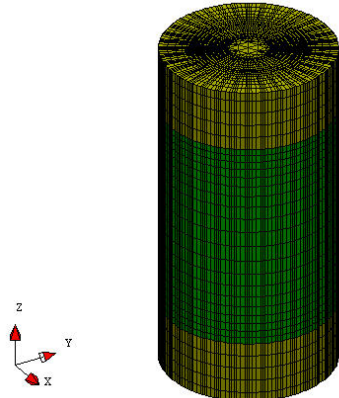
Figure 1 Full meshed model of a 6pole BLDC motor(with endcaps and stator coils)
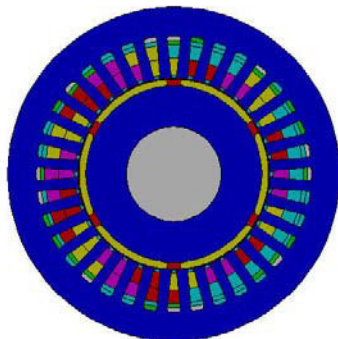
Figure 2: Cross Section of a 6 pole Permanent Magnet Motor

Table 1: Magnetic field for the balanced case.

Observation pts - m	H_r	H_θ	H_ϕ
1, 0, 0	8.098E-3	-5.298E-5	-1.13E-2
10,0,0	4.176E-7	-1.686E-8	-8.115E-8
100,0,0	3.369E-10	-1.436E-11	2.705E-11

Table 2 Magnetic field - unbalanced case.

Observation pts -m	H_r	H_θ	H_ϕ
1, 0, 0	-3.136E-2	-4.389E-5	8.226E-4
10,0,0	-3.672E-5	-1.395E-8	1.067E-5
100,0,0	-3.649E-8	-1.18E-11	1.066E-8

Comparison of sources @1,0,0 meter
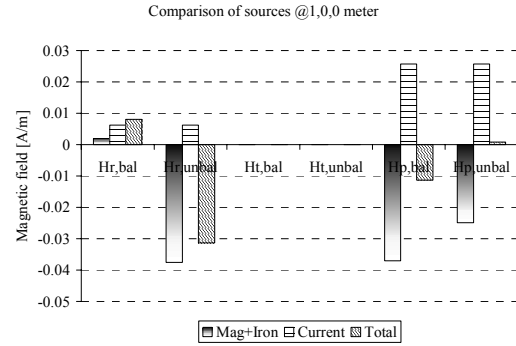
Figure 3: Comparison of the far field from different sources

Table 3 multi-pole components at 1 meter along the x-direction

Pole pair		H_r	H_θ	H_ϕ
Balanced	1	0.3359E-03	-.1409E-04	0.2831E-04
	3	0.8078E-02	-.1077E-04	-.1238E-01
	5	-.3365E-03	0.1154E-05	-.4215E-03
unbalanced	1	-.3645E-01	-.1165E-04	0.1064E-01
	2	-.3601E-02	-.2208E-04	0.1295E-02
	3	0.9005E-02	-.8312E-05	-.1223E-01
	4	0.1583E-03	-.3036E-05	0.4024E-04
	5	-.4937E-03	0.9587E-06	-.4050E-03

CONCLUSIONS:

In this paper we have presented the analysis of far fields due to magnets, stator currents and induced magnetization in iron parts in a six-pole motor by two scalar potential methods. Results of multi-pole expansion of the far (magnetic) field components on a real size motor are illustrated. Results obtained from an alternate spherical harmonic decomposition method will be included in the full paper.

REFERENCES:
[1] Sheppard Salon, O-Mun Kwon, K. Sivasubramaniam, "External Fields of Permanent Magnet Motors", *COMPUMAG*, July 2001
[2] J. A. Stratton, *Electromagnetic Theory*, McGraw-Hill, 1941
[3] J.B.Bronzan, "The Magnetic Scalar Potential ", Am. J. Phys. 39, 1971
[4] M.V.K. Chari and S.J. Salon, *Numerical Methods in Electro Magnetism*, Academic Press 1999.
[5] J.D. Jackson, *Classical electrodynamics -3rd edition*, John Willey & Sons

Design and Analysis of Axial-flux Type Permanent Magnet Synchronous Generator for Wind Power Systems

Don-Ha Hwang, Do-Hyun Kang, Yong-Joo Kim

Industry Applications Research Laboratory,
Korea Electrotechnology Research
Institute (KERI),
P.O. Box 20, Changwon, Gyeongnam,
641-600, Korea
dhhwang@keri.re.kr

Sung-Woo Bae, Dong-Hee Kim

School of Electrical &
Electronic Engineering,
Yeungnam University,
214-1, Daedong,
Gyeongsan, Gyeongbuk,
712-749, Korea

Kyeong-Ho Choi

Dept. of Digital
Electric Design,
Kyungbuk College,
630, Hyuchun 2-dong,
Youngju, Kyungbuk,
750-712, Korea

Abstract – In this paper, design and construction of an axial-flux permanent- magnet generator with power output at 60 [Hz], 10 [kVA], 300 [r/min] for wind energy system is presented. The paper discusses characteristics of an axial-flux permanent-magnet generator for a gearless wind energy system which aims to be satisfied with variable operating conditions. Finite-element method (FEM) is applied to analyze generator performance at variable load. The results of FE analysis show this generator is feasible for use with a wind turbine.

INTRODUCTION

Recently, permanent-magnet (PM) generators in order to convert wind power into electricity are very applied. Especially, PM axial-flux generators are attractive candidate for wind power generation because they have higher efficiency, power facts, output power per mass and better dynamic performance than the other electrical machines [1-3].

In this paper, wind turbine system with direct-driven axial-flux type PM synchronous generator, 10 [kVA], 300 [rpm], is introduced. Generator with axial-flux type or disk type is possible to avoid gearbox which is necessary for conventional generators. Thus it must be light to minimize the requirements for the tower structure and volume.

In order to analyze the characteristics of this generator, finite-element (FE) analysis is applied. Dynamic characteristics analysis of three-dimensional FE is required because of construction of this generator, but it takes long time to calculate. Therefore, equivalent model of 2-dimensional (2-D) is developed.

Both steady and transient-state analysis is performed. Resistive and inductive loads as variable load are applied in order to analyze driving characteristics. The results are very similar to predicted performance of design.

DESIGN AND CONSTRUCTION

The basic specification of PM generator is shown Table 1. One unit module of this generator with axial-flux, double-side and disc-type can be combined 30 [kVA] as shown Fig. 1. Generator consists of a rotor between two stators and winding is connected to a stator as series so that induced voltages from two stators are united together.

A rotor consists of 24-pole and one permanent magnet per a pole. The material of a rotor is stainless and construction of that was designed the leakage flux to be reduced

Single-layer lap winding is used in two stators for economy of construction and volume. The material of core is S-18, and silicon whose thickness is 0.5 [mm] was used. In order to reduce eddy current, the core was laminated roll type. The number of slot is 72 and the number of conductor is one per one phase and one pole.

Table 1. Basic specification of wind generator

Rated power	10000 [VA]
Rated speed	300 [rpm]
Rated voltage	380 [V]
Number of poles	24
Number of phase	3
Type	Axial-flux
Phase connection	Y

Fig. 1. The construction of a permanent-magnet axial modular generator

FINITE-ELEMENT (FE) ANALYSIS

Equivalent 2-D model

The equivalent 2-D model proposed was calculated as average value and 2 poles of 24 poles move between two stators so that dynamic characteristics can be analyzed as shown in Fig. 2. Maxwell is used for performing finite element analysis. In order to calculate induced EMF, external circuit is connected so that driving characteristics at no-load and resistive and resistive-inductive load was analyzed.
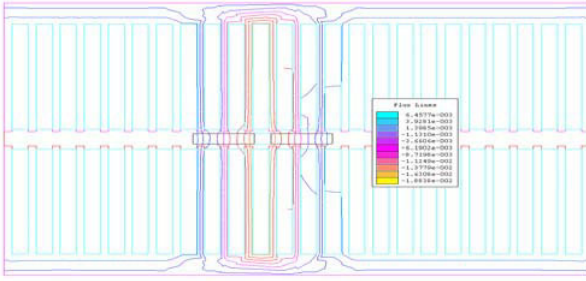
Fig. 2. Equivalent model for characteristics analysis

The magnetostatic field problem of Maxwell may be solved on the base of the following equation (1) [2-4].

$$\nabla \times (\nu \nabla \times \boldsymbol{A}) - \nabla \times (\nu \boldsymbol{B}_r) = 0 \qquad (1)$$

where, A is the magnetic vector potential, ν is the reluctivity given by $|H_c/B_r|$, B_r is the remanent magnetic flux density, and H_c is the coercive magnetic flux of the PM.

The results of FE analysis

The magnetic flux density waveform in air gap is shown at Fig. 3. The calculated RMS value was 0.446 [T], but the result of FE analysis was 0.51 [T].

Three-phase current from 2 poles of 24 poles is shown at Fig. 4. About 1.5 [A] induced current from six coils must multiply 12. When its value is changed rms value, it is about 15.5 [A].

Fig. 5 shows voltage as variable speed at various loads. According to increase speed, voltage is also increase as linear. When the speed is at 300 [rpm], rated voltage that is 226 [Vrms] appears.

The output power as current is increased shows at Fig. 6. When current is 15.53 [A], the output power reached 10 [kVA].
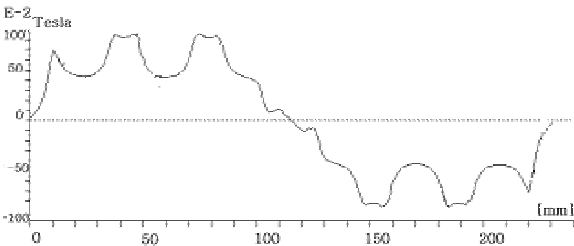
Fig. 3. Air-gap magnetic flux density
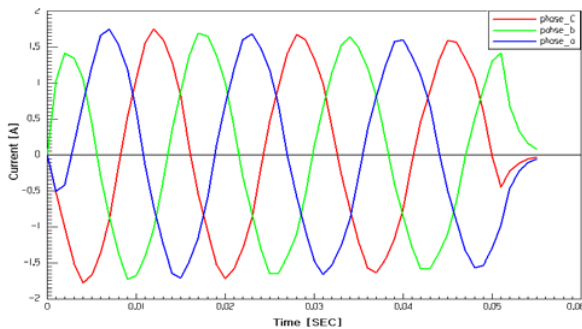
Fig. 4. Current from six coils at resistive load
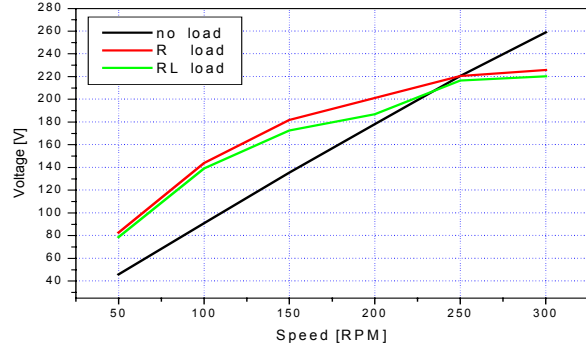
Fig. 5. Voltage according to variable speed at various load
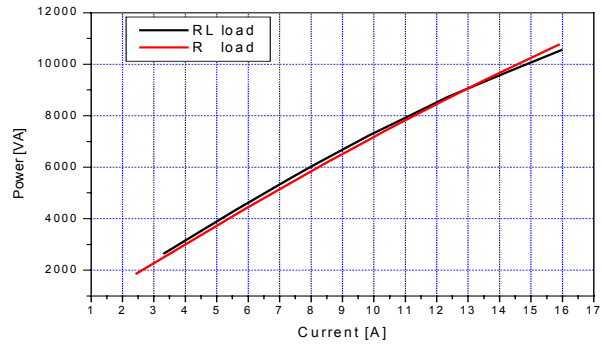
Fig. 6. The output power characteristics as current increases at R and R-L load

CONCLUSION

In this paper, wind turbine system with direct-driven axial-flux type PM synchronous generator, 10 [kVA], 300 [rpm], is presented. In order to analyze the performance of axial PM generator, FE analysis is used, and the 2-D equivalent model is developed. The steady-state and transient-state characteristics is respectively analyzed at no-load and RL-load. The results of FE analysis are very similar at both R-load and RL-load and show this generator is feasible for use with a wind turbine. The added analysis and experimental results will be reported in extend paper in details.

REFERENCES

[1] B.J. Chalmers, W. Wu, and E. Spooner, "An axial-flux permanent-magnet generator for a gearless wind energy system", *IEEE Transactions on Energy Conversion*, Vol. 14, No. 2, pp. 251-257, June 1999
[2] E. Muljadi, C.P. Butterfield, and Y.H. Wan, "Axial-flux modular permanent-magnet generator with a toroidal winding for wind-turbine applications", *IEEE Transactions on Industry Applications*, Vol. 35, No. 2, pp. 831-836, July/Aug. 1999
[3] V. Cingoski, M. Mikami, and H. Yamashita, "Computer simulation of a three-phase brush-less self-excited synchronous generator", *IEEE Transactions on Magnetics*, Vol. 35, No. 3, pp. 1251- 1254, May 1999
[4] J. Chen, C.V. Nayar, and L. Xu, "Design and finite-element analysis of an outer-rotor permanent-magnet generator for directly coupled wind turbines", *IEEE Transactions on Magnetics*, Vol. 36, No. 5, pp. 3802-3809, Sep. 2000
[5] F. Caricchi, F. Crecimbini, O. Honorati, G.L. Bianco, and E. Santini, "Performance of coreless-winding axial-flux permanent-magnet generator with power output at 400 Hz, 3000 r/min", *IEEE Transac-tions on Industry Applications*, Vol. 34, No. 6, pp. 1263-1269, Nov. 1998

An Application of Laurent Expansion of Air Gap Magnetic Field
to Optimizing Motor Geometry with Partially Saturated Iron Core

Masashi Kitamura, Noriaki Hino, and Fumio Tajima
Hitachi Research Laboratory, Hitachi, Ltd.
7-1-1 Omika, Hitachi, Ibaraki 319-1292 Japan
masashi@hrl.hitachi.co.jp

Abstract – The Laurent expansion of air gap magnetic flux density has been applied to the optimal design, based on the combination of the finite element analysis and direct search algorithm, for motors with partially saturated rotor core. It was shown that this technique could remarkably reduce the total elapsed time to obtain the optimal solution.

INTRODUCTION

While going through the process of motor design, we often notice that it includes a variety of electromagnetic optimization problems. Obviously, solving these problems numerically will help us speed up the design process. On the other hand, it is also true that, in some cases, a considerable amount of the computational time is required because the magnetic field computation with the finite element analysis (FEA) must be iterated until the optimization reaches a convergence.

In our previous paper [1], we proposed a numerical method, being limited to torque-related problems, for the purpose of reducing the elapsed time to obtain objective function values. The point of our method is to find out an approximate torque value from the air gap magnetic field calculated for a single time step rather than by computing the torque waveform. Hence, this reduces the elapsed time to compute the functional value, at least, by the order of 1/10. This approach, utilizing the Laurent expansion of the air gap magnetic flux density, is valid as long as the linearity of the machine is preserved even though the torque waveform has a large ripple.

This paper reports an application of the above-mentioned method to optimizing cross-sectional geometry of interior permanent magnet (PM) synchronous motors, in which the magnetic saturation of the rotor core cannot be neglected. The usefulness and limitation of our method are also discussed.

TIME-AVERAGED MOTOR TORQUE

The derivation of the time-averaged motor torque is briefly reviewed [1].

From the 2-D static Maxwell's equations, $\vec{\nabla} \cdot \vec{B} = 0$ and $\vec{\nabla} \times \vec{B} = \mu_0 j$ where μ_0 is the permeability of the vacuum and j is the current density, the x and y components of $\vec{B}$ satisfy $\partial B_x / \partial x + \partial B_y / \partial y = 0$ and $\partial B_y / \partial x - \partial B_x / \partial y = \mu_0 j$. Then, if we introduce the magnetic flux density in complex form written as $B(z) = B_y + i B_x$ as a function of the point, $z = x + iy$, we

can say that the $B(z)$ in a free space ($j = 0$) is a regular function of z since the above relationships are identical to the Cauchy-Riemann relations of $B(z)$ [2]. Consequently, the magnetic flux density in complex form in the ring-shaped air gap of the rotary motor can be expanded at the motor axis ($z = z_0$) into the Laurent series:

$$B(z) = \sum_{n=-\infty}^{\infty} c_n \left(\frac{z - z_0}{R} \right)^n \tag{1}$$

where the coefficient c_n is computed from

$$c_n = \frac{R^n}{2\pi i R} \oint_C \frac{B(\zeta) d\zeta}{(\zeta - z_0)^{n+1}} . \tag{2}$$

Here R is the reference radius, introduced conveniently to give c_n in Tesla, and C is an arbitrary closed loop in the air gap.

Moreover, reconsidering the 2-D Maxwell stress tensor on the basis of the above complex representation, we can show that the torque τ applied to the region inside the closed loop C in the air gap is expressed in complex form as

$$\tau = -\frac{1}{2\mu_0} \text{Re} \left[\oint_C (z - z_0) B^2 dz \right] . \tag{3}$$

Now let us suppose that we have a P-pole synchronous motor rotating steadily at the angular velocity ω and assume that the c_n and the angular velocity ω_n of the magnetic flux density represented by the nth term in (1) are independent of time. Since the fundamental components in (1) respectively due to the stator and the rotor revolve at the same angular velocity, viz., $\omega = \omega_{P/2-1} = \omega_{-(P/2+1)}$ and for other components ($n \neq P/2-1$) the relationship, $\omega_n \neq \omega_{n+2}$, stands, we derive the time-averaged motor torque $\bar{\tau}$ given by

$$\bar{\tau} \approx (2\pi R^2 / \mu_0) \text{Im}[c_{P/2-1} c_{-(P/2+1)}] \tag{4}$$

where $c_{P/2-1}$ and $c_{-(P/2+1)}$ denote the coefficients of the P-pole fundamental magnetic fields, whose flux lines in the case of $P = 8$ are illustrated in Fig. 1. It should be noted that, as long as the above assumptions are satisfied, we can compute the $\bar{\tau}$ using (4) from an instantaneous magnetic flux density in the air gap regardless of the torque waveform.

(a) z^3 (b) z^{-5}
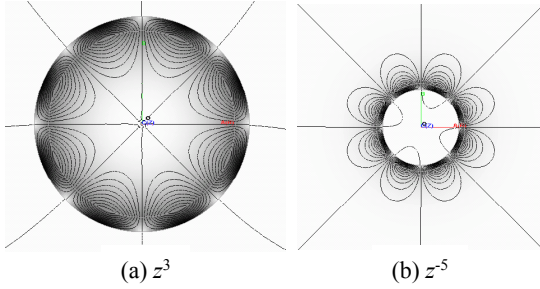
Fig. 1 Magnetic flux lines corresponding z^3 and z^{-5} terms ($P = 8$)

a) Initial shape   b) Optimal shape

Fig. 2 Maximization of motor torque

As an example, we deal with a simple torque maximization problem of a 16-pole, 48-slot interior PM motor shown in Fig 2(a).   To solve this problem, the following objective functions are maximized by the direct search proposed by Rosenbrock [3] combined with the FEA:

Mean of torques computed at time steps with even intervals

$$h_1(x_1, x_2) = \frac{1}{10} \sum_{k=1}^{10} \tau(t_k), \qquad (5)$$

Time-averaged torque computed from (4)

$$h_2(x_1, x_2) = (2\pi R^2/\mu_0)\,\mathrm{Im}[c_7 c_{-9}]. \qquad (6)$$

The optimization variables are PM width (x_1) and the current phase (x_2) measured from the q-axis, as shown in Fig. 2(a).

Our first concern is to know to what extent the assumption we made in the previous section is valid when the rotor core is strongly saturated.   In Fig. 3, the absolute values of c_n are depicted as a function of the time step number.   We see that the assumption is partially satisfied; the 16-pole fundamental components c_7 and c_{-9} are almost constant in time, but other higher order components vary considerably.

For both objective functions, the torque maximization converged very nicely as shown in Fig. 4.   The optimal shape is shown in Fig. 2(b).   Table 1 summarizes the optimal solutions obtained from (6) with c_7 and c_{-9} computed for each time step in Fig. 3.   Though we find that a deviation in the solutions with h_2 is not negligible compared with that with h_1, it can be said that the approximate solutions are obtained quickly. This indicates that, optimizing the problem using (5) with one of the above solutions as initial values, the total computational

Fig. 3 Absolute values of coefficients c_n
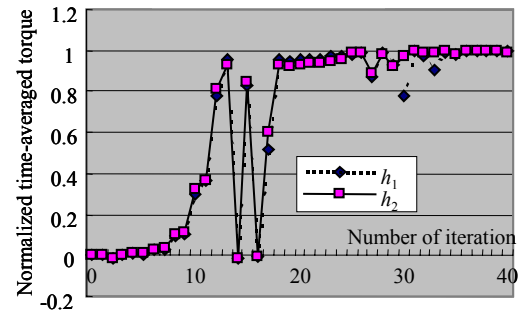
Fig. 4 Convergence of objective functions

time to find the optimal solution can be remarkably reduced. Details of more realistic examples are reported in the full paper.

REFERENCES

[1] M. Kitamura, J. Kaneda, and N. Hino, "Motor Design Approach Utilizing Regularity of a 2-Dimensional Magnetic Field," presented at CEFC 2002
[2] R. Beth, "Complex Representation and Computation of Two-Dimensional Magnetic Fields," *J. of Applied Physics*, Vol.37, No.7, pp.2567-2571 (1966)
[3] D. M. Himmelblau, *Applied Nonlinear Programming*, McGraw-Hill, 1972

Table 1 Comparison of optimal solutions

	Time step	Solutions with h_2										Solutions with h_1
		1	2	3	4	5	6	7	8	9	10	
x_1 (mm)		49.4	49.5	45.8	45.8	45.9	45.9	46	47.3	48.7	49.5	49.4
x_2 (deg)		23.3	17.7	18.6	19.6	18.8	19.5	21.2	17.7	17.9	12.1	15.8

Design and Performance Evaluation of a Linear Micro Switched-Reluctance Motor

Cheng-Tsung Liu[1], *Senior Member, IEEE*,   Da-Chen Pang[2],   Tsung-Shiun Chiang[1]

[1]Department of Electrical Engineering
National Sun Yat-Sen University
70, Lien-Hai Road
Kaohsiung, Taiwan 80424, R.O.C.
ctliu@ieee.org

[2]Department of Mechanical Engineering
National Kaohsiung University of Applied Science
415, Chien-Kung Road
Kaohsiung, Taiwan 807, R.O.C.
pang@cc.kuas.edu.tw

Abstract—To achieve low cost and high precision operational requirements in microelectronics fabrication industry, a new micro linear switched-reluctance motor (µLSRM) design that being integrated with the microelectromechanical system (MEMS) processing scheme has been investigated. With the degraded property of magnetic material after electroplating process and the geometric constraints of MEMS technology all being taken into account, the motor generated propulsive/normal force ratios at various pole shapes and winding excitation levels have been analyzed by three-dimensional finite element analysis. Results showed that the design objectives could be successfully fulfilled by the proposed µLSRM structure.

I. Introduction

With its inherent properties of simple mechanical structure and large force, the switched-reluctance motor preserves its competence in the miniaturized world for microelectromechanical system applications. The mass requirements in minimally invasive surgery, micro positioning stage, micro fluidic devices, relays, and switches have drawn more and more attentions on the possible construction of devices employing such machine concepts. By using the schemes based on semiconductor compatible processes, a micro linear switched-reluctance motor (µLSRM) is thus expected to fulfill these operational objectives.

In 1993, Guckle et al [1], [2] fabricated and tested a three-phase reluctance motor using the x-ray lithography and electroplating processing (LIGA processing) scheme. The motor was designed with 6 stator poles, 4 rotor poles, and a step angle of 30 degrees. With its rotor physical diameter of 285 µm, thickness of 80 µm, air gap of 3 µm, and a much larger stator thickness of 160 µm, the rotor is capable to passively levitated in the air gap to provide a maximum speed of 34,000 rpm and a output torque of 10^{-8} N·m.

Based on the similar LIGA processing scheme, a three-phase linear reluctance motor was then fabricated by Ohnstein et al [3] for the application in a high-pass optical filter with a travel range of 0.78mm. Each phase of the linear motor consists of 10 teeth, with a width of 30 µm and a pitch of 75 µm for each tooth. The linear motor is capable of delivering an output force of 4 mN with an operational power loss less than 200 µW.

Since the magnetic properties of the commonly used materials will be significantly degraded after electroplating, this issue becomes one of the major concerns in fabricating micro motors. Guckle et al [1] reported that the permalloy,

which consists 78% of Ni and 22% of Fe, has a relative permeability of 2000 and will be saturated at a flux density level of 1.0 T. Nevertheless, through a detailed evaluation on various magnetic material processing techniques that are commonly used in micro magnetic devices [4], a general observation can be concluded that the magnetic materials made by electroplating will have much lower permeability.

The other design constraint in the microfabrication process is the cost and geometric limitations for the associated motor construction. For practical consideration, to provide a larger slot for winding allocation and thermal dissipation, contradicting to the conventional motor design prospect, a prerequisite in the µLSRM design and fabrication is to use the number of motor phases as few as possible at a designated operational step length.

Based on the aforementioned material and physical concerns, this paper will present the design and performance evaluation of a µLSRM that is operated with only two phase windings while can still be driven bi-directionally. Detailed comparisons of motor generated propulsive/normal force ratios at various pole shapes and winding excitation levels will all be investigated through three-dimensional finite element analysis (3-D FEA). Validity of the proposed µLSRM can be supported by the analyzed results, and an optimal structure for fabricating such machine under the design constraints can then be identified.

II. The Micro Linear Switched-reluctance Motor

To comply with the simple and two-phase winding configurations, the two-dimensional conceptual view of the basic type µLSRM is depicted in Fig. 1. It can be observed that the stationary primary and movable secondary poles of the motor all have identical size of 1 unit, and the air gap is fixed at 0.1 unit. This motor will move 1 unit per step after each pair of windings being energized, and the exact length of 1 unit will be flexible depending on application objectives and physical fabrication constraints.

III. Operational Forces Analyses

For preliminary investigation, by selecting the unit length as 1 mm, 3-D meshes of the basic type µLSRM are depicted in Fig. 2. The associated mesh sizes are defined in Table I,
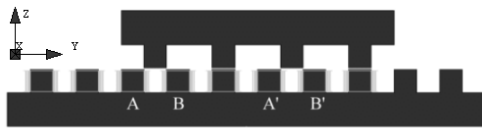
Fig. 1. Conceptual view of the micro linear switched-reluctance motor.

(a) Combination #1. (b) Combination #2. (c) Combination #3.

Fig. 4. Various pole shape combinations of the µLSRM.

and the material selected for electroplating/fabricating this motor has a fairly low relative permeability of 400 and a saturation knee point of 1.2 T. With the total applied base magnetomotive force (MMF) for each step of switching being chosen as 8 A·t, some of the motor generated electromagnetic forces in the propulsive and normal directions at different excitation levels are depicted in Fig. 3. Evidently, due to the low relative permeability and small MMF, the µLSRM will hardly get into saturation.

Since the major operational concern of such a µLSRM, in the miniature aspects and light-load applications, is to provide adequate and smooth force in the propulsive direction that can overcome the generated friction contributed from the normal directional forces of the motor. Especially at the position where one pair of stator and mover poles are aligned and the motor is stalled, the subsequently energized stator pole pairs must generate large enough forces to conquer the entire system static friction. By excluding the applied load, it is thus desired to seek the maximum propulsive/normal force ratios of the µLSRM at various pole shape combinations. Fig. 4 illustrates three of the pole combinations that are feasible for fabrications through present MEMS technology at reasonable overheads, and their corresponding fluxes at

certain MMF excitations as well as force ratios at one step length are provided in Fig. 5. From these calculated results, it is convincible that Combination #3 which providing a designated path for system flux at the propulsive direction in the edges of each pole will be a viable selection.

IV. CONCLUSION

A new micro linear switched-reluctance motor design, by incorporating with the MEMS processing scheme, has been proposed to achieve low cost and high precision operational requirements. With considerations on the degraded property of magnetic material after electroplating process and the geometric constraints of MEMS fabricating technology, the operational performance of those possible motor structures have been thoroughly analyzed by three-dimensional finite element analysis. From these results, the adequacy and feasibility of the proposed µLSRM for possible MEMS applications under the design constraints can then be verified.

REFERENCES

[1] H. Guckel, T.R. Christenson, K.J. Skrobis, T.S. Jung, J. Klein, K.V. Hartojo, and I. Widjaja, "A First Functional Current Excited Planar Rotational Magnetic Motor," Proc. of 1993 IEEE Micro Electro Mechanical Systems, Fort Lauderdale, FL, Feb. 7-10, 1993, pp 7-11.
[2] H. Guckel, T.R. Christenson, K.J. Skrobis, J. Klein, and M. Karnowsky, "Planar Rotational Magnetic Micromotors with Integrated Shaft Encoder and Magnetic Rotor Levitation," Proc. of 2nd Int. Symposium on Magnetic Suspension Technology, NASA CP-3427, Seattle, Aug. 11-13, 1993, pp 501-511.
[3] T.R. Ohnstein, J.D. Zook, and J.B. Starr, "Micromechanical Stepper Motor," US Patent No. 5,929,542, 1999.
[4] J.Y. Park and M.G. Allen, "Development of Magnetic Materials and Processing Techniques Applicable to Integrated Micromagnetic Devices," Journal of Micromechanics and Microengineering, 8, 1998, pp. 307-316.

Fig. 2. Three-dimensional meshes of the µLSRM.

TABLE I. MESH SIZES

Mesh Domain	Size (mm)
Outside Boundary (air)	2.5
Slot (air)	0.3
Air Gap	0.05
Machine Poles	0.4
Pole Tip (0~0.2 mm from the air gap)	0.05

(a) Combination #1. (b) Combination #2. (c) Combination #3.

(a) Propulsive forces. (b) Normal forces.

Fig. 3. Electromagnetic forces generated in the µLSRM.

(d) Propulsive/normal force ratios at different pole displacements.

Fig. 5. Flux paths and force ratios of the µLSRM at various pole shapes.

Optimal Design of Extremely Small Thrust VCM for Nanoindenter

J . H . Cho*, B . I . Kwon*, K . I . Woo**, Y . M . You*

*Graduate school of Hanyang University, Ansan 425- 791, Korea
**Pukyong National University, Busan, 608-739, Korea
E-mail: bikwon@hanyang.ac.kr

Abstract - Purpose of this paper is the optimal design of the extremely small thrust VCM (Voice Coil Motor) for application of the Nanoindenter, which have to control a very small force and displacement. The VCM is designed by the optimization techniques to produce a very small force by the difference of flux density of the lower part from the higher one. As a result, the VCM produces linear driving thrust in a wide range of current.

INTRODUCTION

The VCM has profitable advantages of a miniaturization, precision position control, a fast response, and a linear movement for a relatively long operation distance. Recently, most research of VCM is applied to hard disk, pickup actuator, and LOA (Linear Oscillating Actuator), but research about extremely small force and displacement control is almost not performed. Also, there is research example that applies to extremely small force and displacement control using piezoelectric device (Piezoelectric actuator), but focuses on displacement control. The piezoelectric device is used widely because position control of nano scale is easy, but the complicated circuit system is required for force control [1,2].

In this paper, we propose the shape of extremely small thrust VCM for application of the Nanoindenter, which enable control of a very small force and displacement. And the purposes of optimization are the minimization of the permanent magnet size for the efficient systems and a linearization of thrust for a good control characteristic. The finite element method is used to decide the permanent magnet position. The characteristic analysis time is shortened by the magnetic equivalent circuit analysis considering the saturation, and the steepest descent method is applied to optimize it. As a result, the VCM produces a very small force by the difference of flux density of lower part from higher one. Also, in a wide range of current (0[A]-1[A]), the VCM produces linear driving thrust by saturating the magnetic circuit path.

PROPOSED MODEL FOR SMALL THRUST VCM

Fig. 1 shows the general model of the VCM and the proposed model [3]. The produced force of the VCM is as follows ;

$$F = NBil \quad [N], \tag{1}$$

where, N is the number of coil turns, B [T] the magnetic flux density in the air gap, i [A] the input current, and l [m] the coil effective length. In order to produce extremely small thrust and manufacture the VCM easily, a number of coil turn and an effective length of coil should be limited. Therefore, extremely small thrust is related to the current or the magnetic flux density. It is difficult to control a current less than 1mA. If thrust of serve micro level is needed, the VCM should be operated a 0.01[T] order level of the air gap flux density. However, in case of the small flux density, it is very difficult to keep the linearity of thrust in a wide range of current and to compose the efficient magnetic circuit. We propose a new type VCM to produce an extremely small thrust such as Fig. 1. The thrust of the proposed model is as follows ;

$$F = N(B_1 - B_2)il , \tag{2}$$

where, B_1 [T] is the upper air gap flux density and B_2 [T] the down air gap flux density.
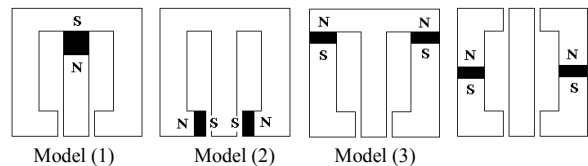
Model (1)	Model (2)	Model (3)
(a) The general models		(b) Proposed model

Fig. 1 The general and proposed model of the VCM

OPTIMAL DESIGN

The minimization of the permanent magnet size for the efficient systems and a linearization of thrust for a good control characteristic are the purposes of the optimization. The optimization technique is applied the steepest descent method[4]. Constraints are decided by a geometrical shape of the VCM and assembly of the whole system. The object function is

$$f(P) = \frac{1}{(B^2/V)^2} , \tag{3}$$

where, B [T] is the magnetic flux density and V [m^3] is the permanent magnet volume. In a wide range of current (0[A]-1[A]), the VCM produces a linear driving thrust because magnetic circuit path is saturated by taking square in value of the flux density. Table I shows the constraints, and Eq. (4) and (5) linear constraints which limit VCM size.

$$2X(1)+2X(4)+2X(6)+5[50 \tag{4}$$

$$2X(3)+X(5)[50 \tag{5}$$

Design variable	Lower limit	Upper limit
X (1)	0mm	13.5mm
X (2)	0mm	20mm
X (3)	10mm	15mm
X (4)	2mm	4mm
X (5)	10mm	30mm
X (6)	7mm	20mm

TABLE I CONSTRAINTS

Fig. 2 shows the design variable and Fig. 3 shows the optimal design process. The characteristic analysis performed by the magnetic equivalent circuit considering the saturation. Also, when the position of the permanent magnet is situated upward from the center position, the leakage flux from the lower air gap becomes much more than that from the upper air gap. Therefore, the flux passing the upper air gap may not pass the lower air gap. Such a phenomenon generates the difference of flux density between the lower and the upper air gaps. This the difference of flux density generates extremely small thrust.

For it is impossible to consider the difference of very small flux density (0.01[T]) using the magnetic equivalent circuit analysis, the most sensitive design variable, upward distance from the center, should be calculated by the finite element method. As a result, the optimum values of each design variable are the same with Table II. Fig. 4 shows the thrust characteristic. As a current increase from 0[A] to 1[A], the thrust is almost linear.

TABLE II OPTIMAL RESULTS OF DESIGN VARIABLES

Design variable	Optimal results
X (1)	12.014mm
X (2)	9.161mm
X (3)	10mm
X (4)	2mm
X (5)	20mm
X (6)	7mm
D_m	0.9mm

Design variable
X(1) : magnet width
X(2) : magnet length
X(3) : yoke length
X(4) : air gap
X(5) : center yoke length
X(6) : yoke width
Dm : magnet position

Fig. 2 Design variables for VCM
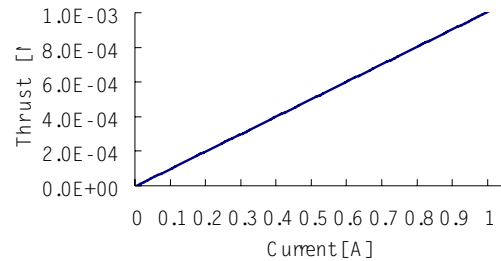
Fig. 4 Thrust characteristic according to the current variation

CONCLUSION

In this paper, we performed the optimal design of extremely small thrust VCM for application of the Nanoindenter, which enable control of extreme small force and displacement. The characteristic analysis time is shortened by the magnetic equivalent circuit analysis considering the saturation. The finite element method is used to decide the position of the permanent magnet, and the steepest descent method is applied to optimize it. As a result, in a wide range of current (0[A]-1[A]), the VCM produces a very small driving thrust which is almost linear.

Fig. 3 Optimal design processes

REFERENCES

[1] Shimamoto A, Tanaka K, "Development of a depth controlling nanoindentation tester with subnanometer depth and submicro-newton load resolutions" Review of Scientific Instruments, V.68 N.9, 1997 .
[2] J . E . Frank, G . H . Koopmann, W . Chen, G . A . Lesieutre, "Design and performance of a high-force piezoelectric inchworm motor" Smart Structures and Materials 1999 : Smart Structures and Integrated Systems, pp.717-723, 1999 .
[3] S.H.Baek, "small size motor design handbook" 12 chapter, fourth paragraph "Voice Coil Motor design" 1988.9
[4] Ashok D. B, Tirupathi R. C, "Optimization concepts and applications in engineering" Prentice hall, pp64~70, 1999.

Design of the Magnetizing System for a Rotor with Surface-mounted NdFeB Permanent Magnets

Y.H.Jeong, D.H.Kang, S.J.Jung, Paul Curiac

Korea Electrotechnology Research Institute

P.O.Box 20, Changwon 641-120, South Korea

yhjeong@keri.re.kr

S.M.Jang

Chungnam Nat'l Univ.

220 Gung-dong , Yuseong-gu , Daejeon 305-764, Korea

smjang@cnu.ac.kr

Abstract – **This paper deals with the magnetizing system for magnetizing a large rotor with surface-mounted NdFeB permanent magnets using the capacitor discharge. In this study, magnetizing-fixture is designed by analytical calculation of the magnetic circuit, and also characteristics of magnetizing system are simulated by a transient finite element method. Finally, magnetizing experiment is done using a 30mF, 1815kJ capacitor bank. As a result, this work has fully magnetized a large rotor with NdFeB permanent magnets.**

INTRODUCTION

In general, it is more difficult to magnetize permanent magnet with high-energy, especially a large synchronous machine rotor with surface-mounted permanent magnets. Recently, a pulsed field approache becomes more attractive than a DC or superconductor magnetizing system. The pulsed excitation current typically lasts only a few milliseconds and the cost of the system power supply is relatively low[1]. In such a system, the excitation field is generated by discharging a large capacitor bank into a magnetizing fixture.

This paper describes design and development of the magnetizing system for magnetizing a large rotor with surface-mounted rare-earth(NdFeB) permanent magnets of a synchronous machine as a whole unit. This system is composed of maximum 30mF, 1815kJ capacitor bank, circuit breaker, and a magnetizing fixture. In this study, magnetizing fixture is designed by analytical method, and magnetizing cirtuit characteristic is simulated by a transient finite element method. Finally, results of the simulation are compared with experimental values.

MAGNETIZING SYSTEM

This work takes anisotropic NdFeB (B_r=1.2T) type of permanent magnet into account. Outer diameter of the rotor under discussion is 153mm, and axial length 200mm. The rotor has several pieces of the NdFeB permanent magnet (W26.7×H9.3×L50mm) with radial magnetization direction on its peripheral surface. To reach high remanent flux density of NdFeB magnets, it is necessary to obtain the peak value of the magnetizing field 2500 kA/m (typically range of 1,600~3,600kA/m^{2}). The corresponding magnetic flux density within the magnets rises up to 4T to 6T peak value, yielding a very saturated magnetic circuit.

The capacitive discharge magnetizer usually contains a DC power supply to charge a capacitor bank. Fig. 1 presents a LRC electric circuit consisted of a loading unit for the capacitor bank, a discharging unit with the breaker, and magnetizing fixture.
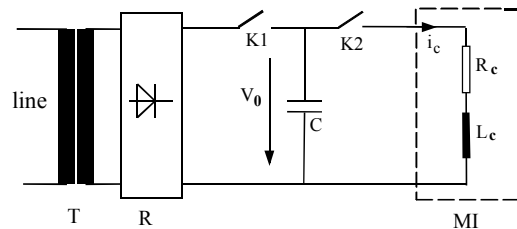
Fig. 1. Condenser bank discharge magnetizer
(T-transformer;R-rectifier;K1-loading switch;K2-discharging switch;C-capacitor bank;MI-magnetizing fixture;R_c, L_c -MI parameters)

Magnetizing fixture is highly saturated during capacitor discharge. Therefore, inductance of winding changes little with rising current. Thus, for simplification, inductance is considered constant and saturated for caculation of the discharge current. For such a system, the LRC circuit and its second order linear differential equation is considered as equation (1).

$$L \frac{di}{dt} + Ri + \frac{1}{C} \int i\, dt = 0 \qquad (1)$$

As a solution, discharge current with exponential impulse is described by equation (2) up to the aperiodic limit, $4L \geq CR^2$ accoring to reference [3].

$$i_c(t) = \frac{V_o}{\omega L} e^{-\frac{t}{\tau}} \sin \omega t \qquad (2)$$

The magnetic ciruit of magnetizing fixture is considered as an one-dimensional magnetic path along the section of the iron core, airgap, permanent magnet, and the rotor core. In one-dimensional magnetic analysis, based on the high saturation of magnetic circuit, B-H curves of the iron and permanent magnet may be simplified as that induction changes from its saturation value by permeability μ_o.

The necessary ampere-turn can be calculated along magnetic path using the Ampere theorem as follow :

$$\int H \cdot dl = i_c N_p \qquad (3)$$

The saturated magnetizing inductance is calculated from the magnetic energy stored within the magnetic circuit. And, leakage inductance by the winding overhang is calculated with the same method as in electrical machines[4].

According to the electric and one-dimensional magnetic analysis[3], magnetizing fixture as fig. 2 was designed for

magnetizing the PM rotor discussed, which has 158mm of inner diameter, 560mm of outer diameter, 210mm of axial length, and total 68 turns of winding number. As a result of circuit analysis, resistance is 0.0678 Ω at 55°C, the magnetizing and leakage inductance are respectively 0.725 [mH] and 0.679 [mH].
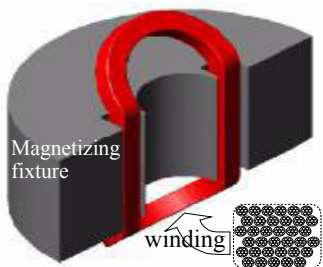
Fig. 2. Configuration of magnetizing fixture

SIMULATION AND EXPERIMENT

Korea Electrotechnology Research Institute, for which author is working, has a capacitor bank with 200 parallel capacitors of 150 μF each, which is adjustable voltage up to 11 kV. So, this work decided capacitance of capacitor bank being 30mF by considering time constant of the electric circuit. As a result of transient FEM analysis, discharge current and radial component of field intensity within the PMs are calculated according to discharge voltage. PMs near the D-axis of rotor become already saturated at 955 V of discharge voltage, which laid on field of about 2500 kA/m. At 2800 V (9.56kA of peak current), about 80% of PMs is expected to be saturated, and at 4745 V about 86%.
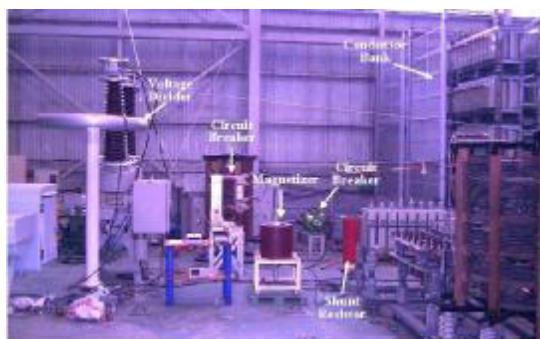
Fig. 3. Test set

Test set of the magnetizing system using capacitor bank is presented in fig. 3. For measuring flux density, hall senor measurable up to 10[T] was used. The results of magnetization experiment are presented in fig.4, and table 1. Experiment results agree finely with those of a transient FEA. In table I, flux densities in parenthese are one that subtract pre-magnetized value in PMs. That is, it is flux density occurred by only discharge current. Of course, at magnetization of 955 V, pre-magnetized value is included a little, too. Fig.5 shows flux density distribution on the surface of the magnetizde rotor in comparison with result of static 3D-FEA. It shows good agreement.
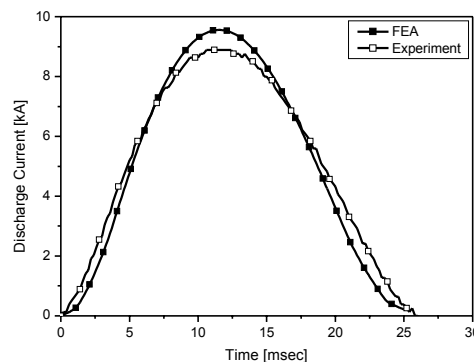
Fig. 4. Discharge current between FEA and experiment (at 2.8kV)

TABLE I. MAGNETIZATION RESULTS

Discharge Voltage		955[V]	2800[V]	4745[V]
Peak current[kA]	FEA	2.77	9.56	16.56
	Test	2.53	9.06	15.29
Peak flux density[T]	FEA	2.48	3.85	5.09
	Test	2.7	4.4(3.45)	5.85(4.9)
Time[ms]	FEA	15.8	11.5	10.5
	Test	15.9	12.3	11.5
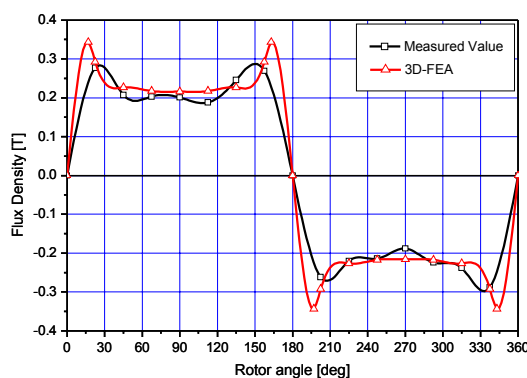
Fig. 5. Flux density on the surface of the magnetized rotor

CONCLUSION

This study dealt with the magnetizing system using a capacitor discharge for magnetizing a large rotor with high energy PMs. This work designed magnetizing fixture and magnetizing sytem using analytical method and a transient FEA, and performed the simulation and experiment for magnetizing a rotor as a whole. As a result, this work obtained a rotor with fully saturated NdFeB magnets.

REFERENCE

[1] Bretchco, Pand and Ludwig, "Open-Loop Pulsed Hysteresis Graph System for the Mgnetization of Rare-earth Magnets", IEEE trans. on magnetics, Vol.36, No.4, pp.2042-2051, 2000.
[2] Walker Scientific Inc., "Magnet Processing–Selecting the Right Equipment", MA01606.
[3] A.Binder, "Design of Coils for Magnetizing Rotors Surface Rare Earth Permanent Magnets", Electrical Engineering, 78, pp.449-454, 1995.
[4]J.F.Gieras, M.Wing,"Permanent Magnet Motor Technology, Marcel Dekker Inc., NewYork, 1997.

The Influence of Magnetization Pattern on the Performance of Permanent Magnet Eddy Current Couplings and Brakes

Sung Ho Lee, Han Wook Cho, Sung Kook Cho, Seok Myeong Jang

Dept. of Electrical Engineering, Chungnam National University,
220 Gung-dong, Yuseong-gu,
Daejeon 305-764, Korea
e-mail: shlee@ee.cnu.ac.kr

Abstract —**This paper examines permanent magnet eddy current couplers and brakes. Specifically, the effect of permanent magnet magnetization patterns on the force production is investigated. A two-dimensional finite element modeling is performed to predict the electromagnetic behavior and the force production of permanent magnet type eddy current couplers and brakes under constant speed operation. The influence of design parameters on the torque-speed characteristics of such devices is also presented.**

I. INTRODUCTION

Drag forces due to eddy currents induced by the relative motion of a conductor and a magnetic field occur in many practical devices: motors, brakes, couplings, magnetic bearings, and magnetically levitated vehicles [1]. In particular, the practicality of using permanent magnets in eddy current couplings and brakes is obviously recent, due to the manifold improvement in magnet materials and technology [2]. The principle behind the operation of such a system relates to basic electromagnetic induction theory. The interaction between the magnetizing field and eddy currents results in forces that oppose (or follow) the movement, producing the braking (or coupling) action [3]. The permanent magnet eddy current devices are also independent of any electric power source and control.

Using two-dimensional finite element analysis, this paper deals with the influence of the magnetization patterns and one of the design parameters on the performance of the permanent magnet eddy current device, specifically the extent to which device performance, in terms of the torque-speed. The calculated results are also compared to the experimental data.

II. STRUCTURE OF PERMANENT MAGNET EDDY CURRENT MACHINES

The permanent magnet eddy current coupling and brake is shown in the cross-sectional schematic of Fig. 1. The basic structure of such a device comprises the moving (or stationary) set of magnets that are separated from the stationary (or moving) conducting cylinder by an air-gap. If held stationary, the conducting cylinder acts as a brake; if free to rotate, the conducting cylinder will follow the magnet cylinder with a relative speed which is a function of the transmitted torque.

As highlighted in Fig. 2, these machines can be configured in a variety of types according to magnetization patterns. Fig. 2(a) shows the topology with the exterior polar Halbach magnetization, while Fig. 2(b) shows the topology with horizontally magnetized magnets separated by iron pole
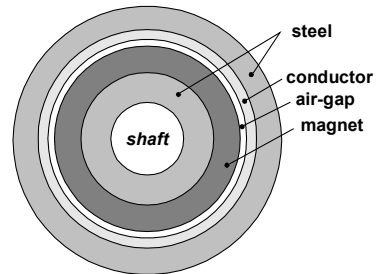
Fig. 1. Schematic of permanent magnet eddy current coupling and brake.

(a) (b)

(c) (d)
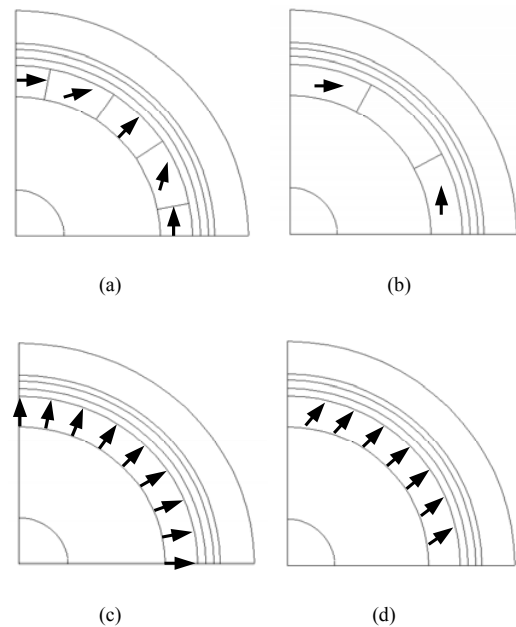
Fig. 2. Permanent magnet eddy current machine topologies according to magnetization patterns : (a) Halbach magnetization, (b) horizontal magnetization, (c) radial magnetization, and (d) parallel magnetization.

pieces. Fig. 2(c) and (d) shows external magnet topologies with radially and parallel magnetized magnets, respectively. In Halbach magnetized topology, the moving (or stationary) part including magnets could be either air- or iron-cored.

III. FINITE ELEMENT MODEL

When the moving part including magnets rotates, currents are induced in the conducting cylinder. The

fundamental equations of the A-ϕ method using a moving coordinate system [4] are given by

$$\text{rot}(\nu\text{rot}\boldsymbol{A}) = \nu_0\text{rot}\mathbf{M} - \sigma\left(\frac{\partial\boldsymbol{A}}{\partial t} + \text{grad}\phi\right)$$

(1)

$$\text{div}\left\{-\sigma\left(\frac{\partial\boldsymbol{A}}{\partial t} + \text{grad}\phi\right)\right\} = 0 \qquad (2)$$

where

$\boldsymbol{A}$ magnetic vector potential;

ϕ electric scalar potential;

ν, σ reluctivity and conductivity of the material, respectively;

$\mathbf{M}$ magnetization vector;

The total eddy current loss in the conducting cylinder is

$$W_e = \sum_{i=1}^{m}\left[I_i^{(e)}\right]^2 R_i^{(e)} h$$

(3)

where, $I_i^{(e)}$ and $R_i^{(e)}$ represents an eddy current and resistance in each element, respectively. h is the axial length of conducting cylinder.

Hence, the torque, T, developed by the brake (or coupler) is related to the total eddy current loss, W_e, and the angular velocity, ω, as follows:

$$T = W_e / \omega$$

(4)

IV. RESULTS AND DISCUSSION

Figure 3 shows the magneto-static field distributions at the air-gap according to magnetization patterns of each magnet cylinder rotor topology, respectively. For a fixed value of the magnet height, Fig. 4 compares the air-gap flux density distributions versus angular position of each topology. The torque variation with speed for various topologies is calculated and plotted in Fig. 5.

The influence of design parameters on the torque-speed characteristics and the comparison between the calculated results and the experimental data will be represented in next extended version.

REFERENCES

[1] W. L. Lorimer and D. K. Lieu, "Correlation of experimental data and three-dimensional finite element modeling of a spinning magnet array", *IEEE Trans. Magn.,* vol. 30, pp. 3004-3007, Sept. 1994.

[2] T. W. Nehl and B. Lequesne, "Nonlinear two-dimensional finite element modeling of permanent magnet eddy current couplings and brakes," *IEEE Trans. Magn.*, vol. 30, pp. 3000-3003, Sept. 1994.

[3] A. Wallace and A. V. Jouanne, "Comparison testing of an adjustable-speed permanent magnet coupling," *IEEE* Pulp & Paper Industry Technical Conference, Atlanta, June 2000.

[4] K. Muramatsu, T. Nakata, N. Takahashi and K. Fujiwara, "Comparison of coordinate systems for eddy current analysis in moving conductors," *IEEE Trans. Magn.*, vol. 28, pp. 1186-1189, 1992.

(a)   (b)

(c)   (d)

(e)   (f)
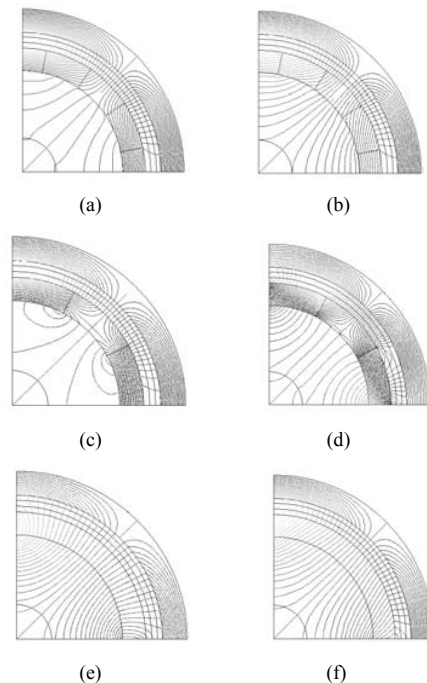
Fig. 3. Magneto-static field distributions according to magnetization patterns: (a) Halbach magnetization without back-iron, (b) Halbach magnetization with back-iron, (c) horizontal magnetization without back-iron, (d) horizontal magnetization with back-iron, (e) radial magnetization with back-iron, and (f) parallel magnetization with back-iron.
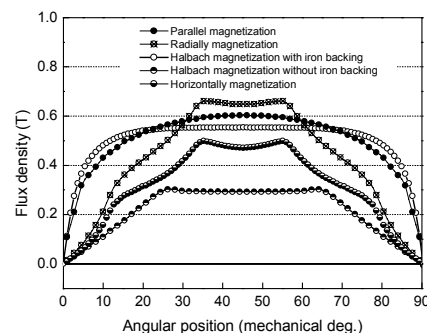
Fig. 4. Comparison of magnetic flux density distributions of each topology versus angular position.

Characteristics of Rotor Losses in High Speed Motor/Generator

Seok Myeong Jang, Han Wook Cho, Sung Ho Lee, Sung Kook Cho
Dept. of Electrical Engineering, Chungnam National University
220 Gung dong   Yusung-gu
Daejeon 305-764, Korea
e-mail: smjang@ee.chungnam.ac.kr

Abstract —**High-speed brushless permanent magnet machines are currently being developed for a number of applications including gas-turbine generator sets and machine tools. Due to the high peripheral speed of the rotor and the relatively high conductivity of the magnets used, rotor eddy current loss can be substantial. On the basis of finite element method, this paper deals the flux density distribution that caused by slotting harmonics, and the contribution of the retaining ring to the total eddy current losses.**

I. INTRODUCTION

High speed brushless permanent magnet machines are good for machine tools, aerospace applications, etc, since they are conductive to high efficiency, high power density, small size and low weight. Due to their high performance characteristics, high-speed electrical machines are likely to be a key technology for many future applications of motion control and drive systems. The most important design consideration in the choice of high speed burshless permanent magnet machine is the need to minimize eddy current losses in the retaining ring and rotor due to slotting harmonics. But , the losses in the rotor elements due to slotting harmonics are not to easy to determine [1]. Therefore, this paper proposes a rectilinear model and governing equation. Field equations are solved in two dimensional model, i.e. the end effects are neglected.

II. ANALYSIS MODEL

A. Analysis Model

Fig. 1(a) shows a 75,000rpm burshless permanent magnet motor with a 24-slot stator carrying a distributed winding, and a 2-pole rotor with diametrically magnetized sintered SmCo magnets which produce an essentially sinusoidal airgap flux density distrubution. And Fig.1.(b) shows that the simplified rectilinear model [2].

B. Governing Equation

The governing equation of the analysis model is given by Maxwell's equations for magnetic field intensity H , magnetic flux density B ,and electric field intensity E simplify to

$$\nabla \times \vec{H} = \vec{J}_0 \qquad (1)$$

$$\nabla \cdot \vec{B} = 0 \qquad (2)$$

$$\nabla \times \vec{E} = -\frac{\partial \vec{B}}{\partial t} \qquad (3)$$
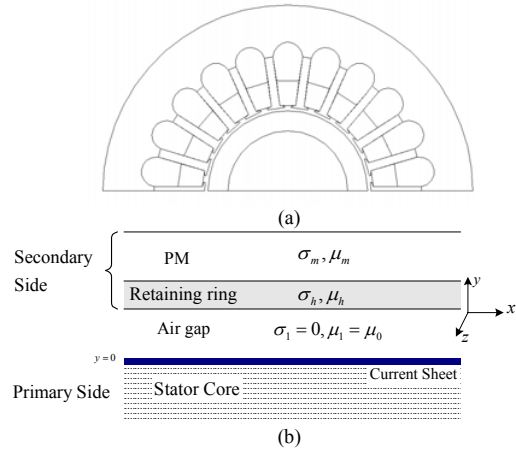
Fig. 1. Analysis models (a) Designed model (b) Simplified Rectilinear model

where $\vec{J}_0$, eddy current density induced in the retaining ring. Eddy current considering the motion represent as follows,

$$\vec{J}_0 = \sigma \vec{E} = \sigma(\vec{u}_x \times \vec{B}) \qquad (4)$$

where σ is the conductivity of retaining ring. Therefore, Eq.(1) becomes,

$$\nabla \times \frac{1}{\mu}(\nabla \times \vec{A}) = \vec{J}_0 \qquad (5)$$

$\vec{A}$ is the magnetic vector potential. Since assuming the motion is only x-direction and the eddy current is z - component, $\vec{A}$ becomes as follows,

$$\vec{A}(x, y, t) = A(y)e^{j(\omega t - v\beta x)}\vec{a}_z \qquad (6)$$

where $\vec{a}_z$ is the z -directed unit vector. And v is the space order of slotted harmonic factor which defined $1 + 2mqn$ ($n = 0, \pm 1, \pm 2, ..$), m and n are the number of phases and the number of slots/pole/phase, respectively. Consequently, the governing equation for the 2-D FEM of analysis model is expressed as,

$$\frac{\partial}{\partial x}\left(\frac{1}{\mu}\frac{\partial A_z}{\partial x}\right) + \frac{\partial}{\partial y}\left(\frac{1}{\mu}\frac{\partial A_z}{\partial y}\right) - \sigma\frac{\partial A_z}{\partial t} = 0 \qquad (7)$$

where μ denotes the permeabillity.

When the high speed permanent magnet machine rotated, induced current density in the retaining ring is,

$$J_z = \sigma\left(-\frac{\partial A_z}{\partial t} - u_x\frac{\partial A_z}{\partial x}\right) \qquad (8)$$

These currents will produce losses in the retaining ring. The losses per muit volume are,

$$P = \frac{1}{2\sigma}\sum_{\nu=-\infty}^{\infty}|J_z|^2 \qquad (9)$$

IV. RESULTS AND DISCUSSION

The curves given in Fig.2(a). shows the flux density distribution over two pole pitches as obtained from numerical flux calculation using finite element method. Fig.2(a). illustrates the considerable decay of the amplitude of the slot harmonics as they propagate through the ring from airgap. This is because of the high leakage of the slot-harmonics due to their small pole pitches.

Therefore more specific losses are expected to take place in the ring rather than in the magnets themselves.

Since the frequency of the eddy currents produced in the rotor elements due to stator slotting is proportional to the rotor speed [1].

Fig.2(b). shows the slotting harmonics characteristics of flux density in airgap. These harmonics are produced due to interaction of rotor fundamental harmonic with airgap permeance harmonics.

(a)

(b)
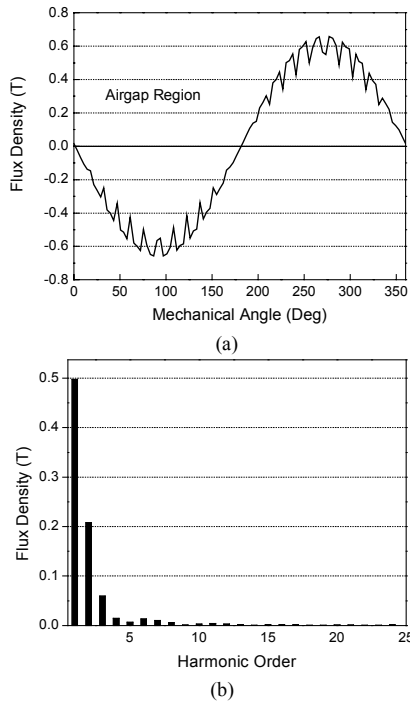
Fig. 2. Airgap flux density distribution and harmonics
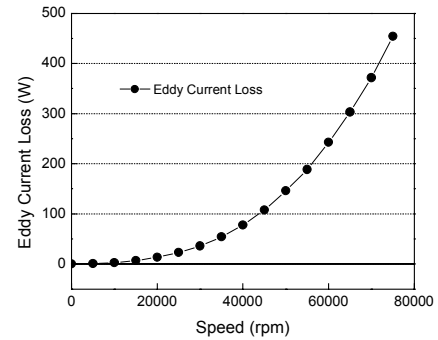
Fig. 3. Eddy current losses in the retaining ring

Fig.3. shows that increasing the speed result in more contribution of the ring to the total eddy current losses. This is due to the increased damping effect of the eddy currents on the side and the faster decay of the slot-harmonics waves on the other side.

V. CONCLUSION

It could be shown, that the total slot harmonics losses in the rotor increase quadratically with speed. However, increasing the speed will increase the contribution of the magnet retaining ring to the total rotor losses. This is because of the damping effect provided by the eddy currents generated in the rotor. Therefore, for high speed applications with critically high speed rotor losses, sectionalizing the ring or even grooving its outer surface would lead to an appreaciable decrease of the rotor losses.

REFERENCES

[1] N. Boules, "Impact of slot harmonics on losses of high-speed permanent magnet machines with a magnet retaining ring", *Electric Machines and Electromechanics*, 6, 527-539, 1981

[2] K.Ng, Z.Q.Zhu, D.Howe, "Open-Circuit Field Distrubution in a Burshless Motor with Diametrically Magnetised PM Rotor, Accounting for Slotting and Eddy Current Effects" ,*IEEE Trans. on Magnetics*, Vol.32, No.5, September 1996

[3] J. R. Hendershot Jr. and T.J.E Miller, *Design of Brushless Permanent-Magnet Motors*, Magna physics publishing, 1994.

Characteristic Analyses of Eddy Current Coupling by Finite Element Method Considering Rotor Pole Shape and Copper-Faced Drum

Seok Myeong Jang, Seong Kook Cho, Sung Ho Lee, Han Wook Cho

Dept. of Electrical Engineering, Chungnam National University

220 Goong-dong Yuseong-Gu Daejeon 305-764, Korea

e-mail: smjang@ee.chungnam.ac.kr

Abstract — **Coupling drives are shown to be applicable to a wide range of control variables. And Electronic control of the coupling offers many new possibilities in process control and industrial control applications. This paper develops three dimensional finite element method of the eddy current coupling. The flux density distributions are also presented using the finite element method. And it focuses on the effect of the copper-faced drum and rotor pole shape. So it deals with eddy current losses in copper-face drum and torque-speed characteristic according to depth of copper.**

I. INTRODUCTION

The eddy current coupling is widely used in industrial applications. This paper gives a theory of steady state operation of eddy current couplings. And the differences in operation between claw-pole and inductor-type eddy-current couplings are shown and the limitations of inductor couplings emphasized. Eddy current couplings always contain two members, which can rotate freely with respect to one another. The magnetic field is generated by the excited coil. The second member is the eddy current cylinder of the coupling[4]. This paper analyze the magnetic field in the drum of the coupling by finite element method for a Lundell type and Inductor type coupling respectively. And then, theoretical torque/slip speed characteristic and drum-loss according to slip speed with various copper depth in the drum are investigated.

II. STRUCTURE AND ANALYSIS

Eddy current coupling is composed of loss drum, inductor and excitation coil. Inductor is simultaneously excited by the exciting coil. When both members are stationary and the field system is excited, a magnetic-field pattern of alternating polarity is established. If the pattern is now rotated, eddy current field interacts with the air-gap flux to produce a torque, which is a function of the field current and slip speed[4].
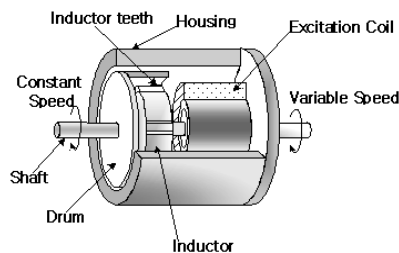
Fig. 1. Structure of eddy current coupling

TABLE I. SPECIFICATION OF THE ANALYSIS MODEL

Item	Value
Pole pairs	3
Pole wavelength	28(mm)
Airgap length	0.5(mm)
Inner diameter of inductor	101(mm)
Axial length of drum	75(mm)
Axial length of pole	70(mm)
Airgap diameter	101.2(mm)
Excitation m.m.f	1500(AT)

Eddy current phenomena are described by the diffusion equation. For the steady state time harmonic case, this equation, in terms of the magnetic vector potential is

$$\frac{\partial}{\partial x}\left(\frac{1}{\mu_y}\frac{\partial A}{\partial x}\right) + \frac{\partial}{\partial y}\left(\frac{1}{\mu_x}\frac{\partial A}{\partial y}\right) = -(J_0 + J_e) \qquad (1)$$

$$J_e = -\sigma\frac{\partial A}{\partial t} - \sigma\frac{\partial \phi}{\partial z} \qquad (2)$$

For the finite element equations for the sinusoidally time varing eddy current case, the result is a matrix equation of the form

$$[S + T]\{A\} = \{J\} \qquad (3)$$

$$S_{i,j} = \iint_{\Delta e}\frac{1}{\mu_e}\left[\frac{\partial N_i}{\partial x}\frac{\partial N_j}{\partial x} + \frac{\partial N_i}{\partial y}\frac{\partial N_j}{\partial y}\right]ds \qquad (4)$$

$$T_{i,j} = j\omega\iint_{\Delta e}\sigma_e N_i N_j ds \qquad (5)$$

where N_i is the shape function associated with node i. In the unconstrained case the right hand side is a vector of known currents which constitute the forcing function of the problem[3]. Next the losses by eddy current in the drum is calculated. The finite element solution gives the complex vector potential at the nodes. The eddy current density is

$$J = j\omega\sigma A \qquad (6)$$

The instantaneous eddy current loss is written in terms of the current density as

$$P = \mathrm{Re}\{1/2\sigma\iint JJ^* dxdy\} \qquad (7)$$

And the expression for force by using the virtual work method then becomes

$$F_{xe} = -\frac{\upsilon_e}{2}[A]^T\left[\frac{\partial S_e}{\partial x}\right][A] \qquad (8)$$

III. RESULTS AND DISCUSSION

Figure 2 shows air-gap flux density distribution of inductor type eddy-current coupling, the operation of this type does not depend, however, on reversal of the polarity of the magnetic field. It is sufficient if the filed varies between a minimum and a maximum value.
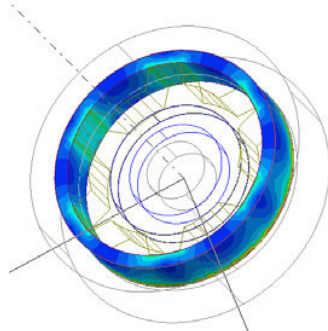
Fig .2. Flux density distribution in the drum of inductor type eddy current coupling

Figure 3 shows flux density distribution of Lundell type eddy-current coupling. Since eddy current of Lundell type takes the more poles in the rotor, it can increase the maximum torque. So it is widely used for the transmission of high power.
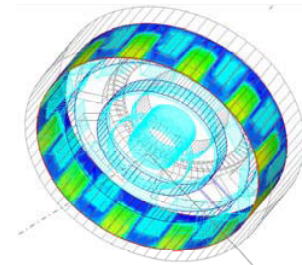
Fig. 3. Flux density distribution in the drum of claw pole type eddy current coupling
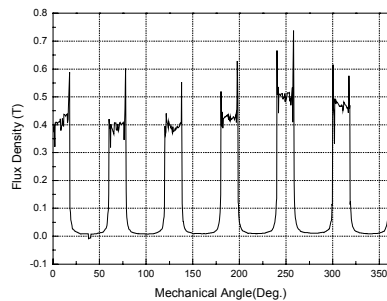
Fig. 4. Radial airgap flux density distribution of inductor type eddy current coupling

Figure 6 shows drum loss according to slip speed . Variable output speed is obtained simply by varying the slip power dissipated in the drum. Torque-Slip speed curves according to depth of copper faced in drum are shown to Fig.7.
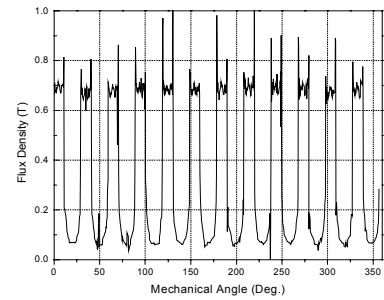
Fig. 5. Radial airgap flux density distribution of claw pole type eddy current coupling

Eddy current coupling is close in nature to the induction motor, it is not surprising that the torque-speed curves of the coupling are almost identical to those of an induction motor with a high-resistance or solid-iron rotor. When the depth of the copper in the drum, torque characteristic about the coupling of TABLE I shown that can used in wide speed range.
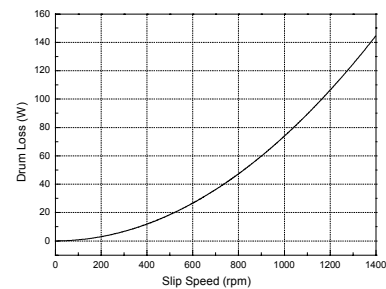
Fig. 6. Eddy current loss in the drum of the inductor type eddy current coupling
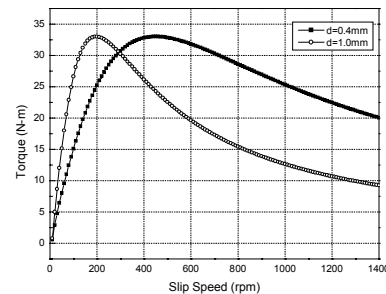
Fig. 7. Torque according to slip speed with 0.4mm and 1mm copper depth

References

[1]E.J.Davies, "Three dimensional theory of eddy-current couplings with copper-faced loss drums", Proc.IEE, Vol 124 DECEMBER 1977
[2]E,J,Davies, "General theory of eddy-current couplings and brakes" , PROC. IEE, Vol. 113, No. 5 MAY 1966
[3]S.J.Salon, *Finite element analysis of electrical machine*, Kluwer Academic Publishers 1995
[4]W.Bahler "An eddy-current coupling employed as a vairable-speed drive", Philips Technical Review Vol 27, No.1 1966.

Some Tricks for Modelling Rotating Electrical Machines Using Finite Elements

D. Rodger H.C. Lai and R.J. Hill-Cottingham
University of Bath,
Bath BNES BA2 7AY, UK

Abstract—**Despite world wide efforts and many recent advances, electrical machine modelling using finite elements can be computationally very expensive, especially if 3D models are required. This contribution is concerned with speeding up the process. Some examples of line start permanent magnet machines and induction motors are provided.**

I. INTRODUCTION

Finite element (FE) models of some classes of rotating electrical machines can be computationally very expensive, mainly due to the frequent need for time transient solutions, complex geometry, coupled circuits and non linearities. Several topics are addressed in this paper, among which are: Time transient modelling of machines containing permanent magnets; obtaining a steady state torque speed curve for induction machines; improving time harmonic models of induction machines using transient time steps; coupled circuits.

II. FINITE ELEMENT SCHEMES

Most electrical machines have a relatively low ratio of conducting regions to non conducting regions, the bars in an induction machine are a typical example. This would imply that in 3D it is advantageous to divide the machine up into non conducting regions in which the magnetic scalar potential ϕ is used and conductong regions in which a vector variable is used (in our case almost always the magnetic vector potential $\mathbf{A}$ but other choices are possible).

A. Non conducting regions

Non conducting regions are modelled using magnetic scalar potentials, either the total scalar ψ, defined as $\mathbf{H}_T = -\nabla\psi$, or the reduced scalar ϕ, defined as $\mathbf{H}_T = -\nabla\phi + \mathbf{H}_S$. Here $\mathbf{H}_T$ is the total magnetic field intensity and $\mathbf{H}_S$ is the field defined as $\nabla\times\mathbf{H}_S = \mathbf{J}_S$, where $\mathbf{J}_S$ is the source current density. The method has been extended to allow voltage forced conditions and to produce cuts for solving multiply connected problems [1]. This is particularly important in electrical machine modelling where the geometry can be very complex and where external circuits are often required. Both scalars give rise to a Laplacian type equation which has to be solved:

$$\nabla\cdot\mu\nabla\psi = 0 \tag{1}$$

B. Conducting regions, **A** scheme

If nodal elements are used to model a rotating conductor in 3D we require a moving Cartesian co-ordinate system which is attached to the moving conductor. The Cartesian components of $\mathbf{A}$ move with the conducting mesh. If edge variables are used this process is automatic.

$$\nabla\times\left(\frac{1}{\mu}\nabla\times\mathbf{A}\right) = -\sigma\left[\frac{\partial\mathbf{A}}{\partial t}\right] \tag{2}$$

For a time transient problem we solve [2], [3],

$$[\mathbf{K}]\boldsymbol{x} + [\mathbf{C}]\dot{\boldsymbol{x}} = \boldsymbol{f} \tag{3}$$

Where $\boldsymbol{x}$ is a vector of ϕ and $\mathbf{A}$ variables.
In 2D usually a scalar version of (2) in terms of A_z is used.

III. TIME TRANSIENT MODELLING OF MACHINES CONTAINING PERMANENT MAGNETS

When modelling a machine containing permanent magnets (PM), a direct implementation of (3) gives rise to unwanted and non physical transients due to the PM being 'switched on' at time zero. If the transient performance is required, it is possible to lock the rotor until the PM switch on effects have decayed and then begin the real transient solution by releasing the rotor and energising the supply. It is also possible to solve a magnetostatic problem including the PM first and then start the transient solution from that state, switching on the supply/external circuit as required. Figure 1 shows the transient switch on of a 60 kW line start PM machine, the graph on the right shows a machine in which the rotor has been clamped until 2s, the graph on the left is a machine started from a magnetostatic solution. Small differences in the graphs may be seen, due to slightly different rotor position at starting and some residual winding currents in the clamped machine windings.
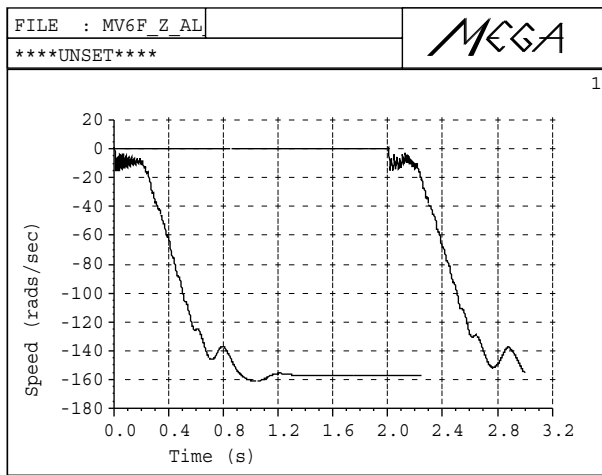
Fig. 1. On line start of a line start machine

IV. STEADY STATE TORQUE SPEED CURVE FOR INDUCTION MACHINES

The steady state torque versus speed curve is one of the most fundamental requirements of an induction machine design program. Unfortunately, it is very expensive to obtain using a standard finite element approach. For the usual slotted rotor and stator a time transient solution is necessary. This is expensive because the time constant of these machines can be of the order of seconds. The time step is governed by the likely distance a rotor will travel over the time step, something of the order of 4° of travel would usually be acceptable, and this means a time step of around 0.22ms for a machine at 3000 rpm. Several methods can be used to speed this up, one is to use a time harmonic solution and ignore the transients [4]. Various schemes are possible but the simplest assumes that only one harmonic is present in the machine appearing as the supply frequency in the stator and slip×supply frequency in the rotor. Making this assumption we can solve (3) with supply frequency everywhere and scale the conductivity σ as slip×σ (taking care to similarly scale frequency dependent rotor external circuit elements).

This may work well where it is valid to ignore such effects as winding harmonics, tooth ripple, saturation and cogging torque. A more accurate solution can be obtained by starting a transient solution from the time harmonic solution, the assumption here is that the fields throughout the former are almost correct and that the true transient solution can be reached quickly using this as a starting point. The time harmonic solution must be found and its value and time derivative at one instant in time is calculated. The transient solution uses this as a starting value. Figure 2 shows a 4 pole motor at 0.8 slip, torque versus time. The result is around -20Nm, with some cogging ripple. It may be seen that the harmonic restart method (small oscillations on Fig 2) converges in about half the time of the transient start from zero. It takes longer to converge results at higher values of slip, because rotor eddy currents are smaller at rotor speeds near to synchronous. This fact can be exploited, a torque speed curve can be generated starting from the higher rotor speeds and using the results as restarts for lower speeds. It is also possible to use point on wave switching and scaled rotor restivites to speed up these calculations, an expanded paper would include these methods.
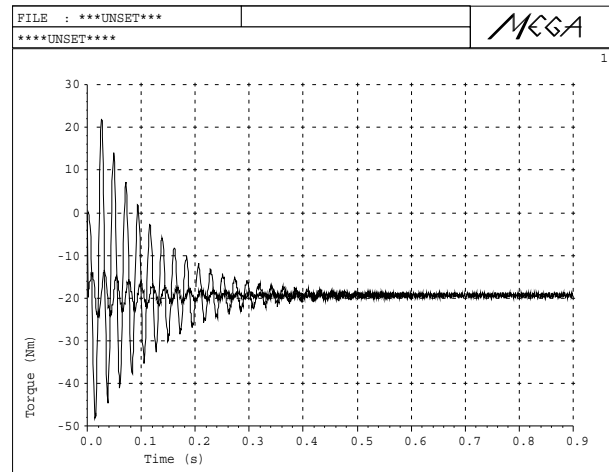
Fig. 2. Four pole induction machine at 0.8 slip

V. CONCLUSIONS

The methods described here can sometimes save computer time which is important to the continued acceptance of FE methods in the design office.

REFERENCES

[1] P.J.Leonard, R.J.Hill-Cottingham, and D.Rodger. "3D Finite element models and external circuits using the **A**ψ scheme with cuts". *IEEE Trans. Magn.*, 30(5):3220–3223, September 1994.
[2] P.J.Leonard and D.Rodger. "A finite element scheme for transient 3D eddy currents". *IEEE Trans. Magn.*, 24(1):90–93, Aug 1987.
[3] D.Rodger, N.Allen, H.C.Lai, and P.J.Leonard. " Calculation of transient 3D eddy currents in non linear media - Verification using a rotational test rig". *IEEE Trans. Magn.*, 30(5):2988–2991, September 1994.
[4] E.Vassent, G.Meunier, and A.Foggia. Simulation of induction machines using complex magnetodynamic finite-element method coupled with the circuit equations. *IEEE Trans. Magn.*, 27(5):4246–4249, September 1991.

Design and Dynamic Analyses of Permanent Magnetic Actuator for Vacuum Circuit Breaker

S.L. Ho[1], Y. Li[2], X. Lin[2], J.Y. Xu[2], W.C. Lo[1], H.C. Wong[1]

[1]Dept. of E.E., Hong Kong Polytechnic University, Hong Kong
[2]Shenyang University of Technology, P.R.China 110023
E-mail: eeslho@polyu.edu.hk

Abstract **Computation of the transient electromagnetic field, actuating force and dynamic characteristics of permanent magnetic actuators for vacuum circuit breakers are reported. Both eddy current and voltage excitations are taken into consideration. Based on the proposed method, a software is developed to analyze and design the permanent magnetic actuators. Besides computing the dynamic characteristics of the actuators, the software will also produce the mechanical drawing together with the electronic control unit details. Finally, a design example is discussed.**

INTRODUCTION

Permanent magnetic (PM) actuator for Vacuum Circuit Breaker (VCB) is a newly developed mechanism having high performance and reliability. Compared with traditional actuators, the PM actuator has a new structural design with relatively less mechanical parts and less maintenance[1]. In order to carry out the optimization study on these actuators, one needs to calculate and analyze their dynamic characteristics and thus it is necessary to (1) calculate the motion speeds of the moving iron (in the PM actuator) and the contact electrodes (of the VCB); (2) determine the relationship of operating force and opposing force during the dynamic process in order to secure reliable mechanical motion and hence improving the mechanical impact strength to result in longer mechanical and electrical life. However the dynamic characteristics of the PM actuator is generally governed by the complex transient electromagnetic field and mechanical motion that are difficult to analyze because (1) the transient electromagnetic field is non-repetitive and non-linear; (2) the presence of permanent magnetic materials in the actuator; (3) the moving iron produces electromotive forces; and (4) presence of eddy current due to the changing magnetic fluxes in the actuator. All these problems require the solution of coupled problems involving electric circuit, transient nonlinear eddy current field and mechanical motion of the iron[2,3]. One possible algorithm to study the aforementioned problems is to solve the dynamic process by calculating the static magnetic field, current and motion of the iron [1]. Even though the excitation voltage source model has been considered in this method, the eddy current is ignored because the magnetic field is considered as a static field. However, it has been pointed that the eddy currents have very significant influences upon the speed of the moving iron[4]. An alternative method is to study the transient eddy current field during the dynamic process with the current being treated as excitation source in the transient model[5,6]. This is nonetheless rather unrealistic since the excitation source is voltage and the current is an unknown. With the algorithm being reported, the transient electromagnetic field, force and dynamic characteristic of PM actuator for vacuum circuit breaker are computed. Eddy current and voltage excitation are also being taken into consideration. A software based on the proposed method is developed to analyze and design the PM actuators. Besides computing the dynamic characteristics of the actuators, the software will also produce the mechanical drawing together with the electronic control unit details. Finally, a design example is analyzed.

METHOD AND DESIGN OF SOFTWARE

Dynamic Model of the PM Actuator

The model to analyze the dynamic characteristics of the PM actuator for the VCB as shown in Fig.1 are given as follows:
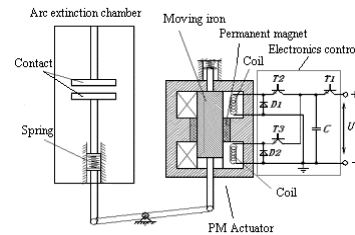
Fig.1 Schematics of a vacuum circuit breaker with PM actuator

The electric circuit with dc excitation is[1,7]

$$U_N = iR + \frac{d\psi}{dt} \qquad (1)$$

For the PM actuator with symmetrical axial structure, the eddy current field can be expressed as

$$\frac{\partial}{\partial z}\left(\frac{1}{\mu r}\frac{\partial(rA)}{\partial z}\right) + \frac{\partial}{\partial r}\left(\frac{1}{\mu r}\frac{\partial(rA)}{\partial r}\right) = -J_s + \frac{\sigma}{r}\frac{\partial(rA)}{\partial t} \qquad (2)$$

where J_s and A are unknown variables.

From the above equations, one obtains:

$$\nabla\frac{1}{\mu r}\nabla(rA) = -\frac{U_N N}{RS_C} + \frac{\sigma\partial(rA)}{r\partial t} + \frac{2\pi N^2}{RS_C}\iint_\Omega \frac{\partial(rA)}{\partial t}d\Omega \qquad (3)$$

where S_c is the cross-sectional area of the coil and N is the number of turns.

Considering the motion equation of the moving parts in the VCB with PM actuator one obtains

$$m\frac{d^2x}{dt^2} = F_{mag} - F_f(x, \frac{dx}{dt}) \qquad (4)$$

where F_{mag} is the electromagnetic force which can be solved

by using the Maxwell's equation, F_f is the opposing force and x is the displacement of the moving iron.

Using eqs. (3) and (4), the electric circuit, electromagnetic and mechanical equations can then be solved simultaneously to analyze the dynamic behavior of the PM actuator. The iron moves under the actuating force when the electromagnetic system is excited. The position of the iron is dependent on the stepping time and new meshes are thus necessary for each new position of the iron.

The Main Units of the Software

Fig. 2 shows the main modules of a computer design software of a PM actuator for 12kV, 40.5kV and 72.5kV VCBs for either indoor or outdoor services.
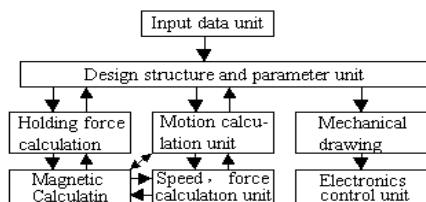
Fig.2 The main modules of the software

Fig.3 The PM actuator(left) and its control unit(right) for the 12kV indoor vacuum circuit breaker

An algorithm which designs and optimises the mechanical, electromagnetic and electronic control system are developed under the Windows environment. The PM actuator can be fed by DC or discharged capacitor. The software outputs automatically the structural parameters, mechanical and electromagnetic dynamic behaviour, electronic control circuit and apparatus as well as the mechanical drawings.

ANALYSIS AND CALCULATION

When the actuator is close and the current excitation circuit is open, the holding force to prevent the actuator from opening is only produced by the PM field, instead of the traditional interlocking mechanism in the proposed VCB. Fig. 4 shows the magnetic field for calculating the holding force. As the coil is excited, the iron of the PM actuator moves quickly. Fig.5 shows the time variation of speed of the moving iron.

In order to validate the method and the software, some tests have been done. Fig. 6 gives the experimental results of the current excitation and displacement of contact electrodes of the VCB. Table I gives the comparison between computed and experimental excitation current in the PM actuator. It

can be seen that the errors are reasonable.
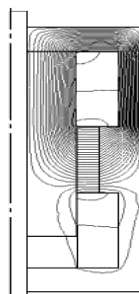
Fig.4 Magnetic field to calculate holding force (1/2 model)
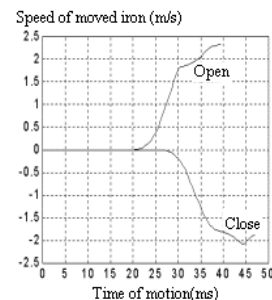
Fig.5 The time variation of speed of moving iron
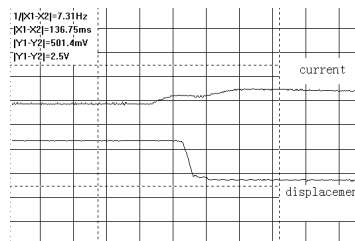
Fig.6 Test results of the coil current and displacement of the contact electrode of the VCB with PM actuator

TABLE I. COMPARISON BETWEEN COMPUTED AND EXPERIMENTAL EXCITATION CURRENT IN PM ACTUATOR

Time(ms)	5.0	10.0	15.0	20.0	25.0	30.0
Test Current(A)	9.4	16.3	21.0	23.7	24.2	22.5
Computed Current(A)	8.2	15.1	19.5	22.7	23.0	20.5
Error(%)	-12.7	-7.2	-7.1	-4.2	-4.9	-8.9

CONCLUSION

A new algorithm has been proposed to calculate the transient electromagnetic field, actuating force, electric circuit and mechanical motion of the moving iron. As the eddy current and voltage excitations are considered in the method presented, very accurate results have been obtained.

REFERENCES

[1] X. Lin, H.J. Gao, J.Y. Xu, "Calculation and Analysis of the Coupled Problem in the Permanent Magnetic Actuator for Vacuum circuit breaker," *IEEE CEFC2000*, Milwaukee, USA, June, 2000.
[2] B.Lepuesne, "Fast-acting, Long-stroke Bitable Solenoids with Moving Permanent Magnets," *IEEE Trans. on Industry Application*, Vol.26, No.3, pp.401-407, 1990.
[3] B. Lequesne, "Dynamic model of Solenoids Under Impact Excitation, Including Motion and Eddy Currents," *IEEE Trans. Magn.*, Vol.26, No.2, pp.1107-1116,1990.
[4] H.J. Fei, "Dynamic analysis and calculation in electromagnetic actuator," Mechanical industry publishing house 1993.
[5] A. Foggia, N. Burais, L. Krahennbuhl, "Finite Element Analysis of a Fast Electromagnetic Actuator," *IEEE Trans.on Mag.*, Vol.20, No.5, pp1942-1944, 1984.
[6] S.C. Tandon, A.F. Armor, M.V.K. Chari, "Nonlinear Transient Finite Element Field Computation for Electrical Machines and Devices," *IEEE Trans. PAS.*, Vol PAS-102, No.5,May,1983, pp1089-1095.
[7] P. Heidrich, "Indirectly Coupling Time-Stepping Techniques for

Numerical Analysis of Transient Force and Eddy Current Loss in a 720MVA Power Transformer

S.L. Ho[1], Y. Li[2], H. C. Wong[3], S.H. Wang[2], R.Y. Tang[2]

[1]Dept. of E.E., [3]Industrial Centre, Hong Kong Polytechnic University, Hong Kong
[2]Shenyang University of Technology, P.R.China 110023
E-mail: eeslho@polyu.edu.hk

Abstract—**The transient eddy current fields and short circuit forces upon the coils of large power transformers is analyzed. The proposed approach is based on the A–V–A formulation in which the eddy current field and the electric circuit equations are solved simultaneously. In order to reduce eddy current loss and reduce local overheating, a magnetic by-pass plate near the coil ends is discussed. A simulation to study the transient short-circuit behaviour of a 720MVA power transformer using the proposed coupled approach is reported.**

INTRODUCTION

The electromagnetic forces on the windings of large transformer due to short circuits are generally detrimental. 3-D nonlinear transient electromagnetic field is used to study these transient short-circuiting forces. A transient field study using current as the source has been reported [1]. However most large transformers are connected to a constant voltage source and the short circuit currents in the coils are unknown. Recently, there are algorithms to couple the magnetic and electric circuits in the simulation of motors [2,3], turbo-generators and other devices [4-6].

Common measure to alleviate the eddy current and overheating problems is to reduce the magnetic flux density in the metallic clamping plates and tank walls. Shields and metals with low permeability are also used to reduce the eddy current. However, these measures are insufficient for transformers rated up to 720MVA having magnetic by-pass plates near the coil ends to reduce the eddy current losses.

Unlike normal pie winding in conventional transformers with negligible axial current and torsional forces[7], the spiral coil in large transformers may be acted upon by torsional forces due to the presence of axial component of the current. Test results show that coil damages due to torsional force are not uncommon, hence it is necessary to calculate the distribution of torsional force on the coils.

This paper presents a 3D, A–V–A coupled formulation in which the eddy current field and the electric circuit equations are solved simultaneously. Some useful results on the transient short-circuit behaviour of a 720 MVA power transformer findings are obtained in the simulation study.

Besides axial and radial force, the distribution of torsional force on the spiral coils is calculated. The mechanical robustness and stability of the coil are checked. The loss density and magnetic flux density in the clamping plate with and without the magnetic by-pass plate is studied.

A-V-A COUPLED FORMULATION

Electromagnetic Field Equations

From the Maxwell's equations, the A−V−A formulations with the Coulomb gauge can be written as [7]

$$\nabla \times \nu \nabla \times \mathbf{A} - \nabla \nu \nabla \cdot \mathbf{A} + \sigma \nabla V + \sigma \frac{\partial \mathbf{A}}{\partial t} = \mathbf{t} \frac{n_c}{S_c} i(t) \quad in \quad \Omega_1 + \Omega_2 \tag{1}$$

$$\nabla \cdot (-\sigma \frac{\partial \mathbf{A}}{\partial t} - \sigma \nabla V) = 0 \qquad in \quad \Omega_1$$

where Ω_1 and Ω_2 are, respectively, the region with and without eddy currents, ν is the reluctivity tensor, σ is the conductivity tensor, $\mathbf{A}$ is the magnetic vector potential, V is the electric scalar potential, $\mathbf{t}$ is a unit coil direction field vector tangential to the windings, n_c is the number of turns, S_c is the total cross-sectional area of the windings and $i(t)$ is the current per turn.

The matrix of the field equation system can be written as

$$[\mathbf{K}]\{\mathbf{A}\} + [\mathbf{M}]\frac{\partial}{\partial t}\{\mathbf{A}\} - [\mathbf{C}]\{\mathbf{I}\} = 0 \tag{2}$$

Equation (2) is the conventional formulation where the current is used as the input.

Equations of the Electric Circuit

Power transformers that are connected to voltage sources typically have the following circuit equation:

$$u = \frac{n_c}{S_c}\frac{\partial}{\partial t}\int_\Omega \mathbf{A} \cdot \mathbf{t} d\Omega + Ri + L \frac{di}{dt} \tag{3}$$

where Ω is the space filled with windings. Moreover, the matrix equation of the equivalent circuit can be written as

$$[\mathbf{C}]^T \frac{\partial}{\partial t}\{\mathbf{A}\} + [\mathbf{L}]\frac{d}{dt}\{\mathbf{I}\} + [\mathbf{R}]\{\mathbf{I}\} = [\mathbf{u}] \tag{4}$$

Magnetic Field and Electric Circuit Coupled Equations

Eqs. (2) and (4) give the following coupled equation:

$$\begin{bmatrix} K & -C \\ 0 & R \end{bmatrix}\begin{Bmatrix} A \\ I \end{Bmatrix} + \begin{bmatrix} M & 0 \\ C^T & L \end{bmatrix}\frac{d}{dt}\begin{Bmatrix} A \\ I \end{Bmatrix} = \begin{Bmatrix} 0 \\ u \end{Bmatrix} \tag{5}$$

The Newton-Raphson algorithm is used to take into account of the magnetic non-linearity.

ANALYSIS AND CALCULATION

Eq. (1) to (5) are employed to compute the transient eddy current fields and the electromagnetic forces upon the coils in a 720MVA/500kV transformer. Fig. 1 shows the sketch of the transformer with the magnetic by-pass plates (1/2 of the structure). Fig. 2 gives the magnetic flux density distribution in the coils.

To validate the approach presented in this paper, a

17MVA transformer is selected as the test model. The corresponding calculated values of magnetic flux density on the surface of the iron core and the tested results are given in Table I which shows the calculated results agree well with the measured ones. For electric equations with known terminal voltages, the coupled method is the most suitable one for transient analyses of transformer.
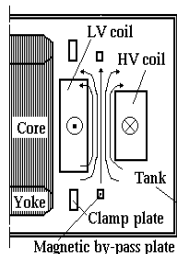
Fig.1 The sketch of transformer with magnetic by-pass plates
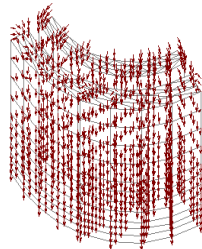
Fig.2 The magnetic flux density distribution in the coils
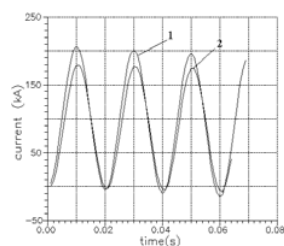
1—convention 2-coupled method
Fig.3 Primary short-circuit currents
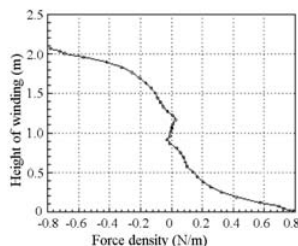
Fig.4 The torsional force of the coil sections

TABLE I COMPARISON BETWEEN COMPUTED AND MEASURED MAXIMUM MAGNETIC FLUX DENSITY (mT)

Height (mm)	442	597	900	1057	1125	1198
Computed	6.64	4.87	4.71	2.91	5.66	9.87
Tested	6.1	4.98	4.62	3.10	6.35	9.05
Error (%)	9.6	-1.6	1.1	-9.4	-12.8	8.7

Fig. 3 is the primary short-circuit currents. It can be seen that the current computed from traditional method is slightly larger than that of the field-circuit coupled method with a maximum current error of about 16.7 percent.

Most power transformers are studied as pie coil models with no axial short circuit current. Unlike traditional ones, the 720MVA transformer uses spiral coils with axial currents. Fig.4 shows the distributions of the torsional force on the B-phase low voltage coil along the z direction (height of coil). It can be seen that the torsional force of the coil sections near the end region of the windings is larger than those near the middle.

In order to study the behaviour of the coils under short circuit forces, it is necessity to check the mechanical robustness and stability of the coils. Based on the calculated results presented, the stresses of the B-phase high voltage coil are computed using the dynamic analysis method. Table II gives stress of the coil sections along the coil height. It can be seen that maximum stress appears near the middle of the coil. The maximum value is 59.6Mpa which is less than the

allowable stress of 100~160Mpa for the copper wire in the coil. Hence the coils have sufficient mechanical rigidity to withstand the short circuit impacts. For low voltage coils, the maximum radial force of the coil section in the transformer is 19207N/m which is less than collapsing critical force of 36355N/m in the radial direction. Hence there is no radial destabilization danger for the coil.

With conventional designs, there are local overheating in the metal clamping plates and pulling plates in transformers. The magnetic by-pass plate for the 720MVA transformer functions to by-pass the leakage magnetic fields at the coil ends from the clamping plates and pulling plates. By optimizing the design of the magnetic by-pass plate, the maximum loss density in the plates can be reduced by 94 percent. Table III gives a comparison of the loss density in the clamping plate from middle to end along the length direction. As the loss in the tank wall is high, a 4mm thick copper shield is used to alleviate the overheating problem in the tank wall. The total losses in the copper shield and tank wall is then reduced by 80 percent as compared to that with an unshielded tank wall. Meanwhile, the maximum loss density is reduced from 200kW/m^3 to 25kW/m^3.

TABLE II. STRESS OF COIL SECTION ALONG THE HEIGHT OF THE COIL

Height (mm)	292	583	875	1167	1460	1751	2043
Stress (MPa)	46.7	55.6	58.5	43.6	59.6	56.2	55.6

TABLE III. LOSS DENSITY IN THE CLAMPING PLATE
(Loss density 1 (kW/m^3)—magnetic by-pass plate, Loss density 2 (kW/m^3)—not magnetic by-pass plate, Length of clamp(m)—length from middle to end of clamp plate)

Length of clamp	0	0.5	1.0	1.5	2.0	2.5	3.0	3.5	4.0
Loss density 1	1.3	1.8	2.2	2.1	1.8	1.3	1.4	1.3	1.1
Loss density 2	40.5	35.1	20.2	14.3	20.1	31.0	39.5	30.2	20.5

CONCLUSION

This paper presents a 3D A−V−A coupled formulation in which the eddy current field and the electric circuit equations in a power transformer are solved simultaneously.

Besides axial and radial forces, the torsional force acting on the spiral coils is computed. By checking the mechanical robustness and stability of the coil, one can evaluate whether the coils can withstand the short circuit forces.

By optimizing the magnetic by-pass plate, the losses are reduced significantly and hence overheating in the clamping plate is avoided.

REFERENCES

[1] Y. Li et al., "Analyses of Transient Force of Coils in Large Transformers," Proc. of CICEM'99, pp.406-409, 1999.
[2] E.G. Strangas, "Coupling the circuit equations to the non-linear time dependent field solution in inverter driven induction motors," *IEEE Trans. Magn.*,Vol.21, No.6, pp.2408-2411, 1985.
[3] A. Bossavit, "Time -stepping finite element analysis of induction motor," Proc.ICEM, Pise, pp275-280, 1988.
[4] Piriou, F., Razek, R., "Coupling of saturated electromagnetic systems to non-linear power electric devices," *IEEE Trans. Magn.*,Vol.24, No.1, pp.274-277, 1988.
[5] A. Nicolet, F. Delince, N. Bamps, A. Grenon and W. Legros, "A coupling between electric circuit and 2D magnetic field modeling,"

Magnetic Force Computation in Permanent Magnets Using a Local Energy Coordinate Derivative Method

W. N. Fu, P. Zhou, D. Lin, S. Stanton and Z. J. Cendes

Ansoft Corporation, 4 Station Square, Pittsburgh, PA 15219, USA

wfu@ansoft.com   ping@ansoft.com   dlin@ansoft.com   stanton@ansoft.com   zol@ansoft.com

Abstract—**The definition of energy/coenergy in permanent magnets for computing magnetic force is still in dispute. There is also the practical problem of computing forces when permanent magnets touch objects. These problems are addressed in terms of a new definition of the energy/coenergy in permanent magnets and by using shell element.**

I. INTRODUCTION

The method of virtual work is widely used to compute magnetic force distributions in permeable materials [1, 2]. While this method has many advantages including good accuracy and the need to compute only one field solution, it is not easily applied in the case of permanent magnets. The problem is that the method of virtual work depends on the expression used to define the energy/coenergy in the system and that several different definitions the energy/ coenergy in a permanent magnet exist [3-7]. The uncertainty in the definition of the energy/coenergy in a permanent magnet creates a practical problem in computing magnetic forces when a permanent magnet touches other objects.

In the paper, a new definition of the energy/coenergy in permanent magnets is proposed and a new method for computing the force involving permanent magnets is developed. The advantages of the new method are: (a) the definition of the energy is based on physical principles; (b) the expressions of the energy/coenergy in permanent magnets and other materials are unified so that energy and coenergy have the same relationship both in permanent magnets and in other materials; (c) the computed force distributions from the energy formulation and coenergy formulation are the same. The method is applied to compute the local and global forces when a permanent magnet touches another object.

II. ENERGY/COENERGY DEFINITIONS IN PERMANENT MAGNET

During the magnetization process [5], the magnetic energy in permanent magnet is stored as

$$W = \int_{\Omega}\left(\int_{B_0}^{B} H^T dB + w_0 \right)d\Omega = \int_{\Omega}\left(|\text{shaded area}|\right)d\Omega + \int_{\Omega} w_0 d\Omega \quad (1)$$

where the shaded area is shown in Figure 1 and w_0 is the magnetic energy density at the initial operating point (H_0, B_0). This initial operating point is generally unknown because of the complicated magnetizing process. It is also impossible to evaluate this operating point from a linear-rigid model of the permanent magnet.

In non-permanent magnet materials, the magnetic energy is

$$W = \int_{\Omega} \int_{B_0}^{B} H^T dB d\Omega + \int_{\Omega} w_0 d\Omega$$
$$= \int_{\Omega} \int_{B_0}^{B} H^T dB d\Omega + \int_{\Omega} \int_{0}^{B_0} H^T dB d\Omega = \int_{\Omega} \int_{0}^{B} H^T dB d\Omega \quad (2)$$

Thus (1) is consistent with the expression used with other materials.

The magnetic coenergy in permanent magnet is defined as

$$W' = \int_{\Omega} H^T B d\Omega - W \quad (3)$$

Expression (3) can be further expressed as:

$$W' = \int_{\Omega} H^T B d\Omega - W = \int_{\Omega} H^T B d\Omega - \int_{\Omega} \int_{B_0}^{B} H^T dB d\Omega - \int_{\Omega} w_0 d\Omega$$
$$= \int_{\Omega} \int_{H_0}^{H} B^T dH d\Omega + \int_{\Omega} H_0^T B_0 d\Omega - \int_{\Omega} w_0 d\Omega$$
$$= \int_{\Omega}\left(\int_{H_0}^{H} B^T dH + w'_0 \right)d\Omega = \int_{\Omega}\left(-|\text{shaded area}| + w'_0 \right)d\Omega \quad (4)$$

where the shaded area is shown in Figure 1 and $w'_0 = H_0^T B_0 - w_0$ is the magnetic coenergy density at the initial operating point (H_0, B_0).

In non-permanent magnet materials, the magnetic coenergy is

$$W' = \int_{\Omega} H^T B d\Omega - W = \int_{\Omega} H^T B d\Omega - \int_{\Omega} \int_{0}^{B} H^T dB d\Omega = \int_{\Omega} \int_{0}^{H} B^T dH d\Omega \quad (5)$$

Thus the proposed definition is also suitable to non-permanent magnet materials.
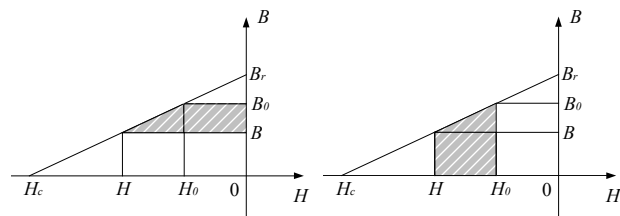
Energy density $w = |\text{shaded area}| + w_0$ Coenergy density $w' = -|\text{shaded area}| + w'_0$

Figure 1   Proposed definition of magnetic energy/coenergy density in permanent magnet

III. LOCAL FORCE COMPUTATION

In each element, the derivative of the energy/coenergy with respect to a displacement s provides the element's contribution to the nodal force [1]

$$F_{se} = -\left.\frac{\partial W}{\partial s}\right|_{\lambda=\text{constant}} = \left.\frac{\partial W'}{\partial s}\right|_{i=\text{constant}} \quad (6)$$

Here λ is the flux-linkage and i is the current. In the coenergy formulation, the contribution to the force from each element is

$$F_{se} = \int_{\Omega_e}\left[-B^T J^{-1}\frac{\partial J}{\partial s}H + \left(\int_{H_0}^{H}\vec{B}\cdot d\vec{H} + w_0'\right)\frac{\partial |J|}{\partial s}|J|^{-1} + \frac{\partial w_0'}{\partial s}\right]d\Omega$$

$$= \int_{\Omega_e}\left[-B^T J^{-1}\frac{\partial J}{\partial s}H + w'\frac{\partial |J|}{\partial s}|J|^{-1} + \frac{\partial w_0'}{\partial s}\right]d\Omega \qquad (7)$$

where J is the Jacobian matrix and $|J|$ is the determinant of the Jacobian matrix. In the energy formulation, the force is

$$F_{se} = \int_{\Omega_e}\left[-H^T\frac{\partial J^T}{\partial s}J^{-T}B + \left(H^T B - \int_{B_0}^{B}H^T dB - w_0\right)\frac{\partial |J|}{\partial s}|J|^{-1} - \frac{\partial w_0}{\partial s}\right]d\Omega \quad (8)$$

Notice that

$$H^T\frac{\partial J^T}{\partial s}J^{-T}B = \left(H^T\frac{\partial J^T}{\partial s}J^{-T}B\right)^T = B^T J^{-1}\frac{\partial J}{\partial s}H \qquad (9)$$

$$H^T B - \int_{B_0}^{B}H^T dB - w_0 = w' \qquad (10)$$

$$\frac{\partial w_0}{\partial s} = \frac{\partial}{\partial s}(H_0^T B_0 - w_0') = -\frac{\partial w_0'}{\partial s} \qquad (11)$$

It is easily demonstrated that (7) and (8) are the same.

It follows from (7) or (8) that the local force depends on the initial energy/coenergy. In the full paper, it will be verified that the global force in permanent magnet is determined purely by dw or dw'. This means that the initial energy/coenergy in a permanent magnet can be any value in the global force computation.

IV. Force Computation when Permanent Magnet Touches Objects

To implement the virtual work method, the expression must be integrated along a layer of elements around the object on which the force is to be computed. If an object touches another object, the integration is along the touched surface. Here we model such touched surfaces by using shell elements [8]. The derivative of the coenergy with respect to displacement s gives the contribution of one shell element to the nodal force

$$F_{se} = \frac{\mu}{2}\sum_{i=1}^{N_e}\sum_{j=1}^{N_e}H_i\left(\frac{\partial m_{ij}}{\partial s}\right)H_j + \int_{\Omega_e}\frac{\partial w_0'}{\partial s}d\Omega \qquad (12)$$

where N_e is the number of edges of one element and

$$m_{ij} = \int_{\hat{\Omega}_e}\hat{\vec{w}}_i^T J^{-T}\cdot J^{-1}\hat{\vec{w}}_j|J|d\hat{\Omega} \qquad (13)$$

Only the Jacobin matrix J depends on the displacement; the shape functions $\hat{\vec{w}}_i$ as well as the area $\hat{\Omega}_e$ of the reference element are independent of s. Therefore

$$\frac{\partial m_{ij}}{\partial s} = \int_{\hat{\Omega}_e}\left[\hat{\vec{w}}_i^T\frac{\partial(J^{-T}\cdot J^{-1})}{\partial s}\hat{\vec{w}}_j|J| + \hat{\vec{w}}_i^T J^{-T}\cdot J^{-1}\hat{\vec{w}}_j\frac{\partial|J|}{\partial s}\right]d\hat{\Omega}$$

$$= \int_{\hat{\Omega}_e}\left[\hat{\vec{w}}_i^T J^{-T}\left(-\frac{\partial J^T}{\partial s}J^{-T} - J^{-1}\frac{\partial J}{\partial s}\right)J^{-1}\hat{\vec{w}}_j|J| + \hat{\vec{w}}_i^T J^{-T}\cdot J^{-1}\hat{\vec{w}}_j\frac{\partial|J|}{\partial s}\right]d\hat{\Omega}$$
$$(14)$$

V. Example

The method has been applied to compute the magnetic force when one permanent magnet touches another. Figure 2 shows two rectangular permanent magnets that attract one another. Each permanent magnet is 20mm×10mm×1000mm and B_r=1.1 tesla, μ=1.0446μ_0. The computed force versus distance between the two objects is shown in Figure 3. The location of the point at zero separation coincides with the extrapolated value as the force versus distance curve approaches zero. Therefore, the value of the force computed when the two permanent magnet objects touch is correctly computed.
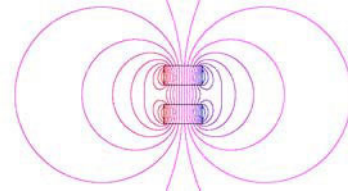
Figure 2 Two permanent magnetobjects attract together
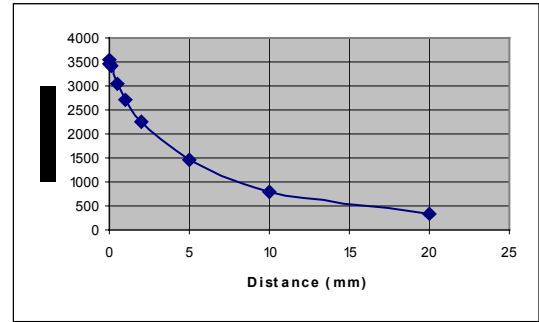
Figure 3 Computed force vs. distance when the two permanent magnets attract together

REFERENCES

[1] J.L. Coulomb, "A Methodology for the Determination of Global Electromechanical Quantities from a Finite Element Analysis and Its Application to the Evaluation of Magnetic Forces, Torques and Stiffness," *IEEE Trans. Mag.*, Vol.19, No.6, Nov. 1983, pp.2514-2519.

[2] Z. Ren and A. Razek, "Local Force Computation in Deformable Bodies Using Edge Elements," *IEEE Trans. Mag.*, Vol.28, No.2, March 1992, pp.1212-1215.

[3] M. Marinescu, "Numerical Computation of Torques in Permanent Magnet Motors by Maxwell Stresses and Energy Method," *IEEE Trans. Mag.*, Vol.24, No.1, January 1988, pp.3012-3015.

[4] R. Wang, E.P. Furlani and Z.J. Cendes, "Design and Analysis of a Permanent Magnet Axial Coupling Using 3D Finite Element Field Computations," *IEEE Trans. Mag.*, Vol.30, No.4, July 1994, pp.2292-2295.

[5] Luiz H. de Medeiros, G. Reyne, G. Meunier and J.P. Yonnet, "Distribution of Electromagnetic Force in Permanent Magnets," *IEEE Trans. Mag.*, Vol.34, No.5, Sept. 1998, pp.3012-3015.

[6] Luiz H. de Medeiros, G. Reyne and G. Meunier, "About the Distribution of Forces in Permanent Magnets," *IEEE Trans. Mag.*, Vol.35, No.3, May 1999, pp.1215-1218.

[7] Luiz H. de Medeiros, "A Unique Distribution of Forces in Permanent Magnets Using Scalar and Vector Potential Formulations," *IEEE Trans. Mag.*, Vol.36, No.5, Sept. 2000, pp.3345-3348.

[8] Z. Ren and Z. Cendes, "Shell Elements for the Computation of Magnetic Forces," *IEEE Trans. Mag.*, Vol.37, No.5, Sept. 2001, pp.3171-3174.

FEM Evaluation of Zero-phase-sequence Characteristics of 3-ph 3-limb Core-type Transformers

Cesare Mario Arturi, Luca Di Rienzo

Dipartimento di Elettrotecnica - Politecnico di Milano, P.za L. da Vinci, 32, 20133, Milano, ITALY;
e-mail: cesaremario.arturi@polimi.it, luca.dirienzo@polimi.it

Abstract – **The paper deals with the zero-phase sequence behavior of 3-phase-3-limb-core-type two-winding power transformers. The zero-sequence-impedance of power transformers depends on both the type of iron core and the presence of the tank, particularly in the case of three-limb core-type two-winding units without a delta-connected winding. A theoretical analysis proposes an equivalent network which allows the simulation of both the open-circuit and the short-circuit zero-sequence behavior of 3-limb core-type units. A finite element simulation procedure allows the computation of the linear and nonlinear parameters of the equivalent network. Experimental verifications have validated the computational procedure and the proposed theoretical approach.**

Keywords – **Devices and Applications, calculation of forces and other device parameters.**

INTRODUCTION

The steady-state and transient analysis of power system networks in asymmetrical conditions require component models accounting not only for 3-ph symmetrical operation but, also, for zero-sequence operation.

The zero sequence impedance of transformers depends on both the type of iron core and the presence of the tank, particularly in the case of three-limb core-type units.

The paper examines the zero-sequence behavior of three-phase three-limb core-type two-winding transformers. The theoretical analysis proposes an equivalent network which allows the simulation of both the open-circuit and the short-circuit zero-sequence behavior of 3-limb core-type units. A finite element simulation procedure allows the computation of the linear and nonlinear parameters of the equivalent network. Experimental verifications made in steady-state ac and in transient dc have validated the computational procedure and the proposed theoretical approach.

The 3-ph 3-limb core-type 2-winding transformer simulated by a 3D-finite element code is rated 40 MVA;132 kV/20.8-10.4 kV; winding connections: Y-Yn, with regulating winding on HV side (Fig. 1). Finite element simulation of open-circuit zero-sequence behavior allows obtaining the magnetizing characteristic shown in Fig. 2. A sample of the flux density vector plot on the surface of the tank of the finite element transformer model, during the open-circuit zero-sequence simulation with the external winding (HV) supplied at 5% of the nominal current is shown in Fig. 3.
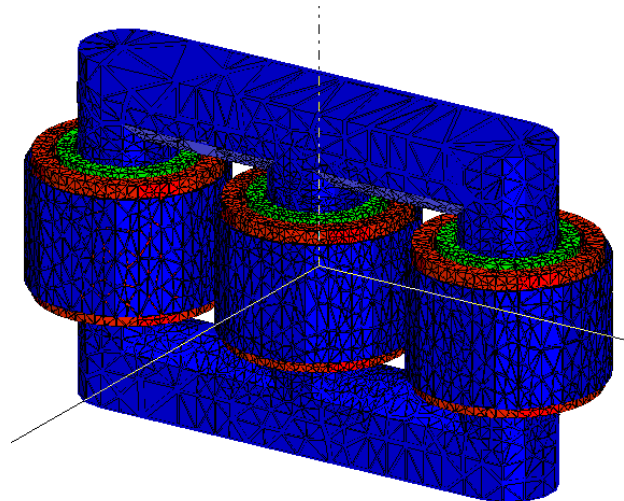
Fig. 1. Three-dimensional finite element model of the 3-ph 3-limb transformer rated 40 MVA; 132 kV/20.8-10.4 kV; Y-Yn, with regulating winding on HV side. The tank has not been represented in this figure.
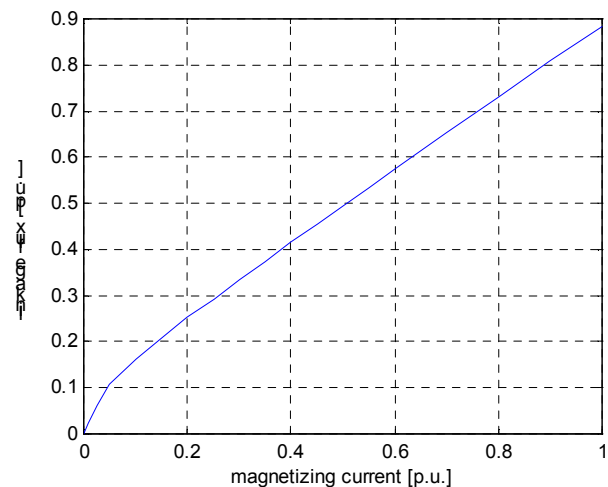
Fig. 2. Open-circuit zero-sequence magnetizing characteristic of the 3-ph 3-limb transformer rated 40 MVA; 132 kV/20.8-10.4 kV; Y-Yn, with regulating winding on HV side.
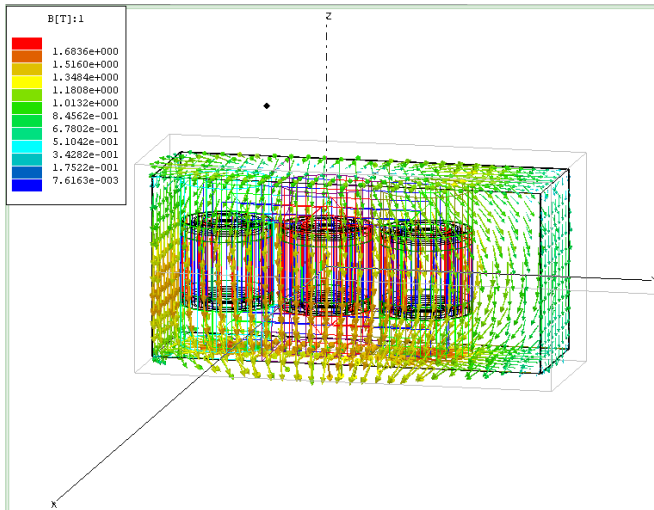
Fig. 3. Flux density vector plot on the surface of the tank of the transformer model, rated 40 MVA, during the open-circuit zero-sequence operation with the external winding (HV) supplied at 5% of the nominal current.

ZERO-SEQUENCE OPERATION OF 3-PH 3-LIMB CORE-TYPE 2-WINDING TRANSFORMERS

It is customary to distinguish between short-circuit and open-circuit zero-sequence operation of a 3-ph 2-winding transformer, with the understanding that, for this sequence, short-circuit indicates that in addition to currents in excited windings, currents also flow in other windings short-circuited for zero-sequence, as in the case of a delta-connected winding, and that open-circuit implies that currents flow only in the excited winding, as with other winding star-connected or open-delta-connected. We also need to specify the supplied winding, internal (usually the low voltage one, LV) or external (high voltage, HV). The open-circuit zero-sequence behavior is more complex than the short-circuit one, because of the role of the tank on the reclosing magnetic flux path.

A physical equivalent network, based on the actual electromagnetic configuration of the transformer, is used for the interpretation of the zero-sequence behaviour of the 3-ph 3-limb transformer with two concentric windings. This equivalent network is obtained from the magnetic network of the transformer by the duality rules.

Fig. 4a schematically shows the structure of the transformer, the tank and a two-node magnetic network constituted by the magnetic flux tubes that discretize and approximate the actual magnetic field. The permeances Λ_{fa}, Λ_{fb}, Λ_{fc} are associated to the flux tubes of the limbs, the permeance Λ_l is associated to the leakage flux of the central phase (the leakage permeance of the lateral phases are not outlined, for simplicity), the permeance Λ_0 is associated to a number of parallel flux tubes connecting the upper and the lower yokes and reclosing outside the external windings. This last magnetic flux tubes flow partially in the space between the

external winding and the tank and partially in a circuit having the air-gaps between the iron-core and the tank (upper and lower side) in series with the tank, usually made by ferromagnetic material. However, when the tank is heavily saturated, the magnetic flux partially recloses outside the tank.

According to the duality rules, the electric network of Fig. 4b is deduced from the magnetic network: each inductance, linear or nonlinear, corresponds, one-to-one, to each permeance of the magnetic network; a voltage of the electric network corresponds to a flux of the magnetic network; a current of the electric network corresponds to a magnetic potential difference (m.p.d.) of the magnetic network. Per unit value of the parameters are used in the analysis of the equivalent network, by assuming as reference the corresponding nominal values.
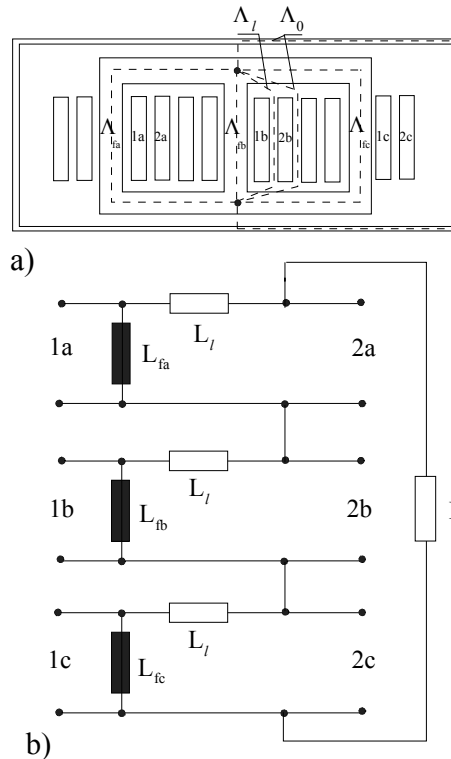
Fig. 4. Three-phase transformer: a) magnetic network; b) equivalent electric network.

The electric equivalent network allows to clearly understand the meaning of the short-circuit ($L_{0SC(LV)}$, $L_{0SC(HV)}$) and open-circuit ($L_{0OC(LV)}$, $L_{0OC(HV)}$) zero sequence inductance of the 3-ph 3-limb core-type 2-winding transformers, seen from the internal (LV) or the external (HV) winding and their relationship with the electric equivalent network parameters. A detailed discussion will be presented in the full paper.

REFERENCES

[1] A. N. Garin: "Zero-phase-sequence Characteristics of Transformers" Part I and II, General Electric Review, March-April 1940, pag. 131.
[2] K. P. Oels: "Ersatzschaltungen des Transformators für das Nullsystem", ETZ-A Bd. 89 (1968) H.3 – pag. 59-62.

Design of Optical Pickup Actuator Using Multi-Pole Magnet for High Performance

In-Ho Choi*, Sam-Nyol Hong* Gina Kim*, and Jin-Yong Kim*

* LG Electronics Digital Media Research Lab. DCT Group

16 WooMyun-Dong, SeoCho-Ku, Seoul

137-724, Korea

E-mail : ciho@lge.com

Abstract --- **To improve the driving sensitivity of an optical pickup actuator for high density and high speed drive, we present a new actuator design using multi-pole magnet by Nd-Fe-B sintered magnet. We expect this actuator to use in 3-axis actuator for tilt compensation as well as conventional 2-axis actuator. The electromagnetic field analysis applying 3-D FEM was performed and several samples were actually tested. From comparing simulated data with experimental results, we verified the accuracy of the simulation and the superiority of the presented method.**

INTRODUCTION

An optical pickup actuator is an objective lens moving mechanism that provides a means to accurately follow the disk displacement, which is commonly used in digital audio/video device such as CDRW, COMBO and DVD. Recently, large-capacity high-density disk and high-speed drive have become popular. Since drive speed and physical density of the optical disc have become higher, better performance and higher servo bandwidth are required of the actuator. The optical pickup actuator requires higher driving sensitivity in both the low and high frequency domain in order to cope with higher servo gain. [1] So far, high driving sensitivity of the actuator has been achieved by optimal design for conventional 2-axis actuator applying one-pole magnet as shown in Fig. 1.[2] However, it did not come up to our more expectations because this method has its own design limitation. Now we need a new idea to improve the driving sensitivity dramatically. [4]

In this paper, we propose novel actuator structures using multi-pole magnet which enables 2 or 3-axis driving including radial tilting as well as focusing and tracking motion as shown Fig 2. [3] In order to calculate the actuator's force, the electromagnetic field analysis applying the three dimension finite elements method and the calculation of the driving sensitivity using programs specially written by us is performed. Also the parametric analysis method that can be changed design variable automatically is used for optimal design of actuator. From this method, we can maximize the actuator's driving force and minimize the non-linearity. Finally, Several samples are actually made and tested for evaluation. Simulated data and experimental results are discussed to prove the validity of the simulation method and superiority of the proposed actuator.

ACTUATOR MODELING
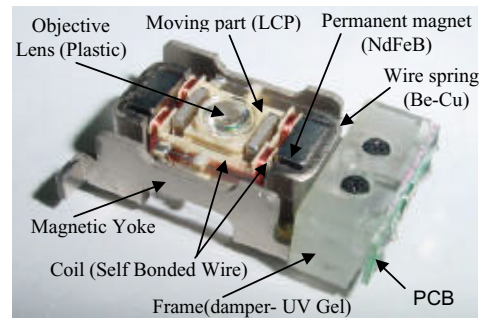
Fig. 1. Conventional 2-Axis Optical Pickup Actuator

The pickup actuators are controlled by Lorentz's force, which is produced between magnet and current carrying coils. There are two basic motions of the pickup actuator. One is a focusing motion having lens move vertically and the other is a tracking motion having lens move horizontally.

In optical pickup actuator, one of the most important performances is the driving sensitivity. The driving sensitivity of the actuator can be easily obtained in a specific frequency domain by the transfer functions of simplified actuator model that is formulated by the classical mechanical motion equation and electric circuit equation as follows.

In the low frequency domain below the first resonance frequency $f_\circ$, so-called DC sensitivity can be calculated from the following equation:

$$S_{VL} = G_A(0) = \frac{B\ell n}{rk} \qquad [\text{mm/V}] \qquad (1)$$

In the frequency domain higher than $f_\circ$, so-called AC sensitivity can be calculated from the following equation:

$$S_{VH} = \frac{B\ell n}{rk} \cdot \left[\frac{f_\circ}{f}\right]^2 \qquad [\mu\text{m/V}] \qquad (2)$$

where r and k are the resistance of the moving coil and the stiffness of the spring, respectively, and *fo* is the first resonance frequency. In addition, n, ℓ and B are available coil turns, length and flux density.

NEW ACTUATOR AND SIMULATION

As a angle on the cost and performance, proposed multi-pole magnetic circuits could be composed of only 2-pole magnet, 2-pole magnet with magnetic yoke, 4-piece 4-pole magnet and 4-pole magnets which are attached to the back yoke as shown in Fig. 2, respectively.

	Focusing	Tracking
DC Sensitivity	0.98 [mm/V]	1.41 [mm/V]
AC Sensitivity	58.7 [μm/V]	84.0 [μm/V]

a) Only 2-pole magnet

	Focusing	Tracking
DC Sensitivity	1.12 [mm/V]	1.39 [mm/V]
AC Sensitivity	66.8 [μm/V]	83.3 [μm/V]

b) 2-pole magnet + Magnetic yoke

	Focusing	Tracking
DC Sensitivity	1.91 [mm/V]	1.43 [mm/V]
AC Sensitivity	114.1 [μm/V]	85.6 [μm/V]

c) 4-piece 4-pole magnet

	Focusing	Tracking
DC Sensitivity	1.77 [mm/V]	1.50 [mm/V]
AC Sensitivity	106.0 [μm/V]	89.4 [μm/V]

d) 4-pole magnet

* DC Sensitivity [at 5 Hz], AC Sensitivity [at 200Hz]
1'st Resonance Frequency : Focus 55 Hz / Track 55 Hz

Fig. 2 Flux-Density Distribution and Driving Sensitivity Calculation

Also figure 2 shows analysis results of the magnetic field that generate *Lorentz* force and calculation results of the driving sensitivity.

Figure 3 shows the magnetic circuit structure for 3-axis actuator, which can drive tilt direction for compensating disc tilt variation as well as focus and track directions.

	Tilting
1'st Resonance Frequency.	120 [Hz]
DC Sensitivity(at 5Hz)	2.12 [degree/V]
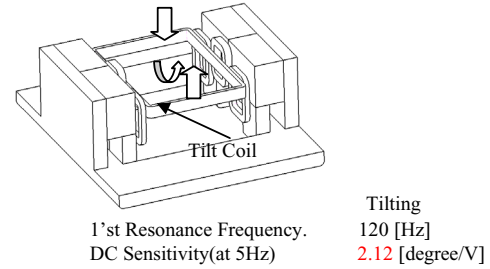
Fig. 3 Magnetic Circuit Structure of 3-Axis Actuator

TEST RESULTS AND CONCLUSION

In this paper, we have newly proposed optical pickup actuator using multi-pole magnet and precise analysis process to improve the driving sensitivity. We can prove the superiority of the proposed model and the accuracy of the simulation, from comparison between the calculation and experimental results as Fig.2 and Table I.

We expect these useful results to be used for similar technical field as well as optical storage field

TABLE I EXPERIMENTAL RESULTS

DC[mm/V]: at the 5Hz, AC[μm/V] :at the 200Hz		FOCUSING		TRACKING	
		DC	AC	DC	AC
One-pole Magnet	Sensitivity	1.26	65.8	1.08	63.2
	Resistance [Ω]	6.00		5.50	
	1'st Frequency [Hz]	52		53	
Multi-pole Magnet	Sensitivity a)	0.92	54.6	1.42	81.3
	b)	1.05	65.2	1.36	78.8
	c)	1.85	108.1	1.38	79.1
	d)	1.68	94.5	1.45	85.2
	Tilt 1'st Frequency[Hz] / DC Sensitivity[degree/v]	125/1.98 (tilt)		-	
	Resistance [Ω]	4.50/5.25(tilt)		4.80	
	1'st Frequency [Hz]	56		57	

REFERENCES

[1] In-Ho Choi,Won-Eull Chung,Young-Joong Kim,In-Seop Eom,Ho-Man Park and Jin-Yong Kim, " Compact Disk/Digital Video Disk (CD/DVD)-Compatible Optical Pickup Actuator for High Density and High Speed Optical Pickup Actuator", Jpn.J.Appl.Phys.Vol.37 Part 1,No.4B, pp.2189-2196, April 1998
[2] Tae-Kyung CHUNG, Gina KIM, In-Ho CHOI, and Sam-Nyul HONG, "Analysis of Optical Pickup Actuator by 3D-EMCN method", IEEE CEFC 2002, P10-17, Jun 2002.
[3] Y.Motegi,M.Nagasato,Y.Ishibashi,H.Someya and N.Kikuiri, "Development of Tilt Servo System using 4-Axis Lens Actuator for Disc Tilt Compensation", ISOM/ODS 99, SPIE Vol 3864, July 1999
[4] In-Ho Choi, Seong-Pyo Hong,Won-Eull Chung, Young-Joong Kim,Man-Hyoung Lee and Jin-Yong Kim, " Concentrated Anisotropic Magnetization for High Sensitivity of Optical Pickup Actuator", IEEE Transactions on Magnetics, Vol. 35, No.3, pp.1861~1864, MAY 1999.

Characteristic Analysis and Modification of PM-type Magnetic Circuit Breaker

K. I. Woo**, B. I. Kwon*, H. D. Jun*
*Graduate school of Hanyang University, Ansan 425-791
**Pukyong National University, Busan 608-739
E-mail: cogging@pknu.ac.kr

Abstract —**This paper presents the operating characteristic analysis of PM-type magnetic circuit breaker with the 2D finite element magnetic field solution including non-linearity of the material and an eddy current. Change of dynamic characteristic by the eddy current of the actuator is quantified from the finite element analysis. A new modified model to decrease the eddy current is proposed. The characterisitcs of the two models are compared.**

INTRODUCTION

The purpose of using the circuit breaker is to protect an electric power system in an accident. The traditional circuit breaker is composed of springs, gears, etc. But, it has a defect that the periodic repair and the exchange of parts are needed after a great number of actions. The PM-type magnetic circuit breaker overcomes its shortcomings and has high reliability of the performance, so the advantages drew great attention recently[1]. Magnetic saturation and eddy current induced in the core body of the linear actuator make the design methodology complicated[2]-[3]. In particular, it is very important to consider the eddy current in the process of linear actuator design, because eddy current led to a time delay in the flux build-up and the force production. And, there is a motion delay by millisecond.

This paper describes the operating characteristics of the PM-type magnetic circuit breaker considering the eddy current caused in the non-laminated plunger, proposes a new modified model. The electromagnetic field, the electric circuit, and the mechanical motion are combined for the analysis. Change of electric and mechanical characteristic with the variation of the conductivity of the plunger is investigated. Also a new laminated plunger model is proposed to decrease the eddy current effect. The characteristics of the non-laminated and laminated model are compared.

ANALYSIS MODEL

The linear actuators can be classified into the moving coil type, the moving magnet type, and the moving core type. The analysis model is the moving core type with the permanent magnet, and shown in Fig. 1. The stator is laminated, but the plunger not due to mechanical effect. A motion of the plunger is controlled by alternate switching of the excitation coils, as shown in Fig. 1. If the current flows across the coil A, the plunger is attracted upwards by the excited magnetic flux. When the coils opened, the plunger is held at its moved

position by the permanent magnet. Table I shows the designed specification of the PM-type magnetic circuit breaker.
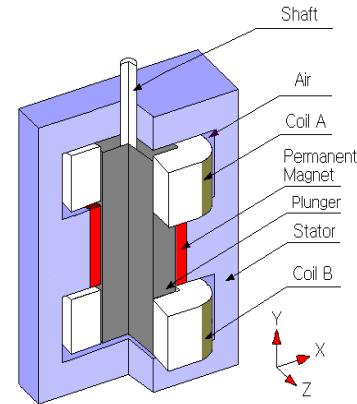
Fig. 1 The designed model of the PM-type magnetic circuit breaker

TABLE I. SPECIFICATION OF DESIGNED MODEL

Input voltage	200 [V]
Residual Flux density of PM	1.005 [T]
Width of plunger	232 [mm]
Height of plunger	77 [mm]
Moving distance of plunger	20 [mm]
Force in the plunger by the PM	3000 [N]

CHARACTERISTICS ANALYSIS

Fig. 2(a) shows the flux plot of the PM-type magnetic circuit breaker when the coils are not excited. The plunger is kept by the permanent magnet. After the coil A is excited with DC 200V, the flux plot at 0.05 [sec] is shown in the Fig. 2(b). At this time, the magnetic field changes with the current, so does the force exerted on the plunger.

A simulation is performed when the conductivities of the plunger are 0, 10^5, 10^6 and 10^7 [mho/m]. Fig. 3 shows the distribution of flux density in the plunger(the region B of Fig. 2(b)) at 0.05 [sec]. When the conductivity of the plunger is not considered, the flux density is almost constant at the region. But the flux of the plunger is concentrated on the surface of the plunger by the skin effect.
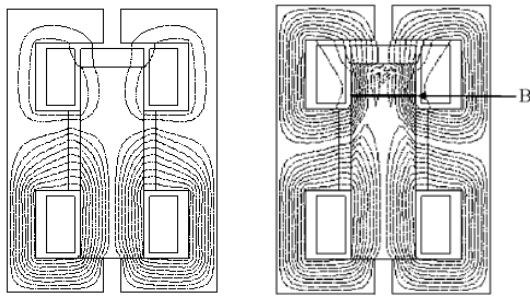
(a) When the coils are not excited   (b) when the coil A is excited only
Fig. 2 The flux plot of the circuit breaker
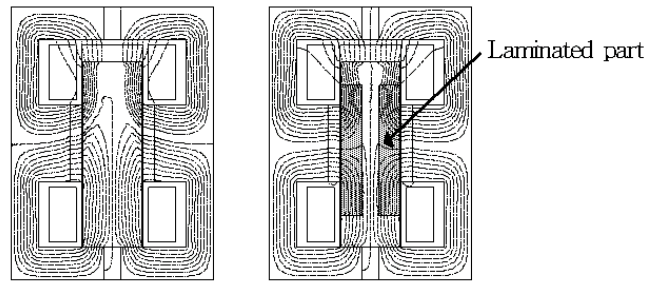
(a) Non-laminated model   (b) Laminated model
Fig. 4 The flux plots at 0.06[sec]
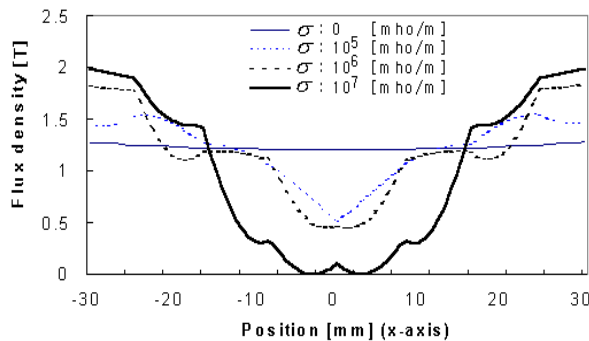
Fig. 3 The flux density of the plunger (σ : conductivity)
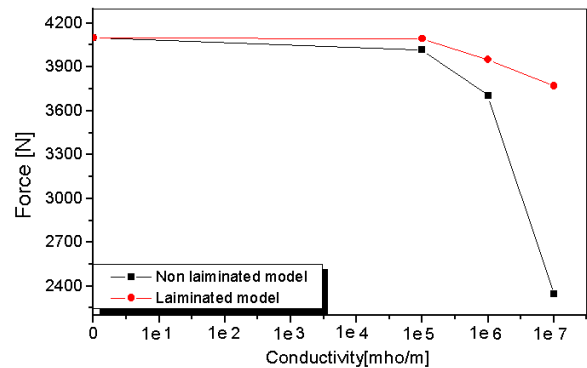
Fig. 5 Force characteristic comparison with variation of conductivity

PROPOSED MODEL

It is general that the plunger of circuit breaker is made of the non-laminated single construction, because the transformation of the plunger occurs in a big mechanical impact. In this paper, a new modified model which has a lamination part in the plunger is proposed to reduce the eddy current effect.

Fig. 4 show the flux plots of the non-laminated model and proposed laminated model at 0.06[sec]. It is shown that the penetration depth of the flux of the proposed laminated model is larger than that of the non-laminated model around the coil A. Because the eddy current effect is reduced by the laminated part.

Fig. 5 shows the force characteristic comparison of the two models. We know that the differences of the characteristics are large when the conductivity of the plunger is 1e7[mho/m] from this figure. It is shown that the force of the laminated model is larger than that of the non-laminated model about 1745[N] when the conductivity is 1e7[mho/m].

CONCLUSION

This paper describes the operating characteristics of the PM-type magnetic circuit breaker considering the eddy current caused in the non-laminated plunger, because it has a mechanical impact. Change of electric and mechanical characteristic with the variation of the conductivity of the plunger is investigated. Also, to minimize the eddy current effect in the plunger, a new modified model has a lamination part in the plunger is proposed and the characteristic is analyzed of it by the finite element method. From the characteristic comparison of the two models, it is shown that the characteristic of the laminated model is better than that of the non-laminated model.

REFERENCES

[1] Lin Xin, Gao Huijun, "The Calculation and Analysis the Coupled Problem in the Permanent Magnetic Actuator Vacuum circuit Breaker", *CEFC –Magnetics, pp. 298,* 2000.
[2] Joachim Fetzer, Stefan Kurz, "Analysis of an actuator with eddy current and iron saturation between a FEM and a BEM-FEM coupling approach", *IEEE Transaction on Magnetics*, pp. 270-273, 1999.
[3] Xiong, Guangyu, Yamada, "Dynamic Analysis of a Cylindrical Moving-core Linear Oscillator Actuator", *LDIA'95 Nagasaki, JAPAN*, pp. 405-408, 1999.

Local Electric Field Analysis for Evaluation of Charge Transfer System Using Sequential Sub-window Technique

Joon-Ho Lee[1], Young-Ki Chung[2], Il-Han Park[1]

[1] School of Information and Communication Eng., Sungkyunkwan Univ., Suwon 440-746, Korea

[2] UI-JAE Electrical Research Institute, Seoul 150-867, Korea

e-mail: jhlee@nature.skku.ac.kr

Abstract — **This paper presents an accurate analyis of electric field for Charge Transfer System which was recently developed to reduce the likelihood of lightning stroke to premise. Since a CTS has many sharp metal points, its geometric modeling is very difficult. To calculate accurate electric field of the CTS, squuential sub-window technique which analyzes local electric field in a small region compared with total system is used. The electric fields of brush tip and top of the CTS which play an import role in lightning mechanism are calculated. The Flanklin rod was also analyzed and compared with the CTS to evaluate the effect of brush of the CTS.**

INTRODUCTION

Lightning rod has been used to protect some premises from direct lightning stroke which can cause fire, explosion, physical damage. In recent years, due to the explosive progress in computer and telecommunication technology, the secondary effect of the lightning stroke became major concern in many cases. Electromagnetic field generated by lightning current near by a conductor connecting the lightning rod to the grounding system may cause malfunction or disruption of sensitive electronic equipment. Therefore, lightning protection of the premises becomes more and more important to provide a specified level of safety. The prevention of the direct lightning strokes into the premise is the only way to eliminate the damages from consequences of the secondary effect.

Charge transfer system (CTS) was recently developed to reduce the likelihood of lightning directly to the premise. Its idea of preventing the lightning stroke is based on the point discharge phenomenon [1]. When sharp-edged object such as pointed electrode is exposed to the strong electric field, it starts to emit electric current into the surrounding air. This current is a result of ionization process in the air surrounding the sharpened points and it weakens the electric field. However, the effectiveness of the CTS has not yet been confirmed [2]. Therefore, some works to evaluate the CTS are needed. First of all, an accurate calculation of local electric field that causes the ionization process is required. But, its accurate numerical analysis is very difficult since the CTS has many sharp metal points whose geometry is too complex to model. In this paper, to resolve this problem a sub-window technique is employed. This technique is good for analyzing a model whose concerned area is too small compared with the total system.

CHARGE TRANSFER SYSTEM

There are several kinds of CTS according to ionizer types: umbrella type, Ball type, Barbed wire type, doughnut type, and cylindrical type [2]. All of these CTS have many spiral brushes along the axis. Since this geometry is real 3 dimensional, its exact modeling is almost impossible and practically not useful. In this paper, the brushes are simplified into many narrow disks and modeled by an axisymmetric problem. For the analysis of the CTS, an accurate calculation of electric field is required since it determines where the initial ionization process will start.

The finite element method (FEM) is most popularly being used for electric field calculation. However, the FE analysis of the CTS has a critical problem in geometrical modeling for the brush of the CTS. The thickness of brush is about 70 [μm] whereas its radius is 25[mm]. It means that the concerned area is too small to analyze the system accurately. In this paper, a sequential sub-window technique using FEM is employed for calculation of local electric field of the CTS.

ANALYSIS OF ELECTRIC FIELD OF CTS AND DISCUSSION

We apply the sub-windows technique method to a cylindrical CTS as shown in Fig. 1(a). To calculate the electric fields due to the lightning, the thunderstorm cloud is represented by a simple electrode on the top line where 1[V] is applied as shown in Fig. 1(b). Since the top brush has a high strength of electric field, this region is concerned. In the first geometrical modeling, the brushes are divided into several groups and simplified as shown in Fig. 1(b).

(a) Cylindrical CTS   (b) Finite element model
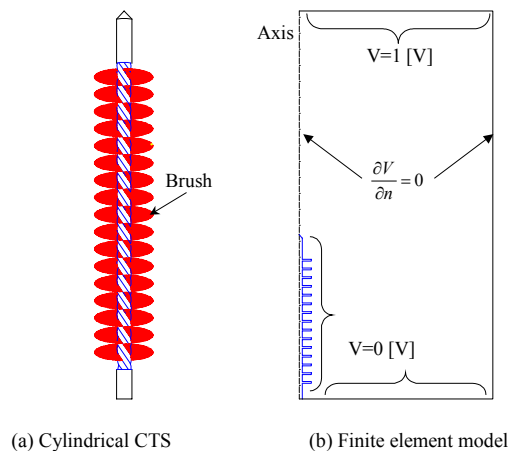
Fig. 1. Model description
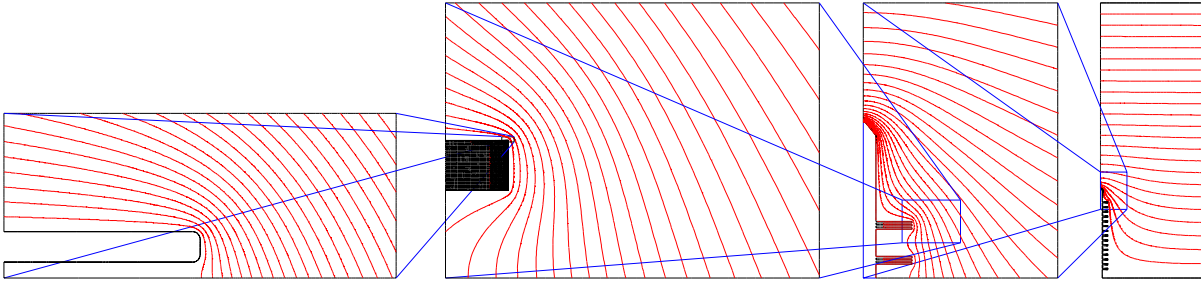
Fig. 2. Closing up by sub-windows

In the first step, the original model is analyzed with a relatively rough mesh. Its numerical result is used for a boundary condition of the second step where the top of CTS and higher brushes region are closed up by sub-window. Next, the higher brush group is closed up again and exactly modeled with 26 brushes. Finally, the top brush is closed up once more and analyzed. So we obtained electric field distribution nearby the top of brush. This procedure is shown in Fig. 2. The electric field at the right top brush is 88 [V/m], which is the maximum value over the entire system. To calculate the electric field at the top of CTS, the sub-window technique is also applied and its results are shown in Fig. 3. The maximum electric field at the top of CTS is 67 [V/m], which is less than that at the brush. It means that the field near the brush can cause the very first ionization.

On the other hand, to evaluate the effect of brushes, the CTS without brushes (Flanklin rod) is also analyzed. The calculated maximum electric field at the top of the rod is 75 [V/m], which is greater than that of the CTS. From this result, we can infer that the air nearby the brushes is ionized before the lightning current is conducted at the top of CTS.

Figure 4 shows the induced charge density along the brush surfaces at the second sub-window in the Fig 2. From this result we can see that the electric field is concentrated at the top part in the brushes and there is almost no field in the region between the brushes.
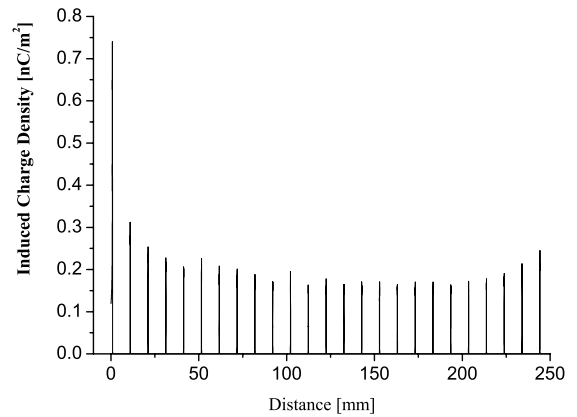
Fig. 4. Induced Charge at brushes of the CTS

CONCLUSIONS

The electric field of brush tip and top of the CTS that play an import role in lightning mechanism was obtained by sequential sub-windows technique. The Flanklin rod was also analyzed and compared with the CTS to evaluate the effect of brushes. This method can be used for evaluating local electric field of all CTS.

REFERENCES

[1] Donald W. Zipse, "Lightning Protection System: Advantage and Disadvantages", *IEEE Transactions on Industry Application*, vol. 30, no. 5, pp. 13511361, September/October 1994.
[2] Abdul M. Mousa, "The Applicability of Lightning Elimination Devices to Substations and Power Lines", *IEEE Transactions on Power Delivery*, vol. 13, no. 4, pp. 1120-1127, October 1998.

(a) Sub-window for the Top of CTS   (b) Original model

Fig. 3. Field intensity of CTS

Electrostatic Comb Accelerometer – Field and Equivalent Circuit Modeling

Sławomir Wiak, Krzysztof Smółka

Institute of Electrical Machines and Transformers
Technical University of Lodz,
ul. Stefanowskiego 18/22, 90-924 Lodz, Poland
e-mail: wiakslaw@p.lodz.pl

Abstract –This paper describes the field and circuit modelling of 2D/3D structure of surface micromachined (MEMS) accelerometers. This comb structure has been able to move only within the plane (two-axes movement). The main goal of investigation is to exploit the field method to extract equivalent capacitance characteristics to be treated as the background for equivalent circuit analysis.

INTRODUCTION

Actually, the task of the designer is complicated by the evidence that different energy domains, in general being mutually coupled, are involved when modeling micro-electro-mechanical devices (MEMD), in the frame of more general micro-electro-mechanical systems (MEMS). Moreover, the designer has to take into account the constraints imposed by the process technology, that limit the feasibility of innovative devices.

MicroElectromechanical Systems (MEMS) technology has generated a significant interest of academic, research and business sectors. The above is caused by very promising technology market and as well cost reduction connected with microscale devices fabricated by use of silicon technology. Due to rapid grow of this market, year after year, the market is just segmented. This is also true in the reference to accelerometer market. Efficiency of the device development is also due to design flexibility, developing of simulation tools and CAD systems, integration of mircodevices and microelectronics, etc. In general, multi-layer surface mircoactuator fabrication process is enough flexible to produce advanced device structures. MEMS structure development requires reliable fabrication processes and flexible CAD/(analysis and optimal design) tools. We could treat mask layout tools as complementary to CAD/(analysis and optimal design) tools. The device geometry is, in general, defined in the mask layout tool, then transferred to integrated circuit layout package, while specific surface micromachining process ahs been employed. Some specific codes based on Finite Element Method could be successfully applied to MEMS designing while microdomain physics are also taken into account. Such a sophisticated software could allow creating 3D structure of the device, full model analysis (structural mechanics, electrostatics, fluid flow, vibration, etc.). The strongest impulse to the development of such advanced tools should come mainly from industrial companies; in fact, virtual prototyping of optimal devices would determine a twofold benefit: decreasing the total time lasting from the device ideation to its implementation as a marketable product; reducing the number of fabrication experiments on real prototypes; identifying the device of minimum cost, given the performance or, conversely, the device of maximum performance, given the cost; increasing the global quality of the industrial product.

ACCELEROMETER DESIGN – PLANAR STRUCTURE

Accelerometers are important devices in the range of variety applications such as air bag actuation (by Analog and Sandia), microrobots, etc (see Fig. 1). The accelerometers available on the market are capable of measuring high values of accelerations. The electrostatic comb accelerometer is fabricated by use of different techniques like CDV, RIE, Wet etching, etc. The relationship between input voltage and output displacement has been widely analysed experimentally and theoretically in the literature [1]. The accelerometer consists of a moving comb teeth, suspended by spring beams on both sides, and fixed teeth. The suspension is designed to be compliant in the x direction of motion and to be stiff in the orthogonal direction (y) to keep the comb fingers aligned. The applied voltages on the force unit causes a net electrostatic force to pull the movable part in the desired direction.
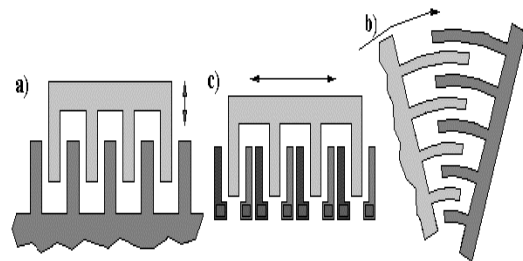
Fig. 1. Selected comb accelerometer structures

EQUIVALENT CIRCUIT MODEL

Energy stored in the device is defined as follows:

$$W = \frac{1}{2}CU^2 \qquad (1)$$

A simplified scheme of a capacitive microaccelerometer is shown in Fig. 2. For the capacitive sensing approach, the displacement is detected by measuring the capacitance change (see formula 2), expressed as a function of displacement of moving comb teeth against fixed comb teeth (see Fig.3).

$$C_p = \varepsilon \frac{a(z-h+y)}{p+x} \qquad C_m = \varepsilon \frac{a(z-h+y)}{m-x} \qquad C_g = \varepsilon \frac{a \cdot d}{h+y} \qquad (2)$$
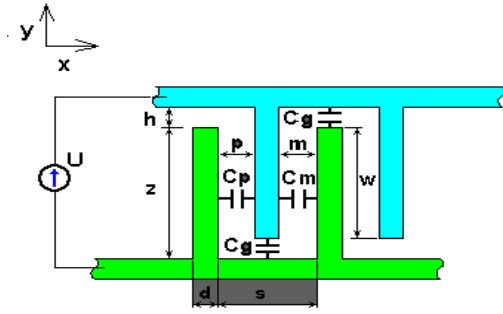
Fig. 2. Analyzed comb accelerometer structure with main dimensions

Total accelerometer capacitance, defined as the symmetrical structure (both symmetrical and unsymmetrical structures are analysed), is the sum of three following terms: Cp, Cm i Cg:

$$Cs = (n-2)C_p + (n-1)C_m + (2n-3)C_g \qquad (3)$$
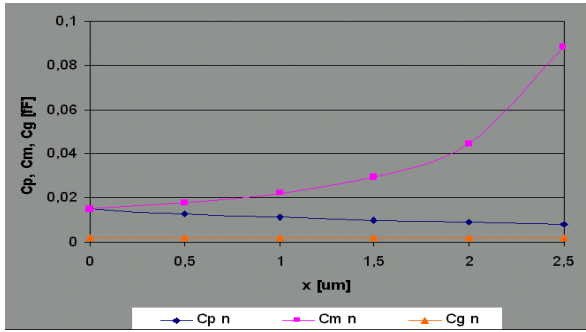
Fig. 3. Capacitance curves versus x displacement (d=2μm, s=8μm, z=1.5μm, m=p=(s-d)/2, a=5μm).

Sensitivity of the circuit model along X and Y we could express as follows:

$$s_y = \frac{\partial C}{\partial y} \qquad\qquad s_x = \frac{\partial C}{\partial x} \qquad (4)$$

Basing on the stored energy evaluation (see expression 1) the acting force in Y and X direction are expressed by the following formulas:

$$F_y = -\frac{\partial W}{\partial y} = \frac{1}{2}U^2 \frac{\partial C}{\partial y} \qquad (5)$$

and finally (s-symmetrical structure):

$$Fy,s = \frac{1}{2}aU^2\left((n-2)\left(\frac{1}{p+x}\right) + (n-1)\left(\frac{1}{m-x}\right) + 2(n-3)\frac{d}{(h+y)^2} \right) \quad (6)$$

Acting force along X axis is expressed as follows:

$$Fx = -\frac{\partial W}{\partial x} = \frac{1}{2}U^2 \frac{\partial C}{\partial x} \qquad (7)$$

and finally (s-symmetrical structure):

$$Fx,s = \frac{1}{2}a(z-h+y)U^2\left((n-1)\left(\frac{1}{(m-x)^2}\right) - (n-2)\left(\frac{1}{(p+x)^2}\right) \right) \qquad (8)$$

COMPARATIVE STUDY BY FIELD MODEL

Since most of the analytical solutions (models) neglect fringing fields, they cannot predict accurately the dependence of the drive force on the moving comb teeth. In order to better determine this dependence, numerical three-dimensional finite-element method (FEM) for electric field simulations in are used. A static FEM computation of electric potential, based on tetrahedron elements was carried out (see Fig. 4). Fixed potential boundary conditions were assumed. The stored electrical co-energy was computed as a function of the movable part position. In particular, detailed field analyses can be developed for investigating local effects in the steady state operation of the device.
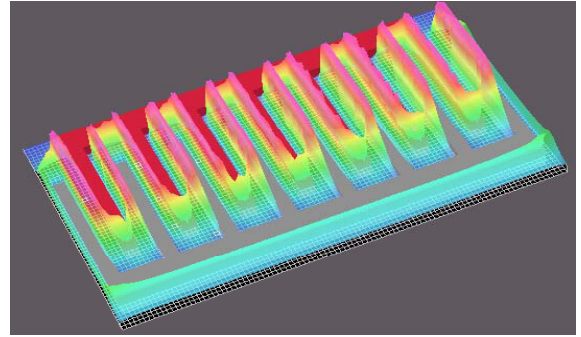
Fig. 4. Mesh and Emod dsitrbution of 3-D comb accelerometer structure

The comparative study performed for equivalent circuit method and field method allows making some improvements in final equivalent capacitance formulas. Therefore, the discrepancy between both values obtained by means field and circuit methods are negligibly small (see Fig. 5). **These improved analytical formulas are in the next step of accelerometer design introduced to optimal design procedure** *(to be presented in full version of the paper).*
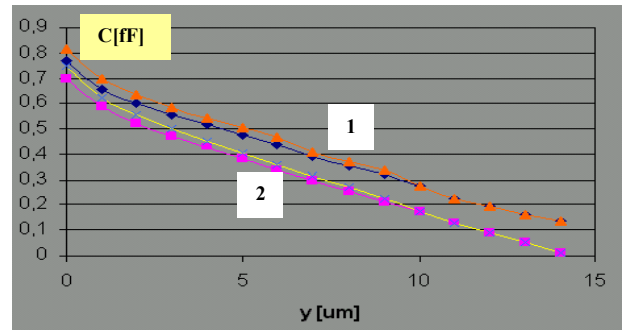
Fig. 5. Capacitance curves versus y displacement (d=2μm, s=8μm, z=1.5μm, m=p=(s-d)/2, a=5μm) (♦,■ -field method, ✕,▲- circuit method; 1-symmetrical structure, 2-unsymmetrical structure)

REFERENCES

1. C. W. Tang. "Electrostatic Comb Drive Levitation and Control Metod", *Jurnal of Micromechanical Systems, 1992, vol.1, no. 4, December* .

2. Julian W Gardner, Vijay K. Varadan, and O. Osama Awadelkarim, *"Microsensor MEMS and Smart Devices", J. Wiley, UK, 2001.*

Optimization of Permanent Magnet Shape for Minimum Cogging Torque Using a Genetic Algorithm

M. Łukaniszyn, M. Jagieła, R. Wróbel

Technical University of Opole,
Department of Electrical Engineering and Automatic Control
PL 45-036, ul. Luboszycka 7, Opole, Poland
E-mail: {luk, mjagiela, rwrobel}@po.opole.pl

Abstract – **The paper presents an approach to minimization of the cogging torque in PM machines using surface-mounted magnets with discrete skew angle. For the purpose of determining the proper arrangement of PM-pole slices, an optimization procedure based on a Genetic Algorithm (GA) is applied. The torque and objective function are determined from a simplified model for torque calculation. The results are validated against the 3D finite element model as well as experimental data obtained from a prototype machine. A new outer-rotor BLDC motor for an electric fan is considered as a sample model.**

INTRODUCTION

Some applications like servodrives or hdd micromotors do not tolerate cogging torque of any level [1, 3 ,4]. Among various approaches, skewing is known to be the most effective method for reducing of the cogging torque in PM machines [1]. There are two alternative solutions, in which skewing of either the stator sheet pack (laminated core) or the rotor permanent magnets is applied. The latter method is a cost-effective solution recommended for the machines with short stack length [3]. This paper demonstrates how the cogging torque can be reduced when replacing continuous skew angle of permanent magnets with discrete one along the machine length (see Fig. 1). Such a construction of the magnetic circuit leads to a great reduction of the cogging torque and its optimization procedure is less complicated than that for the magnets with continuous skew angle. For optimization of skew angle of permanent magnets a Genetic Algorithm is applied.
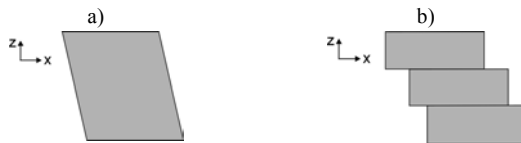
Fig. 1. Two alternative solutions for skewing of the magnets: a) continuous, b) discrete

MODEL FOR TORQUE CALCULATION

The skewed magnets need to be analyzed using 3D field models [3]. In this paper the simplified model for torque calculation, only partially supported by the three-dimensional one, is presented. To describe this model, introduce the symbols shown in Fig. 2.

permanent magnet
yoke
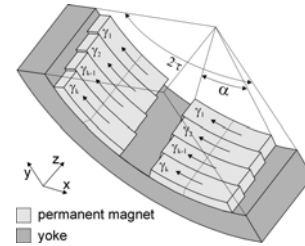
Fig. 2. Symbols

The permanent magnet is divided into k identical slices. Define a vector Γ including angular displacements of consecutive slices: $\Gamma=(\gamma_1, \gamma_2,\ldots, \gamma_{k-1},\gamma_k)$. Due to cross linkage fluxes, the torque density is not constant along the motor axis. It can be assumed that the n-th PM-slice, where $n = 1\ldots k$, generates the cogging torque T_n which can be approximated as:

$$T_n(\Theta) = \frac{f_n}{f} \cdot T(\Theta) \ , \tag{1}$$

where:

f_n – area under the n-th segment of the torque density curve along z direction,

f – total area under the torque density curve along z direction,

f_n/f – weighting coefficient (see Fig. 3),

$T(\Theta)$– angular variation of cogging torque (see Fig. 4).

The above quantities are determined from the standard 3D finite element field model using Maxwell stress tensor method. The overall cogging torque is composed of the torques produced by each pole slice

$$T_{\text{simplified}}(\Theta) = \sum_{n=1}^{k} T_n(\Theta + \gamma_n) \ . \tag{2}$$

Although the cogging torque values obtained from this model are not very accurate, they are useful to indicate a direction of change in the cogging torque while rearranging pole shape in the optimization process.
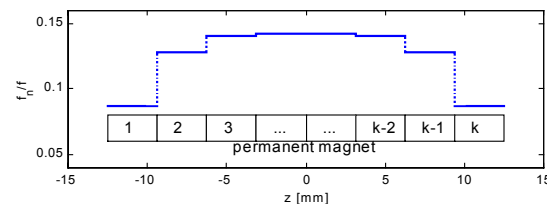
Fig. 3. Variation of f_n/f along z direction for sliced PM poles
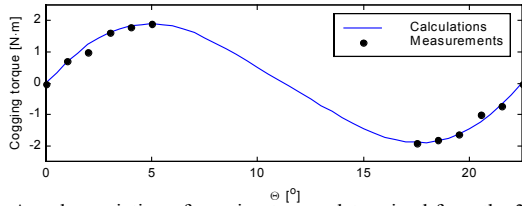
Fig. 4. Angular variation of cogging torque determined from the 3D FEM model

GENETIC OPTIMIZATION ALGORITHM

Genetic Algorithms imitate the natural selection and the genetics of living organisms while searching the global extremum in $\mathbf{R}^n$. A typical GA consists of three operators, i.e. reproduction, crossover and mutation to provide the transfer of best features to the successive generations and to overcome a possibility of falling into a local minimum [1]. The objective function is defined as the absolute average value of the cogging torque for its single period. Decision variables are the consecutive dislocations of PM-pole slices expressed by vector $\mathbf{\Gamma}$, which is constrained with $\|\mathbf{\Gamma}\| \leq 0.5(\tau - \alpha)$.

RESULTS OF OPTIMIZATION

To demonstrate the results of the PM optimization using the Genetic Algorithm, a new outer-rotor BLDC motor for an electric fan is considered (see Fig. 5). The machine specifications are as follows: two-phase, four pole pairs, 150 W, 1,500 rpm. The outer diameter is 112mm and the total length is 30mm. Large armature saliency and high-energy permanent magnets contribute to generation of considerable cogging torque, which produces vibrations transmitted to whole construction of the drive. The reduction of the cogging torque is thus of great importance in this type of motor.
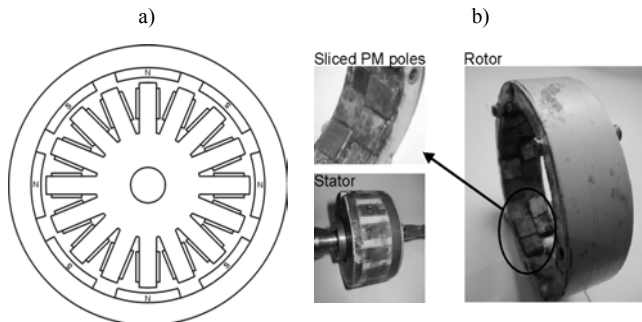
Fig. 5 Cross-section of two-phase BLDC motor a), and its physical model b)

The optimization procedure was performed for the radially-magnetized poles, composed of two, four and eight PM-slices per single pole and for two permanent magnet widths. Fig. 6 shows the optimized magnets shapes for the cases considered. Fig. 7 compares cogging torque variations for different pole shapes. Table 1 summarizes values of torque for the considered magnets shapes.
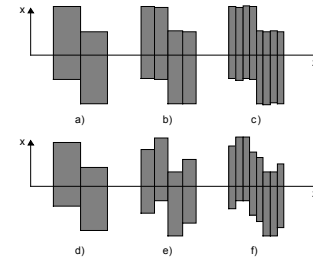
Fig. 6. Optimized magnets shapes for two, four and eight slices: a), b), c)– α/τ=33/45, d), e), f)– α/τ=29/45 (basic shape – all slices in aligned position)
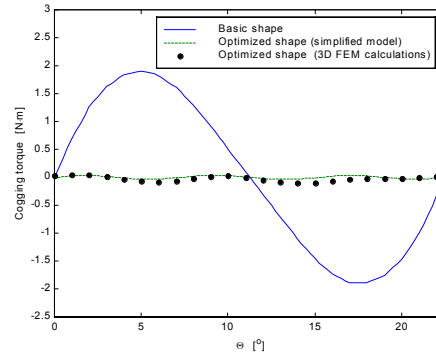
Fig. 7. Angular variations of cogging torque for two pole shapes, optimized shape ($\alpha/\tau = 29/45$, $k = 4$ – see Fig. 6e)

TABLE I. Torque and force values determined from 3D field model for considered magnets shapes (3D FE calculations)

PM type	Maximum Cogging Torque [N·m]			Average Torque [N·m] (at rated current I=20 A)		
Basic shape	α/τ=33/45		α/τ=29/45	α/τ=33/45		α/τ=29/45
	1.90		1.24	0.54		0.51
Optimized shape	k=2	k=4	k=8	k=2	k=4	k=8
α/τ=33/45	0.37	0.27	0.34	0.48	0.48	0.49
α/τ=29/45	0.22	0.05	0.05	0.45	0.48	0.47

CONCLUSIONS

The optimal magnet shape is a four-slice (k=4) with $\alpha/\tau = 29/45$. The reduction of the cogging torque using optimized magnets with respect to the basic version is 97%. The presented method for reduction of the cogging torque can be applied in almost all types of electrical machines with the surface-mounted magnets. The optimized magnet shape can be obtained using either sliced PM poles or a special shape of magnetizing device.

REFERENCES

[1] Jahns T.M., Soong W.L.: *Pulsating torque minimization techniques for permanent magnet AC motor drives - a review*, IEEE Trans. on Industrial Electronics, Vol.43, No.2, 1996, pp. 321-330.

[2] Han K.J., Cho D.H., Jung H.K.: *Optimal Core Shape Design for Cogging Torque Reduction of BLDC Motor Using Genetic Algorithm,* In proc. of Compumag'99, Sapporo, 1999, pp. 332-333.

[3] Jang G. H., Yoon J. W., Ro K. C., Park N. Y., Jang S M: *Performance of a brushless DC motor due to the axial geometry of the permanent magnet*, IEEE Trans. on Magnetics, Vol.33, No.5, 1997, pp. 4101-4103.

[4] Łukaniszyn M., Wróbel R., Jagieła M.: *Reduction of the Torque Ripple in a Brushless DC Torus Motor,* In proc. of ICEM'2002, Brugge, 2002, p. 304.

A Novel Topology Optimization using Density Method
Combined with Modified Evolution Strategy

Yoshifumi Okamoto and Norio Takahashi

Department of Electrical and Electronic Engineering, Okayama University
3-1-1 Tsushima, Okayama 700-8530, Japan
e-mail: [okamoto, norio]@eplab.elec.okayama-u.ac.jp

Abstract — The topology optimization using the density method, which determines the optimal shape by distributing the magnetic material in the design domain, is attractive for designers of magnetic devices because an initial conceptual design can be obtained. But there is no report of global optimal result. Moreover if the density method is combined with the conventional optimal design method, such as an evolution strategy (ES), it is difficult to get a sufficient solution, which can realize an actual magnetic circuit. In this paper, a novel topology optimization technique is proposed by introducing the modified ES, which efficiently utilize the sensitivity analysis to the density method. A global optimal topology of actual magnetic circuit can be obtained by using the method. The effectiveness of the proposed method is illustrated by applying it to the topology optimization of a C-core actuator.

I. INTRODUCTION

In the conventional optimization problem, such as size and shape optimization, the outline of magnetic circuit should be given beforehand. The topology optimization using the density method [1-3] does not need such an initial shape of magnetic circuit, and this method provides useful information for engineers in order to start the design. The topology optimization of magnetic circuit using the density method combined with the sensitivity analysis is reported in references [1-3], but the obtained results are limited to the local minimum, because some of the descent method using sensitivity analysis is utilized. If the global optimization method, such as ES, is used in the density method, it is not easy to get a sufficient solution, which can realize an actual magnetic circuit.

In this paper, ES is combined with the sensitivity analysis (modified ES) in order to get a continuum shape, and then the modified ES is applied to the density method to obtain the global optimal topology of magnetic device. The proposed method combined with the finite element method is applied to the topology optimization of a C-core actuator.

II. METHOD OF ANALYSIS

A. Density Method

In the density method, the material density ρ of each element is the design variable. The expression of relations of ρ and the permeability μ can be written as:

$$\mu = \mu_0 \left\{ 1 + \left(\mu_r - 1 \right) \rho^p \right\}, \quad \left(0 \le \rho \le 1 \right) \tag{1}$$

where μ_0 is the permeability in vacuum, μ_r is the relative permeability of magnetic material (iron), and p is the penalization factor ($= 2$). In order to decide clearly the shape of material, such as iron core, let μ be a discrete value. If ρ is larger than 0.5, μ is set to $\mu_r \mu_0$ (iron), otherwise, it is equal to μ_0 (air). In addition, the relative permeability μ_r of iron is set to 1000 in this analysis.

B. Modified Evolution Strategy

The design variable ρ is updated in the conventional ES by

$$\rho_{oi} = \rho_{pi} + \alpha_j \cdot R_i \tag{2}$$

where ρ_{oi} is an offspring individual, ρ_{pi} is a parent individual, α_j is a mutation step length in the j th generation, and R_i is the random number of [-1,1].

When the conventional ES is applied to the density method, it is difficult to get a continuum result. Then, the sensitivity analysis is combined with ES. This is called as a modified ES. The design variable is updated in the modified ES by

$$\boldsymbol{\rho}_o = \boldsymbol{\rho}_p + \alpha_j \cdot \frac{\boldsymbol{s}_j}{\max(|\,\boldsymbol{s}_j\,|)} \cdot R_i \tag{3}$$

where $\boldsymbol{\rho}_o$ is the offspring vector, and $\boldsymbol{\rho}_p$ is the parent vector. $\max(|s_j|)$ is an absolute value of the maximum component of vector s_j, and $\boldsymbol{s}_j$ is a sensitivity vector with respect to μ. $\boldsymbol{s}_j$ is given by

$$\boldsymbol{s}_j = \left(\frac{\partial W_{j-1}}{\partial \mu_1} \quad \frac{\partial W_{j-1}}{\partial \mu_2} \quad \cdots \quad \frac{\partial W_{j-1}}{\partial \mu_k} \quad \cdots \quad \frac{\partial W_{j-1}}{\partial \mu_n} \right)^T \tag{4}$$

where W_{j-1} is the objective function in the (j-1) th generation, n is the number of design variables. $\partial W_{j-1} / \partial \mu_k$ is approximated by the forward difference method as follows:

$$\frac{\partial W_{j-1}}{\partial \mu_k} = \frac{W_{j-1}(\mu_k + \Delta \mu) - W_{j-1}(\mu_k)}{\Delta \mu} \tag{5}$$

where $\Delta \mu$ is the perturbation in the k th permeability μ_k. In this optimization problem, the initial value of mutation step length α_j is chosen as equal to 1.0. If α_j becomes less than 0.3, the calculation is stopped. The number of searches per one generation is set to 600.

A. Analyzed Model and Objective Function

Fig.1 shows an analyzed model of C-core actuator. The 2-D finite element method using quadrilateral elements is used. The number of elements is 13650. The initial material is air in the design domain, where there are 2400 design variables (elements).

The design goal in this problem is to maximize the x-component of the electromagnetic force f_x of armature. The objective function W is given by the following equation:

$$W = 1/|f_x| \tag{6}$$

The nodal force method [4] is used for the calculation of f_x.
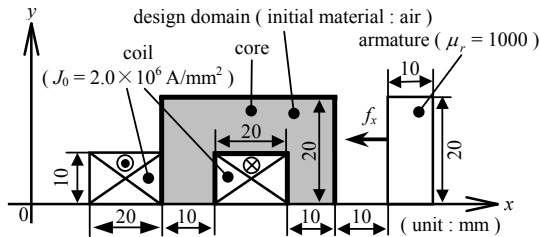
Fig. 1. Analyzed model.

B. Results and Discussion

The obtained shape by the conventional ES and the modified ES are shown in Fig. 2. The shape obtained by using the conventional ES is not continuum. This is because there are too many combinations of design variables, and the search of the global optimal solution is failed. On the contrary, the solution obtained by the modified ES can be realized as an actual magnetic circuit, and is considered as a global solution.

Fig. 3 shows the flux distributions. Since there are many voids in the core obtained by the conventional ES, the flux distribution is distorted. On the contrary, the flux distribution

(a) conventional ES
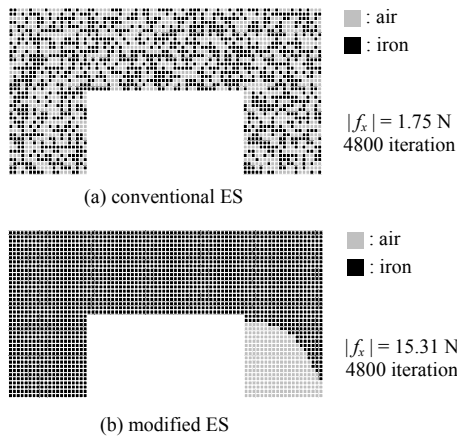
(b) modified ES

Fig. 2. Optimal shapes.

is smooth in the shape obtained by the modified ES. The force $|f_x|$ obtained by the modified ES is 15.31 N, and considerably larger than that obtained by the conventional ES ($|f_x|$ = 1.75 N). Fig. 4 shows the change of the objective function. The convergence in the case of using the modified ES is better than that of the conventional ES.

(a) conventional ES

(b) modified ES
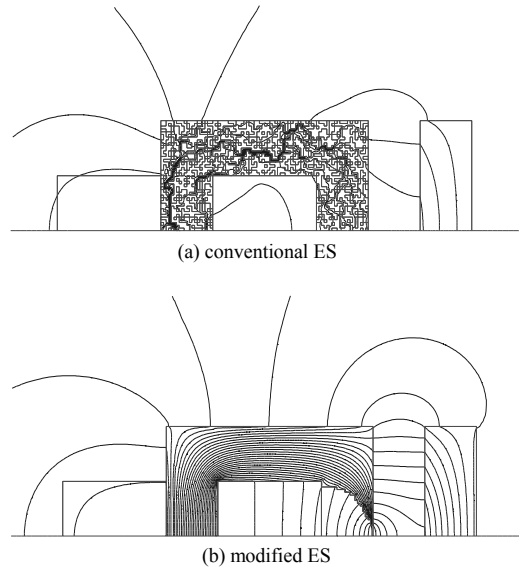
Fig. 3. Flux distributions.
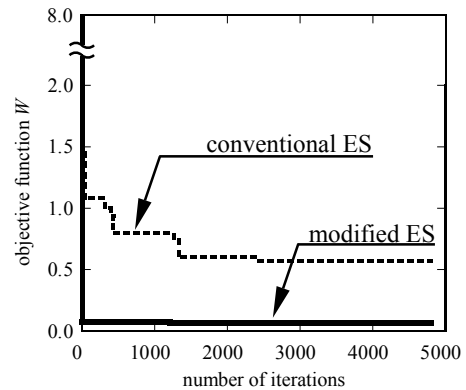
Fig. 4. Change of objective function.

REFERENCES

[1] D. N. Dyck and D. A. Lowther, "Automated design of magnetic devices by optimizing material distribution", *IEEE Trans. Magn.*, vol. 32, no. 3, pp. 1188-1193, May 1996.
[2] S. Wang and J. Kang, "Topology optimization of nonlinear magnetostatics", *IEEE Trans. Magn.*, vol. 38, no. 2, pp. 1029-1032, March 2002.
[3] S. Wang and J. Knag, "Topology optimization of electromagnetic system in multi-domain", Conference Digest of CEFC'2002, No. P1-23, 2002.
[4] A. Kameari, "Local force calculation in 3D FEM with edge elements", International Journal of Applied Electromagnetics in Materials, vol. 3, pp. 231-240, 1993.

Crossover-Controlled Genetic Algorithm and Its Application to
Inverse Problem in SF$_6$ Interrupter

Youhua Wang, Xiaoguang Yang and Weili Yan
School of Electrical Engineering & Automatization
Hebei University of Technology
No. 8, Guangrong Str., Tianjin, 300130, China
yhwang@hebut.edu.cn

Egon Sommer
Department of EE & IT
Munich University of Applied Sciences
No. 98b, Dachauer Str., Munich, D-80335, Germany
sommer@ee.fhm.edu

Abstract—From the application of genetic algorithm (GA) to the optimal design of some electromagnetic devices, it is found that its convergence speed is directly affected by the similarity of crossover codes. Based on the analysis for crossover operation a crossover-controlled genetic algorithm (CCGA) is presented. On the basis of finite element analysis the optimal magnetic field distribution in sulfur hexafluoride interrupter is obtained by applying CCGA. As a result 18.8 percent of CPU time taken by GA is saved and the interrupting performances at no load and short circuit currents are improved.

I. INTRODUCTION

Generally speaking, global optimization methods, such as simulated annealing, evolution strategy and genetic algorithm (GA), exchange optimal solution with many function evaluations, i.e. many numerical field computations. Although GA is the most powerful, it is necessary to do further research for accelerating its convergence.

One of the further developments for sulfur hexafluoride (SF$_6$) circuit breakers is the application in power distribution systems which rated voltages are not more than 35kV. When utilized for power distribution, SF$_6$ circuit breakers sometimes use arc-rotated interrupters because of their simple structure. But its interrupting capability depends on the value of current to be interrupted. The lower the interrupting current is, the weaker the flux density induced, the slower the arc rotation, the longer the arcing time, and even interruption failure occurs. For this reason some permanent magnets are used in the interrupter to increase the flux density at no load. On the other hand, at short circuit current optimal magnetic field distribution can decrease arc curling, which is mainly caused by some parts of rotating arc with different angular frequencies.

II. CROSSOVER-CONTROLLED GENETIC ALGORITHM

Genetic algorithms have been shown to be highly efficient in design optimization applications for electromagnetic devices [1]. Crossover is their most important operation to generate new points, i.e. individuals, in the feasible domain in the search for the minimum. This operation is carried out between a pair of parents chosen randomly. After the exchange of genetic codes new points are generated and have a part of the genetic characteristics of their parents.

Crossover has several models, e.g. one-point, two-point, multi-point, uniform crossover, and so on. Now use binary string to codify design variables. In case of similarity or even identity between a pair of bits to be exchanged, such as 1111111 and 1111110 or 1111111 and 1111111 it is very likely or even sure that this crossover operation does not exchange any genetic characteristics of the parents, no matter what kind of crossover model is applied. So it is necessary to consider the similarity before crossover, and then determine whether the crossover operation is made or not. The genetic algorithm, in which crossover is not operated for every pair of bits predetermined, is named crossover-controlled genetic algorithm (CCGA).

Let L be the length of bits that are randomly selected in chromosome, Ls the number of same corresponding codes between a pair of bits to be exchanged, and Ls/L the similarity. If Ls/L $> \varepsilon$, cancel the crossover and continue between another pair of parents, where $\varepsilon \in$ [0.8, 0.95] generally and Ls/L $\in$ [0, 1]. If ε =1, CCGA becomes GA.

A global optimization example:

$$\min f(X) = 30 + \sum_{i=1}^{3} (\frac{1}{10}(x_i - 20)^2 - 9\cos\frac{2\pi}{5}x_i) \qquad (1)$$

s. t. $1 \leqslant x_i \leqslant 39$ for i=1, 2, 3

where $X=(x_1, x_2, x_3)^T$ and $f(X)$ are variable vector and objective function, respectively.

If using population number np=100, generation number ng=100, crossover probability pc=0.8, mutation probability pm=0.1 and inversion probability pi=0.01, the optimization results with GA and CCGA are shown in Table I. It is found that 12.1 and 15.5 percent of CPU time taken by GA can be saved by CCGA with ε equal to 0.833 and 0.875, respectively.

TABLE I. RESULTS FROM (1) WITH GA AND CCGA

ε	CPU Time (s)	Function Evaluations	Optimal Point X^*	$f(X^*)$
1.000	0.116	3833	$(19.95, 20.04, 20.08)^T$	3.07
0.833	0.102	3551	$(20.07, 20.07, 19.93)^T$	3.11
0.875	0.098	3578	$(20.02, 19.97, 20.09)^T$	3.06

III. INVERSE PROBLEM IN SF$_6$ INTERRUPTER

Desirable Flux Density Distribution

The arc-rotated interrupter with permanent magnets is shown in Fig. 1. The moving arc column in the magnetic field is driven by Lawrence force and encounters gas flow resistance. If some simplifications are made and the arc is not bent during rotation, the transverse flux density at a given point j on the arc can be approximately expressed as [2]

$$B_j = \frac{K \, \omega^2 r_j^2}{(\omega \, r_j + 10)^{0.5} i^{0.5}} \qquad \text{for j=1,2, } \cdots \text{,n} \qquad (2)$$

where K is constant, ω angular frequency of arc rotation, r_j radius of given point j, n number of given points on arc, and i arc current, i.e. coil current.

To avoid arc curling, ω at any point on the arc is required to be almost identical. So the flux density distribution following (2) is expected.
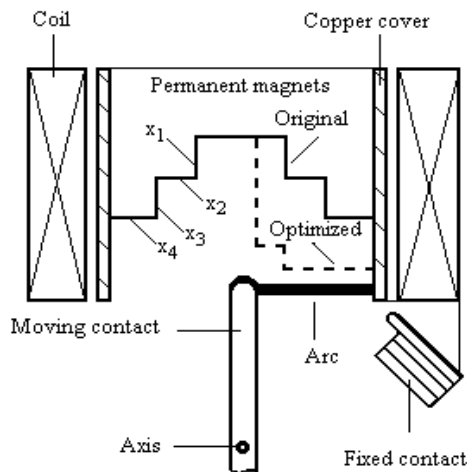
Fig. 1. Original and optimized magnet structures in SF$_6$ interrupter

Inverse Problem

The diameter of the copper cover is unchanged and to fix the structures of the permanent magnets needs four design variables, as shown in Fig. 1.

To prevent arc curling it is necessary to make every point on the arc rotate at as closely the same angular frequency as possible. Therefore the inverse problem can be written as the following optimization problem.

$$\min f(X) = \frac{1}{n \varpi} \sum_{k=1}^{n} |\omega_k - \varpi|$$
$$\text{s. t.} \quad a_i \leq x_i \leq b_i \quad \text{for } i=1,2,3,4 \qquad (3)$$
$$x_1 + x_3 \leq c_1$$
$$x_2 + x_4 \leq c_2$$

where $X = (x_1, x_2, x_3, x_4)^T$ is the design variable vector, $f(X)$ objective function, ϖ the mean value of n angular frequencies, and a_i, b_i, c_1 and c_2 are constants.

Optimization Results

If taking current density $J_0 = 50A/mm^2$, the original and optimized results are given in Table II.

TABLE II. RESULTS FROM (3) WITH GA AND CCGA AT $J_0 = 50A/mm^2$

	x_1 (mm)	x_2 (mm)	x_3 (mm)	x_4 (mm)	$f(X)$	Function Evaluations	CPU Time (h)
Original	30.0	30.0	30.0	30.0	0.581		
GA	79.2	20.4	19.7	61.0	0.494	6288	3.73
CCGA	80.3	19.2	20.1	60.4	0.501	5102	3.03

It is found from Table II that the global solution can be obtained with CCGA, using 18.8 percent less CPU time compared to GA.

IV. CONCLUSIONS

Compared with GA, CCGA has higher convergence speed and better convergence for applying a more efficient crossover operation.

Permanent magnets used in the arc-rotated interrupter of SF$_6$ circuit breakers can increase its interruption capability without load current. On the other hand, the optimal structure of the permanent magnets to decrease arc curling in short circuit current interruption is obtained by combining FEM with GA or CCGA.

REFERENCES

[1] O. A. Mohammed, F. G. Uler, S. Russenschuck and M. Kasper, "Design Optimization of a Superferric Octupole Using Various Evolutionary and Deterministic Techniques", *IEEE Trans. Magn.,* vol.33, pp. 1816-1821, March 1997.
[2] Wang Qiping, *Theory of Electrical Apparatus Arc*, China Machine Press, 1992, pp. 37-38.

An Emigration Genetic Algorithm and its Application to Multiobjective Optimal Designs of Electromagnetic Devices

Yuhuai WANG, Shiyou YANG, Guangzheng NI

Zhejiang University, Hangzhou, 310027, China

Abstract—Tanks to the success of the design of an emigration operator and the introduction of other approaches such as the fitness sharing, the clustering method, and the elitism strategy, an emigration genetic algorithm is proposed for the vector optimizations of electromagnetic devices. Numerical results are reported to demonstrate the effectiveness of the proposed algorithm for solving engineering multiobjective optimal design problems.

INTRODUCTION

Most of the real-world optimal design problems involve several incommensurable and often conflicting objectives. The traditional exact ways such as linear programming and gradient-based searches will encounter great difficulties when they are used to solve such Multi-objective Optimal Problems (MOP). Fortunately, the recently developed Evolutionary Algorithms (EA) have been proved to be one of the most efficient MOP solvers, and thus have attracted increasing attentions of both academics and engineers alike [1]-[2]. For a multiobjective solver, the following two issues must be addressed carefully: (1) how to accomplish the fitness assignment and selection in order to guide the search towards the Pareto-optimal set, and (2) how to maintain a diversity population in order to prevent premature convergences and to smooth the sampled Pareto front. In this point of view, a Pareto emigration genetic algorithm is proposed in this paper. To preserve the diversity of the searched Pareto solutions and to smooth the Pareto front, an emigration operator is introduced. The approaches such as the fitness sharing, the clustering method, and the elitism strategy to strength the robustness of the proposed algorithm are also improved and used. To validate and to show the advantages of the proposed algorithm, computer simulation results on two numerical examples are presented.

A PARETO EMIGRATION GENETIC ALGORITHM

Emigration Operator

In a real-life society, when a town is populated with too many residents, there will be great competitions and the living resources may be scarce. Then some people may immigrate to other towns to survive rather than to stay in the city for dieing out. In view of an optimization problem, the effect of this emigration operation is to maintain a diversity of the total national populations. In this point of view, an emigration operator is introduced and explained as:

Step 1 Find out the maximum distance among those of every two solutions in the population, and define a town radius which is proportional to this maximum distance. The number of solutions which will emigrate to near towns is proportional to the population size.

Step 2 Determine the neighbor size of every individual by comparing its distances to neighborhood solutions with the pre-defined town radius. The neighbor size of an individual is proportional to the number of the neighborhood solutions whose distances to the specified individual exceed the pre-defined town radius.

Step 3 Identify, respectively, the solutions with the maximum and minimum neighborhood sizes, and then replace the maximum one by a new generated individual. The new individual is generated from the individual of minimum neighbor size by adding a small perturbation to it.
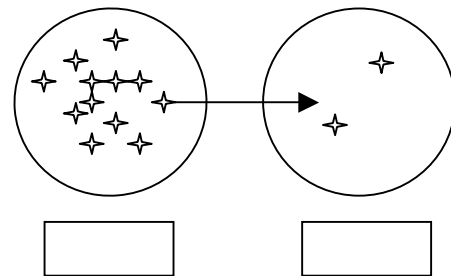
Fig. 1. A schematic diagram of the emigration operation

Fitness Assignment

Similar to but different from the Pareto based fitness assignment strategy [1], the fitness value of a individual in the proposed algorithm is assigned in the following steps:

Step 1 Fitness assignment of the excellent tribe. Introduce an external population which is called the excellent tribe, and copy the non-dominated solutions of the population to it. The fitness value of a solution i in the external excellent tribe is determined from

$$f_i = 1 + \frac{N-n}{N} \qquad (1)$$

Step 2 Fitness assignment of the population. The fitness assignment of an individual j in the population is evaluated according to the following procedures: (1) firstly, one identifies the solution with the smallest fitness value among solutions in the excellent tribe which dominate individual j, and define the smallest fitness value as *smallestfitness*; (2) one then sums up all the num of the nondominated solutions in the excellent tribe which dominate individual j as totalnum (the num of a nondominated solution is given by $num = N \times (2 - f_i)$); (3) the fitness value of the individual j

of the population is then given by

$$f_j = \frac{smallestfitness - 1}{totalnum} \qquad (2)$$

where n in (1) is the number of individuals in the population which is dominated by the specific solution of the excellent tribe, N is the size of the population.

An illustration of the fitness assignment of the proposed algorithm for a minimization problem with two objectives is given in Fig. 2. From Fig. 2 and (2), one can see that a non-dominated solution always has larger fitness values than those of individuals in the population. Moreover, the solutions in densely populated regions have smaller fitness values than those in the sparsely populated regions, other things being equal; and the individuals of population which is dominated by more nondominated solutions have relatively smaller fitness values. Since the smaller the fitness value of a solution is, the lower the probability of accepting the specific solution as new parent, the proposed fitness assignment strategy would have the ability to obtain a uniform and smooth Pareto front.

The details about other improvements such as the local search, the fitness sharing, the clustering method, and the elitism strategy will be explained in the full paper.
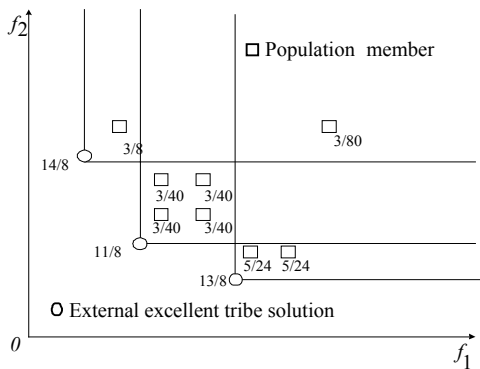
Fig. 2. Fitness assignment for a minimization problem with two objectives

NUMERICAL EXAMPLES

Two numerical examples are solved by using the proposed algorithm to validate its feasibility and robustness for solving multiobjective optimal problems.

Example1: A two decision variable and two objective mathematical function as formulated as

$$\begin{cases} f_1(x_1, x_2) = 2.0 \times \sqrt{x_1} \\ f_2(x_1, x_2) = x_1 \times (1.0 - x_2) + 5.0 \end{cases} \qquad (3)$$

$$(1 \le x_1 \le 4, 1 \le x_2 \le 2)$$

Example 2: The geometry design of the multi-sectional pole arcs of large hydro-generators as detailed in [3].

The comparison of the searched Pareto solutions obtained by the proposed algorithm and a traditional genetic algorithm for the mathematical function is shown in Fig. 3. And the sampled Pareto front for example 2 are depicted in Fig. 4. It is

very clear that (1) the Pareto front of the mathematical function obtained by using the proposed algorithm are more uniform and smooth compared with those by using a traditional one, which suggests that the proposed algorithm is more robustness in sense of producing a satisfactory Pareto front, (2) the proposed algorithm yielded almost the same Pareto solutions as those searched by a tabu based approach [3], demonstrating its feasibility for solving practical engineering multiobjective optimal design problems.

REFERENCES

[1] Eckart Zitzler and Lothar Thiele, "Multiobjective evolutionary algorithms: a comparative case study and the strength Pareto approach," *IEEE Transactions on Evolutionary Computation*, vol. 3, pp. 257-271, 1999.
[2] Hisao Ishibuchi and Tadahiko Murata, "A multive-objective local search algorithm and its Application to flowshop scheduling," *IEEE Transaction on System, Man and Cybernetics-Part C: Applications and Reviews,* vol. 28, No. 3, pp. 392-403, 1998.
[3] S.L. Ho, Shiyou Yang, Guangzheng Ni, H.C. Wong, " A tabu method to find the Pareto solutions of multiobjective optimal design problems in electromagnetics, " *IEEE Trans. Magn.*, 38, pp.1013-1016, 2002.
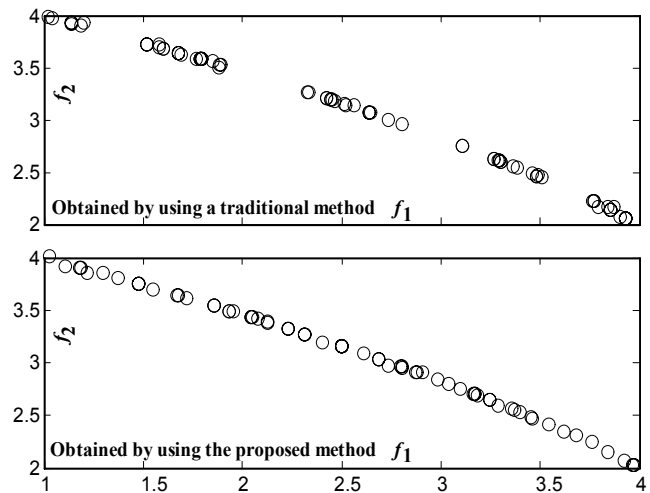
Fig. 3. The Searched Pareto front by different methods for example 1
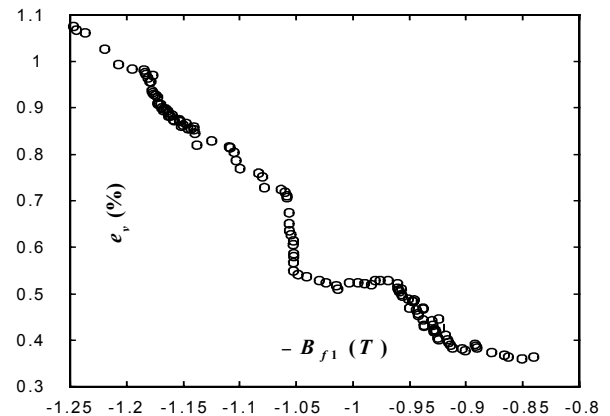
Fig. 4. The Searched Pareto front by the proposed method for example 2

Analysis of Cogging Torque Considering Tolerance of Axial Displacement on BLDC Motor by Using a Stochastic Simulation Coupled with 3D-EMCN

Young-Kyoun Kim, Jeong-Jong Lee, Jung-Pyo Hong, Senior Member, IEEE, and Yoon Hur*

Dept. of Electrical Eng., Changwon National University, #Sarim, Changwon, Kyungnam, 641-773, Korea
*Automotive Motor division / Advanced R&D Team, Kumjeong, Busan, 609-600, Korea
e-mail: ensigma@hitel.net

Abstract —**This paper describes a tolerance analysis concerned with an axial displacement on a BLDC motor. The axial displacement occuring in productions of a BLDC motor directly affect its torque ripple. Therefore, the tolerance analysis is vary important for improving a robustness of its production and this work is accomplished by a stochastic simulation introduced to overcome a disadvantage of Monte Carlo Simulation.**

INTRODUCTION

Permanent magnet BLDC motors are increasingly being used in high performance applications. In many case of applications, torque ripple characteristics of BLDC motor are of basic concern. There is no exception for a BLDC motor employed as the electric power steering of vehicles. This motor is requiring low level of the torque ripple for comfortable steering of a vehicle [1].

Generally, the production of the electric machine needs allowance for dimensional or positional tolerances of design variables due to limitations on the manufacturing and measuring precision on every part. These dimensional tolerances, however, can effect on a electrical performance of electric machines. A axial displacement between the stator and the rotor occurs when the BLDC motor is produced. And the axial displacement has an influence on a cogging torque of the BLDC motor. So, this torque directly affect a torque ripple of the motor. Therefor, it is necessary for an tolerance analysis concerned about the axial displacement on a design stage before manufacturing the BLDC motor.

The tolerance commonly can be treated as random parameters, and an expression for an uncertainty of design variables and ouputs can be accomplished by a stochatc simulation. One of the widely used methods, which is based on sampling for the stochatc simulation, is Monte Carlo Simulation. This method is powerful tool to predict the effects of manufacturing variation. But, the biggest disadvantage of the Monte Carlo Method is that it requires large samples to achieve reasonable accuracy. On the other hand, introduced in this paper, the Stochastic Response Suface Methodology (SRSM) treats the uncertainty of design variables as stochastic variables. And the SRSM approximates the output function by using a polynomial fitting and samples the approximation to calculate statistical distribution of outputs .

The SRSM is based on sample points, which could be obtained by using 3D-EMCN combined with 2D-FEM, which is proposed to analyze the cogging torque having the axial displacement on the BLDC motor.

CONCEPT OF FORMULATION METHOD

Concept of Stochastic Response Surface Methodology

In the SRSM, a relationship of the uncertainty between the outputs and inputs is addressed by the series expansion of standard normal variables in terms of Hermite polynomials. Therefore, the output can be approximated by an expansion known as polynomial chaos expansion as follows [1];

$$y = a_0 + \sum_{i1=1}^{n} a_{i1}\Gamma_1(\xi_{i1}) + \sum_{i1=1}^{n}\sum_{i2=1}^{i1} a_{i1i2}\Gamma_2(\xi_{i1},\xi_{i2}) + \sum_{i1=1}^{n}\sum_{i2=1}^{i1}\sum_{i3=1}^{i2} a_{i1i2i3}\Gamma_3(\xi_{i1},\xi_{i2},\xi_{i3}) + \cdots \quad (1)$$

where, y is the random variable representing the output of a model, the $\Gamma_p(\xi_{i1},\cdots,\xi_{ip})$ are Hermite polynomials of degree of p and a's are unknown coefficients to be estimated.

Introductory Statistics for tolerance Analysis

A variation band and uncertainty of design variables with assuming the distribution of a normal distribution. In this symmetrical distribution, the tolerance band of design variables is easy to quantify in terms of the percentage of the area that will occur between one, two and more standard deviation from the mean μ as follows [1];

$$\Delta x = \pm n\sigma \quad (n = 1, 2, 3, \cdots) \quad (2)$$

Modeling variation of outputs according to tolerance of design variables is built by the SRSM. From a set of N samples, the basic moments of the distribution of an output y_i can be calculated as follows;

$$\boldsymbol{\mu}_{y_i} = \mathrm{E}\{y_i\} = \frac{1}{N}\sum_{j=1}^{N} y_{i,j} \quad (3)$$

$$\sigma_{y_i}^2 = \mathrm{E}\{(y_i - \boldsymbol{\mu}_{y_i})^2\} = \frac{1}{N-1}\sum_{j=1}^{N}(y_{i,j} - \boldsymbol{\mu}_{y_i})^2 \quad (4)$$

$$\sigma_{y_i} = \sqrt{\sigma_{y_i}^2} \quad (5)$$

where, μ_{yi} is a mean, σ_{yi}^2 is a variance and σ_{yi} is a standard deviation, respectively.

Fig. 1 shows the longitudinal cross-section of the analysis model. The stator of the permanent magnet BLDC motor has 18 slot and the rotor is bult with 12 tiles of radial and skewed magnetic. Axial displacement in the manufacturing of the skew mounted permanent magnet BLDC motor needs to be analyzed by a full 3D-analysis, such as, 3D-FEM. This approach, however, is too computationally expensive to produce results in a reasonable time, therefore, an alternative method must be found. In this paper, a proposed method is taken with two sections shown in fig. 2, so called, lateral section and radial section. The former is constructed with both the lateral flux and the radial flux, flowing from the rotor to the stator. The latter is composed of radial flux only crossing from the rotor to the stator. In order to analyze the cogging torque of each section, the lateral section employed the 3D-EMCN [2], and the radial section used a multi-slice technique based on 2D-FEM, where is assumed that the radial flux only acting on the air-gap. The totality of the analysis is found by superimposing both the 3D-analysis and the 2D-analysis.
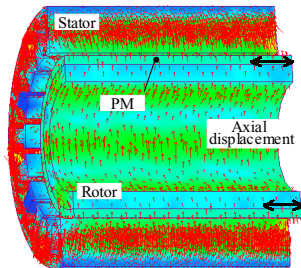
Fig. 1. Longitudinal cross-section of analysis model
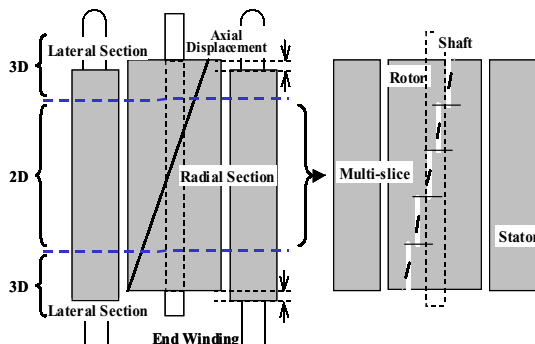
Fig. 2 Proposed sections of analysis model and multi-slice technique

RESULTS AND DISCUSSION

Fig. 3 shows a comparison between both results of the cogging torque obtained form the actual experiment and the proposed analysis method. So, a validity of proposed analysis method is verified from the experimental results. And then, by using a combination technique employing the SRSM and the proposed analysis method, results according to the analysis of the tolerances were obtained with 10 (%) and 5(%) tolerance of all design variables, as shown in Fig 4. These results show that, when design variables are controlled with tighter tolerance, the scatter of the set of the cogging torque is extremely centralizd in the mean of its population.

CONCLUSIONS

In this paper, the tolerance analysis is accomplished by the SRSM combined with 3D-EMCN and 2D-FEM. It offers the predicted variations of the cogging torque according to the axial displacement of the motor. In most cases of manufacture the axial displacement can be inevitably happening in the BLDC motor. Therefore, the tolerance ananlysis must be considered on the design stage, because that would lead a production of the BLDC motor to be robust. In full paper, more descriptions of this work will be presented in detail.

REFERENCES

[1] Young-Kyoun Kim et al, "Torque Characteristics Analysis Considering the Tolerance of Electric Machine by Stochastic Response Surface Method ", Proceeding of IAS' 2002, pp. 752-758, October 2002.
[2] Jin Hur et al "A Method Reduction of Cogging torque in Brushless DC Motor Considering the Distribution of Magnetization by 3DEMCN," *IEEE Transactions on Magnetics,* vol. 34, No. 5, pp. 3532-3535, Sep., 1999.
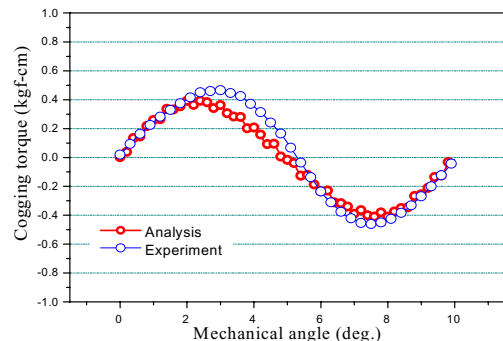
Fig. 3 Comparison of cogging torques at axial displacement = 0 (mm)
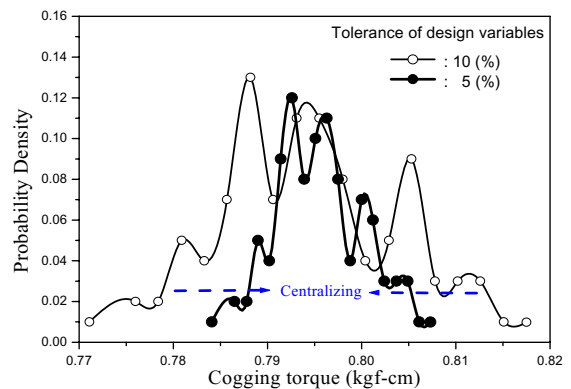
Fig. 4 Estimated probability distribution of cogging torque

A Novel Algorithm for Multimodal Function Optimization
Based on Evolution Strategy

Chang-Hwan Im[1], Hong-Kyu Kim[2] , Hyun-Kyo Jung[1], and Kyung Choi[3]

[1]School of Electrical Engineering, Seoul National University, San 56-1, Shillim-dong, Kwanak-gu, Seoul, 151-742, KOREA
[2]Advanced Power Apparatus Group, KERI, P.O Box 20, Changwon, 641-600, KOREA
[3]Kwangwon National University, 192-1, Hyoja2-dong, Chunchon, Kwangwon-do, 200-701, KOREA
e-mail : ichich2@snu.ac.kr

Abstract — In this paper, a novel algorithm for multimodal function optimization is developed based on the concept of evolution strategy. A new concept, named as restricted evolution, can yield more improved characteristics than conventional approaches used for the multimodal function optimization. The efficiency and usefulness of the proposed method will be verified by the application to various cases.

INTRODUCTION

Recently, algorithms to find more than one local optimum of a function, which is usually referred to as a multimodal function optimization, have been widely studied. Most of the studies were based on the genetic algorithm (GA). Various concepts have been introduced, such as sharing [1], deterministic crowding (DC) [2], restricted competition selection (RCS) [3,4] and so on. Basically, however, algorithms based on the GA tend to converge slowly compared to other heuristic algorithms.

Nowadays, there have been some attempts to apply the evolution strategy (ES) to the multimodal function optimization [5]-[7]. Most of the approaches adopted some concepts of GA, such as crossover and sharing. The main characteristic of them is to cluster neighboring solutions around a peak. However, excessive application of the GA concept may lose the powerful advantage of the ES, deterministic-like convergence that yields faster convergence characteristic than the GA.

In this paper, a novel algorithm for the multimodal function optimization is developed based on the concept of the ES. A new concept, named as restricted evolution, is proposed to realize the multimodal function optimization scheme. The concept excludes solutions from clustering with their neighbors and makes only one solution survive for each peak. Hence, the proposed concept is more efficient and practical than the conventional ones because the smaller number of population is required. Moreover, it has additional advantages that it is easy to implement and shows fast convergence because it keeps the basic process of the ES. The efficiency and usefulness of the proposed method will be verified by the application to various functions.

PROPOSED ALGORITHM

As stated before, the main feature of the proposed algorithm is the separation of neighboring solutions, which is very different from the conventional ES applications in [5]-[7]. In the case of the GA, the concept of the RCS is somewhat similar to that of the proposed method [3,4]. However, in the case of the RCS-GA, niche radius should be determined preliminarily before the optimization process, which is very hard to determine because the shape of an objective function cannot be estimated. Whereas, for the proposed method, the evolution range can be modified during optimization process by checking the convergence rate. The proposed method adopts the concept of *elite set*, which can store superior solutions with some distance between each other. The members of the elite set are replaced with much superior or improved solutions during the evolution. Total process of the proposed algorithm is as follows. Detailed explanations will be shown in the full paper with illustrations.

Step 0 – Initialization

Setting $\alpha_{\min,i}$, $\alpha_{\max,i}$, and $\alpha_{\text{init},i}$ for each design variable.

α_i : Evolution range for i-th design variable. If i-th design variable is p_i, the child generation is generated within [p_i - α_i, p_i + α_i], where $\alpha_{\min,i}$ < α_i < $\alpha_{\max,i}$. This factor is modified during the evolution and every elite set has different ranges except at the starting time.

$\alpha_{\min,i}$: Minimum distance between two elite solutions. This factor controls minimum distance between two closest extrema.

$\alpha_{\max,i}$: Maximum distance between two elite solutions. This factor controls the convergence rate.

$\alpha_{\text{init},i}$: Initial value for α_i

Step 1 – Generating initial elite set

Making initial population (the number of it is $\mu \times \lambda$) and elite set. Among them, μ solutions are selected as members of an elite set. Elite set is determined by following rules.
- Put current best solution to elite set and remove solutions inside the mutation range of the best solution.
- Find best solution except the removed solutions, and repeat the previous step until μ members are found.

Step 2 – Generating Children, Restricted Evolution

Making new λ children within mutation width of each elite set. This process is the same as $(1+\lambda)$ ES.

Step 3 – Mutation

If the objective function for a child generation is improved compared to its parent, replace the parent (a member of elite set) with the child. After finishing the mutation, check if each elite solution is located in the mutation range of other elite solutions. If it is 'true' and its objective function has worse value than other solution, eliminate it (remove from elite set). The number of removed solution is denoted by ξ.

Step 4 – Shaking

$(\xi + \rho)$ solutions are randomly generated in the whole search space outside the mutation ranges of existing elite solutions (ρ : the number of shaking solutions). During the generation process, they should not invade other solutions' mutation range, $\alpha_{init,i}$.

Step 5 – Annealing

Form a new elite set. The ξ removed solutions are replaced by the new solutions generated by *shaking* process (superior solutions are selected among $(\xi + \rho)$ solutions). Existent elite solutions that are worse than remaining ρ solutions are also replaced with new solutions. If an elite solution is improved within the mutation range, the mutation range is increased by dividing it by 0.85. If the elite solution is not improved, the mutation range is decreased by multiplying it by 0.85. Initial mutation range $\alpha_{init,i}$ is given to the newly generated solutions.

Step 6 – Convergence Check

Repeat *Step 2* - *Step 6*, until all solutions are not improved any more.

NUMERICAL TESTS AND RESULTS

The proposed algorithm was applied to the optimization of the mathematical function. Fig. 1 and Fig. 2 show two examples of the test functions and optimized results. From the figures, we can see that the results show very fast convergence speed and the proposed method is very efficient to find multiple peaks. Practical application of the method to electromagnetic optimization problems and comparison with other coventional methods will be shown in the full paper.

CONCLUSION

In this paper, a novel algorithm for multimodal function optimization was proposed. The algorithm is based upon combination of the evolution strategy and the restricted evolution. The usefulness of the proposed method was verified by the application to various test functions.

REFERENCES

[1] D. E. Goldberg and J. Richardson, "Genetic algorithms with sharing for multimodal function optimization," *Proc. 2nd ICGA*, pp. 41-49, 1987.
[2] S. W. Mahfoud, *Niching methods for genetic algorithms*, Ph. D. dissertion, Univ. Illinois at Urbana-Champaign, Illinois Genetic Algorithm Lab., Urbana, IL, 1995.
[3] Cheol-Gyun Lee, Dong-Hyeok Cho, and Hyun-Kyo Jung, "Niching genetic algorithm with restricted competition selection for multimodal function optimization," *IEEE Trans. Magn.*, vol. 34, pt. 1, pp. 1722-1725, May 1999.
[4] Jae-Kwang Kim, Dong-Hyeok Cho, Hyun-Kyo Jung, Cheol-Gyun Lee, "Niching Genetic Algorithm Adopting Restricted Competition Selection Combined with Pattern Search Method," *IEEE Trans. Magn.*, vol. 38, no. 2, pp. 1001-1004, March 2002.
[5] Jian Zhang, Xiaojing Yuan, Zhixiang Zeng, Saud Amer, "Niching in as ES/EP Context," *Proceedings of the 1999 Congress on Evolutionary Computation* (CEC 99), vol. 2, pp. 1426-1433, 1999.
[6] Osamu Takahashi, Shigenobu Kobayashi, "An Adaptive Neighboring Search Using Crossover-like Mutation for Multimodal Function Optimization," *Proceedings of IEEE International Conference on Systems, Man, and Cybernetics*, vol. 1, pp. 261-267, 2001.
[7] O. Aichholzer, et. Al., "Evolution Strategy and Hierarchical Clustering," *IEEE Trans. Magn.*, vol. 38, no. 2, pp. 1041-1044, March 2002.

(a) test multimodal function   (b) iteration 1

(c) iteration 4   (d) iteration 15
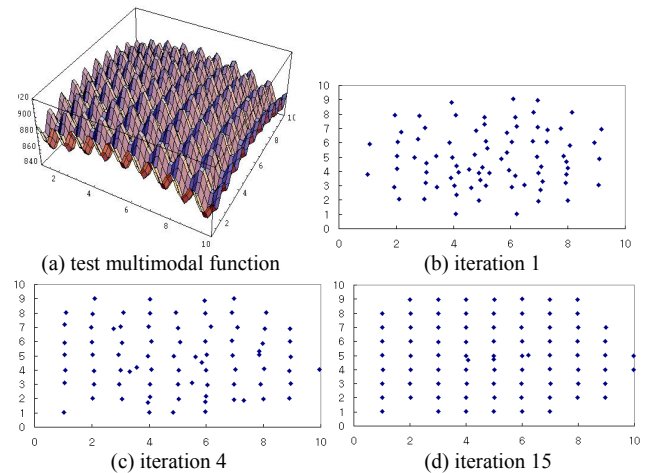
Fig. 1. Optimization result for a test function ($\mu = 80$, $\lambda = 5$, $\rho = 10$).

(a) 2-D Sinc function   (b) iteration 1

(c) iteration 4   (d) iteration 15
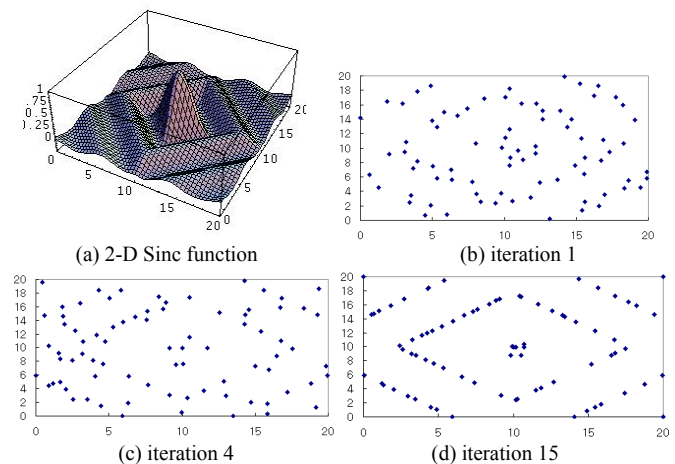
Fig. 2. Optimization result for 2-D Sinc function ($\mu = 80$, $\lambda = 5$, $\rho = 10$).

Optimization of Geometric and Electric Parameters in Switched Reluctance Motor Based on Response Surface Method

Jae-hak Choi and Ju Lee

Energy Conversion Lab., Dept. of Electrical Engineering, Hanyang University

Haengdang-dong, Seongdong-gu, Seoul,

133-791, South of Korea

E-mail: ivy@ihanyang.ac.kr

Abstract — **This paper presents an optimum design technique, which is able to determine optimal geometric and electric variables of switched reluctance motor (SRM). SRM has essentially high torque ripple due to its salient structure. In order to increase average torque and reduce torque ripple causing noise and vibration, an optimization design technique has been investigated variables by means of combining finite element method (FEM) considering driving circuits and the progressive quadratic response surface method (PQRSM).**
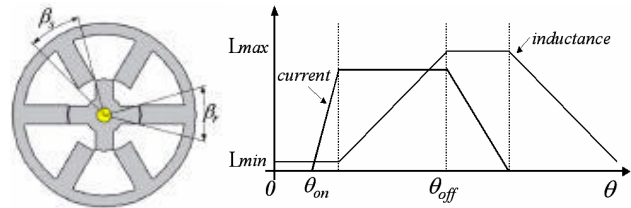
Fig. 1. The initial model and equivalent self-inductance

Ⅰ. INTRODUCTION

The switched reluctance motor (SRM) has a lot of advantages such as simple and rugged motor construction, high reliability, and low cost [1]. However, SRM has some problems that limit its applications because of its inherent structure. One of the major problems is the torque ripple that causes undesirable acoustic noise and high vibration. The torque ripple depends essentially on geometric design variables and electric design variables, which have been adopted as two-dimensional design variables. As shown in Fig. 1, the electric design variables are relative to turn-on angle (θ_{on}), turn-off angle (θ_{off}). The geometric design variables are relative to the salient pole shapes such as stator pole arc (β_s), rotor pole arc (β_r)[2].

Ⅱ. OPTIMIZATION ALGORITHMS AND FINITE ELEMENT METHOD

A. Optimization algorithm; Progressive quadratic RSM

Gradient-based nonlinear optimization methods like conjugate gradient method (CGM) are inefficient in applications where expensive function evaluations are required, and in applications where objective and constraint functions are noisy due to modeling and cumulative numerical inaccuracy since gradient evaluation results cannot be reliable. In this research an effective optimization technique named PQRSM has been used to overcome aforementioned difficulties. The PQRSM approximates objective and constraint functions to quadratic functions within the reasonable design space and sequentially optimizes the approximate optimization problems in the context of the trust region model management strategy. The trust region model management strategies adaptively restrict design

moves within trust regions, where the approximate function produces information that agrees with the actual function within an acceptable tolerance to error. Because PQRSM uses only function information of objective and constraints to build approximate functions and does not use gradient information it is a very useful method for problems where gradient information cannot be obtained. The object function and constraints are represented by (1) and (2)

Objective Function:
Maximize average torque (T_{ave}) or
Minimize torque ripple (T_{rip}) (1)

Subject to:
Phase current; (I_{max}) ≤ 6(A),
Stator pole arc; $\beta_s = 30°$,
Rotor pole arc; $30° \leq \beta_r < 60°$,
Turn-on angle; $0° \leq \theta_{on} \leq 30°$,
Turn-off angle; $30° \leq \theta_{off} \leq 45°$ (2)

B. Finite Element Method

If the magnetic vector potential and current density have only a *z*-axis component, the governing equation for SRM can be expressed in a magnetic vector potential A as follows:

$$\partial/\partial x (v\, \partial A/\partial x) + \partial/\partial y (v\, \partial A/\partial y) + J_o = 0 , (3)$$

where v is the inverse of permeability, A is the magnetic vector potential, and J_0 is the input current density.

The electrical input equation of the voltage source is expressed as

$$V = R_m I_m + E_m , (4)$$

where V is the voltage source, R_m is the phase resistance, I_m is the phase current, and E_m is the electromotive force induced in the coil.

After applying the Gelerkin method in (3) and coupling the voltage equation (4), system matrix equation is obtained by using the time difference scheme as follows.

$$\begin{bmatrix} [s] & [Q] \\ 1/\Delta t[F] & [R_m] \end{bmatrix}\begin{bmatrix} A^{t+\Delta t} \\ I_m^{t+\Delta t} \end{bmatrix} = \begin{bmatrix} 0 & 0 \\ 1/\Delta t[F] & 0 \end{bmatrix}\begin{bmatrix} A^t \\ I_m^t \end{bmatrix} + \begin{bmatrix} 0 \\ V^{t+\Delta t} \end{bmatrix} \qquad (5)$$

The moving line technique is introduced to carry out the dynamic analysis [3].

The force is calculated by the surface integral of the Maxwell stress tensor on the line and the thrust is given by following equation:

$$\vec{F} = \int_l \frac{w}{2\mu_o}\{n_x(B_x^2 - B_y^2) + 2n_y B_x B_y\}dl , \qquad (6)$$

where, n_x and n_y are the unit normal direction vectors, w is the stack width, and B_x and B_y are the magnetic flux density.

C. Optimization procedure with Finite Element Method

Fig. 2 shows the automatic optimal design process. The β_s, β_r, θ_{on}, and θ_{off} are adopted as a design variables to obtain the optimal results. To calculate the object functions, two-dimensional time stepping FEM considering the driving circuit is used.

III. ANALYSIS RESULTS AND DISCUSSION

Various optimization algorithms are implemented in the switched reluctance motor design. The effectiveness of the PQRSM is verified in torque ripple and average torque as shown Fig. 2.

Fig. 2 shows the total torque characteristics comparison between the initial model and the optimal model. The torque ripple of initial model is very large, which is almost 95.4(%). Fig. 2 also shows that of the optimal model for minimizing torque ripple. The torque ripple of optimal model is drastically improved to 6.2(%). It can be known that the average torque of optimal model is completely much higher than that of initial model. In order to compare the PQRSM with conventional RSM, we also suggest the results of the conventional RSM will be released to in the final paper.

IV. CONCLUSION

This paper presented the results of this optimum design for maximizing the average torque and minimizing torque ripples specified according to SRM applications. In that work,

the time stepping FEM has been effectively used in taking the drive circuit and the switching condition into account. In order to identify the approaches on SRM, optimal design variables and the performances were investigated in detail. A trade-off characteristic between the average torque and the torque ripple was also investigated. The optimal design process proposed in this article may be also used effectively for various electric machines.

REFERENCES

[1] T. J. E. Miller, *Switched Reluctance Motors and their control,* Hillsboro, OH: Magna Physics Publishing and London: Oxford University Press, 1993.
[2] S. Brisset and P. Brochet, "Optimization of Switched Reluctance Motors using Deterministic Methods with Static and Dynamic Finite Element Simulation," *IEEE Transactions on Magnetics,* vol. 34, pp. 2853-2856, September 1998.
[3] Youn- Hyun Kim, Jae-Hak Choi, Sung–In Jung, Yon–Do Chun, Ju Lee, Min–Sik Chu, Kyung–Jin Hong, and Dong-Hoon Choi, "Optimal design of switched reluctance motor using two-dimensional finite element method," *Journal of Applied Physics*, vol. 91, no. 10, 6967, May 2002.
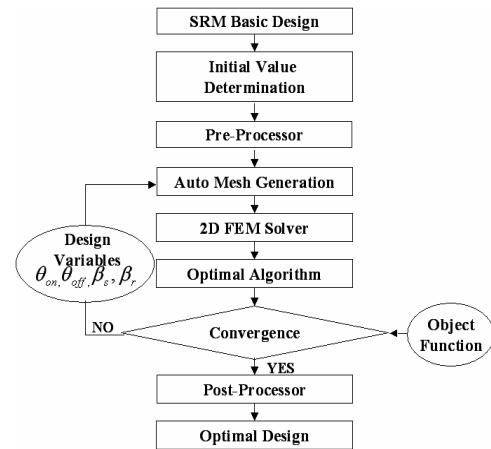
Fig. 2. The automatic optimization procedure
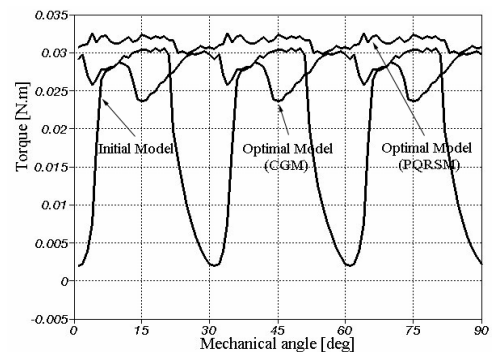
Fig. 3. Torque characteristic; optimum design vs. initial design

A Modified Genetic Algorithm in Electrotechnical Applications

Jarosław Jajczyk, Ryszard Nawrowski

Poznań University of Technology, Institute of Industrial Electrical Engineering

ul. Piotrowo 3A

60-965 Poznań, Poland

E-mail: Jaroslaw.Jajczyk@put.poznan.pl, Ryszard.Nawrowski@put.poznan.pl

Summary – **The paper presents an analysis of several variants of genetic algorithms, that have been used for optimization of geometric dimensions of three-phase high current busways with permanent insulation.**

INTRODUCTION

The process of finding optimal structures of complex technological systems requires the choice of the most effective optimization method. In case of multi-dimensional problems, the objective functions of which are characterized by several local optima, the method of finding a global optimum is of important meaning. Such problems are satisfactorily solved by means of the genetic algorithm [1, 2].

The work presents and visually shows the optimization course of the busway and the effect of its various modifications on obtained results.

THE GENETIC ALGORITHM AND ITS MODIFICATIONS

An elementary form of the genetic algorithm was considered by K.A. De Jong and A. Brindle (random choice with repetitions). It includes the following three basic operations: selection according to the roulette principle, simple crossing with random coordination, and simple mutation [1].

The work presents a modification, implementation, and consequences of modification of a selection process of an elementary genetic algorithm, based on the model of De Jong's expected values and Brindle's random selection with the use of remainders without repetitions. In the proposed method for each individual an expected number of copies e_i is calculated:

$$e_i = \frac{f_i}{\sum\limits_{j=1}^{n} f_j} \cdot n \qquad (1)$$

where: f – accommodation factor, n – the size of the population.

Integer part of the number determines the number of transfers of given individual to the parent pool, while the fraction part is equal to the probability of copying into the parent pool in result of Bernoulli's trials.

In result of the crossing and mutation operations the best already found individual might be lost, that would usually impair convergence of the algorithm. In order to avoid such an instance a method of keeping the best of existing solutions

was proposed. Similar modification was analyzed by De Jong in his exclusivity model of expected values.

Copying of the best individual from the $\mathbf{P}(t)$ to the $\mathbf{P}(t+1)$ generation with a view to replacing an individual of the least accommodation factor or a randomly selected one is carried out only provided that the accommodation factor of the best individual of the $\mathbf{P}(t+1)$ population is lower than for the best individual of the $\mathbf{P}(t)$ one.

In the genetic algorithms, for which the numbers of individuals are not additionally adjusted, a premature convergence (in the preliminary phase) or random migrating among similar solutions (the end of optimization process) may occur. In order to avoid such a condition adjustment scaling is applied. In the presented algorithm a linear scaling was used:

$$f' = m \cdot f + n \qquad (2)$$

where f – preliminary accommodation factor, f' – after-scaling accommodation factor

The m and n coefficients are selected with a view to obtain the average after-scaling accommodation (f'_{avg}) equal to the preliminary accommodation (f_{avg}). The m and n coefficients are described by the relationships (3):

$$m = \frac{(C_{multi} - 1) \cdot f_{avg}}{f_{max} - f_{avg}}, \qquad n = \frac{f_{avg} \cdot (f_{max} - C_{multi} \cdot f_{avg})}{f_{max} - f_{avg}} \qquad (3)$$

where C_{multi} – multiplication coefficient. In the current implementation $C_{multi} = 2.0$ is adopted.

THE MODEL OF THE OPTIMIZED OBJECT

The object subject to optimization with the modified genetic algorithm was a three-phase high current busway with permanent insulation [3], the cross-section of which is shown in Fig. 1.
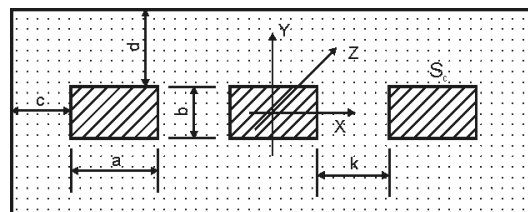
Fig. 1. Cross-section of the high current busway with permanent insulation

The objective function depends on geometric variables affecting the area of cross-section of the busway:

$$\mathbf{S(u)} = f(a,b,c,d,k) = k_{invest} + k_{operat} \qquad (4)$$

where: k_{invest} – the investment cost, k_{operat} – the operation cost.

An optimization criterion is minimal consumption of structural material of the conductors and the insulator (the investment cost) and minimal loss of effective power within assumed period of time (the operation cost).

The objective function $\mathbf{S(u)}$ so defined must fulfill a set of constraints provided in a general form (5):

$$\mathbf{Z_i(u)} = [\mathbf{Z_1(u)}, \mathbf{Z_2(u)}, ..., \mathbf{Z_k(u)}] \qquad (5)$$

among which the following conditions may be reckoned: maximal temperature of working conductor T_{Cmax}; maximal insulator temperature T_{Imax}; maximal electric stress E_{max}, maximal forces acting in steady state and short-circuit F_{max}, requirements of the standards related e.g. to the results of short-circuit currents.

Such definition of the problem is converted to optimization problem without constraints, formulated in the form of a modified criterion function $\mathbf{S_z(u)}$ (6):

$$S_z(u) = S(u) + \sum_{i=1}^{k} P_i(Z_i)^2 N[Z_i] \qquad (6)$$

where: $N[Z_i]=1$ for $Z_i>0$ (breach of the constraints) or $N[Z_i]=0$ for $Z_i \leq 0$ (fulfillment of the constraints).
P_i is a so-called punishment factor of large absolute value.

CALCULATION

Results of the calculation carried out with the use of given modifications of genetic algorithm are shown in graphical form in Figs 2 and 3. The following parameters were assumed: – intensity of phase current 10 [kA]; – conductor voltage 20 [kV]; – exploitation time 10 years; the phase conductors made of aluminum and the insulator made of an epoxy resin.
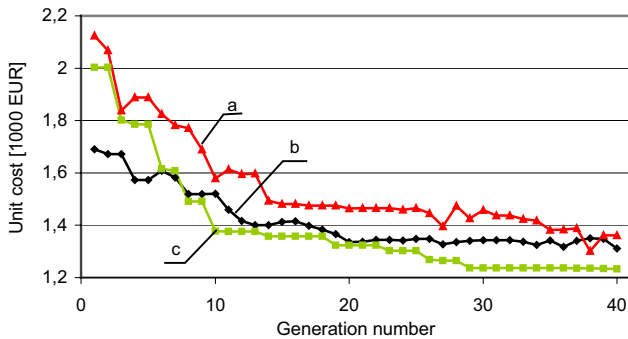
Fig. 2. The course of optimization process: a – selection according to the roulette principle, b – selection according to remainders without repetitions; c – selection according to remainders without repetitions with transferring of the best individual "always" to randomly selected location with adjustment scaling

The averaged plots have been obtained for 100 trials (Fig. 3). They enable the most reliable visualization of the effectiveness of the introduced modifications.
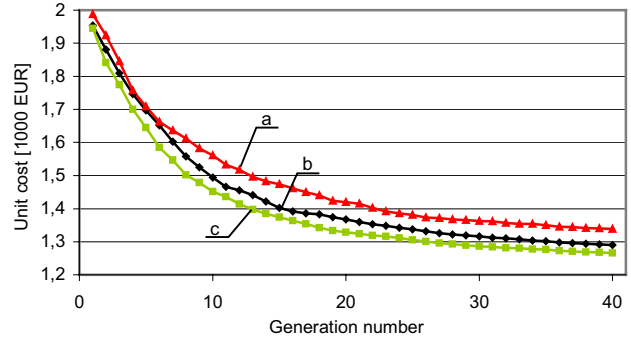
Fig. 3. The course of optimization process (100 trials): a – selection according to the roulette principle, b – selection according to remainders without repetitions; c – selection according to remainders without repetitions with transferring of the best individual "always" to randomly selected location with adjustment scaling

The effect of the proposed modifications on the course of optimization calculations was observed for 40 generations. Crossing and mutation probabilities were constant and amounted to 0.8 and 0.005, respectively. The size of the population was constant and equal to 30 items.

NOTES AND CONCLUSIONS

The calculation and the results enabled formulating of the following conclusions:

- The selection based on the roulette principle distinguishes with worse results than the method of selection according to remainders without repetitions. For example using the first method the costs at the level of EUR 1400 was achieved after 22 generations, while with the second one – already after 15 generations (Fig. 3).

- Adjustment scaling and transferring of the best individual improves the rate and accuracy of achieving the optimal point, that, in consequence, leads to reduction of the number of generations and cuts down the computation time. In result a 6-percent cost reduction was obtained (Fig. 3).

- Modification consisting in transferring of the best individual prevents the loss of promising solutions and protects from inappropriate course of the computation process, occurring for the case of the lack of such modifications (Fig. 2, curves a and b).

REFERENCES

[1] D.E. Goldberg, "Genetic Algorithms in Search, Optimization and Machine Learning", Addison-Wesley Publishing Company, Inc. Reading, Massachusetts, 1989.
[2] L. Fausett, "Fundamentals of Neural Networks: Architectures, Algorithms and Applications", Prentice Hall International Inc., 1994.
[3] Bednarek K., Nawrowski R., Paruch W.: Coupling between electromagnetic and thermal fields in three-phase rectangular shield conductors, International Symposium on Electromagnetic Fields in Electrical Engineering, Thessaloniki, 25-27 September 1995, p.315-318.

Application of A Hybrid Algorithm Based on Chaotic Optimization Method to Underwater Thruster Motor

Chen Zhifei   Shi Hongyan   HuYan   An Yuejun   Sun Changzhi

College of Electrical Engineering

Shenyang University of Technology

58 Xinghua South Street, Tiexi District

110023,P.R.China

Zhifeichen@163.com,   Shihong_yan@eyou.com

Abstract **Based on the analysis of the properties of Alopex and chaotic optimization algorithm, a hybrid optimal method is proposed to solve nonlinear constraint optimization of underwater thruster motor design by the use of properties of ergodicity, randomicity and regularity of chaotic motion, which can enhance the local rate of convergence and improve the accuracy of solution. The mathematical model of thruster motor is set up and demonstrated by using numerical simulations under the condition of different starting, Computer-aided electromagnetic field calculation are employed to solve force and torque of underwater thruster.**

INTRODUCTION

Underwater robots are applied mainly to oil and gas exploration and production, marine science(including environmental impact assessment), hydrographic survey, salvage and military field for general scientific experimentation and for data acquisition. Because neodymium-iron-boron (Nd-FeB) Permanent magnets have high-energy with suitable magnetic and physical properties for applications, Nd-Fe-B permanent magnet(PM) direct current (DC) motors have played an important role in high performance underwater thruster systems.

In computational design optimization of underwater thruster motors, there are two tools that cooperate to obtain the optimal result. The fundamental tool of the scheme is the search tool. As every point in the search space represents a different design, the heuristic optimization algorithms transfer this particular design to the other tool of the optimization, the analysis tool, to get a performance measure. The analysis tool's task is to solve the field equations for the submitted design and to return the relevant parameters back to the search tool.

In recent years, increasing attention has been given to the development of novel heuristic optimization algorithms for a wide range of applications[1,2], the emergence of intellectual algorithms combined with advances in computer have facilitated the realization of high efficient PM motors. In this paper, a hybrid algorithm on the basis of Alopex and chaotic optimization is proposed for the underwater motor.

HYBRID OPTIMIZATION

Alopex Algorithm

The Alopex process[3] is a biologically-influenced computational paradigm that uses a stochastic procedure to find the optimum of nonlinear functions and uses the Boltzmann probability distribution function to generate probabilities of taking positive or negative steps away from its current position on the path toward the optimal solution. It is distinguished from the other methods by the following features:

1). The procedure is iterative, with the variables that determine the cost function updated simultaneously by small increments during each iteration. Following the update, the new value of the cost function is computed.

2). The change in the variable x_i depends stochastically upon the change in the value of the cost function and the change in x_i over the preceding two iterations.

3). All increments in parameter values are retained and carried over into the next iteration.

4). The process is guided by two parameters: the step size and the stochastic element called the effective temperature.

5).Alopex contains additional algorithms which automatically adjust step size and temperature as the run progresses.The equations satisfying the algorithm are

$$x_i(n) = x_i(n-1) + \delta_i(n) \tag{1}$$

$$\delta_i(n) = \begin{cases} +\delta & with \quad probability \quad p_i^+(n) \\ -\delta & with \quad probability \quad (1-p_i^+(n)) \end{cases} \tag{2}$$

where $p_i^+(n) = \dfrac{1}{1+\exp(-\Delta_i(n)/T)}$ (3)

Chaotic Optimization

By the use of inherent special properties chaotic motion, the approximate optimal solution obtained from Alopex algorithm is transferred to the chaos optimization search to enhance the local rate of convergence and improve the accuracy of solution.
The mathematical expression of the logistic mapping

of chaos optimization method is given in (4) .

$$x_{n+1}(x) = rx_n(1-x_n), \qquad n = 0,1,2,\cdots, x_0 \in [0,1] \quad (4)$$

where r =the growth rate or fecundity

x_0 =initial value

The type of orbit depends on the growth rate parameter. When the growth rate equals 4, all orbits zoom to infinity.

After the initial steps of problems are implemented to search according to the requirements of Alopex, if the value of cost function keeps constant and unchanged, namely, then the local optimal point x_i^* is obtained. Chaotic number generator typically generate values between –1 and 1, if such chaotic variable as $o_{i,n}$ is designated, the following formula can be used to generate new value x_i'

$$x_i' = x_i^* + \alpha_i o_{i,n} \qquad (5)$$

where α_i =adjusting coefficient

x_i^* =present optimal value

and continue to search, set $x_i(k) = x_{i,n}'$,and calculate the value of objective function $f(k)$.

if $f(k) < f^*$, then $f^* = f(k)$, $x_i^* = x_i(k)$;

if $f(k) \ge f^*$,then abandon $x_i(k)$

$k = k+1$ where k =iterative number

FINITE ELEMENT METHOD

A 2-D FEM is perfect to a 3-D FEM because the overhang leakage flux of the motor is relatively significant while the corresponding computation program and time are much shorter. The x-y plane is selected as the cross section of the motor and the z-axis is along its axial direction. Thus, the nonlinear partial differential equation and boundary conditions for this motor are given by

$$\begin{cases} \Omega : \dfrac{\partial}{\partial x}\left(\dfrac{1}{\mu}\dfrac{\partial A_z}{\partial x}\right) + \dfrac{\partial}{\partial y}\left(\dfrac{1}{\mu}\dfrac{\partial A_z}{\partial y}\right) = -J_z \\ \Gamma_1 : A_z = 0 \\ \Gamma_2 : A_z = 0 \end{cases} \qquad (6)$$
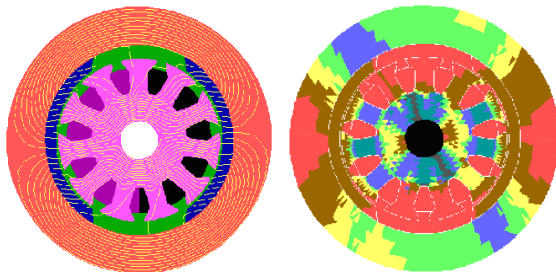
Fig. 1. Distributions of magnetic field
and flux density at load
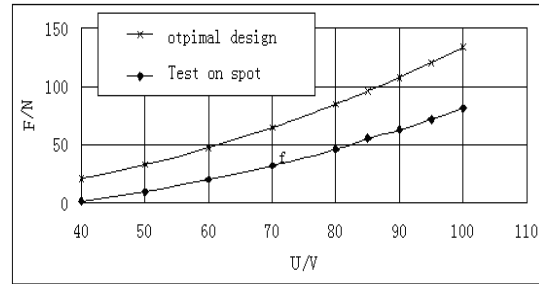
Fig.2 Thrust of underwater thruster
at different voltage

NUMERAL SIMULATION

Owing to starting directly at rated voltage 90V, the starting current is 28 times as high as the rated current, the peak current reaches 140A, thus, the motor is easy to be damaged as well as its gearing. How to choose starting reasonably is necessary. By setting up the numeral simulation model, the two starting methods are considered.
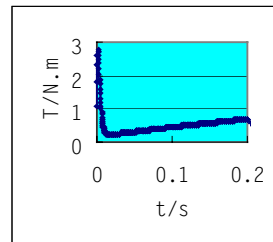
Fig.3. Starting by decreasing

Voltage
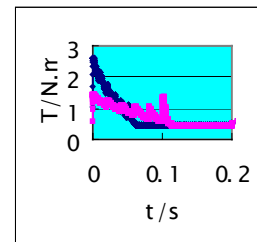
Fig.4.Starting under resisters

in series

CONCLUSION

In this paper a hybrid method for global minimization of function with continuous and discrete variables based on Alopex and chaotic algorithms has been presented. This optimization technology has been demonstrated on multimodal functions and applied to design of a series of underwater thruster motors.

REFERENCES

[1] K.F. Man, K.S.Tang and S. Kwong, Genetic algorithms, concepts and designs, Springer Verlag, London 1999, ISBN 1852330724.

[2] E Aarts and J. Korst, Simulated annealing and Boltzmann machines, John Wiley & Sons, Chichester 1989, ISBN 0471921467.

[3] Pandya A.S.," A stochastic parallel optimization algorithm", Ph. D. Dissertation. Syracuse University (U.S.A.). 1988

An Optimization Design Method for Enhancing Efficiency of PM Motor by Using Voltage Driven Finite Element Method with Adjusting Supply Voltage

Shinya Matsutomo[1], So Noguchi[1], Hideo Yamashita[1], Shigeya Tanimoto[2]

1) Graduate School of Engineering, Hiroshima University, 1-4-1 Kagamiyama, Higashihiroshima, 739-8527, Japan
2) Manufacture Engineering Research Center of Toshiba Corporation, 33 Shin-isogo-cho, Yokohama, 235-0017, Japan
E-mail: yama@eml.hiroshima-u.ac.jp

Abstract — In this paper, we propose the adjusting technique of the supply voltage of permanent magnet motor when carrying out the optimal design by finite element method and genetic algorithm. In calculation for the optimal design, it is difficult to keep a desirable balance of the supply voltage and the induced electromotive force. By using the proposed method, the supply voltage is appropriately decided to generate the rated torque. Owing to adopting this adjusting technique, the computation time of optimal design can be reduced and the solution can escape from local minima because the needless computation can be drastically reduced.

I. INTRODUCTION

The total amount of electric power consumed by motors is more than 50% of the whole electric power in Japan. In recent years, from the point of view of energy saving, it is desired to improve the efficiency of motors. Furthermore a high-power and highly efficient motor is desired for electric vehicle (EV), electrical machinery and so on.

Therefore it is necessary to improve properties (e.g. efficiency) of permanent magnet (PM) motors by applying an optimal design method. In the conventional optimimal design methods (e.g. [1]), the simplified model was dealt with in order to shorten calculation time; for example, the magnitude of the load current was decided or the waveform of the load current was assumed to be sinusoidal. In these methods it is impossible to obtain enough accurate results about the motor properties such as torque and loss and it is also impossible to consider the drive circuit of motor. Therefore, in this paper, the voltage driven finite element method is adopted to take into consideration the drive circuit of motor. However in the calculation for the optimal design, it is difficult to keep a desirable balance of the supply voltage and the induced electromotive force. In order to solve this problem, we propose the adjusting technique for supply voltage of permanent magnet motor when carrying out the optimal design for enhancing efficiency of PM motor. By using the proposal method, the supply voltage can be appropriately changed to generate the rated torque, so that the computation time of optimal design can be reduced even when to consider the drive circuit of motor.

II. OPTIMAL DESIGN OF PM MOTOR

In optimal design of PM motor, it is desirable to take into account the electric circuit and the magnetic circuit of the PM
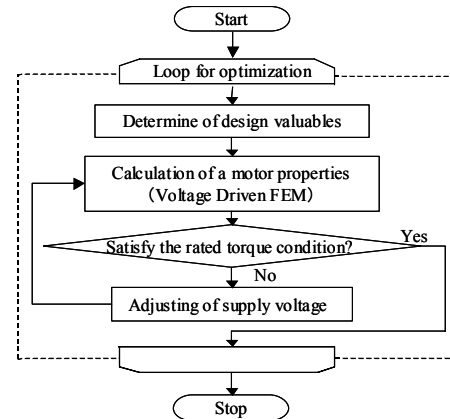
Fig. 1. Flowchart of the optimal design for PM motor
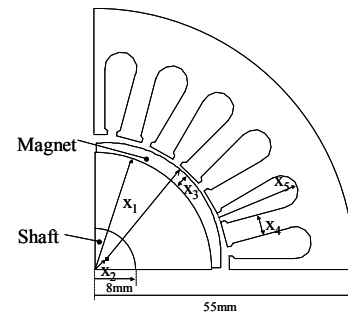
Fig. 2. Design variables for shape of SPMSM

motor at the same time. A useful method in such a case is to adopt the voltage driven finite element method [2][3]. However, this method needs to input a supply voltage to analyze the properties of motor, and the supply voltage to generate a rated torque can't be decided at design stage. Therefore a desirable balance of the supply voltage and the induced electromotive force can't be kept. If the supply voltage is too high, the generated torque is larger than the rated torque. From this reason, many useless computations for analyzing the properties of PM motor are performed in searching the global optimal solution.

In order to solve this problem, we propose a method to determine the supply voltage of the PM motor at the optimal design stage. Figure 1 shows a flowchart of the proposed optimization process. In the proposal method, the supply voltage is adjusted to generate the rated torque. Since the torque is almost proportional to the supply voltage, the

adjustment of the supply voltage is possible by performing the calculation a few times. As a result, during the optimization process, it is able to compare the specifications of motor under the condition that the torque is rated.

III. MODEL OF PM MOTOR TO BE OPTIMIZED

The model of Surface PM Synchronous Motor (SPMSM) for optimal design is shown in Fig.2. The number of design variables in this model is nine in all; five variables are shown in Fig. 2, the other three are the length of motor, the number of turns of winding and the diameter of wire. Furthermore the phase of a supply voltage is treated as a design variable, because it is impossible to specify an optimal torque angle beforehand. The rated torque in this model is 1.7[Nm] at 2400[rpm]. The maximum permissible torque ripple is 5% of the rated torque. And the genetic algorithm was adopted as an optimization method.

IV. RESULT

For verification of the proposed method, the SPMSM was optimized. Figure 3 shows that the plots of torque at every generation of GA are widely distributing in the case using the ordinary method. The white circles represent the effective
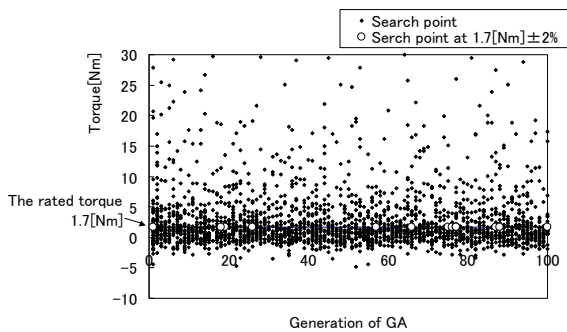
Fig. 3. Distribution of torques at every generation of GA by using the non-proposed method
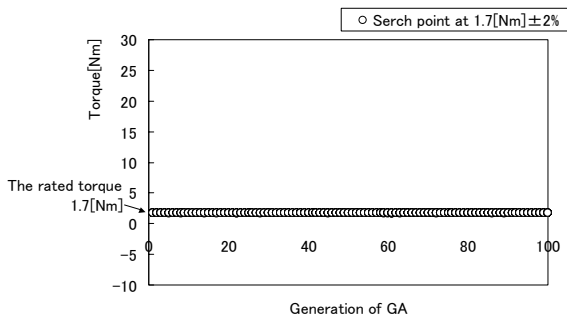
Fig. 4. Distribution of torques at every generation of GA by using the proposed method

calculation at the rated torque. While, the dots represent the useless calculation at the non-rated torque. The number of dots is mush lager than that of the circles, that is, the ordinary method spent much unnecessary computation time. It is because the matching of the supply voltage and the induced electromotive force could not be taken. The efficiency of the optimized SPMSM is 90.12% and the calculation time was 36 hours (Pentium4, 2.0 GHz) in this case (see Table I).

On the other hand, in the case of adjusting the supply voltage, the efficiency of the optimized SPMSM is 97.17% and the calculation time was 25 hours (see Table I). In Fig. 4, the plots of torque are concentrated on the line of the rated torque. By using the proposed method, the calculation time can be shortened because the time for needless numerical calculations" can be reduced drastically. The magnetic flux density distribution of the optimized SPMSM is shown in Fig .5.

As a result, the performance of the proposed method was better than that of the non-adjusted supply voltage method.

TABLE I. Characteristics of Optimized SPMSM

	Non-adjusting supply	Adjusting supply
Rated torque	1.72 [Nm]	1.70 [Nm]
Output power	720 [W]	712 [W]
Cupper loss	39.81 [W]	7.98 [W]
Iron loss	39.20 [W]	12.75 [W]
Torque ripple	0.17 [Nm]	0.11 [Nm]
Load current	14.75 [A]	4.88 [A]
Supply voltage	99 [V]	121 [V]
Efficiency	90.12 [%]	97.17 [%]
Calculation time	36 [h]	25 [h]
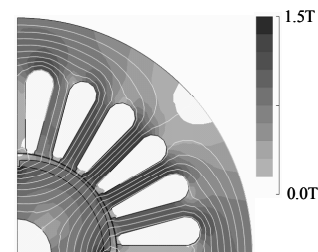
Fig. 5. Magnetic flux density distribution and flux lines in optimized SPMSM

REFERENCES

[1] Y. Hosokawa, S. Noguchi, H.Yamashita and S. Tanimoto, "An Optimal Design Method for Efficiency of Permanent Magnet Motors" *T.IEE Japan,* vol. 121-D, no.2, pp. 171-177, 2001.
[2] T. Nakata, N. Takahashi, "Direct Finite Element Analysis of Flux and Current Distributions Under Specified Conditon", *IEEE Trans. Magn.,* vol. MAG-18. no. 2, pp. 325-330,1982.
[3] V. Cingoski, M. Mikami, H. Yamashita and K.Inoue, "Computer Simulation of three-phase Brushless Self-Excited Synchronous Generator", *IEEE Trans. Magn.,* vol. 35. no. 3, pp. 1251-1254,1999.

Analysis and Optimization of Photonic Crystal Fibers by the FEM/GA Technique

Rui Yang[1], Yilong Lu[1] [†], and Erping Lee[2]

[1] Nanyang Technological University, Singapore 639798
[2] Institute of High Performance Computing, Singapore 117528
[†] Corresponding author: eylu@ntu.edu.sg

Abstract--An efficient full-wave numerical analysis for photonic crystal fibers is achieved by finite element method using hybrid edge/nodal elements with triangular shapes. Genetic algorithms are proposed with a view to optimize the geometrical parameters to get desired dispersion and polarization parameters of these fibers.

Index Terms--Finite Element Methods, Genetic Algorithms, Photonic Crystal Fibers.

I. INTRODUCTION

OPTICAL fibers and integrated optical waveguides are finding wide use in areas covering telecommunications, sensor technology, spectroscopy, and medicine. Photonic crystal fibers (PCFs) have attracted a lot of intension recently because of their unusual optical properties such as extra large chromatic dispersion, a wide range single mode operation [1-2]. The complex nature of the cladding structure of the PCFs does not allow for the direct use of methods from traditional fiber theory. Especially for the novel PCF, operating by the photonic band gap (PBG) effect, the full vectorial nature of the electromagnetic waves has to be taken in account.

A PCF usually consists of a hexagonal arrangement of air holes running down the length of a silica fiber surrounding a central core of solid silica or, in some cases, air. PCFs can exhibit a number of unique properties, including zero dispersion at visible wavelengths and low or high effective nonlinearity. By varying the size of the holes and their number and position, one can also design PCFs with carefully controlled dispersion and modal properties.

In this paper, we present finite element magnetic and electric field models for determining the propagation modes in dielectric wave guiding structures. A combination of edge elements for the transverse field and nodal elements for the longitudinal field is used together with Perfect Match Layer (PML) to cope with the open domain.

Genetic algorithms (GAs) are stochastic search and optimization techniques modeled on the mechanics of biological genetics and natural evolution. Based on FEM solver mentioned previously, we employ GAs to achieve accurate and optimal design of PCFs.

II. FEM FORMULATION

To analyze electromagnetic wave propagation in an inhomogeneous wave guiding structures, the finite element method is employed in the framework of the Galerkin formulation of the weighted residual method to solve the vector Helmholtz equation:

$$\nabla \times \frac{1}{\mu_r} \nabla \times \mathbf{E} = k_0^2 \bar{\varepsilon}_r \mathbf{E} \qquad (1)$$

where $\bar{\varepsilon} = \varepsilon + \sigma /(j\omega)$ and ε and σ represent the permittivity and conductivity, respectively, of dielectric materials. $k_0^2 = \omega^2 \mu_0 \varepsilon_0$ and $\bar{\varepsilon}_r = \bar{\varepsilon}/\varepsilon_0$. Assuming for all of the field components the dependence from the spatial coordinate z of the form $\exp(-\gamma z)$, with $\gamma = \alpha + j\beta$ as the complex propagation constant, and subdividing the electric field into its transverse ($\mathbf{E}_t$) and longitudinal (E_z) parts, we get:

$$\mathbf{E}(x,y,z) = [\mathbf{E}_t(x,y) + \hat{z} E_z(x,y)]e^{-\gamma z} \qquad (2)$$

Substituting (2) into equation (1), and splitting it into its transverse and longitudinal parts, we can get:

$$\nabla_t \times (\frac{1}{\mu_r} \nabla_t \times \mathbf{e}_t) - \gamma^2 \frac{1}{\mu_r}(\nabla_t e_z + \mathbf{e}_t) = k_0^2 \bar{\varepsilon}_r \mathbf{e}_t \qquad (3)$$

$$\gamma^2 \nabla_t \times [\frac{1}{\mu_r}(\nabla_t e_z + \mathbf{e}_t) \times \hat{z}] = \gamma^2 k_0^2 \bar{\varepsilon}_r e_z \hat{z} \qquad (4)$$

where $\mathbf{e}_t = \gamma \mathbf{E}_t$ and $e_z = E_z$.

To apply the weighted residual procedure, two sets of basis functions and two corresponding sets of weighted functions have to be defined. Since the Galerkin formulation is adopted, each set of weighting functions is equal to the corresponding set of basis functions. We use the vectorial shape functions $\boldsymbol{\alpha}_i^{(e)}$ as the set of basis function to express the approximate $\bar{\mathbf{e}}_t^{(e)}$ to the exact transverse part $\mathbf{e}_t$ of the electric field on the element (e), and we use the nodal shape functions $\alpha_i^{(e)}$ to express the approximate $\bar{e}_z^{(e)}$ to the exact longitudinal

component e_z of the electric field on element (e). By using the finite element expansion of the unknown field on element (e), we substitute these approximations into (3)(4) and annihilate the residue, we can get:

$$\begin{bmatrix} 0 & 0 \\ 0 & \frac{1}{\mu_r}\left[S_t^{(e)}\right]-k_0^2\bar{\varepsilon}_r\left[T_t^{(e)}\right] \end{bmatrix}\begin{bmatrix} \left[\bar{E}_z^{(e)}\right] \\ \left[\bar{E}_t^{(e)}\right] \end{bmatrix}$$
$$= \gamma^2 \begin{bmatrix} \frac{1}{\mu_r}\left[S_z^{(e)}\right]-k_0^2\bar{\varepsilon}_r\left[T_z^{(e)}\right] & \frac{1}{\mu_r}\left[G^{(e)}\right]^T \\ \frac{1}{\mu_r}\left[G^{(e)}\right] & \frac{1}{\mu_r}\left[T_t^{(e)}\right] \end{bmatrix}\begin{bmatrix} \left[\bar{E}_z^{(e)}\right] \\ \left[\bar{E}_t^{(e)}\right] \end{bmatrix} \quad (5)$$

where the entries of the local matrices are given in [3]. After assembling all elements and zeroing the residuals, we can get the final generalized eigenvalue problems. Once the normalized operating frequency k_0 is fixed, we can compute the propagation and attenuation constants of the characteristic modes of the guiding structures.

III. FEM/GA Optimization Design Approach

Any genetic algorithm should consist of following basic operations: a) construction of chromosomes, b) initial population, c) mating, d) crossover, e) mutation, f) fitness evaluation}, and g) survival selection, etc. The detailed description of the efficient GA can be found in [4]. The optimization progress of the GA is illustrated by the flow chart in Fig. 1.
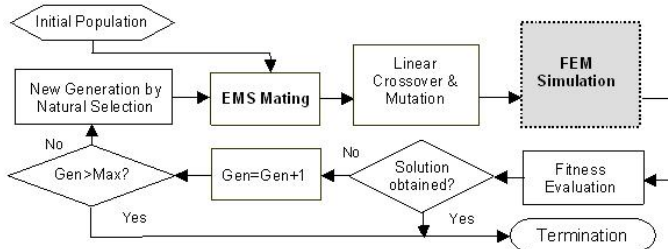
Figure 1 The flow chart of the FEM/GA optimization algorithm.

Unlike most GAs using binary coding and binary genetic operations, the proposed approach applies direct expression of original decimal parameters, i.e., a chromosome is just a real number or complex number vector associated with the model. For PCFs, the structures of a chromosome for the fiber design optimization are just the number, location, and the size of the holes. The mating scheme plays a very important role on the convergence and robustness of a GA. There are various mating schemes. After extensive comparative study, we have found that the Emperor-Selective (EMS) scheme is more effective than many other popular ones such as Roulette Wheel, Tournament Selection, Adjacent-Fitness-Pairing, etc. EMS mating scheme allows the fittest individual to procreate freely with virtually the rest of the population, resulting in a greater diversity and faster convergence.

IV. Preliminary Results And Conclusion

Here we specifically analyzed this kind of photonic crystal fibers, which have several rings of air holes around the core. In Fig. 2., the geometry of PCFs with a ring and two rings of six airs holes is given. In Fig. 3 the calculated propagation constant verse working frequency band is plotted. Where the dotted line, is just the main propagation mode of common circular air waveguide. The solid line is when there are several rings of air holes around the core, no matter how many rings around the core; there is almost no any difference. Because that the most part of the transmission power are confined in the area inside the first ring. The effect of holes to the propagation properties will be presented in more details at the conference and the full paper.
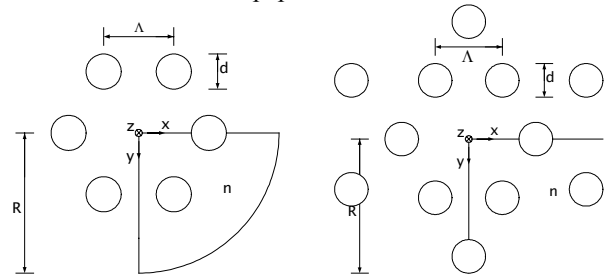
Figure 2 PCFs with a ring and two rings of air holes
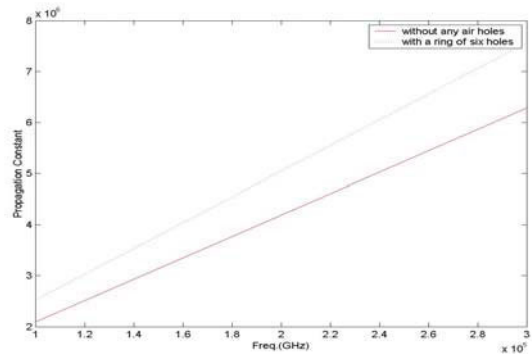
Figure 3 Frequency VS Propagation Constant

Based on this efficient analysis method, we can carefully study the unusual optical properties of PCFs. We can optimize the design of the geometry of PCFs by using FEM/GA optimizer. More results for optimized design will be presented at the conference and in the extended paper.

References

[1] J. Broeng, "Photonic Crystal Fibers: A New Class of Optical Waveguides". Optical Fiber Technology **5**, pp. 305-330, 1999.

[2] A. Bjarklev. and J. Riishede, "Photonic crystal fibers - a variety of applications". Proceedings of the 2002 4th International Conference on Transparent Optical Networks, Vol. 2, pp.97 –97, 2002.

[3] M. Koshiba and K. Inoue, "Simple and efficient finite-element analysis of microwave and optical waveguides". Microwave Theory and Techniques, IEEE Transactions on, Vol. 40, pp. 371-377, 1992.

[4] B. K. Yeo and Y. Lu, "Array failure correction by using the genetic algorithm," IEEE Trans. on Antennas and Propagation, Vol. 47, pp.823-828, 1999.

Interface Reconstruction Between Two Conducting Fluids Applying Genetic Algorithms

Marek Ziolkowski[1,2], Hartmut Brauer[1], Milko Kuilekov[1]

[1] Technische Universitaet Ilmenau, Helmholtzplatz 2, D-98684 Ilmenau, Germany

[2] Technical University of Szczecin, Sikorskiego 37, PL-70313 Szczecin, Poland

e-mail: marek.ziolkowski@tu-ilmenau.de

Abstract—- **In magnetic fluid dynamics appears the problem of reconstruction of free boundary between conducting fluids, e.g. in aluminum electrolysis cells. We have investigated how the interface between two fluids of different conductivity of a highly simplified model of an aluminum electrolysis cell could be reconstructed by means of external magnetic field measurements using simple genetic algorithm.**

INTRODUCTION

There are a variety of problems in material processing where it would be useful to know the time-dependent distribution of the electrical conductivity of a single fluid or a multiphase flow. For instance, the knowledge of the position of the interface between highly conducting molten aluminum and poorly conducting liquid cryolite is important to prevent unwelcome instabilities in aluminum reduction cells [1].

The purpose of the present work is to demonstrate that concepts of *Magnetic Field Tomography (MFT)* which have been successfully applied to a variety of problems in *biomagnetism* can be used in order to detect interfaces between current carrying fluids of different electrical conductivity. We demonstrates that the external magnetic field generated by the electrical current flowing through a highly simplified model of an aluminum reduction cell provides sufficient information to reconstruct the unknown interface shape.

HIGHLY SIMPLIFIED CELL MODEL

If we consider typical figures of aluminum electrolysis cells it must be noticed that the cross section has a length of about $L = 8m$, whereas the interface displacement is very small compared to the lateral extent of the system. Industrial practice shows that already such small interface displacement can perturb significantly the operation of the cell [2]. Consequently, our physical model is characterized by a very small ratio η/L.

The considered problem is shown in Fig. 1. Two fluids with different electrical conductivity σ_1 (upper) and σ_2 (lower) are situated in a long cylinder with the radius R. The cylinder walls are nonconducting. Along the length axis of the cylinder a homogeneous electrical current density $\mathbf{J_0}$ is applied.
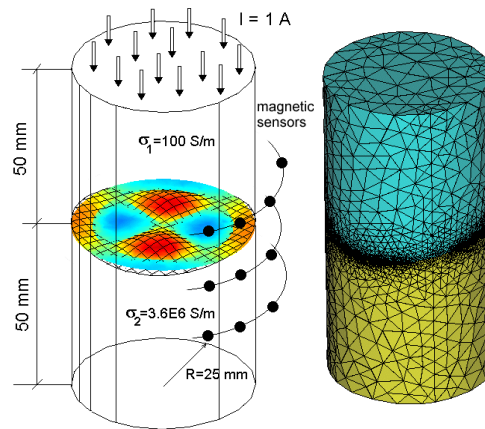
Fig. 1. Aluminum electrolysis cell model with a non-axisymmetric interface and FEM model used in forward calculations.

The complete interface perturbation can be found solving the Euler equation and the mass conservation law as

$$\eta(r,\alpha) = \sum_{m=-M}^{M} \sum_{n=1}^{N} \eta_{mn} J_m(k_{mn}r) e^{jm\alpha} \qquad (1)$$

The value n is called the radial mode number and the value m the azimuthal mode number. Although the quantity of modes is usually unlimited, the highest modes have the smallest amplitudes and can be neglected.

The validity of the above interface representation is limited by the amplitude of the interface oscillations. We consider only small interface oscillations because the larger interface oscillations lead to instabilities due to drop formation [2].

MAGNETIC FIELD MODELING

If the interface between fluids is flat, the current density $\mathbf{J}$ is homogeneous everywhere. As soon as the interface deviates from its flat shape due to interfacial waves or an external forcing, the current density $\mathbf{J}$ will become inhomogeneous near the interface (Fig. 2).
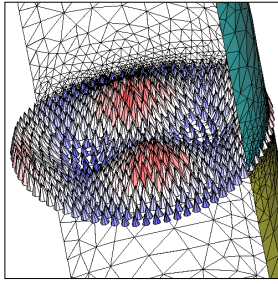
Fig. 2. Distribution of current density 0.5 *mm* under the interface.

The inhomogeneity of **J** can be represented by the perturbation current density **j**. If the perturbation of the fluid interface is non-axisymmetric, it leads to a perturbation of the magnetic field outside the cylinder. This fact is used for the interface reconstructions.

To model the magnetic field we have calculated first the current density distribution in the cylinder using FEM method or the semi-analytical approach described in [3, 4]. Then using the Biot-Savart law:

$$\mathbf{b}(\mathbf{r}) = \frac{\mu}{4\pi} \int_V \frac{\mathbf{j} \times (\mathbf{r} - \mathbf{r}')}{|\mathbf{r} - \mathbf{r}'|^3} dV' \qquad (2)$$

we have calculated the magnetic flux density in the sensors area. Fig. 3 shows the distribution of magnetic flux density components (B_r, B_z) on the evolved cylindrical surface of the radius 10 *mm* greater than the cell with fluids (*R*=25 *mm*)
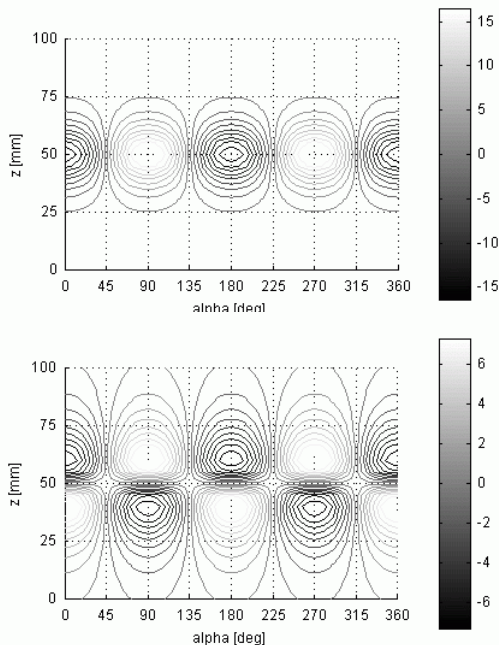
Fig. 3. Distribution of magnetic flux density (B_r - top, B_z – down, in [*nT*]) produced by mode 22.

To reconstruct the interface between two fluids we have applied a simple genetic algorithm (GA) [5]. As an example we have reconstructed the shape of the pure mode η_{22}. We have restricted the search space to the 12 parameters consisting of amplitudes of the interface perturbation given by (1), where *m*=1…4 and *n*=1…3. The simulated magnetic field has been calculated around cylinder at the radius 35 *mm* in 16x7 equally distributed positions. As an objective function we have used a sum of squared differences of B_r and B_z produced by the actual individual and the original field in the sensors positions. The perfect result of reconstruction is shown in Fig. 2. In that case, the population size was equal 60, the mutation probability 0.01 and the crossover one point probability 0.6.
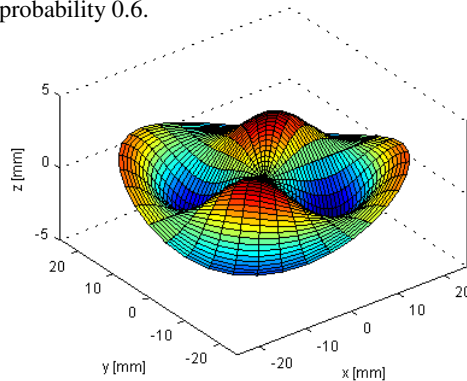
Fig. 4. Shape of reconstructed interface (mode 22).

CONCLUSIONS

We have shown that it is possible to reconstruct the shape of the interface between two fluids on the basis of magnetic flux density measurements using simple GA. In the full paper, we would like to present the reconstruction of hybrid modes and the influence of the noise on the quality of reconstruction.

REFERENCES

[1] P.A.Davidson, "Magnetohydrodynamics in material processing," *Annu. Rev. Fluid Mech.,* vol. 31, pp. 273-300, 1999.
[2] J. Miles, and D. Henderson, "Parametrically forced surface waves," *Annu. Rev. Fluid Mech.,* vol. 22, pp. 143-165, 1990.
[3] A. Kurenkov, and A. Thess, "Reconstruction of interfaces between electrically conducting fluids from electrical potential measurements," 4th Int. Conf. of Magnetohydrodynamics, Giens/France, September 2000, Proc. vol. 1, pp. 45-50, 2000
[4] H. Brauer, M. Ziolkowski, M. Dannemann, M. Kuilekov, D. Alexeevski, „Forward Simulations for Free Boundary Reconstruction in Magnetic Fluid Dynamics," 10th IGTE Symposium, Graz, 2002.
[5] Z. Michalewicz, *Genetic Algorithms + Data Structures = Evolution Programs*, 3rd ed., Springer Verlag, Berlin, Heidelberg, New York, 1996.

Optimal Design of Brushless DC Motor for Electric Wheel Chiar using Parallel Genetic Algorithm

Cheol-Gyun Lee, Mi-Hyun Kang, Hyun-Kyo Jung*, T.A. Lipo**

Dept. of Eelctrical Eng.
Dong-eui Univ.
Mt. 24 Gaya-dong, Busanjin-gu
Busan, KOREA 614-714
cglee@dongeui.ac.kr

*School of Elec. and Comp. Eng.
Seoul Nat. Univ
Shinlim-dong, Gwanak-gu
Seoul 614-714, Korea

**Dept. of Elec. and Comp. Eng.
Univ. of Wisconsin-Madison, Madison
1415 Engineering Drive
Madison, WI 53706, USA

Abstract – **Parallel genetic algorithms (PGAs) have been developed to reduce the large execution times that are associated simple genetic algorithms (SGAs). They can also be used to solve larger problems and to find better solutions in single processor. In this paper, we use a particular kind of parallel GA, called coarse-grain GA as an optimization algorithm. To verify its validity, this method is applied to some traditional mathematical problems. The optimal design of a brushless DC motor using PGA is presented.**

INTRODUCTION

In the area of design of traction motor for electric wheel chair, the weight and the efficiency of the traction motor is very important because of the limitation of electric power from batteries. The high starting torque for good acceleration and low manufacturing cost are also required. Therefore, many aspects have to be considered in designing traction motor for electric wheel chair. To meet these requirements at once the optimal design is needed than the experience of the motor designer.

Genetic algorithms (GAs) are a promising search heuristic for finding near-optimal solutions in large space. GA's are now widely recognized as an effective search paradigm in artificial intelligence, image processing, VLSI circuit layout, solving non-linear equations, optimization of electric machine design, and many other areas. But in case of the optimization problems that have many design variables, such as the design of Brushless DC motor, the conventional GA's fall into a trap of local minima with high probability. This problem is called premature convergence problem. To overcome this problem, the parallel genetic algorithm is introduced in this paper. Originally parallel genetic algorithms (PGAs) using multiple processors have been proposed to reduce the large amount of computation time associated with simple genetic algorithms (SGAs). But they can also be used to solve larger problems and to find better solutions in single processor.

In this paper, we use a particular kind of parallel GA, called coarse-grain GA's, which aid in global search and retard premature convergence [1]. Coarse-grain GA's maintain multiple and independent populations with occasional interchange of solutions between these populations. And new techniques for genetic operator are introduced to advance the characteristic of parallel GA.

PARALLEL GENETIC ALGORITHM

To avoid premature convergence problem in GA many researches have been proposed. Of course, a parallel GA may be seen as a particularly natural and efficient version of such researches. There are three main types of parallel GA: (1) global single-population master slave GA, (2) single population fine-grained, and (3) multiple-population coarse-grained GA. A multi-population parallel GA called coarse-grained GA is very popular. It uses several subpopulations which evolve independently from each other for a certain number of generation and exchanges individual occasionally [2]. Fig. 1 is the structure of coarse-grained GA. To advance the characteristic of parallel GA, we introduce real-coded algorithm, scaling window and elitism.

NUMERICAL EEXAMPLES

Two test functions are used to compare the performance of
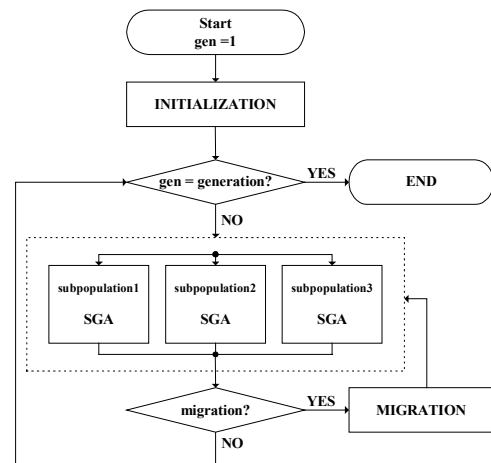
Fig. 1. Structure of coarse-grained GA

simple and parallel GA. The first is a two-dimensional function

and the second is four-dimensional function. Both of them have a minimum value at x=1. The functions are specified by the following equations:

$$F_2(x) = 100(x_1^2 - x_2^2) + (1 - x_1)^2, \quad -2.047 \le x_1, x_2 \le 2.048 \quad (1)$$

$$F_4(x) = 100(x_1^2 - x_2^2) + (1 - x_1)^2 + 90(x_4 - x_3^2) + (1 - x_3)^2$$
$$+ 10.1\{(x_2 - 1)^2 + (x_4 - 1)^2\} + 19.8(x_2 - 1)(x_4 - 1)$$
$$\text{, where } -10 \le x_1, x_2, x_3, x_4 \le 10 \quad (2)$$

We run each algorithm 50 times on test functions and average the searched result. The parallel GA has three sub-populations. So the size of sub-populations for PGA is one-third of SGA. The iteration of generation is 2000. Table I summarize all results. Fig. 2 is the comparison of convergence to F4 test function at two algorithms. As shown Table I and Fig. 2, PGA works better than SGA especially in four-dimensional function. PGA found the lower minimum value of test function and converged it faster than SGA for the high dimensional problem.

TABLE I. PERFORMANCE COMPARISON

	SGA	PGA
F2	0.00000	0.00000
F4	0.00558	0.00138
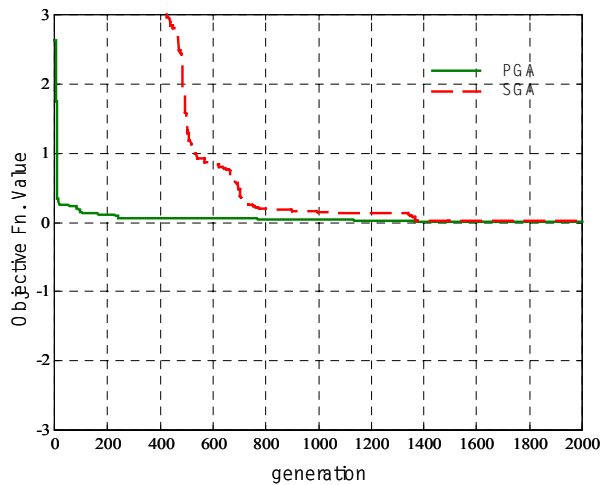
Fig. 2. Convergence comparison for F4 test function

OPTIMIZATION OF BLDC MOTOR DESIGN

Now, the proposed parallel method is applied to the optimal design of BLDC motor for electric wheel chair. The first step of optimization is a design synthesis of BLDC motor. The synthesis is a procedure for producing the motor on the basis of a set of design variables, other design data, and the motor specification. We select the five independent design variables

consisting of one maximum flux density for the stator and rotor punching and four geometric variables. Four geometric variables are the stator outside radius, motor axial length, rotor outside radius and the depth of rotor magnet. Air gap length and stator slot opening are dictated by mechanical considerations.

The designer of traction motor for electric wheel chair should try to design lower weight motor in order to improve driving performance, running distance and low material cost. From the above result, the weight of a motor is selected for the objective function of optimal design. And the other characteristics such as the efficiency of motor are selected as a constraint of optimization. The 210[w], 4-pole, three-phase BLDC motor for electric wheel chair is designed as a sample design. The rated speed is 2,500[rpm] and battery voltage is 24[V]. Fig. 3 is the convergence characteristics of motor weight. Through the optimal design, we reduce the weight of motor by 23[%]. It is being manufactured for test.
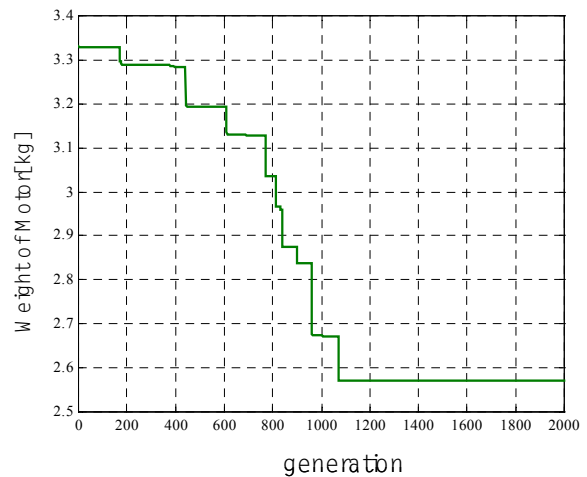
Fig. 3. Convergence characteristics of motor weight

CONCLUSION

To overcome the premature convergence problem, an advanced parallel GA is introduced in this paper. We showed that parallel GA works better than simple GA especially in high dimensional problem which fall into a trap of local minima with high probability. Through the application of parallel GA to optimization of BLDC motor design for electric wheel chair, we designed lighter motor.

REFERENCES

[1] E. Cantu-paz, "Survey of Parallel Genetic Algorithm", Techinal Report. Illinois Genetic Algorithm Laboratory, 1997.
[2] S. Oh, C. Kim and J. Lee, "Balancing the Selection Pressures and Migration Schemes in Parallel Genetic Algorithm for Planning Multiple Pathss", Proceeding of the 2001 IEEE Int. Conf. On Robotics and Automation, Seoul, Korea, pp.3314-3319, 2001.

Robust Design of MR Head to Minimize Side-Fringing and its Variation Using Finite Element Method and Response Surface Methodology

H. T. Wang, Z. J. Liu, Y. H. Wu, and D. You

Data Storage Institute, 5 Engineering Drive 1, Singapore 117608

wanght@dsi.a-star.edu.sg

Abstract—The fringing field of the write element of the merged magnetoresistive (MR) head is minimized while restraining its deviation due to uncontrollable factors such as variability in material properties. Finite Element Method (FEM) is applied in combination with Response Surface Methodology to search for the robust solution. The influence of the geometrical parameters of MR head on the fringing field and its deviation is investigated.

INTRODUCTION

With the demand for increased recording density of Hard Disk Drive, it is necessary to design high performance MR head with narrow track width and minimum side-fringing. A merged MR head with trimmed shared pole can reduce side-fringing field and therefore improve off-track performance while keeping well-defined narrow track width [1][2].

It is obviously inadequate to search for an optimal design by conventional optimization technique if the design is very sensitive to perturbations of its parameters. Compared to traditional optimization techniques, the robust design provides a solution to achieve not only the optimal target but also reduce the its sensitivity to noise factors, which may be caused by the variability due to manufacturing or environmental conditions [3]. Response Surface Methodology (RSM) [4] is a set of statistical methods and can be used for conducting experiments, analyzing experiments' results and searching optimal solution in engineering design.

In the present work, Finite Element Method (FEM) is utilized to simulate the side-fringing field of MR head. To achieve robustness of MR head, RSM is introduced and applied together with the concept of Orthogonal Array (OA) for conducting noise factor settings [5], and Signal-to-Noise (S/N) [5] to evaluate the performance and its deviation.

DESCRIPTION OF DESIGN PROBLEM

A part of the write element of the MR head with trimmed shared pole is shown in Fig. 1. The thickness of trimmed pole is 2μm, the width of trimmed pole is 16μm, the inner throat height of shared pole is 0.25μm, P2W and P3W are 0.27μm, the height of P2 is 2.5μm and the length of air-gap is 0.1μm. In the present work, the dimensions of trimmed shared pole, P2, and P3 are investigated as the design parameters. The objective of this study is to reduce the side-fringing field in order to obtain narrower track width.

Selection of quality characteristic, and design parameters

In this study, the inner trimmed height of shared pole, h, the trimmed depth of shared pole, w, the depth of P2, $p2d$ and the height of P3, $p3h$, are selected as design parameters (Control factors). The B-H properties of soft material for the pole and the width of P2, $p2w$, are the noise factors due to fabrication variability. The objective is to reduce the side-fringing field; therefore the displacement of certain point, in which the field intensity is less than one time of the medium coervicity, is considered as the quality characteristic (response).
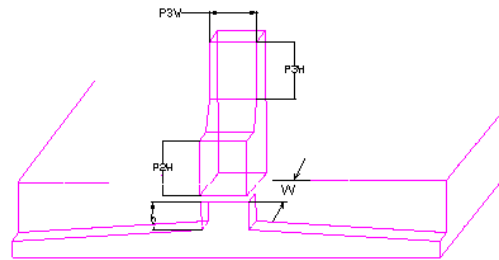
Fig. 1 a partial design of MR head with trimmed shared pole

DESIGN METHOD AND ANALYSIS

Response Surface Methodology (RSM)

At this stage, RSM is applied to conduct design of experiments, analyze the results and search for the robust solution. It is designed to quantify the relationship between the values of some measurable response values and those of a set of experimental factors presumed to affect the response, and find the values of the factors that produce the best value of the response. A polynomial presentation of a response surface could be written as a first-degree model or a second degree one, even higher. A second-degree model presented in this paper is described as Equ. 1.

$$y = \beta_0 + \sum_{i=1}^{n} \beta_i x_i + \sum_{i=1}^{n} \sum_{j=i}^{n} \beta_{ij} x_i x_j + \sum_{i=1}^{n} x_i^2 \qquad (1)$$

By linear regression, the coefficients in the above equation can be obtained and therefore the response is quantified with the values of experimental factors. The solution of factors, which will produce the best value of the response, can be calculated.

Design of Experiments and Simulation

The central composite design (CCD) is applied to construct the second order polynomial model. In the study the nominal values of h, w, $p2d$, and $p3h$ are 0.25μm,

3.5μm, 0.5μm, and 2.5μm respectively. The values for one unit of coded factor level are also resumed to 0.03μm, 0.2μm, 0.05μm, and 0.2μm respectively. The inner array of design of experiments is shown as Table 1. For noise factors, the BH properties with 5% tolerance and *p2w* with 0.2μm tolerance, the outer array of design of experiments is conducted as Table 2.

TABLE I. INNER ARRAY (Control Factors Settings)

Run	h	w	p2d	p3h	Run	h	w	p2d	p3h
1	0.22	3.3	0.45	2.3	14	0.28	3.7	0.45	2.7
2	0.22	3.3	0.45	2.7	15	0.28	3.7	0.55	2.3
3	0.22	3.3	0.55	2.3	16	0.28	3.7	0.55	2.7
4	0.22	3.3	0.55	2.7	17	0.19	3.5	0.5	2.5
5	0.22	3.7	0.45	2.3	18	0.31	3.5	0.5	2.5
6	0.22	3.7	0.45	2.7	19	0.25	3.1	0.5	2.5
7	0.22	3.7	0.55	2.3	20	0.25	3.9	0.5	2.5
8	0.22	3.7	0.55	2.7	21	0.25	3.5	0.4	2.5
9	0.28	3.3	0.45	2.3	22	0.25	3.5	0.6	2.5
10	0.28	3.3	0.45	2.7	23	0.25	3.5	0.5	2.1
11	0.28	3.3	0.55	2.3	24	0.25	3.5	0.5	2.9
12	0.28	3.3	0.55	2.7	25	0.25	3.5	0.5	2.5
13	0.28	3.7	0.45	2.3					

TABLE II. OUTER ARRAY (Noise Factors Settings)

Run	1	2	3	4
Material	95%	95%	105%	105%
P2w	0.25	0.29	0.25	0.29

Commercial FEA software ANSOFT is used to evaluate product performance, which is the side-fringing field of MR head. Fig. 2 shows the typical field intensity along the track direction. It should be noted that the point with 0.05μm displacement X is the center of gap and track.
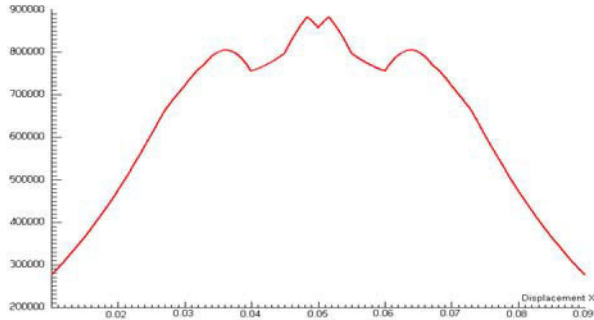
Fig. 2 A Sample of Side-Fringing Field intensity Curve (H unit: A/m, X: μm)

Linear Regression Analysis

Applying the results of simulations, the second-order

$$y = 26.71 + 0.22x_1 - 0.48x_2 - 0.34x_3 - 0.032x_4$$
$$- 0.84x_1x_2 - 0.85x_xx_2 - 0.21x_1x_4 - 0.34x_2x_3$$
$$- 0.22x_2x_4 + 0.1x_3x_4 - 0.04x_x^2 + 0.05x_2^2 - 0.09x_x^2 - 0.02x_4^2$$

(2)

regression model is fitted as Equ. 2.

It is noted that *y* presents the displacement X, x_1 represents *h*, x_2 represents w, x_3 represents *p2d* and x_4 represents *p3h*. The stationary point at *h*=0.234μm,

w=3.566μm, *p2d*=0.489μm and *p3h*=2.508μm can be searched easily. The prediction displacement X, in which field intensity is much less than one time of medium coercivity, is 0.003μm. In other words, the half of track width is only 0.094μm. Fig. 3 shows fitting response surface corresponding to h, and w.

The analysis of variance is carried out in order to check the adequacy of fitting in the design region. The result of analysis is shown in Table III.

TABLE III. ANALYSIS OF VARIANCE (ANOVA)

Source	DF	SS	MS	F	R^2	R_A^2
Regression	14	13.249	0.946	1.021	0.588	0.0121
Residual	10	9.267	0.927			
Total	24	22.516	0.938			

CONCLUSION

In the design study, the side-fringing field has been markedly reduced while keeping the response more insensitive to the variability of design parameters. Compared to the original design, which is of 2.084μm track width and 0.002748 standard deviation, the robust solution provides an optimal setting of the design parameters for high product quality. It is shown that the robust design based combined with FEM technique RSM can be used as an efficient and effective tool in engineering design.
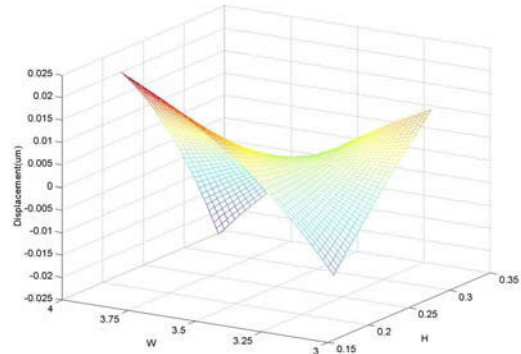
Fig. 3 Fitting Surface Model

REFERENCE

[1] Y. Guo, J. Chang and K. Ju, "Low Fringing-Field and Narrow-Track MR Heads", *IEEE Trans. Magnetics, Vol. 33, No. 5*, Sept. 1997
[2] A. M. Choukh and I. E. Kim, "Recording Performance of MR Head with Trimmed Shared Pole", *IEEE Trans. Magnetics, Vol. 32, No. 5*, Sept. 1996.
[3] H. T. Wang, Z. J. Liu, T. S. Low, S. S. Ge and C. Bi, "A Genetic Algorithm Combined with Finite Element Method for Robust Design of Actuators", *IEEE Transactions on Magnetics, Vol. 36, No. 4*, July 2000
[4] S. S. Shapiro and E. F. Mykythka, "The ASQC basic References in Quality Control: Statistical Techniques", Florida International University, 1984
[5] P. J. Ross, "Taguchi Techniques for Quality Engineering", McGraw-Hill, New York, 1996.

Modeling of Eddy Currents
in Magnetic Materials and Laminated Materials

Bernard Bandelier, Françoise Rioux-Damidau

U2R2M, Université Paris XI, UMR 8081, Bat 220, 91405 Orsay - France

e-mail: Bernard.Bandelier@u2r2m.u-psud.f

Abstract—We adapt the classical formulations in field h and e and also a mixed formulation in h, e in order to compute the eddy currents in a magnetic and/or laminated medium. The results obtained with the 3 formulations for the Joule losses are compared. We show the interest of the mixed formulation for inhomogeneous conductors.

INTRODUCTION

The computation of eddy currents by associating a FEM and a BIM can be made with different formulations using h ([2]) or e ([3]) or h and e ([4]). We here modify them in order to be abble to consider magnetic and/or laminated materials and we compare their performances.

THE FORMULATIONS

We consider a domain Ω with a boundary Γ. Ω is made of steel sheets perpendicular to Ox. The conductivity of the steel is σ and its magnetic permeability $\mu = \mu_0 \mu_r$. The conductivity of the insulating material is 0 and its magnetic permeability is μ_0. The stacking factor f is:

$$f = \frac{thickness\ of\ steel\ plate}{thickness\ of\ (steel\ +\ insulator)} \quad (1)$$

When Ω is put in a alternative source field h^s, e^s at frequency ω, it appears induced currents in it. If the steel sheets are thin enough, we may compute the electromagnetic fields e and h by treating Ω as an homogeneous anisotropic material having the following equivalent electric conductivities and magnetic permeabilities [1]:

$$\sigma_x = 0, \quad \sigma_y = \sigma_z = f\,\sigma$$

$$\frac{1}{\mu_x} = \frac{f}{\mu} + \frac{1-f}{\mu_0}, \quad \mu_y = \mu_z = \mu + (1-f)\mu_0 \quad (2)$$

We already used 3 formulations which permit to compute eddy currents in an homogeneous domain. They all associate a finite element method in Ω and a boundary element method on Γ and we finally have to solve a system

$$Ax = b. \quad (3)$$

where A is a symmetrical matrix.

We will here slightly transform our 3 codes in order to be able to use anisotropic characteristics in Ω and first of all we will briefly recall the formulations.

The h formulation **hF** *[2]*

$$\int_\Omega i\omega\mu h \cdot h' + \int_\Omega \rho\,\mathrm{curl}h \cdot \mathrm{curl}h' - i\omega\mu_0 \int_\Gamma (R\varphi)\varphi'$$
$$= i\omega\mu_0 \int_\Gamma h^s \cdot n\ \varphi' \quad (4)$$

The unknown quantities are:
- the circulations of the magnetic field h on the N_{ied} internal edges of Ω,
- the reduced potential φ at the N_v vertices of Γ.
The dof (degrees of freedom) number is $N_h = N_{ied} + N_v$.
The stiffness matrix corresponding to R is a full (N_v, N_v) matrix.
When μ and $\rho = \frac{1}{\sigma}$ are anisotropic, $\rho_x = \frac{1}{\sigma_x}$ is ∞ and it is not possible to introduce such a value in the equations. We then have to take a "great" value for ρ_x and test how are the results.

The e formulation **eF** *[3]*

$$\int_\Omega \sigma e \cdot e' + \int_\Omega \frac{1}{i\omega\mu}\,\mathrm{curl}e \cdot \mathrm{curl}e' - \int_\Gamma Z(e^r \times n) \cdot e' =$$
$$\int_\Gamma h^s \times n \cdot e' \quad (5)$$

The unknown quantities are the circulations of the total electric field e on the N_{ied} internal edges of Ω, and of the reduced electric field e^r on the $N_{\Gamma ed}$ edges of Γ.
The dof number is N_e, the total number of edges.
The stiffness matrix corresponding to Z is a full $(N_{\Gamma ed}, N_{\Gamma ed})$ matrix.

The he formulation **heF** *[4]*

$$\int_\Omega i\omega\mu h \cdot h' + \int_\Omega e \cdot \mathrm{curl}h' - i\omega\mu_0 \int_\Gamma (R\varphi)\varphi' = i\omega\mu_0 \int_\Gamma h^s \cdot n\ \varphi'$$
$$- \int_\Omega \sigma e \cdot e' + \int_\Omega \mathrm{curl}h \cdot e' = 0. \quad (6)$$

The unknown quantities are:
- the circulations of h on the N_{ied} internal edges of Ω,
- the values of φ at the N_v vertices of Γ,
- the circulations on all the N_{ed} edges of total field e.
The dof number is $N_{he} = N_{ied} + N_v + N_{ed}$.
R is the same as for **hF**.

TABLE I. JOULE LOSSES IN HOMOGENEOUS SPHERE

μ_r	$W_J^{\mathbf{ana}}$	$Q^{\mathbf{hF}}$	$Q^{\mathbf{eF}}$	$Q_e^{\mathbf{heF}}$	$Q_{curlh}^{\mathbf{heF}}$
1	5.900	1.000	1.005	1.001	1.068
4	6.089	0.992	0.994	0.993	1.059
10	3.848	0.988	0.994	0.988	1.055
40	1.264	0.985	1.103	0.986	1.051
100	0.536	0.984	1.743	0.985	1.051
400	0.138	0.984	27.500	0.985	1.051
1000	0.056	0.983	—	0.985	1.051

TABLE II. CPU IN HOMOGENEOUS SPHERE

μ_r	1	4	10	40	100	400	1000	stf
hF	45.	45.	48.	53.	58.	60.	62.	9.
eF	193.	216.	215.	246.	314.	598.	—	26.
heF	54.	63.	65.	72.	77.	80.	82.	9.

COMPARISON OF THE FORMULATIONS

We take as Ω a sphere of radius $R = 1$ m, meshed with 6192 tetrahedra, 6704 internal edges, 720 edges on Γ and 362 vertices on Γ. The dof number are $N_h = 7066$, $N_e = 7724$, $N_{he} = 14790$ and for the stiffness matrices $N_R = 362$, $N_Z = 720$.

We computed the Joule losses
- from curl$h$ with **hF**,
- from e with **eF**,
- from e and from curl$h$ with **heF**,

for an homogeneous source field. We choose the data such that the skin-depth in the steel $\delta = .89$ m and is thus very great compared to the thickness of the plates.

Joule losses in an homogeneous medium

We considered several couples μ, σ giving the same δ.

Table I gives the analytical Joule losses $W_J^{\mathbf{ana}}$ [5] and the ratio Q between the computed and analytical losses. Table II gives the CPU time used for the code and the one (stf) used for the computation of the stiffness operator.

It appears that $Q \simeq 1$ when the losses are obtained from curl$h$ with **hF** or from e with **heF**. The losses are a little not so good when obtained from curl$h$ with **heF**. Those obtained with **eF** are good only if μ_r is not too great (i.e. if σ is great enough) and when it is great the system $Ax = b$ cannot be solved; this comes from the fact that the weight of stiffness Z for **eF** becomes more important than the weight of $\int_\Omega$ in matrix A and that the computation of the stiffness Z is then not accurate enough.

Joule losses in a laminated medium

We take $\mu_r = 10$, $\delta = 89$ cm and $h^s = $HX or $h^s = $HY. As the plates are very thin and perpendicular to Ox the induced currents are to be nil for $h^s = $HY.

When using **hF**, as ρ_x cannot be infinite, we test several values of ρ_x/ρ but we compute the Joule losses by taking

TABLE III. JOULE LOSSES IN LAMINATED MEDIUM

	ρ_x/ρ	W_{Je}	W_{Jcurlh}	CPU
HX=100				
hF	10		2.61	121.
hF	100		2.61	180.
hF	1000		—	
eF		4.71		1129.
heF		2.62	2.72	238.
HY=100				
hF	10		0.06	91.
hF	100		$7.e^{-4}$	265.
hF	1000		$3.e^{-4}$	577.
hF	10000		—	
eF		0.09		1098.
heF		0.04	0.12	241.

$\sigma_x = 0$. In table III, we see that the CPU time increases with ρ_x/ρ; the solution is no more obtained (—) when ρ_x/ρ is too high. We see that, in the case of a HX field:
- The Joule losses given by **hF** and **heF** are very similar, the CPU time for **heF** being generally smaller.
- With **eF** the Joule losses are, as in the homogeneous case, very different from those given by **hF** and **heF** and CPU time is very great.

As expected, the Joule losses with a HY field are low, in particular with **hF**.

Other tests have confirmed these results.

CONCLUSION

The tests made on a homogeneous or laminated magnetic sphere embedded in a homogeneous magnetic field show that:
- **eF** is never competitive,
- **hF** and **heF** give similar results with an homogeneous sphere and the CPU time is somewhat lower for **heF**,
- **hF** and **heF** give similar results with a laminated sphere but we cannot take $\sigma_x = 0$ with **hF** and the more σ_x is small the more CPU time is great. The **heF** formulation is thus the better one in this case.

REFERENCES

[1] T. Tokumasu, S. Doi, K. Ito and M. Yamamoto, "An electric vector potential approach for 3-D electromagnetic field in turbine generator core end", *IEEE Transactions on Power Apparatus and Systems*, vol. 103, pp. 1330-1338. 1984.

[2] A. Bossavit and J. C. Vérité, "A mixed FEM-BIEM method to solve eddy currents problems", *IEEE Transactions on Magnetics*, vol. 18, pp. 431-435, 1982.

[3] M. Djennah, B. Bandelier and F.Rioux-Damidau, "Computation of electric charges and eddy currents with an e-formulation", *IEEE Transactions on Magnetics*, Vol. MAG-33, 1997, pp. 1322-1325.

[4] D. Korichi, B. Bandelier and F.Rioux-Damidau, "Adaptative 3D mesh refinement based on a two fields formulation of magnetodynamics", *IEEE Transactions on Magnetics*, vol. 36, pp. 1496-1500, 2000.

[5] W. R. Smythe, Static and dynamic electricity, McGraw-Hill Book Company, Inc. New-York, 1950.

A Computational Effective Material Data Representation for Fast Simulation Models of Giant Magnetostrictive Materials

Y. Sato

Department of Mechanical Engineering
Yokohama National University
79-5 Tokiwadai, Hodogaya, Yokohama 240-8501, Japan
sato@post.me.ynu.ac.jp

G. Engdahl

Department of Electric Power Engineering
Royal Institute of Technology
SE-100 44 Stockholm, Sweden
goran.engdahl@ekc.kth.se

Abstract – **Aiming at time reduction and high efficiency in computation, a set of simple formulae characterizing a giant magnetostrictive material is proposed. It can represent non-linearity of the magnetic properties with respect to both the magnetic field intensity and the mechanical stress, using easy-to-handle function form with some adjustable parameters given by from experimental data resources.**

INTRODUCTION

The properties of giant magnetostrictive materials (abbreviated by GMM in followings) are known to have non-linearity with respect to both the magnetic field and the mechanical stress. The linearized modeling of GMM presents a high computational efficiency, but is insufficient to represent the entire properties of GMM [1]. A powerful model representing the non-linearity of GMM has been presented by Benbouzid, et al, [2]. It directly refers to the state of GMM by means of the spline interpolation, as a point on the mathematical surface transformed from static experimental data; therefore it performs accurate but needs memory space for the resources of the complicated surface and more computational processes for the interpolation. As the alternative modeling approach, this paper proposes 2-dimensional approximate formulae, which need no data resources during the computation.

PREPROCESS ARRANGEMENT FOR MEASURED DATA

Measured properties of GMM are simply visualized by anhysteresic curves $S_{an}(H, T)$ for the relation between the strain S and magnetic field intensity H, and $B_{an}(H, T)$ between the magnetic flux density B and H, which are transformed from the measured hysteresic loops by calculating the averages of the upper and lower branches. The examples of anhysteresic curves are depicted in Fig. 1-2, where the parameters used in the approximate formulae are superimposed. As observed in those figures, the corves $S_{an}(H, T)$ and $B_{an}(H, T)$ are smooth, symmetric and saturable. Exponent-base functions, such as Sigmoid and Gaussian, are applicable for the representation of those features.

STRAIN REPRESENTATION

Arranging Gaussian function, the approximate formula for strain representation is proposed as;

$$S(H,T) = S_H(T)\left\{1 - \exp\left[-\left(\frac{H}{H_{Sw}(T)}\right)^2\right]\right\} + S_{sat}\left\{1 - \exp\left[-\left(\frac{H}{H_{ws}}\right)^2\right]\right\} + S_d(T) \quad (1)$$

where, the first term represents the fundamental curve assuming perfect saturation, the second the gradual increment at saturation region, and the last the drop of the bottom due to the compressive stress. In case of $T = 0$ or $= T_{max}$, the circled parameters in Fig. 1 are directly detected from $S_{an}(H, T)$, but others need some graphical procedures for estimation. At first, $S_H(0)$ is determined as the intercept of the tangent line I at the point $P_1 = (H_{max}, S_{an}(H_{max}, 0))$, then the curve II corresponding to the second term in (1) is applied so that it could start from $P_2 = (0, S_H(0))$ and could have a common tangent line with $S_{an}(H, 0)$ at P_1. The shape of curve II depends on both values of H_{ws} and S_{sat}, but they have little affect on the shape between P_1 and P_2. Therefore any couple of H_{ws} and S_{sat} is usable as long as the condition of the common tangent is fulfilled. Then, the curve II is determined passing through some adjusting

Fig.1 Anhysteresic curves of magnetostriction (strain) $S_{an}(H, T)$ transformed from the measured data
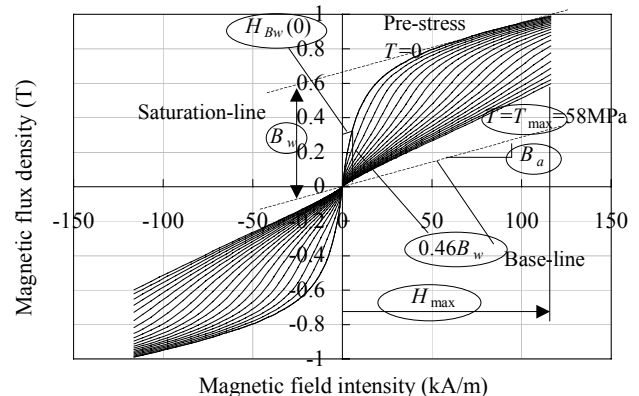
Fig.2 Anhysteresic curves of magnetic flux density $B_{an}(H, T)$ transformed from the measured data

trials. If once the curve II is fixed, the curve III can be drawn by shifting the curve II to $P_3 = (0, S_d(T_{max}))$. $S_H(T_{max})$ is estimated as the height of the perfect saturable component corresponding to the first term in (1). For this procedure, an appropriate extension for $S_{an}(H, T_{max})$ such as the curve IV is necessary because the saturation of $S_{an}(H, T_{max})$ usually cannot be found below H_{max} in Fig. 1.

In the intermediate state between at $T = 0$ and $T = T_{max}$, the parameters determining the shape of the curve are unknown. It would be natural to assume that the shape of curve changes smoothly against the change of T. And then, the following functional expressions are introduced;

$$S_H(T) = S_H(0) - \left(S_H(0) - S_H(T_{max})\right)\left(\frac{T}{T_{max}}\right)$$
$$- a_s\left(S_{Hmax} - S_H(0)\right)\left(\frac{T}{T_{max}} - \frac{1}{a_s}\right)^2 + \left(S_{Hmax} - S_H(0)\right) \quad (2)$$

where, a_s is a adjustable constant, $a_s > 1$, and

$$H_{Sw}(T) = \left(H_{Sw}(0) - H_{Sw}(T_{max})\right) \cdot \left(1 - \frac{T}{T_{max}}\right)^a + H_{Sw}(T_{max}) \quad (3)$$

$$S_d(T) = S_d(T_{max}) \cdot \left(\frac{T}{T_{max}}\right)^b \quad (4)$$

Equation (4) expresses the nature of GMM that the maximum magnetostriction appears under an appropriate pre-stress; therefore, a convex second order function that has the peek S_{Hmax} at a certain stress below T_{max} is applied. S_{Hmax} and a_s cannot be given directly by Fig.1, but roughly estimated by rearranging the measured data to $S_{an}(H_{max}, T)$-$S_{an}(0, T)$ vs. T. The exponents a and b works as distribution weight factors, which are adjusted by comparison with the measured data.

MAGNETIC FLUX DENSITY REPRESENTATION

$B_{an}(H, 0)$ can be expressed by the combination of Sigmoid and the first-order functions, and $B_{an}(H, T_{max})$ can be estimated as nearly linear. "Saturation-line" and "base-line" are herein defined; the former is the tangent line for the wholly saturated curve at $T = 0$, the latter parallel to that and passing through the origin. The approximate formula for the magnetic flux density representation is proposed as;

$$B(H, T) = B_w\left[\frac{2}{1 + \exp\left(-\frac{H}{H_{Bw}(T)}\right)} - 1\right] + B_a H \quad (5)$$

where, B_a is the inclination of the base-line. All the parameters except $H_{Bw}(T)$ are given by the measured data, as shown in Fig. 2. $H_{Bw}(0)$ with respect to $0.46B_w$ can be read from Fig.2, whereas $H_{Bw}(T_{max})$ is unknown. A very large value compared with $H_{Bw}(0)$ should be applied so that the curve $B(H, T_{max})$ could approach to $B_{an}(H, T_{max})$.

Intermediate state can be expressed by similar technique for the strain representation. Then, the following function is introduced;

$$H_{Bw} = H_{Bw}(T) = \left(H_{Bw}(T_{max}) - H_{Bw}(0)\right) \cdot \left(\frac{T}{T_{max}}\right)^c + H_{Bw}(0) \quad (6)$$

where, exponents c is an adjustable parameter.

EVALUATION OF THE APPROXIMATE FORMULAE

Fig. 3 and 4 show the comparison of the approximate formulae (right; solid) with measured data (left; broken), by each half curve. It can be said that the proposed formulae fit well to the measured data except for stresses below $\approx$ 3MPa (e.g. T=0, 2.57MPa) in the strain representation. However, these errors can be ignorable in case of modeling for an actuator application operated under higher stress than those.

CONCLUSIONS

A set of approximate formulae for the strain and magnetic flux density representations of GMM has been proposed. It expresses the non-linear properties of GMM with good agreement with the measured data.

REFFERENCES

[1] G. Engdahl, ed., *Handbook of Giant Magnetostrictive Materials*. Academic Press, San Diego, 2000.
[2] M.E.H. Benbouzid, et al, "Dynamic Modeling of Giant Magnetostriction in Terfenol-D Rods by the Finite Element Method," *IEEE Transactions on Magnetics*, vol.31, pp. 1821-1824, May 1995.

Fig.3 Approximate formula for strain representation $S(H, T)$ compared with the measured data $S_{an}(H, T)$
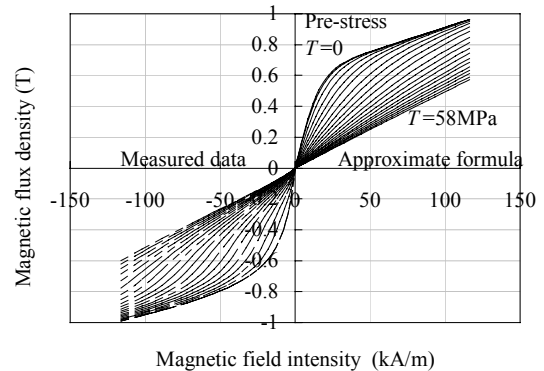
Fig.4 Approximate formula for magnetic flux density representation $B(H, T)$ compared with the measured data $B_{an}(H, T)$

3-D Finite Element Analysis of Current Distribution in HTS Power Cable

Taking Account of *E-J* Power Low Characteristics

Daisuke Miyagi[*1], Tomohiro Wakatsuki[*1], Norio Takahashi[*1], Shinji Torii[*2], Kiyotaka Ueda[*3]

*1:Dept. Electrical and Electronic Eng., Okayama Univ., Okayama 700-8530, Japan

({miyagi, wakatuki, norio}@eplab.elec.okayama-u.ac.jp)

*2:Central Research Institute of Electric Power Industry, Komae, Tokyo 201-8511, Japan (tori@criepi.denken.or.jp)

*3:Super-GM, 5-14-10 Nishitenma , Osaka 530-0047, Japan (super-gm@nifty.com)

Abstract — **A method for analyzing the current distribution in high-T_c superconducting power cable is examined by the aid of novel use of anisotropic conductivity and 3-D finite element method in consideration of *E-J* power low characteristics. The detailed current distribution in the cable is illustrated and the shielding effect of HTS shield is also examined.**

I . INTRODUCTION

Controlling the current distribution in each layer of a multi-layer superconducting cable uniformly is important in order to realize a compact and large capacity high-T_c super conducting power cable [1]. The phenomenon of current imbalance should be exactly investigated by analyzing, for example, the effect of twist pitch etc. on flux and current distribution to design efficient cable. However, the accurate analysis of current distribution of a HTS cable taking account of the *E-J* characteristic is seldom reported. This is mainly because the 3-D analysis of current distribution in multi-layer superconducting cable consisting of superconducting tapes spirally wound of a former is complex.

In this paper, 3-D finite element analysis taking account of the non linear *E-J* power law characteristic is carried out by modeling such spirally wound superconducting tapes as conductors having an anisotropic conductivity [2][3].

II . METHOD OF ANALYSIS

A. Modeling of Cable Structure

A HTS cable should consist of multi-layered conductors to increase its current loading. The structure of HTS cable is shown in Fig.1. When there are many layers of superconductor in a superconducting cable, it is difficult to analyze magnetic fields in the cable using the conventional 3-D finite element method, because the number of finite elements increases greatly. If the cable is treated as a macroscopic one having anisotropic conductivity, as shown in Fig.2, the calculation can be carried out within the acceptable computer storage and CPU time. Moreover, since it is not necessary generate a mesh again even if the twist pitch is changed, it is useful to examine the optimal twist pitch.

The conductivity $\sigma_{//}$ parallel to the superconducting tape is equal to infinity. The conductivity $\sigma_{\perp}$ perpendicular to the superconducting tape can be given by [2]

$$\sigma_{\perp} = \frac{1+\lambda}{1-\lambda}\sigma_m \qquad (1)$$

where σ_m is the conductivity of the silver sheath. λ is the volume fraction of superconductor in the HTS layer. The conductivity σ_m of silver sheath is 3.45×10^8 S/m (at 77K) and the volume fraction λ is assumed as equal to 0.6. Then, $\sigma_{\perp}$ is 1.38×10^9 S/m according to Eq.(1).

The conductivity of the anisotropic conductor is a tensor, of which the off-diagonal elements are all zero. The current density J_u, J_v and J_w in *u*-, *v*- and *w*-directions defined along the superconducting tape as shown in Fig.3 can be written using each component E_u, E_v and E_w of electric field strength E and $\sigma_{\perp}$ and $\sigma_{//}$ as follows [3]:

$$\begin{Bmatrix} J_u \\ J_v \\ J_w \end{Bmatrix} = \begin{bmatrix} \sigma_{\perp} & 0 & 0 \\ 0 & \sigma_{\perp} & 0 \\ 0 & 0 & \sigma_{//} \end{bmatrix} \begin{Bmatrix} E_u \\ E_v \\ E_w \end{Bmatrix} \qquad (2)$$

The relationship between J_x, J_y and J_z and E_x, E_y and E_z can be obtained as follows [2]:

$$\begin{Bmatrix} J_x \\ J_y \\ J_z \end{Bmatrix} = [K] \begin{bmatrix} \sigma_{\perp} & 0 & 0 \\ 0 & \sigma_{\perp r} & 0 \\ 0 & 0 & \sigma_{//} \end{bmatrix} [K]^{-1} \begin{Bmatrix} E_x \\ E_y \\ E_z \end{Bmatrix}$$
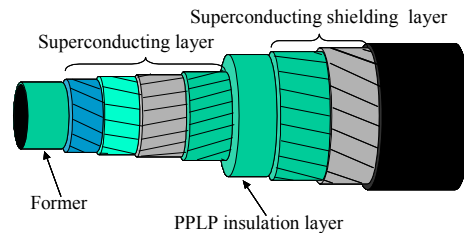
Fig. 1. Structure of HTS cable composed of multi-layered conductors.
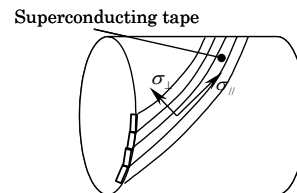
Fig. 2. Modeling of cable conductors with anisotropy of conductivity.

$$= \begin{bmatrix} \sigma_a & \sigma_b & \sigma_c \\ \sigma_d & \sigma_e & \sigma_f \\ \sigma_g & \sigma_h & \sigma_i \end{bmatrix} \begin{Bmatrix} E_x \\ E_y \\ E_z \end{Bmatrix} \tag{3}$$

[K] is the transformation matrix[3].

The superconducting cable is treated as a conductor having large conductivity. The magnetic field is analyzed using the 3-D edge-based hexahedral finite element method(A-ϕ method, A: magnetic vector potential, ϕ: electric scalar potential).

B. Conductivity of Superconductor to be used in Numerical Analysis

The infinite conductivity σ_{sc} ($\sigma_{//}$) of the supercondcutor cannot be treated in the numerical calculation. One needs to determine a suitable value for the conductivity $\sigma_{//}$ (σ_{sc}) in Eq.(2) for the numerical calculation. The superconducting property is given by the E-J characteristic (Fig.4) represented with a power law

$$E = E_c \left(\frac{J}{J_c} \right)^n \tag{4}$$

where J_c is a critical current density and E_c is equal to 1×10^{-4} V/m. Then, the equivalent conductivity of superconductor σ_{sc} is derived as,

$$\sigma_{sc} = \frac{J}{E} = \frac{J_c^{\,n}}{E_c} J^{1-n} \tag{5}$$

σ_{sc} is determined iteratively at each time step until the final result is obtained. The maximum value of σ_{sc} is limited to 1×10^{11} S/m to enhance the efficiency of calculation.

C. Boundary Condition

Fig.5 shows the boundary condition. The Dirichlet boundary condition (A=0) is given on the boundary γ of air region. Let us assume that a point p on the boundary α of the HTS conductor corresponds to a point q on the boundary β. The periodic boundary condition is given at the points p and q, by assuming that the vector potential A_p at the point p is equal to A_q at the point q ($A_p=A_q$). The unknown equi-potential condition of electric scalar potential ϕ_1 is given on the boundary α of the HTS conductor, and the unknown equi-potential ϕ_2 is given on the boundary β.

III. RESULTS AND DISCUSSION

The flux and current distribution in the HTS cable model of 1-layer conductor shown in Fig.5 are analyzed. The thickness of the conductor is 0.3mm. The twist pitch is equal to 300mm. n value is assumed to be 16, and J_c is 2.0×10^7. The frequency of the current is 50Hz.

Fig.5 shows an example of flux and current distribution at $\omega t = 90$deg. The deviation of current is remarkable.

This work has been carried out as a part of Super-ACE (R&D of fundamental technologies for superconducting AC power
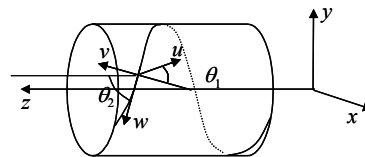
Fig. 3. Local coordinates.
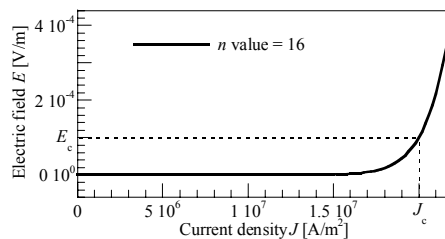
Fig.4. E-J characteristics.
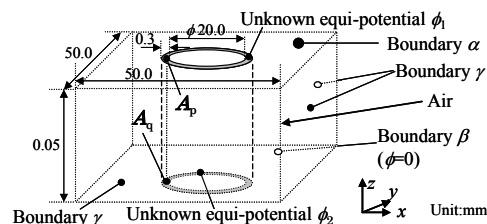
Fig. 5. Boundary condition and the HTS cable mode used for numerical calculation.

(a) flux   (b) current
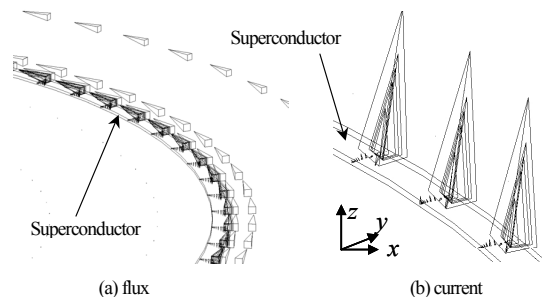
Fig. 6. Flux and current distribution.

equipment) project of METI, being consigned by NEDO.

REFERENCES

[1]S. Honjo, K. Matsuo, T. Miura and Y. Takahashi: "High-Tc superconducting power cable development", *Physica* C, 357-360, pp.1234-1240, 2001.

[2]W. J. Carr, Jr.: "AC loss and macroscopic theory of superconductors", *Gorden and Breach Science Publishers*, 1983.

[3]N. Takahashi, T. Nakata, Y. Fujii, K. Muramatsu, M. Kitagawa and J. Takehara: "3-D finite element analysis of coupling current in multifilamentary ac superconducting cable", *IEEE Trans. Magn.*, vol.27, no.5, pp. 4061-4064, 1991.

Power-law Characteristic for 3D Macroscopic Modelling of Superconductors via an Integral Formulation

Guglielmo Rubinacci, Fabio Villone

Ass. EURATOM/ENEA/CREATE, DAEIMI, Università di Cassino, Via Di Biasio 43 – 03043 Cassino (FR) – Italy

Walter Zamboni

DIEL, Università degli Studi di Napoli "Federico II", Via Claudio 21 – 80125 Napoli – Italy, zamboni@unina.it

Abstract – **In this paper we solve the eddy currents problem in presence of superconductors in 3D geometries. An integral formulation of the electromagnetic part of the problem is complemented by a variational form of the macroscopic constitutive relationship of a superconductor, obtained by the use of a suitable power -law characteristic. This formulation allows us to solve the problem as an unconstrained minimization of a convex functional.**

INTRODUCTION

The industrial applications of superconducting materials are growing in number and importance in the last years. For instance, in addition to energy storage systems and transportation via levitation, one very important field of application is the realization of superconducting magnets, successfully used in common applications and also in complex devices.

A suitable numerical model of superconductors is needed in order to help and test the design of such magnets and other devices. Due to the complexity of the systems, it is rather practical to use macroscopic models, i.e. constitutive relationships expressing the (macroscopic) electric field in the material as a function of the current density. Indeed, a topic of growing interest is to assess the performances of different possible macroscopic numerical modelling tools for superconductors [1].

One of the first macroscopic models of superconductors was the Bean model [2], and successive variations [3]. This model prescribes that the electric field is zero when the current density is below a critical value. However, many other macroscopic laws have been proposed, like the flux flow and creep model [4], and the power-law model [5], which is probably one of the most used. In addition, once a model has been chosen, many (both numerical and theoretical) difficulties must be tackled when a fully 3D geometry must be solved [6,7].

In the past, a very promising way of formulating the Bean model has been proposed in [8], where the problem is recast as the minimization of a proper convex functional. Recently [9, 10], the authors have presented an implementation of such a model in a 3D integral formulation of the eddy current problem, based on the electric vector potential and solved using edge elements.

Aim of this paper is to extend this previous piece of work to include a power-law characteristic, whose limit is the usual Bean model. Hence, the present formulation solves the eddy currents problem in the presence of fully 3D superconductors described by a power-law characteristic, allowing the meshing of the (super)conducting materials only and

requiring the unconstrained minimization of a convex functional.

In perspective, also some other aspects will be dealt with, as possible non-isotropy of the constitutive relation, feeding the superconductors with some electrodes, and the dependence of the critical current density on the magnetic field and on the temperature. These issues are fundamental in order to pursue simulations of real-world applications, but pose also some theoretical and numerical difficulties. In particular, a variable critical current density may lead to a possible non-convexity of the functional to be minimized.

THE MATHEMATICAL MODEL AND THE NUMERICAL FORMULATION

The integral formulation for the computation of the magneto-quasistatic field in presence of superconductors is recast as a minimization problem. The functional to be minimized is:

$$F(\mathbf{J}) \triangleq \frac{Y(\mathbf{J})}{\Delta t} + U(\mathbf{J}), \qquad (1)$$

where $\mathbf{J}$ is the current density.

The first part of the functional, $Y(\mathbf{J})$, takes into account inductive effects, as it is clearly shown in [9].

The second part $U(\mathbf{J})$ depends on the non-linear constitutive relationship of the superconductor, that can be expressed as the following variational inequality [8]:

$$\textit{find } \mathbf{J} \textit{ such that} \quad U(\mathbf{J}') - U(\mathbf{J}) \geq \int_{V_c} \mathbf{E} \cdot (\mathbf{J}' - \mathbf{J}) d\mathbf{x} \quad \forall \mathbf{J}', \ (2)$$

where $\mathbf{x}$ is the spatial variable, $\mathbf{E}$ is the electric field, and $U(\mathbf{J})$

$$U(\mathbf{J}) = \int_{V_c} u(\mathbf{x}, \mathbf{J}(\mathbf{x})) dV \quad \text{where} \quad u(\mathbf{x}, \mathbf{J}(\mathbf{x})) = \int_0^{J(\mathbf{x})} f(j) dj. \ (3)$$

The function f represents the non-linear link between $\mathbf{E}$ and $\mathbf{J}$, that reduces to a link between their amplitudes in the isotropic case. In Fig. 1 the case of power-law model is represented: the continuous function f is defined as follows:

$$f(J) = \begin{cases} \eta J_c (J/J_c)^n & \text{for } J \leq J_c \\ \\ \eta J & \text{for } J > J_c \end{cases} \qquad (4)$$

The continuity of the subgradient of the functional F is guaranteed by the use of the power-law characteristic.

From the numerical point of view, we discretize only the conducting region, introducing the electric vector potential $\mathbf{T}$ such that $\mathbf{J} = \nabla \times \mathbf{T}$, expanded in term of edge elements: $\mathbf{T} = \Sigma I_k \mathbf{N}_k$.
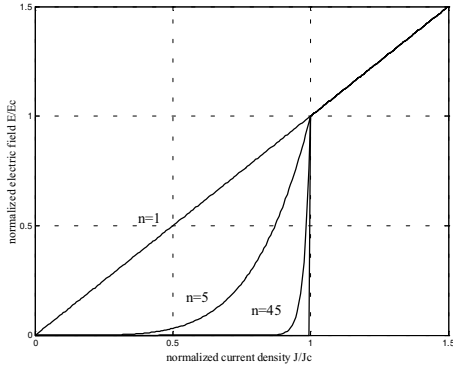
Fig. 1. Power-law characteristic for a superconductor

Fig. 2. Solution at t=0.75 for different values of *n* compared with the analytical (solid line) and numerical (O) solution obtained with the classical Bean model

A two component gauge is imposed using tree-cotree decomposition of the mesh [11]. Expanding **J** we have:

$$\mathbf{J} = \sum I_k \nabla \times \mathbf{N}_k , \qquad (5)$$

so, our discrete unknown becomes

$$\mathbf{i} = \left(... \quad I_k \quad ...\right)^T \qquad \text{for } k = 1...\text{N}_{\text{active edges}}$$

For a type II superconductor characterized by (4), the discrete functional $U_D(\mathbf{i})$ can be calculated by numerically integrating on V_c the following expression, obtained from (3):

$$u(\mathbf{x},\mathbf{J}) = \begin{cases} \dfrac{\eta}{n+1} \dfrac{J^{n+1}(\mathbf{x})}{J_c^{n-1}} & \text{for } \mathbf{x} \in V_c - V_n \\[3mm] \eta \dfrac{J^2(\mathbf{x})}{2} - \eta \dfrac{J_c^2}{2} \dfrac{n-1}{n+1} & \text{for } \mathbf{x} \in V_n, \end{cases} \qquad (6)$$

where V_n is the volume of the superconductor in the normal state ($J>J_c$). It is easy to show that, for $Y_D(\mathbf{i})$, we have [9]:

$$Y_D(\mathbf{i}) = \frac{1}{2}\mathbf{i}^T \mathbf{L}\mathbf{i} - \mathbf{i}^T \mathbf{L}\mathbf{i}_n + \mathbf{i}^T \left(\mathbf{v}_{0,n+1} - \mathbf{v}_{0,n}\right) \qquad (7)$$

$$L(i,j) = \frac{\mu_0}{4\pi} \iint_{V_c V_c} \frac{\nabla \times \mathbf{N}_i \cdot \nabla \times \mathbf{N}_j}{|\mathbf{x} - \mathbf{x}'|} d\mathbf{x}d\mathbf{x}' \qquad (8)$$

$$V_{0,k}(i) = \int_{V_c} \mathbf{A}_{0,k} \cdot \nabla \times \mathbf{N}_i d\mathbf{x} , \qquad (9)$$

where $\mathbf{A}_{0,k}$ is the discretized magnetic vector potential due to external sources at the instant k, $\mathbf{i}_n$ is the solution at the previous time instant.

The unique solution of the unconstrained minimization problem is guaranteed by the convexity of the functional $F_D(\mathbf{i})$ [8]. The minimum can be obtained with successive line minimizations along directions that can be estimated by a numerical computation of the gradient (continuous thank to the power-law characteristic).

In the full paper, we will also introduce the possibility of feeding the superconductor through some electrodes. This will be done, as described in [12], introducing some additional degrees of freedom linked to non-local basis functions connecting the electrodes. This is fundamental for retrieving the *E-J* characteristic on the basis of the experimental *V-I* characteristic.

As a preliminary result, a simple 1D test-case, already reported in [9] for Bean characteristic, is solved with the application of the fully 3D code. A thin superconducting disk (radius 1m, thickness 1cm) is immersed in an axial uniform external magnetic field, linearly increasing with time: eddy currents are induced in the toroidal direction. In Fig. 2, some numerical solutions (at t=.75s), obtained for different values of *n* in the power-law characteristic, are plotted. The agreement with the numerical and theoretical solutions obtained using the Bean model improves increasing *n*.

REFERENCES

[1] S. Stavrev et al., "Comparison of Numerical Methods for Modeling of Superconductors", *IEEE Trans. Mag.*, vol. 38, pp. 849-852, March 2002.
[2] C. P. Bean, "Magnetization of hard superconductors," *Phys. Rev. Lett.*, vol. 8, pp. 250-253, March 1962.
[3] Y. B. Kim, C. F. Hempstead, and A. R. Strnad, "Critical persistent currents in hard superconductors," *Phys. Rev. Lett.*, vol. 9, pp. 306-309, October 1962.
[4] Y. Yoshida, M. Uesaka, and K. Miya, "Magnetic Field and Force Analysis of High Tc Superconductor with Flux Flow and Creep," *IEEE Trans. Mag.*, vol. 30, no. 5, pp. 3503–3506, September 1994.
[5] J. Rhyner, "Magnetic properties and AC losses of superconductors with power-law current-voltage characteristics," *Physica C*, vol. 212, pp. 292–300, 1993.
[6] H. Hashizume, S. Toda, "Three dimensional evaluation of current distribution in twisted superconductors," *IEEE Trans. Mag.*, vol. 32, pp. 1152-1155, May 1996.
[7] H. Hashimoto et al., "Finite Element Analysis of AC Losses in Double Helix Superconducting Cables," *IEEE Trans. Mag.*, vol. 36, pp. 1205-1208, July 2000.
[8] A. Bossavit, "Numerical modeling of superconductors in three-dimensions: a model and a finite element method," *IEEE Trans. Mag.*, vol. 30, pp. 3363–3366, 1994.
[9] G. Rubinacci, A. Tamburrino, F. Villone, "Three Dimensional Finite Elements Modelling of Superconductors," *IEEE Trans. Mag.*, Vol. 36, No. 4, pp. 1276-1279, July 2000.
[10] G. Rubinacci, A. Tamburrino, S. Ventre, F. Villone, "Macroscopic Electrodynamic Modeling of Superconductors", *Cryogenics*, vol. 40, no. 8-10, pp. 671-676, 2000.
[11] R. Albanese, G. Rubinacci, "Finite Element Methods for the Solution of 3D Eddy Current Problems", *Advances in Imaging and Electron Physics*, vol. 102, pp. 1-86, Academic Press, 1998.
[12] G. Rubinacci, A. Tamburrino, F. Villone, "Circuits/fields coupling and multiply connected domains in integral formulations", *IEEE Trans. Mag*, vol. 38, pp. 581-584, March 2002.

Micromagnetic Simulation of Fine Structures in Asymmetrical Landau-Lifshitz Domain Pattern

Mai Lu, Paul J. Leonard

Department of Electronic and Electrical Engineering, University of Bath,

Claverton Down, Bath BA2 7AY, United Kingdom

E-mails: m.lu@bath.ac.uk, P.J.Leonard@bath.ac.uk

Abstract– **A 3D micromagnetic simulation has been implemented to investigate the asymmetrical Landau-Lifshitz domain pattern (one 180° domain wall and four 90° domain walls with a vortex structure) in FeSi (3.25% Si) platelet. The magnetization distributions in platelet plane and cross section of platelet are presented. The dependence of vortex structure on domain pattern is discussed.**

I. INTRODUCTION

The Landau-Lifshitz(LL) domain pattern, which consists of one 180° domain wall and four 90° domain walls has been extensively investigated by experemental observations and numerical calculations. Recently, a new kind of LL domain pattern, an asymmetrical Landau-Lifshitz domain pattern (Fig.1) has been predicted[1]. In this paper, a 3-dimensional micromagnetic model is implemented in a rectangular FeSi (3.25% Si) platelet. Structures in asymmetrical Landau-Lifshitz domain pattern are simulated and discussed.

II. MICROMAGNETIC MODEL

Fig.2 shows the geometry of the FeSi platelet domain model. The computational region $1320\AA \times 780\AA \times 3000\AA$ is 3-dimensional meshed. The total free energy E_{tot} in the absence of applied field is the sum of three contributions: exchange energy $E_{ex} = \int_V A[(\nabla\alpha)^2 + (\nabla\beta)^2 + (\nabla\gamma)^2]dv$, cubic anisotropy energy $E_{an} = \int_V (K_1(\alpha^2\beta^2 + \beta^2\gamma^2 + \gamma^2\alpha^2) + K_2\alpha^2\beta^2\gamma^2)dv$, and magnetostatic interaction energy $E_{mag} = -\frac{1}{2}\int_V \vec{H}_d \cdot \vec{M} dv$. Where α, β, and γ are directional cosines of the magnetization with respect to the axes x, y, and z. A is the exchange constant, K_1 and K_2 are the cubic anisotropy constants, and $\vec{H}_d$ is the demagnetizing field. The method for the energy minimization was previously presented[2]. The intrinsic parameters adoped here are: A=10^{-6} erg/cm, M_s=1590 emu/cm^3, $K_1 = 3.6 \times 10^5$ erg/cm^3 and $K_2 = 2.0 \times 10^5$ erg/cm^3. The computational region is discretized into $22 \times 13 \times 50$ cubic elements with size of $60\AA$. A free boundary condition $\frac{\partial M}{\partial y}$=0 is used at the planes $y = 0$ and $y = 780\AA$, respectively. Imposed boundary condi-
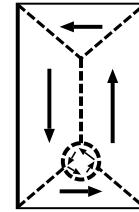
Fig.1 Schematic asymmetrical Landau-Lifshitz domain pattern
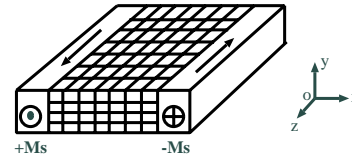
Fig.2 3-dimensional partition for the computational region between two antiparallel domains

tions ($\alpha = 0, \beta = 0, \gamma = \pm 1$) are used at the $x = 0$, $x = 1320\AA$ planes, respectively.

III. RESULTS

In film plane (xoz plane), the asymmetrical Landau-lifshitz domain pattern is simulated. The vortex structure is dependent on the variation of magnetization directions in 180° domain wall. Typical magnetization distributions for the 1st layer and 11th layer are shown in Fig.3 and Fig.4, respectively. In cross-section plane (xoy plane), the magnetization distributions show complicated configurations, and can be simply classfied as: transverse type, quasi-C-shaped type, and C-shaped type. Typical distributions are shown in Fig.5 to Fig.9.

1

Fig.3 Magnetization distribution in the 1st layer in xoz plane
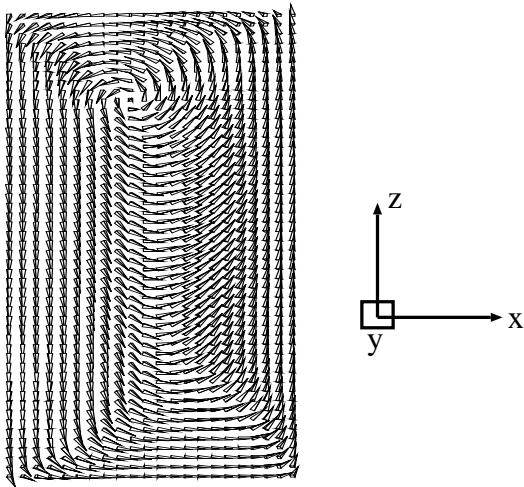
Fig.4 Magnetization distribution in the 11th layer in xoz plane
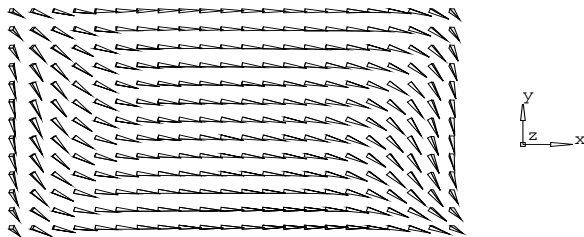
Fig.5 Transverse type in the 1st layer in xoy plane
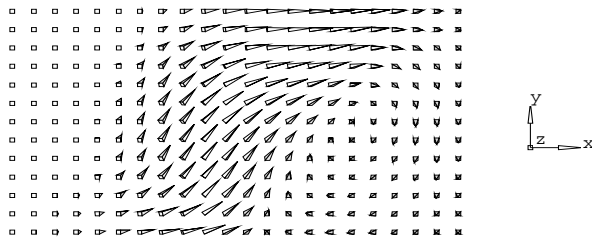
Fig.6 Quasi-C-shaped type in the 9th layer in xoy plane

IV. CONCLUSIONS

In an asymmetrical Landau-Lifshitz domain pattern, vortex structure plays an important role. The vortex structure in platelet plane is dependent on the variation of magnetization direction in 180° domain wall. In cross section plane, the magnetization distributions have three different types: transverse type, quasi-C-shaped type, and C-shaped type, and the vortex structure is directly related to the formation of quasi-C-shaped magnetiztion distribution. Those results on the one hand improve our understanding and enrich our knowledge on domain structure, and on the other hand have potential values in studying wall pinning and energy loss during wall mobility.

Fig.7 C-shaped type in the 25th layer in xoy plane
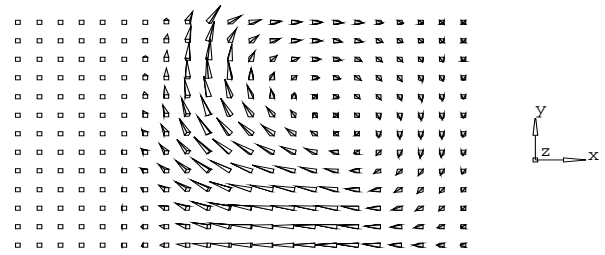
Fig.8 Quasi-C-shaped type in the 41th layer in xoy plane
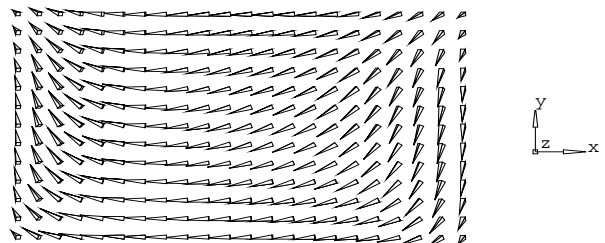
Fig.9 Transverse type in the 49th layer in xoy plane

REFERENCES

[1] H. Kronmuller and R. Hertel, "Computational micromagnetism of magnetic structures and magnetisation processes in small particles", Journal of Magnetism and Magnetic Materials, vol.215-216, pp.11-17, 2000.

[2] M. Lu and P.J. Leonard, "Micromagnetic simulation of magnetization reversal processes in ferromagnetic cubes from quasisaturation state", Journal of Physics: Condensed Matter, vol. 14, pp.8089-8101, 2002.

2

Time Domain Analysis of Shielding Current Density in HTS
by Element-Free Galerkin Method

Atsushi Kamitani, Ayumu Saitoh

Faculty of Engineering, Yamagata University, Yonezawa, Yamagata 992-8510, JAPAN

kamitani@yz.yamagata-u.ac.jp

Soichiro Ikuno

School of Engineering, Tokyo University of Technology, Hachioji, Tokyo 192-8580, JAPAN

Abstract—The numerical code for calculating the shielding current density in the high-Tc superconductor is developed by using the element-free Galerkin method. The behavior of the shielding current density is expressed by the integro-differential equations. In order to solve the initial-boundary-value problem of the equations, the equivalent weak form is derived. Since the form satisfies the essential boundary conditions automatically, it is discretized easily. In the numerical code, the resulting nonlinear system is solved at each time step. By means of the code, the spectral analysis of the magnetic field is performed.

INTRODUCTION

Among the applications of the high-Tc superconductor (HTS), the magnetic levitation and the magnetic shielding have recently become promising. Since the quantitative evaluation of the shielding current density is indispensable for the design of the magnetic levitation system and the magnetic shielding apparatus, various methods [1-3] have been proposed for calculating the shielding current density. However, in all of the methods, the finite element method (FEM) has been employed as the discretization method.

In spite of its quite convenience, the FEM has been plagued by two inherent difficulties: the time consumption of the element generation and the limited smoothness of the approximate solution. In order to resolve the above difficulties, several meshless approaches [4,5] have been proposed.

The purpose of this study is to develop the numerical code for analyzing the time evolution of the shielding current density by using the element-free Galerkin (EFG) method and to perform the spectral analysis of the magnetic field by use of the code.

GOVERNING EQUATIONS

Let us first assume that the HTS plate has the same cross section through the thickness direction and that it is exposed to the ac magnetic flux density $B_0 = B_0 \sin 2\pi f t \, e_z$. Here, e_z denotes a unit vector along the z-axis. We further assume the multiple-thin-layer approximation [1] to simulate an anisotropy in the critical current

density of the HTS. In the following, the shielding current density and the electric field in the pth layer are denoted by j_p and E_p, respectively, and Ω is the cross section of the HTS plate.

Under the above assumptions, there exists a scalar function $S_p(x, t)$ such that $j_p = (1/\varepsilon) \, \nabla S_p \times e_z$ and the behavior of j_p is governed by the following integro-differential equations [1,2]:

$$\mu_0 \frac{\partial}{\partial t} \sum_{q=1}^{M} \int_{\Omega} Q_{pq}(|x-x'|) \, S_q(x', t) \, dx' + \frac{\mu_0}{\varepsilon} \frac{\partial S_p}{\partial t}$$

$$+ \frac{\partial}{\partial t} (B_0 \cdot e_z) + e_z \cdot (\nabla \times E_p) = 0 \quad (p = 1, 2, 3, \cdots, M) \, , \quad (1)$$

where 2ε and M are the layer thickness and the total layer number, respectively, and the explicit form of the function $Q_{pq}(r)$ is given in [2]. Throughout this study, x and x' denote vectors in the xy plane. In addition, the flux-flow and flux-creep model [1-3] is adopted for the J-E constitutive relation, and both the flow resistivity ρ_f and the critical current density j_C are assumed as constants. By solving (1) with the initial and the boundary conditions, we can investigate the time evolution of $j_1, j_2, \cdots, j_M$.

NUMERICAL METHOD

By means of the backward Euler method, (1) can be easily discretized with respect to time. The boundary-value problem of the resulting equations is equivalent to the following weak form:

$$\mu_0 \sum_{p=1}^{M} \sum_{q=1}^{M} \int_{\Omega} \int_{\Omega} \delta S_p(x) \, Q_{pq}(|x-x'|) \, S_q^n(x') \, dx' dx$$

$$+ \frac{\mu_0}{\varepsilon} \sum_{p=1}^{M} \int_{\Omega} \delta S_p \, S_p^n \, dx + \Delta t \sum_{p=1}^{M} \int_{\Omega} E_p^n \cdot (\nabla \delta S_p \times e_z) \, dx$$

$$+ \sum_{p=1}^{M} \oint_{\partial \Omega} (\delta S_p \, \lambda_p + S_p^n \, \delta \lambda_p) \, d\ell$$

$$= \mu_0 \sum_{p=1}^{M} \sum_{q=1}^{M} \int_{\Omega} \int_{\Omega} \delta S_p(x) \, Q_{pq}(|x-x'|) \, S_q^{n-1}(x') \, dx' dx$$

$$+ \frac{\mu_0}{\varepsilon} \sum_{p=1}^{M} \int_{\Omega} \delta S_p \, S_p^{n-1} \, dx - \sum_{p=1}^{M} \int_{\Omega} \delta S_p \, [e_z \cdot (B_0^n - B_0^{n-1})] \, dx$$

for $\forall \delta S_p \, \forall \delta \lambda_p \, (p = 1, 2, \cdots, M) \, , \quad (2)$

where the superscript n indicates the value at time $t = t^n \, (\equiv n\Delta t)$, e.g., $S_p^n(\mathbf{x}) = S_p(\mathbf{x}, t^n)$. In addition, the Lagrange multiplier $\lambda_p(s)$ is a function of an arclength s along $\partial\Omega$, and both δS_p and $\delta\lambda_p$ denote test functions. Note that the essential boundary conditions are incorporated into (2) through Lagrange multipliers. In this sense, the test and the trial functions can be selected arbitrarily.

By using the shape functions of the moving least-squares approximation [4,5], the weak form (2) can be discretized as

$$G(\mathbf{z}) \equiv \begin{bmatrix} W & B \\ B^T & O \end{bmatrix} \mathbf{z} + \Delta t \begin{bmatrix} \mathbf{e}(s) \\ \mathbf{0} \end{bmatrix} - \begin{bmatrix} \mathbf{u} \\ \mathbf{0} \end{bmatrix} = \mathbf{0} \; , \; \left(\mathbf{z} \equiv \begin{bmatrix} s \\ \lambda \end{bmatrix} \right) \quad (3)$$

where the nodal vectors, s, $\mathbf{e}(s)$ and $\boldsymbol{\lambda}$, correspond to the scalar function S_p^n, the electric field $\mathbf{E}_p^n$ and the Lagrange multiplier λ_p, respectively, and the matrices, W and B, are calculated from the shape functions and the function $Q_{pq}(r)$. In addition, $\mathbf{u}$ is a nodal vector irrelevant to s. As is apparent from (3), s can be determined by solving the nonlinear system (3). Thus, the initial-boundary-value problem of (1) is reduced to the problem in which the nonlinear system (3) is solved at each time step.

<center>NUMERICAL RESULTS</center>

The 3D simulation code for solving the initial-boundary-value problem of (1) has been developed by means of the method explained above. For simplicity, the HTS plate is assumed to have a square cross section of side length $2a$, and its thickness is denoted by D. Throughout this study, the geometrical and the physical parameters are fixed as follows: $a = 20$ mm, $D = 2$ mm, $M = 6$, $f = 100$ Hz, $\rho_f = 7 \times 10^{-9}$ $\Omega \cdot$m and $j_C = 1.3 \times 10^7$ A/m^2. A typical distribution of the shielding current density is shown in Fig. 1. We see from this figure that the smoother distribution is obtained by using the EFG method. This is mainly because the shape functions are continuously differentiable in the EFG method.
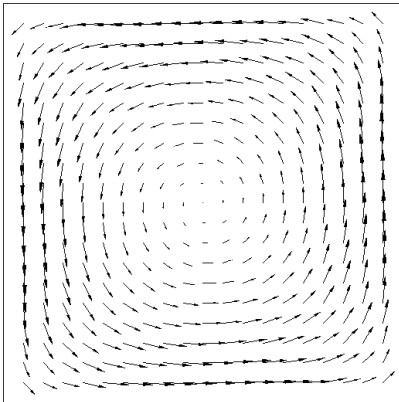
Fig. 1. Spatial distribution of the shielding current density at $t = 42/(25f)$ for the case with $B_0 = 1.0$ T. The distribution is calculated at $z/a = 1/120$.
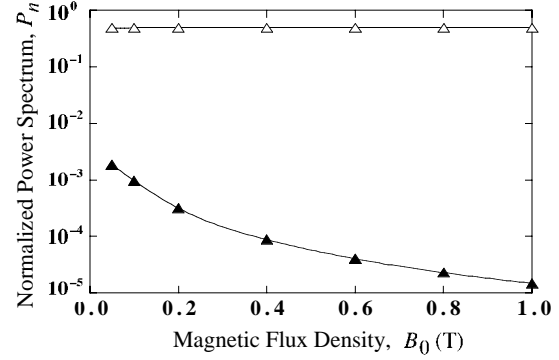
Fig. 2. Dependence of the normalized power spectrum on the applied magnetic flux density. The magnetic flux density is calculated at $= (0, 0, -0.06)$. $\triangle$: $n = 1$ and $\blacktriangle$: $n = 3$. Here, n denotes the index of the Fourier mode.

Once the spatial distribution of the shielding current density is given, the magnetic flux density can be evaluated at an arbitrary location. After calculating z-component B_z of the magnetic flux density at a specific point, we get the time sequence, $B_{z\,0}, B_{z\,1}, \cdots,$ $B_{z\,N-1}$. By using the FFT algorithm, the sequence is easily transformed to $\hat{B}_0, \hat{B}_1, \cdots, \hat{B}_{N-1}$.

By using the axisymmetric FEM program, the authors investigated the time variation of the shielding current density in cases where ρ_f and j_C depend strongly on B. Furthermore, they performed the spectral analysis of the generated magnetic flux density to find that the third harmonics are excited abruptly with an increase in B_0 [3]. Such a sudden onset of the third harmonics was also observed in the experiments by Claassen $et\ al$. [6] Unlike our earlier work, the B-dependence of ρ_f and j_C is neglected in this study. The power spectrum of the magnetic flux density is calculated by using the 3D code and is depicted in Fig. 2. Although the intensity of the $n = 1$ mode does not change, the $n = 3$ mode is weakened with an increase in B_0. Therefore, we cannot reproduce the sudden onset of the third harmonics numerically if the B-dependence of ρ_f and j_C is neglected. From the above results, we might conclude that its sudden onset is closely related to their B-dependence.

<center>REFERENCES</center>

[1] Y. Yoshida, M. Uesaka and K. Miya, *Int. J. Appl. Electromagn. Mater.*, vol. 5, pp. 83-89, 1994.

[2] A. Kamitani and S. Ohshima, *IEICE Trans. Electron.*, vol. E82-C, pp. 766-773, 1999.

[3] A. Kamitani, K. Hasegawa and T. Yokono, *Physica C*, vol. 378-381, pp. 853-857, 2002.

[4] T. Belytschko, Y. Y. Lu and L. Gu, *Int. J. Numer. Methods Eng.*, vol. 37, pp. 229-256, 1994.

[5] S. N. Atluri and T. Zhu, *Comput. Mech.*, vol. 22, pp. 117-127, 1998.

[6] J. H. Claassen, M. E. Reeves and R. J. Soulen, Jr., *Rev. Sci. Instrum.*, vol. 62, pp. 996-1004, 1991.

Design of Anisotropic Magnetic Material in Switched Reluctance Motor Using Finite Element Method

Jae-hak Choi, Youn-hyun Kim and Ju Lee

Energy Conversion Lab., Dept. of Electrical Engineering, Hanyang University
Haengdang-dong, Seongdong-gu,
Seoul, 133-791, South of Korea
E-mail: ivy@ihanyang.ac.kr

Abstract—**The design of anisotropic magnetic material is an important area of electromagnetic fields because these materials are used in a large number of electromagnetic devices. This paper presents a design method to maximize the average torque in 6/4 Switched Reluctance Motor (SRM) used anisotropic and isotropic magnetic materials. In order to confirm design results, Finite Element Method in which the time varying magnetic field is combined with driving circuit of SRM has been used effectively. In order to see the difference between anisotropic model and isotropic model, the conventional SRM designed as isotropic material was also calculated.**

. INTRODUCTION

Switched Reluctance Motor (SRM) has doubly salient poles and generates the electromagnetic force by the variation of inductance according to a position. Therefore, it is possible to increase the average torque with more accurate modeling and understanding of flux behavior within SRM. The difference (dL) between the unaligned inductance and the aligned inductance influences the performance of SRM [1]. To make the inductance difference larger, it is desirable to make the unaligned inductance smaller or aligned inductance bigger. For this purpose, the existing papers were focused on pole shape design of the rotor and stator, but this paper suggests new model that improve inductance characteristic by substituting anisotropic iron-core material for the stator teeth. The proposed model may be effective in the point of the inductance difference. In this paper, we investigate the effectiveness of the proposed SRM model, which has anisotropic iron-core material structure.

. MODEL DESCRIPTION AND FINITE ELEMENT FORMULATION

A. Description of Analysis model

When the saturation is neglected, the instant motor torque (T) is calculated by derivative of the inductance (L), which is a function of rotor position (θ), as shown in (1)

$$T(\theta, i) = \frac{1}{2} \cdot i^2 \cdot \frac{dL(\theta)}{d\theta} \tag{1}$$

Fig. 1 shows cross section view of the proposed SRM. The direction of the magnetic flux density **B** and the magnetic field **H** in stator teeth of SRM is always in the same direction. Stator teeth can be designed anisotropic material to reduce magnetic resistance and leakage flux. As shown Fig. 1, the large arrows indicate that the easy magnetizing direction of the anisotropic steel sheet is radial in each pole. On the other hand, rotor and back yoke cannot be designed anisotropic material, because their directions of magnetization vary along the motor rotation.

B. Finite Element Formulation

Anisotropic nonlinear magnetic field has to be analyzed to evaluate the effectiveness of proposed model. Most of conventional anisotropic analyses are applied to transformer and there are not difficulties because the easy axes are *x*-axis or its perpendicular [2, 3]. But the proposed model has a difficulty to analyze in an *x-y* coordinate because the easy axis of an element, $E_{\alpha\beta}$, in a stator pole is α -axis as shown in Fig. 1.

If the magnetic vector potential and current density have only a *z*-axis component, the governing equation for SRM can be expressed in a magnetic vector potential *A* as follows:

$$\partial/\partial x \left(\nu \, \partial A/\partial x\right) + \partial/\partial y \left(\nu \, \partial A/\partial y\right) + J_o = 0 , \tag{2}$$

where ν is the inverse of permeability, *A* is the magnetic vector potential, and J_0 is the input current density.

There are two formulation methods in this case. First, formularize governing equation (2) for *x-y* coordinate using tensor of inverse permeability as shown in (3). Secondly, transform coordinate from *x-y* coordinate to $\alpha - \beta$ coordinate

Fig. 1. Cross section view of switched reluctance motor

as shown in (4). Equation (4) is more profitable in the point of the computation time. This paper applies (4) to anisotropic analysis after converting *x-y* coordinate into easy-axis coordinate for each element of the stator poles.

$$S_{ij} = \int_{\Omega} \{ v_{xx} \frac{\partial N_i}{\partial y} \frac{\partial N_j}{\partial y} - v_{xy} \frac{\partial N_i}{\partial x} \frac{\partial N_j}{\partial y} -$$

$$v_{yx} \frac{\partial N_i}{\partial y} \frac{\partial N_j}{\partial x} + v_{yy} \frac{\partial N_i}{\partial x} \frac{\partial N_j}{\partial x} \} A_j d\Omega \qquad (3)$$

$$S_{ij} = \int_{\Omega} \{ v_{\alpha} \frac{\partial N_i}{\partial \beta} \frac{\partial N_j}{\partial \beta} + v_{\beta} \frac{\partial N_i}{\partial \alpha} \frac{\partial N_j}{\partial \alpha} \} A_j d\Omega \qquad (4)$$

. ANALYSIS RESULTS AND DISCUSSION

Fig. 2 shows the magnetic flux distributions of SRM at unaligned position. In the figures, more large fluxes of the proposed model flow into the air between the stator and rotor than that of conventional model. Therefore, it is possible to predict that the reluctance of the proposed model may be larger at unaligned position.

Fig. 3 shows the inductance profiles according to the rotor position. The difference of the inductance of the proposed model is large than that of the conventional model. This inductance characteristic effect on SRM performance, especially the torque density and torque ripples. We will presents additional results in the full paper.

. CONCLUSION

The design of material in switched reluctance motor has been presented and expressed using finite element method. In order to increase the average torque with more accurate modeling and understanding of flux behavior within SRM, anisotropic and isotropic materials have been considered in motor design. The proposed design method can also be used wide range of electromagnetic devices.

REFERENCES

[1] T. J. E. Miller, *Switched Reluctance Motors and their control,* Hillsboro, OH: Magna Physics Publishing and London: Oxford University Press, 1993.
[2] Changhwan. Lee, Hyun-Kyo Jung, "Two-Dimensional Analysis of Three-Phase Transformer with Load Variation Considering Anisotropy and Overlapped Stacking," *IEEE Transactions on Magnetics*, vol. 36, no. 4, July 2000.
[3] Jin Liu, G. H. Shirkoohi, "Anisotropic magnetic material modeling using finite element method, " *IEEE Transactions on Magnetics*, vol. 29, no. 6, November 1993.
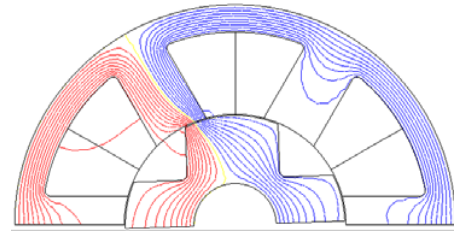
(a) Conventional model; isotropic
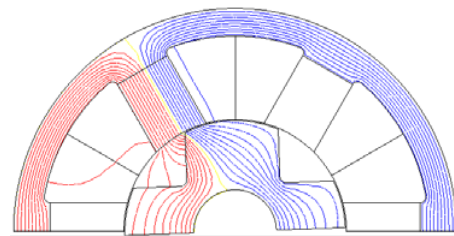
(b) Proposed model; Anisotropic

Fig. 2. Flux distribution of switched reluctance motor
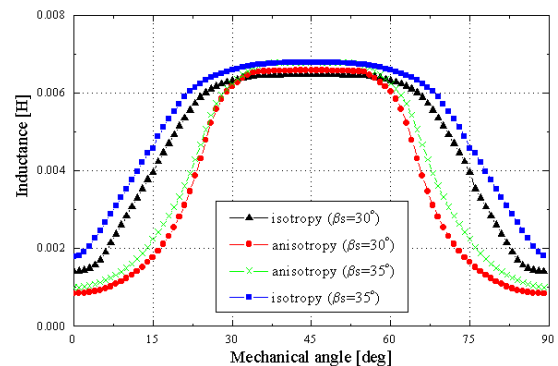
Fig. 3. The inductance profiles according to the rotor position

Vector Hysteresis in Magnetization Model of Anisotropic Magnet Rings

Y. Zhilichev

MAGNEQUENCH INTERNATIONAL
Technology Center – 9000 Development Drive – P.O.Box 14827
Research Triangle Park – NC 27709-4827 – USA
e-mail: yzhilich@mqii.com

Abstract — **The paper describes a simplified vector hysteresis model developed for a pulse magnetization of anisotropic permanent magnets. The model is tested on the magnetization of sintered and hot deformed anisotropic rings. The magnetization problem is solved by integral method, and the distribution of the magnetization vector is used to calculate a static field around the ring. The predicted magnetic field is compared against the measured one in the open and closed magnetic circuits.**

INTRODUCTION

The radially anisotropic permanent magnet rings are widely used in servomotors. They can be produced through sintering process or hot deformation of the fully dense preformed magnets. The microstructure and, therefore magnetic properties are dependent on the production process. The sintered ring has a steeper virgin curve and highly nonlinear minor demagnetization curves. The extruded rings in general are less homogenous in axial direction. However they have minor demagnetization curves with much smaller slopes that is a significant benefit when shaping the poles is required. Together with skewing, shaping the poles is often used to control a content of high harmonics in the back-emf and torque of electrical motor. Unlike isotropic magnets different pole's profiles can be achieved in anisotropic rings only by its partial magnetization. Obviously a hysteresis model with minor loops is required to predict the distribution of magnetization vector across the pole. A simplified model of vector hysteresis [1] has been incorporated in the 2D finite element solver to simulate the pulse magnetization of anisotropic magnets. In this paper, results from 3D modeling along with the test data are presented for the radially oriented ring. Some possible improvements in the model like including the off-diagonal components in the susceptibility tensor are discussed.

HYSTERESIS MODEL

The characteristics of magnet along both easy (radial direction) and transverse (circumferential/axial directions) axes are defined by a virgin curve in the first quadrant of the B-H plane and a series of demagnetization curves in the first and second quadrants. A table for the virgin curve is used until B_{sat} when the permeability reaches one. Each demagnetization curve is approximated by a quadratic
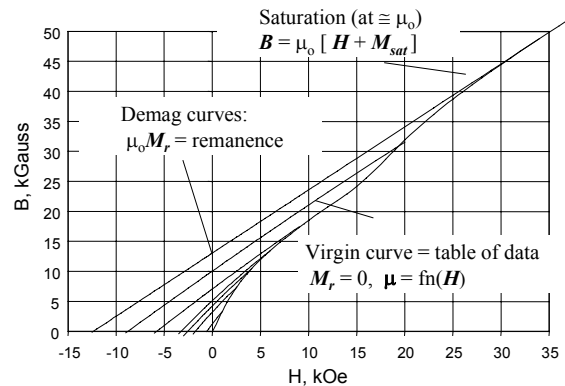
Fig. 1. Major and minor hysteresis loops along the easy axis

polynomial with three coefficients a,b,c (Fig.1). To determine the demagnetization characteristics between the defined set of quadratic polynomials, a nonlinear interpolation between the polynomial coefficients are used. Because some of the minor loops for sintered rings have a complicated shape, the quadratic approximation is applied separately to two portions of the demagnetization curves in the first and second quadrants, respectively (Fig.2). This requires two different sets of coefficients for the same material. The first set is used for the simulation of the pulse magnetization, while the second one is loaded in the magnet model when the solution is exported into the application model
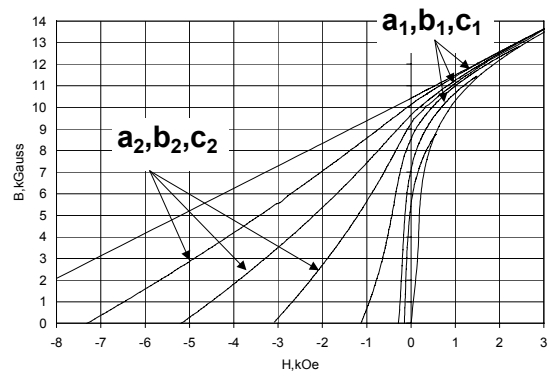
Fig. 2 Approximation of minor B-H curves of a sinered ring in the first and second quadrants

Although normally more than two poles are required for the servomotor, a straight magnetization (Fig. 3) is considered for validation of the model. To find a distribution of magnetization vector across the magnet the following transient problem is solved

$$\vec{H} = \vec{H}_e - \frac{1}{4\pi} \nabla \int_{V_m} \frac{\vec{M}\,\vec{R}}{R^3} dv + \frac{1}{4\pi} \int_{V_m} \frac{\vec{J}_e \times \vec{R}}{R^3} dv \qquad (1)$$

$$\vec{J}_e = -\frac{\sigma\mu_0}{4\pi} \frac{\partial}{\partial t} \nabla \times \int_{V_m} \frac{\vec{M} + \vec{H}}{R} dv \qquad (2)$$

$$\left[\vec{M}(\vec{H})\right] = \begin{bmatrix} M_r(H_r) & 0 & 0 \\ 0 & M_\phi(H_\phi) & 0 \\ 0 & 0 & M_z(H_z) \end{bmatrix} \qquad (3)$$

where H_e is the magnetizing field varied with time, M is the magnetization vector, J_e is the eddy current density , σ is the ectrical conductivity of magnet.

When applying a time-variable field, the magnet follows its virgin curve. The field vector is resolved into components along the easy (radial) and transverse axes, so that each axis is treated independently. The transition from the virgin to demagnetization curves along each axis occurs when the corresponding field component starts to decrease. Once the material has switched onto a demagnetization curve, the magnetization corresponding to the intersection of this curve with the virgin curve is remembered

RESULTS

The magnetization problem (1)-(3) was solved by an integral method with iterations on the magnetization at each time step The distribution of the magnetization vector was used to calculate the static field around the ring.

The straight magnetization of ring magnet in a solenoid was used for experimental study. The surface field profile was measured with a resolution of 1000 points per one degree. The comparison shows that test results are in good agreement with the predicted magnetization distribution only for hot extruded rings when the field is measured in the presence of back iron inside and outside of the ring (Fig.4). The discrepancy between the model and test increases for the open-circuit measurements when operating points in the magnet move towards H-axis. This is especially crucial for the sintered rings having highly nonlinear demagnetization curves. Extra minor hysteresis loops around an origin are required to predict the field oscillations near the ring neutral zone. The further improvement of the model to increase its overall accuracy is under way.
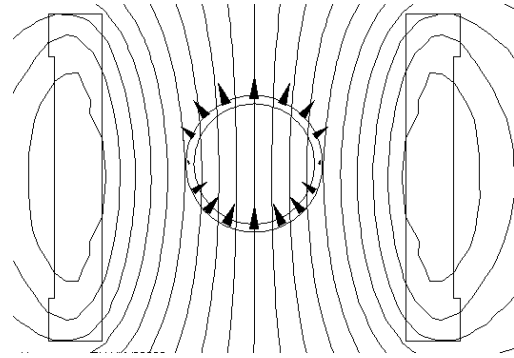
Fig.3. Pulse magnetization of anisotropic ring in the parallel field
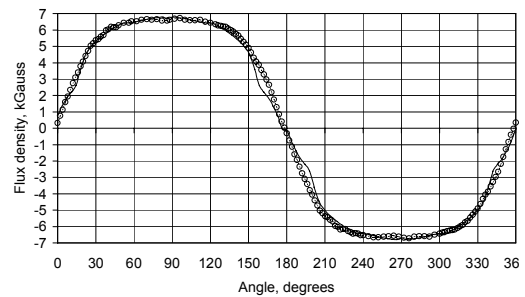
Fig.4. Flux density distribution along the air gap between the back-extruded ring and outer back iron : solid line = model, o = test
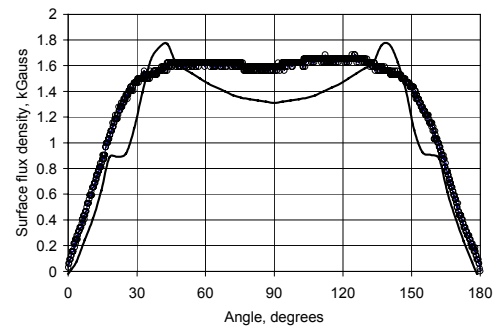
Fig.5. Flux density distribution on the surface of the back-extruded ring with the inner core inside : solid line = model, o = test

REFERENCES

[1] Y. Zhilichev, D. Miller, P. Campbell, J. Simkin, "Accurate model for pulse magnetization of anisotropic permanent magnets", Proc.17th Int'l Workshop on Rare Earth Magnets and their Applications, Ed. by G.Hadjipanayis, Delaware, pp. 115-126, 2002

B-H loop Modeling of Magnetics Based on Normal Distribution

K. W. E. Cheng, L. Yan and S. L. Ho

Department of Electrical Engineering, the Hong Kong Polytechnic University, Hung Hom, Kowloon, Hong Kong
Emails: eeecheng@polyu.edu.hk; 01901820r@polyu.edu.hk; eeslho@polyu.edu.hk

Abstract—A novel modeling method based on the normal distribution of the dipoles is used to represent the B-H loop of magnetic materials. The dipole representation can be expressed in 2-orientation and 4-orientalisation. Depending on the accuracy, the modeling method typically requires only the magnetic saturation parameter, the critical H-field and a few control parameters. Experimental results show the method can be used to represent the B-H loop of materials very accurately.

INTRODUCTION

The modeling of B-H loop using finite element [1] and Preisach mode [2-3] has been proposed by many researchers with success. On the other hand, the dipole theory of the magnetics facilitates the consideration of the magnetic dipoles in two or more orientations and that can be computed using the accumulation effect.

In the absence of magnetisation, the domains are randomly distributed and the total number of dipoles in either orientation is equal. When magnetisation occurs, the dipoles distributions are then aligned towards one orientation.

DIPOLE ORIENTATION THEORY

Assume N_0 and N_{180} are the total number of dipoles in the two orientations, the total number N_T which is a constant is:

$$N_T = N_0 + N_{180} \tag{1}$$

The normally distributed domains tend to align along the same direction as that of the applied magnetisation. Therefore the B-field for a given H is:

$$B(H) = k\left(\int_{-\infty}^{H} p(x)dx - \int_{-\infty}^{0} p(x)dx \right) \tag{2}$$

where k is a scaling constant and p is the normal distribution function which is:

$$p(x) = e^{-\frac{(x-m)^2}{2\sigma^2}} \tag{3}$$

where m is the mean value of $p(x)$ and σ is the standard deviation. The first integral of (2) is to describe the distribution of the dipoles whereas the second integral is to ensure the B-H hysteresis is balanced between the positive and negative values. Its value can be approximated by:

$$\int_{-\infty}^{0} p(x)dx = 1.25\sigma \tag{4}$$

A B-H loop is formed by an upward trajectory and a downward trajectory. Eq. (2) is in fact a function of four independent variables. Therefore the trajectory is re-written as $B(H,k,m,\sigma)$. The upward trajectory can then be represented by:

$$B_u = B(H, k, -H_c/2, B_{sat}/(1.25k)) \tag{5}$$

the downward trajectory is represented by:

$$B_d = B(H, k, H_c/2, B_{sat}/(1.25k)) \tag{6}$$

where B_{sat} is the saturated field and the domains are either aligned to 0° or 180° of the applied field; H_c is the critical H-field when B=0. It should be noted that:

$$B_{sat} = 1.25k\sigma \tag{7}$$

$$H_C = m \tag{8}$$

The B_u and B_d form a limiting loop. The above equations form a simple and realistic mechanism to model the B-H loop of a magnetic material. The method can also be used to calculate the minor loop under DC and AC operations. Once B-H is determined, the hysteresis loss P_h can be determined easily by calculating the area enclosed by B-H loop.

Higher orders orientations such as 4, 8, etc can also be used. The basic equation for four orientations of 0°, 90°, 180° and 270° can be described by 2 normal distribution functions as:

$$B(H) = k\left(\int_{-\infty}^{H} p_1(x)dx - \int_{-\infty}^{0} p_1(x)dx \right) + k\left(\int_{-\infty}^{H} p_2(x)dx - \int_{-\infty}^{0} p_2(x)dx \right) \tag{9}$$

COMPUTATION RESULT

Fig 1 shows the normal distribution of the domains for the upward magnetisation of m = -300A/m and downward magnetisation of m = 300A/m for a typical ferrite. The corresponding B-H is shown in Fig 2 with the following describing parameters: B_{sat}=0.31T, H_c=300A/m that are based on k=0.02 H/m, σ=250A/m.
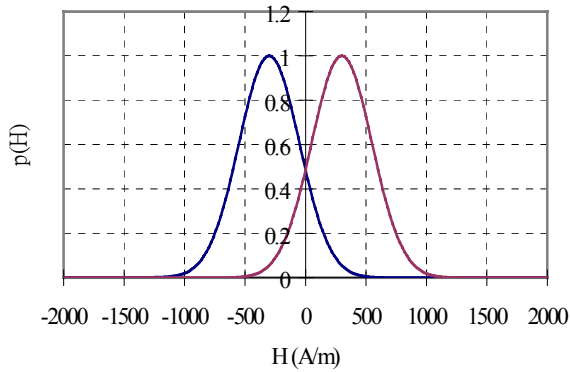
Fig 1 Probability distribution function of the domain
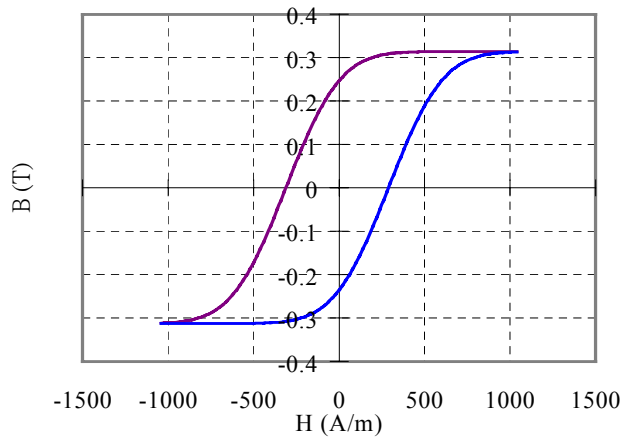
Fig 2 B-H loop formed by the probability distribution function

Fig 3 shows the B-H curve of the low-permeability materials poly10 with a composition of Co and Ni in the ratio of 20:10. The H-field is increased to 33kA/m in order to produce a B-field of 0.11T. It can be seen that the materials have a very low relative permeability of only 2.7. The corresponding hysteresis loss is 480J/m³.
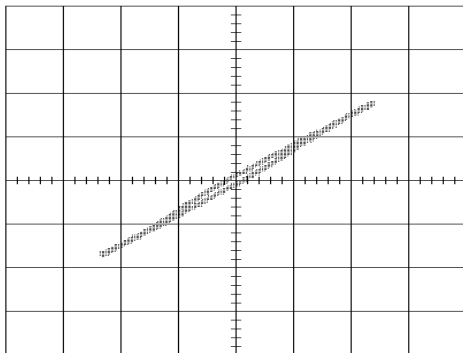
Fig 3 Measured B-H loop of the new material poly7
(y: 0.06T/div, x: 13.3kAm⁻¹/div)

The above modelling techniques can be used to model new materials. Fig 4 shows the computed B-H loop. The parameters used in the simulations are:

k=0.0035 H/m, m= 1000 A/m, σ=45000 A/m

It can be seen that the proposed method represents a simple method to model the B-H loops of magnetic materials.
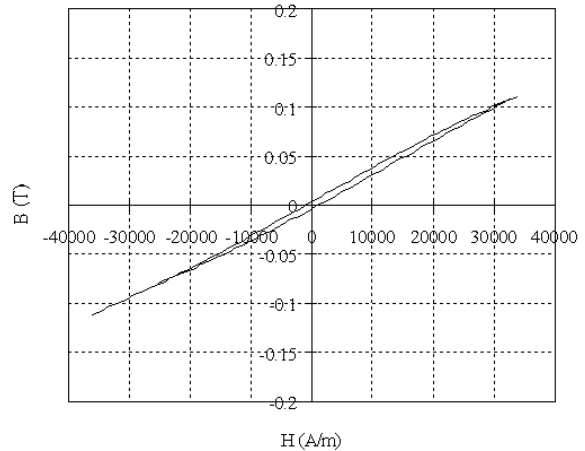
Fig 4 Simulation of the B-H loop of material poly10

CONCLUSIONS AND DISCUSSIONS

The proposed modeling method gives a simple but powerful representation of the characteristics of magnetic materials. It can be shown that the higher the number of orientations being used, the more accurate is the model. Nevertheless, the amount of input data is typically quite small. In the case of two orientations, only the values of k, m, σ are necessary.

ACKNOWLEDGEMENT

REFERENCES

[1] H.L.Toms, R.G..Colclaser, M.P.Krefta, "Two-dimensional finite element magnetic modeling for scalar hysteresis effects", *IEEE Transactions on Magnetics* , Volume: 37 (2), March 2001, pp. 982 -988

[2] S.R.Naidu: "Time domain model for the ferromagnetic core including the effects of hysteresis and eddy currents", *IEE Proceedings–A*, Vol. 138, No. 1, Jan 1991, pp. 44-50.

[3] S.Y.Rui, J.G.Zhu and V.S.Tamsden: "A generalised dynamic circuit model of magnetic cores for low- and high-frequency applications", *IEEE Trans Power Electronics*, Vol. 11(2), March 1996, pp. 251-259.

Calculation of Losses in Laminated Ferromagnetic Materials

Imre Sebestyén, Szabolcs Gyimóthy, József Pávó

Department of Electromagnetic Theory, Budapest University of Technology and Economics,
Egry József u. 18. Budapest, H-1521 Hungary
si@evtsz1.evt.bme.hu, gyimothy@evtsz1.evt.bme.hu, pavo@evtsz1.evt.bme.hu

Oszkár Bíró

Institut für Grundlagen und Theorie der Elektrotechnik, Technical University of Graz,
Kopernikusgasse 24, Graz, A-8010 Austria
biro@igte.tu-graz.ac.at

Abstract — **Numerical method for calculation of the power losses of nonlinear laminated ferromagnetic cores is presented. The calculation is made in two subsequent steps. In the first step, the approximate magnetic field distribution in the material is determined assuming a non-laminated bulk nonlinear ferromagnetic material with anisotropic conductivity. In the second step the nonlinear ferromagnetic material of the laminated core is replaced to linear material with spatially inhomogeneous permeability. The actual permeability distributions of the lamination are determined based on the magnetic field obtained from the first calculation and the nonlinear B-H curve of the material. In this paper the outlined method is verified through calculations made by FEM studying a simple benchmark arrangement. Different methods for assigning the inhomogeneous permeability are also investigated.**

INTRODUCTION

Calculation of losses in laminated ferromagnetic cores pose a quite time consuming task for conventional electromagnetic field calculations. The main reason of the required huge computational work is the fact that the thickness of the sheets forming the laminated core is very small (0.3-0.5 mm) compared to the other dimensions of the devices. Consequently, a very large number of elements (and unknowns) is resulted for the accurate analysis of the ferromagnetic core of such devices. In a previous paper [1] we presented three efficient methods for the approximate prediction of the eddy current losses in the case of linear core material. These methods process the field distribution obtained from anisotropic solution considering the real laminated geometry. The computational costs are drastically reduced and predictions of losses are significantly improved applying this treatment. Recently we intended to extend these methods for the treatment of nonlinear ferromagnetic materials. In order to perform this, we developed a method to model the homogeneous nonlinear material as spatially inhomogeneous but linear material. In the present paper we describe this method. The validity of the described method will be studied through the analysis of a benchmark arrangement. In the following sections the method calculation of inhomogeneous permeability, the studied benchmark configuration and reference solution is presented, following which the power loss prediction is compared with the reference data. In the final paper we will investigate the way of the discretization of the inhomogeneous materials coupled to the method of the permeability assignment in order to further improve the loss prediction; moreover the proposed method also will be verified comparing the calculated results to measured ones.

CALCULATION OF INHOMGENEOUS PERMEABILITY AND LOSSES

The real electromagnetic field inside the laminated core is approximated in two subsequent steps. In the first step the laminated core is modeled as a homogeneous medium whose B-H curve is nonlinear and whose conductivity is anisotropic having zero conductivity in the direction perpendicular to the laminations. This so-called anisotropic solution gives an agreeable approximation of the overall electromagnetic field distribution for the core, but the power loss obtained from this solution is not correct [1].

During the second step of the calculations the sheets of the laminated core are discretized on a regular grid. In each brick, the material is substituted by a linear material whose permeability is determined based on the nonlinear B-H curve and the magnetic field obtained from the anisotropic solution. In the paper we used two different methods for this purpose. In case of method #1 the equivalent permeability of a brick is calculated as the slope of the line on the B-H plane connecting the origin with the actual point of the B-H curve corresponding to the maximum value of the first harmonic of the magnetic field average calculated on the given brick. To get physically more realistic permeability prediction, this very simple method can be replaced by a more sophisticated one (method #2), when the effective permeability is calculated by the RMS method described in [2]. In this case assuming the magnetic field strength $H(\mathbf{r},t)$ is a time harmonic function everywhere in the core material, the permeability is calculated as

$$\mu = \frac{\sqrt{\dfrac{1}{T}\int\limits_{<T>} B^2(t)\,dt}}{\hat{H}/\sqrt{2}} = \frac{B_{rms}}{H_{rms}}, \qquad (1)$$

where $B(t)$ is calculated for every time step using the B-H curve of the material, and $\hat{H}$ is the first harmonic amplitude of the magnetic field intensity. T denotes the length of one period.

In the second step of the calculations the obtained linear and inhomogeneous laminated core is analyzed. During this analysis, the sheets of the laminations are processed one by one using the averages of the field values tangential to the laminate as input data. Detailed presentations of these methods can be found in [1]. Having the result of this calculation, the power loss produced by small eddy currents flowing in the cross-sections of the sheets is also obtained.

BENCHMARK ARRANGEMENT

The geometry of the benchmark problem studied is shown in Fig. 1 where the dimensions of the arrangement are also displayed. The exciting coil is driven with a sinusoidal current that frequency is 50Hz and the total exciting current is $24 \cdot 10^3$ AT. The conductivity of the core material is 5,875 MS/m. The B-H curve of the applied core material is shown in Fig. 2.
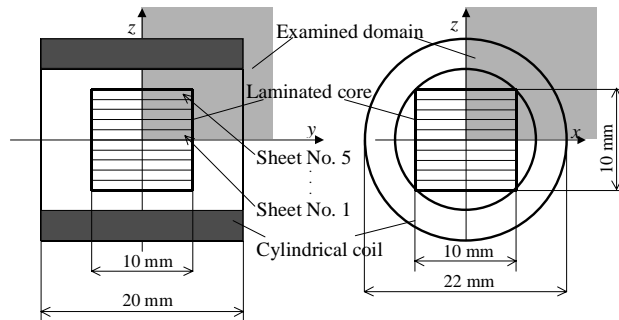
Fig. 1. Geometry of the benchmark configuration
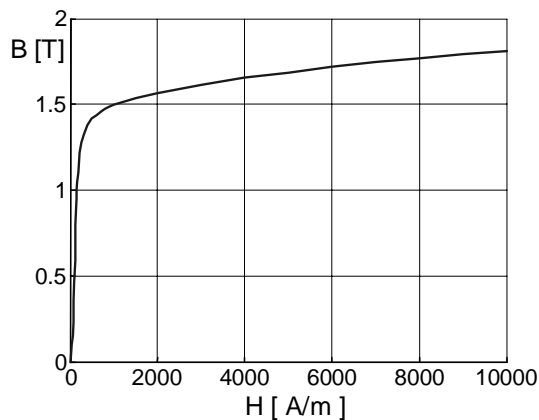
Fig. 2. B-H curve of the ferromagnetic core

REFENCE SOLUTION

In order to evaluate the results of the described methods, the transient analysis of the laminated nonlinear core is also done. The result of this calculation will be referred as the reference solution. The calculations used as reference are carried out by FEM code using second order hexahedral elements. For the solution of the problem the T, Ψ-Ψ formulation is used. This method gives the possibility to model the laminations by prescribing the tangential component of the current vector potential, T, to zero on the boundaries between the sheets. The average power loss is calculated as the mean value of the instantaneous losses determined for a whole period of the transient solution.

RESULTS

In Table I, the power losses of the core material calculated from the reference and the anisotropic solutions and the loss approximation obtained by FEM using the spatially inhomogeneous permeability are compared. We can see that the loss predicted using the proposed method gives considerably better result than the anisotropic solution.

TABLE I. CALCULATED LOSSES

Sheet #	Power Loss [mW]		Method #1		Method #2	
	Reference	Anisotropic	Loss [mW]	Error [%]	Loss [mW]	Error [%]
1	6.0970	-	8.3561	37.05	7.9717	27.80
2	6.8711	-	7.9452	15.63	7.3249	6.60
3	8.2701	-	9.5844	18.89	8.6550	4.65
4	9.4344	-	12.2224	29.55	10.8752	15.27
5	10.1223	-	15.1951	50.12	13.3599	31.98
Σ	40.7949	5.2052	53.3032	30.66	48.0067	17.68

REFERENCES

[1] J. Pávó, I. Sebestyén, Sz. Gyimóthy and O. Bíró, "Approximate Prediction of Losses in Transformer Plates," *10th International IGTE Symposium, Graz, Austria,* Sept. 16-19, 2002, to be appeared
[2] G. Paoli, O. Bíró and G. Buchgraber, "Complex Representation in Nonlinear Time Harmonic Eddy Current Problems," *IEEE Trans. Magn. Vol. 34,* pp. 2625-2628, Sept. 1998

Variability analysis applied to cable accessories made of composite materials

B.De Vivo[#], G.Spagnuolo[#], V.Tucci[#], M.Vitelli[*]

[#] DIIIE - Università di Salerno
I-84084, Fisciano (SA) – ITALY
e-mail: spanish@ieee.org

[*] DII - Seconda Università di Napoli
I-81031, Real Casa dell'Annunziata, Aversa (CE), Italy
e-mail: vitelli@unina.it

Abstract - **In this paper, an evolutionary approach to the variability analysis applied to a cable termination equipped with a composite material based stress control tube (accessory used for the stress relief in cable terminations) and modeled by means of a lumped non-linear circuit is presented. The evolutionary algorithm allows minimizing the underestimation error that affects classical Monte Carlo-based methods. The technique gives reliable results also whenever large parameters variations need to be taken into account and performance functions that are non-linear with respect to parameters are considered.**

I. INTRODUCTION

In recent years, variability analysis has become a crucial task in system design because of the increasing demand of high-performances and high reliability devices. Modern CAD tools need to be capable of handling large variations and uncertainties that may affect the system parameters. Aging, temperature stress, field stress, radiation, distorted operation give rise to an increase of the factory tolerance, which only depends on system manufacturing technologies. Moreover, if parasitics are considered, their uncertainty is intrinsically large, the statistical distribution of their values is in general not known and often no prior knowledge about their correlation is available. In such conditions, variability analysis results in Worst-Case Analysis (WCA), with parameters' values uncorrelated and uniformly distributed. Performing an effective and reliable WCA in presence of large parameter variations means to be able to provide a neither too optimistic nor too pessimistic foreseeing. A too optimistic True-Worst-Case (TWC) foreseeing in systems design compromises the compliance with regulations and/or performance constraints. On the other side, a too pessimistic foreseeing leads to badly sized systems and/or to products less competitive for the market.

II. PROBLEM FORMULATION

In fig.1a a Stress Control Tube (SCT) in a cable termination is depicted. SCT's are tubes of suitable stress grading materials characterised by a rather high non linear permittivity and a non linear resistivity. Such materials are used in order to reduce the electric field enhancement in high voltage cables-terminations and are obtained by loading the polymeric matrix with suitable fillers such as carbon-black. SCT's can be modelled with the simple transmission line RC network [2] shown in fig.1b. The cable termination is divided in N elements of length Δz, characterised by a transversal capacitance C_t, a longitudinal capacitance C_l and a longitudinal conductance G. Such parameters assume the following expressions:

$$C_t = \frac{2\pi\varepsilon_0\varepsilon_r\Delta z}{\ln(r_2/r_1)}; C_l = \frac{\pi\varepsilon_0\varepsilon_{rt}(V)((r_2+\delta)^2 - r_2^2)}{\Delta z}; G = \frac{\pi((r_2+\delta)^2 - r_2^2)}{\rho(V)\Delta z}$$

The capacitance C_t is associated to the elementary flux tube inside the cable primary insulation; ε_r is the relative permittivity of the cable main insulation while r_1 and r_2 represent its inner and outer radii. Capacitance C_l and conductance G are associated to the SCT; in particular δ is its thickness and $\rho(V)$ and $\varepsilon_{rt}(V)$ are respectively the nonlinear resistivity and the nonlinear relative permittivity of the SCT.
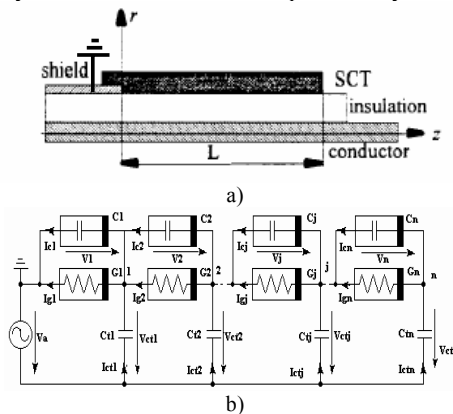
Figure 1. a) Schematic setup of a cable termination based on a heat shrinkable SCT; b) equivalent lumped parameter network.

The potential vector $v(t)=[v_1(t),v_2(t),\ldots,v_n(t)]$, obtained by evaluating the potential in the sections represented by the nodes $(1,2,\ldots,n)$ in fig.1.b, gives the discretized potential distribution along the cable. To verify the design reliability, we need to keep into account uncertainties and variations of materials characteristics, which bring about variations of the potential and field distribution along the cable with respect to the "nominal" one obtained giving "nominal" values to the SCT parameters. Parameters set include both geometrical and electrical parameters. The varying parameters considered in this paper are the main insulation relative permittivity ε_r spanning the range [2,7], the SCT thickness δ in the range [0.1,0.3]cm. Moreover, SCT permittivity has been expressed by a third order polynomial, whose four coefficients have been supposed to be affected by a ±10% variation, to keep into account manufacturing tolerances. The resulting band is reported in fig.2, together with the non linear, but certain, resistivity. Our goal is to determine the upper and lower bounds for the maximum value of the vector $v(t)$, $V=[V_{1max},V_{2max},\ldots,V_{nmax}]$, embedding all the possible solutions admitted by the variations of the mentioned parameters, supposed uncorrelated and uniformly distributed.
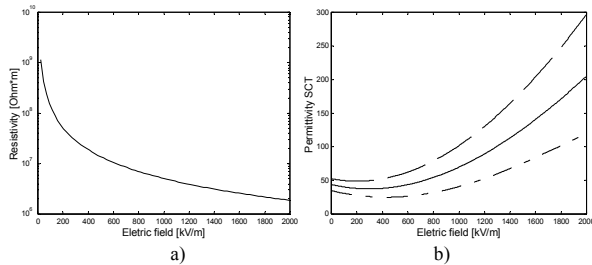
Figure 2. a) non linear resistivity adopted, b) uncertainty permittivity bound (-=nominal, --=upper and lower bounds).

The vector V is evaluated after the steady state has been reached; due to system non-linearity, V does not have an explicit expression and it is strongly non-linear with respect to parameters. The WCA is usually performed by Monte-Carlo (MC) analysis, at a high computational cost due to the big amount of trials required to get a solution that is sufficiently close to the True Worst Case (TWC). This drawback is as much evident as larger the parameters' variations and sensitivities are. A great improvement in computation time and accuracy can be obtained by the evolutionary "intelligent" MC approach illustrated in Sect. II.

II. THE EVOLUTIONARY ALGORITHM

The Evolutionary Algorithm (EA) works on a population of real-coded individuals, each one represented by a six components vector, each component being related to one of the uncertain parameter, which are free to assume values within the ranges of variation mentioned in Section I. Each set of parameters corresponds to a unique vector V of node potentials. Consequently, a Worst-Case Envelope (WCE) can be built up for each EA generation picking, for each node, the maximum and the minimum values among the potential distributions associated to the individuals. The fitness associated to each individual is an integer number in the range $[1,n]$: it has been chosen equal to the number of nodes wherein the potential value improves the WCE obtained up to the current generation. For example, referring to the evaluation of the upper bound of the worst case, at each generation the WCE is updated by taking, for each node, the maximum value among the ones given by the individuals of the current population. In place of blindly taking sets of parameters within the tolerance ranges as in MC WCA, the new trial sets of parameters are generated using the fitness value to drive the reproduction: the larger is the number of nodes wherein the solution overcomes the WCE, the higher the surviving probability of the genetic wealth of the individual. This makes the proposed EA-based approach a kind of intelligent MC analysis. Note that the current WCE does not correspond to a given set of parameters: it is a collection of the best parts of all the solutions explored during the evolution. This notably increases the selection capability of the EA.

III. SIMULATION RESULTS

Fig.3 shows the envelope obtained by EA (40 individuals over 15 generations to evaluate the upper bound and the same for the lower bound), compared with the one given by MC (3500 trials) and vertex analysis (2^6 evaluations). Each marker indicates one of the n=30 nodes of the circuit model of fig.1b. The nominal solution has been also plotted, to put in evidence the potential sensitivity with respect to the varying parameters. Fig.3b highlights the discrepancy between the MC and EA results, in spite of the larger number of MC evaluations (EA=1200, MC=3500). By fixing the number of evaluations at 1200, the discrepancy increases, as shown in fig.3c. Note that the computation time required by the evaluation of the vector V is in fact quite high with respect to the one the EA needs to generate offspring. Finally, the EA approach gives a better estimation of the TWC, namely a potential WCE that in every node is larger than the one achieved by the MC analysis.
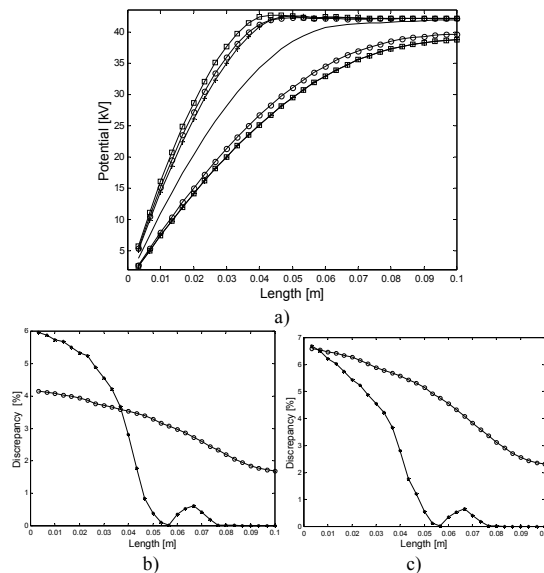
Figure 3. a) final WCE (□=EA, O=MC, +=VA, -=nominal solution); discrepancy between EA and MC (O=lower bound, *=upper bound): b) 3500 MC trials, c) 1200 MC trials.

IV. CONCLUSIONS

In this paper, the worst-case tolerance analysis of a cable termination employing a composite material based SCT is presented. The calculation of an underestimation of the true worst-case is performed by means of an evolutionary algorithm, with a considerable gain in terms of accuracy or saving of computation time with respect to classical MC based methods.

V. REFERENCES.

[1] Michalewickz, Z.: Genetic Algorithms + Data Structures = Evolution Programs, Artificial Intelligence, Springer-Verlag, 1992.
[2] Lupo, G. et al.: "Electric field calculation in HV cable terminations employing heat-shrinkable composites with non linear characteristics", Proc. of the 4th Int. Conf. on Prop. and Appl. of Diel. Mat., 1994, Vol.1, pp. 278 -281.

New Design of the Magnetic Fluid Linear Pump to Reduce the Discontinuities of the Pumping Forces

Gwan Soo Park and Kang Seo

Dept. of Electrical Engineering, Korea Maritime University
Youngdo-Ku, Dongsam-Dong, Pusan 606-791, South Korea
e-mail: gspark@hanara.kmaritime.ac.kr

Abstract — **In this research, a new design to reduce the discontinuities of the pumping forces of the magnetic fluid linear pump (MFLP) is studied. Forming shapes of the magnetic fluid at the intermediate moment is computed based on magneto-hydrodynamic analysis[1-2] so as to reduce the pumping discontinuities. Continuous pumping of the newly designed MFLP increases pumping efficiency and reduces the pumping shock. All the more, because back flow pressure is reduced remarkably, 4 yokes instead of 7 yokes are turned out to be enough to operating the MFLP without weakening of the pumping forces.**

I. INTRODUCTION

In previous works [1-2], we developed the magnetic fluid linear pump (MFLP). In this device, the sequential currents are needed to produce pumping forces so that pumping forces are mainly depended on the current patterns. The excessive forces at pumping moment could cause the medical shock [3], and weak forces at intermediate moment could cause the back flow of the pumping liquid. In this research, instead of DC, AC with 90 degree's phase differences are studied to reduce the excessive forces and back flow of the pump. Forming shapes of the magnetic fluid at the intermediate moment are analyzed to reduce the discontinuities of the pumping forces. Continuous pumping forces increase the pumping efficiency so that the length of the MFLP could be reduced to half size.

II. FORMING OF THE MAGNETIC FLUID

The forming shapes of the magnetic fluid are determined by the the driving currents. From the magneto-hydrodynamic analysis, the mass conservation law and moment conservation law gives,

$$\frac{\partial \rho}{\partial t} + \rho \nabla \cdot \mathbf{V} = \frac{d\rho}{dt} \tag{1}$$

$$\mathbf{F} = \rho \frac{d\mathbf{V}}{dt} = \rho \frac{\partial \mathbf{V}}{\partial t} + \rho \, (\mathbf{V} \cdot \nabla)\mathbf{V} \tag{2}$$

In the equation, ρ is the mass density and $\mathbf{V}$ is the velocity vector. The forces include the gravitational force, mechanical force and ectromagnetic force. So, (2) becomes

$$\rho \frac{\partial \mathbf{V}}{\partial t} + \rho(\mathbf{V} \cdot \nabla)\mathbf{V} = -\nabla U - \nabla P - \nabla \Psi \tag{3}$$

By using vector notation, we could have the following equation in steady flow.

$$\nabla \left(P - \int \mathrm{Md}H + \frac{1}{2}\rho v^2 + \rho gh \right) = \rho \mathbf{V} \times (\nabla \times \mathbf{V}) \tag{4}$$

If the fluid is irrotational such as potential flow, (4) becomes

$$P_i - \int \mathrm{Md}H + \frac{1}{2}\rho v^2 + \rho gh = C \tag{5}$$

In this equation, P_i is the pressure inside the fluid and C is called dynamic constant. At the boundary surface of the magnetic fluid, the forces inside the fluid are equal to the forces outside the fluid because liquid is free to move to the equilibrium state, which leads

$$P_o = P_i + \int MdH + \frac{1}{2\mu_o}M_n^2 \tag{6}$$

From (5) and (6),

$$P_o = 2\int MdH - \frac{1}{2}\rho v^2 - \rho gh + \frac{1}{2\mu_o}M_n^2 + C \tag{7}$$

So, the dynamic constant is represented as following,

$$C = P_o - 2\int MdH + \frac{1}{2}\rho v^2 + \rho gh - \frac{1}{2\mu_o}M_n^2 \tag{8}$$

Right hand side terms of (8) are applied pressure difference, magnetic field energy, momentum energy, gravitational energy and surface tention energy, respectively. The dynamic constant C in (8) is always the same value at the fluid surface. From the conventional nonlinear finite element method, right hand side of (8) could be computed at the given shape of the fluid. Because the geometry of the system is free to move with respect to net forces, (8) should be solved iteratively to obtain the forming shapes of the magnetic fluid[1-2].

III. NEW DESIGN OF THE MFLP TO REDUCE THE PUMPING DISCONTINUITIES

Fig. 1 shows the Magnetic Fluid Linear Pump(MFLP)[1]. There are 7 yokes and DC pulses as in Fig. 2 are used to operating the MFLP[1-2]. In the operation, there are driving force discontinuity as in Fig. 3 because of the space between yokes. In Fig. 3, the space d between the changes of each mode reduces the pumping efficiency and this could cause the back flow of the liquid.

In this research, AC driving as in Fig. 4 is studied to increase the pumping efficiency and reduce the pumping shock at the pumping moment. In each state in Fig. 4, the forming shapes of the magnetic fluid are computed as shown in Fig. 5 and Fig. 6. Magnetic field and forming shape inside the MFLP along with time and space is plotted in Fig. 7. Between each mode, the transient state reduces the pumping discontinuities so that pumping efficiency is increased and pumping shock is reduced. All the more, because back flow pressure is reduced remarkably, 4 yokes are turned out to be enough to operating the MFLP without weakening of the pumping forces.
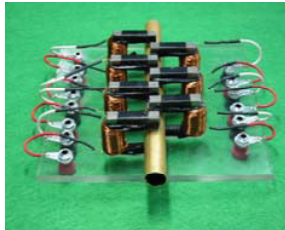
Fig.1 Magnetic Fluid Linear Pump
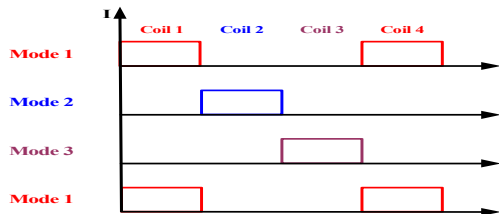
Fig. 2 Operating Current (DC Driving)
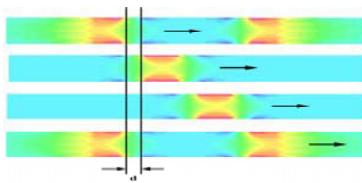
Fig. 3 Discontinuities of the Driving Forces between each mode
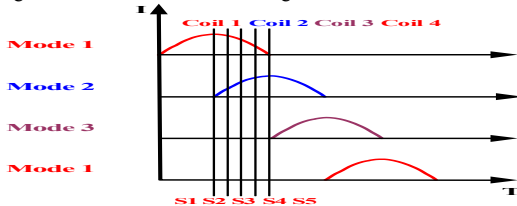
Fig. 4 Operating Current (AC Driving)
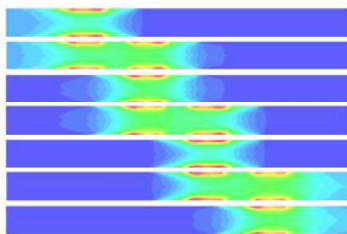
Fig.5 Computed Forming Shapes in AC Driving
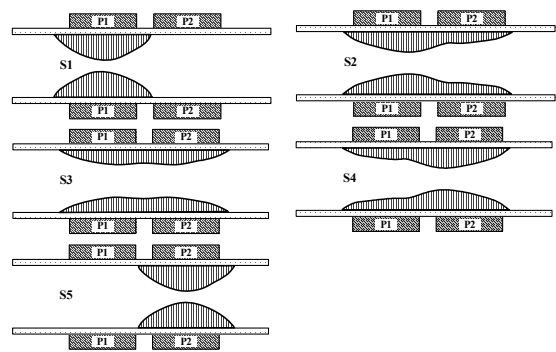
Fig.6 Changes of the Forming Shapes in AC Driving

Fig. 7 ... g Forces between each mode
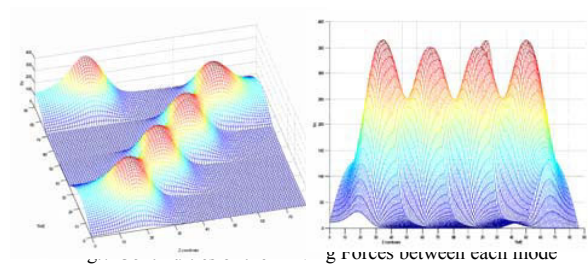
IV. CONCLUSIONS

In this research, the pumping discontinuity of the MFLP is analyzed and a new design to reduce the discontinuties are studied by magneto-hydrodynamic analysis. Forming shapes of the magnetic fluid at the intermediate moment is computed so that continuous pumping of the newly designed MFLP increases pumping efficiency and reduces the pumping shocks. All the more, because back flow pressure is reduced remarkably, 4 yokes instead of 7 yokes are turned out to be enough to operating the MFLP without weakening of the pumping forces.

V. REFERENCES

[1] G. S. Park and S. H. Park, "New Structure of the Magnetic Fluid Linear Pump", IEEE Trans. Magn., vol. 36, no. 5, pp.3709-3711, September 2000.
[2] G. S. Park, S. H. Park," Design of Magnetic Fluid Linear Pump", *IEEE Trans. Mag.,* vol. 35, no. 5, pp. 4058-4060, September 1999.
[3] Yamaguchi M, et. al., "Design investigation of linear motor for artificial heart driving", *Trans. Institute of Elect. Eng. of Japan D-A Publication of Industry Applications Society*, V.117-D, N. 5, 1997.
[4] Zou Jibin and Lu Yongping, "Numerical calculations for ferrofluid seals," *IEEE Trans. on Mag.*, vol.28, No. 6, pp 3367-3371. Nov. 1992.

Method of Nonlinear Magnetic Field Analysis
Taking into Account Eddy Current in Laminated Core

Kazuhiro Muramatsu, Takashi Okitsu and Hidefumi Fujitsu

Department of Electrical and Electronic Engineering, Saga University
1 Honjo-Machi, Saga 840-8502, Japan
e-mail: muramatu@cc.saga-u.ac.jp

Abstract − In this paper, the method for modeling laminated core by solid model is investigated. The method for taking into account eddy current in each steel plate used for laminating, which is developed in the linear analysis, is expanded to the nonlinear analysis. The space factor of the lamination is also considered. The effectiveness of the proposed method is shown by using a simple model.

INTRODUCTION

In electrical machines, laminated cores are commonly used in order to reduce the eddy current losses. In the finite element analysis of the magnetic field in such a machine, the laminated core is normally modeled by the solid model in order to save the computation cost. In the ordinary method, the eddy current in the core is neglected because the eddy current loops in laminated cores are much different from those in solid cores. However, it seems that the eddy current in the steel plate used for laminating sometimes cannot be neglected, such as a machine with an inverter power supply of which voltage has harmonic components.

Recently, the method of magnetic field analysis taking into account eddy current in laminated core is proposed in the linear analysis [1]. In this method, the laminated core is modeled by the solid one with anisotropic permeability and conductivity, and the analytical solution is adapted for cases that take into account the eddy current in the steel plate. In this paper, the method is expanded to nonlinear analysis by using the 1-dimensional (1D) eddy current analysis instead of the analytical solution in the steel plate. Moreover, the space factor of the lamination is also considered in order to obtain more accurate results. Finally, the effectiveness of the proposed method is investigated by using a simple model.

METHOD OF ANALYSIS

Laminated core and Solid Core Model

The core constructed by laminating steel plates (permeability μ^*, conductivity σ^*) and the approximated solid model are shown in Fig. 1. In this paper, the laminated core is modeled by the solid core model with anisotropic permeability μ_α, μ_β and conductivity σ_α, σ_β [1]. The subscripts α and β denote values in parallel and perpendicular directions to the lamination, respectively. The method for determining each constant is described below.

Conductivity

As both paths of the eddy currents, Je_α^* and Je_α, parallel to the lamination in laminated and solid cores are the same, as shown in Fig. 1, Je_α is considered. Then, σ_α is given by the following equation using the space factor F:
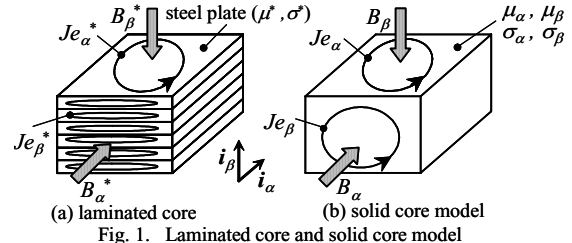
Fig. 1. Laminated core and solid core model

$$\sigma_\alpha = F\sigma^* \tag{1}$$

On the other hand, the perpendicular components, Je_β^* and Je_β, of the eddy currents are much different in the two cases. Therefore, Je_β is neglected, and the effect of Je_β^* is taken into account by the permeability μ_α. Namely, the conductivity σ_β becomes zero as follows:

$$\sigma_\beta = 0 \tag{2}$$

Permeability

In order to determine the permeability μ_α taking into account Je_β^*, the flux distribution in the steel plate is calculated by the 1D nonlinear eddy current analysis (called "sub-analysis" in this paper). The mesh for the sub-analysis of the steel plate with thickness $2d$ is shown in Fig. 2. The vector potential, $A_d^{(jp)}$, at node jp on the Dirichlet boundary at $z=d$ is given by the flux density $B_\alpha^{(ie)}$ of element ie in the 3D nonlinear eddy current analysis of the solid model (called "main-analysis") as follows:

$$A_d^{(jp)} = B_\alpha^{(ie)}d \tag{3}$$

In the nonlinear iteration, the flux density, $B_h^{(je)}$, for evaluating the nonlinearity in the element je in the sub-analysis is defined by not only the flux density $B_\alpha^{(je)}$, but also the flux density $B_\beta^{(ie)}$ in the main-analysis as follows:

$$B_h^{(je)} = \sqrt{B_\alpha^{(je)2} + B_\beta^{(ie)2}} \tag{4}$$
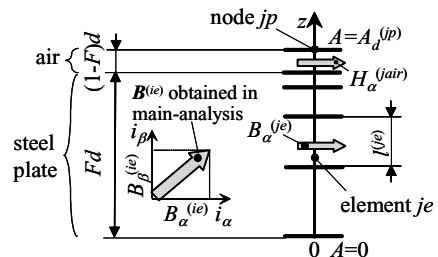
Fig. 2. Mesh for sub-analysis (1D)

Finally, the permeability $\mu_\alpha^{(ie)}$ used in the main-analysis is determined by the following equation:

$$\mu_\alpha^{(ie)} = B_\alpha^{(ie)} \Big/ H_\alpha^{(jair)} \qquad (5)$$

where $H_\alpha^{(jair)}$ is the magnetic intensity in the air obtained from the sub-analysis.

The permeability $\mu_\beta^{(ie)}$ is given by the following equation:

$$\mu_\beta^{(ie)} = d \Bigg/ \left(\sum_{je=1}^{Nej} l^{(je)} \Big/ \mu^{(je)} \right) \qquad (6)$$

where N_{ej} is the total number of elements and l is the length of element in the sub-analysis.

Flowchart

The flowchart for the proposed method is shown in Fig. 3. The sub-analysis is carried out for each element *ie* at each nonlinear iteration in the main-analysis. The Newton-Raphson method is used for both nonlinear iterations:

Ne_i: number of elements in core in main-analysis
Fig. 3.   Flowchart
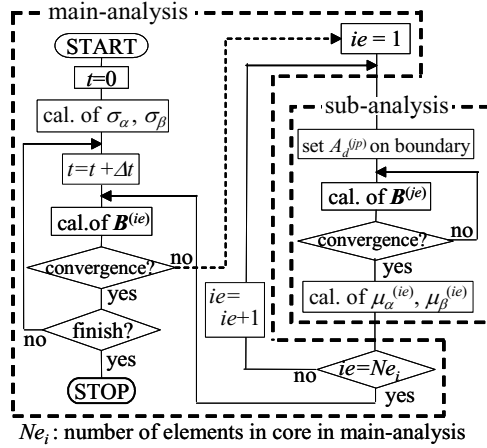
INVESTIGATION OF EFFECTIVENESS

Model and Analyzed Condition

In order to investigate the effectiveness of the proposed method, the nonlinear magnetic field in the model shown in Fig.4 is analyzed. The laminated cores are assumed to be placed in a row with gaps in *y*-direction infinitely. Each core is constructed by laminating 20 sheets of steel plates in *z*-direction, and the space factor *F* is equal to 0.96. A uniform magnetic field B_{oy} is applied in *y*-direction.

Fig. 4.   Laminated cores
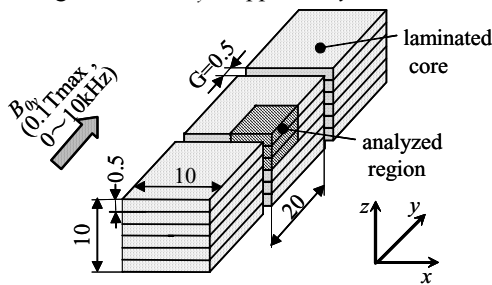
Only 1/8 region of a core is analyzed using the finite element method with 1st order brick edge elements. Two kinds of meshes for real and solid models are used as shown in Fig. 5. In the analysis of solid model, the ordinary method, that completely neglects the eddy currents in the core and the space factor *F*, is also used for comparison. The transient analysis for a cycle *T* is carried out using the step-by-step method. The time interval Δt is equal to 1/16 *T*.

Results and Discussions

The average flux densities, B_{yave}, interlinking the core at *y*=7.7mm at time *t*=0.75*T* are represented against frequency in Fig. 6. This figure shows that the result of the proposed method are in much better agreement with that of the real model, compared with the ordinary method. Table I shows the discretization data and the CPU time for each method. This table shows that the computation cost for the proposed method is much smaller than that for the real model.

(a) real model   (b) solid model
Fig. 5.   Mesh (core region)

Fig. 6.   Average flux density interlinking core
(t=0.75T, y =7.7mm)

TABLE I   DISCRETIZATION DATA AND CPU TIME
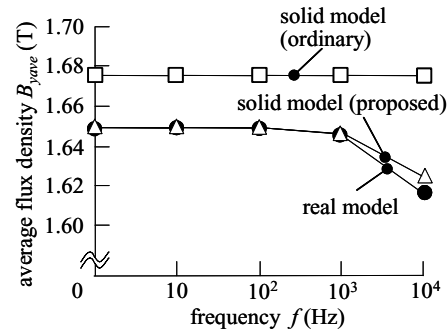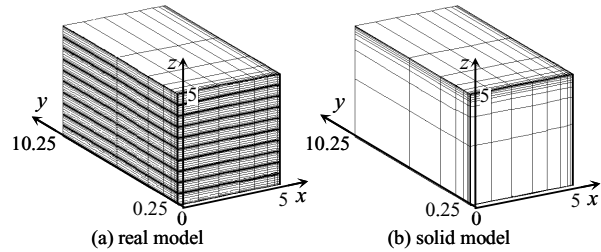
method	real model	solid model	
		ordinary	proposed
no. of elements	30,300	5,187	
computer storage (MB)	306	58	70
CPU time (h)	14.2	0.3	1.9

computer used : Intel Pentium IV 2.4GHz

REFERENCE

[1] P. Dular et al, "A 3d magnetic vector potential formulation taking eddy currents in lamination stacks into account," The conference digests of CEFC 2002, p.123, Perugia, Italy, 2002.

Homogenisation of Lamination Stacks in Linear Magnetodynamics

Laurent Krähenbühl*, Patrick Dular[+], Tarek Zeidan*

*CEGELY-CNRS, ECL, F-69134 Écully cedex, France – Laurent.Krahenbuhl@ec-lyon.fr
[+]F.N.R.S., University of Liège, Dept. of Electrical Engineering, Institut Montefiore, B28, B-4000 Liège, Belgium

Abstract— **An effective numerical modelling of devices with lamination stacks cannot be done without replacing the laminations by an equivalent solid region. So far, no convincing model has been proposed, even in the "simple" case of linear magnetodynamics – particularly if the resultant current in each sheet does not cancel. In this paper, we define the homogenised fields, and the related material properties. The noteworthy precision of the homogenised solution is shown by comparing it with the exact solution of the problem with laminations in the case of a simple "1.5D" analytical test problem.**

I. Introduction

Two papers published over the last three years propose new ideas concerning the homogenisation of lamination stacks, to lead to simplified but accurate models for finite elements. In [1] a static anisotropic problem is first solved, then the eddy currents are processed as a second order effect. The analytical space and time changes of fields and current are correctly taken into account; however, this method cannot be applied if the eddy currents have a perceptible effect on the static solution. Very recently in [2], the same analytical 1-D solutions have been a priori integrated into the test functions of the finite element formulation. The results obtained by this way are valid for a very large frequency range; on the other hand, only situations with a symmetrical magnetic flux density distribution in the normal direction of the iron sheets have been taken into account. In this paper, the validity of these formulations is extended.

II. Homogenisation

The well-known analytical solutions in a linear and conducting iron sheet concern the values of the tangential components of the magnetic flux density and magnetic field (in a direction α) on one hand, of the current density and electric field (in the direction β perpendicular to α) on the other hand. All these quantities vary in the direction γ normal to the sheets, following the same shape functions $\underline{f}(\gamma)$ et $\underline{g}(\gamma)$, which are respectively odd and even functions :

$$\underline{f}(\gamma) = \sinh[(1+j)\gamma/\delta]/\sinh[(1+j)d/2\delta] \quad (1)$$
$$\underline{g}(\gamma) = \cosh[(1+j)\gamma/\delta]/\cosh[(1+j)d/2\delta] \quad (2)$$

where d is the plate thickness and γ is equal to zero at the mid thickness of the plate.

The integral value of $\underline{g}$ will also be used in the following:

$$\underline{G} = \frac{1}{d}\int_d \underline{g}(\gamma).d\gamma = \tanh[(1+j)d/2\delta] / [(1+j)d/2\delta] \quad (3)$$

If these particular variations in the sheets are accepted, the values of the tangential component of each field (h_α, b_α, e_β or j_β) on the surfaces of the sheets define it everywhere; we get

for any tangential quantity $\underline{x}$:

$$\underline{x}(\gamma) = \tfrac{1}{2}[\underline{x}(d/2)+\underline{x}(-d/2)].\underline{g}(\gamma) + \tfrac{1}{2}[\underline{x}(d/2)-\underline{x}(-d/2)].\underline{f}(\gamma) \quad (4)$$

If the function $\underline{x}$ is continuous at the limit between two sheets, we can build a new function $\underline{X}$, which is equal to $\underline{x}$ on these limits and vary linearly in the sheets. Then we get:

$$\underline{X}(\gamma=0) = \tfrac{1}{2}[\underline{x}(d/2)+\underline{x}(-d/2)] \quad \text{and} \quad (5)$$
$$\partial\underline{X}/\partial\gamma . d/2 = \tfrac{1}{2}[\underline{x}(d/2)- \underline{x}(-d/2)] \quad \text{for } \gamma \in \;]-d/2,d/2[\quad (6)$$

$\underline{X}$ is a possible homogenisation of $\underline{x}$. We could also build an homogenised function $\widetilde{\underline{X}}$ from the mean value of $\underline{x}$ through the sheets:

$$\widetilde{\underline{X}}(\gamma=0) = \frac{1}{d}\int_d \underline{x}(\gamma).d\gamma \quad (7)$$

The homogenisation requires also to write again the Maxwell's equations – here the Ampère's theorem and the Lenz's law – in an integral form, on a scale greater than (or equal to) the thickness d of the sheets:

$$[\underline{h}_\alpha(d/2)-\underline{h}_\alpha(-d/2)] - d.\lim_{a\to 0}\frac{\underline{h}_\gamma(\alpha+a)-\underline{h}_\gamma(\alpha)}{a} = \int_d \underline{j}_\beta(\gamma).d\gamma \quad (8)$$

$$[\underline{e}_\beta(d/2)-\underline{e}_\beta(-d/2)] - \varepsilon.\lim_{b\to 0}\frac{\underline{e}_\gamma(\beta+b)-\underline{e}_\gamma(\beta)}{b} = -j\omega.\int_d \underline{b}_\alpha(\gamma).d\gamma \quad (9)$$

where $\varepsilon \ll d$ is the thickness of the insulating between two iron sheets[1] ($\underline{e}_\gamma$ is supposed to be zero *in* the sheets, but not *between* them). That is to say, with notations (6), (7) and $\underline{E}_\gamma=\underline{e}_\gamma.\varepsilon/d$ (that means that the circulations of the homogenised and actual electric fields $\underline{E}$ and $\underline{e}$ are equal in the direction γ):

$$\partial\underline{H}_\alpha/\partial\gamma - \partial\underline{H}_\gamma/\partial\alpha = \widetilde{\underline{J}}_\beta \quad \text{and} \quad \partial\underline{E}_\beta/\partial\gamma - \partial\underline{E}_\gamma/\partial\beta = -j\omega.\widetilde{\underline{B}}_\alpha \quad (10)$$

It remains to be written the phenomenological relations between the homogenised quantities. It can be seen that equations (3), (7), (4) and (5) lead to $\widetilde{\underline{X}} = \underline{X}\underline{G}$; using the relations between the local fields $\underline{b}=\mu\underline{h}$ and $\underline{j}=\sigma\underline{e}$ we get[2]:

$$\widetilde{\underline{B}}_\alpha = \underline{\mu}_{\alpha\beta}\underline{H}_\alpha \text{ and } \widetilde{\underline{J}}_\beta = \underline{\sigma}_{\alpha\beta}\underline{E}_\beta \text{ with: } \underline{\mu}_{\alpha\beta} = \mu\underline{G} \text{ and } \underline{\sigma}_{\alpha\beta} = \sigma\underline{G} \quad (11)$$

In the normal direction γ, we will simply write:

$$\widetilde{\underline{B}}_\gamma = \mu\underline{H}_\gamma \text{ and } \widetilde{\underline{J}}_\gamma = 0 \text{ that means: } \underline{\mu}_\gamma = \mu. \text{ and } \underline{\sigma}_\gamma = 0 \quad (12)$$

Consequently, the homogenised permeability and conductivity are defined as complex tensors: $\underline{\mu}$ and $\underline{\sigma}$.

At this stage of our chain of reasoning, the homogenised fields and properties that we have defined, coupled with the shape functions $\underline{f}$ and $\underline{g}$, are only an other way to write the analytical solutions in the laminated stack.

---

[1] Compared with d, the thickness ε of the insulation will be neglected in the following: it could easily be taken into account in the homogenised properties (11) and (12), which just become more complicated.

[2] As far as possible, the notations of paper [2] are used here. Even if it is not obvious, it can be shown that the term F_R of paper [2] is equal to $1/\underline{\mu}_{\alpha\beta}$: the two approaches are consistent.

The *homogenisation principle* itself consists in assuming that the homogenised fields are a continuum following – as a first step – equations (10) and (11), and more generally speaking the Maxwell-like equations:

$$\nabla\times\underline{H} = \underline{\widetilde{J}} \quad \nabla\times\underline{E} = -j\omega\cdot\underline{\widetilde{B}} \quad \nabla\cdot\underline{\widetilde{B}}=0 \quad \underline{\widetilde{B}}=\underline{\mu}\cdot\underline{H} \quad \underline{\widetilde{J}}=\underline{\sigma}\cdot\underline{E} \quad (13)$$

Replacing an actual discrete system of equations by a continuous one, we clearly do an approximation; it will be more and more accurate, as far as the number of sheets will increase.

III. ENERGETIC INTERPRETATION

In the real system, the losses are solely due to the eddy-currents, and depend on γ. For one sheet, the mean value of these losses is: (14)

$$\widetilde{P} = \frac{1}{d}\int_d \underline{e}_\alpha(\gamma)\cdot\underline{j}_\alpha^*(\gamma)d\gamma = \underbrace{\frac{\left|\underline{j}(d/2)+\underline{j}(-d/2)\right|^2}{4\sigma d}\int_d g^2(\gamma)d\gamma}_a + \underbrace{\frac{\left|\underline{j}(d/2)-\underline{j}(-d/2)\right|^2}{4\sigma d}\int_d f^2(\gamma)d\gamma}_b$$

After some calculations, we can prove that:

$$\widetilde{P} = Re(\underbrace{\underline{E}\cdot\underline{\widetilde{J}}^*}_a - \underbrace{j\omega\underline{H}\cdot\underline{\widetilde{B}}^*}_b) \qquad [\text{W/m}^3] \qquad (15)$$

In the same way, the imaginary part in (15) can be expressed as the mean value of $-\omega\underline{hb}^*$. This confirms the relevance of our choices for the homogenised quantities and properties.

The first term (a) is linked to the *even* part of the local current density $\underline{j}(\gamma)$; it will be represented in the continuous model by the losses of the homogenised current density $\underline{\widetilde{J}}$, which could be regarded as the "macroscopic" current density.

The term (b) is linked to the *odd* part of the local current, which cannot be observed on a "macroscopic" level; it will be represented by the losses due to the difference of phase between the homogenised fields $\underline{\widetilde{B}}$ et $\underline{H}$.

IV. TESTING THE MODEL

Manifold tests could be managed in 2D or 3D to compare finite element solutions obtained either with the "sheet by sheet" description of a laminated region, or with the homogenised model. For this two page paper, we rather chose to present an other test, which points out the accuracy of the homogenised equations (10) and (11) in comparison with the real solution: this is actually the main point.

The test device (Fig. 1) is excited on its front and back faces by a harmonic tangential magnetic field in direction γ. The global current (direction α) in each sheet is controlled by circuit equations, equivalent to resistances R (all identical and connected to a common point). For R→∞, each sheet is completely insulated from the others, the solution is the same in each sheet, with a zero global current. For R=0 (short circuit) the lamination has no more effect, and the solution is that of a solid conductor (global skin effect); as a consequence, the global current in each sheet is not zero. The analytical solutions for this "1.5D" problem exist, for the "real" stack as for the homogenised equivalent system. It is therefore possible to show the error due to the homogenisation itself, independently of any finite element formulation.

For the results presented in Fig. 2, we chose R to obtain non-zero global currents in each sheet, but, however, a solution very different from the simple short circuit one. The comparison shows how the solution of the homogenised equations represents the real laminated device. This practically perfect agreement was also verified for all the configurations we have processed.

V. CONCLUSION

The implementation of equations (13) in a finite element software does not pose any technical problem, because the form of the classical equations is preserved. Only complex tensors have to be used for the material properties, instead of real numbers; the post-processing may be modified, if local values are required in the laminations.

REFERENCES

[1] Karl Hollaus and Oszkar Biro, "*Estimation of 3-D eddy-currents in conducting laminations by an anisotropic conductivity and a 1-D analytical model,"* COMPEL, Vol. 18, no. 3, pp. 496-499, 1999.
[2] P. Dular, J. Gyselinck, C. Geuzaine, N. Sadowski and J.P.A. Bastos, "*A 3D magnetic vector potential formulation taking eddy currents in lamination stacks into account,"* CEFC 2002, Sorrento. To be published in IEEE T-Mag.
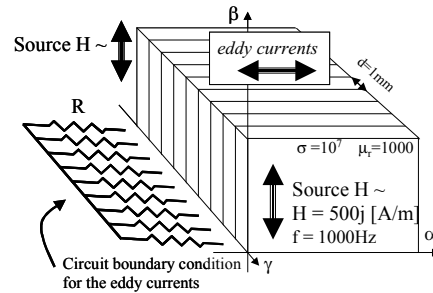
Fig. 1: Definition of the test device
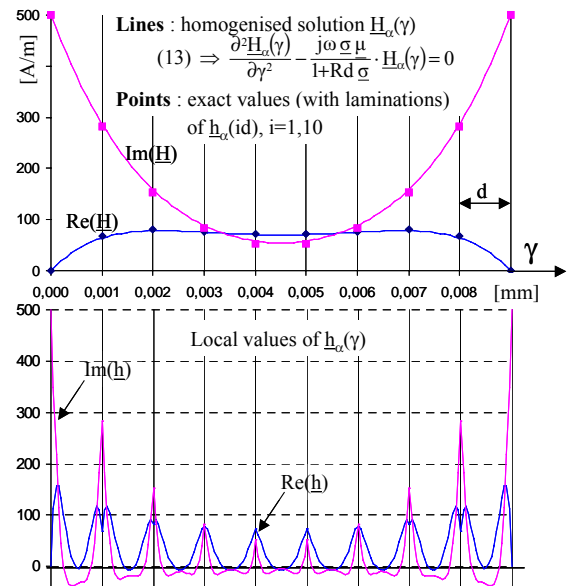
Fig. 2: Comparison homogenized/exact solutions for the magnetic field, and local variations of $\underline{h}$.

Engineering-Oriented Benchmarking of Problem 21 Family and Experimental Verification

Z.Cheng[1], R.Hao[2], N.Takahashi[3], Q.Hu[1], C.Fan[1]

(1) R & D Centre of Baoding Tianwei Group, Baoding, 071056, China (E-mail: emlab@btwtc.com)
(2) Dept. of Electrical Engineering, Hebei University of Technology, Tianjin, 300130, China
(E-mail: ruixianghao@eyou.com)
(3) Dept. of Electrical and Electronic Engineering, Okayama University, Okayama, 700-8530, Japan
(E-mail: norio@eplab.elec.okayama-u.ac.jp)

Abstract **This paper shows the results concerning both the TEAM Problem 21 and the TEAM-based test models, and details the stray-field loss behaviors via engineering-oriented benchmarking.**

INTRODUCTION

TEAM Problem 21 is an engineering-oriented loss model, which was approved by the International TEAM Board in 1993[1] and updated in TEAM-Sapporo, 1999[2]. A number of results and some valuable conclusions concerning TEAM Problem 21 have been presented [1-14]. The TEAM activities have played an important role in progress of electromagnetics in engineering. Fortunately, thrice TEAM Workshops have been taken place in China: TEAM-Qiandaohu(1992), TEAM-Yichang(1996) and TEAM-Chengde(2000)[14]. Some important suggestions regarding TEAM have been made in TEAM-Chengde.

As the further development of TEAM Problem 21, a TEAM-based benchmark family has been proposed [13]. In this paper the features and the essentiality of the Problem 21 family are discussed and the newly obtained behaviors of iron loss are shown.

PROBLEM 21 AND BENCHMARKING FAMILY

TEAM Problem 21 shown in Fig. 1 has two models: Model A and Model B [1]. Model A consists of two exciting coils of the same dimensions and two steel plates. In the center of one steel plate, there is a rectangular hole. Model B consists of two exciting coils and one steel plate without hole. The direction of exciting current of one coil is different from that of the other coil.

In order to solve the key problems encountered in electromagnetic design, the engineering benchmarking is really necessary, because the bottleneck problems cannot be detailed and the analysis methods cannot be verified through a complicated engineering system. For example, the iron loss generated in the transformer parts, such as oil-tank, or core-plates with different number of slits, or the losses produced in the hybrid structure made of different materials. For this reason, the authors have proposed other benchmarking models based on TEAM Problem 21, named as Problem 21+(with slit-plate) [10] and Problem 21*(with the magnetic and non-magnetic plates) [13], as shown in Fig. 2 and Fig. 3. Those models compose a Problem 21 family. The corresponding eddy current distributions for Problem 21+ and Problem 21* are shown in Fig. 2 and Fig. 4, respectively.

(a) Model A (b) Model B
Fig. 1. TEAM Problem 21

Prob. 21+-0

Prob. 21+-1

Prob. 21+-2

Prob. 21+-3

Fig. 2. TEAM-based Problem 21+

Non-magnetic plate Magnetic plate

Coil Coil
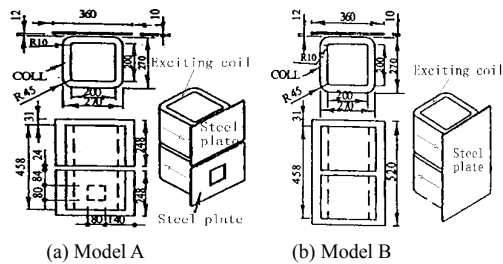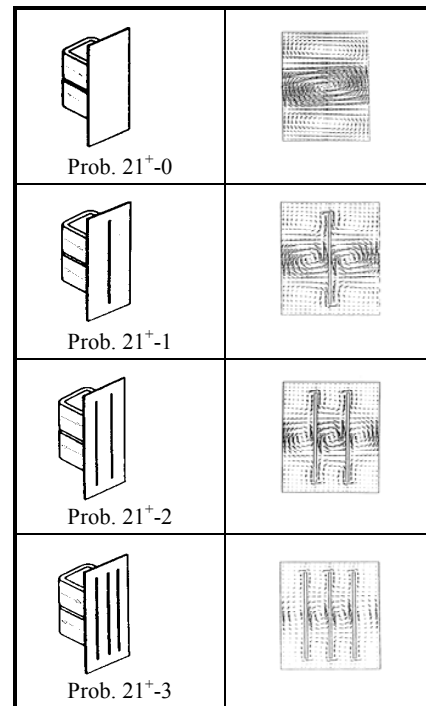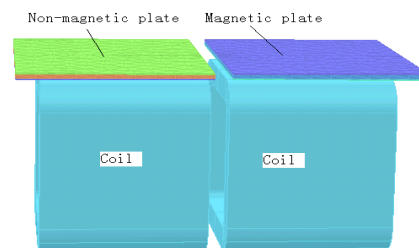
Fig. 3. TEAM-based Problem 21*
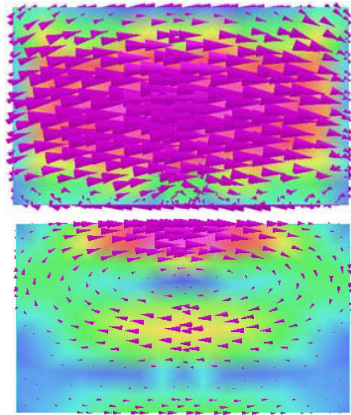
Fig. 4. Eddy current distributions in both the magnetic (upper) and non-magnetic plates of Problem 21*(calculated by OPERA)

RESULTS AND CONCLUSIVE SUMMARY

A number of the calculated and measured results of magnetic flux densities, eddy currents and power losses concerning Problem 21 family have been obtained by the authors[1,2,10-13], as partly shown in TABLES I, II and III.

TABLE I. EDDY CURRENT AND HYSTERESIS LOSSES
(TEAM PROBLEM 21)

Model		Calculated (W)			
	Methods	P_e	P_h	P_t	P_h/P_t(%)
A	1	5.32	2.92	8.24	35.4
	2	5.36	3.04	8.40	36.2
B	1	7.24	3.54	10.78	32.8
	2	7.70	4.11	11.81	34.8

P_e: Eddy current loss; P_h: Hysteresis loss; P_t: Total loss.

Notes:

(a) The measured total losses (P_t) for TEAM Problem 21 are:
Model A: 9.28(W); Model B: 12.56(W);
(b) The definition of the methods in TABLE 1 is as follows:
Method 1denotes nonlinear transient method [11-12] (step by step, with fine FEM mesh);
Method 2 denotes quasi-nonlinear method [2, 15] (with fine FEM mesh).

TABLE II. EDDY CURRENT LOSSES (PROBLEM 21+)

Number	Measured	Calculated(W)	
of slits	(W)	2-D method	3-D method
0	9.17	14.75	9.31
1	3.40	6.23	3.34
2	1.68	3.07	1.66
3	1.25	1.86	1.14

TABLE III. LOSS RESULTS FOR PROBLEM 21*
(INCLUDING 2 COMPARATIVE MODELS)

Model	Eddy current loss(W)		Hysteresis loss(W)	Total loss(W)
	Plate 1	Plate 2		
Problem 21*	0.669	4.626	1.531	6.826
Compar. 1	3.720	3.720	2.440	9.880
Compar. 2	0.685	0.685	___	1.370

Notes:
(a)Problem 21*: plate1: magnetic; plate2: non-magnetic;
(b)Comparative model 1: plates1 and 2: magnetic;
(c)Comparative model 2: plates1 and 2: non-magnetic.

The presented results are summarized as follows:
(1) For Problem 21, the hysteresis loss, as a part of total stray loss, can not be neglected, even if the flux densities in the air region are small; the skin effect must be taken into account; the proposed method to deal with the hysteresis loss problems in electrical engineering is effective[11].
(2) For Problem 21+, the 3-D calculated loss results are in good agreement with the measured ones, which detail the loss distributions and are really important for EM design. However, 2-D results of Problem 21+are useless.
(3) For Problem 21*, the hybrid model clearly shows the loss behavior of both the magnetic and non-magnetic parts, which is concerned by the designers.

REFERENCES

[1]Z.Cheng,Q.Hu, S.Gao,Z.Liu,C.Ye,M.Wu,J.Wang,H.Zhu, An engineering-oriented loss model (Problem 21), Proc. of the International TEAM Workshop, (ed. by O.A.Mohammed), pp.137-143, 1993.
[2]Z.Cheng, N.Takahashi, S.Gao, Q.Hu, T.Sakura, Loss analysis on revised version of TEAM Problem 21, TEAM Workshop, Sapporo, 1999.
[3]T.Nakata, N.Takahashi, K.Fujiwara, H.Ohashi, H.Zhu, Analysis of an engineering oriented loss model (Problem 21), Proc. of the TEAM Workshop, Seoul, pp.51-55, 1994.
[4]J.P.A.Bastos, N.Ida, R.C.Mesquita, J.Hector, Problem 21: Solution using edge elements and a vector potential A, Proc. of the International TEAM Workshop, Berlin, pp.71-75, 1995.
[5]L.Li,X.Cui,J.Yuan, Numerical calculation of 3D eddy current loss and magnetic field(Problem 21), Proc. of the International TEAM Workshop, Berlin, pp.67-70, 1995.
[6]O.Biro,K.Pries,K.R.Richter, Various FEM formulation for the calculation of 3D eddy currents in nonlinear media, IEEE Trans. on Magn., vol.31, no.3, pp.1307-1312, 1995.
[7]J.Fetzer,S.Kurz,G.Lehner, The solution of TEAM workshop Problem 21 using BEM-FEM coupling, Proc. of the International TEAM Workshop, Okayama, pp.19-22, 1996.
[8]C.Golavanov, Y.Marechal, G.Meunir, Solution of TEAM workshop Problem 21, Proc. of the International TEAM Workshop, Okayama, pp.26-30, 1996.
[9]G.Ciuprina, D.Ioan, P.J.Leonard, D.Rodger, Solution of TEAM Problem No.21, Proc. of TEAM Workshop, Graz, pp.17-19, 1996.
[10]Z.Cheng, N.Takahashi, S.Gao, Z.Liu, Some new developments of Problem 21, Proc. of the International TEAM Workshop, Brazil, pp.21-24, 1997.
[11]N.Takahashi,T.Sakura,Z.Cheng, Nonlinear analysis of eddy current and hysteresis losses of 3-D stray field loss model (Problem 21),   IEEE Trans. on Magn.,Vol.37,No.5, pp.3672-3675, 2001.
[12]N.Takahashi, T.Sakura, Z.Cheng, Practical approach in estimation of iron losses of 3-D stray-field loss model(invited), Proc. of ICEF and TEAM Workshop, China, pp.489-493, 2001.
[13]Z.Cheng, N.Takahashi, Q.Hu, C.Fan, TEAM-based benchmark family: Problem 21+/21+/21*, Proc. of the 4th CEM, UK, 2002.
[14]Proc. of the TEAM Workshops, Qiandaohu1/Yichang2/Chengde3, China, 1992/1996/2000.
[15]G.Paoli,O.Biro,G.Buchgraber, Complex representation in nonlinear time harmonic eddy current problems, IEEE Trans. on Magn., Vol.34, No.5, pp.2625-2628, 1998.
[16]O.Bottauscio, M.Chiampi, D.Chiarabaglio, Iron loss in soft magnetic materials under periodic non-sinusoidal supply conditions, Physica B, Vol.275, Pp.191-196, 2000.

Working Transient Eddy Current Problems with Velocity using Modified Green's Functions and Impedance Matrices

Kent R. Davey

2275 Turnbull Bay Rd., New Smyrna Beach, FL 32168-5941, USA

Abstract - It is known that boundary element techniques can analyze problems with velocity by modifying the Green's function. Technically, the solution is only applicable if media in either the stationary or moving reference frame do not vary in the direction of motion. It is hypothesized that these solutions can be used to predict motion not only when the above condition is not met, but also during a transient. It is further conjectured that knoledge of the impedance matrix for this system at the excitation frequency can be used to simulate the transient. Team problem 28 is used to test this hypothesis.

Index terms - Transient, eddy current, Green's function, impedance matrix.

I. INTRODUCTION

Nearly all transient field problems are solved using a time stepping procedure in which the incremental are either explicitly or implicitly determined. Velocity effects are integral to the field equations and are treated as such. Burnet Fauchez [1] was perhaps the first to employ boundary element methods with modified Green's functions to solve constant velocity problems in which either the laboratory or moving frame remained unchanged in the direction of travel. Part of the intent of this manuscript is to determine how it performs when changes occur in the direction of movement, and whether it can be applied to a transient problem.

A second intent of this paper is to examine the use of impedance matrices in problems of this nature. The use of impedance matrices has been explored [2], but not for transient eddy current problems. The matrix relates the elements of the problem in a mixed circuit sense. Velocity is added in the computation of the current for this transient problem.

IV. TRANSIENT PREDICTION USING BEM WITH THE ALTERED GREEN'S FUNCTION

Consider predicting the force on the aluminum disk using a parametric analysis for a range of vertical positions and velocities. A double iteration was used to determine that the velocity ranged between -0.235 and 0.305 m/s, while the height varied from the starting position at y=3.8 mm up to 20 mm. A

simple nested do loop was employed as follows:

```
for v = vmin : vmax (60 steps)
    for y = ymin:ymax (20 steps)
        Compute force on the disk at 50 Hz
    end;
end;
```

Next a divariate spline was employed to construct a continuous function of the disk force F(v,y). A Runge Kutta algorithm was then used to model the disk position as a function of time, fitting the equation

$$m\frac{d^2y}{dt^2} = -mg + F(v,y) \ . \tag{1}$$

The two unknowns in the Ringe Kutta algorithm were y and v as a function of time. The Jacobian of this system was employed to speed up the algorithm,

$$J = \begin{bmatrix} 0 & 1 \\ \dfrac{1}{m}\dfrac{\partial F}{\partial y} & \dfrac{1}{m}\dfrac{\partial F}{\partial v} \end{bmatrix} . \tag{2}$$
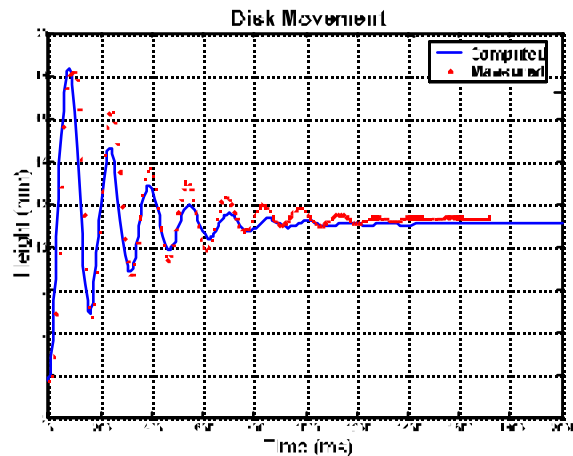
Fig. 1 Disk trajectory using BEM altered Green's function.

Computation of the spline fit, the derivatives, and the Runge Kutta algorithm requires 1.95 s on a 2 GHz Pentium IV. A comparison of the computed height and that from the measurement is shown in Fig. 2.

V. TRANSIENT PREDICTION USING IMPEDANCE MATRICES

An impedance matrix can be determined for any problem by imposing a current of unit value in any region and computing the flux linkage with any other region at the frequency of interest. Consider numbering the conductors as annotated in Fig. 1. By iteratively following this procedure for each conductor, an equation governing the current induced in the solid disk results as

$$\frac{di_3}{dt} + R i_3 + \frac{d}{dt}(i_1 M_{13}) + \frac{d}{dt}(i_2 M_{23}) + i_1 R_{13} + i_2 R_{23} = \tag{3}$$

With sinusoidal excitation, and the disk moving with velocity v, the current i_3 is

$$i_3 = \frac{1}{(R - j w L)}\left\{ -j w (M_{23} i_2 + M_{13} i_1) \right.$$
$$\left. - v\left(i_2 \frac{dM_{13}}{dy} + i_1 \frac{dM_{11}}{dy} \right) - R_{13} i_1 - R_{23} i_2 \right\}. \tag{4}$$

The coenergy for this system is

$$W = i_1 i_3 M_{13} + i_2 i_3 M_{23}. \tag{5}$$

Force is the rate of change of this with respect to displacement. Both the current i_3 and the mutual inductances have a y directed dependance.

$$\frac{di_3}{dt} = \frac{1}{(R + j w L)}\left\{ -j w \left(\frac{dM_{23}}{dy} i_2 + \frac{dM_{13}}{dy} i_1 \right) \right.$$
$$\left. - v\left(i_2 \frac{d^2 M_{23}}{dy^2} + i_1 \frac{d^2 M_{13}}{dy^2} \right) - \frac{dR_{13}}{dy} i_1 - \frac{dR_{23}}{dy} i_2 \right\}. \tag{6}$$

Using this relation, the force on the disk can be written as

$$F_y = \frac{dW}{dy} = \Re\left\{ i_3\left(i_1 \frac{dM_{13}}{dy} + i_2 \frac{dM_{23}}{dy} \right) \right.$$
$$\left. + \frac{di_3}{dy}(i_1 M_{13} + i_2 M_{23}) \right\}. \tag{7}$$

Here $\Re$ denotes real part, and the rms value of current must be used for coils 1 and 2 Equation (20) to compute the disk trajectory with time yields the result shown in Fig. 3. Note that the timing of the peaks for both the modified Green's function approach, also plotted, and the impedance approach maintain a close relation to one another.

These calculations require 5.04 s on a 2 GHz Pentium IV, while the impedance matrix requires about 15 minutes to generate with a boundary element code.
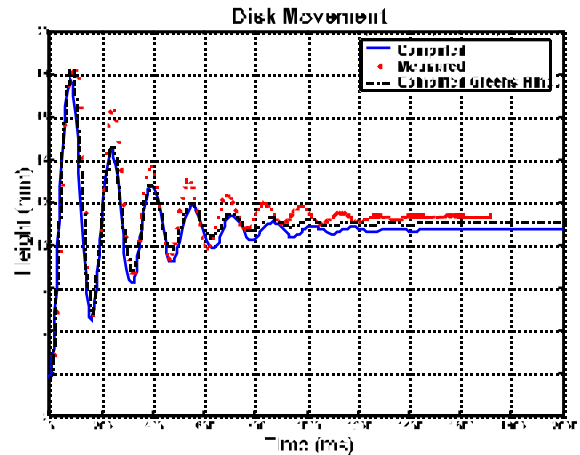
Fig. 2 Disk movement predicted using impedance matrices.

VI. CONCLUSIONS

Both the modified Green's function approach and the impedance matrix approach model the disk transient reasonably well. This is especially true when the sources of error are considered.

1. Both approaches use the average force during one complete waveform. Small differences should be expected since the disk movement during 20 ms is not insignificant.

2. Slight tilting and lateral movement are expected during the actual experiment. Such affects are ignored in the computations. Of the two approaches, the modified Greens function is to be preferred since it circumvents the requirement of taking analytical derivatives of impedances. Differentiation is always a source of additional error. The full paper will also look at a finite element time step solution.

VII. REFERENCES

[1]. M. Burnet Fauchez, "Calculation of eddy currents in moving conductors using a boundary element method", Compumag Colorado, June 1986, p. 156.

[2]. K. R. Davey and Dalian Zheng, " Prediction and Use of Impedance Matrices for Eddy Current Problems", *IEEE Transactions on Magnetics*, vol. 33, no. 4, pp. 2478-2485, July 1997.

[3]. Dalian Zheng and Kent R. Davey, "A Boundary Element Formulation for Thin Shell Problems," *IEEE Transactions on Magnetics*, Vol. 32, No. 3, pp. 675-677, May 1996.

[4]. Kent R. Davey and Bruce Klimpke, "Coupling Circuit Constraints into Boundary Element Methods", *IEEE Transactions on Magnetics*, Vol. 36, No. 4, pp. 1444-1447, July, 2000.

Surface Current Reconstruction Using Magnetic Field Tomography

H. Brauer, M. Ziolkowski

Technische Universitaet Ilmenau, Dept. Electrical Engineering and Information Technology
Am Helmholtzplatz 2, P.O.Box 100565
D – 98684 Ilmenau, Germany
e-mail: hartmut.brauer@tu-ilmenau.de

Abstract —The identification of characteristics or the reconstruction of the shape of free boundaries are inverse problems arising in industrial applications, e.g. in magnetic fluid dynamics. We have studied the reconstruction of interfaces between two conducting fluids using external magnetic field measurements which were applied to a highly simplified model of an aluminum electrolysis cell. Because semi-analytical solutions for the electrical and magnetic field are known numerical simulations (FEM or BEM) can be evaluated. Measured magnetic fields are available due to an experimental setup of the object under consideration.

We propose a new TEAM benchmark problem for evaluation of inverse methods which can be applied to the reconstruction of the surface current distribution representing the interface between the two fluids.

INTRODUCTION

There is a variety of problems in material processing where it would be useful to know the electrical conductivity profile of a single fluid or a multiphase flow. The knowledge of the position of the interface between good conducting molten aluminum and poorly conducting liquid cryolite is important to prevent unwelcome instabilities in aluminum reduction cells [1-3]. But conductivity distributions are also of interest in glass melting furnaces or metal-slag interfaces in steel and iron making.

In a previous work [5] we have demonstrated how the concept of *Magnetic Field Tomography*, which has been successfully applied to the source localization and source reconstruction in biomagnetism [6], can be used to detect the interface between fluids with different electrical conductivities. In particular, we have shown that the external magnetic field generated by the electrical current flowing through a cylindrical volume conductor (a highly simplified model of an aluminum reduction cell) provides sufficient information to reconstruct the shape of the interface between two fluids.

PHYSICAL MODEL

If we consider typical figures of aluminum electrolysis cells it must be noticed that the cross section has usually a length of a few meters, whereas the interface displacement is very small compared to the lateral extent of the system. The applied high electrical currents (about 100 kA) will result in a interface displacement of the order of several centimeters. But from industrial practice is known that already such small interface displacements can disturb significantly the operation of the cell.

The simplified model of an aluminum electrolysis cell we have considered is shown in Fig. 1. Two fluids with different electrical conductivity κ_1 and κ_2, respectively, are situated in a long cylinder with the radius R. The cylinder wall is non-conducting. At the top of the cylinder a homogeneous electrical current density J_0 is impressed.
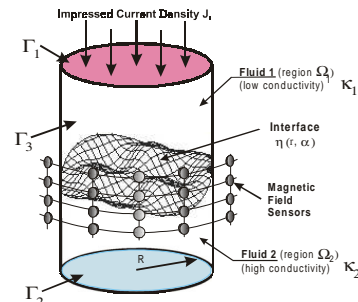
Fig. 1. Physical model with a non-axisymmetric interface, impressed homogeneous current density J_0 and magnetic field sensor positions.

If the interface is flat, the current density J is homogeneous and the total electrical potential Φ is equal to the electrical potential $\Phi_0 = -J_o z/\kappa$, induced by the impressed current density J_o. As soon as the interface is deformed (due to interfacial waves or an external forcing), the current density J will become inhomogeneous near the interface. Then the inhomogeneity of J can be represented by the perturbation of the current density j which induces a perturbation of the electrical potential φ.

The problem is now to reconstruct the interface shape using the magnetic flux density B measured outside the cylinder. Non-axisymmetric perturbations of the fluid interface lead to perturbations of the magnetic field outside the cylinder which can be measured and used for the interface reconstruction.

FLUID-MECHANICAL CURRENT FLOW MODELING

If we consider a long cylinder containing two incompressible fluids with different densities, an equation for the velocity potential can be derived [1]

$$\phi_i = C_i J_m (k_{mn} r) e^{-k_{mn}|z|+jm\alpha - j\omega t} \tag{1}$$

where the constants C_i can be complex; J_m is the Bessel

function of the first kind, $k_{mn} = y_{mn}/R$, y_{mn} is the n-th solution of the equation $J'_m(r) = 0$ at $m>0$ and $(n+1)$-th solution at $m=0$. Using (1) the interface perturbation $\eta(r,\alpha)$ can be derived

$$\eta(r,\alpha) = \sum_{m=-M}^{M} \sum_{n=1}^{N} \eta_{mn} J_m(k_{mn}r) e^{jm\alpha} \qquad (2)$$

The value n is called the radial mode number, whereas m is the azimuthal mode number. The validity of the interface representation described by (2) is restricted to small amplitudes of interface oscillations.

MAGNETIC FIELD MODELING

The main difference for magnetic field modeling is that we will assume non-oscillating interface functions $\eta(r,\alpha)$ which are caused by external mechanical forcing.

The interface perturbation η leads to an inhomogeneous distribution of the total electrical current density $\boldsymbol{J}$ in the fluids which can be written as $\boldsymbol{J} = -J_0\, \boldsymbol{e_z} + \boldsymbol{j}$, where J_0 is the impressed current density and $\boldsymbol{j}$ the perturbation of this current density. The total electrical potential is then $\Phi = \Phi_0 + \varphi$, where φ is the perturbation of the electrical potential.

Similar to the fluid flow modeling the perturbed potential can be calculated approximatively based on a linearization of the boundary condition for the potential on the interface (at $z = h/2$)

$$\Phi_1 - \Phi_2 = J_0 \cdot \eta \cdot \left[\frac{1}{\kappa_2} - \frac{1}{\kappa_1} \right] \qquad z = \frac{h}{2} \qquad (3)$$

This means, that only small interface deviations from the plane at $z = h/2$ are allowed.

We finally end up with the magnetic field $\boldsymbol{b}$ related to the interface perturbation (4):

$$\mathbf{b(r)} = \frac{\mu \cdot J_0}{4\pi} \frac{\kappa_1 - \kappa_2}{\kappa_1 + \kappa_2} \int sign(z') \frac{\nabla\left(\eta(r'_h) \cdot e^{-k_{mn}|z'|}\right)}{|\mathbf{r}-\mathbf{r'}|^3} \times (\mathbf{r} - \mathbf{r'}) \cdot dV'$$

MAGNETIC FIELD MEASUREMENTS

Magnetic field distribution outside the cylinder is measured be means of a set of 16 sensors (fluxgates) placed on a ring which can be shifted vertically (Fig. 3). Different interfaces can be generated by modifying magnitude and frequency of the pneumatic shaker. Depending on magnitude and frequency of the mechanical excitation different stable oscillations of the interface, i.e. the liquid metal surface, can be generated (Fig. 4).

A transparent plastic cylinder (height 100 mm, diameter 50 mm) filled with *Galinstan* (metal mixture of Ga, In, and Sn, with conductivity $\kappa_2 = 3.6 \cdot 10^6$ S/m, liquid at room temperature) and the electrolyte KCL (conductivity $\kappa_1 = 10^{-2} ... 10^2$ S/m) was used. A current of I = 1A was uniformly impressed to the electrode covering the complete top of the cylinder.
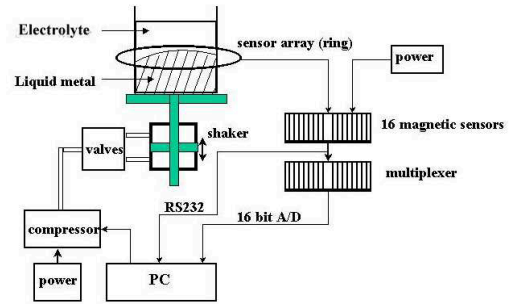
Fig. 3. Experimental setup for the magnetic field measurements at the cylindrical object filled with liquid metal (*Galinstan*) and KCL as electrolyte.
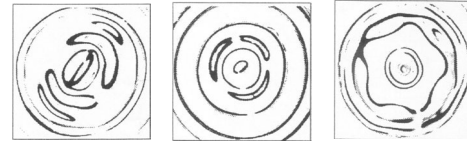
Fig. 4. Optical snapshots (negatives) of interface modes which have been observed in an experiment after mechanical excitation.

INTERFACE RECONSTRUCTION

Using the experimental setup (Fig. 3) different surface shapes of the liquid metal can be generated, their shapes can be observed applying optical or laser techniques. For numerical simulations the interface functions $\eta(r,\alpha)$ can be described by superposition of Bessel´s and trigonometric functions. To reconstruct these surfaces the parameters η_{nm} have to be estimated using the magnetic field distribution measured in a set of grid points outside the cylinder. Thus, the number of optimization parameters depends on the chosen interface mode.

REFERENCES

[1] P.A. Davidson, "An energy analysis of unstable, aluminium reduction cells*," European Journal of Mechanics, B/Fluids,* vol. 13, No. 1, pp. 15-32, 1994.
[2] K. Fujisaki, K. Wajima, and T. Ohki, "3-D magnetohydrodynamics analysis method for free surface molten metal," *IEEE Transaction on Magnetics,* vol. 36, No. 4, pp. 1325-1328, 2000.
[3] I. Panaitescu, M. Repetto, L. Leboucher, and K. Pericleous, "Magneto-hydro-dynamic analysis of an electrolysis cell for aluminum production," *IEEE Transaction on Magnetics,* vol. 36, No. 4, pp. 1305-1308, 2000.
[4] A. Kurenkov, and A. Thess, "Reconstruction of interfaces between electrically conducting fluids from electrical potential measurements," 4th Int. Conf. of Magnetohydrodynamics, Giens/France, September 2000, Proc. vol. 1, pp. 45-50, 2000
[5] H. Brauer, M. Ziolkowski, M. Dannemann, M. Kuilekov, and D. Alexeevski, „Forward simulations for free boundary reconstruction in magnetic fluid dynamics", 10th IGTE Symposium, Graz, 2002
[6] H. Brauer, J. Haueisen, M. Ziolkowski, U. Tenner, and H. Nowak, "Reconstruction of extended current sources in a human body phantom applying biomagnetic measuring techniques," *IEEE Transaction on Magnetics,* vol. 36, No. 4, pp. 1700-1705, 2000.

Development of Network-Oriented Education System for Learning Finite Element Method Using JAVA

Masashi Ohchi, Tatsuya Furukawa and Shin-ichiro Tanaka

Saga University

1, Honjo-machi, Saga,

840-8502, Japan

E-mail: masashi@ace.ec.saga-u.ac.jp

Abstract —**The numerical simulation has become an important technology in various research and development fields. The finite element method (FEM) is a popular technique of computational analyses among various numerical methods which are aided by the EWS and the PC. The FEM will require the pre-processing to discretize the analyzed domain into triangular elements and the post-processing to visualize the results. Taking account such backgrounds, it is necessary to educate the numerical analysis at universities. In the paper, the authors will present the implementation of the education system including prepost-processors and solver for the learning FEM based on server client model using JAVA.**

INTRODUCTION

We have developed the highly interactive and portable pre-processor [1] for 2-D FEM analysis. Moreover the automatic mesh generator [2] has been implemented for the linear induction motors (LIM). Since the tools were made the best use of Graphical User Interface (GUI) in the environment of the *X window System* on the UNIX operating system, even a novice user can make the discretized domain easily. We have also developed the post-processor [3] to visualize calculated results.

Recently an object-oriented programming language "Java" has been widely adopted in the computer science. There has been some report on numerical analysis using Java [4]. However that is not an available application but only benchmark test.

In this paper, we will present the new education system that is all in one package, based on server client model using Java. The system is adopted to a practical curriculum of a student laboratory in our Department of Electronics, Saga University.

DEVELOPMENT OF EDUCATION SYSTEM FOR LEARNING FINITE ELEMENT METHOD

Fig. 1 shows the system configuration of the present education system. The system is based on the server client model for the load distribution. The flow of numerical analysis using the system is as follows. (1) A student uses a client computer for the input data of model for analysis. (2) The analyzed domain is discretized by the Delauney-Volonoi triangular method on the client computer. (3)The boundary conditions and parameters of material are inputted. Subsequently, since the JAVA Applet program is not possible to create the data file at the local computer, the discretized domain data is sent to the server computer through the network. (4)The coefficient matrix is computed. (5)The "Gauss Elimination Method", that is coded by JAVA Applet, solves the Rayleigh-Ritz matrix equation. At the last step, (6)the numerical results are visualized on the client computer using JAVA Applet, such as equipotential lines, electric field vector and magnetic vector. If the discretized domain data stored in the server is transmitted to the client Applet through the network, it is able for student to simulate the electromagnetic fields using the previous discretized domain data.
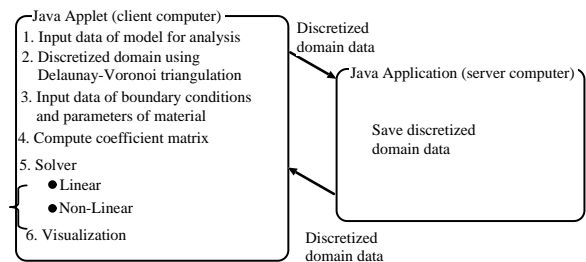
Fig. 1. System configuration
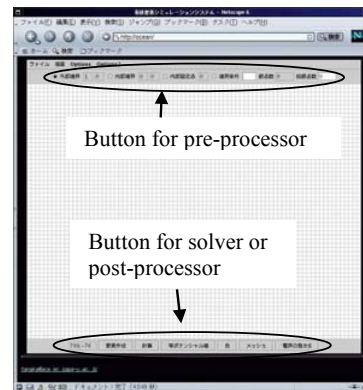
Fig. 2. Operating window of present system using Netscape Navigator

---

Fig.2 shows the snapshot of the implemented education system in case of using Netscape Navigator. The buttons for pre-processor, such as inputting data of model for analysis or boundary conditions, are arranged at the top of the window. The post-processor buttons, such as illustration the equipotential lines, electric field vector and magnetic vector, are located at the bottom.

| (a) Initial two domains | (b) Making a new domain based on AND operation |

(c) Making a new domain based on OR operation
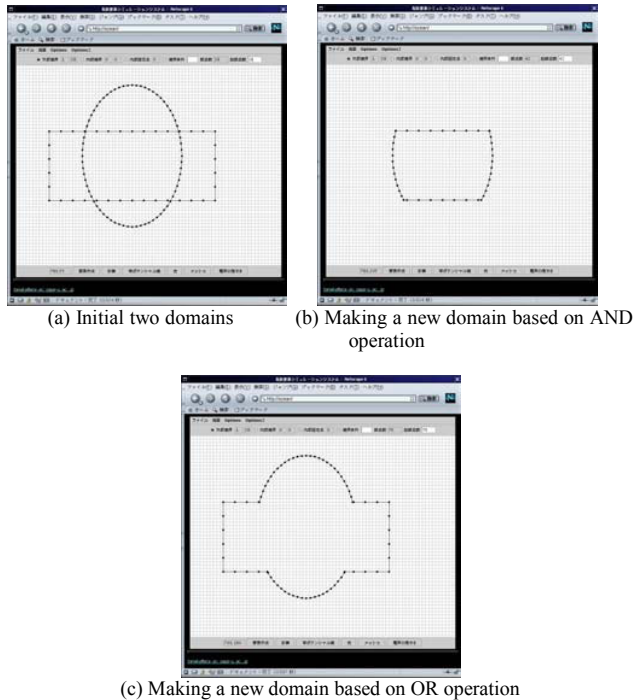
Fig. 3. View of making a new domain from two domains

TABLE I. CPU TIME FOR PROCESSING

	Number of Nodes			
	1,000	2,000	3,000	4,000
Delauney(Client1)	1.87	2.72	3.84	6.02
Gauss(Client1)	29.79	245.02	837.53	1958.34
Delauney(Client2)	0.87	1.39	1.80	2.38
Gauss(Client2)	5.01	37.91	132.47	320.87
Gauss(Server)	5.16	32.37	107.21	257.06

(sec.)

Client1 CPU:Dual Pentium III Processors 450MHz, Memory:512MB
    OS:Linux (Kernel 2.2.18)
Client2 CPU: Pentium IV Processor 1.8GHz, Memory:512MB
    OS: Linux (Kernel 2.4.18)
Server CPU:Dual Pentium Xeon Processors 1.7GHz, Memory:2GB
    OS:Linux (Kernel 2.4.18)

Fig.3 shows a generation method of new domain from two objects based on the "AND" or "OR" operation. The ellipse and square exist in Fig. 3 (a). The result of "AND" operation at two objects shows in the Fig. 3 (b). Fig. 3 (c) illustrates the generation of new domain based on "OR" operation at two objects.

Table.I describes CPU time for processing each discretized domains, whose numbers of nodes are 1000, 2000, 3000 and 4000. It takes very short time to compute the Delauney-Volonoi triangular even if the low performance computer (client1) uses. However, it takes long time to execute Gauss Elimination Method on the client1. Using client2 or server, the CPU time is reduced approximately by 85% than client1.

CONCLUSION

We have implemented the education support system including the prepost-processors and solver for learning the FEM based on the server/client model through the network. Nevertheless students use the JAVA Applet program on the client, it is possible to save the discretized domain data on the server.

The present system has been adopted to a practical curriculum of a student laboratory in our department. It is found out that the present education system will support the understanding the numerical analysis and FEM satisfactorily.

ACKNOWLEDGEMENT

REFERENCES

[1] M. Ohchi, T. Furukawa and M. Matsuo, "Development of Highly Interactive and Portable Pre-Post Processors for 2-D FEM Analysis," *The Third World Congress on Computational Mechanics Extended Abstracts*, Vol II, P6-5, pp. 1846-1847, August 1994.
[2] T. Furukawa, H. Homan, M. Ohchi and T. Nitta, "Design and Implementation of a Graphical User Interface for Finite Element Analysis of Linear Induction Machines," *The 12th COMPUMAG Conference on the Computation of Electromagnetic Fields*, Vol. 1, PB5-3, pp. 210-211, October 1999.
[3] T. Furukawa, T. Eguchi and M. Ohchi, "Development of EWS Aided Graphical Facilities for Computational Electromagnetism," *IEEE Transactions on Magnetics*, vol. 33, no. 2, pp. 1978-1981, March 1997.
[4] K. Watanabe and T. Honma, "Post-Process Using Java Servelet in BEM," The Papers of Joint Technical Meeting on Static Apparatus and Rotating Machinery, IEE Japan, SA-0213, RM-02-13, pp.7-11, January 2002.

TEAM Workshop Problem 25: a multi-objective analysis

Luiz LEBENSZTAJN

LMAG Laboratǔrio de Eletromagnetismo Aplicado, Escola PolitÈcnica da Universidade de S„o Paulo

05508-900 ñ S„o Paulo/SP ñ Brazil

leb@pea.usp.br

Jean-Louis COULOMB

LEG: Laboratoire dí..lectrotechnique de Grenoble - INPG/UJF- CNRS UMR 5529 ENSIEG, BP 46, 38402

Saint Martin díHËres France

Jean-Louis.Coulomb@leg.ensieg.inpg.fr

Abstract-- **In this work we propose a multi-objective analysis for TEAM workshop problem 25. In order to obtain the Pareto frontier, the objective functions are replaced by approximations. A straightforward method, based on the use of approximations, is used to obtain a Pareto set.**

*Index Terms*ó Approximation techniques, multi-objective optimization, finite element method.

I. Introduction

TEAM Workshop has two problems on electromagnetic device optimization: Problems 22 and 25. The first one deals with the optimization of superconducting magnetic energy storage (SMES) arrangement [1] and the second one deals with the Optimization of Die Press Model [2].

The optimization of superconducting magnetic energy storage (Problem 22) has already been solved as a multi-objective problem [3].

The Optimization of Die Press Model (Problem 25) is always analyzed as a single objective problem. There are several approaches on the optimization process. The first work [4] is a very interesting analysis on the use of the simulated annealing method on a electromagnetic device and the objective function was not approximated. There are other works that use approximations of the objective function [5]. This is due to one of the main characteristics of this problem: the objective function is very flat around the global minimum, so a good approximation could save a lot of computational effort.

The optimization of die press model has another nice characteristic, without any change on the geometry of the problem: it could be solved as a multi-objective problem.

II. A brief Problem Description

The geometry of Problem 25 is shown on Fig.1. The goal is to obtain a radial magnetic induction distribution on a specified path. Four parameters (R_1, L_2, L_3 and L_4) could be changed in a specified range. The coils are fed on DC and there are two ampere-turns conditions. In this paper, we will deal only with the small ampere-turn (4253 AT). So, the radial magnetic induction must be equal to 0.35 T along the line e-f.
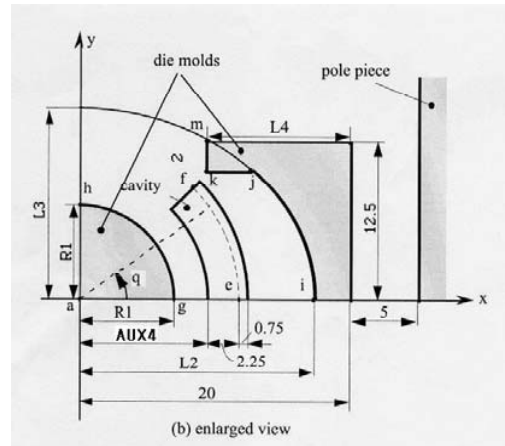
Fig. 1. Team Workshop problem 25, model of die press: enlarged view[1,4]

The objective function is defined as:

$$W = \sum_{i=1}^{n} \left\{ \left(B_{xip} - B_{xio}\right)^2 + \left(B_{yip} - B_{yxio}\right)^2 \right\} \tag{1}$$

where the subscript p denotes a calculated value and the subscripted o the specified value. The number of points (n) is equal to 10.

There are two important parameters (or indexes) on the problem description: the maximum deviation on the amplitude and the maximum error on the angle of magnetic induction vector. They are defined to compare the optimization methods.

The maximum deviation on the amplitude is defined as follows:

$$\varepsilon_{B\max} = \max \left| \frac{B_p - B_o}{B_o} \right| \times 100 \quad \% \tag{2}$$

and the maximum error on the angle of magnetic induction vector is calculated by:

$$\varepsilon_{\theta\max} = \max \left| \theta_{Bp} - \theta_{Bo} \right| \tag{3}$$

The objective function measures the homogeneity of the magnetic distribution. The parameters $\varepsilon_{B\max}$ and $\varepsilon_{\theta\max}$ measure the local quality of the induction magnetic distribution.

III. A multi-objective approach

On TEAM Workshop Problem 25, the minimization of (1) is performed and then indexes are calculated. It is possible that we can lose some *nice* solutions, which have low indexes, but a less homogeneous distribution.

So, we propose to analyze the "Optimization of a Die Mold" as follows: it is necessary to obtain a magnetic induction radial distribution on a specified line (e-f), with the following attributes:

1- the magnetic induction distribution must be as homogeneous as possible;
2- the local deviation on the magnetic induction amplitude must be minimized;
3- the local deviation on the magnetic induction vector angle must be minimized.

Thus, on this approach: instead of minimize (1) and then calculate (2) and (3), a multi-objective analysis will be carried out. We are dealing with another concept: usually there is not *a solution*, but a *set of solutions*. They are superior to the others, when all the objectives are taken into account: this set of solutions is called the Pareto-set or the non-dominated set [6].

One possible solution to a multi-objective problem is to create a new objective function, which is a weighted sum of the all the objectives. If the weights are changed, then a new solution could be obtained and all the Pareto-set could be obtained. This approach can solve several problems, but it has a high drawback: when the Pareto frontier is non-convex, the method is not able to capture all the solutions.[7].

IV. METHODOLOGY

In this work, we will use a methodology based on approximations, proposed by Wilson [7]. It is a straightforward method and the first step is the replacement of the objective functions with a set a low computational cost approximations.

In order to compute the Pareto-set:

1. Kriging approximations [8] are performed based on a regular 13x13x13 grid to replace the objective functions;
2. The design space is explored and all the approximated objective functions are evaluated.
3. Each function is then scaled between zero and one, as follows:

$$f_1 = (f_1-min(f_1))/ (max(f_1)-min(f_1)) \quad (4)$$

4. A function F_i is defined for each explored point:

$$F_i = [1 - \max_{i \neq j} (min(f_{1i}-f_{1j} ; f_{2i}-f_{2j} \; Ö \; .. \; ;f_{Ni}-f_{Nj} ;))] \quad (5)$$

where f_1 is the first objective function and f_2 is the second objective function.

This function F_i is greater or equal to one for every Pareto design. The value F_i for dominated designs is always less than one.

V. RESULTS

The method was applied to TEAM Workshop problem 25 [1, 4]. The magnetic field computations were done with finite element analysis [9]. Four geometric parameters can be varied [1,4], but the significant parameters showed to be R1, L2 and L4 [5]. Approximations were then constructed on the parallelepiped [5, 9.4]*[12.6, 18]*[4, 19].

Fig. 2 shows the Pareto Set and the coordinates of the

Global Error and the Local Errors of the magnetic induction (amplitude and angle).
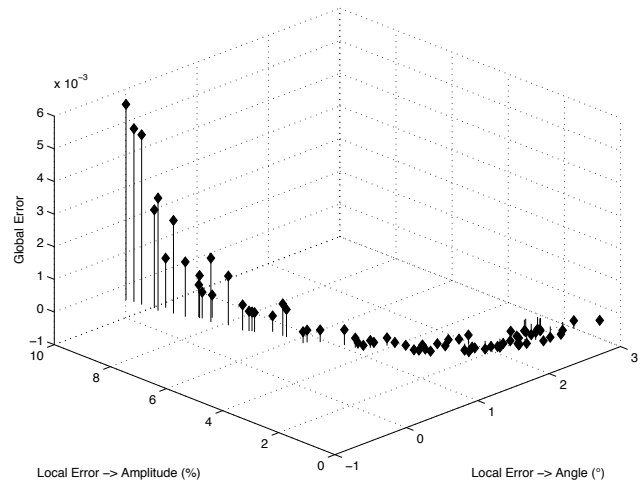
All the actual objective functions are positive. Nevertheless, two approximation functions (the Global Error and the Local Error on the Angle) have some very small negative values on the Pareto-Set. This is due to some oscillations on approximations functions, because the actual functions are very flat. Fig. 2 shows a very important result: Problem 25 has several points with high homogeneity distribution and low local errors on the magnetic induction.

VI. CONCLUSIONS

A multi-objective analysis to TEAM Workshop Problem 25 was proposed. It is a straightforward method and low cost method, based on approximation functions and it is a very good starting point to the solution of real-world problems.

REFERENCES

[1] http://www-igte.tu-graz.ac.at/team/index.htm
[2] http://ics.ec-lyon.fr/team.html
[3] Dias, A.H.F.; de Vasconcelos, J.A. "Multiobjective genetic algorithms applied to solve optimization problems" IEEE Transactions on Magnetics, Volume: 38 Issue: 2 Part: 1 , March 2002 Page(s): 1133 - 1136
[4] N. Takahashi et alli ì Investigation of simulated annealing method and its application to optimal design of die mold for orientation of magnetic powderî, IEEE Transactions on Magnetics, vol. 32, no.3, 1996.
[5] Kobetski, A. et alli "Comparison of radial basis function approximation techniques", IGTE 2002 : 10th International IGTE Symposium on Numerical Field Calculation in Electrical Engineering September 16-18, 2002 Graz, Austria
[6] E. Zitzler and L. Thiele. "An Evolutionary Algorithm for Multiobjective Optimization: The Strength Pareto Approach", Technical Report 43, Computer Engineering and Communication Networks Lab (TIK), Swiss Federal Institute of Technology (ETH), Zurich, Switzerland, May 1998.
[7] Wilson, B. et alli "Efficient Pareto Frontier Exploration using Surrogate Approximations", Optimization and Engineering, 2, 31ñ50, 2001, Kluwer Academic Publishers, 2001, The Netherlands.
[8] Simpson, T. W. et alli "Comparison of Response Surface and Kriging Models for Multidisciplinary Design Optimization", 7th Symposium on Multidisciplinary Analysis & Optimization, St. Louis, MO, September 2-4, AIAA, 1 (381-391) AIAA-98-4755. 1998
[9] Flux, Cedrat, 10, Chemin de PrÈCarrÈ ñ ZIRST, 38246 Meylan, France. http://www.cedrat.com

Some results on a SMES device optimization problem using stochastic methods

O. Hajji, S. Brisset, and P. Brochet

L2EP

Ecole Centrale de Lille – Cité Scientifique – BP 48 – 59651 Villeneuve d'Ascq cedex - France

E-mail: omessaad.hajji@ec-lille.fr, stephane.brisset@ec-lille.fr, pascal.brochet@ec-lille.fr

Abstract — The optimization of superconducting magnetic energy storage (SMES) is performed by means of different stochastic methods: genetic algorithms, genetic algorithms with response surface, simulated annealing, improved simulated annealing, tabu search and new tabu search. An analytical comparison among them is performed. Finally, results on different methods are discussed.

INTRODUCTION

Superconducting magnetic energy storing systems consisting of a single superconducting solenoid coil offer the opportunity to store a significant amount of energy in magnetic fields. However, such arrangements usually suffer from their remarkable stray fields. A reduction of the stray field can be achieved if a second solenoid is placed outside the inner one, with a current flowing in the opposite direction. A correct design of the system should then couple the right value of energy to be stored with a minimal stray field. This optimal design problem has been accepted as a benchmark problem and inserted in the list of TEAM Workshop problems [1].

The aim of this type of problem is to test several optimizations methods. These algorithms include simulated annealing (SA), improved simulated annealing (ISA), genetic algorithm (GA), Hu's tabu search (HuTS), universal tabu search (UTS), and an original new tabu search (NTS) presented in a companion paper [2].

The first section presents the SEMS problems, the second section presents different stochastic studied methods and finally results and comparison are summarized out.

SMES PROBLEM

This problem consists of determining the optimum design parameters of superconducting magnetic energy storage (SMES) device [1]. The device is composed of two axisymmetric concentric coils with current densities equal to 22.5 A/mm² in opposite direction.

Besides usual geometrical constraints, there is a material related constraint: the given current density and the maximum magnetic flux density value on the coil must not violate the superconducting quench condition which can be well represented by linear relationship.

The objective function (OF) of this problem has to take both the energy and the stray field requirements into account, which can be done using a weighted sum as given in (1)

$$OF = \frac{B_{stray}^2}{B_{norm}^2} + \frac{\left| Energy - E_{ref} \right|}{E_{ref}} \quad (1)$$

$$B_{stray}^2 = \frac{1}{22}\sum_{i=1}^{22} B_{stray,i}^2 \ , \ E_{ref} = 180 \ MJ \ , \ B_{norm} = 3 \cdot 10^{-3} \ T$$

B_{stray} is evaluated along equidistant points at a distance of 10 meters, the problem investigated here is the three variables continuous case.

GENETIC ALGORITHM

GA [3] is an iterative procedure which maintains constant size of population of candidate solutions. During each iteration, called a generation, the individuals in the current population are evaluated. By a randomized selection procedure a new population is selected that ensures that the expected number of times an individual is chosen is approximately proportional to its relative performance. In order to search other points in the design space, the two genetic operators' crossover and mutation are applied. To maintain the focus of the processes on the best solution found so far, an elitist approach can be built into the selection process.

Genetic algorithm with new stop criterion

The optimization process is performed in two steps. In the first step, the standard GA process is performed until the error between the objective function and its approximation is sufficiently low. In the second step, the approximation of the objective function is used to locate quickly the global optimum point in the confidence domain of the approximation function using recursive canonical analysis [4].

SIMULATED ANNEALING

SA is a procedure for optimization that has been firstly proposed to solve complicated combinatorial problems. It has proved to be an effective and powerful global optimization algorithm in many combinatorial optimization problems such as the traveling salesman problem. It is based on an analogy with thermodynamics where a system is slowly cooled in order to achieve its lowest energy state. The main stochastic rule used in SA is the Boltzmann probability [5].

Improved simulated annealing

The improved SA algorithm used in this paper is derived directly from the one applied to multimodal functions of continuous variables [4].

A new method to determine the step vector is proposed here, based on the proposition of Hu [6]. The steps lengths are taken from a list of realizable steps computed using [6]. The search starts with large steps in order to cover all the search space. Decreasing the step vector and the control parameter, the search is performed in a smaller space.

Simulated annealing and auto-tuning steps

In standard SA, during the constant temperature phase, the step vector is periodically adjusted in order to be well fitted on OF variation. After thermal equilibrium, the temperature is reduced. The step vector is changed a certain amount of times that is set by the user. This number depends on the optimization problem. Therefore, a more efficient criterion is searched to determine if the thermal equilibrium is reached.

The criterion proposed here depends on the step vector. In optimization process, it is preferable to keep the ratio between the numbers of accepted and rejected configurations equal to 1 in order to explore all the space search. Therefore, the step is changed as proposed in [5]. The process of thermal equilibrium is stopped when the step becomes very small

TABU SEARCH

TS is a metaheuristic method recently developed by Glover specifically for combinatorial optimization problem. It guides the search for the optimal solution making use of memory systems, which exploit the history of the search

Among all the visited solutions the best one is chosen. This strategy can lead to cycling on previously visited solutions. To prevent this effect, the algorithm set as tabu moves that had led to improvement of the objective function for a certain number of iterations, depending of the tabu list size. The performance of a TS algorithm depends on the size of neighborhood of a solution, and on the number of iterations for which a move is kept as tabu. There are two fundamentals structure of TS algorithms implemented here: Hu's TS (HuTS) and Universal TS (UTS), they are described respectively in [6] and [7].

New Tabu Search

In this proposed TS method, points are generated using normal law, the tabu list contains all points and a prohibited zone around each point. The size depends on the value of the objective function and decreases as the number of iteration increases. Alternation of intensification and diversification phases allows finding the global optimum with a good

accuracy. More details are available in a companion paper [2].

RESULTS AND COMPARISON

The SMES problem [1] is optimized using the previously described stochastic algorithms.

Table I give the comparison of the computed results using the previously described stochastic standard and improved algorithms. From these results it can be seen that the improved algorithms use less iterations than the standard one and reach almost the same optimal. The time is expressed as the number of computations of the objective function (OF).

TABLE I. OPTIMIZATIONS RESULTS

Method	OF	B^2_{stray}	Energy	R_2	h_{22}	d_2	Time
Unit	-	$10^{-6} T^2$	10^6 J	m	m	m	-
GA	0.090	7.668	179.19	3.04	0.24	0.386	2400
GA+RS	0.0862	7.775	180.02	3.084	0.238	0.395	945
SA	0.087	7.59	179.36	3.078	0.237	0.39	5025
ISA	0.0864	7.79	179.95	3.089	0.246	0.381	859
HuTS	0.0864	7.67	179.79	3.08	0.246	0.381	3821
UTS	0.0868	7.7	179.75	3.077	0.245	0.385	901
NTS	0.0864	7.78	179.99	3.08	0.254	0.37	1800

CONCLUSION

Improved version of standard stochastic algorithms have presented and tested on the SMES problem with three parameters. A comparison of the different optimization methods has been performed. Improved algorithms use less time and provide better solutions than standard ones.

REFERENCES

[1] SMES Optimization Benchmark, definition of the 3 parameter problem, discrete case, http://www-igte.tu-graz.ac.at/team/team3dis.htm.
[2] O. Hajji, S. Brisset, P. Brochet, "A new Tabu Search Method for Optimization with Continuous Parameters", COMPUMAG 2003.
[3] Y. Rahmat-Samii, E. Michielssen, Electromagnetic Optimization by Genetic Algorithms, John Willey, 1999.
[4] O. Hajji, S. Brisset, P. Brochet, A stop Criterion to accelerate Magnetic Optimization Process using Genetic Algorithms and Finite Element Analysis, CEFC 2002, pp.304.
[5] A. Corana et al, "Minimizing multimodal Functions of Continuous Variables with the Simulated Annealing Algorithm", ACM Trans, Math. Soft, Vol. 13, Sept. 1987, pp. 262-280
[6] N.Hu, "Tabu search method with random moves for globally optimal design", *Int. J. Num. Meth. Engineering*, Vol. 35, pp. 1055-1070, 1992.
[7] Y. Shiyou, L. Yan, "An universal Tabu Search Algorithm for Global Optimization of Multimodal Functions with Continuous Variables in Electromagnetics", *IEEE Trans. Mag.*, Vol. 34, No. 5, pp. 2901-2904, September 1998.

An NDT pulse shape study with TEAM Problem 27

Derek N. Dyck, Geoff Gilbert, Behzad Forghani, Jon P. Webb

Infolytica Corporation, Montreal, Quebec, Canada

Abstract- This paper performs a study of the effect of pulse shape on signal amplitude for TEAM Problem 27 – Eddy Current NDT and Deep Flaws. A procedure is described to reduce the discretization errors in the finite element mesh. The results are compared with experimental waveforms.

INTRODUCTION

TEAM problem 27 was originally introduced at the TEAM Workshop in Rio de Janeiro, Brazil in 1997. The problem geometry consists of a round hole through a conducting (aluminum alloy) plate. Partway down the hole is a flaw. As stated in the problem description [1], "The aim of this problem is to be able to optimize the dimensions of the coil and the excitation current to have the highest level of the signal as possible".

Previous work on this problem calculated differential flux densities horizontally and vertically for various size flaws, but using a sinusoidal excitation [2]. Other work also included the design of a genetic optimization algorithm to design a well adapted sensor [3]. More recently an algebraic multigrid approach to this problem was presented [4].

This paper performs a study of the pulsed current turn-off time to aid in selecting the optimal pulse shape. These results are compared with the experimental results given in [1]. The analyses were performed using the MagNet transient analysis software from Infolytica, which is based on the T-Ω method [5].

PROBLEM SETUP

The detection of flaws and cracks through the use of the finite element method is notoriously mesh sensitive. For this reason the problem was setup so that meshing errors could be removed from the solution by gathering results with the flaw on opposite sides of the screw hole. In one analysis the flaw is on the left side of the screw hole and in the subsequent analysis it is on the right side. The same mesh is used for both analyses, with only the material properties of the flaws changing (from air to aluminum-alloy and vice-versa). The Horizontal Differential Flux Densities (HDFD's) from these two analyses are then averaged. This method removes much of the discretization errors and has the added advantage of reducing the other numerical errors in the signal by a factor of two (due to the averaging step). There is still a small discretization error because the T-Ω formulation uses different basis functions in conductor (edge-based basis functions) and non-conductor (node-based basis functions), however this error appears to be much less significant. The magnetic flux densities in the experiment were reportedly measured using Hall effect sensors as described in TEAM problem definition. This is simulated by sampling the flux density at specific points. Thus the HDFD is calculated from the analyses as follows:

$$HDFD = \frac{[B_r^R(r_0,z_0) - B_r^R(-r_0,z_0)] + [B_r^L(-r_0,z_0) - B_r^L(r_0,z_0)]}{2}$$

where is B_r^R and B_r^L are the radial components of the flux density from the analyses with the flaw on the right and left hand sides of the hole, respectively. The original TEAM problem proposal [1] specifies the radial position of the Hall sensors at $r_0 = 5$ mm, but their vertical position is not specified. A plot of flux density as a function of vertical position indicates that the strongest signal is found at the base of the coil or at $z_0 = 0.5$mm above the plate.

DETERMINATION OF THE TURN-OFF RATE

The TEAM problem proposal suggests either a time-harmonic source or a pulsed source, with the pulse consisting of a turn-off of a coil carrying a specified current. This latter method has advantages because the source waveform is effectively composed of many frequencies, instead of a single frequency. Since the optimal frequency for flaw detection depends on the size and depth of the flaw, a single pulse can, in principle, generate a strong signal for a wide variety of flaws. The strongest signal would be produced if the current were turned off instantaneously, however this would require an infinite voltage. To determine a practical turn-off rate, a series of transient simulations were performed using a pulse with varying turn-off time. Fig. 1 shows the coil current at each time step. This same waveshape was used for different time steps ranging from 5 μs to 60 μs. The finite element mesh contained 198,212 tetrahedra, and for each transient time step there were 184,362 unknowns in the linear system of equations, which were solved using an average of 613 conjugate gradient iterations. A transient solution for 10 time steps required approximately 40 minutes on an AMD Athlon 2000+.
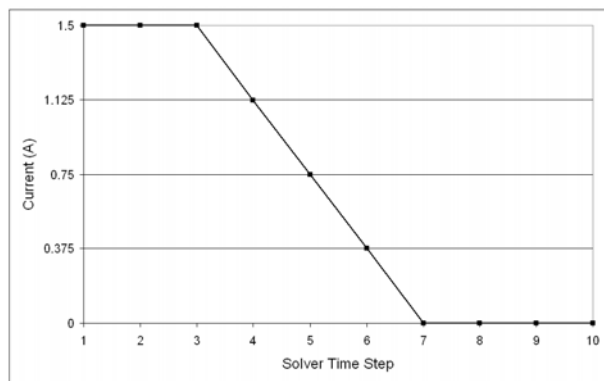
Fig. 1. Current waveform

The result is the peak signal amplitude as a function of the turn-off time as shown in Fig. 2 for the horizontal flaw with length l=4mm and height h=1mm. This behavior is approximately modeled by a quadratic, also shown in the figure, and it can be seen that turn-off times less than 50 μs do not yield a significant gain in signal amplitude.

$$y = -40.601x^2 - 17.099x + 46.148$$
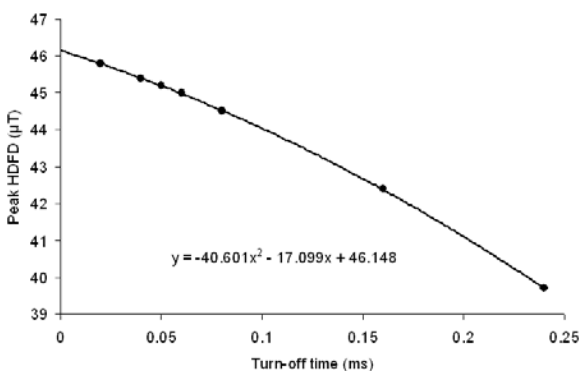
Fig. 2. Differential flux densities for various turn-off rates.

COMPARISON WITH EXPERIMENT

The authors [1] state that their current generator has a bandwidth of 10kHz, but give no other details as to slew rate or peak voltage. To generate waveforms to compare with the experimental data in [1], simulations were performed from 0 to 2 ms using a time step of 25 μs for the first 400 μs after the start of current turn-off, and 50 μs subsequently. The turn-off time was 50 μs (two time steps). The zero of the experimental data was aligned with the time instant at which the current first begins to turn-off, although a better fit to the experimental data could be obtained by adjusting this slightly. Overall this method agrees well with experiment results as shown in Fig. 3, where the experimental data is shown as individual points and simulation results are the solid and dashed lines. Note, however, that the simulation achieves the larger signal for the horizontal flaw (l=4,h=1) while experimentally a

larger signal was obtained for the vertical flaw (l=1,h=4). Also note that the oscillations in the data indicate an experimental error of at least 5%.
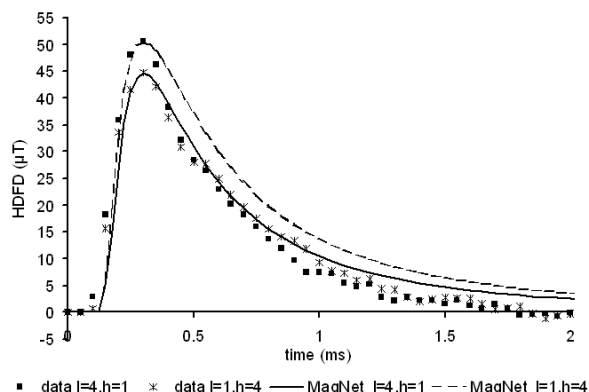
Fig. 3. Differential flux density response

DISCUSSION AND CONCLUSION

A study to determine an optimal turn-off rate for a pulse-driven NDT sensor has been performed. It has been shown that good results can be obtained in reasonable computation times. This is useful both in terms of demonstrating that optimization is feasible using transient analyses, as well as in providing a baseline for comparing with experimental results.

REFERENCES

[1] F.Thollon, "Eddy current NDT and deep flaws", Presented at the TEAM Worksop in Rio de Janeiro, Brazil, 1997.
[2] J.L.Rasolonjanahary, F.Thollon, N.Burais, X.Brunotte, "Study of Eddy Currents NDT Systems in Riveted Assemblies", *IEEE Transactions on Magnetics*, Vol. 32, No. 3, pp. 1585-1588, 1996.
[3] F.Thollon, N.Burais, "Geometric optimization of sensors for eddy current NDT and NDE", *IEEE Transactions on Magnetics*, Vol. 31, No.3, pp. 2026-2031, 1995.
[4] M.Kaltenbacher, S.Reitzinger, "Nonlinear three-dimensional magnetic field computations using Lagrange finite-element functions and algebraic multigrid," *IEEE Transactions on Magnetics*, Vol. 38, No.3, pp. 1489-1494, 2002.
[5] J.P.Webb, B.Forghani, "T-Ω method using hierarchal edge elements," *IEE Proc.-Sci. Meas. Technol.*, Vol. 142, No. 2, March 1995.

Optimise: A Computational Environment for Teaching Optimization in Electrical Engineering

Jaime A. Ramírez, Frederico G. Guimarães, and Paulo H. L. Barros

Universidade Federal de Minas Gerais

Departamento de Engenharia Elétrica, Av. Antônio Carlos, 6627

Belo Horizonte, MG, 31270-010, Brazil

e-mail: jramirez@cpdee.ufmg.br

Abstract— **This paper presents Optimise, a computational optimization environment tool for education in electrical engineering. Optimise has been developed using software engineering process and object-oriented programming philosophy. This educational tool incorporates a set of deterministic and stochastic methods and also a set of computational intelligence techniques. Optimise offers a friendly interface and allows the students to practice the theory learned to verify and compare the features of the optimization methods. A general view of the software is presented describing its modules and class libraries. Some optimization problems are discussed to illustrate the flexibility and power of the Optimise as an educational tool.**

Introduction

Many undergraduate courses in electrical and electronic engineering, control engineering etc., are incorporating the subject of optimization in their curricula. This fact is certainly due to the need of using numerical optimization techniques in engineering. The optimization methodology provides a rational and scientific support in a decision-making process. Although some authors have developed educational tool software, such as to understand electromagnetic scattering phenomena [1] and in the analysis of electromagnetic fields [2], there are few, if none, software in optimization conceived for that purpose.

Optimise has been developed for Windows using a software engineering process and object-oriented programming philosophy. The software has a friendly interface and is capable of tackling restricted and irrestricted linear and nonlinear problems using deterministic (BFGS, penalty functions, ellipsoidal algorithm etc.) or stochastic (genetic algorithm) methods and a combination of both. Optimise has also a module of computational intelligence techniques to generate a multidimensional function that can be used in optimization when the objective function is not known and a data set is given. There is also a numerical library that implements mathematical entities like vector and matrix.

General View

A general optimization problem can be stated mathematically as:

$$\min F(\vec{x}) \in \Re \qquad (1)$$

subject to:

$$\begin{cases} g_i(\vec{x}) \leq 0 & i = 1, \ldots, m \\ h_j(\vec{x}) = 0 & j = 1, \ldots, n \\ A \cdot \vec{x} \leq \vec{b} \\ A \cdot \vec{x} = \vec{b} \\ x_k^{min} \leq x_k \leq x_k^{max} & k = 1, \ldots, p \end{cases} \qquad (2)$$

where $\vec{x}$ is the vector of variables, $F(\vec{x})$ is normally called objective function, $g_i(\vec{x})$ and $h_j(\vec{x})$ are the inequality and equality constraints respectively.

Optimise has been developed following a software engineering process, consisting of requisites specification, object-oriented analysis, software design, testing and coding. The software was coded in C++ for Windows.

The use case view of the requisites specification to accomplish (1) and (2) is illustrated below.
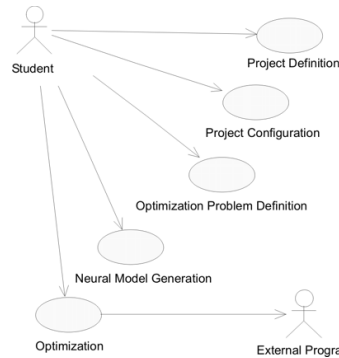
Fig. 1. Use Case View of the Requisites Specification.

It can be seen that Optimise also communicates with external programs. This is particularly important when the objective function (1) implicitly involves the solution of common engineering problems such as an electromagnetic field analysis, a circuit analysis, a control analysis etc. In such cases Optimise would invoke an external program to solve the specific engineering problem that is part of the optimization process.

The class libraries conceived at the design process phase are shown in Fig. 2. Details of the class hierarchy will be given in the full paper.

User Interfaces

The main window of the Optimise is illustrated in Fig. 3. The interface presents buttons to define the free param-
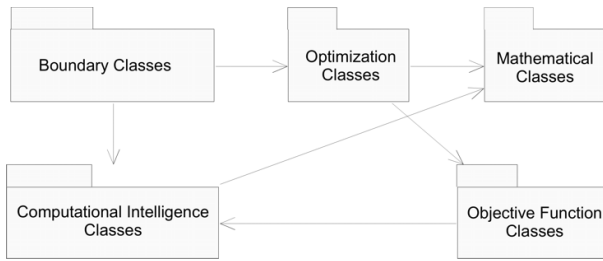
Fig. 2.   The class libraries.

eters, the objective functions and its constraints, to configure and start the optimization process, to train a neural network, and to simulate the objective function provided that a set of values for the free parameters.
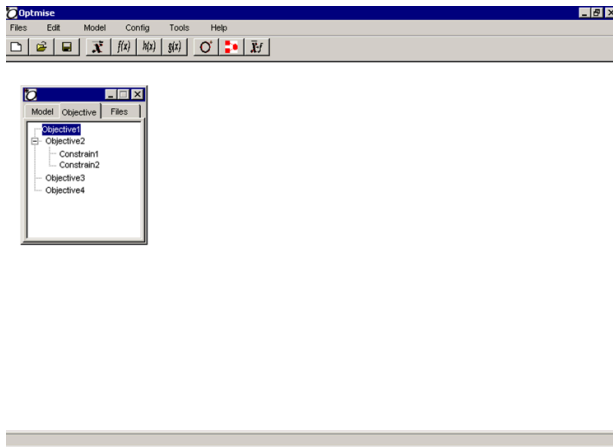
Fig. 3.   Main window of the Optimise.

The objective functions are divided in three categories: (i) analytical objective function, which is described by means of an analytical expression relating the free parameters with the objective function, (ii) approximate objective function, which is obtained by training a neural net with a data training set, and (iii) external objective function, which is partially or entirely evaluated by another program.

To initiate an optimization process, the user first defines the optimization model, that is, the number of free parameters, its names and ranges. Next, (s)he selects the type of objective function. Depending of the type selected, new data must be entered to completely define the objective function. Finally, (s)he selects the optimization method and configures its specific parameters. After initiating the optimization process, the results window is opened. It shows the evolution of the optimization process along the iterations. In the full paper, details of other user interfaces will be illustrated.

Results

To illustrate an application of Optimise, the following analytical optimization problem was studied. The problem consists in optimizing

$$F(x, y) = x\sqrt{1 + y^2} \qquad (3)$$

with the following nonlinear constraints:

$$\begin{cases} g_1(x, y) = 0.124\sqrt{1 + y^2}\left(\frac{8}{x} + \frac{1}{xy}\right) - 1 \le 0 \\ g_2(x, y) = 0.124\sqrt{1 + y^2}\left(\frac{8}{x} - \frac{1}{xy}\right) - 1 \le 0 \end{cases} \qquad (4)$$

Also, the variables must respect the upper and lower limits $0.2 < x < 4.0$ and $0.1 < y < 1.6$.

This problem was solved using the BFGS method coupled with a penalty function to treat the constraints. Starting from $x = (-3, 3)$ the optimization process converged to the minimum in 11 iteration, at which $F(x, y) = 1.5087$, $(x, y) = (1.4116, 0.3771)$, $g_1(x, y) = 0$, $g_2(x, y) = -0.4979$. These results are in agreement with the analytical solution. Figure 4 illustrates the surface of the objective function and the evolution of the optimization process.
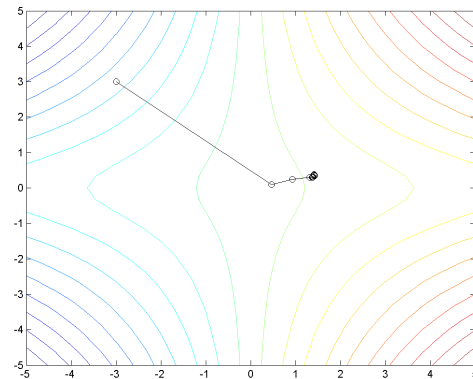
Fig. 4.   Evolution of the optimization process.

Conclusions

The results show that Optimise is a flexible and efficient educational optimization tool that can be used in the classroom. It incorporates a set of optimization methods that can used to solve a broad range of problems. It also has a computational intelligence module that widens its applicability. Optimise has a friendly interface that enables the student to investigate the features of the opimization methods. The software was conceived using object-oriented programming to facilitate its maintenance and evolution. Optimise is planned to be available in public domain. It is hoped that this ideal will enhance its audience.

References

[1] F. Thollon and L. Nicolas, *"A Computer Aided Education Tool for Electromagnetic Scattering Phenomena"*, IEEE Transactions on Magnetics, vol. 36, no. 4, pp.880-883, 2000.
[2] K. Preis, O. Biro, T. Ebner, and I. Ticar, *"An Electromagnetic Field Analysis Tool in Education"*, IEEE Transactions on Magnetics, vol. 38, no. 2, pp. 1317-1320, 2002.

An Analysis of the Performance of a MEMS Micro-Mirror

J. Wen, X. Hoa, A. Kirk, D. Lowther
Department of Electrical and Computer Engineering
McGill University
3480 University Street, Montreal, Quebec Canada
e-mail: lowther@ece.mcgill.ca

Abstract —**The paper describes the structure and analysis of a particular MEMS micro-mirror device that can be used as an optical switch. The predicted performance is compared with measurements. Sufficient details are given to enable this device to be used as a benchmark problem for electric field analysis systems.**

INTRODUCTION

The ability to switch optical signals without the need to convert them to and from electronic form is important for several applications. Examples include optical communications networks and video projectors. The switching of light signals can be achieved by the use of small mirrors which can be moved to deflect the incoming beam into a desired direction [1]. These mirrors are of the dimensions of microns and are moved by the use of micro-electromechanical- systems (MEMS) devices. At the sizes being considered, the actuation of the MEMS device usually involves electrostatics.

The devices are constructed by using techniques which are very similar to those used in fabricating integrated circuits, i.e. by a series of deposition and etching processes.

The intention of this paper is to present the structure of one such device that might provide a future benchmark for analysis systems and to compare measurements of its performance with numerical predictions.
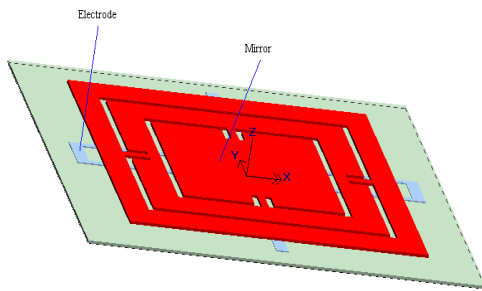
Fig. 1. View of the micro-mirror system.

THE MICRO-MIRROR STRUCTURE

The MEMS device being considered in this comparison is shown in Fig. 1, [2]. The mirror structure (the central
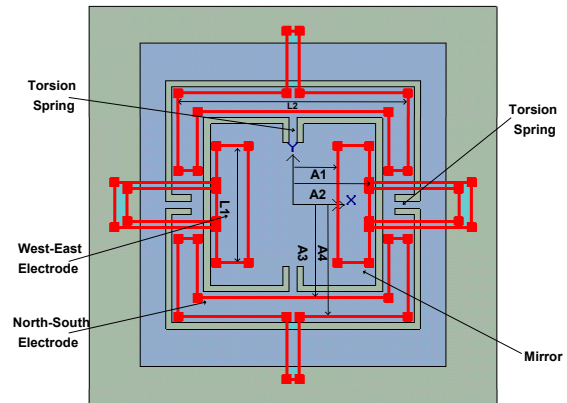
Fig. 2. Layout of Electrodes and Torsion Springs.

rectangle) is gimbaled through two torsion springs at right angles to allow motion in two orthogonal directions. The mirror can be rotated about the x-axis (North-South) by one pair of electrodes and about the y-axis (East-West) by a second pair of electrodes, orthogonal to the first. A view of the electrode structure and springs is shown in Fig. 2.

TABLE I. DIMENSIONS OF THE MEMS MICRO-MIRROR.

Item	Value
Overall dimension	240*260 μm
Flat mirror surface	65*65 μm
Torsion spring	6*20 μm
A1	35 μm
A2	60 μm
A3	75 μm
A4	90 μm
L1	120 μm
L1	180 μm

The device was manufactured using the MUMPs process. In this system, a 0.6 μm film of silicon nitride is deposited on a silicon substrate followed by a 0.5 μm layer of polysilicon which is used to form the electrodes. Next a 2 μm of phosphosilicate glass (PSG) is deposited on top of which is placed 2 μm of polysilicon. These last two layers are repeated to create an entire structure 9.1 μm thick. Each layer is etched after deposition to create the desired structure. Once the layers have been constructed, the PSG layers are etched away to leave the top layers free to move. The overall dimensions of the mirror structure are given in Table I. And the material data is given in Table II.

TABLE II. MATERIAL DATA FOR THE MEMS MIRROR.

Material	Relative Permitivity
Polysilicon	11.0
Silicon Nitride	9.4

ANALYSIS

The mirror can rotate around the y-axis by twisting about the inner gimbal structure or the x-axis by twisting about the outer gimbal. In each case, the electrostatic forces rotate the mirror while a restoring torque is generated by the twisting of the rectangular beams (torsion springs) which support the mirror structure. The restoring torque generated by twisting a rectangular cross-section beam has an analytical solution:

$$T_{mech} = K_\alpha \alpha \quad (1)$$

where T_{mech} is the mechanical torque at an angle α and K_α is the spring constant. For a torsion spring of length l, width w, and thickness t, the spring constant is given by:

$$K_\alpha = 2 \times \frac{Gwt^3}{3l}\left[1 - \frac{192}{\pi^5} \cdot \frac{t}{w}\tanh\left(\frac{\pi w}{2t}\right)\right] \quad (2)$$

and G is given by :

$$G = \frac{E}{2(1+\nu)} \quad (3)$$

where $\nu = 0.28$ for polysilicon and E (Young's modulus) is $1.35*10^{11}$ (for the current material).

The torque due to the electric field was computed from a 3-D electrostatic analysis [3] and the curve of deflection angle versus applied voltage was obtained by determining the angle at which the electric and mechanical torques balanced for each voltage.

RESULTS
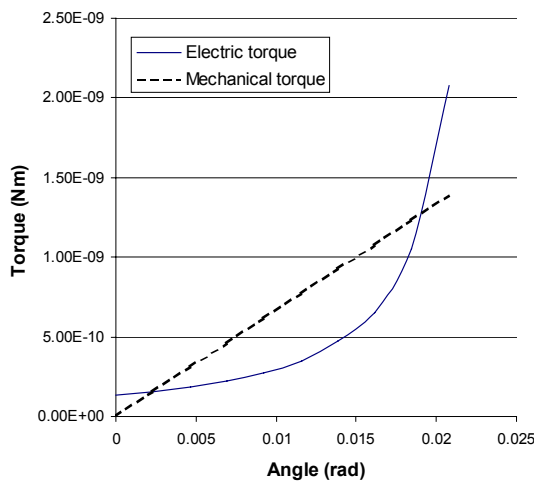
Fig. 2.Mechanical and Electric torques versus Angle for an applied East-West Voltage of 20 volts.
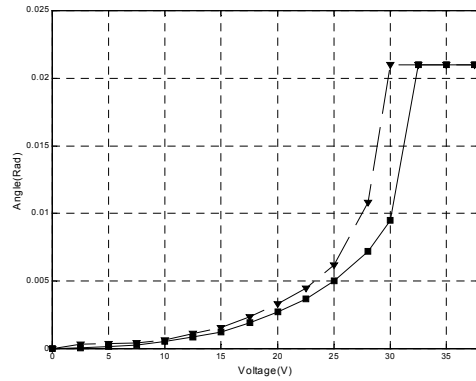
Fig. 3. Voltage versus Tilt Angle in the East-West direction. The Solid line is the calculated result, the dashed line is the measurement.

Typical curves of mechanical restoring torque and electric torques plotted against angle for a particular voltage are shown in Fig.2. It can be seen that there are two crossing points. The first point at which the curves cross is the stable rotation angle for the applied voltage.

Fig.3. shows the computed and measured torques for the device. As can be seen, the agreement is fairly good and certainly, the curves follow the same general shapes. The errors are probably due to three sources. The first is the permittivities of the materials and the second is the mechanical rotque. Due to etching, the beam may not be perfectly rectangular and a full numerical analysis allowing for possible variation in the cross-section from a rectangle should probably be applied. The third source of error is due to the fact that the electric forces are distributed over the surface of the mirror and there is probably some bending of the mirror structure itself, in addition to the beams. It is intended to add a further analysis to estimate this bending but this requires a full structural analysis of the mirror under a distributed force.

CONCLUSIONS

The paper has described a MEMS device and provided a geometric description and a set of experimental measurements. The numerical predictions of the device performance show reasonable agreement with the measurements. This model can be used as a benchmark for both electrostatic analysis and for a coupled structural-electrostatic analysis. More details on the measurements and the device performance will be given in the full version of the paper.

REFERENCES

[1] J.I.Young, A.M.Shkel, "Comparative Study of 2-DOF Micromirrors for Precision Light Manupulation", *Proc. Of SPIE: SPIE Smart Structures and materials Conference*, 2001.

[2] J.E.Lin, F.S.J.Michael, A.G.Kirk, " Investigation of improved design for rotational micromirrors using multi-user MEMS processes", *Journal of Microlithography, Microfabrication and Microsystems*, Vol.1, No.1, pp.70-78, 2002.

[3] "ElecNet User's Manual", Infolytica Corporation, Montreal, 2002.

Scalar and Vector Potentials
in the Dynamical Equations of Electromagnetism

José A. Camberos

United States Air Force Research Laboratory, Dayton, OH 45433

Abstract—**The solution of the complete set of electromagnetic equations, including the two divergence equations, is proposed by the addition of two pseudo–variables that represent the presence of magnetic monopoles and scalar vacuum polarization (both set to zero to prevent solutions not supported by physical theory). The added symmetry, which bestows a degree of aesthetic beauty to the governing equations, also has the practical benefit that couples the divergence equations to the curl equations, thus representing a complete solution in the sense that all four equations can be solved together. Hence, the divergence–free conditions in the absence of electromagnetic sources are explicitly enforced, suppressing spurious solutions.**

INTRODUCTION

The speed, memory, and power available in modern computer architectures makes it possible to obtain numerical solutions of partial differential equations in diverse theoretical fields. The numerical solution to Maxwell's equations in particular began as soon as computers were available. Recently, finite–element and finite–volume methods have received attention. Every numerical method has its strengths and weaknesses; its champions and detractors. As yet, no ideal numerical method, acceptable by even a majority of users, provides sufficient flexibility, accuracy, robustness, and ease of use to declare further research and development obsolete.

The lack of complete symmetry in the Maxwell equations of electromagnetism has been well-noted and lamented[1]. The author presents the results of a search to fully couple and solve a completely symmetric set of electromagnetic equations inspired by the work of Harmuth[2], Cornille[3], and Jiang[4]. Some of these works have provoked controversy and perhaps remain on the fringes of research in computational electromagnetics, where standard algorithms for finite–difference time–domain methods continue to dominate. By abstracting from the common elements and ideas in the scalar and vector potential formulation of Maxwell's equations, it is possible to infer additional terms in the partial differential equations that represent phenomena not presently supported by theory but that may nevertheless be useful in numerical solutions, where spurious terms with no physical source often arise and need to be controlled or suppressed. Jiang[4] solved this problem by developing a mathematical formulation in context of the finite–element method that fully coupled the full Maxwell equations, including the two divergence equations.

Because the divergence equations can be derived from the curl equations, it was recognized early on that these are not independent and instead have the form of initial and boundary conditions. However, once the formulas contain complete symmetry, the divergence equations no longer appear redundant and in fact explicitly represent a conservation law for electric and magnetic charge.

Electromagnetic Equations: In the presence of simple material media, (isotropic, linear properties), the Maxwell equations (also known by their respective historical names) describe electromagnetic phenomena:

$$\text{Curl Eqns.:} \quad \nabla \times \vec{E} = -\frac{\partial \vec{B}}{\partial t} \quad ; \quad \nabla \times \vec{H} = \frac{\partial \vec{D}}{\partial t} + \vec{J}_e \quad (1)$$

$$\text{Div Eqns.:} \quad \nabla \cdot \vec{D} = \rho_e \quad ; \quad \nabla \cdot \vec{B} = 0 \quad (2)$$

Constitutive relations for simple media (linear, isotropic, and homogeneous) include: $\vec{D} = \epsilon \vec{E}$, $\vec{B} = \mu \vec{H}$, and $\vec{J}_e = \sigma_e \vec{E}$. These allow for some flexibility in choosing the dependent variables so the Maxwell equations can be written in various ways. The symbols ϵ and μ represent the electric and magnetic constants of the medium respectively; these are related to the speed of light in the medium: $c^2 = 1/\epsilon\mu$.

VECTOR AND SCALAR POTENTIALS

Vector and scalar potentials for Maxwell's theory are now standard practice in college courses on electromagnetism, even introductory ones since the concept and ideas are relatively easy to grasp. They also make evident the connection between electric and magnetic fields and their sources (electric charge and current). Standard practice (e.g., Stratton,[6]) in developing electromagnetic theory considers the vector $\vec{A}_e$ and scalar potential ϕ_e fields such that

$$\vec{B} = -\mu\nabla \times \vec{A}_e \quad , \quad \vec{D} = \epsilon\mu\frac{\partial \vec{A}_e}{\partial t} + \nabla\phi_e \; . \quad (3)$$

On choosing the Lorenz[1] gauge

$$\frac{\partial \phi_e}{\partial t} + \nabla \cdot \vec{A}_e = 0 \quad (4)$$

and substituting into the Maxwell equations gives a set of wave equations, one for the scalar potential and one for the vector potential:

$$\nabla^2\phi_e - \epsilon\mu\frac{\partial^2\phi_e}{\partial t^2} = \rho_e \quad , \quad \nabla^2\vec{A}_e - \epsilon\mu\frac{\partial^2\vec{A}_e}{\partial t^2} = \vec{J}_e \; . \quad (5)$$

---

[1]The gauge is nowadays attributed to H. A. Lorentz, although it was L. Lorenz who first published the concept, as detailed by Nevels[5].

Using a Green's function approach, the proper solutions to the scalar and vector wave equations (5) are given by

$$\implies \quad \phi_e(\vec{r}, t) = \frac{-1}{4\pi} \iiint [\rho_e] \frac{dV_1}{R} \qquad (6)$$

$$\implies \quad \vec{A}_e(\vec{r}, t) = \frac{-1}{4\pi} \iiint [\vec{J}_e] \frac{dV_1}{R} \qquad (7)$$

where the notation $[\xi] = \xi(\vec{r}, t - R/c)$ and $R = |\vec{r} - \vec{r}_1|$ represents the time–delayed quantities.

MAGNETIC MONOPOLES

Maxwell's electromagnetic theory does not exclude magnetic monopoles, although these have no experimental evidence as yet. Nevertheless, it is possible to postulate magnetic charge carriers for the practical purpose of obtaining solutions for the Maxwell equations that may not be possible otherwise[2]. Towards that end, consider the vector and scalar potential functions that satisfy the differential equations as given by (5). By analogy, one may postulate a corresponding set of magnetic vector and scalar potential functions satisfying

$$\nabla^2 \vec{A}_m - \epsilon\mu \frac{\partial^2 \vec{A}_m}{\partial t^2} = \vec{J}_m \ , \quad \nabla^2 \phi_m - \epsilon\mu \frac{\partial^2 \phi_m}{\partial t^2} = \rho_m \ . \ (8)$$

Lorenz–type gauge conditions provide the coupling of the scalar and vector fields:

$$\frac{\partial \phi_e}{\partial t} + \nabla\cdot\vec{A}_e = 0 \ , \quad \frac{\partial \phi_m}{\partial t} + \nabla\cdot\vec{A}_m = 0 \ . \qquad (9)$$

Abstracting from (3), define the $\vec{B}$ and $\vec{D}$ fields as

$$\vec{B} = \epsilon\mu \frac{\partial \vec{A}_m}{\partial t} + \nabla\phi_m - \mu\nabla\times\vec{A}_e \qquad (10)$$

$$\vec{D} = \epsilon\mu \frac{\partial \vec{A}_e}{\partial t} + \nabla\phi_e + \epsilon\nabla\times\vec{A}_m \qquad (11)$$

Taking the divergence and curl of each quantity gives a form of the electromagnetic equations, after some simplification and manipulation, that exhibit a striking symmetry, endowed by postulating magnetic charge and current. From solutions to (8) and the Lorenz gauge condition (9), the conservation of magnetic charge equation gives

$$\frac{\partial \rho_m}{\partial t} + \nabla\cdot\vec{J}_m = 0 \qquad (12)$$

Consider now a more general method for deriving the governing equations in terms of electric and magnetic field quantities. First, postulate a set of vector and scalar potentials. Second, select a generalized Lorenz gauge. Third, define the electric and magnetic fields. Fourth, obtain the differential equations for these by taking the divergence and curl of each and manipulating in combination with the appropriate time–derivative.

EM EQUATIONS WITH POLARIZATION GAUGE

As an alternative to the Lorenz gauge condition, define the scalar–polarization condition as

$$\frac{\partial \phi_m}{\partial t} + \nabla\cdot\vec{A}_m = -P_m \qquad (13)$$

$$\frac{\partial \phi_e}{\partial t} + \nabla\cdot\vec{A}_e = -P_e \qquad (14)$$

which represent vacuum polarization[3]. Now the electro–magneto dynamic equations with polarization gauge exhibit complete symmetry:

$$\frac{\partial \vec{B}}{\partial t} + \nabla\times\frac{\vec{D}}{\epsilon} + \nabla P_m = -\vec{J}_m \qquad (15)$$

$$\frac{\partial \vec{D}}{\partial t} - \nabla\times\frac{\vec{B}}{\mu} + \nabla P_e = -\vec{J}_e \qquad (16)$$

$$\epsilon\mu \frac{\partial P_m}{\partial t} + \nabla\cdot\vec{B} = \rho_m \qquad (17)$$

$$\epsilon\mu \frac{\partial P_e}{\partial t} + \nabla\cdot\vec{D} = \rho_e \qquad (18)$$

Contrast these with Equations (10),(11), (13), and(14), which have identical mathematical properties.

Continuity equations for electric and magnetic charge now represent a wave equation for the scalar polarization:

$$\nabla^2 P_m - \epsilon\mu \frac{\partial^2 P_m}{\partial t^2} = -\left(\nabla\cdot\vec{J}_m + \frac{\partial \rho_m}{\partial t}\right) \qquad (19)$$

$$\nabla^2 P_e - \epsilon\mu \frac{\partial^2 P_e}{\partial t^2} = -\left(\nabla\cdot\vec{J}_e + \frac{\partial \rho_e}{\partial t}\right) \qquad (20)$$

A Green's function approach readily provides the solutions:

$$P_m(\vec{r}, t) = \frac{1}{4\pi} \iiint \left\{ \nabla_1 \cdot [\vec{J}_m] + \left[\frac{\partial \rho_m}{\partial t}\right] \right\} \frac{dV_1}{R} \qquad (21)$$

$$P_e(\vec{r}, t) = \frac{1}{4\pi} \iiint \left\{ \nabla_1 \cdot [\vec{J}_e] + \left[\frac{\partial \rho_e}{\partial t}\right] \right\} \frac{dV_1}{R} \qquad (22)$$

Remark: The scalar–polarization solution given by (21) and (22) demonstrate explicitly that a violation of charge conservation (electric or magnetic) gives rise to a different gauge condition than that theoretically proposed Lorenz. In numerical solutions of Maxwell equations, be it finite–difference, finite–volume, or finite–element, will not necessarily satisfy charge conservation unless strategically designed to do so. For general purpose computational electromagnetic solvers, this may not be possible if the divergence equations are ignored or taken for granted as redundant.

REFERENCES

[1] C.-D. Munz, et. al., "Divergence Correction Techniques for Maxwell Solvers Based on a Hyperbolic Model", *Journal of Computational Physics*, **161**, 2000, pp. 484–511.

[2] H. F. Harmuth "Electromagnetic Transients not Explained by Maxwell's Equations." *Essays on the Formal Aspects of Electromagnetic Theory*, A. Lakhtakia, editor. River Edge, NJ: World Scientific Publishing Co. Pte. Ltd., (1993) pp. 87–126.

[3] P. Cornille. "Inhomogeneous Waves and Maxwell's Equations." *Essays on the Formal Aspects of Electromagnetic Theory*, A. Lakhtakia, editor. River Edge, NJ: World Scientific Publishing Co. Pte. Ltd., 138-182 (1993).

[4] Bo–Nan Jiang, J. Wu, and L. A. Povinelli. "The Origin of Spurious Solutions in Computational Electromagnetics." *Journal of Computational Physics* Vol. 125, pp. 104–123 (1996).

[5] R. Nevels and C. S. Shin, "Lorenz, Lorentz, and the Gauge", *IEEE Antennas and Propagation Magazine*, Vol. 43, No. 3, June 2001, pp. 70–71.

[6] J. A. Stratton, *Electromagnetic Theory*, McGraw–Hill Book Co.: New York, NY, 1941, pp. 23–26.

Analysis of the thin plate eddy current problem by Finite Volume Method

J. Zou, Y. Q. Xie, J. S. Yuan, X. S. Ma

Department of Electrical Engineering, Tsinghua University, Beijing, 100084, China

zoujun@tsinghua.edu.cn

X. Cui

Department of Electrical Engineering, North China Electric Power University, Baoding, Hebei, 071003, China

hjbdcuix@heinfo.net

Abstract—The eddy current distribution in a thin nonferrous steel plate is calculated by using the finite volume method excited by a 50Hz sinusoidal magnetic field. Based on the flux conversation conception of control volume, an equation group with unknown nodes of current vector potential T can be formed in a straightforward way. The numerical results show very good agreements with the experimental data of TEAM problem 21.

INTRODUCTION

The analysis of eddy current field is an important problem for the engineering design and scientific research. In the past years, the finite element method is widely used in many engineering applications. However, there are few papers to report calculation of the eddy field by the finite volume method (FVM)[1]. In this paper, an eddy current problem analyzed by FVM is presented and TEAM Problem 21[2] with a nonmagnetic steel plate is picked out as an example to verify the effectiveness of approach proposed.

PRINCIPLE

The schematic diagram of TEAM problem 21 is shown in Fig. 1. The model consists of two rectangle coils with the same geometrical dimension and a nonmagnetic steel plate with 3 rectangle slots. Since the steel plate is thin as compared with its skin depth, the eddy current J in the plate has no normal component, that is, $J = J_y j + J_z k$, where i, j and k are unit vectors of the coordinate axis respectively. Obviously, the rotation of J has only the component along the x axis, so

(a) side view   (b) front view   (c) planform
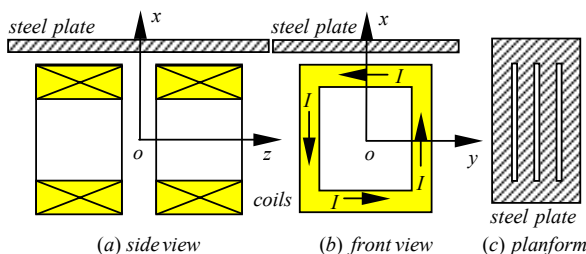
Fig. 1 Model of TEAM problem 21

$$\nabla \times J = -k^2 (H_{rx} + H_{sx}) i \qquad 1$$

where $k^2 = j\omega\mu_0\sigma$, $j = \sqrt{-1}$. σ is the conductivity of the steel. H_{sx} and H_{rx} are the magnetic field intensities of x axis components generated by the exciting current of coils and the eddy current within the thin plate respectively. It is convenient to use $T - \Omega$ potential to analyze the eddy current field, i.e.,

$$\nabla \times T = J, \qquad H_r - T = -\nabla\Omega \qquad 2$$

where H_r is in corresponding with the magnetic field intensity generated by the eddy current. It should be noted that the direction of T is only along the unit vector i. By substituting (2) into (1), (1) can be rewritten as

$$\nabla \times J = -k^2 (T_x - (\nabla\Omega)_x + H_{sx}) i \qquad 3$$

Similar to the finite element method, the steel plate is discreted by a number of hexahedron elements as shown in Fig.2. The central point scheme is employed, which means that the unknown is the current vector potential in the center of each element. By referring to the diagram of element 1234 shown in Fig.2(b), (3) can be recasted as

$$\nabla \times J \approx \frac{-\oiint_s J \times ds}{\Delta v} = (\frac{J_{za} - J_{zc}}{\Delta y} - \frac{J_{yb} - J_{yd}}{\Delta z}) i \qquad 4$$

where $\Delta v = \Delta x \cdot \Delta y \cdot \Delta z$ is the control volume and S is its surface. J_{za}, J_{zc}, J_{yb} and J_{yd} are the eddy current flowing along four sides of each element. Taking the element 5678 as an example and choosing the integral path efgh shown in Fig.2(c), in terms of the identical equation
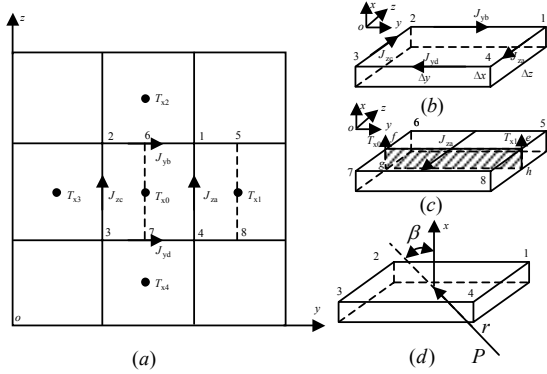
Fig. 2 Central point scheme of FVM

$\oint_l T \mathrm{d}l = I$, one can obtain $T_{x0}\mathrm{d}x - T_{x1}\mathrm{d}x = J_{za}\mathrm{d}x\mathrm{d}y$, i.e.,

$$J_{za} = \frac{T_{x0} - T_{x1}}{\Delta y} \qquad 5$$

Similarly

$$J_{zc} = \frac{T_{x3} - T_{x0}}{\Delta y}, J_{yb} = \frac{T_{x2} - T_{x0}}{\Delta z}, J_{yd} = \frac{T_{x0} - T_{x4}}{\Delta z} \qquad 6$$

According to Fig.2(d), the magnetic intensity of field P generated by the element 1234 is $\nabla\Omega = -\iint_s \frac{\rho_s \mathrm{d}s}{4\pi r^2} \cdot \frac{r}{r}$, where ρ_s is the surface density of magnetic charge and r is the distance between the field and source point. Then the x component of $(\nabla\Omega)_x$ is $-\iint_s \frac{\rho_s \mathrm{d}s}{4\pi r^2}\cos\beta$, where β is the angle between the vector r and i. Because the thickness of steel plate is rather small, ρ_s equals to the current vector potential T approximately, in addition, the solid angle θ of field point P with respect to each element is $-\iint_s \frac{\cos\beta \mathrm{d}s}{r^2}$, so $(\nabla\Omega)_x = \frac{T \cdot \theta}{4\pi}$. By adding up the contribution of neighboring element, for the center of the element 1234, one can get

$$(\nabla\Omega)_{x0} = 2\frac{\sum_{i=1}^4 T_{xi}\cdot\theta_i}{4\pi} = \frac{\sum_{i=1}^4 T_{xi}\cdot\theta_i}{2\pi} \qquad 7$$

where T_{xi} is the current vector potential of element surrounding element 1234. θ_i is the solid angle of the center of element 1234 with respect to its neighboring elements. The coefficient 2 is due to accumulating the contribution of magnetic charge on the upper and lower plate surface. Substituting (4),(5),(6) and (7) into (3) and recasting (3), for the element 1234, the unknown current vector

potential of FVM scheme can be expressed as

$$\frac{T_{x0} - \sum_{i=1}^4 T_{xi}}{k^2 h^2} + T_{x0} - \sum_{i=1}^4 T_{xi}\cdot\theta_i = -H_{sx0} = -\frac{B_{sx0}}{\mu_0} \qquad (9)$$

where $h = \Delta y = \Delta z$, B_{sx0} is the magnetic induction intensity generated by the coils and can be calculated by using Boit-Savart's law. Then an equation group with the unknown T_x can be formed by applying (9) to each element, and the eddy current J can be evaluated by T_x in terms of (2).

NUMERCIAL EXAMPLES

The steel plate shown in Fig.1 is made of non-magnetic steel with $\mu_r = 1$, $\sigma = 1.39\times10^6\,\mathrm{S/m}$ and its length, width and height is 820 , 360 and 10 mm respectively. The direction of the exciting current in one coil is opposite to that of another, and the ampere-turn of two coils are both 3000 AT (RMS, 50Hz). Fig. 3 shows the comparison curves between the numerical and measured magnetic flux density at some specified positions of steel plate.
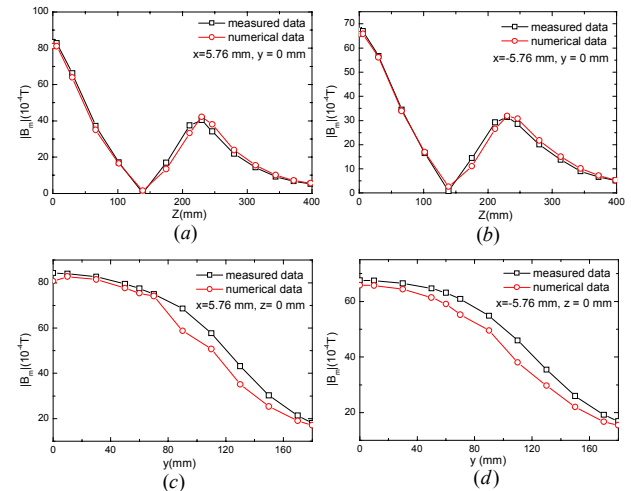
Fig. 3 numerical and measured results

CONCLUSION

The TEAM problem 21 is analyzed by using the finite volume method. The numerical results show that FVM is another good candidate approach to calculate the eddy current problems.

REFERENCES

[1] M. Rosenfeld, R. Tanami, and S. Abboud "Numerical solution of the potential due to dipole sources in volume conductors with arbitrary geometry and conductivity", *IEEE transactions on biomedical engineering,* Vol.43. No.7 pp.679-688, July 1996.
[2] J. Wang, Z. Cheng, and Y. Zhang, "Experiment and Analysis on Model Simulating 3D Eddy Current Losses in Non-Magnetic Steel Plate," *J. of North China Electric Power University,* vol. 24, pp.8-14, July 1997.

Calculation of Eddy Current Energy Losses in Thin Sheets under Saturation

G. Szymański and M. Waszak

Institute of Control and System Engineering - Poznań University of Technology

ul. Piotrowo 3a, PL 60-965 Poznań, Poland

Email: grzegorz.szymanski@put.poznan.pl

Abstract— **This paper presents an approach for eddy current energy losses computations. The approach is based on the A-V formulation. The Newton-Raphson algorithm with the jacobian matrix calculated numerically has been applied. It has been focused on devices with parts consisting of thin sheets. Influence of saturation effects has been studied. For such devices very high accuracy of field solution is required in order to calculate energy losses precisely. The simulation of permanent magnet rotating machine with enforced movement is presented.**

I. INTRODUCTION

A common problem is magnetic field analysis in systems with thin conductive layers [3]. One obvious issue is discretization using finite elements mesh since the skin effect depth remains unknown as transient simulation is performed. This can be, however, overcome for instance, when adaptive or local mesh refinement is applied [4]. Alternatively, skin effect depth can be precisely enough estimated when sufficient details about exciting waveform are provided. Additional problems in thin sheets analysis arise when saturation effects become important. In particular, convergence difficulties during transient simulation may arise as iterative method, used to solve nonlinear equations, lead to high flux density values during solution process. Similarly, substantial changes of magnetization curve slope impede convergence process.

The accuracy of field solution is of great importance in systems with eddy currents. It is well-known that eddy current density depends on derivative of magnetic flux density with respect to time. The derivative is a function of working point locus. Therefore, high accuracy in evaluation of the operating point is required in the systems working near the saturation. In such systems flux density changes remain very small during relatively substantial changes of magnetic field strength. Whereas, in non-saturated region, the same field strength changes correspond to considerably larger shifts along the flux density axis. It leads straightforward to inconsistencies in eddy current energy losses calculations. Therefore, considering the saturation in thin sheets and its accuracy aspects are the major contribution of this paper.

We propose to take advantage of the Newton-Raphson algorithm with the jacobian matrix calculated numerically. This method is characterized by unique approach to the magnetization characteristics on the H-B plane. The method is proper and remains unchanged for both initial magnetization curve and permanent magnet demagnetization curve as well as for hysteresis loops. Thus, one can control the accuracy of the whole field problem by parameters and stopping criteria of only one routine.

The paper is organized as follows. After the introduction a brief description of problem formulation is given. Next, we propose an approach to saturation effects. After that some numerical example is presented. The last section covers some further remarks.

II. PROBLEM FORMULATION

We exploit the A-V formulation. The field distribution in non-conducting region is described by

$$rot\frac{1}{\mu}rot\boldsymbol{A} = \boldsymbol{j}_0 + \frac{1}{\mu_0}rot\boldsymbol{M}, \qquad (1)$$

whereas in conducting area governs

$$rot\frac{1}{\mu}rot\boldsymbol{A} = \boldsymbol{j}_e \qquad (2)$$
$$div\,\boldsymbol{j}_e = 0; \qquad (3)$$

where $\boldsymbol{j}_e$ stands for eddy current density

$$\boldsymbol{j}_e = -\sigma\frac{\partial\boldsymbol{A}}{\partial t} - \sigma\,grad\,V.$$

Using the finite element method, one obtains the equations (1)-(3) in matrix form

$$\begin{bmatrix} S & E \\ 0 & G \end{bmatrix}\begin{Bmatrix} A \\ V \end{Bmatrix} + \begin{bmatrix} F \\ E^T \end{bmatrix}\frac{\partial}{\partial t}\{A\} = \begin{bmatrix} C+M \\ 0 \end{bmatrix}, \qquad (4)$$

where
$\{A\}$ is vector of unknown nodal components of magnetic vector potential,
$\{V\}$ is vector of unknown nodal values of scalar electric potential,
$[C]$ is exciting current density vector and
$[M]$ is magnetization vector.

The permeability tensor μ and the magnetization $\boldsymbol{M}$ are usually functions of magnetic flux density, hence they depend on magnetic vector potential, therefore the operator $[S]$ and the vector $[M]$ tend to be nonlinear ones with respect to the unknown vector $\{A\}$. To deal with the nonlinearities the Newton-Raphson method has been chosen [5].

III. Saturation Effects

Consider an operating point on the magnetization curve on the H-B plane. The eddy current energy losses depend on the derivative of the operating point flux density component with respect to time. Thus high accuracy in the evaluation of the working point is essential, especially when relevant changes of magnetization curve slope occur in the neighborhood of the working point.

Since the fixed point method proposed in [1] loses accuracy near the saturation, we have proposed another approach. Our idea is to calculate the jacobian matrix of the system (4) numerically using forward difference formula [6]. In order to perform the calculations efficiently each element is considered individually.

Let us focus on the nonlinear components of (4), i.e. $[S]$ and $[M]$, expressed in terms of the element nodal components of magnetic vector potential $\{A^e\}$. We use the notation R^e for the element remainder vector and J^e for the corresponding jacobian matrix, respectively. The calculation of the jacobian is performed for column j as follows

$$ J^e_{\cdot,j} = \frac{R^e(A^e + A^e_j) - R^e(A^e)}{\Delta_j}, \qquad (5) $$

where: $A^e_j = [0 \cdots \Delta_j \cdots 0]^T$.
The remaining issue is evaluation of the increment Δ_j. The choice of the increment cannot be arbitrary due to the fact that Δ_j influences the flux density hence the working point locus on the H-B plane. We assume that from the magnetization curve slope a proper increment of flux density ΔB can be obtained. Thus the increment Δ_j fulfills equation

$$ B\left(A^e + A^e_j(\Delta_j)\right) = B\left(A^e\right) + \Delta B\left(A^e\right); \qquad (6) $$

where the above equation can be solved either as vector equation or in terms of absolute values. The flux density is related to magnetic vector potential by means of $\boldsymbol{B} = rot\,\boldsymbol{A}$.

IV. Numerical Example

As numerical example we use a permanent magnet rotating machine. The discretized three dimensional model is presented in Fig. 1. It is assumed that field distribution of a single sheet is representative of the entire machine. The mesh consists of 297 689 elements. The teeth material magnetization characteristic is depicted in Fig. 2. The nominal operating point is located near the saturation.

V. Further Remarks

In the full paper it is intended to cover some further details concerning implementation of the jacobian matrix evaluation.

The results of transient idle state simulations for varying sheet thinness will be presented in the full paper; the comparison with measurements will be given.
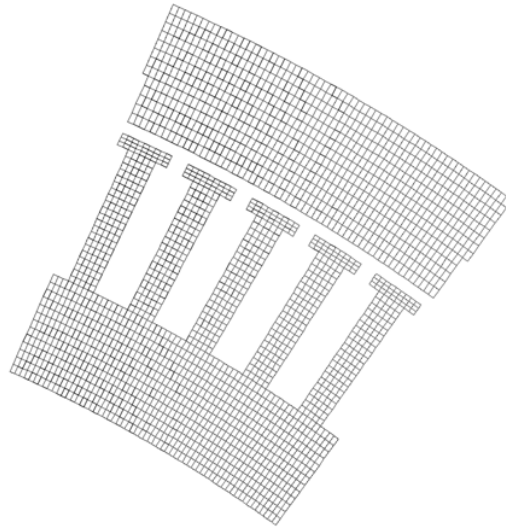
Fig. 1. Permanent magnet rotating machine
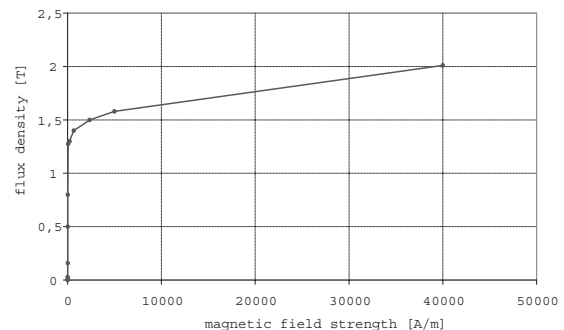
Fig. 2. Magnetization characteristic of teeth material

References

[1] A. Patecki and G. Szymański, "Calculation of 3D Eddy Current Transient Process with Enforced Movement,", *Proceedings of CEFC 2000*, Milwaukee, Conference Record, p. 243, June 2000.

[2] L. Jänicke, A. Kost, R. Merte, T. Nakata, N. Takahashi, K. Fujiwara, K. Muramatsu, "Numerical Modeling for Anisotropic Magnetic Media Including Saturation Effects," *IEEE Transactions on Magnetics*, Vol. 33, No. 2, pp. 1788-1791, March 1997.

[3] H. Igarashi, A. Kost, T. Honma, "A Three Dimentional Analysis of Magnetic Fields around a Thin Magnetic Conductive Layer Using Vector Potential," *IEEE Transactions on Magnetics*, Vol. 34, No. 5, pp. 2539-2542, 1998.

[4] A. Hahn, A. Kost, L. Jänicke, K. Miethner, "Fields and shielding by eddy currents in perforated boxes," *Proceedings of ISTET 2001*, Linz, Conference Record, pp. 75-78, August 2001.

[5] J. O'Dwyer and T. O'Donnell, "Choosing the Relaxation Parameter for the Solution of Nonlinear Magnetic Field Problems by the Newton-Raphson Method," *IEEE Transactions on Magnetics*, Vol. 31, No. 3, May 1995.

[6] W. H. Press et al., *Numerical Recipes in C*. Cambridge University Press, Cambridge, 1997.

Transient 3D FEM Computation of Eddy-Current Losses in the Rotor of a Claw-Pole Alternator

Christian Kaehler and Gerhard Henneberger

Department of Electrical Machines (IEM), Aachen University (RWTH),

Schinkelstrasse 4, D-52056 Aachen, Germany

christian.kaehler@iem.rwth-aachen.de

Abstract—**The 3D Finite-Element method (FEM) allows for the calculation of eddy currents in the claws of synchronous claw-pole alternators taking the rotational geometry movement into account. A transient edge-based vector formulation is utilized to compute the induced eddy-current losses in the rotor caused by the stator slotting. The theory of this formulation is outlined and the FEM model of the alternator is described. On a model built in series-production the local loss distribution on the rotor claw is discussed as well as the speed characteristics of the eddy-current losses. The use of adaptive mesh optimization leads to corrected results which will be compared to measurements in the full paper.**

Index Terms— **Transient 3D FEM computation, Eddy-current losses, Geometry movement, Adaptive h-refinement**

I. INTRODUCTION

The efficiency of electric machines is decreased by different loss mechanisms. In the case of the claw-pole alternator, these are dominantly ohmic losses in the coils, that define the loss behavior in the lower speed range of the alternator. Additionally, iron losses, consisting of hysteresis and eddy-current losses, define the high-speed loss characteristics of this machine [1]. Both can be broken down into rotor and stator parts. Whereas the ohmic losses can be directly calculated in dependence on the coil currents, an analytic description of the iron losses is not possible due to the geometric complexity of the three-dimensional field distribution.

Measurements of the total losses and a subtraction of all analytically defined loss mechanisms lead to a separation of the iron losses. These separated losses are error-prone due to the long series of measurements.

Usage of the Finite-Element Method (FEM) combined with a time-stepping approach allows to calculate the eddy currents in conducting materials which are induced by an alternating magnetic field. In the case of the claw-pole synchronous machine, the eddy-current losses in the rotor claws are caused by the rotor movement in combination with the stator slotting. The magnetic flux pulsates with the slot frequency e.g. $f_{slot} = 1800$ Hz at speed $n = 3000$ rpm. The flux pulsations induce the eddy currents in the claws made of massive steel.

In this paper the applied transient edge-based FEM approach [2] is outlined. The 3D model of the claw-pole alternator is described. The characteristic curve of the rotor eddy-current losses depending on the alternator speed in generator mode is presented. Adaptive refinement in eddy-current regions with two different local error estimation strategies is applied. The calculation results are compared to measurements.

II. THEORY OF THE EDGE-BASED SOLVER

The applied edge-based solver is part of an object-oriented solver package [3]. It applies a transient edge-based FEM formulation on simply-connected eddy-current regions taking the rotational movement into account by means of time stepping.

The transient $\vec{A}$-approach applies only the magnetic vector potential $\vec{A}$ in all regions Ω utilizing the following equation (in Galerkin formulation):

$$
\int_\Omega \nabla \times \vec{\alpha}_i \cdot \nu \nabla \times \vec{A}(t) + \sigma \frac{d\vec{A}(t)}{dt} d\Omega =
$$
$$
\int_\Omega (\vec{\alpha}_i \cdot \vec{J}_0(t) + \nabla \times \vec{\alpha}_i \cdot \nu \vec{B}_r(t)) d\Omega \quad . \tag{1}
$$

The material parameters ν and σ represent the non-linear reluctivity and the linear conductivity, respectively. $\vec{\alpha}_i$ defines the shape function of an edge element (in this solver first-order tetrahedra). $\vec{J}_0(t)$ describes the given coil current density while $\vec{B}_r(t)$ defines remanence. Note, that external currents ($\vec{J}_0(t) > \vec{0}$) are only allowed in non-conducting regions ($\sigma = 0$) while remanence is valid in all regions ($\sigma \geq 0$).

The time-stepping algorithm interpolates the time-dependent variables linearly:

$$
\vec{A}(t) = \tau \cdot \vec{A}_{n+1} + (1 - \tau)\vec{A}_n \quad \text{ditto for } \vec{J}_0(t), \vec{B}_r(t);
$$
$$
\frac{\partial}{\partial t}\vec{A}(t) = \frac{1}{\Delta t}(\vec{A}_{n+1} - \vec{A}_n) \quad , \tag{2}
$$

where n represents the number of the transient step, Δt the time in between transient steps and τ the relaxation factor. The relaxation factor in between transient steps is chosen as $\tau = \frac{2}{3}$ (Galerkin-scheme) [4].

The resulting global matrix is symmetric, thus allowing the storage as lower or upper triangular matrix and the use of the Cholesky-CG combination [2] of the ITL package [5]. Saturation effects are computed with an overlaying Newton-Raphson procedure for each transient step.

To represent rotational movement a lock-step method is utilized. Boundary conditions pair edges in a sliding area mesh. In each step a search function connects the edges in this area depending on the displacement in between the transient steps, while the mesh remains stationary [6].

III. FINITE-ELEMENT MODEL

A model of the alternator in production is depicted in Fig. 1 with translucent stator regions.
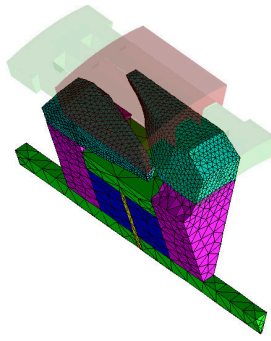
Fig. 1

MODEL OF SERIES-PRODUCTION ALTERNATOR

Fig. 2

LOSS ENERGY OF STARTING MESH AND OF ADAPTIVE STEP 3

The edge-grouping routine of the transient solver described in section II depends on a special air-gap discretization. To implement the change of geometry, the FEM mesh of the alternator is separated into moving elements in the rotor and stationary elements in the stator. The boundary area of these two meshes is located in the middle of the air gap. It is meshed identically in both separate meshes.

IV. CALCULATIONS AND RESULTS

All calculations are conducted at constant speed. The material conductivity of iron $\sigma = 7.5 \cdot 10^6\,[\Omega m]^{-1}$ is used for the massive steel regions of the claws.

The computations are started on a coarse mesh of about 150 000 first-order elements. In order to calculate the discretization error, the eddy-current density of a full loss period is taken into account by using the arithmetic mean value of the local error for each element. In each adaptive step a given ratio of the elements with the highest local error is refined by h-partitioning.

Two strategies for the local error estimation are evaluated. The first strategy defines the highest error in dependence of the gradient of the eddy-current density $\vec{J}$:

$$\varepsilon_1 = |\nabla \cdot |\vec{J}||\quad. \tag{3}$$

The second strategy evaluates the error of the joule loss in each element e rated by the total loss of the conducting region [7]:

$$\varepsilon_2 = \frac{\int_{\Omega_e}(\vec{J}_e - \vec{J}_{avr})\cdot \vec{E}_e\, d\Omega_e}{\int_{\Omega}\vec{J}\cdot \vec{E}\, d\Omega}\quad. \tag{4}$$

$\vec{J}_e$ and $\vec{E}_e$ are the eddy-current density and the electric field strength of element e while $\vec{J}_{avr}$ defines the average eddy-current density of all contact elements.

Both error estimators lead to mesh refinements on the surface of the rotor claw interfacing the air gap. Figure 2 depicts the density of the mesh on the claw tip comparing the starting grid to a mesh after 3 adaptive steps.

With finer meshes the average eddy-current loss decreases (Fig. 3). The adaption is ended when the difference of the average loss values before and after the adaptive step falls below a given limit of 5%. This limit is reached after 3 to 4 steps.
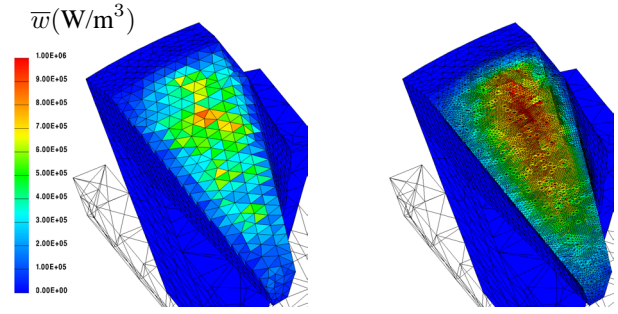
The working points of the alternator are varied from $n = 1500\,\mathrm{rpm}$ to $n = 10000\,\mathrm{rpm}$. These computations lead to the characteristic speed curve of the average eddy-current losses in the rotor in generator mode on a half-logarithmic scale as presented in Fig. 3.
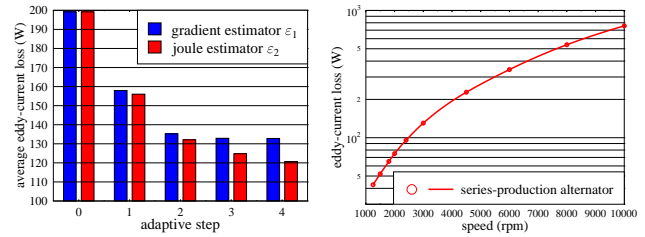
Fig. 3

EDDY-CURRENT LOSSES VS ADAPTIVE STEP AND VS ALTERNATOR SPEED

V. CONCLUSION

A transient 3D FEM approach to calculate the eddy currents in the claws of a synchronous claw-pole alternator is applied taking the rotational movement into account. Two different error estimators are compared that lead, in combination with adaptive remeshing, to the characteristic speed curve of the eddy-current losses in the rotor. Comparison to measurements as well as discussion of both error estimators will follow in the full paper.

REFERENCES

[1] K. G. Bürger, H. P. Gröter, H. J. Lutz, F. Meyer, and W. Schleuter, "Generatoren im Kraftfahrzeug - Stand der Technik und Entwicklungstendenzen," in *Tagung: Nebenaggregate im Fahrzeug*, Haus der Technik, Essen, October 1994.

[2] A. Kameari and K. Koganezawa, "Convergence of ICCG method in FEM using edge elements without gauge condition," *IEEE Transactions on Magnetics*, vol. 33, no. 2, pp. 1223–1226, March 1997.

[3] Guido Arians, Thomas Bauer, Christian Kaehler, Wolfgang Mai, Christoph Monzel, Dirk van Riesen, and Christoph Schlensok, "Innovative modern object-oriented solving environment - iMOOSE," Available: http://imoose.sourceforge.net, [Online].

[4] O. C. Zienkiewicz and R. L. Taylor, *The Finite Element Method*, McGraw-Hill Book Company, London, New York, 1991.

[5] Andrew Lumsdaine, Jeremy Siek, and Lie-Quan Lee, "The iterative template library - itl," Available: http://www.lsc.nd.edu/research/itl, [Online].

[6] Christian Kaehler and Gerhard Henneberger, "Eddy-current computation on a one pole-pitch model of a synchronous claw-pole alternator," in *Conference Record of the 15th International Conference on Electrical Machines*, Brugges, Belgium, August 2002, ICEM.

[7] Koji Tani, Takashi Yamada, and Yoshihiro Kawase, "Error estimation for transient finite element method using edge elements," *IEEE Transactions on Magnetics*, vol. 36, no. 4, pp. 1488–1491, July 2000.

Crack detection in ferromagnetical materials

Abbas Farschtschi[1], Amor Benmansour[2]

Lehrstuhl für Allgemeine und Theoretische Elektrotechnik

Technische Universität Chemnitz

D-09107 Chemnitz - GERMANY

E-MAIL: (1) LATE@e-technik.tu-chemnitz.de, (2) amor.benmansour@e-technik.tu-chemnitz.de

Abstract- **Nowadays the non-destructive material testing is increasingly important. This work deals with eddy current testing. The finite network method (FNM) is used as numerical computation method.**

INTRODUCTION

A further application of the finite network method (FNM) consists of detecting material defects by means of eddy current testing (ECT) in the context of non-destructive material testing. For this raison a physical model, consisting of an exciting coil and a massy conductor, is selected. With this numeric method is necessary to discretize only areas with conducting material and the surfaces of the iron domains.

NUMERICAL COMPUTATION MODEL

In an eddy current area with magnetizable matter, there are magnetizing currents flowing on the surface as well as inside the magnetizable matter, in addition to the eddy currents. A homogeneous isotropic and linear matter presumed, eddy currents and magnetizing currents inside could be summarized [3]:

$$I_{ges} = I_m + I_w \tag{1}$$

where I_m is the magnetizing current and I_w is the eddy current in the massy conductor.

Through the discretisation of a three-dimensional model results a spatial network, which consists of rectangular solid volume elements. The corner points of these volume elements are called grid-points of the network. Each centre-point of such an element is a network-node and each connection between neighbouring network-nodes is a network-branch. According to FNM, the conducting parts will be transformed into a network of resistances and (mutual-)inductances [1,2]. The current density within a network-branch is assumed to be constant. For this reason, the current density may be replaced by the current that flows in the related network-branch. Such a network created by disretisation may be extended with additional elements (voltage sources, for example). In order to be able to analyse the network with the mesh current procedure, the characteristic values of its elements, voltage supplies, resistances and inductances must be specified [3]. The voltage supplies are considered here as given.

The configuration in this work is composed of a very thin exciting coil and a massy conductor of iron. The exciting coil and the massy conductor, which, as describes above, discretised into many short circuit loops, form a primary and a secondary system.

For a sinusoidal exciting voltage the system equation, in matrix notation, yields:

$$\begin{bmatrix} \underline{Z}_{ss} & j\omega\underline{M}_{ps} \\ j\omega\underline{M}_{ps}^{T} & \underline{Z}_p \end{bmatrix} \begin{bmatrix} I_{ges} \\ I_p \end{bmatrix} = \begin{bmatrix} \mathbf{0} \\ \underline{U} \end{bmatrix} \tag{2}$$

with:

$\underline{Z}_{ss}$ a (nxn) matrix on their diagonal the impedances and on the secondary diagonal the mutual inductances of the short-circuit loops to each other in the secondary system (n to be the number of independent loops in the massy conductor),

$\underline{M}_{ps}$ one dimensional matrix of the length n of all mutual inductances between the short-circuit loops in the massy conductor and the exciting coil,

$\underline{M}_{ps}^{T}$ the transpose matrix of $\underline{M}_{ps}$

$\underline{Z}_p$ impedance of the primary system,

I_{ges} one dimensional matrix of the length n of all currents of the short-circuit loops in the secondary system,

I_p current at the primary system

$\underline{U}$ voltage of excitation at the primary system

Further it could be noted:

$$\underline{U} = \left[\underline{Z}_p - (j\omega)^2 \underline{M}_{ps}^{T} \underline{Z}_{ss}^{-1} \underline{M}_{ps} \right] I_p \tag{3}$$

It is also valid:

$$\underline{U} = \underline{Z} \cdot I_p \tag{4}$$

From (3) and (4) it results:

$$\underline{U} = \left[\underline{Z}_p - (j\omega)^2 \underline{M}_{ps}^{T} \underline{Z}_{ss}^{-1} \underline{M}_{ps} \right] I_p \tag{5}$$

The impedance of the system yields:

$$\underline{Z} = R_{sys} + j\omega M_{sys} \tag{6}$$

where

R_{sys} is the real part of system impedance and M_{sys} is the imaginary part of the system impedance.

If a crack is in the massy conductor, the system impedance changes. This change can be expressed as follows:

$$\Delta R(x, \omega, \mu_r) = R_{sysR}(x, \omega, \mu_r) - R_{sysoR}(x, \omega, \mu_r) \quad (7)$$

$$\Delta M(x, \omega, \mu_r) = M_{sysR}(x, \omega, \mu_r) - M_{sysoR}(x, \omega, \mu_r) \quad (8)$$

with

$R_{sysR}(x, \omega, \mu_r)$ the resistance of the systems with crack,

$M_{sysR}(x, \omega, \mu_r)$ the inductance of the system with crack,

$R_{sysoR}(x, \omega, \mu_r)$ the resistance of the Systems without crack,

$M_{sysoR}(x, \omega, \mu_r)$ the inductance of the system without crack.

EXAMPLE OF APPLICATION

An alternating voltage of constant amplitude (1V) is applied at a one-winding copper coil. The numerical computation is performed for 50Hz as well as for 100Hz. The relative permeability of the massy conductor is set to be 100. The exciting coil moves with a constant velocity along the massy conductor [4]. The position of the coil center refered to the crack center is (x). The crack length is set to be 3mm and the coil width 4mm. Alteration of impedance of the sensor coil was evaluated at different positions. Furthermore the alteration of impedance was determined at a frequency of 900Hz and for different μ_r-values.

RESULTS

The variation of coil impedance is determined according to the equations (7) and (8). The impedance variation depending from the distance (x) between the coil center and the crack center is shown in Fig. 1 resp. Fig. 2 for 50Hz as well as for 100Hz. The dependence of impedance variation from relative permeability of the medium is illustrated in Fig. 3 at x=0 mm.

Fig. 2: Impedance variation at f=100Hz and μ_r =100
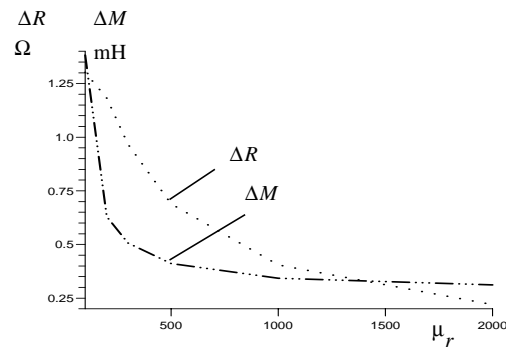
Fig. 3: Impedance variation at f=900Hz and for variable μ_r -values

CONCLUSION

In case of ferrousmagnetic media a noticeable variation of impedance may be observed only in the proximity of the material defect. The sensitivity of the coil-sensor is smaller by encreasing distance(x)-values. Similar observation of impedance variation may be seen in dependence of permeability.

REFERENCES

[1] Farschtschi, A.: „Dreidimensionale Wirbelstromberechnung nach der Netzwerkmethode". Archiv für Elektrotechnik, S. 165-169, 1986

[2] Farschtschi A., Drechsler S.: „Dreidimensionale Wirbelstromberechnung mit der finiten Netzwerk Methode (FNM)" 40. IWK Ilmenau 1995 2:180-185

[3] Farschtschi A., Plontke J., Roscher H.-J., Drechsler S.: „Berücksichtigung von ferromagnetischem Material in der FNM durch Einführung von Magnetisierungsstromdichten"
Electrical Engeneering 81 (1998) 65-68, Springer-Verlag

[4] Farschtschi; Benmansour:„eddy current in moving Media", COMPUMAG 2001 (Evian (F)), Volume IV, 80-81

Fig. 1: Impedance variation at f=50Hz and μ_r =100

Eddy Current Analysis of Surface Permanent Magnet Motor Using 3-D Finite Element Method

Yoshihiro Kawase, Tadashi Yamaguchi, Tomohiro Ono and Shinya Sano

Department of Information Science, Gifu University

Yanagido 1-1, Gifu, 501-1193, Japan

E-mail : kawase@info.gifu-u.ac.jp

Abstract — It is important for the high efficient design of motors to clarify the iron loss (the eddy current loss and the hysteresis loss). In this paper, the eddy current loss and the hysteresis loss of a piece of silicon steel sheet of a surface permanent magnet motors (SPM motors) are calculated using the 3-D finite element method. It is clarified that the skin effects increase the iron loss by our calculation. Furthermore, we calculated the eddy current distribution in the permanent magnet.

INTRODUCTION

Recently, the development of high efficient motors is strongly desired for the environmental issues[1][2]. In order to operate the SPM motors high efficiently, it is important to clarify the iron loss. However, the analysis techniques of the eddy current loss and the hysteresis loss have not been established as yet.

Then, we calculated the three dimensional distributions of eddy current and flux in a piece of silicon steel sheet of a SPM motor using the 3-D finite element method. It is clarified that the eddy current loss and the hysteresis loss in the SPM motor. Furthermore, we calculated the eddy current loss in a permanent magnet of a SPM motor with or without the overhang of the permanent magnet.

As the results of computation, it is found that the iron loss with skin effects is different from the iron loss without skin effects, and the effects of overhang of permanent magnet on the eddy current loss in the permanent magnet and the iron loss are also quantitatively clarified.

ANALYSIS METHOD

A. Magnetic Field Analysis

The fundamental equations of the magnetic field using the 3-D FEM can be written using the magnetic vector potential A and the electric scalar potential ϕ as follows [3]:

$$\mathrm{rot}(\nu\,\mathrm{rot}\,\boldsymbol{A}) = \boldsymbol{J}_e + \nu_0\,\mathrm{rot}\,\boldsymbol{M} \qquad (1)$$

$$\boldsymbol{J}_e = -\sigma\left(\frac{\partial \boldsymbol{A}}{\partial t} + \mathrm{grad}\ \phi\right) \qquad (2)$$

$$\mathrm{div}\,\boldsymbol{J}_e = 0 \qquad (3)$$

where, ν is the reluctivity, ν_0 is the reluctivity of vacuum, $\boldsymbol{J}_e$ is the eddy current density and σ is the conductivity.

B. Calculation of Eddy Current Loss

The eddy current loss W_{ed} is given as follows [3]:

$$W_{ed} = \frac{1}{\tau/2}\int_t^{t+\tau/2}\left\{\int_{V_e}\frac{(\boldsymbol{J}_e)^2}{\sigma}dv\right\}dt \qquad (4)$$

where, τ is the period of the eddy current waveform, V_e is the region of the conductor with the eddy current, $\boldsymbol{J}_e$ is the eddy current density and σ is the conductivity.

C. Calculation of Hysteresis Loss

The hysteresis loss W_{hy} taking into account the major and minor loops of the hysteresis loop can be estimated as follows [4]:

$$W_{hy} = \frac{K_h D}{T}\sum_{i=1}^{NE}\frac{\Delta V_i}{2}\left(\sum_{j=1}^{Npr^i}\left(B_{mr}{}^{ij}\right)^2 + \sum_{j=1}^{Np\theta^i}\left(B_{m\theta}{}^{ij}\right)^2 + \sum_{j=1}^{Npz^i}\left(B_{mz}{}^{ij}\right)^2\right) \quad (5)$$

where, K_h is the coefficient of the hysteresis loss, D is the density of the steel sheet, T is the period of analysis time, NE is the number of the elements in the steel sheet and ΔV_i is the volume of the i-th element. $N_{pr}{}^i$, $N_{p\theta}{}^i$ and $N_{pz}{}^i$ are the number of the maximum or minimum value of the flux density of the radial direction, the rotation direction and the z-direction of the i-th element, respectively. $B_{mr}{}^{ij}$, $B_{m\theta}{}^{ij}$ and $B_{mz}{}^{ij}$ are the amplitude of the flux density of major and minor hysteresis loops of the radial direction, the rotation direction and the z-direction, respectively.

EDDY CURRENT ANALYSIS OF A PIECE OF SILICON STEEL SHEET

A. Analyzed Model and Condition

Fig. 1 shows the analyzed model of a piece of silicon steel sheet, which thickness is 0.5mm, of a SPM motor. It is 1/8 of the whole region because of the symmetry and the periodicity. The analyzed SPM motor is built up by 80 silicon steel sheets.

In this case, the rotor rotates 1500rpm by another motor to clarify the iron loss without a coil current.

B. Results and Discussion

Fig. 2 shows the eddy current loss and hysteresis loss. It is found that the 3-D analysis value is slightly larger than the 2-D analysis[4] value which is taking into no account the skin effects. It is found that the skin effects in a piece of silicon steel sheet increase the eddy current loss.

(a) plan view (x-y plane)

(b) flont view (x-z plane)
Fig. 1. Analyzed model.
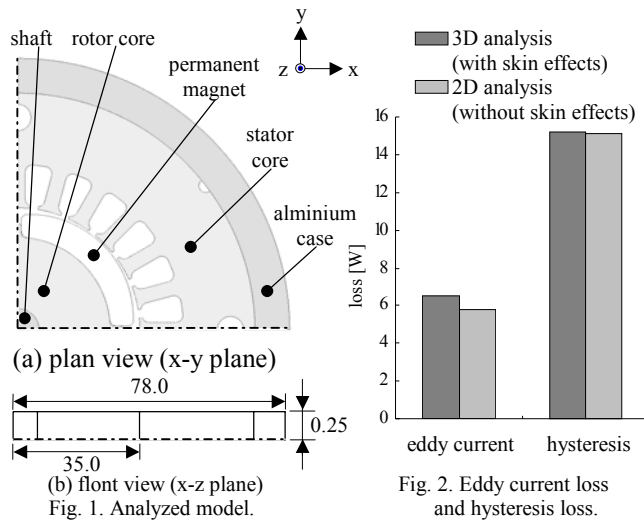
Fig. 2. Eddy current loss and hysteresis loss.

EDDY CURRENT ANALYSIS OF PERMNENT MAGNETS

A. Analyzed Model and Condition

Fig. 3 shows the analyzed model. It is 1/4 of the whole region because of the periodicity. We calculate two type models. One is with the overhang of permanent magnet, and the other is without the overhang of permanent magnet. The analyzed condition is the same as the analysis of a piece of silicon steel sheet. However, the skin effects in the cores are not taken into account.
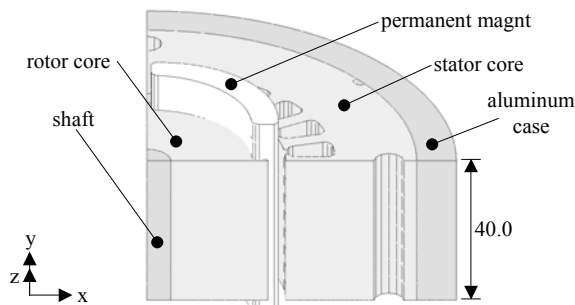
Fig. 3. Analyzed model (1/4 region, with overhang model).

B. Results and Discussion

Fig. 4 shows the contours of eddy current loss in the permanent magnet. It is found the large eddy current loss on the surface at the center of the permanent magnet. In the case of the calculation of the overhang model, it is also found that there are eddy current loss in the overhang area of the permanent magnet.

Fig. 5 shows the eddy current loss in the permanent magnet and the iron loss in the cores. It is found that the overhang of the permanent magnet increases the iron loss in the cores as well as the eddy current loss in the permanent magnet.

(a) without overhang (b) with overhang
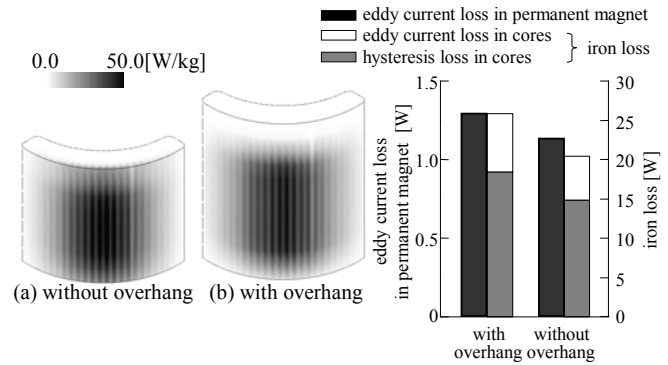
Fig. 4. Contours of eddy current loss in permanent magnet.

Fig. 5. eddy current loss in permanent magnet and iron loss in cores.

CONCLUSIONS

In this paper, we calculate the eddy current loss and the hysteresis loss in a piece of silicon steel sheet, and the eddy current loss in the permanent magnet in a SPM motor using the 3-D finite element method. As the results of computation, it is found that the skin effects in a piece of silicon steel sheet increase the eddy current loss, and the overhang of the permanent magnet increases the iron loss of cores as well as the eddy current loss in the permanent magnet. The usefulness of the 3-D eddy current analysis is confirmed by this analysis of a SPM motor.

REFERENCES

[1] Y. Kawase, N. Mimura and K. Ida : "3-D electromagnetic force analysis of effects of off-center of rotor in interior permanent magnet synchronous motor", *IEEE Transactions on Magnetics,* vol. 36, no. 4, pp. 1858-1862, July 2000.
[2] Y. Kawase, T. Yamaguchi, N. Mimura, M. Igata and K. Ida : "Analysis of magnetizing process using discharge current of capacitor by 3-D finite element method", *IEEE Transactions on Magnetics,* vol. 38, no. 2, pp. 1145-1148, March 2002.
[3] Y. Kawase and S. Ito, *New Practical Analysis of Electrical and Electronic Apparatus by 3-D Finite Element Method,* Morikita Publishing Co., 1997.
[4] K. Yamazaki, "Efficiency analysis of induction motor considering rotor and stator surface loss caused by rotor movement", Proceedings of The 10th International Symposium on Applied Electromagnetics and Machines, pp.107-108, 2001.

Crack Shape Reconstruction in Ferromagnetic Materials using a Novel Fast Numerical Simulation Method

Haoyu Huang, Toshiyuki Takagi and Tetsuya Uchimoto

Institute of Fluid Science, Tohoku University, Katahira 2-1-1, Aoba-ku, Sendai 9808577, Japan
E-mail: takagi@ifs.tohoku.ac.jp

Abstract — **This paper describes research on crack shape reconstruction in ferromagnetic materials using a novel fast numerical simulation method. The fast numerical method developed here, which can treat ferromagnetic materials, is an extension of a pre-computed database approach based on the reduced magnetic vector potential method. It provides a fast forward simulator about 80 times faster than a conventional one even in the case of ferromagnetic materials without losing accuracy. The fast simulator is applied to the inverse problem of ECT, crack shape reconstruction, and results of some EDM cracks on a ferromagnetic plate are shown.**

INTRODUCTION

Eddy current testing (ECT) is a nondestructive testing method of metal materials. Numerical analysis methods are applied to predict the ECT signals, to aid the design of ECT probes, and to reconstruct the crack shape from its ECT signals. Research of forward and inverse problems of ECT are carried out in these few years and great results are achieved.

For the non-ferromagnetic materials, high accuracy of some numerical simulation techniques has been demonstrated and several fast computational methods are presented. Z. Chen and K. Miya [1] presented a fast analysis method using a small part of the inverse matrix of the coefficient matrix and FEM-BEM. H. Huang and T. Takagi [2] also presented a pre-computed database approach based on edge based finite element and reduced magnetic vector potential (A_r) method [3]. The ECT signals can be achieved in short CPU time with high precision, which allows the inverse problems to be solved in practical time. Up to now, inverse problems from ECT signals of a single EDM crack of non-ferromagnetic materials have already been solved. Some problems remained for natural cracks and multi-cracks, but few papers have solved the ECT inverse problems of ferromagnetic materials.

The numerical analysis method based on edge based FEM and A_r method [3] can be applied to ferromagnetic material problems. It is verified by axisymmetric FEM program as well as the benchmark problems proposed by the Japan Society of Applied Electromagnetics and Mechanics (JSAEM). However, numerical analysis of ferromagnetic materials remains a hard and time-consuming job. The fast analysis method [2] based on A_r method is extended to solve the forward and inverse problems when ferromagnetic noise source exists [4]. However, this research [1,2,4] is restricted that a crack exists in non-ferromagnetic materials only.

Recently, a novel fast method [5] is proposed by the extension of the pre-computed database approach based on the A_r method. Different from the improvement in [4], not only governing equations but also the expressions of ECT signals

are newly developed. This method can be applied to the ECT of ferromagnetic materials, and computing time is reduced significantly. In this paper, the novel fast simulator is applied to ECT inverse problem of ferromagnetic materials. For the first time, the crack sizing in ferromagnetic materials is considered and excellent reconstruction results are shown.

FAST SIMULATION METHOD OF FERROMAGNETIC MATERIALS

Systems with and without a crack are considered as shown in Fig. 1, where the source in the figure is the exciting current in a coil, the conductor is a sample going to be tested. Instead of a crack, a secondary source is introduced [2,4,5]. The region includes the crack is called "suspect region" hereafter. The secondary source includes two parts when considering ferromagnetic materials: a secondary electric current source due to the change of conductivity and a secondary magnetic current source due to the change of permeability. More details of this fast simulator can be found in references [2,4,5]
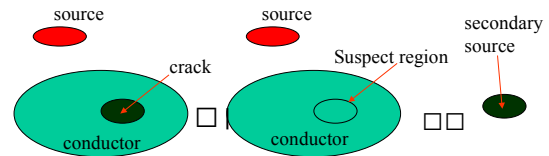
Fig. 1. Secondary source due to the crack

Denoting exciting source region by superscript *s* and crack region by superscript *f*, two sets of alternating current sources may be considered: J_e^s and J_m^s are exciting electric and magnetic source current density respectively, and J_e^f and J_m^f are secondary sources (exists in the crack region Ω_f only). Considering that J_e^s exists only in source region Ω_s and J_m^s is zero, the reciprocity theorem appears as follow:

$$\oint_{\Omega_s} E^f \times J_e^s dV = \oint_{\Omega_f} E^s \times J_e^f dV - \oint_{W_f} H^s \times J_m^f dV . \tag{1}$$

The left-hand side is the energy change $I^2 \Delta Z$, thus the impedance change of the coil can be computed by the integration inside the crack region only. In order to deduce the expression of the secondary electric and magnetic current source, the generalized Maxwell equations including both electric and magnetic sources are considered. As a result, the expressions are finally obtained as follows [5]:

$$J_e^f = -\sigma E = j\omega\sigma(A^f + A^u) , \tag{2}$$

$$J_m^f = -j\omega(\mu - \mu_0)H = -j\omega\frac{(\mu - \mu_0)}{\mu_0}\tilde{N} \cdot (A^f + A^u) . \tag{3}$$

It is a normal approach to solve inverse problems by minimizing the least square error function between the estimated signals and observation signals. The following evaluation function is used:

$$J(x) = \sum_{i=1}^{N_{pos}} \left| S_{comp}^i(x) - S_{obs}^i \right|^2 \bigg/ \sum_{i=1}^{N_{pos}} \left| S_{obs}^i \right|^2 , \qquad (4)$$

where x is the vector characterizing the shape of the cracks, $S_{comp}^i(x)$ are the predicted signals related to the vector x, and S_{obs}^i are the observation signals. N_{pos} is the observation points.

Initial shape used here corresponds the case when half of the depth of the suspect region is cracked. Crack shape reconstruction is performed by the combination of the fast forward ECT simulator and the steepest descent method. Flow chart of the inverse scheme is shown in Fig. 2.

RESULTS AND DISCUSSIONS

ECT applied to the inspection of a ferromagnetic metal plate is simulated by numerical methods. The size of the plate is $20{\times}20{\times}1.25\text{mm}^3$, and the size of a suspect region is $6{\times}0.2{\times}1.25\text{mm}^3$, where 0.2mm is the width and 6mm is the length. Relative permeability and conductivity of the conductor is 100 and 10^6S/m respectively. The pancake coil (140 turns) is used for the inspection, whose inner diameter is 1.2mm, outer diameter is 3.2mm, and height is 0.8mm.

The results of the conventional A_r method [3] are compared with those of the fast simulation method, excellent agreements are shown [5]. Using exciting frequency of 1.5kHz, the pancake probe moves along the direction of the crack from -5mm to 5mm by 1mm step. Comparisons of computational costs are shown in table I. The fast forward simulator presented here is about 80 times faster than a conventional one with same computational accuracy.

Applying this fast forward analysis method, crack reconstruction is performed by a parameter estimation method. Using a steepest decent method, the number of iteration will be large but total computational time will be short because of the fast simulator. Some fixed width (0.2mm) EDM cracks are considered within the suspect region. ECT signals from forward numerical analysis are used. Reconstructed crack shapes are shown in Fig. 3. ID and OD in the captions indicate the cracks on the same side and the opposite side of the probe respectively. Both depth and length of the cracks are reconstructed satisfyingly comparing the true shapes shown by squares within the error of 0.5% in one or two minutes.

CONCLUSIONS

A Novel fast simulator and its applications to ECT inverse problems of ferromagnetic materials are discussed.

1. The fast forward simulator of ECT of ferromagnetic materials is about 80 times faster than a conventional method and still have the same computational accuracy.
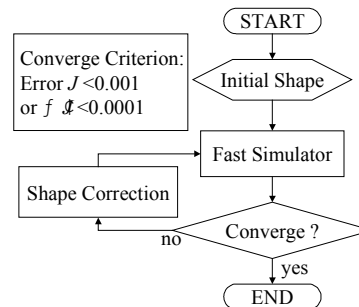
Fig. 2. Flow chart of the inverse analysis

(a) ID40%, 6mm   (b) ID40%, 4mm

(c) ID20%, 6mm   (d) OD40%, 6mm
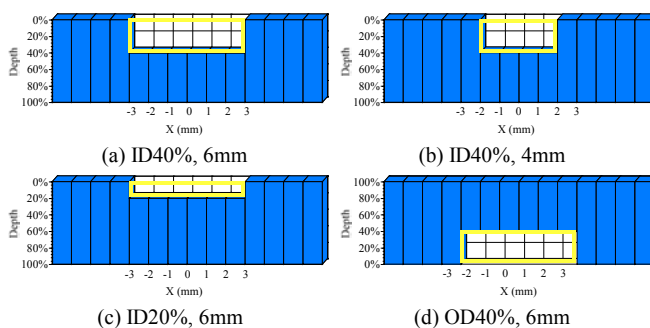
Fig. 3. Reconstruction results of EDM cracks on a ferromagnetic plate

TABLE I. COMPARISON OF THE PRESENT AND CONVENTION METHODS

	Computer	Nodes	Elements	Time
Present Method	VT alpha667	84*	30*	8 s
Conventional Method	VT alpha667	6460	5472	660 s

* Values correspond to a suspect region

2. Crack sizing in the ferromagnetic materials are performed. Satisfactory results are obtained in practical time by applying the fast simulator.

REFERENCES

[1] Z. Chen and K. Miya, "ECT inversion using a knowledge-based forward solver," *J. Nondestructive Evaluation*, vol.17, no.3, pp.167-175, 1998.

[2] T. Takagi, H. Huang, H. Fukutomi and J. Tani, "Numerical evaluation of correlation between crack size and eddy current testing signal by a very fast simulator," *IEEE Trans. Magnetics*, vol.34, no.5, pp.2581-2584, 1998.

[3] H. Fukutomi, T. Takagi, J. Tani, M. Hashimoto, T. Shimone and Y. Harada, "Numerical evaluation of ECT impedance signal due to minute cracks," *IEEE Trans. Magnetics*, vol.33, no.2, pp.2123-2126, 1997.

[4] H. Huang, T. Takagi, and H. Fukutomi, "Fast signal prediction of noised signals in eddy current testing," *IEEE Trans. Magnetics*, vol. 36, no. 4, pp.1719-1723, 2000.

[5] H. Huang, T. Takagi and T. Uchimoto, "Crack Modeling in Eddy Current Testing of Ferromagnetic Materials and a Novel Fast Numerical Analysis Method," submitted to J. Applied Physics.

Eddy Currents Effects in Circuit Breakers During Arc Displacement Phase

O. Chadebec[1], G. Meunier[1], V. Mazauric[2], Y. Le Floch[1,3], P. Labie[1]

[1] Laboratoire d'Electrotecnique de Grenoble, ENSIEG/INPG, 38402 Saint Martin d'Hères, France

[2] Schneider Electric, A2 plant, Corporate Research Division, 38050 Grenoble, France

[3] Cedrat, 10 chemin Pré Carré, Zirst, 38246 Meylan, France

Abstract – **This paper deals with the modeling of eddy currents generated by arc motion during opening phases of circuit breakers. Two kinds of modeling are tested. While the first one consists in determining eddy currents in splitter plates, the second one is devoted to the calculation of eddy currents in electrodes. All simulations are carried out with a lagrangian T-Φ FEM formulation and no new mesh at each time step is required.**

I. INTRODUCTION

The goal of circuit breakers is to switch off currents in electric circuits. During this process, the contact opening ignites an electric arc which slides between two electrodes and is extinguished in splitter plates.

The force that yields the arc motion has two origins. The first one is the loop effect (the trend to increase the self-inductance of the circuit composed by the electrodes and the arc itself). The second one is due to the presence of ferromagnetic splitter plates which creates a classic reluctance variation effect and provides an arc attraction (see Fig. 1).
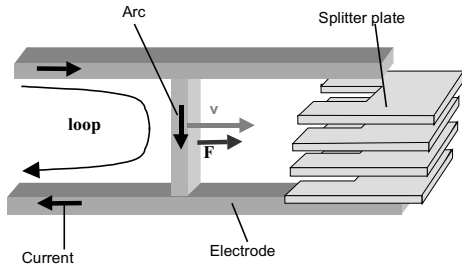
Fig.1. Circuit breaker with electrodes, splitter plates, arc and representation of loop effect.

The calculus of the force acting on arc has led to numerous previous works [1]. In most part of them, only magnetostatic approaches are provided. However, the motion of the arc creates eddy currents in both electrodes and splitter plates. These eddy currents limit the force and decrease the performance of the current interruption process. In order to increase the efficiency of circuit breakers, it is then necessary to develop accurate models to calculate these eddy currents.

II. FEM FORMULATION

In this paper, we are focussed on electrotechnical aspects. So, we have defined a very simple model for the arc. It is considered as a line with a square section and a constant translation velocity **v** is affected to it. Previous works have shown that eddy current in arc can be neglected [2]. It is then possible to consider that the current density in it is uniform.

Two kinds of description can be used to describe moving conductors [3]. In the Eulerian approach, only one resolution is needed. It leads to low CPU computation times but it is limited to invariant geometries and requires upwind elements. To take into account the specific geometry of our device, it is necessary to develop a Lagrangian description, where each moving conductor has its own co-ordinate system. A step by step resolution is adopted and, at each time step, the arc position is shifted of a distance of v×Δt. The following equations are solved by a finite difference time-stepping approach with an implicit scheme. In conducting regions with a translation motion, we have:

$$\mathbf{curl}\,(\rho\,\mathbf{curl}\ \mathbf{H}) = -\frac{d\,(\mu\,\mathbf{H})}{dt} \qquad (1)$$

$$\mathrm{div}\,(\mu\,\mathbf{H}) = 0 \qquad (2)$$

where ρ is the conductivity of the material, μ is the permeability and $\mathbf{H}$ is the magnetic field. d/dt denotes the convective derivative. In the air, we only have to solve (2).

To solve (1) and (2), a **T-Φ** formulation based on the electric vector potential **T** and scalar magnetic potential Φ [4] with nodal approximation is used. The expression of the field and the current are then:

$$\mathbf{H} = \mathbf{T} - \mathbf{grad}\ \Phi \qquad (3)$$

$$\mathbf{J} = \mathbf{curl}\ \mathbf{T} \qquad (4)$$

This formulation has two advantages. Firstly, it leads to one unknown per node in the air region and secondly it ensures high current density conservation in conductors that is convenient for Lorentz force calculation.

To limit CPU times and validate our model, we have decided to separate the evaluation of eddy current in splitter plates and in electrodes. It is based under the assumption that eddy currents in one region does not influence the other one.

III. EDDY CURRENTS EFFECT IN SPLITTER PLATES

In this section, eddy currents in the electrodes are neglected. Only reluctance effect is then evaluated. It is then possible to take into account the effect of the source current (electrodes + arc) with a simple moving inductor. To restore the Ampere's law, it is convenient to reduce the potential Φ with respect to the current in the inductor. We have in the air region:

$$\mathbf{H} = \mathbf{T_{0ind}} - \mathbf{grad}\Phi \qquad (5)$$

where $\mathbf{T_{0ind}}$ is the field created by the inductor and calculated by Biot and Savart's formula.

In the splitter plates region, in order to circumvent the so-called cancellation error in ferromagnetic part, Φ is reduced only with respect to eddy currents with a jump condition at the interface with the air region:

$$\mathbf{H} = \mathbf{T_f} - \mathbf{grad}\,\Phi \qquad (6)$$

It remains to introduce (5) and (6) in (1) and (2). At each time step, the position of the inductor is changed and a new $\mathbf{T_{0ind}}$ is calculated. After resolution, $\mathbf{T_f}$ and Φ are obtained. Eddy currents density in splitter plates is then calculated with the following expression:

$$\mathbf{J} = \mathbf{curl}\,\mathbf{T_f} \qquad (7)$$

This formulation has been tested on a geometry composed of three splitter plates. Figure 2 shows eddy currents density and figure 3 the Lorentz force acting on the arc (i.e. $\mathbf{J}\times\mathbf{B}$ integrated on the volume of the arc).
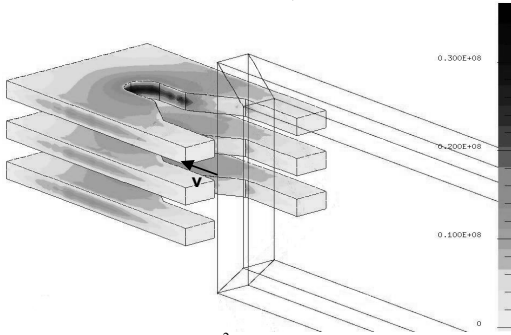
Fig. 2. Eddy current density (A/m^2) in splitter plates when the arc enters the slots (v=20m/s, $\rho=1.10^7\Omega/m$, μ_r=1000, I=1000A)
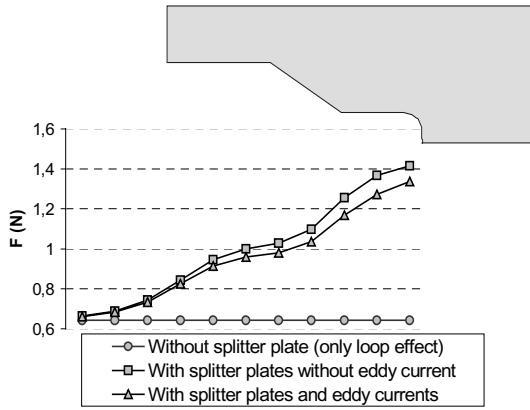
Fig. 3. Force (N) acting on arc versus arc position. Comparison between loop effect without any splitter plate (analytical calculation [2]), magnetostatic force due to splitter plates and magnetostatic force combined with eddy currents effects.

IV. EDDY CURRENTS EFFECTS IN ELECTRODES

In this section, we are focussed on eddy currents in electrodes (i.e. the loop effect), splitters plates are then replaced by air. Like in previous section, it is necessary to restore Ampere's theorem. Two kinds of conductors generate source field: the arc and the electrodes. The arc is still without any eddy currents and an inductor model it. Its effect $\mathbf{T}_{0arc}$ is still calculated by Biot and Savart's formula. However, it is necessary to introduce another auxiliary vector potential $\mathbf{T}_{0elec}$ which is created by the two electrodes. Two approaches are possible to calculate $\mathbf{T}_{0elec}$

The first one is to use an inductor, which crosses the electrode and carries total current [3]. $\mathbf{T}_{0elec}$ is then calculated by Biot and Savart's law. The expression of $\mathbf{T}_0$ is then strictly equivalent to $\mathbf{T}_{0ind}$ in previous section. The main advantage of this approach is its convenience of implementation to take into account the motion of the arc. However, this method needs a high mesh density everywhere in the conductor and is often too much memory consuming.

We preferred to use a preliminary static current flow. This is carried out by a FEM resolution imposing the potential on the output and the input faces of the electrode and a Newman boundary condition elsewhere. We obtain in each electrode i a static current density $\mathbf{J}_{0i}$. $\mathbf{T}_{0eleci}$ is then calculated by solving a second FEM system:

$$(\mathbf{curl}\,\mathbf{T}_{0eleci} - \mathbf{J}_{0i})^2 = \mathbf{0} \qquad (8)$$

The magnetic expression of the field in air region is:

$$\mathbf{H} = \mathbf{T}_{0\,arc} + \sum_{i=1,2} \mathbf{T}_{0\,eleci} - \mathbf{grad}\,\Phi \qquad (9)$$

where Φ is then reduced with respect of current sources.
In the electrodes, Φ is reduced with respect to currents sources and eddy currents:

$$\mathbf{H} = \mathbf{T}_{0\,arc} + \sum_{i=1,2} \mathbf{T}_{0\,eleci} + \mathbf{T}_f - \mathbf{grad}\,\Phi \qquad (10)$$

After these two preliminary FEM resolutions, it remains to introduce (9) and (10) in (1) and (2). Each step, the arc is displaced to obtained a new $\mathbf{T}_{0arc}$ and the boundary conditions of the static current flow resolution are changed to obtained new $\mathbf{T}_{0eleci}$. Then, the global system is solved. The total current in the electrode i is:

$$\mathbf{J} = \mathbf{curl}\,\mathbf{T}_f + \mathbf{J}_{0i} \qquad (11)$$

We applied this approach to an electrodes geometry (see Fig. 4). Force acting on arc has been computed as described in previous section.
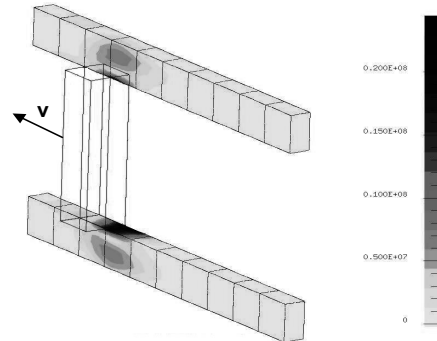
Fig. 4. Eddy currents density (A/m^2) in electrodes (v=20m/s, $\rho=5.10^7\Omega/m$, μ_r=1, I=1000A). Only half geometry is represented.

V. CONCLUSIONS AND PERSPECTIVES

We have developed new formulations to calculate eddy currents that appear in a circuit breaker during current interruption phases. These two formulations can be combined to obtain a global model. Moreover, it is possible to apply it with distorted arc models and with non-constant velocity. The main advantage of this approach is that no new mesh at each time step is required. Full paper will give more details about the influence of eddy currents on force acting on arc versus its speed and versus the circuit breaker geometry.

REFERENCES

[1] H.-C. Song, U.-Y. Lee, S.-H. Kang, K.-J. Lim ,"3D finite elements analysis of magnetic force on the arc chamber design of modeled case circuit breaker," presented at Numelec, Poitiers, France, 2000.
[2] A. Slama, V. Mazauric, Y. Marechal, G. Meunier, P. Wendling, "Electric railgun 3D modeling: computation of eddy current and Lorentz force," *IEEE Trans. Mag.*, vol. 37, pp 139-142, 2001.
[3] A Slama, V. Mazauric, G. Meunier, Y. Marechal, "From an Eulerian description the electromagnetic launcher," presented at Compumag, Evian, France, 2001.
[4] O. Biro, K. Preis, W. Renhart, G. Vrisk, F. Ricter, "Computation of 3D current driven skin effect problem using current vector potential," *IEEE Trans. Mag.*, Vol 29, pp. 1325-1332, 1993.

Generalization of the ideal crack model in Eddy-Current Testing

Philippe Beltrame, Noël Burais

Ecole Centrale de Lyon

69134 Ecully Cedex – France

e-mail: {Philippe.Beltrame, Noel.Burais}@eea.ec-lyon.fr

Abstract —For the ideal cracks, in Eddy-Current Testing (ECT), the field-flaw is equivalent to a currents dipoles layer on its surface. This model proved very powerful, as well on the level of the accurating as of the computing CPU time. The goal of this paper is to improve this model to take account of an inclination, a low conductivity and low thickness of the crack.

INTRODUCTION

The thin crack problem in ECT - i.e. the crack width e (Fig. 1) is small compared to its other dimensions and to the skin depth δ - constitutes a major difficulty for the simulation. It is commonly assumed that a surface crack is "ideal": being infinitesimally thin and allowing no current to flow across it. Then, Bowler [1] showed that the crack is equivalent to a currents dipoles surface of density $\mathbf{p} = p\mathbf{n}$, where $\mathbf{n}$ is the normal of the crack (Fig. 1). A boundary integral method is used because only the flaw domain has to be meshed. The density p is solution of an integral equation on the surface crack. The variation ΔZ of the coil impedance is directly obtained from this density.

Because of the hypersingular kernel of this equation, a regularization method is required to solve it [2]. This is applied to compute the density p for a straight crack, i.e. $\alpha = 0$ (Fig. 1), using a collocation method with second order shape functions. The case of two straight parallel cracks in a tested piece was treated in [3]. A particular interest was related to the representation of the eddy-current distribution in the cracks neighborhood which posed a problem of evaluation of quasi-singular integrals.

The goal of this paper is to generalize the ideal crack model to take into account others parameters: equivalent crack conductivity σ_f, low thickness e and the inclination α.
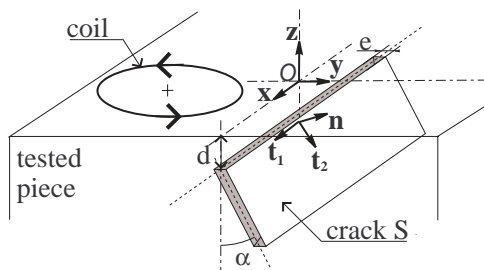
Fig. 1. Schematic configuration for the crack detection.

FORMULATIONS

The electromagnetic values are dimensionless.

Low Crack Conductivity

The closure of crack may ultimately produce electrical contacts. In order to simulate the effects of current leakage across crack, an equivalent conductivity σ_f of the crack is introduced. Then, the flow crossing this surface is proportional to the density p [4]. Let us define the relative conductance γ :

$$\gamma = \frac{\sigma_f}{\sigma - \sigma_f} \frac{\delta}{e}. \tag{1}$$

The eddy-current $\mathbf{J}$ is related to the density p by the following adimensional relation:

$$\mathbf{J_0(r_f)}.\mathbf{n} = -2j\mathbf{FP}\int_S \mathbf{n}.\mathbf{G(r_f,r)p(r)}\,\mathrm{d}S_r + \gamma p(\mathbf{r_f}), \tag{2}$$

with $\mathbf{J_0}$: incident current, $\mathbf{FP}$: Finite Part of Hadamard, and $\mathbf{G}$: electric-electric Green tensor in the tested piece [1].

Thin Thick Model

In the ideal crack model, a term, corresponding to the energy change in the crack volume, is neglected in the expression of the impedance change [5]. This term P_0 is written:

$$P_0 = j\int_V \mathbf{J_0}.\mathbf{A}\,\mathrm{d}\tau, \tag{3}$$

where $\mathbf{A}$: the magnetic vector potential with the Coulomb gauge. This potential is continuous through the crack [5]. If it is supposed constant on the thickness e then it can be proved that $\mathbf{J_A} = j\mathbf{A}$ is given by integrals of the density p on the crack surface:

$$\mathbf{J_A(r_f)}.\mathbf{n} = \gamma p(\mathbf{r_f}) - \mathbf{FP}\int_S g_{s,nn}(\mathbf{r_f,r})p(\mathbf{r})\,\mathrm{d}S_r$$

$$(\mathbf{J_A(r_f)} - \mathbf{J_0(r_f)}).\mathbf{t_i} = -\int_S g_{r,nt_i}(\mathbf{r_f,r})p(\mathbf{r})\,\mathrm{d}S_r \tag{4}$$

$$+ \left(\int_S \mathbf{G_R(r_f,r)p(r)}\,\mathrm{d}S_r\right).\mathbf{t_i},$$

where g_S : elementary solution of the Poisson equation in the whole space, g_R : reflexion term of the elementary solu-

tion of the Poisson equation in the piece test domain, and $\mathbf{G_R}$: reflexion terms of $\mathbf{G}$. The proof of the expression of $\mathbf{J_A}$ will be detailed in the full paper.

Inclined Crack

If the crack is straight ($\alpha = 0$) then eddy-current on the crack deduces directly from the differentiation of the density p . On the other hand, if the crack is inclined of an angle α , it is necessary to take into account the reflexion terms:

$$\begin{aligned}
\left(\mathbf{J}(\mathbf{r_f^\varepsilon}) - \mathbf{J_0}(\mathbf{r_f})\right)\!.\mathbf{t_i} &= -\frac{\varepsilon}{2} p_{,t_i}(\mathbf{r_f}) \\
&+ \left(\int_S \mathbf{G}_R(r_f, r)\mathbf{p}(r)dS_r \right)\!.\mathbf{t_i}
\end{aligned} \tag{5}$$

where, $i \in \{1,2\}$, $\varepsilon = \pm 1$ and designates the positive or negative of the crack face.

RESULTS

In order to validate the thin thick model, the TEAM Workshop Problem n° 15 [1] has been solved. The computation of the ideal crack was improved by using special elements at the crack edges (Fig. 2). When we take account of the thickness, the theoretical value differs from less than 1% from the experiment while in the case of the ideal crack it was about 2.5% with special elements (Fig. 2).

For the same problem, an inclination of the crack is introduced. The figure 3 shows signatures associated with a displacement of sensor according to (Oy) axis for different inclinations.

The figure 3 shows the distribution of the eddy-current for a crack at the depth $d = \delta$ with $\alpha = 45°$, the others parameters being the same as previous.

CONCLUSION

The ideal crack model was improved by introducing three parameters: σ_f, e and α . By adding a term to the impedance change, a low thickness of the crack can be take account with a good agreement with experiment. The limit of validity of the thin thick model will be developed in the extended paper. The study of the influence of these parameters allows determining the relevance of their taking into account for the inverse problem.

REFERENCES

[1] J. Bowler, "Eddy-current interaction with an ideal crack. The forward problem," *In J. Appl. Phys.*, vol. 75 (12), pp. 8128-8137, 1994.

[2] Ph. Beltrame, and N. Burais "Computing Methods of Hypersingular Intergal Applied to Eddy-Current Testing," *IEEE Transactions on Magnetics*, vol. 38, pp. 1269-1272, 2002.

[3] Ph. Beltrame, and N. Burais "Application of regularization method to compute eddy-current distribution near cracks," *COMPEL*, Vol. 24, No 4, 2002.

[4] N. Harfield, J. R. Bowler, "A thin-skin theory of current leakage across surface cracks," Electromagnetic Nondestructive Evaluation (II), R. Albanese et al. (Eds.), *IOS Press*, 1998.

[5] Z. Badics, K. Miya *et al.*, "An effective 3-D Finite Element Scheme for Computing Electromagnetic Field Distortions Due to Defects in Eddy-Currents Nondestructive Evaluation," *IEEE Transactions on Magnetics*, Vol. 33, n° 2, pp. 1012-1020, March 1997.
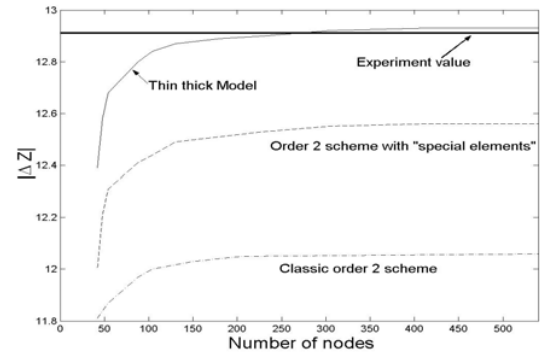
Fig. 2. Convergence with (solid line) and without (dashed lines) the thickness e of the crack for the coil position $(x, y) = (9mm, 0mm)$.
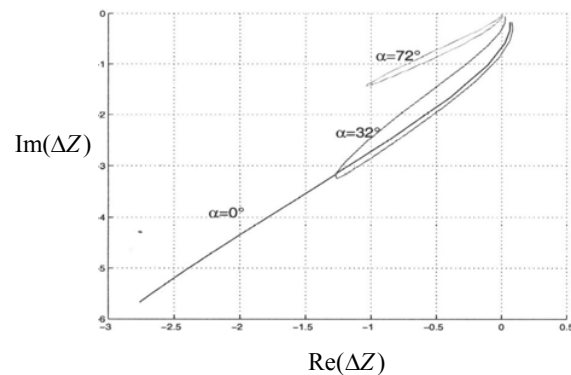
Fig. 3. Signature for three different inclinations of the crack.
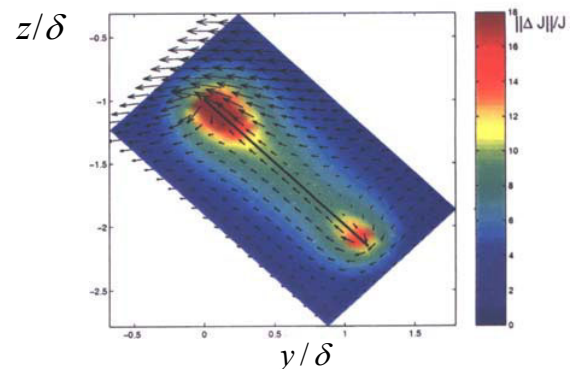
Fig. 4. Eddy-current distribution in the plane $x = 0$ for an inclined crack ($\alpha = 45°$) for the coil position $(x, y) = (9mm, 0mm)$.

Three-dimensional FEM analysis of an eddy current braking system

F. Rapetti[1], L. Santandrea[2], F. Bouillault[2], A. Razek[2]

[1]Lab. J.-A. Dieudonné, UMR 6621 CNRS, Univ. Nice et Sophia-Antipolis, Parc Valrose, 06108 Nice cedex 02, France
[2]Lab. de Génie Electrique de Paris, UMR 8507 CNRS, Univ. Supelec, Plateau de Moulon, 91192 Gif-Sur-Yvette, France

Abstract—**We present a method and some related results for the calculation of eddy currents in a 3D braking system. The approximation is based on the mortar element method combined with finite differences in time and node/edge elements in space.**

INTRODUCTION

This contribution deals with the numerical treatment of three-dimensional eddy current problems in moving rigid bodies, as for example a braking system. We address the question how to calculate the electromagnetic fields if the motion of the bodies is known in advance. In Lagrange variables, it may be less expensive from the computational point of view the use a method that allows to work with nonmatching grids at the sliding interface and avoids re-meshing procedures. The *mortar element method* (see [3] for the problem we consider here) is a nonconforming nonoverlapping domain decomposition technique which allows for independent meshes in adjacent subdomains. The idea of the method is to weakly impose the transmission conditions at the interfaces by means of Lagrange multipliers suitably chosen to ensure optimal properties on the discrete problem.

THE MODEL

The mathematical model describing the distribution of eddy currents in conductors at low frequencies is given by the quasi-stationary Maxwell's equations [1], [2]. The magnetic quantities can be eliminated from the equations and set up a formulation in terms of the electric ones, as in [5]. Here we do the other way, by restricting ourselves to the so called $\mathbf{T} - \varphi$ formulation of the magnetodynamic problem. More in detail, let $\Omega \subset \mathbb{R}^3$ be an open bounded set; we assume that $\Omega = \Omega_c \cup \Omega_{nc}$ where Ω_c is the conducting part and Ω_{nc} is the non-conducting one (containing airgaps and ferromagnetic parts, as in Figure 1 (left)). For the current density $\mathbf{J}$, the condition $\operatorname{div}\mathbf{J} = 0$ suggests the introduction of a vector potential $\tilde{\mathbf{T}}$ such that $\mathbf{J} = \operatorname{curl}\tilde{\mathbf{T}}$. Then, in Ω_c, the difference between $\tilde{\mathbf{T}}$ and the magnetic field $\mathbf{H}$ can be written as the gradient of a scalar function $\tilde{\varphi}$. A similar argument holds for Ω_{nc} where we assume knowing a vector potential $\mathbf{T}_0$ such that $\mathbf{J}_0 = \operatorname{curl}\mathbf{T}_0$, where $\mathbf{J}_0$ is a given external source. Being $\mathbf{J}_0$ zero in Ω_c, the magnetic field $\mathbf{H}$ is given by $\tilde{\mathbf{T}} - \operatorname{grad}\tilde{\varphi}$ in Ω_c and $\mathbf{T}_0 - \operatorname{grad}\tilde{\varphi}$ in Ω_{nc}. Thus, we obtain a magnetodynamic problem in terms of the vector potential $\tilde{\mathbf{T}}$ defined only in Ω_c and the scalar potential $\tilde{\varphi}$ defined everywhere in Ω. The system is completed with boundary conditions on $\partial\Omega$ and interface conditions on $\gamma_c = \partial\Omega_c \setminus (\partial\Omega_c \cap \partial\Omega)$ stating, e.g., that $\tilde{\Omega}$ is continuous and $\tilde{\mathbf{T}} \times \mathbf{n}_c = \mathbf{0}$. The magnetic permeability μ and the electric
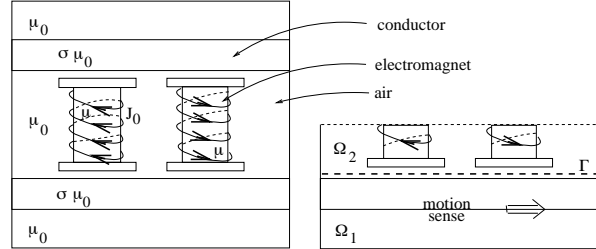
Fig. 1. Domain geometry on the x-z section.

conductivity σ are assumed to be linear, bounded, time-independent scalar functions. We set $H_{0,\gamma_c}(\operatorname{curl}, \Omega_c) = \{\mathbf{v} \in L^2(\Omega_c)^3 | \operatorname{curl}\mathbf{v} \in L^2(\Omega_c)^3 \text{ with } (\mathbf{v} \times \mathbf{n}_c)_{|\gamma_c} = \mathbf{0}\}$ and $H^1_{0,\gamma_{nc}}(\Omega) = \{u \in L^2(\Omega) | \operatorname{grad}u \in L^2(\Omega)^3 \text{ with } \varphi_{|\gamma_{nc}} = 0\}$, where $\gamma_{nc} \subset \partial\Omega$ with positive measure. The variational formulation of the considered problem reads: given $\mathbf{T}_0 \in L^2(\Omega_{nc})^3$, find $\tilde{\mathbf{T}} \in H_{0,\gamma_c}(\operatorname{curl}, \Omega_c)$ and $\tilde{\varphi} \in H^1_{0,\gamma_{nc}}(\Omega)$ s.t.

$$\frac{d}{dt}\int_{\Omega_c}\mu(\tilde{\mathbf{T}} - \operatorname{grad}\tilde{\varphi})\cdot\mathbf{w} + \int_{\Omega_c}\frac{1}{\sigma}\operatorname{curl}\tilde{\mathbf{T}}\cdot\operatorname{curl}\mathbf{w}$$
$$+ \int_{\partial\Omega_c\setminus\gamma_c}\frac{1}{\sigma}(\mathbf{n}_c\times\operatorname{curl}\tilde{\mathbf{T}})\cdot\mathbf{w} = 0,\ \forall\mathbf{w}\in H_{0,\gamma_c}(\operatorname{curl},\Omega_c),$$

$$-\frac{d}{dt}\int_{\Omega_c}\mu\tilde{\mathbf{T}}\cdot\operatorname{grad}v + \frac{d}{dt}\int_{\Omega}\mu\operatorname{grad}\tilde{\varphi}\cdot\operatorname{grad}v$$
$$-\frac{d}{dt}\int_{\partial\Omega\setminus\gamma_{nc}}\mu\frac{\partial\tilde{\varphi}}{\partial n}v = \frac{d}{dt}\int_{\Omega_{nc}}\mu\mathbf{T}_0\cdot\operatorname{grad}v,\ \forall v\in H^1_{0,\gamma_{nc}}(\Omega).$$
$$(1)$$

It is easy to see that if $(\tilde{\mathbf{T}}, \tilde{\varphi})$ is a solution of (1), then $(\tilde{\mathbf{T}} + \nabla\phi, \tilde{\varphi} + \phi)$, $\phi \in H^1_0(\Omega_c)$, is a solution as well. In order to get uniqueness, we can choose ϕ such that $\varphi = \tilde{\varphi} + \phi$ is harmonic on Ω_c. To this purpose, as in [4], we involve the harmonic extension operator $\mathcal{H}$ satisfying, for $v \in H^{1/2}(\partial\Omega_c)$, the conditions $\mathcal{H}v \in H^1(\Omega_c)$, $(\mathcal{H}v)_{|\partial\Omega_c} = v$ and $\int_{\Omega_c}\operatorname{grad}\mathcal{H}v\operatorname{grad}w = 0$, $\forall w \in H^1_0(\Omega_c)$. Problem (1) is then modified as follows: given $\mathbf{T}_0 \in L^2(\Omega_{nc})^3$, find $\mathbf{T} \in H_{0,\gamma_c}(\operatorname{curl}, \Omega_c)$ and $\varphi \in H^1_{0,\gamma_{nc}}(\Omega)$ s.t.

$$\frac{d}{dt}\int_{\Omega_c}\mu(\mathbf{T} - \operatorname{grad}\mathcal{H}\varphi_{|\partial\Omega_c})\cdot\mathbf{w} + \int_{\Omega_c}\frac{1}{\sigma}\operatorname{curl}\mathbf{T}\cdot\operatorname{curl}\mathbf{w}$$
$$+ \int_{\partial\Omega_c\setminus\gamma_c}\frac{1}{\sigma}(\mathbf{n}_c\times\operatorname{curl}\mathbf{T})\cdot\mathbf{w} = 0,\ \forall\mathbf{w}\in H_{0,\gamma_c}(\operatorname{curl},\Omega_c),$$

$$-\frac{d}{dt}\int_{\Omega_c}\mu\mathbf{T}\cdot\operatorname{grad}\mathcal{H}v_{|\partial\Omega_c} + \frac{d}{dt}\int_{\Omega_{nc}}\mu\operatorname{grad}\varphi\cdot\operatorname{grad}v$$
$$-\frac{d}{dt}\int_{\partial\Omega\setminus\gamma_{nc}}\mu\frac{\partial\varphi}{\partial n}v = \frac{d}{dt}\int_{\Omega_{nc}}\mu\mathbf{T}_0\cdot\operatorname{grad}v,\ \forall v\in H^1_{0,\gamma_{nc}}(\Omega).$$
$$(2)$$

As proved in [4], problem (2) has a unique solution.

Due to symmetry reasons, from now on we work in half domain, as in Figure 1 (right). When dealing with moving structures, translating in our case, we suppose that the domain Ω is divided into (at least) two sub-domains Ω_1 and Ω_2 separated by the interface Γ; Ω_1 can move in the x-direction with a speed V. Here we set $\Omega_1 = \Omega_c \cup \{\text{airgap}\}$ and $\Omega_2 = \Omega \setminus \Omega_1$. We call $r_t : \Omega_1 \to \Omega_1$ the operator at time t which moves the domain Ω_1 of the quantity $s = V t$ and r_{-t} the inverse operator. If $V = 0$, r_t is the identity

operator. We assume the existence of a *reference* configuration, say $\Omega_1(0)$, and we denote by $\Omega_1(t) := r_t \Omega_1(0)$: the material particle occupies a position $\mathbf{x}$ in the reference picture $\Omega_1(0)$ and its position in the *actual* configuration $\Omega_1(t)$ at time t will be $r_t\mathbf{x}$. Defined $\Omega(0) = \Omega_1(0) \cup \Omega_2$, in the *piecewise Lagrange approach* we look for $(\mathbf{T}_1, \varphi_1)$ and $(\mathbf{0}, \varphi_2)$ such that $\mathbf{T}_1 = \mathbf{0}$ in the airgap contained in Ω_1 and φ_k, $k = 1, 2$, verify two time-dependent transmission conditions at $\Gamma = \partial \Omega_1(0) \cap \partial \Omega_2$ that read:

$$(TC_1) \quad \varphi_1(r_{-t}\mathbf{x}, t) = \varphi_2(\mathbf{x}, t),$$

$$(TC_2) \quad \mu(r_{-t}\mathbf{x})\frac{\partial \varphi_1}{\partial n_\Gamma}(r_{-t}\mathbf{x}, t) + \mu(\mathbf{x})\frac{\partial \varphi_2}{\partial n_\Gamma}(\mathbf{x}, t) = 0.$$

The conditions (TC_1) and (TC_2) describe, respectively, the continuity of the two components $\mathbf{H} \times \mathbf{n}_\Gamma$ and $\mathbf{B} \cdot \mathbf{n}_\Gamma$ across the interface Γ. In the considered framework, we introduce the functional space at each time t

$$\mathcal{U}(t) = \{(\varphi_1, \varphi_2) \in H^1(\Omega_1) \times H^1(\Omega_2) \mid$$
$$\varphi_1(r_{-t}\mathbf{x}, t) = \varphi_2(\mathbf{x}, t), \, \forall \mathbf{x} \in \Gamma, \, \varphi_{k|\partial\Omega_k \cap \gamma_{nc}} = 0 \}; \quad (3)$$

the new variational formulation is then given by (2) replacing $\mathbf{w} \in H_{0,\gamma_c}(\mathrm{curl}, \Omega_c)$ by $\mathbf{w}_1 \in H(\mathrm{curl}, \Omega_1)$ that verifies $\mathbf{w}_1 = \mathbf{0}$ in the airgap contained in Ω_1 and $v \in H^1_{0,\gamma_{nc}}(\Omega)$ by $v \in \mathcal{U}(t)$. Moreover, $\int_\Omega \mu \, \mathrm{grad} \, \varphi \cdot \mathrm{grad} \, v$ has no more sense and has to be replaced by $\sum_{k=1}^2 \int_{\Omega_k} \mu_{|\Omega_k} \, \mathrm{grad} \, \varphi_k \cdot \mathrm{grad} \, v_k$. Note that the essential condition (TC_1) is strongly imposed in the definition of $\mathcal{U}$, while the natural one (TC_2) can be recovered by integrating by parts.

We now discretize the new variational formulation by using edge elements for $\mathbf{T}_1$ and node elements for φ_k on tetrahedrical meshes. Let $\mathcal{T}_{k,h}$ be two triangulations of $\overline{\Omega}_k$, $k = 1, 2$, independently generated (h is the maximum size of the mesh tetrahedra); we then introduce the edge element space $X_{1,h}$, the node element ones $Y_{k,h}$, and, as explained in [3], M_h a proper subspace of the trace space $W_h = \{\psi \in L^2(\Gamma) \mid \exists v_{2,h} \in Y_{2,h} \text{ such that } (v_{2,h})_{|\Gamma} = \psi\}$. In the mortar setting, the value at Γ of each discrete function on the mortar (master) side Ω_1 will define *weakly* the values at Γ of the discrete function on the nonmortar (slave) side Ω_2. The discrete version of $\mathcal{U}(t)$ is the space

$$\mathcal{U}_h(t) = \{(\varphi_{1,h}, \varphi_{2,h}) \in Y_{1,h} \times Y_{2,h} \mid \varphi_{k|\partial\Omega_k \cap \gamma_{nc}} = 0 \text{ and}$$
$$\int_\Gamma (\varphi_{1,h}(r_{-t}\mathbf{x}, t) - \varphi_{2,h}(\mathbf{x}, t))\psi_h(\mathbf{x}) \, d\Gamma = 0, \, \forall \psi_h \in M_h\}.$$

The presence of the *weak coupling condition* prevents $\mathcal{U}_h(t)$ from being a subspace of $\mathcal{U}(t)$, i.e., we are using a nonconforming method to approximate the scalar potential φ. There are two main difficulties (see [3] for details): the construction of a basis for the Lagrange multiplier space M_h and the computation of $\int_\Gamma \varphi_{1,h} \psi_h$ with $\varphi_{1,h}$ and ψ_h leaving on different (a priori nonmatching) grids.

To write the discrete version of the new variational problem in a matrix form, we involve a rectangular matrix Q that allows for coupling at Γ the information coming from Ω_1 and Ω_2. The fully discrete problem results from the application of a first order implicit Euler scheme with time step δt to discretize the time variable. The final system has a matrix form

$$(M_c + \delta t \, A_c)\mathbf{T}^{n+1} + BQ\varphi^{n+1} = \mathbf{F}_c,$$
$$\tilde{Q}^t_{n+1}B^t \, \mathbf{T}^{n+1} + \tilde{Q}^t_{n+1}KQ_{n+1} \, \varphi^{n+1} = \tilde{Q}^t_{n+1}\mathbf{F}. \quad (4)$$

The vectors $\mathbf{F}_c$ and $\mathbf{F}$ depend on the approximations of $\mathbf{T}$ and φ at the previous time step ($\mathbf{F}$ depends also on $\mathbf{T}_0$). M_c, A_c are the mass and stiffness matrices with edge elements, K is the stiffness matrix with node elements, B is the matrix associated to the bilinear form $-\int_{\Omega_1} \mathrm{grad} \, \mathcal{H}\varphi \cdot \mathbf{w}$ and B^t is associated to $-\int_{\Omega_1} \mathbf{T} \cdot \mathrm{grad} \, \mathcal{H}v$. Matrix Q_{n+1} is responsible for the coupling at the interface Γ at time t_{n+1} and $\tilde{Q}^t_{n+1}$ is its "transposed". There are at least two ways of computing $\int_\Gamma \varphi_{1,h} \psi_h$ while preserving the optimality of the nonconforming approximation. The first is based on the introduction of a third discretization of Γ, which is independent of the ones induced by $\mathcal{T}_{k,h}$ and on which we define a quadrature formula, see [5]. In this case, $\tilde{Q}^t_{n+1} = Q^t_{n+1}$ and problem (4) has a symmetric matrix that can be inverted by a Conjugate Gradient procedure. In the second case, we do not need a third mesh on Γ; the integral $\int_\Gamma \varphi_{1,h} \psi_h$ is computed by means of a quadrature formula defined, for Q_{n+1}, on the slave (Ω_2) side of Γ and, for $\tilde{Q}^t_{n+1}$, on the master (Ω_1) side of Γ, see [3]. In this case, $\tilde{Q}^t_{n+1} \neq Q^t_{n+1}$ and problem (4) has a nonsymmetric matrix that can be inverted by a stabilised Bi-Conjugate Gradient procedure.

Results

Figure 2 shows, on the left, the distribution of $\mathbf{B}$ in a y-z section of the domain and, on the right, the distribution of $\mathbf{J}$ in a x-y section of the bottom conductor. Both distributions are computed in half domain (see Figure 1 (right)): the electromagnet heigth is 55 mm, the coil radii are 55 mm and 45 mm. Note that $\mathbf{T}_0$ can be analytically defined thank to the simple (circular) geometry of the coils. The airgap is 1.5 mm, the conductor is $130 \times 150 \times 15$ mm^3 and Ω is a cube of 150 mm per side. The data are $\mu = 10^3 \, \mu_0$ H/m, $\sigma = 6.67 \, 10^6$ S/m, $J_0 = 10^6$ A/m^2 and $\delta t = 10^{-3}$ s.
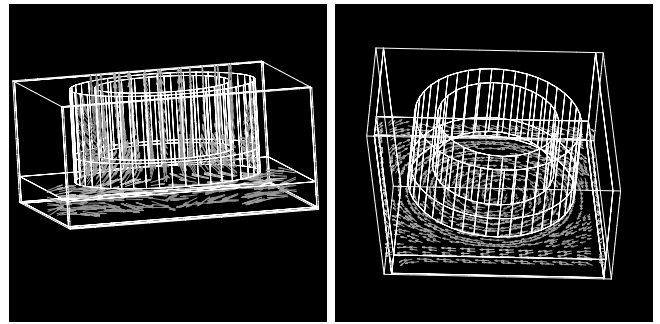
Fig. 2. (Left) Distribution of $\mathbf{B}$ in a y-z section of half domain. (Right) Distribution of $\mathbf{J}$ in a x-y section of the bottom conductor.

References

[1] R. Albanese, G. Rubinacci, "Formulation of the eddy-current problem", *IEE Proc.*, A 137, 16-22 (1990).

[2] A. Bossavit, *Computational Electromagnetism: Variational Formulations, Complementarity, Edge Elements*, 1st ed., Academic Press (1998).

[3] Y. Maday, F. Rapetti, B. I. Wohlmuth, "The influence of quadrature formulas in 2D and 3D mortar element methods", *Lecture Notes in Computational Science and Engineering*, 23, 119-137, Springer (2002).

[4] Y. Maday, F. Rapetti, B. I. Wohlmuth, "Coupling between scalar and vector potentials by the mortar element method", *C. R. Acad. Sci. Paris*, Sér. I 334, 933-938 (2002).

[5] F. Rapetti, Y. Maday, F. Bouillault, A. Razek, "Eddy current calculations in three-dimensional moving structures", *IEEE Trans. Magn.*, 38, 2, 613-616 (2002).

Study of the Local Eddy Current Loss Density near the Edges in Steel Laminations of Finite Width

P. G. Pereirinha[1,2], J. Gyselinck[3], C. Lemos Antunes[1]

[1]ISR – Institute of Systems and Robotics, Dep. Engenharia Electrotécnica
Universidade de Coimbra - Pólo II, P-3030-290 Coimbra, Portugal, e-mail: ppereiri@isr.uc.pt

[2] Instituto Superior de Engenharia de Coimbra
Rua Pedro Nunes, P-3030-199 Coimbra – Portugal

[3] Department of Electrical Engineering, Institut Montefiore, University of Liège,
Sart Tilman Campus, Building B28, B-4000 Liège, Belgium

Abstract — **This paper deals with the eddy current losses in a steel lamination. In particular, the effect of the finite lamination width on the local loss density is studied. Taking the analytical expression for the loss density in an infinitely wide lamination as a reference, a relative loss density curve (relative losses vs. distance to edge) can be considered for laminations of various widths, with either a constant surface magnet field or average induction excitation. It is shown that in the former case this relative function is independent of the width to thickness ratio, and may thus present a suitable tool in homogenization techniques.**

INTRODUCTION

When performing FE analyses of electromagnetic devices comprising a stack of ferromagnetic laminations, it is for practical reasons impossible to model each lamination separately. As a consequence, it is difficult to accurately incorporate the iron losses in the FE model, in particular the eddy current loss (ECL) component, which depends on the eddy current loops in the individual laminations. The eddy current losses can be accounted for in an approximate way by means of homogenization techniques. In [1] and [2] such techniques are proposed for 2D and 3D FE models respectively. In a (linear) frequency domain calculation, the skin effect can be easily included. Edge effects, due to the finite width of the laminations, are ignored as the aforementioned homogenization techniques are based on 1D lamination models (in which only the variation throughout the lamination thickness is considered). In order to also include the edge effect in a 3D homogenization technique, a 2D lamination model [3][4] can be studied. In this paper is studied the influence of the width of the lamination on the local ECL density, and is shown that an equivalent conductivity can be derived that could be applied for including the edge effect in the homogenization technique for the 3D model. This is limited to the linear case, for the time being.

2D LAMINATION MODEL

For a lamination (Fig. 1) the 2D harmonic diffusion equation expressed in terms of the y component of the magnetic field strength H_y is [3]:

$$\nabla^2 H_y - j\omega\mu\sigma H_y = 0 \tag{1}$$

with $\omega=2\pi f$ the pulsation, μ the magnetic permeability and σ the electrical conductivity. A constant H on the lamination boundary, H_s, is either imposed or floating. In the latter case, the flux or average induction B_a is imposed. The ECL (W/m^3) can be averaged over the thickness d from the FE solution, by

$$P_J = \frac{1}{d}\int_d \frac{J^2}{2\sigma} dz \tag{2}$$

where J is the amplitude of the sinusoidal eddy currents (A/m^2). In case of an infinitely wide lamination, an analytical expression of the loss density can be used either in terms of the surface magnetic field [3] or the average induction [1][3]

$$P_{1DHs}(H_s, f) = \frac{H_s^2}{d\sigma\delta}\frac{\sinh\lambda - \sin\lambda}{\cosh\lambda + \cos\lambda} \tag{3}$$

$$P_{1DBa}(B_a, f) = \frac{1}{6}\sigma\pi^2 d^2 f^2 B_a^2 F_{sk}(f) \tag{4}$$

where the skin effect for (4) is comprised in the dimensionless function $F_{sk}(f)$ given by

$$F_{sk} = \frac{3}{\lambda}\frac{\sinh\lambda - \sin\lambda}{\cosh\lambda - \cos\lambda} \tag{5}$$

with $\lambda = d/\delta$, where $\delta = \sqrt{1/\pi f\sigma\mu}$ is the skin depth.
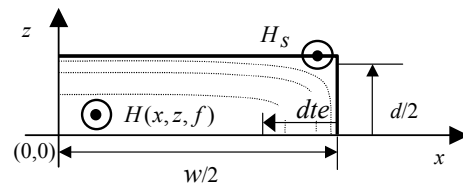
Fig.1. *H* and eddy currents in ¼ of a lamination, and *dte* origin.

APPLICATION EXAMPLE

A steel lamination with $\sigma = 4.5\times10^6$ S/m, $\mu=6.667\times10^{-3}$ H/m ($v=150$ m/H), $d=0.5$ mm, of various widths w ranging from $2d$ to $25d$ is considered. Different frequencies, ranging from 0.42 Hz to 4.2 kHz ($\lambda = d/\delta$ ranging from 0.1 to 10) are considered. As, due to the edge effect, the ECL given by (2)

start to change as the distance to the edge *dte* decreases, a equivalent conductivity σ_{eq} (S/m) is introduced that used in (3) or (4) will give the same results as (2) for each *dte*:

$$\sigma_{eq} = \frac{1}{P_J} \frac{H_s^2}{d\delta} \frac{\sinh\lambda - \sin\lambda}{\cosh\lambda + \cos\lambda} = \left(\frac{P_J}{P_{1DHs}}\right)^{-1} \sigma \qquad (6)$$

$$\sigma_{eq} = \frac{P_J}{\pi^2 d^2 f^2 B_a^2 F_{sk}/6} = \frac{P_J}{P_{1DBa}} \sigma \qquad (7)$$
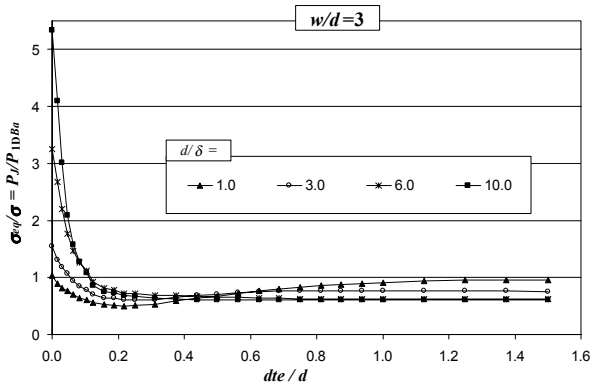
Fig. 2. P_J/P_{1DBa} (constant B_a) for w/d=3.

From Fig. 2, for constant B_a it can be seen that σ_{eq}/σ is different from 1 on the central zone of the lamination, what might complicate its use in homogenization techniques. However this problem does not occur when using H_s constant (Fig. 3 and Fig. 4) as σ_{eq}/σ =1 on the central zone of the lamination and for a $dte \leq 1.5d$ it can be applied a σ_{eq} at the border of the bulk material, given by a lookup table that incorporates the values of Fig. 3 and Fig. 4, or by fitted expressions obtained from the same data, to use in homogenization technique.
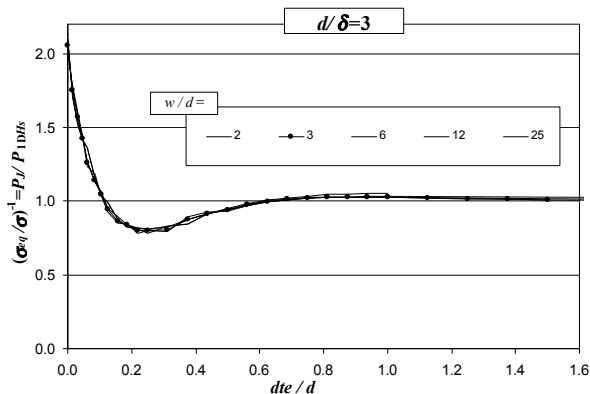
Fig. 3. P_J/P_{1DHs} (constant H_s) for d/δ=3.
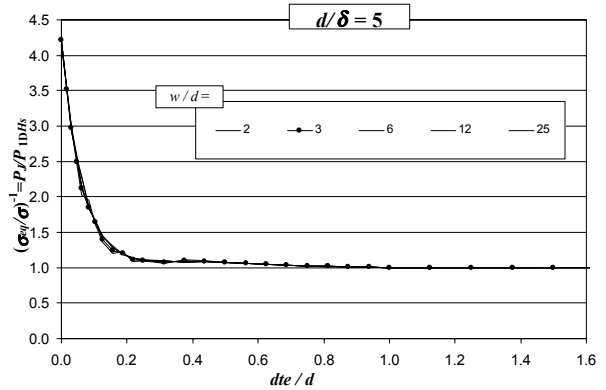
Fig. 4. P_J/P_{1DHs} (constant H_s) for d/δ=5.

CONCLUSIONS

From the results obtained, the following conclusions can be presented:

- Using the methodology with constant B_a leads to P_J/P_{1DBa} (in general) different from 1, and depending on w/d and d/δ.
- Using the methodology with constant H_s leads to P_J/P_{1DHs} depending only on d/δ and equal to 1 for dte>1.5d.
- It was shown that both methodologies could be related to an equivalent conductivity, specially the one with H_s constant that we expect to apply in homogenization techniques.

In the full paper some more interesting cases and conclusions will be presented.

REFERENCES

[1] J. Gyselinck, L. Vandevelde, J. Melkebeek, P. Dular, F. Henrotte and W. Legros, "Calculation of eddy currents and associated losses in electrical steel laminations", *IEEE Transactions on Magnetics*, Vol. 35, No. 3, pp.1191-1194, May 1999.
[2] P. Dular, J. Gyselinck, C. Geuzaine, N. Sadowski, J. Bastos, "A 3D magnetic vector potential formulation taking eddy currents in lamination stacks into account", *Proc. of CEFC2002*, 16–19 June 2002, Perugia, Italy, pp. 123.
[3] C.L. Antunes, P.G. Pereirinha, "Finite element computation of eddy current losses in steel lamination considering the skin effect, the lamination width and thickness", *Proc. of the ICEM*, Brugge, Belgium, 25-28 Aug. 2002, paper 159 (in CD ROM).
[4] P.G. Pereirinha, C.L. Antunes, "Generic abacus and analytical model for eddy current loss calculations in steel lamination derived from finite element numerical results in 2D", *Proc. of CEFC2002*, 16–19 June 2002, Perugia, Italy, pp.238.

Managing Uncertainties in Electromagnetic Design Problems with Robust Optimization

Gerald Steiner[*], Andreas Weber[†] and Christian Magele[†]

[*]Institute of Electrical Measurement and Measurement Signal Processing
Email: steiner@emt.TUGraz.at

[†]Institute for Fundamentals and Theory in Electrical Engineering
Email: christian.magele@TUGraz.at

Graz University of Technology
Kopernikusgasse 24
8010 Graz, Austria

Abstract—Numerical optimization techniques are widely used in electromagnetical design, but uncertainties in the design variables are neglected in the majority of cases. A robust formulation of nonlinear programs that incorporates uncertainties and their effects on target performance and feasibility directly into the optimization process is proposed. Applicability and benefits of this method are discussed with the TEAM Workshop problem 22.

INTRODUCTION

The solutions of electromagnetic design problems from usual optimization are highly tuned to precise numerical values of the design variables. In real-world implementations of designs the values can often only be realized within some tolerance or they may be affected by external perturbations. This can result in considerable deterioration of the target performance and even infeasibility of the implemented design.

With the presented Robust Optimization framework uncertainties in the design variables can be included in the problem formulation. Given a model of the possible deviations, the optimization algorithm is forced to converge to a solution that is optimal regarding the target values and remains feasible in the whole domain of uncertainty.

PROBLEM FORMULATION

The conventional constrained nonlinear programming problem often evolving in electromagnetic design is

$$\min_{\mathbf{x}} \quad f(\mathbf{x}) \\ s.t. \quad g_i(\mathbf{x}) \leq 0 \quad i = 1, \ldots, m \tag{1}$$

with the vector of the n design variables $\mathbf{x} \in \Re^n$, the target function f and m inequality constraints g_i. This formulation does not account for uncertainties in the design variables. It contains no information about the behavior of the target function in a neighborhood of the nominal point, and the design may become infeasible in the presence of perturbations.

Uncertainty Set   A simple model of the possible fluctuations around every nominal point $\mathbf{x}$ is introduced [1]. This

Uncertainty Set $U(\mathbf{x})$ is a compact sub-domain of the design space and is uniquely defined for every point $\mathbf{x} \in \Re^n$. It can e.g. be modelled as hyper-rectangle centered at $\mathbf{x}$,

$$U(\mathbf{x}) = \{\boldsymbol{\xi} \in \Re^n \mid \mathbf{x} - \boldsymbol{\Delta} \leq \boldsymbol{\xi} \leq \mathbf{x} + \boldsymbol{\Delta}\} \subset \Re^n \tag{2}$$

where $\boldsymbol{\Delta} = [\delta_1 \ \delta_2 \ \cdots \ \delta_n]^T \in \Re^n$ is the vector of the biggest possible variations from the nominal values for all design variables.

Robust Formulation   Problem (1) has to be adjusted in the presence of uncertainties. Solutions should be robust regarding target performance and feasibility. For the target function flat regions with best performance in U are preferred to steep valleys with the best value at the nominal point. The constraints have to be satisfied for all points in U for robust solutions.

In the majority of cases it is essential to treat both demands simultaneously. Feasibility robustness ascertains the effects of uncertainty in relation to the constraints and target robustness detects the effects of the abberations to the quality function. The following formulation combines both tasks,

$$\min_{\mathbf{x}} \ \max_{\boldsymbol{\xi} \in U(\mathbf{x})} f(\boldsymbol{\xi}) \\ s.t. \ \max_{\boldsymbol{\xi} \in U(\mathbf{x})} g_i(\boldsymbol{\xi}) \leq 0 \quad i = 1, \ldots, m \tag{3}$$

The resulting target function is continuous but not continuously partially differentiable at unconstrained minimizers [2]. The new constraint functions are also continuous but possibly not continuously partially differentiable at certain points, depending on the shape of the original constraints [1].

ROBUST OPTIMIZATION PROCEDURE

Uncertainty Set Evaluation   It is tried to identify the worst values of the target functions and constraints in U to directly compute the max-functions. The worst values are assumed to appear at one of the vertices of the uncertainty set. This is true if the original functions g_i and f, respectively, are convex or if all their partial derivatives with respect to the design variables do not change the sign in a set $F \supseteq U$. Instead of evaluating

all vertices, a prediction for the worst one is used [2]. Two function values, at $\mathbf{x}_{i+}$ and $\mathbf{x}_{i-}$, have to be calculated for every coordinate direction. For a nominal point $\mathbf{x}_0$, the point $\mathbf{x}_{i+}$ is $\mathbf{x}_0$ with Δ_1 added in the ith element. The predicted worst vertex is assumed in the directions where the higher values were determined,

$$\mathbf{x}_{pred} = \mathbf{x}_0 + \begin{pmatrix} sign\Big(f\big(\mathbf{x}_{1+}\big) - f\big(\mathbf{x}_{1-}\big)\Big) \cdot \Delta_1 \\ \cdots \\ \cdots \\ sign\Big(f\big(\mathbf{x}_{n+}\big) - f\big(\mathbf{x}_{n-}\big)\Big) \cdot \Delta_n \end{pmatrix} \quad (4)$$

and the predicted worst value is

$$\max_{\boldsymbol{\xi} \in U(\mathbf{x}_0)} \{f(\boldsymbol{\xi})\} \approx f(\mathbf{x}_{pred}) \quad . \quad (5)$$

For problems where all functions are derived from the solution of one forward problem, as usual in electromagnetic design, $l = (2 \cdot n + m)$ problem evaluations are necessary to estimate all the worst values.

Optimization Algorithm A two step procedure was used to solve the design problem described in the following section. First a Genetic Algorithm (GA) was used to find the region of the global optimum in the design space containing lots of local minima. The non-differentiable functions are no limitation for the GA.

In the second step Sequential Quadratic Programming (SQP) was launched from the solution of the first stage to explore the local structure of the problem. With some modifications to the standard SQP algorithm convergence can be guaranteed for minimax problems [3]. The possible discontinuities in the partial derivatives of the constraint functions were smoothed implicitly by finite difference gradient calculations.

TEAM PROBLEM 22: SMES DEVICE

Superconducting Magnetic Energy Storage (SMES) systems consisting of two coaxial solenoids allow the storage of large amounts of energy in a fairly economical way and can be rather easily scaled up in size. The optimization of such a device is the task of the TEAM Workshop problem 22 [4], where the following objectives have to be satisfied:

- The energy stored in the device should be $180\ MJ$.
- The stray field along a line at a distance of 10 meters should be as small as possible.
- The generated magnetic field inside the solenoids must not violate a certain physical condition which guarantees superconductivity (quench condition).

The design problem is finding the set of 6 geometrical parameters and the current densities J_1 and J_2 that best fit the objectives. For the robust problem the current densities were assumed uncertain. The results from optimization runs with different uncertainties $\Delta_J = \Delta_{J1} = \Delta_{J2}$ are shown in Fig. 1. The upper two and the lower left plot illustrate the stray
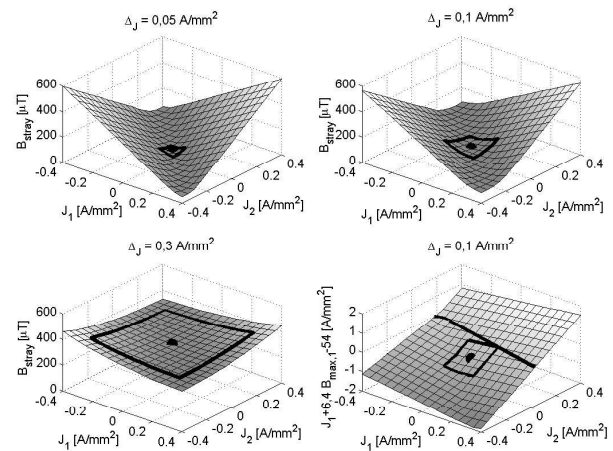
Fig. 1. SMES Optimization results for different uncertainties.

field around the nominal solutions. The unperturbed designs are marked by the black dots. The black rectangles represent the limits of the corresponding uncertainty sets. For growing uncertainties the curves get flatter while the stray field at the nominal points increase. But all the different solutions are optimal regarding their worst values in U. The lower right plot shows the constraint function describing the quench condition in the first coil for $\Delta_J = 0.1\ A/mm^2$. All points below the black line are feasible. Only a corner of U touches the boundary, so the design will not quench if the perturbations remain within the assumed limits of uncertainty. This solution illustrates the importance of considering robustness issues for both target and constraint functions.

CONCLUSION

The presented procedure for performing robust optimization can find solutions that are insensitive to variations in the design parameters. The solutions can support the designer in finding the best trade-off between peak performance tuned to exact parameter values and accepting a certain amount of uncertainty. This will be further exploited in the extended paper by directly comparing optimal designs for varying amounts of uncertainty.

REFERENCES

[1] P. Alotto, T. Fortuna, C. Magele, H. Pflügl, G. Steiner and A. Weber, "Robust Optimization in Electromagnetic Design", presented at *IEEE CEFC 2002*, Perugia, Italy, to be published, 2002.
[2] P. Alotto, C. Magele, W. Renhart, G. Steiner and A. Weber, "Robust Target Functions in Electromagnetic Design", *Proceedings of the 10th IGTE Symposium*, Graz, Austria, pp. 84-88, 2002.
[3] J.L. Zhou and A.L. Tits, "Nonmonotone Line Search for Minimax Problems", *Journal of Optimization Theory and Applications*, vol. 76, no. 3, pp. 455-476, 1993.
[4] Ch. Magele et. al, "SMES optimization benchmark", *Proceedings of the TEAM Workshop in the Sixth Round*, March 20-21, Okayama, Japan, 1996.

Stochastic Handling of Tolerances in Robust Magnets Design

M. Cioffi, A. Formisano and R. Martone

Dipartimento di Ingegneria dell'Informazione - Seconda Università di Napoli
Via Roma, 29
Aversa CE, 81031, Italy
marco.cioffi@unina2.it

Abstract—**Due to construction tolerances, the performances of actual electromagnetic devices differ from those of the nominal design. A strategy for the search of robust design solutions against construction tolerances is here presented. The approach is based on the statistical analysis of the tolerances effects on the Objective Function to evaluate. The application of the proposed strategies to the optimal design of MRI magnets by a Genetic Algorithm shows the possibility to direct the search towards robust solutions.**

INTRODUCTION

The main requirement to fulfil in the optimal design of superconducting (SC) magnets for Magnetic Resonance Imaging (MRI) is the high uniformity of the magnetic field inside a wide Volume of Interest. Unfortunately, in practical realisations, the actual magnet differs from the optimal one due to construction and assembling tolerances [1]. In addition, in the normal operating conditions, the generated magnetic forces can deform the coils, with the consequence that the working geometry is different from the design one [2]. In both cases a performances degradation has to be expected. It is therefore very important to look for robust design configurations characterised by a reduced sensibility to little changes of the magnet geometry.

IMPACT OF THE TOLERANCES ON THE DESIGN STRATEGY

To design purposes, a SC magnet has to be properly modeled by defining the key design parameters and its performance figures. The magnet geometry and the field are here supposed to be axially symmetric and the tolerances are assumed to not break the symmetry. In real cases, however, a lack of symmetry could appear and thus the field distribution exhibits multipole components [3]: therefore a full 3D check of the final design is recommended.

The optimal design can be formulated in terms of the minimization of a suitable Objective Function (*OF*), able to quantify the performance figures as a function of all design parameters [4]. Scalar *OFs* are usually assumed as the weighted sum of the different figures (objectives). The main design objective is the magnet field uniformity; other important requirements are the device compactness and superconducting material volume, which is an index of the total cost [1]. In addition, a number of geometrical and physical constraints have to be considered in the design process, including, as an example, the limit on the current density in the coils, which must not exceed a critical value, depending on the field and on the temperature, in order to preserve the SC state.

The uncertainness associated with assembling tolerances has an important effect for the formulation of the optimal design search. In the following, the main aspects of such impact are examined and discussed.

Assembling tolerances

When considering the assembling tolerances, the performances of a possible design solution have to be redefined taking into account the uncertainness impact. A possible new definition of the *OF* can be its statistical average [4]:

$$\overline{OF}(\mathbf{x}) = \int_{\Omega(\mathbf{x})} p(\mathbf{x}')OF(\mathbf{x}')d\mathbf{x}' \tag{1}$$

where $p(\mathbf{x})$ is the probability density function (PDF) of the configuration described by the parameters vector $\mathbf{x}$ and $\Omega(\mathbf{x})$ is the tolerances interval around the nominal configuration $\mathbf{x}$. Mechanical and assembling tolerances are usually modelled as random variables with Gaussian PDF. A different approach is presented in [6], where just the worst *OF* on the tolerance range boundary is considered: this correspond to the choice of an uniform PDF.

Preliminary step: Design of Experiment

The introduction of the assembling tolerances in optimal design implies a relevant impact on the computational costs because, for each trial solution, the computation of the solution local behaviour is required (see for instance [1]). The increase of the computational load can become too high for the available computing resources, especially when the number of design parameters is high and the adopted search strategy is stochastic. Therefore, techniques for the reduction of the computational burden are crucial.

Aim of the present paper is to propose a strategy to reduce the computational cost by a preliminary ranking of the design parameters on the base of the impact of their uncertainness on the *OF* (parametric sensibility) inside the tolerance region. For low impact parameters, the average (1) can be, neglected reducing to the classical *OF*. The ranking is based on a Design of Experiment (DOE) type technique, suitably adapted to the

requested parametric sensibility evaluation. A number of random samples in the feasible regions are selected for Monte Carlo Analysis (MCA) around each of them, in order to compute the correlation indices between each design parameter and the *OF*: the larger the correlation index appears, the more critical is the parameter. In the optimisation process just the most critical parameters can then be considered affected by tolerances, achieving the foreseen reduction of the computational cost.

Another possible ranking index is also proposed: the overall sensitivity of each design variable with respect to the assembling tolerances is evaluated using the mean value over the MCA runs of the ratio $\overline{OF};_k(\mathbf{x})/OF(\mathbf{x})$, where:

$$\overline{OF}_k(\mathbf{x}) = \int_{\Omega(\mathbf{x}_k)} p(x'_k) \, OF(x_1,\ldots,x'_k,\ldots x_n) \, dx'_k \ , \tag{2}$$

$p(x_k)$ is the probability of x_k and $\Omega(x_k)$ is the tolerances interval of x_k. It should be noted that the global effect of the variation of a parameter is related to the mean of MCA results among different test points, while the local effect on the solution robustness inside the tolerance range is expressed by $\overline{OF};_k(\mathbf{x})/OF(\mathbf{x})$ values for each sample point.

Statistical dependence of design tolerances

The simplest approach to numerical evaluation of (1) is to consider statistical independence among tolerances, assuming the joint PDF p(**x**) as the product of the marginal probabilities relative to each parameter: however this strategy is computationally heavy for the evaluation of the integral in (1). On the other hand, due to technological and constructive issues, there could be some dependencies among design parameters or tolerances due to machine tools and construction methodologies, and advantage can be taken by considering that the joint PDF should no longer be considered the product of marginal PDF, eventually leading to a reduction of the computational cost for evaluation of (1). As an example, for MRI magnets the minimum radius of the coils are subjected to the same tolerance. The exploitation of such concepts provide a better exploration of the search space in the neighborhood (tolerance range) of each design trial solution: the integration points can be reduced by locating them only in a subregion of $\Omega(\mathbf{x})$, while keeping the same accuracy.

PRELIMINARY RESULTS

The practical effectiveness of the proposed method has been evaluated with reference to the design of a superconducting magnet for MRI. The main goals of the device are a central magnetic field of 3 T and a field homogeneity of 2 ppm. Preliminary results are presented here for a test case magnet with 4 coils, symmetrically placed with respect to a central plane, with the minimum radius and the coil lengths kept fixed. There are therefore four design variables: the axial position $Z_{b,1}$ and $Z_{b,2}$ of the two (respectively inner and outer) coils baricentres and the radial thickness ΔR_1 and ΔR_2. Mechanical tolerances of 1% affect just the inner coil 1 thickness, and have been modelled by using Gaussian distributions. The optimal design is performed by using a Genetic Algorithm (GA), which is well suited for *OF* with multiple minima [4]. The *OF* has been assumed as the sum of three terms, related to field homogeneity, volume and compactness respectively [5].

A MCA has been performed for a set of five test points, randomly selected inside the admissible parameter ranges. In Table I the Correlation Indices (CI) between the design parameters and the *OF* are reported for each test point and for each parameter. In addition, the *OF* for each point is reported. Note that the most relevant parameter for the *OF* is the thickness of the coil 1 either for global and local variations. Consequently, in the optimization phase, just the tolerance on ΔR_1 will be taken into account in (1).

TABLE I
CORRELATION INDICES OF THE DESIGN VARIABLES WITH *OF*

	$Z_{b,1}$	$Z_{b,2}$	ΔR_1	ΔR_2	*OF*
Point 1	0.214	0.002	-0.940	-0.147	0.199
Point 2	0.523	0.002	-0.832	0.055	0.042
Point 3	0.338	0.211	-0.869	-0.115	0.028
Point 4	0.457	0.053	-0.874	0.072	0.009
Point 5	0.088	0.052	-0.974	0.015	0.009

In the full paper, a more detailed discussion about the proposed technique and the ranking indices will included, and extended results for a larger six coils more realistic magnet will be presented, with particular reference to computation al costs reduction.

REFERENCES

[1] V. Cavaliere, M. Cioffi, A. Formisano, R. Martone, "Improvement of MRI Magnets Design Through Sensitivity Analysis", *IEEE Trans. on Applied Supercond.*, Vol. 12, Issue 1, pp. 1413-1416, March 2002.

[2] A. Yamamoto, *et al.* , "Analysis of Mechanical Tolerances of a Low-β Quadrupole Magnet for the LHC", *IEEE Trans. on Applied Supercond.*, Vol. 10, N. 1, pp. 131-134, March 2000.

[3] S. Russenschuck, T. Tortschanoff, "Estimation of the Errors of Conductor Positioning in the LHC Main Magnets from a given Multipole Content", *IEEE Trans. on Magnetics*, Vol. 29, N. 2, pp. 2060-2063, March 1993.

[4] S. Russenschuck, "Synthesis, inverse problems and optimisation in computational electromagnetics", *Int. Journal of Numerical Modeling*, Vol. 9, pp. 45-57, 1997.

[5] M. Cioffi, A. Formisano, R. Martone, "Increasing Design Robustness in Evolutionary Optimisation", Proc. of PMAPS 2002, Napoli, Italy, September 22-26, 2002.

[6] P. Alotto, C. Magele, W. Renhart, G. Steiner, A. Weber, "Robust Target Functions in Electromagnetic Design", Proc. of the IGTE 2002, Graz, Austria, September 16-18, 2002.

Optimization Design of Electrode Contour of SF₆ Circuit Breaker Using Artificial Neural Network

Cao Yundog, Liu Xiaoming, Liu Dong, Wang Erzhi

Shenyang University of Technology

58#, Xinghua South Street, Tiexi District

Shenyang 110023, China

caoyundong@hotmail.com

Abstract- **In this paper, the artificial neural network (ANN) is applied to solve the inverse problem of electric field in SF6 circuit breaker. Taking the high nonlinear approaching ability of ANN and the numerical analysis of electromagnetic field into consideration, the demonstration examples have been solved. From calculation result, it can be seen that the proposed method is feasible and valid.**

INTRODUCTION

Presently, some contributions have been reported using modern optimization methods, such as genetic algorithm, simulated annealing, taboo search algorithm and ANN for solving the global optimization problems [1,2]. And the inverse problem computation of electric field play a very important role for optimizing and investigating the insulation performance and interrupting characteristic of high voltage (HV) electrical apparatus. However, there exist many optimized variables for solving the inverse problem and longer calculation time is required. For the above optimization techniques, ANN possesses the ability to simulate the intricate nonlinear problem. Moreover, in application of ANN, some tedious modeling of the complicated system can be simplified because it is unnecessary to know the pre-konwledge of the computation structure. So ANN is introduced to solve the inverse problem of electric field in HV SF6 circuit breaker in this paper.
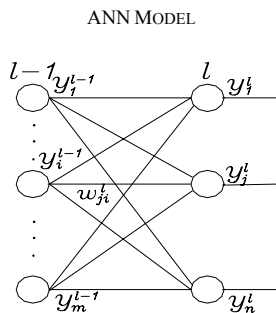
ANN MODEL

Fig.1. Diagram of multi-layer feed-forward ANN

By determining a rational ANN structure, the intricate inverse problem can be solved. ANN model with multi-layer feed-forward network is established, as shown in Fig.1. Suppose $y_j^l(n)$ is the output of the jth unit of the lth layer in the nth iteration step, thus

$$y_j^l(n) = \sum_{i=0}^{l} \omega_{ji}^l(n) y_i^{l-1}(n) \tag{1}$$

Where $y_i^{l-1}(n)$ is the working signal of the ith unit of the former layer, $\omega_{ji}^l(n)$ is the connecting weight between the ith and the jth unit.

E_{AV} is the learning objective function, which is the average of calculation error, that is

$$E_{AV} = \frac{1}{2N} \sum_{n=1}^{N} \sum_{k=1}^{M} e_k^2(n) \tag{2}$$

Where $e_k(n) = T_k(n) - O_k(n)$ and $O_k(n)$ is an output in the nth iteration step for the kth unit in output layer, and $T_k(n)$ is the corresponding teaching patterns.

The back propagation method (BP) is applied to correct weight according to the following approach:

$$\Delta\omega_{ji}^l(n) = \alpha\Delta\omega_{ji}^l(n-1) + \eta\delta_j^l(n)y_j^l(n)$$
$$(0 < \alpha < 1) \tag{3}$$

For $\delta_j^l(n)$ of the lth layer, when the jth unit is in the output layer, then

$$\delta_j^l(n) = e_j(n)O_j(n)[1 - O_j(n)] \tag{4}$$

While the jth unit is on the hidden layer

$$\delta_j^l(n) = y_j^l(n)[1 - y_j^l(n)] \sum_{k=1}^{m} \delta_k^{l+1}(n)\omega_{kj}^{l+1}(n) \tag{5}$$

NUMERICAL CALCULATION OF DEMONSTRATION EXAMPLES

Simulation of the Nonlinear Oscillating Function

The nonlinear oscillating function is applied to test the simulation characteristic of ANN with three layers, that is

$$y = Sinc(x) = \begin{cases} 1 & x = 0 \\ \dfrac{\sin(x\pi)}{x\pi} & x \neq 0 \end{cases} \tag{6}$$

The calculation results are shown in Table I, where "Ne" represents the number of neurons in the hidden layer. For reflecting the effect of the number of neurons on the mean squared error in the hidden layer, the training times is fixed at 500. And when the number of neurons in the hidden layer is 7, the training error is the least and simulation results are shown in Fig.2.

TABLE I. CALCULATION RESULTS

Ne	Mean squared error	Training times	Training time(second)
1	8e-2	500	10.27
2	2e-3	500	49.3
5	3e-7	500	97.6
7	1e-11	500	84.42
9	1e-10	500	108.4
10	3e-11	500	81.57
11	2e-11	500	85.2
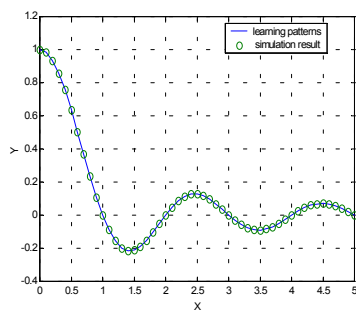
Fig.2. Simulation results of the nonlinear oscillating function

OPTIMIZATION OF THE ELECTRODE CONTOUR IN SF6 CIRCUIT BREAKER

The electrode contour of HV SF6 circuit breaker is optimized using the proposed method. The objective function is $f = \max\{E(r)\}$, Where $E(r)$ represents the electric field intensity of the electrode. For the concrete structure, 8 neurons in input layer, which represents the corresponding X coordinates of 8 equated optimized points along Y axis on the electrode, have been determined. And 3 neurons in output layer, which gives the E_{max} and its corresponding X, Y coordinates. In comparison with calculation results of different approaching ability and computing time, 10 neurons of hidden layer are selected. The calculation configuration and optimized electrode contour are illustrated in Fig.3 and Fig.4. Optimization results are given in Fig.5 and Table II.

TABLE II. OPTIMIZATION RESULTS

Optimized points	1	2	3	4	5	6	7	8
Original coordinates X (mm)	572.0	572.0	572.0	572.0	572.0	574.0	576.5	581.0
Optimized coordinates X (mm)	573.82	573.25	572.0	574.83	578.0	579.53	582.57	585.03
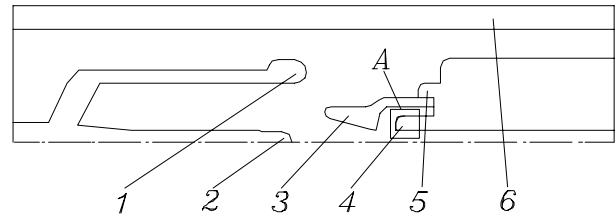
Fig.3. Calculation configuration of SF6 circuit breaker
1- Stationary main contact 2- Stationary arc contact 3- Nozzle
4- Movable arc contact   5- Movable main contact   6- Porcelain casing
A- optimized domain
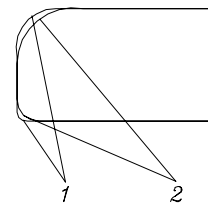
Fig.4. Zoom of the optimized domain A
1-The initial electrode contour   2-The optimized electrode contour
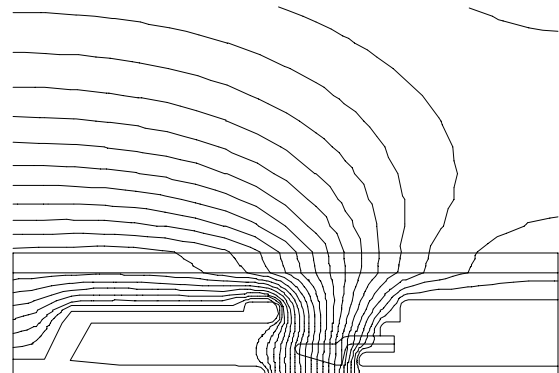
Fig.5. Equal electric potential distribution with optimized contact

CONCLUSIONS

In this paper, the feed-forward ANN is applied to solve the nonlinear oscillating function and to compute the inverse problem of electric field. Taking the simulation error and training time into account, there exists an optimum range of number of the neurons on the hidden layer. The simulation results show that the combination of ANN and electromagnetic numerical analysis is feasible and valid.

REFERENCES

[1] Nickolai S. Rubanov, "The layer-wise method and the back propagation hybrid approach to learning a feed forward neural networks," IEEE Trans on Neural Networks, Vol.11, No.2, pp. 295-305, March 2000.

[2] Liu Xiaoming, Cao Yunong, Wang Erzhi etc, "Optimization design of the contact and shield in vacuum interrupter based on the genetic algorithm," 19th ISDEIV, pp.463-466, Sep 2000.

Optimization of an Offset Reflector Antenna using Genetic Algorithms

S.L. Ávila   W.P. Carpes Jr.

GRUCAD / EEL / CTC / UFSC, C.P. 476, Florianópolis, SC, 88040-900, Brazil

avila@grucad.ufsc.br   carpes@grucad.ufsc.br

J.A. de Vasconcelos

GOPAC / EEL / EE / UFMG, Belo Horizonte, MG, 31270-010, Brazil

joao@cpdee.ufmg.br

Abstract – **This paper presents the application of genetic algorithms in the optimization of an offset reflector antenna. The antenna shape is designed in order to obtain a uniform radiation pattern on the Brazilian territory. Modified genetic operators are proposed with the aim to increase the efficiency of the real coded GA used here.**

INTRODUCTION

Genetic algorithms (GAs) are robust, stochastic-based methods which can handle the common features of electromagnetic optimization problems that are not readily handled by other traditional optimization methods. An overview of GAs for electromagnetic optimization can be found in [1]-[2].

In the design of reflector antennas, the required radiation pattern is generally obtained by using a set of feeds and a parabolic reflector [3]. However this technique can be difficult to implement and the structure is bigger and more expensive than that using a single reflector with a single feed.

In this paper, a GA is used to design the shape of a single-feed offset reflector antenna. The main goal is to obtain an antenna whose radiation pattern covers uniformly the Brazilian territory. After a simple revision about GAs, we propose modified genetic operators with the aim to increase the efficiency of the real coded GA.

GENETIC ALGORITHMS

Nowadays an important issue is related to the techniques used to increase the efficiency of GAs. Particularly, the strategy used in coding the variables is of crucial importance. It is also very important to have an efficient exploration of the search space (the space of all possible solutions). The latter requires that the GA operators (selection, crossover and mutation) be properly implemented.

We carried out some simulations in order to compare the most used coding schemes: binary and real. We used the Rastrigin function as test function and we used the same procedures presented in [4]. The results obtained with real coding were practically the same obtained using binary coding. So, the coding scheme must be chosen according to the nature of the variables and the programming language used.

Real coding is well suited to a large class of programming languages and to problems with a great number of variables. For this reason, we have developed genetic operators for a real coded GA that allow an effective exploration of the search space. We consider a case where the population is given by

$$
X^{n} = \begin{bmatrix} X_1^{n,1} & X_2^{n,1} & \cdots & X_{n\,var}^{n,1} \\ \vdots & \vdots & \vdots & \vdots \\ X_1^{n,nbpop} & X_2^{n,nbpop} & \cdots & X_{n\,var}^{n,nbpop} \end{bmatrix} , \quad (1)
$$

where each line represents an individual, $nbpop$ is the number of individuals of the population, $nvar$ is the number of variables of each individual and n represents the current generation. In the evolutionary process, we group the individuals in pairs and, for each pair, it is verified if crossover will take place (with a probability P_c). If it is the case, crossover is performed to yield two offspring according to:

$$
X_{kcross\ldots dir}^{n+1,i} = 0.9\,X_{kcross\ldots dir}^{n,i} + 0.1\,X_{kcross\ldots dir}^{n,j} , \quad (2)
$$

$$
X_{kcross\ldots dir}^{n+1,j} = (1-\alpha)X_{kcross\ldots dir}^{n,i} + \alpha\,X_{kcross\ldots dir}^{n,j} , \quad (3)
$$

where $kcross$ is a random integer with uniform distribution on the interval $1 \le kcross \le nvar$ defining the crossover cut point [5]; α is a random multiplicative coefficient with uniform distribution on the interval $-0.1 \le \alpha \le 1.1$ [6]; and dir is a random binary variable that indicates the direction in which the crossover will be performed. It is equal to $nvar$ if the direction is from the cut point to the last variable and equal to 1 in the other direction. Also, $X_{kcross\ldots dir}^{n,i}$ represents a portion of the individual i containing all variables from $X_{kcross}^{n,i}$ to $X_{dir}^{n,i}$ (or from dir to $kcross$ if $dir < kcross$). The variables of the offspring not included in the interval $kross\ldots dir$ are directly copied from the respective progenitor. With this approach, known as biased crossover, one child inherits most of its genetic material from one of the parents. In this case, in order to improve the average fitness of the population at each generation, it is necessary that

$$
f\left(X^{n,i}\right) > f\left(X^{n,j}\right) , \quad (4)
$$

where $f(\cdot)$ represents the fitness function.

In a similar fashion, mutation is performed (with a probability P_m) with the sum of a perturbation vector (γ) to the portion of the individual that will suffer mutation. In the beginning of the evolutionary process the perturbation vector is taken as:

$$
\gamma_{kmut\ldots dir}^{n,i} = 0.05\beta\ range_{kmut\ldots dir}^{n,i} , \quad (5)
$$

where $range$ is defined by the allowable limits of each variable and β is a random number with uniform distribution

on the interval $0 \leq \beta \leq 1$. In this case, the mutation corresponds to a maximum change of $\pm 5\%$ of the range for each variable. This amount of mutation allows an efficient exploration of the search space without making the process too erratic. At the end of the evolutionary process, the perturbation vector changes to

$$\gamma_{kmut\ldots dir}^{n,i} = 0.05\beta \frac{\sum\limits_{i=1}^{nbpop} X_{kmut\ldots dir}^{n,i}}{nbpop} \quad . \tag{8}$$

In order to investigate the efficiency of the genetic operators proposed here, they have been applied in the minimization of a rotated Rastrigin's function [6] with 30 variables. The allowed range for all variables corresponds to the interval $-5.12 \leq X \leq 5.12$. The values give an objective function with 10^{30} minima. The global minimum for the rotated Rastrigin's function is $X_{1\ldots30} = 0$. The simulation was run 100 times and in all cases convergence has been attained in about 100 generations with a population of 200 individuals (convergence criterion: $\|x_i\|_2 \leq \sqrt{0.02}$). The improvement techniques proposed in [4] were also used. We observed that convergence was reached with approximately 200×100 evaluations of the objective function for a search space containing 10^{30} possible solutions. This demonstrates the great efficiency of the real coded GA presented here.

OFFSET REFLECTOR ANTENNA

The offset reflector antenna to be optimized is a single-feed and single-reflector structure with circular aperture. Its surface is parameterized according to [7]:

$$z'(t,\phi) = \sum_{n=0}^{N} \sum_{m=0}^{M} \left(C_{nm} \cos n\phi + D_{nm} \sin n\phi \right) F_m^n(t) \quad , \tag{10}$$

where t and ϕ are spherical coordinates of the paraboloid, C_{nm} and D_{nm} are expansion coefficients and $F_m^n(t)$ is the modified Jacobi polynomial.

The antenna analysis is performed with the Physical Optics (PO) approximation [8] corrected by equivalent edge currents (FR) [9]. Therefore, the total electric field radiated is:

$$\vec{E} = \vec{E}_f + \vec{E}_{PO} + \vec{E}_{fr} \quad . \tag{11}$$

ANTENNA OPTIMIZATION

The optimization procedure has as goal to design a reflector surface shape that produces a uniform coverage of Brazilian territory [10] with maximum average gain. Table I presents the maximum and average gain of the optimized antenna along with the corresponding values of the parabolic antenna (used as reference). Fig. 1 shows the footprints of the radiated field.

TABLE I. COMPARISON BETWEEN ANTENNAS

Reflector	Max. Gain (dBi)	Average Gain G_{av} (dBi)
Paraboloid	44.64	18.37
Optimized	39.13	30.74

Fig. 1 and Table I clearly show that the optimized antenna gives a more uniform illumination with a higher average gain over the covering area than that of the reference antenna. The optimized antenna made it possible to obtain a directive gain of 25 dB on practically all the Brazilian territory and at least 30dB on 80% of it. Fig. 2 is a contour graph showing the difference between the z-coordinates of the optimized reflector and reference one. More results will be presented in the extended version of the paper.
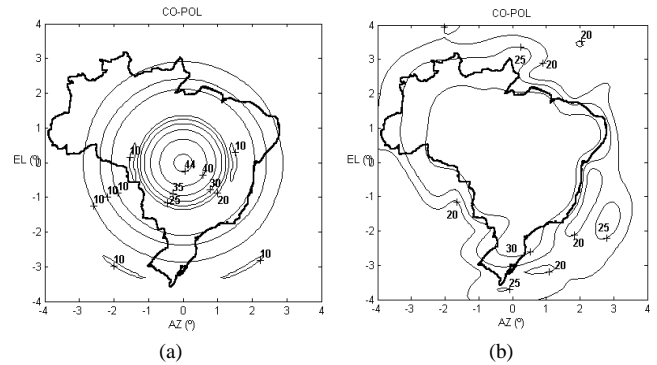
Fig. 1. Radiation patterns (in dBi) for: (a) reference parabolic reflector and (b) optimized shape.
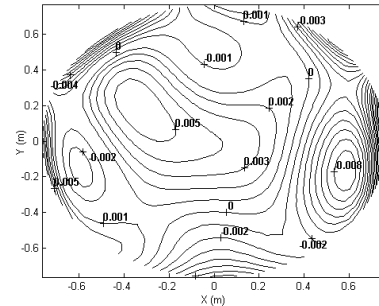
Fig. 2. Difference between optimized and reference parabolic shapes.

REFERENCES

[1] Haupt, R. L. "An Introduction to Genetic Algorithms for Electromagnetics," *IEEE AP-Mag.*, v. 37, n. 2 (Apr), pp. 7–15, 1995.
[2] Johnson, J.M.; Rahmat-Samii, Y. "Genetic Algorithm in Engineering Electromagnetics," *IEEE AP-Mag.*, v. 39, n. 4 (Aug), pp. 7–22, 1997.
[3] Saka, B.; Yazgan, E. "Pattern Optimization of a Reflector Antenna with Planar-Array Feeds and Cluster Feeds," IEEE Trans. on AP, v. 45, n. 1 (Jan.), pp. 93–97, 1997.
[4] Vasconcelos, J. A.; et al. "Improvements in Genetic Algorithms," IEEE Trans. on AP, v. 37, n. 1 (Sep), pp. 3414–3417, 2001.
[5] Qing, A.; et al. "Electromagnetic Inverse Scattering of Two-Dimensional Perfectly Conducting Objects by Real-Coded Genetic Algorithm," *IEEE Trans. on GRS*, v.39, n.3 (Mar), pp.665–676, 2001.
[6] Takahashi, R. H. C.; et al. "A Multiobjective Methodology for Evaluating Genetic Operators," *IEEE Trans. on Mag.*, subm. 2002.
[7] Duan, D-W; Rahmat-Samii, Y. "A Generalized Diffraction Synthesis Technique for High Performance Reflector Antennas," *IEEE Trans. on AP*, v. 43, n. 1 (Jan), pp. 27-40, 1995.
[8] C. A. Balanis, *Antenna Theory – Analysis and Design,* John Wiley & Sons, 2° ed., New York, 1997.
[9] Rego, C. G.; Hasselmann, F. J. V. "Time-Domain Analysis of Pulse-Excited Reflector Antennas," *In: IEEE AP-S Int. Symp.*, v. 4, pp. 2046-2049, Salt Lake City, (Jul) 2000.
[10] Spring-GeoMinas and DPI/Inpe-http://www.dpi.inpe/spring/, 2002.

Optimization of radar cross section by a gradient method

A. Bondeson[1], Y. Yang[1], P. Weinerfelt[2]

[1]Department of Electromagnetics, Chalmers University of Technology, S-412 96 Göteborg, Sweden

[2]Saab Aerospace, S-581 88 Linköping

E-mails: elfab@elmagn.chalmers.se, elfyang@elmagn.chalmers.se, per.weinerfelt@saab.se

Abstract— **A gradient method for radar cross section (RCS) optimization is derived from Maxwell's equations. The method uses the adjoint problem and finds the derivatives of the RCS with respect to all design parameters from a single solution of the scattering problem. In two-dimensional test problems it converges with a small number of iterations to shapes with strongly reduced RCS in specified angular intervals. The optimal shapes have sharp corners in directions where the RCS is minimized and corrugations. The corrugations can be suppressed by means of penalty functions.**

Keywords—**optimization, radar cross section, gradient method, adjoint equation**

OPTIMIZATION PROBLEM

WITH few exceptions [1]-[3], optimization of microwave devices has relied on evolutionary methods such as the genetic algorithm. Here, we derive a gradient method, based on the adjoint problem [4], for the minimization of radar cross sections (RCS), and show that it is highly efficient.

First, consider a 3D scattering problem with an incident wave $\vec{E}_i = \vec{E}_0 \exp(-j\vec{k}_0 \cdot \vec{r})$. The mono-static RCS is $\sigma = 4\pi |A_\perp|^2 / E_0^2 k_0^2$, where the scattering amplitude

$$\vec{A} = \frac{k_0}{4\pi} \oint_{NTF} \left[\hat{n} \times (\nabla \times \vec{E}) - j\vec{k}_0 \times (\vec{E} \times \hat{n}) \right] e^{-j\vec{k}_0 \cdot \vec{r}} dS \quad (1)$$

is computed on the Near-To-Far-field transformation surface, and $\perp$ refers to the back-scatter direction.

The incident wave is imposed on a Huygens surface S, so that the electric field $\vec{E}$ is the total field inside S and only the scattered field outside. The incident field gives rise to sources in the curl-curl equation for $\vec{E}$, which we write in weak form as

$$L(\vec{w}, \vec{E}) = L_0(\vec{w}, \vec{E}) + E(\vec{w}, \vec{E}_0) = 0, \quad (2)$$

where $\vec{w}$ is a testing function,

$$L_0(\vec{w}, \vec{E}) = \int_\Omega \left(\nabla \times \vec{w} \cdot \nabla \times \vec{E} - k_0^2 \vec{w} \cdot \vec{E} \right) dv$$
$$+ \oint_{\partial \Omega} (\hat{n} \times \vec{w}) \cdot (jk_0 \hat{r} \times \vec{E}) dS \quad (3)$$

describes the homogeneous system and

$$E(\vec{w}, \vec{E}_0) = -\vec{E}_0 \cdot \oint_S [\hat{n} \times (\nabla \times \vec{w}) - j\vec{k}_0 \times (\vec{w} \times \hat{n})] e^{-j\vec{k}_0 \cdot \vec{r}} dS \quad (4)$$

represents the incident wave.

We use methods of optimal shape design [4] to find how the solution changes if the boundary Γ of the PEC scatterer is displaced by an infinitesimal distance ξ in the outward normal direction. The first order variation $\delta \vec{E}$ is determined by requiring the weak form of the differential equation (2) to hold for $\vec{E} + \delta \vec{E}$ in the modified geometry:

$$L_0(\vec{w}, \delta \vec{E}) = \oint_\Gamma \xi \left(\nabla \times \vec{w} \cdot \nabla \times \vec{E} - k_0^2 \vec{w} \cdot \vec{E} \right) dS. \quad (5)$$

Using (1) we find that the first variation of the RCS is

$$\delta \sigma = -E(\delta \vec{E}, \vec{A}_\perp^*) / E_0^2 k_0 + \text{c.c.} \quad (6)$$

Let $\vec{p}_E$ be the solution of the adjoint equation

$$L_0(\vec{w}, \vec{p}_E) + E(\vec{w}, \vec{A}_\perp^*) = 0, \quad (7)$$

which is the same scattering problem as $\vec{E}$, except that the incident wave is $\vec{p}_{E,i} = \vec{A}_\perp^* \exp(-j\vec{k}_0 \cdot \vec{r})$. Therefore, the adjoint solution $\vec{p}_E$ can be constructed from solutions of the original problem. This is because Maxwell's equations are self-adjoint and we consider backscattering.

If we choose $\vec{w} = \delta \vec{E}$ in (7), Eq. (6) gives the first order variation of the radar cross section $\delta \sigma = L_0(\vec{p}_E, \delta \vec{E}) / E_0^2 k_0 +$ c.c. Therefore, (5) with $\vec{w} = \vec{p}_E$ gives

$$\delta \sigma = \frac{2}{E_0^2 k_0} \text{Re} \left[\oint_\Gamma \xi \left(\nabla \times \vec{p}_E \cdot \nabla \times \vec{E} - k_0^2 \vec{p}_E \cdot \vec{E} \right) dS \right],$$

which can be expressed in terms of the surface current and charge densities on the PEC scatterer as

$$\delta \sigma = -\frac{2k_0 Z_0^2}{E_0^2} \text{Re} \left[\oint_\Gamma \xi \left(\vec{J}_{\text{adj}} \cdot \vec{J}_{\text{orig}} + c^2 \rho_{\text{adj}} \rho_{\text{orig}} \right) dS \right]. \quad (8)$$

The surface currents in the adjoint problem contain information on how the surface currents in the direct problem contribute to the radar cross section. The variation of the RCS can be weighted with respect to angle of incidence and frequency in obvious ways.

Similar formulas hold for scattering in 2D. For TM polarization, with an incident wave $E_i = E_0 \exp(-j\vec{k}_0 \cdot \vec{r})$, we define the scattering amplitude $A = -\frac{1}{4} \oint_{NTF} (j\vec{k}_0 E + \nabla E) \cdot \hat{n} \exp(-j\vec{k}_0 \cdot \vec{r}) dl$, and find the variation of the scattering length:

$$\delta L = -\frac{2Z_0^2 k_0}{|E_0^2|} \text{Re} \left(\oint_\Gamma \xi J_{\text{adj}} J_{\text{orig}} dl \right), \quad (9)$$

where $J_{\text{adj}} = (A^* / E_0) J_{\text{orig}}$.

For TE polarization, with an incoming field $H_i = H_0 \exp(-j\vec{k}_0 \cdot \vec{r})$, and scattering amplitude $C = -\frac{1}{4} \oint_{NTF} (j\vec{k}_0 H + \nabla H) \cdot \hat{n} \exp(-j\vec{k}_0 \cdot \vec{r}) dl$, we find

$$\delta L = -\frac{2k_0}{|H_0^2|} \text{Re} \left[\oint_\Gamma \xi \left(J_{\text{adj}} J_{\text{orig}} + c^2 \rho_{\text{adj}} \rho_{\text{orig}} \right) dl \right], \quad (10)$$

with $\{J_{\text{adj}}, \rho_{\text{adj}}\} = (C^*/H_0)\{J_{\text{orig}}, \rho_{\text{orig}}\}$.

Using the surface integrals for the RCS variation from a surface displacement, we obtain the derivative of the RCS with respect to any shape parameter by means of the chain rule [5].

RESULTS FOR A 2D TEST CASE

Coupled RCS and aerodynamical optimizations are in progress, but here, we limit the scope to RCS optimization. We have minimized the RCS of a PEC scatterer in the angular intervals $[-\theta_m, \theta_m] \cup [\pi - \theta_m, \pi + \theta_m]$. The design parameters were taken as the coefficients in a Fourier series for $r(\theta)$, describing the boundary of the scatterer, with the constant term fixed to unity to prevent the optimization from shrinking the scatterer to zero. As optimization routine, we have mainly used Matlab's lsqnonlin, which solves a least square problem by the Levenberg-Marquardt method.

The surface currents are computed by a boundary element code [6] that solves the 2D Complex Field Integral Equation (CFIE) for both TM and TE polarization.

The shape derivatives in Eqs. (6), (9) and (10) involve squares of the complex surface currents and vary twice as fast as the incoming wave. For proper averaging, the angles of incidence have to be resolved with a maximum separation of $\Delta\theta < \lambda/8d$, where d is the transvers extent of the scatterer. We find that, even with sufficient averaging, the optimal shapes contain oscillations, at about half the wavelength of the incoming radiation. To remove such corrugations, we have added terms penalizing boundary curvature to the goal function of the minimization.
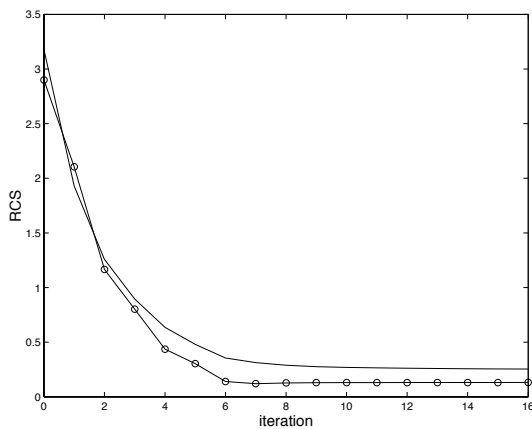
Fig. 1. Evolution of the average RCS for TE (-o-) and TM (-) polarization in $0 < \theta < \pi/4$ with the Levenberg-Marquart algoritm and a small penalty.

For moderately large objects ($k_0 = 4\pi$), the shape optimization converges rapidly, see Fig. 1. The optimized shapes shown in Fig. 2 tend to have large flat regions and sharp corners pointing in the directions where the RCS is minimized. This conforms with expectations from geometrical optics. When the optimization interval becomes large, $\theta_m \gtrsim 80^\circ$, the algorithm
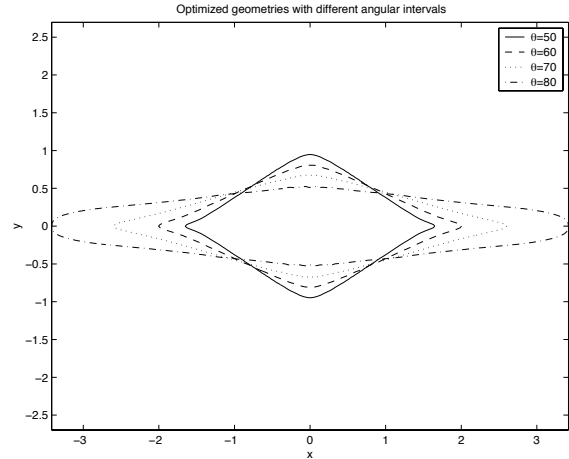
Fig. 2. Optimized shapes for some different widths of the reduction interval for a relatively small scatterer, $k_0 = 4\pi$.
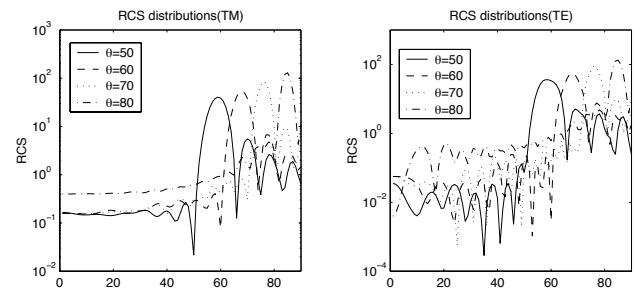
Fig. 3. RCS vs. angle of incidence $\theta \in [0, \pi/2]$ for the optimized shapes in Fig. 2. Generally, the algorithm reduces σ in the specified interval by increasing it outside.

no longer produces sharp tips, see Fig. 2, and the RCS in the forward direction $\theta = 0$ increases, as shown by Fig. 3.

We conclude that the gradient method using the adjoint problem, combined with a suitable penalty term, is efficient for RCS optimization. We believe that the method has great potential for more general microwave problems.

REFERENCES

[1] J. Kim, H.B. Lee, H.K. Jung, S.Y. Hahn, C. Cheon, H. Kim, "Optimal design technique for waveguide device," *IEEE Trans. Magn.*, vol. 32(3), pp. 1250-1253, 1996.
[2] H.B. Lee, T. Itoh, "A systematic optimum design of waveguide-to-microstrip transition," *IEEE Trans. Microw. Theory Tech.*, vol. 45(5), pp. 803-809, 1997.
[3] Y.S. Chung, C. Cheon, I.H. Park, S.Y. Hahn, "Optimal shape design of microwave device using FDTD and design sensitivity analysis" *IEEE Trans. Microw. Theory Tech.*, vol. 48(12), pp. 2289-2296, 2000.
[4] O. Pironneau, *Optimal shape design for elliptic systems*, Springer Verlag (New York, 1984).
[5] P. Weinerfelt, O. Enoksson, "Aerodynamic Shape Optization and Parallel Computing Applied to Industrial Problems," in *Parallel Computational Fluid Dynamics*, Elsevier Science (Oxford, 2001).
[6] A. Bendali, "Numerical analysis of the exterior boundary-value problem for the time-harmonic Maxwell equations by a boundary finite-element method," *Math. Comput.* vol. 43, pp. 29-68, 1984.

Optimization of 3D SAR Distribution in Local RF Hyperthermia

N. Siauve[(1)], L. Nicolas[(1)], C. Vollaire[(1)], A. Nicolas[(1)], J.A. Vasconcelos[(2)]

[(1)] CEGELY - UMR CNRS 5005
Ecole Centrale de Lyon - 69134 Ecully cedex - France

[(2)] Universidade Federale de Minas Gerais
Av. A. Carlos 4434 – Belo Horizonte - Brazil

Abstract — A procedure to optimize the specific absorption rate in patient during hyperthermia treatment. is presented. It is based on a genetic algorithm coupled to a finite element formulation. The optimization is applied to real human body.

INTRODUCTION

Hyperthermia is used in oncology treatment to treat localized cancerous tumours [1]. Its purpose is to heat (42-44°C) the tumour while keeping the temperatures in healthy tissues at acceptable levels. The elevation of temperature is obtained by submitting locally the patient to a radiofrequency (RF) electromagnetic field. The Specific Absorption Rate (SAR) maybe related to the distribution of temperature in a first approximation. A 3D Finite Element (FE) formulation has been previously developed in order to calculate it [2]. It is directly written in term of electric field **E**. It is coupled to a first order Engquist-Majda absorbing boundary condition. Space discretization is performed using incomplete first order edge elements. The sparse complex symmetric matrix equation is solved using conjugate gradient solver with SSOR preconditionning. The formulation has been validated by comparison of calculated SAR distribution on a phantom to temperature measurements.

All the success of hyperthermia treatment lies in the focalization of the heat inside the cancerous tumour. It is obtained by using several RF sources having specific phases and amplitude. In this paper, a tool to optimize the SAR distribution in the patient including the specification of constraints is presented. Optimization procedure is first presented. Results are then given for two types of applicators.

OPTIMIZATION

Energy deposited into the part of the body to be heated is accompanied by energy deposition into other regions. It is impossible to predict intuitively phases and amplitudes of the sources leading to the best focalization. A Genetic Algorithm (GA) is then used to optimize the SAR distribution [3].

Objective function

Several Objective Functions (OF) have been tested. In this paper, two OF are presented. They are defined as the ratio between the SAR in the tumour and the SAR in healthy tissues (1) or in all tissues (2). The GA maximize the result of these OF in order to obtain maximum SAR in cancerous tissues and the minimun in other tissues.

$$OF_1 = \frac{\int\limits_{tumour} SAR(r).d^3r}{\int\limits_{healthy\_tissues} SAR(r).d^3r} \quad (1) \qquad OF_2 = \frac{\int\limits_{tumour} SAR(r).d^3r}{\int\limits_{all\_tissues} SAR(r).d^3r} \quad (2)$$

Optimization Procedure

For an hyperthermia system that consists of n applicators, each applicator contributes to a part of the total **E** field. The **E** field distribution due to each source is first computed with the FE method, each source having an amplitude equal to 1 and a phase equal to 0. The GA modifies in a second step amplitudes and phases, and by application of the principle of linearity and the theorem of superposition, the corresponding **E** field distribution is obtained.

On the other hand, several constraints are prescribed for an optimal treatment: the SAR in tumour has to be close to 50 W/kg, and the total power absorbed by the patient has to be lower than 1250 W.

MODELED DEVICES

Two types of applicators are studied. The first one (A1) is made of two waveguides filled with conducting water and radiating at 27.12 MHz (fig. 1). The second applicator (A2) is an Annular Phased Array (APA) made of a dielectric ring with four 110 MHz sources. A pocket of water (bolus) fills the space around the patient in order to avoid excessive heating at the skin level. For both devices, the patient model is created from 60 Computerized Tomography (CT) scans. The mesh is made of 203989 elements and 42089 nodes, leading to 261500 degrees of freedom. Electromagnetic characteristics of the media are obtained from [4].
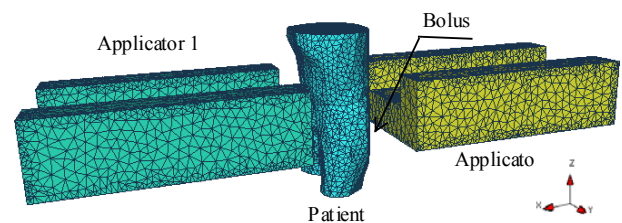
Fig. 1. Mesh of the waveguides applicator A1.
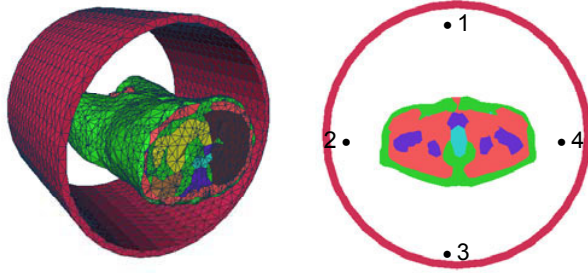
Fig.2. APA applicator A2. Left: 3D mesh, right: location of the sources

Fig. 3. Default (3.a) and optimal (3.b) SAR distribution

OPTIMIZATION RESULTS

The results of the optimization for applicator A1 are presented in Table I. Different configurations are compared, with only one source functioning (Source 1 or Source 2), with the two waveguides operating simultaneously with default adjustments (Default). A and $\phi°$ denote respectively the amplitude and the phasis of the sources. The optimal configurations obtained with the GA for the two OF (1) and (2) are also presented (Optimal OF_1 and OF_2). Fig. 2 shows the SAR ratio between SAR in healthy tissues and in tumour. The SAR distribution on bone and tumour is presented in fig. 3, for the default and optimal configurations (OF_1 and OF_2). Table II gives the CPU times on a HP J5000 computer for the optimization procedure with the OF_1 and the E field computation.

TABLE II. CPU TIMES FOR WAVEGUIDES APPLICATOR A1

		CPU time (s)	%
Electric fields distribution	Source 1	41 670	54
	Source 2	34 349	45
Optimization		750	1
Total		76 769	100

Results of optimization for applicator A2 are given in Table III. Optimal results obtained with objective function OF_1 are compared to those obtained with only one source and to whose obtained with all sources in phasis.

TABLE III. OPTIMIZATION RESULTS FOR THE APA APPLICATOR A2

	Source 1		Source 2		Source 3		Source 4		SAR_{ratio}
	A	$\varphi°$	A	$\varphi°$	A	$\varphi°$	A	$\varphi°$	A
Source 1	1	0							0.29
Default	1	0	1	0	1	0	1	0	0.90
OF_1	13.1	185.4	33.7	246.4	2.9	0	8.0	108.2	2.25

CONCLUSIONS

A 3-dimensional optimization tool based on a coupled GA-FE method has been developed for hyperthermia treatment. The developed model allows to obtain a better focalization of the SAR into the tumour.

TABLE I. OPTIMIZATION RESULTS FOR THE WAVEGUIDES APPLICATOR A1

Configuration	Source 1		Source 2		OF	$P_{patient}$	P_{tumour}	SAR_{tumour}
	A	$\varphi°$	A	$\varphi°$		W	W	W/kg
Source 1	1	0	-	-	1.30	213	1.62	7.5
Source 2	-	-	1	0	1.75	133	1.22	5.6
Default	1	0	1	0	1.52	484	4.31	19.9
Optimal OF_1	1.30	0	2.99	235	2.30	1066	11.5	53.3
Optimal OF_2	1.18	0	2.71	235	2.03	878	9.51	43.9

REFERENCES

[1] O.S. Nielsen, M. Horsman and J. Overgaard, "A Future for Hyperthermia in cancer Treatment," European Journal of Cancer, vol. 37, pp. 1587-1589, 2001.
[2] N. Siauve, L. Nicolas, C. Vollaire and C. Marchal, "3D Modeling of the SAR Distribution for RF hyperthermia with external waveguide applicator," Compumag-Evian, pp. 164-165, July 2001.
[3] B. Sareni, L. Krähenbühl and A. Nicolas, "Niching Gentic Algorithms for Optimization in Electromagnetics, I. Fundamentals," IEEE Trans. on Magnetics, vol. 34, no. 5, pp. 2984-2987, 1998.
[4] S. Gabriel, R.W. Lau and C. Gabriel, "The Dielectric Properties of Biological Tissues: III. Parametric Models for the Dielectric Spectrum of Tissues," Phys. Med. Biol. pp. 2271-2293, no. 41, 1996.

Fig. 2. SAR distribution ratio between tissue and tumour

Author Index

Author Index

Author Index

Author Index

The 14th COMPUMAG Conference on the Computation of Electromagnetic Fields will be held in Saratoga Springs, NY USA, from July 13 to 18, 2003.

❦

Previous COMPUMAG Conferences were held at
Oxford, UK · 1976
Grenoble, France · 1978
Chicago, USA · 1981
Genoa, Italy · 1983
Fort Collins, USA · 1985
Graz, Austria · 1987
Tokyo, Japan · 1989
Sorrento, Italy · 1991
Miami, USA · 1993
Berlin, Germany · 1995
Rio de Janeiro, Brazil · 1997
Sapporo, Japan · 1999
Evian, France · 2001

WWW.COMPUMAG2003.COM

For more information, please e-mail the Secretariat for Compumag 2003 at secretariat@compumag2003.com

❦

Chairman
Dr. Sheppard Salon,
Rensselaer Polytechnic Institute
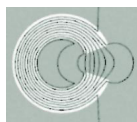
COMPUMAG
2003

Conference on the Computation of Magnetic Fields

SARATOGA SPRINGS, NY, USA
JULY 13–18, 2003